AIR FORCE OFFICE OF SCIENTIFIC RESEARCH

2000 CONTRACTORS' MEETING IN TURBULENCE & ROTATING FLOWS

REPORT DOCUMENTATION PAGE

AFRL-SR-BL-TR-00-

0538

1. AGENCY USE ONLY *(Leave blank)*	2. REPORT DATE	3. REPORT TYPE AND DATES COVERED
	16 August 2000	Contractor's Meeting Abstracts Aug 1999-Aug 2000

4. TITLE AND SUBTITLE
2000 Contractor's Meeting in Turbulence and Rotating Flows

5. FUNDING NUMBERS

6. AUTHOR(S)
Various
Edited by Thomas J. Beutner

7. PERFORMING ORGANIZATION NAME(S) AND ADDRESS(ES)
Various

8. PERFORMING ORGANIZATION REPORT NUMBER

9. SPONSORING/MONITORING AGENCY NAME(S) AND ADDRESS(ES)
Air Force Office of Scientific Research
AFOSR/NA
801 N. Randolph St.
Arlington, VA 22203-1977

10. SPONSORING/MONITORING AGENCY REPORT NUMBER

11. SUPPLEMENTARY NOTES

12a. DISTRIBUTION AVAILABILITY STATEMENT
Unlimited

12b. DISTRIBUTION CODE

13. ABSTRACT *(Maximum 200 words)*

A collection of 54 abstracts from various principal investigators is included which discuss progress on research projects in the AFOSR Turbulence and Rotating Flows Program during the August 1999 to August 2000 period. Topics include fundamental turbulence measurements, turbulence modeling,transition mechanisms, experimental and computational investigations of flow control, and complex turbomachinery flow interactionss. Abstracts are approximately 4-6 pages long, and contain figures and references to other published works on the same topics.

20001024 016

14. SUBJECT TERMS	15. NUMBER OF PAGES
Turbulence, Rotating Flows, Turbomachinery, Flow Control, Transition	320
	16. PRICE CODE

17. SECURITY CLASSIFICATION OF REPORT	18. SECURITY CLASSIFICATION OF THIS PAGE	19. SECURITY CLASSIFICATION OF ABSTRACT	20. LIMITATION OF ABSTRACT
Unclassified	Unclassified	Unclassified	Unl

AIR FORCE OFFICE OF SCIENTIFIC RESEARCH

2000 CONTRACTORS' MEETING IN TURBULENCE & ROTATING FLOWS

Air Force Office of Scientific Research
Directorate of Aerospace and Materials Sciences
AFOSR/NA
801 N. Randolph Road, Room 732
Arlington, VA 22203-1977

AFOSR Contractors' Meeting in Turbulence & Rotating Flows
TABLE OF CONTENTS

A 3D PIV SYSTEM FOR GAS TURBINE ENGINE APPLICATIONS

AFOSR F49620-00-1-0187

Sumanta Acharya and Dimitris Nikitopoulos
Department of Mechanical Engineering
Louisiana State University, Baton Rouge

Abstract

The proposed research deals with the acquisition of a Particle Image Velocimetry (PIV) system for application to turbomachinery research of interest to DOD. Two specific projects of interest to AFOSR will be significantly benefited by the acquisition of the PIV system. The first project deals with the flow and heat transfer in rotating channels. This configuration is of interest in internal cooling of gas turbine blades and is relevant to the "*Turbulence and Rotating Flows*" Program. A unique optical beam-transmission and receiving system, mounted on the rotating frame, will be employed, so that, time-resolved velocity data, and the associated heat transfer data can be obtained. The second project deals with an improved concept for flame stabilization in gas turbine combustors using a trapped vortex (TV) cavity. This project is currently supported by the AFOSR "*Propulsion*" program. Additional details on these projects are provided next.

PIV Measurements in a Rotating Channel

Flow and heat transfer in the internal coolant passages of a rotating smooth or ribbed channel is of interest in a variety of applications, most notably, internal cooling of gas turbine blades. A cutaway section of a typical turbine blade is shown in Fig. 1, and illustrates the ribbed serpentine passages. The flow in the serpentine coolant passages of a gas turbine blade are complicated by the presence of Coriolis forces, centrifugal-buoyancy forces, and secondary flows induced by the bends and anisotropies in the Reynolds-stresses. The dominant effects appear to be due to the *Coriolis forces* which are responsible for secondary flows directed from the leading to the trailing surface along the radially-outward flow passage and from the trailing to the leading along the radially-inward flow passage. These secondary flows destabilize the near-wall flow along the trailing surface of the radially-outward flow leg and the leading surface of the radially-inward flow leg (see Wagner et al., 1991), and enhance heat transfer along these surfaces. Correspondingly, they stabilize the flow and degrade heat transfer along the leading surface of the radially-outward leg and the trailing surface of the radially-inward leg. A factor of 2 or greater in the Nusselt numbers between trailing and leading surfaces have been reported (Han et al., 1993; Bons and Kerrebrock, 1998).

The literature dealing with flow measurements under rotating conditions is extremely limited, due partly to the complexities associated with measurements in a rotating frame. Such measurements have been reported by Tse and Steuber (1997), Iacovides et al. (1998), Bons and Kerrebrock (1998) and Servouze (1998). However, these flow measurements have all been made with the instrumentation on the stationary frame, and only provide conditionally sampled data. Since the

data at a specific point or plane is sampled for a short time interval during one revolution, and this process is repeated over many cycles, only conditionally-averaged statistics can be reliably obtained. To obtain time-resolved velocity measurements, the instrumentation must be mounted on the rotating frame. This is a primary objective of the present research.

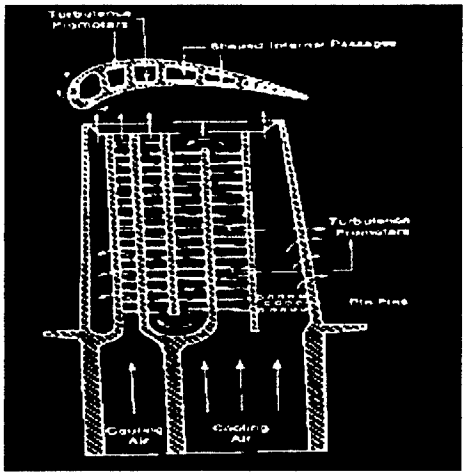

Fig. 1: Schematic of the cooling passages of a gas turbine blade

A multi-pass smooth and ribbed rotating channel will be studied. For the measurements, a rotating facility is already available in the PI's laboratory (Fig. 2), and this facility has been used by the co-PIs to study heat transfer in the coolant channels with rotation (*Hibbs et al.,* 1996; *Eliades et al.*, 1999) and without rotation (*Hibbs et al., 1997; Hibbs et al., 1998*).

The velocity measurements proposed will include primarily Particle Image Velocimetry (PIV). These measurements will be done under conditions of rotation for Reynolds number, Rotation number and centrifugal buoyancy parameter relevant to gas turbine applications. A unique optical beam-transmission and receiving system, mounted on the rotating frame, will be employed, so that, time-resolved velocity data, and the associated heat transfer data can be obtained.

The current rotating facility (Fig. 2) is housed in the PI's laboratory, and the test section consists of a two-pass ribbed coolant channel mounted inside a pressure vessel. The test-section is located on a vertical arm that is connected to a hydraulically-driven hollowed shaft. The hollowed shaft is connected at both ends to rotating seals. Compressed air is delivered at one end of the hollow shaft, and is fed to the conditioning plenum upstream of the test section through rigid rubber tubing. Compressed air exiting from the test section is then delivered through a rubber tubing back to the hollow shaft and discharged through the other rotating seal. A dummy counter weight is placed diametrically opposite to the test section for load balancing. The entire rotating system is encased in an outer enclosure for safety and reduction of form drag.
The current facility can be driven to rotation numbers of around 0.5, and air handling capacity has been enhanced to reach Reynolds number as high as 10^6. Till this point, all measurements

made in this facility have been mass-transfer (naphthalene-sublimation) measurements (*Hibbs et al., 1996, 1997, 1998; Eliades et al., 1999*). This facility will be modified for the present research to accommodate velocity measurements on the rotating frame.

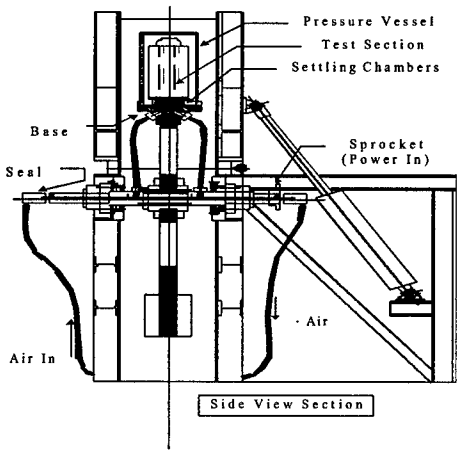

Figure 2 Rotating Channel Facility

Both local and field velocity measurements will be pursued. The former are necessary for obtaining statistically meaningful mean velocity and velocity correlation distributions, while the latter will provide both quantitative and qualitative insight of the velocity field on 2-D planes. The field velocity measurements will help visualize instantaneous details of the flow that are very helpful in understanding the dynamics of the complex flows under study. Local velocity measurements will be pursued through Laser Doppler Velocimetry (LDV) and field velocity measurements will be obtained using Particle Image Velocimetry. The velocity measurements will be performed in the rotating reference frame so that time-resolved data, without errors associated with shifting of the illumination plane or measurement location, can be obtained and used to compute the relevant statistics.

The principal obstacle in performing PIV measurements on a rotating frame stems from the necessity to transfer "information" to and from the rotating frame. This could be eliminated if it were possible to mount all of the instrumentation on the rotating frame. However, this is not feasible due to size, mass and strength limitations. Thus, the bulk of the instrumentation used in the proposed study will be on the stationary frame. Electrical signals are going to be transferred between the rotating and stationary frames through the use of slip rings. Optical signals will be transferred through a specially designed optical de-rotator.

Almost all the hardware of the PIV system will be on the stationary frame as shown schematically in Figure 3. The pulsed laser source beams are going to be directed along the axis of rotation, through the hollow shaft, and to the measurement location by means of a periscope assembly with compact and ruggedized light sheet generating optics (a combination of spherical and cylindrical lenses) at the end. Two possible arrangements are shown in Figure 3. The first arrangement shown on the side view of Figure 3 allows for PIV on planes perpendicular to the

main flow direction so that the cross-stream secondary flows, which are most relevant to this study, can be captured. The second arrangement shown on the front view of Figure 3 allows for PIV on planes parallel to the stream-wise direction. The illuminated plane images are going to be directed to a color CCD camera on the stationary frame through a periscope assembly and the use of a rotating triple-reflection prism which is also going to "de-rotate" the back-scattered light. The triple-reflection prism has the property of rotating an image by 180 degrees if the prism is rotated by 90 degrees. Thus a rotating image can be made into a stationary one if the prism rotates at half the rotation speed of the image and in the same direction. The triple-reflection prism will be housed on a casing which will be rotated at half the speed of the test section through a 1:1 timing chain and 2:1 gear transmission as shown schematically in Figure 3. The images are going to be processed using appropriate software to render the instantaneous velocity vector field. An ensemble average of a number of images will render the mean flow field. Seed particles necessary for the application of PIV will be selected carefully depending on an estimate of the flow turbulence so that they have good frequency-response in the rotating environment. Micron-size Al_2O_3 particles are a good candidate as seed.

On the rotating frame the optical paths are going to be directed to and from the measurement location through the use of ruggedized periscope assemblies in combination with step-motor driven traverses. The traverses will be controlled either by a pre-programmed on-board mini-computer, or a computer on the stationary frame through the use of digital slip rings. The periscope assemblies and traverses will be supported on a lightweight, yet stiff, frame, which will be attached to the rotating shaft the test-section housing and counterbalance.

PIV Measurements in a Trapped Vortex Combustor

The ongoing research deals with the fundamental issues pertaining to an improved concept of flame stabilization. In this concept, termed the Trapped-Vortex (TV) combustor, a circumferential cavity with a trapped vortex, into which secondary fuel and air is injected, provides the flame stabilization. Hot combustion products emanating from within the cavity get entrained into the main combustion zone thus providing ignition of the primary fuel/air mixture and the necessary flame stabilization mechanism. Stable combustion with Lean Blow Out (LBO) equivalence ratio limits as low as 0.005 have been obtained (Hsu et al., 1995). However, very little is known about the important hydrodynamic and combustion mechanisms that are responsible for the improved behavior.

Two separate trapped vortex configurations are currently being investigated. These are shown schematically in Figure 4. In one concept (Fig. 4a), the central fuel-air delivery system is replaced by a circular forebody-afterbody arrangement similar to that of Hsu et al. (1995). The fuel-air injection is performed through discrete locations in the afterbody. A co-annular airflow generates a vortex trapped between the fore- and after-bodies, and a fairly stable flame can be sustained under these conditions. In the second arrangement

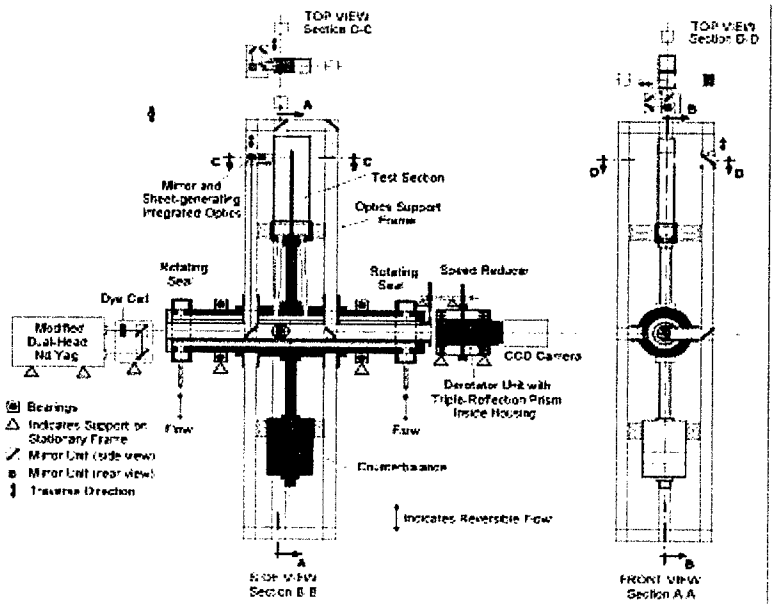

Figure 3: Implementation of two-color digital PIV on the rotating frame.

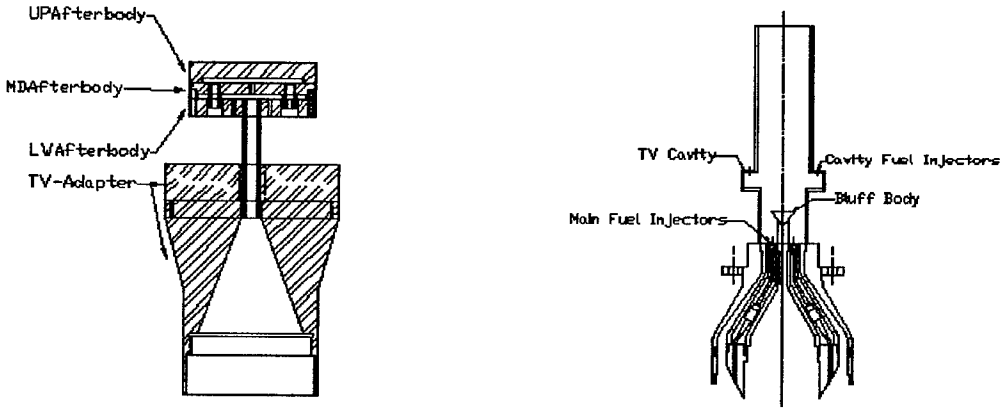

(a) (b)

Figure 4: (a) Central TVC Combustor (b) TVC Incorporated on a Can-Combustor

(Fig. 4b), a can-combustor is retrofitted with a trapped-vortex cavity, and a stable flame is generated in the cavity. The role of this flame is to provide the heat source for stabilizing the flame in the primary combustor.

A fundamental goal of the ongoing study is to understand the interaction between the primary annular flow and the flow in the trapped vortex cavity, so that, conditions that promote flame stability can be identified. This interaction can be highly unsteady, as LES computations have indicated, and a careful understanding of this interaction is necessary before conditions that provide a stable trapped vortex over a range of conditions can be identified. Under non-optimal

conditions, unsteady three-dimensional vortices that are detrimental to flame stability can be generated. Since the flow is highly three-dimensional a 3D PIV system will provide instantaneous realizations of the flowfield along the illuminated plane, and provide a great deal of information on the behavior of the vortical flow structures, and their evolution with time. The 3D PIV system requested can be implemented without any major modifications, since the combustor currently has orthogonal optical windows needed for the PIV measurements.

Finally, the PIV measurements, along with other diagnostic measurements, can be used to compute the statistics of the turbulent flowfield, that can then be used to validate the CFD calculations and aid in the modeling process.

Acknowledgment/Disclaimer

This work was sponsored (in part) by the Air Force Office of Scientific Research, USAF, under grant/contract number F49620-00-1-0187. The views and conclusions contained herein are those of the authors and should not be interpreted as necessarily representing the official policies or endorsements, either expressed or implied, of the Air Force Office of Scientific Research or the U.S. Government.

References

1. J. H.. Wagner, B. V. Johnson, and F. C. Kopper, *ASME Journal of Turbomachinery*, 1991, 113: 321-330.

2. J. C. Han, Y. M. Zhang, and K. Kalkeuhler, *ASME Journal of Heat Transfer*, 1993, 115: 912-920.

3. J. P. Bons, and J. L. Kerrebrock, 1998, ASME Paper 98-GT-464.

4. D. G. N. Tse, and G. D. Steuber, 1997, ASME Paper 97-GT-529.

5. H. Iacovides, H., D. C. Jackson, H. Ji, G. Kelemenis, B. E. Launder, and K. Nikas, *ASME Journal of Turbomachinery*, 1998, 120, 386-391.

6. Y. Servouze, 1998, ASME Paper 98-GT-123.

7. R. Hibbs, S. Acharya, Y. Chen, D. Nikitopoulos, and T. Myrum, *ASME-International Mechanical Engineering Congress and Exposition (IMECE),* Atlanta, November 1996

8. V. Eliades, D. E. Nikitopoulos, and S. Acharya, *ASME-IGTI Intl. Gas Turbine Conference*, Indianapolis, June 1999

9. R. Hibbs, S. Acharya, Y. Chen, D. Nikitopoulos, , *ASME-International Gas Turbine Conference,* 1997, Orlando

10. R. Hibbs, S. Acharya, Y. Chen, D. Nikitopoulos and T. Myrum, 1998, *ASME Journal of Turbomachinery*, 1998, 120: 724-734.

11. S. Acharya, T. A. Myrum, and S. Dutta, 1998, *ASME Journal of Heat Transfer,* 1998, 120: 550-562

12. S. Acharya, S. Dutta, T. Myrum, and R. S. Baker, , *ASME Journal of Fluids Engineering,*1994, 116: 238-246

13. K. Y. Hsu, L. P. Goss, and D. D. Trump, 1995, AIAA 95-0810

DEMONSTRATION OF ROBUST MICROMACHINED JET TECHNOLOGY AND ITS APPLICATION TO REALISTIC FLOW CONTROL PROBLEMS

Mark G. Allen and Ari Glezer
School of Electrical and Computer Engineering & School of Mechanical Engineering,
Georgia Institute of Technology, Atlanta, GA

Abstract

In this work, we are investigating the use of microfabrication technology to create a micromachined fluidic control system (consisting of micromachined actuators, sensors, and control/drive circuitry) with a goal of application in practical fluids problems, such as UAV-scale aerodynamic control. Our approaches include: (1) the development of suitable micromachined synthetic jets (*microjets*) as actuators, which obviate the need to physically extend micromachined structures into an external flow; and (2) a non-silicon alternative micromachining fabrication technology based on metallic substrates and lamination (in addition to traditional MEMS technologies) which will allow the realization of larger scale, more robust structures and larger array active areas for fluidic systems. In the previous report, we demonstrated independently fabricated sensors and actuators. These devices were fabricated using stainless steel as a substrate and a combination of lamination and traditional micromachining processes as fabrication technologies. This report covers the initial fabrication process of pressure sensors and microjet modulators co-integrated on the same substrate, the successful design of a switched capacitor amplifier as an interface to the pressure sensor, and advances in vortex generation.

1. Progress in Robust Micromachining Technology

Figure 1 shows a robust modulator and pressure sensor co-integrated on the same stainless steel substrate. The sensor contains a stainless steel membrane extended over the pressure inlet hole. When pressure is applied, the membrane deflects toward the fixed back plate. This increases the capacitance between membrane and back plate. The actuator contains a disc, supported by three or four beams. The channel between the disc

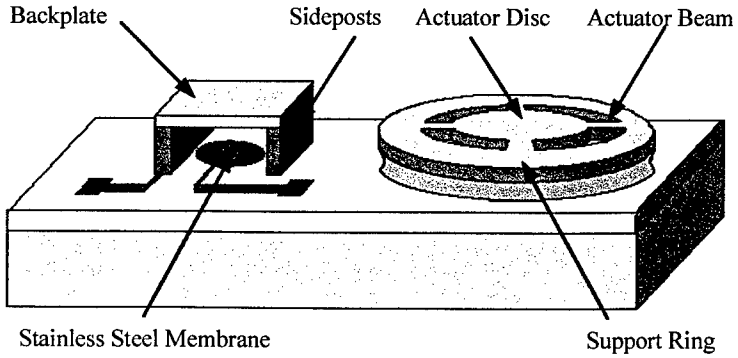

Figure 1: System of robust pressure sensor (L) and microjet modulator (R).

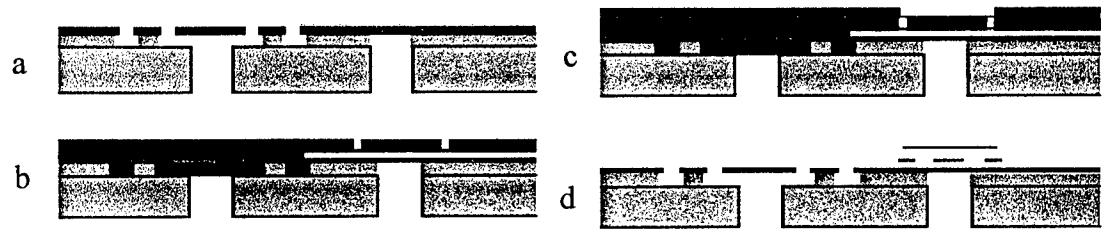

Figure 2: Fabrication sequence for sensors and actuators.

and an orifice conventionally machined in the substrate permits airflow when the actuator is in the 'off' position. When the actuator is energized, the disc is deflected toward the substrate, constricting the airflow and ultimately blocking the orifice. Currently, the actuators are driven electrostatically, by application of a voltage between the flexible sheet and the substrate. Synthetic jets are formed by addition of a piezoelectric driver attached to the actuator side of the substrate orifice.

The co-fabrication sequence of robust pressure sensors and robust modulators starts on a square stainless steel substrate with a side length and thickness of 60mm and 0.9 mm, respectively. Pressure inlet and jet holes with diameters of 2mm are milled through the stainless steel substrate. Figure 2 shows the fabrication sequence in greater detail.

A 50μm thick Kapton HN200 polyimide film and 12.5μm stainless steel film are laminated on the milled stainless steel substrate using a hot press. To form the actuator disc, the support ring, and the actuator beam, polyimide 2611 is spin coated on the stainless steel film, cured and patterned. Then the stainless steel film is etched. Next, the Kapton film under the stainless steel film is dry-etched through the backside holes of the sensors and actuators. The Kapton under the suspensions of the actuator plates is etched from the front side. (Fig. 2a).

Then the bonding pads, interconnection lines and bottom electrodes, and the seed-layers for the electroplating steps are formed. Ti/Cu/Ti (300/6000/300A°) is deposited and patterned. Positive photoresist AZ 4620 forms the molds of the side posts of the sensor. Finally, NiFe is electroplated through the mold (Fig. 2b).

To fabricate the back plate of the sensor, a seed-layer is deposited and patterned. AZ 4620 positive photoresist defines a mold. Then NiFe is electroplated, (Fig. 2c). Finally the two photoresist layers, and the second seed layer are removed, (Fig. 2d). The final system of sensors and actuators is shown in Figure 3.

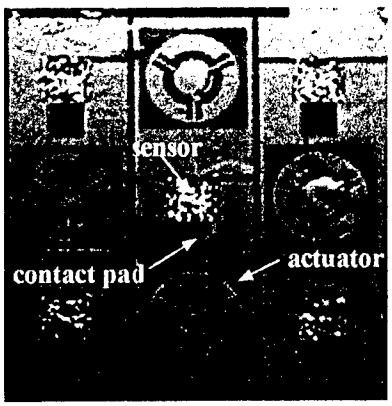

Figure 3: Photograph of fabricated sensor and actuator array.

Characterization

The capacitance of individual pressure sensors has been measured using a Keithley 3322 LCZ meter. Measured capacitances for undeflected pressure sensors were in the range of

73.4 pF to 93.5 pF. A large fraction of these values originates from parasitic capacities of the connection lines and bonding pads on the substrate. The capacitance change as a function of applied pressure is shown in the Figure 4.

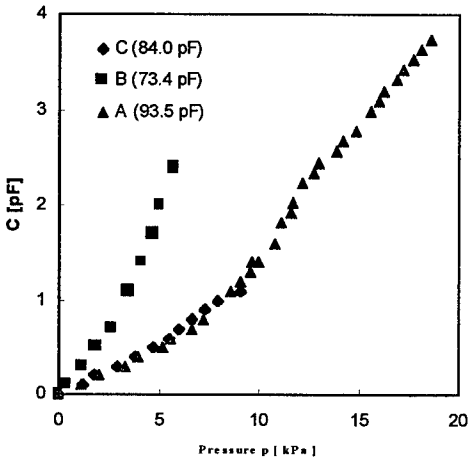

Figure 4: Capacitance of sensors as a function of applied pressure.

The modulators co-fabricated with the pressure sensors do not yet operate satisfactorily due to some fabrication issues currently under investigation. Therefore, the discussion below centers on the characterization of actuators on independently fabricated modulators with similar cross-section.

In order to reduce actuation voltages and achieve significant process yields, several parameters have been varied: beam length, gap size, actuator disc diameter d_a, and orifice diameter d_o. A new shape of the support ring, with preliminary results shown in the last report, allowed retaining the beam length while maximizing the support area. This increased the yield to 90%.To increase the electrostatic force, the effective area of the capacitor, i.e. the overlap between substrate and diaphragm can be increased. The effective capacitor area is $A_{eff} = \pi(d_a^2 - d_o^2)/4$. To increase A_{eff} the size of the orifice was reduced. The 1mm orifice devices repeatedly exhibited pull down voltages under 200 V. However, the centerline flow velocity was reduced to approximately 1 m/s. Previous testing has produced jets with centerline flow velocity of approximately 3 m/s.

We conclude that the actuation voltage of the electrostatically actuated modulators can be reduced below 200 V. Significant reduction of the voltage, however, can not be achieved without reducing the flow velocity of the air jet. To achieve better performance we are currently investigating the use of thermally actuated Cu/Ti bimorph structures to modulate microjets. For a cantilever length of 3.0 mm we get deflections of 36 μm at a heat dissipation of 235 mW.

2. Interface Circuitry for an array of Robust Pressure Sensor

The characterization of pressure sensors and the activation of modulators are both currently performed remotely. Local read-out circuitry is desirable for three reasons. First, the capacitance changes of a pressure sensor are small. Parasitic capacitances and pick-up of noise through the connection cables induce measurement errors. Second, a bandwidth of 1kHz should be achieved to resolve aerodynamic fluctuations of the pressure. In the previous report we demonstrated an oscillator built in proximity to the sensor, based on discrete components. Its resonance frequency depends on the capacitance of the pressure sensor, which is used to measure the pressure. This scheme is accurate if the integration time of the frequency counter is larger than 0.1s. The method can not resolve aerodynamic pressure fluctuations. An additional restriction of this approach is that only one sensor can be interfaced with the circuit.

We designed and characterized a custom ASIC that solves these two limitations. One of four sensors can be selected. The chip uses a standard switched capacitor (SC) architecture to measure the difference between the capacitance of the selected sensor and an on-chip reference. The transfer function from the sensor capacitance C_{sensor} to the output voltage V_{out} is the following

$$V_{out} - V_{cm} = -5(V_{sig} - V_{icm})\frac{C_{sensor} - C_{ref}}{C_{ref}} + 5(V_{ref} - V_{sig}),$$

where the reference capacitance C_{ref} can be adjusted between 10pF and 70pF in seven steps to compensate for the process dependent sensor capacitance at zero pressure. It can be further tuned by the voltage V_{ref}-V_{sig}. The voltage V_{sig}-V_{icm} determines the sensitivity.

The operational amplifier is based on a standard folded cascode architecture. At a bias current of 40 μA the op-amp dc power consumption is 1.2mW. The open loop gain is 62dB and the gain bandwidth product is 11.9MHz with a phase margin of 59° for a load capacitance of 5pF. The first and second poles are at 12kHz and 32MHz, respectively. With a SC feedback gain of 5 a gain inaccuracy of 0.4% is achieved when switch noise is neglected. For $C_{sensor} = C_{ref} = 70$pF the bandwidth is 394kHz.

The amplifier was designed on a MOSIS ABN 1.5μm run. It was integrated with additional circuitry for clock generation, bias generation, and on-chip trimming. The total core area is 2.3 mm^2. To achieve reasonable settling, a clock speed of 50 kHz was chosen. The ASIC was characterized using a standard capacitor of 49pF instead of the sensor, a supply voltage of 4.993V, and control voltages V_{cm} and V_{sig} of 2.995V and 2.492V, respectively. The gain of V_{out} versus V_{ref} was 4.89 to be compared with 5.0 for ideal on-chip capacitor ratios and infinite op-amp gain. These chips have just been received back from the foundry. As a next step, the ASIC will be characterized together with a sensor described in Section 1.

3. On-demand Synthetic Jet Vortex Generation

Vortex generators of varying scales are widely utilized in numerous aerodynamic applications to prevent or delay flow separation by inducing the formation of streamwise vortices of a prescribed sign near the flow surface. In current realizations, vortex generators are typically made of spanwise rows of passive plates that are permanently mounted on the flow surface and thus affect the flow and contribute to the aerodynamic drag even in the absence of separation. Compton and Johnston (1992) proposed to emulate the effect of a vortex generator by using a jet that issues normal to the surface (having the advantage that it can be "removed" when not needed). Pitching or skewing of the jet relative to the oncoming flow leads to the evolution of a *single sign* streamwise vortex where the sense of the rotation is determined by the skew direction and vortex strength is determined by the skew angle. However, with a fixed nozzle, this vortex generator is limited to a fixed sign vortex.

This part of the project focuses on the development of batch-fabricated arrays of fluidic-based vortex generators that are capable of generating streamwise vortices having *prescribed sign and strength.* Each element in the array is comprised of a pair of adjacent rectangular synthetic (zero net mass flux) jets where the jet spacing (along their

long dimensions) is comparable to the width of the jet orifice. Each jet can be produced over a broad range of scales by an actuator comprised of a closed chamber having an orifice and an oscillating diaphragm that is built into one of the chamber walls. When the jets are operated in concert, the combined jet can be vectored towards one of the jets by advancing the phase of the actuation signal of that jet (Smith and Glezer[1]) resulting in a single-sign streamwise vortex where the sense of rotation and strength are controlled by the sign and magnitude of the phase difference between the driving signals. The interactions between arrays of synthetic jet pairs and a cross flow of varying speed is investigated in the cross-stream (x-y) and spanwise (y-z) planes of a small scale wind tunnel. Arrays of rectangular (0.5 mm wide, and 25 mm long) jet pairs (spaced 14 mm apart on center) are fabricated using lithographic techniques and driven using piezoelectric membranes (at 980 Hz) and integrated into the test section wall so that their axes are aligned with the streamwise (x) direction.

As the velocity ratio between the jet and the cross flow VR is decreased, the jet bends in the streamwise direction and its penetration distance into the cross flow decreases. Figures 5 is a composite of three streamwise stations for VR = 0.8 (a) and 0.48 (b). While the penetration height of the jet into the cross flow decreases, the vorticity concentrations that originate from the downstream edge of the jet orifice persist through the downstream edge of the measurement domain. These successive concentrations are advected at the speed of the free stream, and the spacing between them increases with decreasing velocity ratio (the jet frequency is invariant).

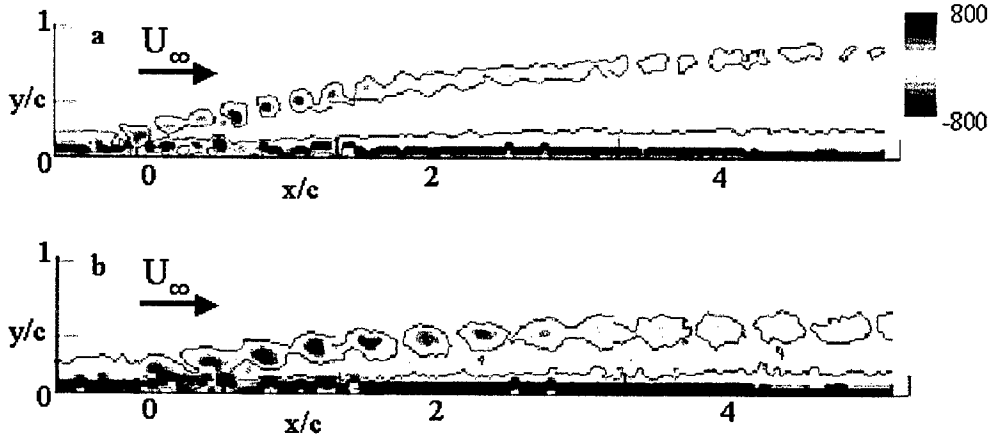

Figure 5. Jet penetration into cross flow, VR = 0.8 (a), 0.48 (b) (Negative vorticity is bounded with a single contour at lowest level.).

The evolution of the ensuing streamwise vortices in the cross-stream y-z plane (looking in the streamwise direction) is shown in Figures 6(a,b) for x/c = 3 for an array of 5 jet pairs. When the two jets in each pair are in phase, symmetric counter-rotating vortex pairs much like those of conventional jets are present (Figure 6a). These data also show pairs of secondary streamwise vortices that are induced near the wall (in the wake of the jet). Vectoring the jet pair using an imposed phase difference of 150° between the jet pair

[1] B. L. Smith and A. Glezer, "The formation and evolution of synthetic jets," *Phys. Fluids,* **10**, 1998, pp. 2281-2297.

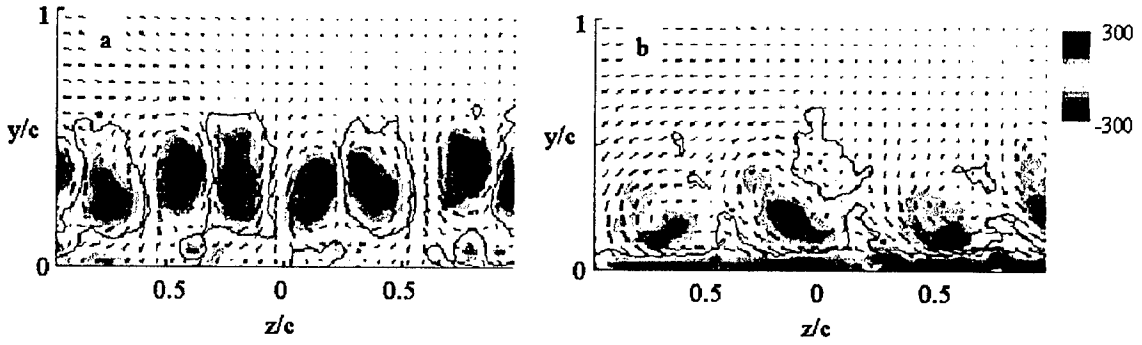

Figure 6. Cross stream vorticity contour maps of a jet array for VR = 0.8, x/c = 3 (a) Φ = 0° (b) Φ = 150° (vorticity concentrations as in Figure 5).

(Figure 6b), leads to the formation of an array of strong single-sign CCW vortices. This pattern persists in the streamwise direction and the formation of the opposite sense secondary vortices near the wall is apparently suppressed while the (primary) vortex cores remain at nearly the same elevation (although the cores are stretched).

Conclusions

We reported an initial fabrication procedure of an array of pressure sensors and microjet modulators, co-fabricated on the same substrate. The array is based on robust stainless steel shim stock, lamination processing, and stainless steel diaphragms for the pressure sensor, and stainless steel actuator discs for the microjet modulators. The sensors were successfully characterized. A study of various device geometries for the microjet modulators shows that actuation voltages can be reduced below 200 V, but with the expense of reduced jet center velocities achievable. To achieve higher actuation forces we are currently fabricating a thermally actuated bimorph structure. To achieve higher resolution and interfacing to multiple sensors an ASIC read-out circuit has been successfully designed and tested and will be co-integrated with the pressure sensor array. Arrays of streamwise vortex generators are developed using lithographic techniques. Single-sign streamwise vortices are formed by spanwise vectoring of a pair of rectangular synthetic jets issuing into a cross-flow thus providing on-demand vortex generation without alteration of surface geometry.

Acknowledgement/Disclaimer

This work was sponsored in part by the Air Force Office of Scientific Research, USAF, under grant/contract number F49620-97-1-0519. The views and conclusions contained herein are those of the authors and should not be interpreted as necessarily representing the official policies or endorsements, either expressed or implied, of the Air Force Office of Scientific Research or the U.S. Government.

Personnel

The work discussed in this report has been performed by Sung Pil Chang, Brian English, and Dr. Martin von Arx of the School of Electrical and Computer Engineering, and Chris Rinehart of the School of Mechanical Engineering, in addition to the authors.

AFOSR Aerodynamics and Turbulence Conference, Dayton, OH. August 15-16, 2000

TURBULENT SPOT CHARACTERIZATION AND THE MODELING OF TRANSITIONAL HEAT TRANSFER IN TURBINES

Grant Number F49620-97-1-0524

Richard J. Anthony
Dept. Engineering Science
University of Oxford, U.K.

John E. LaGraff
MAME Department
Syracuse University, NY

Terry V. Jones
Dept. Engineering Science
University of Oxford, U.K.

Abstract

Optimum design of gas turbine blades depends on accurate prediction of boundary layer transition. The purpose of this research is to obtain more information on the generation, propagation, and coalescence of turbulent spots in a transitional boundary layer, and examine the effects of freestream turbulence along with adverse and favourable pressure gradients. Experimental data from this study may be used to improve existing CFD models, allowing designers to make more accurate predictions of transitional heat transfer in turbines.

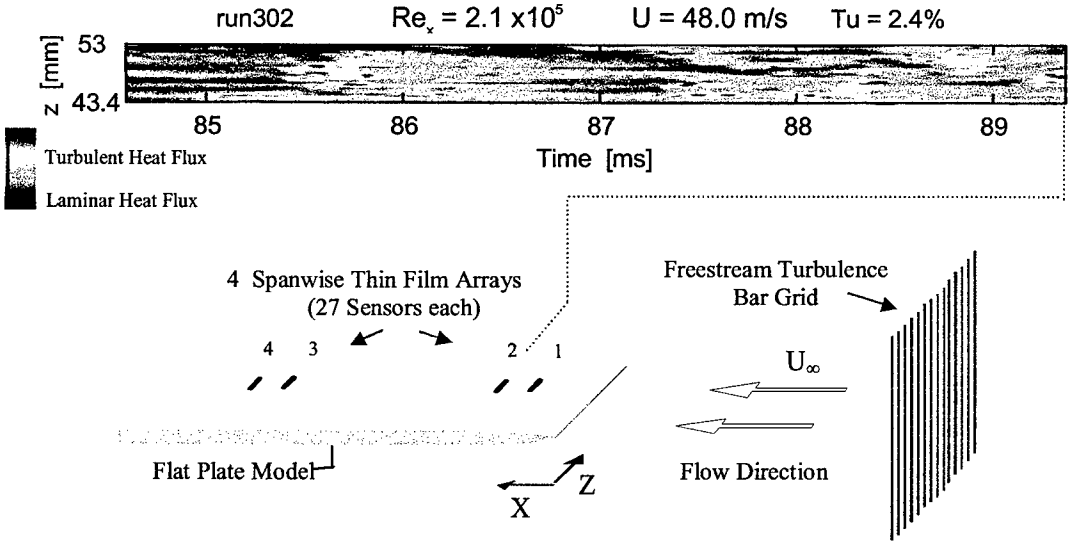

Figure 1 Experimental setup showing the flat plate wind tunnel model instrumented with high-density thin film arrays. The spanwise arrays shown are perpendicular to the flow direction. The top image is a view of transitional heat flux in the *z-t* plane from array #2 which shows the heat flux events crossing a 9.6 mm span in less than 4.5 ms. The high frequency, high spatial resolution measurements can capture turbulent spot detail in a high speed transitional boundary layer.

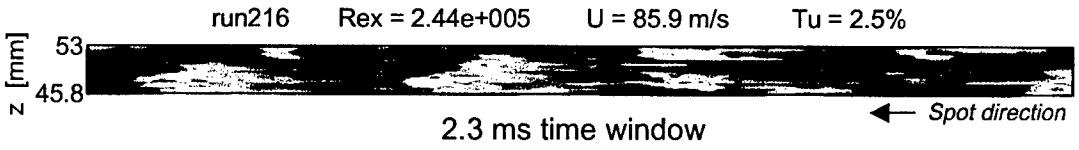

Figure 2 Turbulent spots captured across a 7.2 mm wide spanwise array in 2.3 ms. Data is taken from array #1 in Figure 1.

Measuring turbulent spots in a high speed transitional boundary layer requires instrumentation capable of resolving very small, and very fast, surface heat flux events. New thin film sensor arrays, developed especially for this project (Anthony et. al. 1999), allow high frequency, high spatial resolution surface heat flux measurements to be made. The new thin film arrays allow direct measurement of turbulent spot generation rate, spot size, and spot/streak shapes. Figure 1 illustrates their use on a flat plate wind tunnel model used in this study.

Flat plate experiments are being carried out in a subsonic wind tunnel at Oxford where experiments are run over a range of Reynolds number and Mach number (0.1-0.4). Surface heat flux is driven by a temperature difference between the model and the freestream airflow. The run time is very short (~0.3 sec) allowing 1-D semi-infinite transient heat conduction analysis to be used (Schultz and Jones 1973).

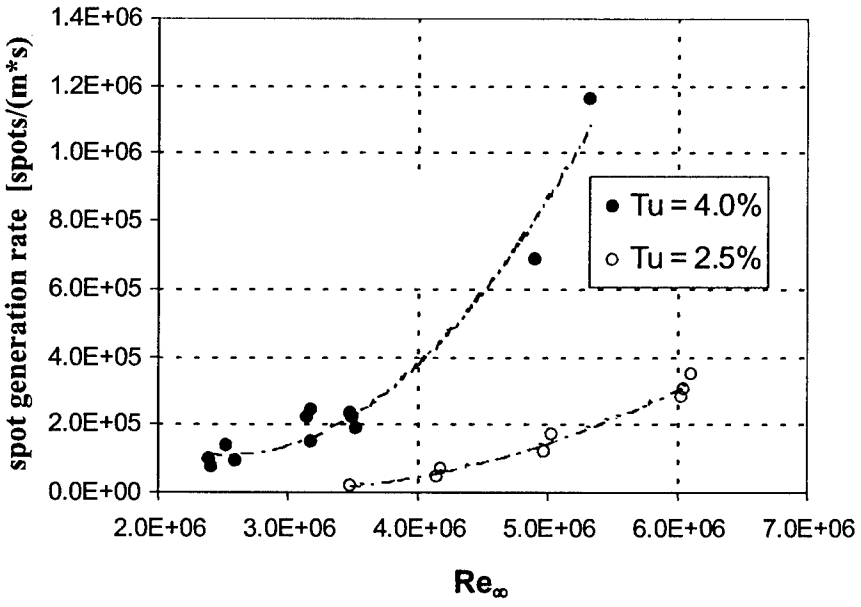

Figure 3 Direct measurement of turbulent spot generation rate shows that an increase in turbulence intensity from 2.5% to 4.0% significantly increases the number of spots generated per meter per second

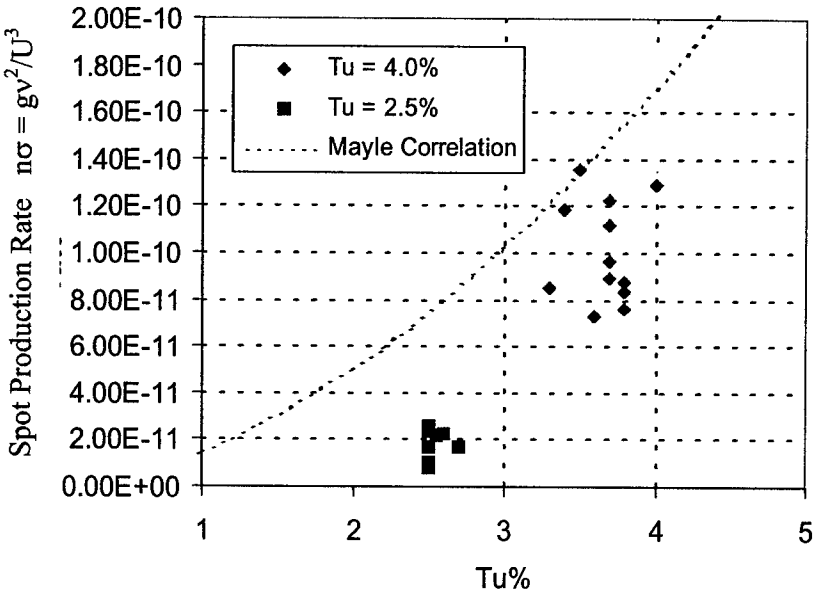

Figure 4 Non-dimensional spot production rate compared with correlation by Mayle (1991) based on indirect measurements.

The top image in Figure 1 is a view of transitional heat flux in the *z-t* plane showing the heat flux events crossing a 9.6 mm spanwise array in less than 4.5 ms. This array is located within the transition region at a local Reynolds number of 2.1×10^5 under a freestream turbulence intensity of 2.4%. The figure shows intermittent turbulent heat flux, but also defines the shape and structure of the turbulent spots that have appeared in the laminar boundary layer.

It is found that the small initial turbulent vortices are likely to induce additional vortices slightly behind and to the side of each other forming an irregular patch of turbulent heat flux streaks. Given time to convect in this manner, the patch of turbulent vortices, known collectively as a turbulent spot, grows and develops into a regular arrowhead shape. A striated tail of calmed fluid follows behind the growing turbulent patch. In cases where transition length is short, such as affected by freestream turbulence, turbulent spots coalesce into a fully turbulent boundary layer before they are able to form the more developed regular arrowhead shape.

The imaging capability of the arrays reveals a lot of information, but one key result is the ability to directly measure turbulent spot generation rate. Most methods infer generation rate from intermittency curves or use some other indirect method. The present technique allows us to distinguish between individual spots and count the number that pass over a spanwise length. Figure 2 shows a small time segment of data recorded over a 7.2mm wide spanwise array located at $Re_x=2.44 \times 10^5$. Hundreds of spots are counted over the 0.3 second run time and used to obtain a value for spot generation rate.

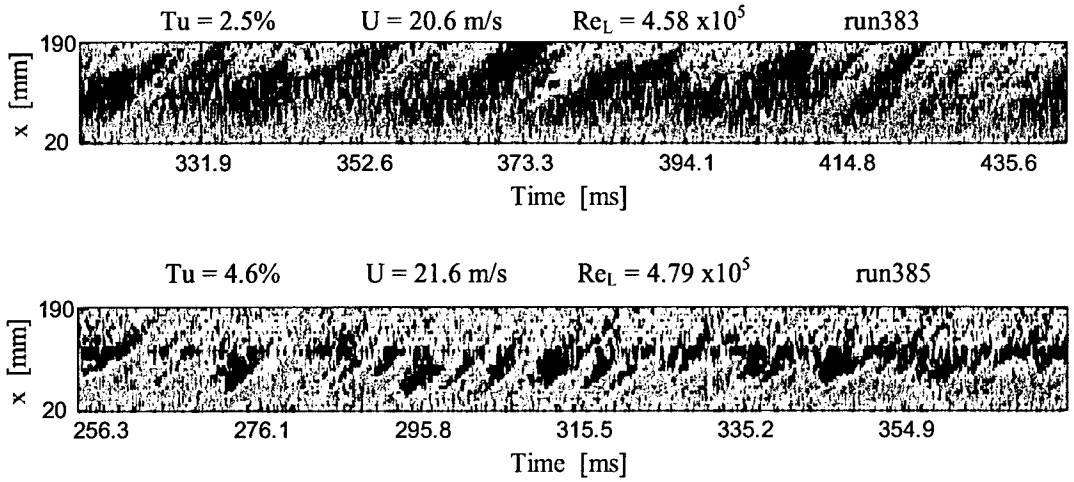

Figure 5 Image of transition in the x-t plane, where x is streamwise distance, showing the inception and propagation of turbulent spots down the model surface. Increasing freestream turbulence intensity moves the onset of transition forward on the plate.

Values of spot generation rate have been obtained under varying levels of freestream turbulence intensity *(Tu*= 2.4%, 4.2%, and 15%) while holding the turbulent length scale constant. Figure 3 is a plot of spot generation rate g vs. the freestream unit Reynolds number Re_∞. Increasing freestream turbulence intensity *Tu* causes bypass transition to occur at lower Reynolds number. Assuming initial spot size scales with the thickness of the boundary layer at the inception point, one would expect this to increase the number of spots generated per unit span. The data shown in Figure 3 supports this showing a significant rise in generation rate from *Tu*=2.5% to *Tu*=4%.. A plot of non-dimensional spot production rate is shown in Figure 4 along with an indirect correlation by Mayle (1991). The slight difference may be due to the difference between direct and indirect methods of measurement. Distinguishing turbulent spots under the high *Tu* case of 15% was nearly impossible. It appears at this level that most of the heat transfer fluctuations are actually caused by freestream eddies entering deep into the boundary layer.

While some thin film arrays are aligned in the spanwise direction, others are aligned in the streamwise direction to track spot development and propagation rates. Figure 5 shows two images in the *x-t* plane, which can be used to measure spot convection velocities and inception locations. Both runs are at nearly the same Reynolds number, but under two different turbulence intensities. It can be seen from the figure that increasing *Tu* from 2.5% to 4.6% moves the onset of transition closer to the front of the plate and increases the overall heat transfer across the surface.

Experiments have also studied the effects of adverse pressure gradient. A variable geometry test section was built to adjust the pressure gradient across the model. Relatively constant acceleration parameters of K = -1 x10^{-7}, -7 x10^{-7}, and –10 x10^{-7} were tested. The stronger adverse pressure gradients appear to cause a short laminar separation

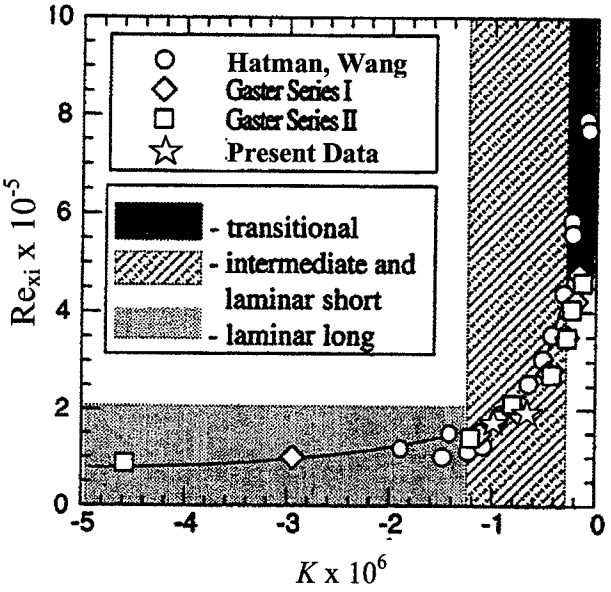

Figure 6 Correlation between separation Reynolds number and pressure gradient parameter at separation. Present data agrees with separated flow transition map from Hatman and Wang (1998) .

bubble that is transitional in the free shear layer and reattaches turbulent. Tests at K = -7 x10^{-7} appear to separate at a Reynolds number of about 1.83 x10^{5} and reattach turbulent shortly after. Tests at K = -10 x10^{-7} separate a little sooner near a Reynolds number of 1.69 x10^{5} and also reattaches turbulent shortly downstream. This data was compared with a previous AFOSR supported study on separated flow transition by Hatman and Wang (1998). Data from the strongest adverse pressure gradients match their correlation well and fall into the region predicting laminar separation, short bubble mode transition (Figure 6). It should be noted that adding a small amount of freestream turbulence initiates transition before separation occurs. The turbulence effect seems to dominate up until separation. Since the laminar boundary layer can handle only a weak adverse pressure gradient, it is very likely for separated flow transition to occur under a positive pressure gradient.

Experimental work is continuing with studies of favourable pressure gradient effects and spanwise pressure gradient effects. Results from all the tests are in the process of being analyzed and documented to aid the better understanding of boundary layer transition in complex flows.

Acknowledgement/Disclaimer

This work was sponsored (in part) by the Air Force Office of Scientific Research, USAF, under grant/contract number F49620-97-1-0524. The views and conclusions contained herein are those of the authors and should not be interpreted as necessarily representing the official policies or endorsements, either expressed or implied, of the Air Force Office of Scientific Research or the U.S. Government.

Personnel Supported

Richard J. Anthony Doctorate Student, University of Oxford, U.K.

References

Anthony, R.J., Jones, T.V., LaGraff, J.E., 2001 "Visualization of High Speed Transitional Boundary Layer Heat Flux using High Density Thin Film Arrays", Paper submitted to the *39th AIAA Aerospace Sciences Meeting and Exhibit*, 8-11 January 2001, Reno, NV.

Anthony, R.J., Oldfield, M.L.G., Jones, T.V., LaGraff, J.E., 1999, "Development of High-Density Arrays of Thin Film Heat Transfer Gauges", *Proceedings of the 5th ASME/JSME Thermal Engineering Joint Conference*, San Diego, CA. AJTE99-6159.

Clark, J.P., Jones, T.V., and LaGraff, J.E., 1993, 'On the Propagation of Naturally-Occurring Turbulent Spots," *Journal of Engineering Mathematics*, special issue on turbulent spots, ed. F.T. Smith.

Hatman, A., and Wang, T., 1998, "A Prediction Model for Separated-Flow Transition," ASME Paper 98-GT-237.

Hofeldt, A., 1997, *The Investigation of Naturally-Occurring Turbulent Spots Using Thin-Film Gauges*, D.Phil. Thesis, Dept. of Engineering Science, Oxford University, U.K.

Mayle,R.E., 1991, "The Role of Laminar-Turbulent Transition in Gas Turbine Engines", *ASME J. Turbomachinery*, Vol. 112, pp. 188-195.

Schultz, D.L. and Jones, T.V., 1973, "Heat Transfer Measurements in Short-Duration Hypersonic Facilities," AGARD AG-165.

MEMS-BASED CONTROL OF AIR-BREATHING PROPULSION

AFOSR/DARPA Grant No F49620-97-1-0526

J. Bae
Department of Aeronautics and Astronautics
Massachusetts Institute of Technology, Cambridge, MA

K.S. Breuer
Division of Engineering
Brown University, Providence, RI

C.S. Tan
Department of Aeronautics and Astronautics
Massachusetts Institute of Technology, Cambridge, MA

ABSTRACT

Compressor tip clearance flow control schemes are explored using fluidic actuators, the so-called "synthetic jets", on the casing wall acting over the clearance region. Three actuation schemes are under investigation. The first scheme is to use a synthetic jet to create a virtual wall (or flow curtain) in the tip clearance and to reduce the leakage flow. In the second approach, the leakage jet (which has the characteristics of a wall jet) is forced at an appropriate frequency and amplitude in order to enhance the momentum transfer from the main flow to the low momentum region and subsequently to reduce the non-uniformity. The third approach is to direct the synthetic jet in the streamwise direction to energize the low momentum fluid in the tip clearance vortex. Experiments in test rigs show that all three schemes are successful in alleviating the effects of tip leakage, although the efficiency and net gain (relative to the cost of actuation) has not yet been demonstrated.

PROGRAM OBJECTIVES AND APPROACH

The objectives of the research program are to demonstrate effective and efficient flow control methods to alleviate problems associated with tip leakage flows in axial compressors. Two test rigs were fabricated to measure the control performance. The first is a simple two-dimensional leakage jet rig and the second is a linear cascade rig with variable tip clearances.

EXPERIMENTAL METHODS AND RESULTS

Gap Reduction Scheme

First, a simple model experiment has been designed to evaluate the gap reduction scheme in a more manageable environment compared to the tip leakage flow in compressor blade passages. A two-dimensional tip leakage flow is generated without the complication of the axial core flow and chordwise variations. Discharge coefficient of the leakage flow was measured over a range of actuator parameters. The results showed that the discharge coefficient could be reduced by up to 50% with actuation. However, the required amplitude, i.e. momentum out of the synthetic jet actuator, was quite high and was about 40 times the momentum of the leakage flow to achieve 50% reduction. This was not realizable with the actuator developed for the cascade experiment and hence was not pursued in the cascade rig.

Mixing Enhancement Scheme

To investigate the response of the tip clearance flow to the actuation in a compressor blade passage, a linear cascade was designed and fabricated. The design was intended to be representative of a moderately loaded rotor tip section in a modern aero-engine compressor with a diffusion factor of 0.40. The schematic of the wind tunnel is shown in Figure 1. Three central blades in the test section are cantilevered to allow variable tip clearances. The periodicity was achieved by adjusting the bleed ports on the sidewalls.

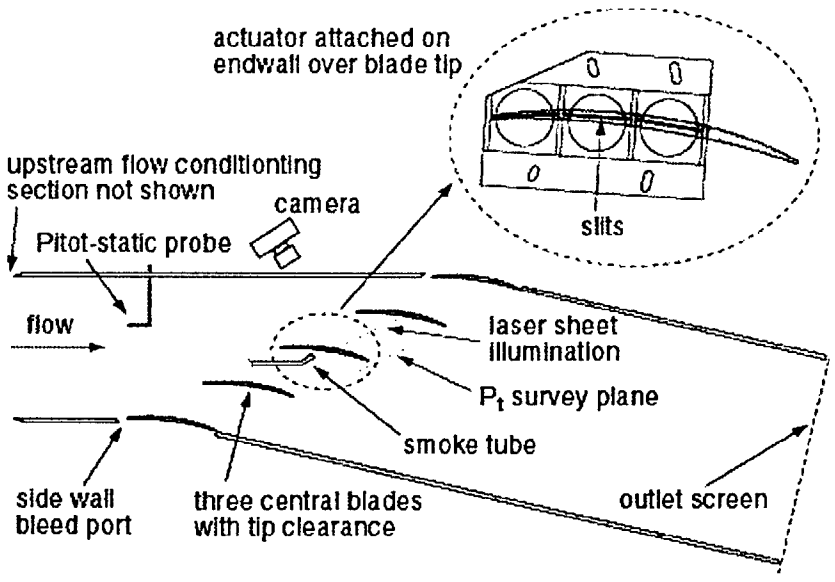

Figure 1. Schematic of cascade wind tunnel test section.

The actuator was attached in a slot on the casing wall. The actuator, widely known as synthetic jet actuator (Amitay *et al.* [1], Smith *et al.* [2]), comprises of a vibrating membrane, a cavity, and a slit (or hole). Three straight slits of three isolated actuator sections are shaped

to approximately follow the camberline of the blade. The actuator covers about 70% chord from the leading edge. Hot wire measurements at the slit exit in a bench test showed that the actuator produces a synthetic jet of up to 65m/s.

To assess the effectiveness of the actuation, the total pressure loss coefficient, $\omega = (P_{t,\infty} - P_t)/q_\infty$ was measured using a Kiel probe in the survey plane, 5% chord downstream of the trailing edge plane as shown in Figure 1. The traversing was programmed and performed automatically over the survey area (1 pitch × 0.5 span).

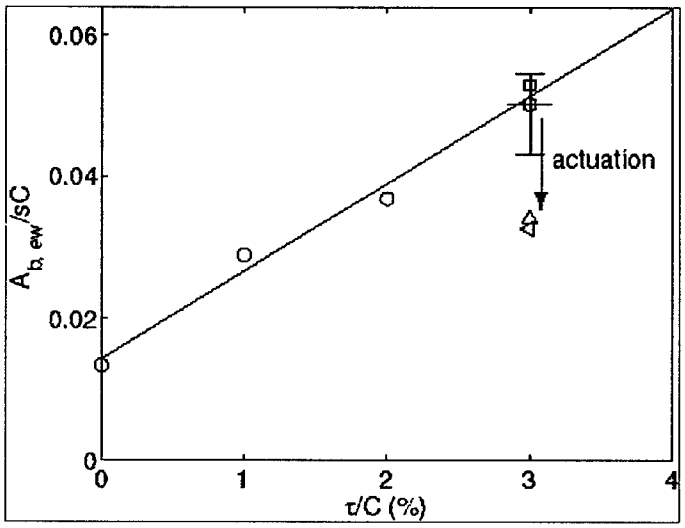

Figure 2. Blockage vs tip clearance. Actuation: $F^+ = 1.0$ and $C_\mu = 0.031$.

The integrated endwall blockage is estimated from the total pressure loss coefficient ω measurements. The total pressure loss coefficient of 0.03 is used to define the edge of the blocked region. The total blocked area, A_b is calculated by integrating over the blocked region. The endwall blocked area, $A_{b,ew}$ is then calculated by subtracting the blocked area related to the blade surface boundary layer, $A_{b,2D}$ from A_b. The endwall blocked areas normalized by the pitch, s times the chord, C are plotted with circular symbols (○: $Re_C = 1.5\times10^5$) in Figure 2 for tip clearance $\tau = 0$, 1, 2, and 3% chord. The estimated uncertainty (20 to 1) in the blockage for the data point with 3% chord clearance is shown with an error bar. The endwall blockage linearly increases with the tip clearance. The blockage directly related to the tip clearance begins at the vertical axis-intercept of the least square fit line and the blockage below the vertical axis-intercept is attributed to the endwall boundary layer. The square symbol (□) is the blockage measured at $Re_C = 1.0\times10^5$.

The triangular symbols (△: $Re_C = 1.5\times10^5$, ◁: $Re_C = 1.0\times10^5$) in Figure 2 are the blockages with actuation at 3%C clearance. The actuator slit was aligned with the camberline of the

blade and its size was 0.25mm. Three voice coils vibrate in unison driven by the same signal. The non-dimensional frequency (reduced frequency = fC/U_∞) was $F^+ = 1.0$ and the non-dimensional amplitude (momentum coefficient = $(\rho U_j^2 \delta L)/(\rho U_\infty^2 sC)$) was $C_\mu = 0.031$. The tip clearance related blockage is reduced by about 50% with actuation. The reduction in the blockage results in the increased static pressure rise (by a few percent) across the cascade as the static pressure measurements on the casing wall indicate. There is no appreciable net change in the mass-average total pressure loss coefficients with actuation as the actuation simply redistributes the retarded fluid to reduce flow non-uniformity and hence the blockage.

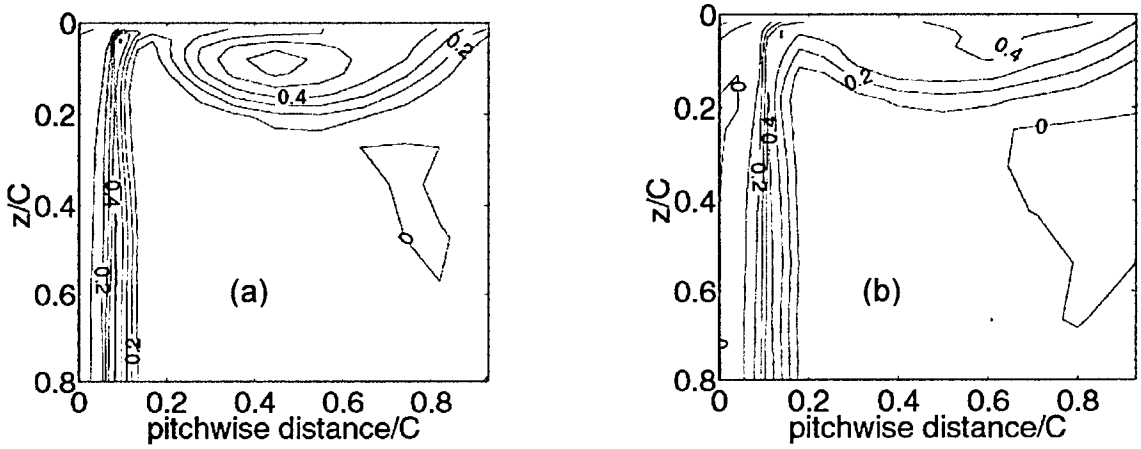

Figure 3 Contour of total pressure loss coefficient with 3%C tip clearance. (a) baseline without actuation. (b) with actuation: Reduced frequency $F^+ = 1.0$ and momentum coefficient $C_\mu = 0.031$.

Figure 3 shows the contour plots of total pressure loss coefficient ω. Figure 3a shows the baseline without actuation at 3%C clearance. Figure 3b shows data collected with actuation at the reduced frequency $F^+ = 1.0$ and the momentum coefficient $C_\mu = 0.031$. The maximum value of ω in the endwall region is reduced from 0.65 to 0.47.

To examine the frequency-dependence of the blockage reduction, the tip leakage flow was forced at different frequencies. Figure 4 shows the blockage against the forcing frequency F^+ for three tip clearances. In all cases, the non-dimensional amplitude of the actuation C_μ was kept constant at 0.031. The tip clearance size was 2, 3, and 4%C. There exists a clear preference to the forcing frequency with optimum at $F^+ = 1.0$. The trend in Figure 4 is similar to the change in mixing level obtained in an image analysis of flow visualization implying the important role of the enhanced mixing in reducing the blockage.

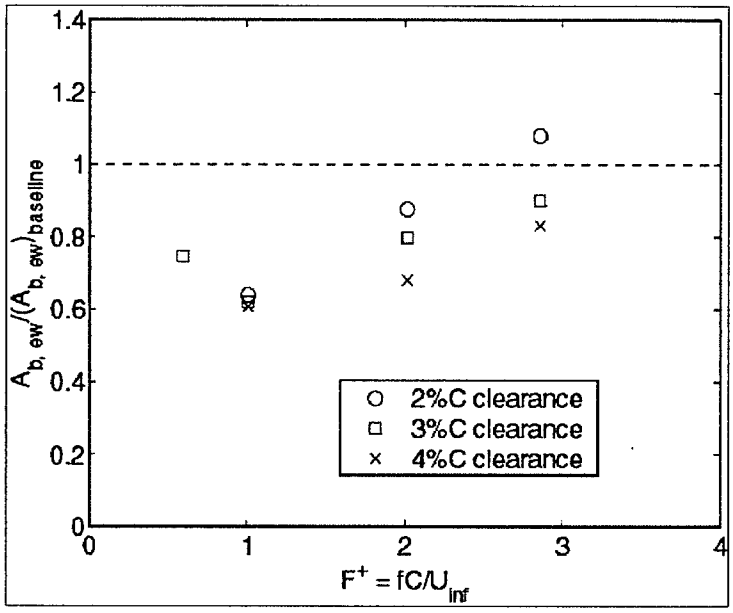

Figure 4. Frequency dependence of actuation on reduction in tip clearance related blockage.

Directed Synthetic Jet Scheme

Only a limited number of measurements are available with the directed synthetic jet scheme at this point. The preliminary measurements show that the directed synthetic jet reduces the tip clearance related blockage and loss as expected. Also found is that the effectiveness of the directed synthetic jet is less sensitive to the forcing frequency and the location relative to the blade tip compared to the normal synthetic jet discussed above. Further investigation is planned during the coming year.

SUMMARY AND CONCLUSIONS

- Synthetic jet was applied to control behavior of tip clearance flow in compressor cascade.
- Reduction of discharge coefficient was demonstrated in a simple two-dimensional leakage flow rig. However, it requires large actuator amplitude.
- Mixing enhancement scheme was studied in a linear cascade rig. The flow blockage associated with tip clearance flow was reduced by about 40-50% with actuation.
  - Blockage reduction is sensitive to forcing frequency with optimum at $F^+ = 1.0$.
  - The power consumption is still large. Time-average flow power from the synthetic jet actuator is about 8% of the flow power in one blade passage.
  - The blockage reduction is sensitive to location of actuator slit. It needs to be right over the blade tip.
- Directed synthetic jet scheme was accessed.
  - Reduction in both blockage and loss.
  - Less sensitive to forcing frequency and location.

FUTURE PLANS

There are three remaining research tasks. They are listed in the following with research questions to be answered:

- Parametric characterization of directed synthetic jet actuation
  - How effective is the streamwise momentum injection?
  - What does the effectiveness depend on?
- Quantification of the actuation schemes at higher loading
  - How does the effectiveness of the actuation schemes vary with the blade loading?
- Identification of changes in flow processes with actuation
- Synthesis of the results
  - What are the implications and recommendations for rotating machines?

ACKNOWLEGEMENT/DISCLAIMER

This work was sponsored by the AFOSR/DARPA under grant/contract number F49620-97-1-0526. The views and conclusions contained herein are those of the authors and should not be interpreted as necessarily representing the official policies or endorsements, either expressed or implied, of the Air Force Office of Scientific Research or the U.S. Government.

REFERENCES

[1] Amitay,M., Honohan,A., Trautmann,M., and Glezer, A., "Modification of the Aerodynamic Characteristics of Bluff Bodies Using Fluidic Actuators", AIAA 97-2004, 1997.

[2] Smith,D.R., Amitay,M., Kibens,V., Parekh,D., and Glezer,A., "Modification of Lifting Body Aerodynamics Using Synthetic Jet Actuators", AIAA 98-0209, 1998.

PERSONNEL SUPPORTED

Graduate Students:	Jinwoo Bae, Eugene Kang
Faculty and Research Staff:	Kenneth S. Breuer, Choon S. Tan
Administrative Staff:	Holly E. Anderson

PUBLICATIONS

"Control of Tip Clearance Flows in Axial Compressors", J. Bae, K.S. Breuer, and C.S. Tan, AIAA 2000-2233, June 2000.

"Control of Leakage Flows using Periodic Excitation", E. Kang, K.S. Breuer, and C.S. Tan, AIAA 2000-2232, June 2000.

LOW PRESSURE TURBINE SEPARATION CONTROL USING VORTEX GENERATOR JETS

AFOSR/AFIT MOA Project Order #QAF185005203215

Jeffrey P. Bons
Department of Aeronautics and Astronautics
Air Force Institute of Technology

Rolf Sondergaard and Richard Rivir
Propulsion Directorate
Air Force Research Laboratory

Abstract

During high altitude cruise, the operating Reynolds number (based on axial chord and inlet velocity) for the low-pressure turbine (LPT) in an aircraft gas turbine engine can drop below 25,000. At these low Reynolds numbers, the boundary layers on the LPT blades are largely laminar, even in the presence of freestream turbulence, making them susceptible to flow separation near the aft portion of the blade suction surface, with associated loss increase and performance drop. Sharma et al. (1998), Matsunuma et al. (1998,1999), and Helton (1997) have all reported increased separation and secondary flow losses when operating LPTs at low inlet Reynolds numbers. Altering the blade shape to avoid this low Reynolds number separation problem is not desirable since such a modification is likely to impair the engine operation at higher (design) Reynolds numbers. As such, flow control techniques which can be practically implemented on a separating turbine blade are of current interest.

This effort investigates the application of pulsed vortex generator jets (VGJs) to control separation on the suction surface of a low pressure turbine blade. Blade Reynolds numbers in the experimental, linear turbine cascade match those for high altitude aircraft engines and aft stages of industrial turbine engines with elevated turbine inlet temperatures. The vortex generator jets have a 30 degree pitch and a 90 degree skew to the freestream direction. Jet flow oscillations up to 100 Hz are produced using a high frequency solenoid feed valve. Results are compared to steady blowing at jet blowing ratios less than 4 and at two chordwise positions upstream of the nominal separation zone. The steady VGJ work was accomplished previously under AFOSR funding and was reported in Bons et al. (1999).

Results to date indicate that pulsed vortex generator jets produce a bulk flow effect comparable to that of steady jets with an order of magnitude less massflow. Figure 1 shows the effect of pulsed vs. steady blowing on the integrated wake total pressure loss (vs. the jet velocity to local freestream blowing ratio, B). The data was taken at a blade inlet Reynolds number of 25,000 with the VGJs located at 63% axial chord (just upstream of the natural separation location). The pulsing frequency of 10Hz corresponds

to an F^+ (or reduced frequency) of approximately 0.74 based on the axial chord and inlet velocity. Control is effective at higher F^+ values while at lower F^+ values the separated flow becomes periodic. From the figure, pulsed VGJs effectively reduce the blade wake at c_μ values down to 0.005. Boundary layer traverses and blade static pressure distributions show that separation is almost completely eliminated with the application of unsteady blowing.

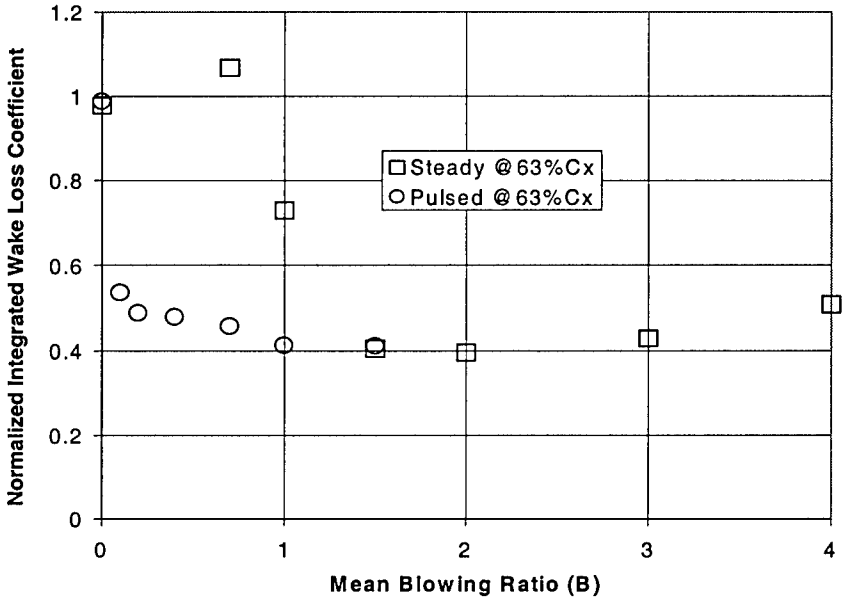

Figure 1: Integrated wake loss coefficient (γ_{int}) normalized by loss coefficient for B=0 vs. mean blowing ratio (B). Data for pulsed blowing at 10Hz and 50% duty cycle vs. steady blowing at Re=25k.

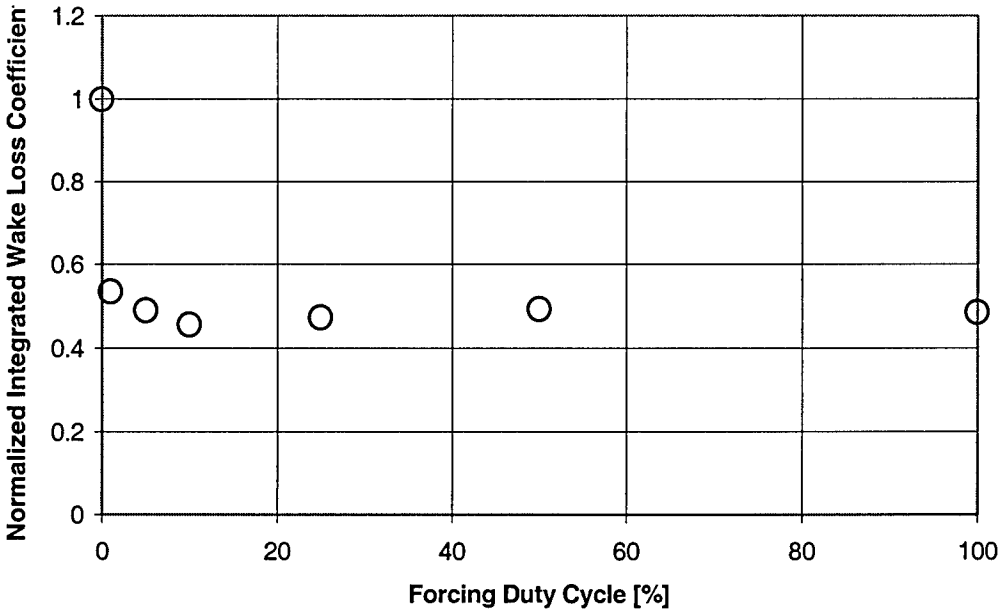

Figure 2: Normalized integrated wake loss coefficient ($\gamma_{int}/\gamma_{int0}$) vs. pulsing duty cycle for constant maximum blowing ratio (B_{max} = 2). Data for pulsed blowing at 10Hz. Re=25k.

A second test was conducted to determine the effect of reducing the pulsed jet duty cycle at constant frequency and peak amplitude (figure 2). The near constant effectiveness from 100% down to 1% duty cycle ($c_\mu = 0.001$) suggests that the mechanism for unsteady control lies in the starting and ending transitions of the pulsing cycle rather than the injected jet stream itself. Boundary layer spectra support this conclusion and highlight significant differences between the steady and unsteady control techniques.

Finally, the pulsed vortex generator jets are effective at both chordwise injection locations tested (45% and 63% axial chord) covering a substantial portion of the blade suction surface. This insensitivity to injection location bodes well for practical application of pulsed VGJ control where the separation location may not be accurately known a priori.

Acknowledgement/Disclaimer
This work was sponsored in part by the Air Force Office of Scientific Research, USAF, under the AFOSR/AFIT MOA Project Order #QAF185005203215. The views and conclusions contained herein are those of the authors and should not be interpreted as necessarily representing the official policies or endorsements, either expressed or implied, of the Air Force Office of Scientific Research or the U.S. Government.

References
1. Bons, J., Sondergaard, R., and Rivir, R., 1999, "Control of Low-Pressure Turbine Separation Using Vortex Generator Jets", AIAA paper #99-0367.
2. Helton, D., 1997, private communication.
3. Matsunuma, T., Abe, H., Tsutsui, Y., and Murata, K., 1998, "Characteristics of an Annular Turbine Cascade at Low Reynolds Numbers.", presented at IGTI 1998 in Stockholm, Sweden, June 1998, paper #98-GT-518.
4. Matsunuma, T., Abe, H., and Tsutsui, Y., 1999, "Influence of Turbulence Intensity on Annular Turbine Stator Aerodynamics at Low Reynolds Numbers.", presented at IGTI 1999 in Indianapolis, Indiana, June 1999, paper #99-GT-151.
5. Sharma et al., 1998, private communication.

Personnel Supported
None

Publications
"Control of Low-Presure Turbine Separation Using Vortex Generator Jets" by Sondergaard, R., Bons, J., and Rivir, R.. Submitted (May, 2000)for publication in the AIAA Journal of Power and Propulsion.

"Control of Low-Pressure Turbine Separation Using Vortex Generator Jets," by R. Sondergaard, J.P. Bons, and R.B. Rivir. Presented at the 2000 International Gas Turbine Institute (IGTI) Conference in Munich, Germany, (paper #2000-GT-262) and accepted for publication (Jan, 2000) in the ASME Journal of Turbomachinery.

REAL-TIME FEEDBACK CONTROL OF MIXING IN A HEATED JET

CONTRACT NUMBER: F49620-97-C0021

W. W. Bower, Y. Ikeda
Phantom Works
The Boeing Company

P. Moin
Center for Turbulence Research
Stanford University

J. B. Freund
Department of Mechanical and Aerospace Engineering
University of California, Los Angeles

D. E. Parekh
Aerospace & Transportation Laboratory
Georgia Tech Research Institute

Abstract

Objectives

Increased mixing is sometimes desired in aircraft jet exhaust to disperse hot gases quickly. Similarly, in combustors enhanced mixing increases the net reaction rate and thereby combustor efficiency. The primary objectives of this program are to investigate methods for open-loop optimization and real-time feedback control of mixing in a heated jet and to demonstrate the resulting techniques in a laboratory environment. The techniques developed in this program would be applicable to C-17 plume temperature reduction.

Approach

The approach to achieving the program objectives has involved systems modeling, control law design, and control law implementation in a real-time laboratory-scale jet. The systems modeling has involved various levels of sophistication ranging from large-scale direct numerical simulations to an inviscid linear stability theory approach. The controller development process focused on various controller design methods based on a weak solution of the linearized flow equations with a forcing term, a linearized system model determined by the input-output relationship of the flow system, and a nonlinear inverse system model. The latter was chosen to construct the baseline controller for the laboratory implementation and demonstration. For this demonstration a RAM 750 microjet model aircraft engine was selected which provides a realistic exhaust flow to be controlled. A new compact, high-bandwidth, high-flow-rate fluidic actuator was designed and fabricated and operated under computer control such that the classical

controller or a genetic algorithm could automatically regulate the actuator frequency, phase, and amplitude to affect the jet mixing.

Progress/Results

1. Simulations: Numerical simulations were used to study the dynamics of jets subject to different types of forcing and to develop tools for their optimization. Large-scale direct numerical simulations of jets forced with different types of actuation were conducted to perform detailed analysis of their dynamics. The compressible Navier-Stokes equations were solved without modeling approximations. Fluidic actuators were included in the computations by adding specifically designed body force terms to the governing equations. By taking this novel approach the computational cost was avoided that would have been required to represent the actuators in detail, but still it was possible to provide high-amplitude, low-mass-flux forcing that was similar to that used in the corresponding experiments. Forcing was done at Strouhal numbers of 0.2 and 0.4. These values were chosen since the former was found to be the most effective at reducing the potential core length and the latter was found to be the most amplified frequency in the unforced jet.

Several measures of mixing effectiveness were investigated. Potential core length measurements and scalar concentrations both showed that forcing at either Strouhal number dramatically increased mixing. The streamwise mass flux was significantly increased for the forced cases, with St = 0.2 forcing inducing marginally more entrainment than St = 0.4 forcing. Aside from the potential core length difference, the most dramatic difference found between the two forced cases was in the scalar dissipation and in the integral of the squared radial velocity in the jet. It was found that the single period average of the measures is very close to its longtime average, which is important for the application of these control techniques.

In the second step, the simulations were combined with optimization strategies to automatically search for the optimal actuation. Testing various optimization procedures it was found that evolution strategies are suitable for the optimization of this computationally expensive problem. Starting from a set of initial parameter vectors which contains the Strouhal numbers and amplitudes of the actuation $x = (St_a, St_h, A_a, A_h)$, new vectors were obtained by random variation.

An initial population of parameter vectors is subjected to repeated mutation and selection until a sufficiently good solution is found. The advantage of evolution programs is that they are efficient, ensuring a rapid convergence of the procedure by evaluating several search trajectories in parallel. The approach for optimizing jet mixing requires 100-200 numerical simulations of the jet. In order to reduce the CPU time, use was made of the observation that the jet is sensitive to the external forcing already at early stages of the simulation. Since the flow is governed by the dynamics of the large scale structures, a coarse grid was used for the evaluation of the objective function.

For the test case of an incompressible jet flow at low Reynolds number Re = 1500, a systematic search was performed for helical and combined axial and helical forcing of the jet. The direct numerical simulation used a second order finite volume method to solve

the incompressible Navier-Stokes equations on a staggered spherical grid. The actuation was imposed on the velocity profile at the inflow. An important result is that combined axial and helical actuation is much more efficient with respect to jet mixing than a helical actuation alone. The combined actuation leads to a large spreading of the jet, resulting in a large mixture fraction and a fast decay of the center line velocity and scalar concentration. The most pronounced spreading was found when the helical Strouhal was $St_h = 0.3$, which is close to the preferred Strouhal number of the jet, and for an axial Strouhal number $St_a = 2 \cdot St_h$. This is in very good agreement with experimental results (Ref. 1 and 2). Figure 1 shows a snapshot of the scalar concentration of the jet obtained for the optimal actuation found by the evolution strategy. This dual-frequency actuation leads to a large spreading. The jet column is completely dispersed near the end of the domain, indicating good mixing of the jet with the ambient fluid. In Figure 2 the centerline velocity obtained from the flapping and bifurcating jet computations is shown. For comparison of the profile for a round axisymmetric jet (standard jet) at comparable Reynolds number is included. For both the flapping and bifurcating jets the centerline velocity starts to drop much earlier than in the standard jet. The decay rate (slope of the curve in Fig. 2 (right)) of the flapping jet is comparable to that of the standard jet while the bifurcating jet decays much faster. For the flapping jet the decay is approximately linear; for the bifurcating jet it is superlinear.

Finally, the optimization procedure was applied to jets at higher Reynolds number Re = 6000 using a large eddy simulation. Including the dynamics procedure to model the small scales of the flow, the optimization procedure was used to search for the optimal actuation. Although the large eddy simulation of the jet is computationally expensive, it was possible to find good solutions within reasonable time. Figure 3 shows a snapshot of the jet with the best mixing properties obtained for combined axial and helical actuation. The actuation leads to a large scale flapping of the jet column and a spreading rate which is higher than that for flows at lower Reynolds numbers.

2. Controller Information: A baseline controller was formulated using a C-17 experimental data base for pulsed jet excitation. The baseline controller was constructed by the inverse system identification, and to compensate the inversion error, an integrator was used in the feedback path. The resulting control architecture is illustrated in Fig. 4. This control design was coded in FORTRAN and delivered to GTRI for laboratory demonstration.

3. Laboratory Demonstration of Turbulent Jet Mixing Control: The GTRI laboratory demonstration has focused on pulsing air into the jet exhaust stream to reduce the temperature by increasing mixing of the exhaust with ambient air. The miniature engine used in the experiments has the model name RAM 750, and is manufactured by R.A. Microjets. It is a single stage axial turbine, and it is capable of producing approximately 20 lbs. of thrust. It is shown installed on the test stand with the compact actuators on opposite sides of the nozzle in Fig. 5.

Two actuators located at the jet exit pulse air into the exhaust stream. Inside each actuator is a high-aspect-ratio drum with 12 slots. As the drum's slot aligns with the outer

actuator slot, air flows from the actuator. The actuators are supplied with compressed air, and the pulsing frequency is controlled using two Maxon motors and motor controllers. These compact, computer-controlled actuators can provide pulsed fluidic excitation at frequencies up to 1200 Hz at flow rates up to 10% of the jet engine flow rate. This provides the important capability of simultaneously achieving both high frequency and high flow rate in a compact system. Exhaust temperature is measured at the immediate jet exit as well as downstream of the exit with a movable aspirated thermocouple. The downstream centerline temperature is used as a figure of merit for the mixing and provides the single input to the controller.

All data acquisition and control are performed with a personal computer using the Lab View software package. The Boeing-supplied control algorithm, originally written in FORTRAN, was also implemented in Lab View. The control systems consist of the jet engine throttle and the actuator pulsing frequency. The measurement systems consist of mass flow to the actuators, jet exhaust velocity, and jet exhaust temperature. Since this controller was developed based on data from a generic axisymmetric round jet, it could not be directly ported to control flow from this jet engine which has both a centerbody and some residual swirl. We are currently exploring whether a simple length-scale transformation that maps the jet engine flow to that of the axisymmetric jet reference is an adequate adjustment to make the controller suitable for controlling this jet engine flow. Recent work has also includedimplementation of a genetic algorithm to provide an automated means for optimizing actuator forcing frequency and amplitude.

Acknowledgement/Disclaimer
This work was sponsored by the Air Force Office of Scientific Research, USAF, under contract number F49620-97-C0021. The views and conclusions herein are those of the authors and should not be interpreted as necessarily representing the official policies or endorsements, either expressed or implied, of the Air Force Office of Scientific Research or the U.S. Government.

References

1. D.E. Parekh, V. Kibens, A. Glezer, J.M. Wiltse, and D.M. Smith, "Innovative Jet Flow Control: Mixing Enhancement Experiments," 34th Aerospace Sciences Meeting and Exhibit, AIAA Paper 96-0308, 1996.

Personnel Supported

William W. Bower	Phantom Works, The Boeing Company
Yutaka Ikeda	Phantom Works, The Boeing Company
Parviz Moin	Mechanical Engineering Dept., Stanford University
John B. Freund	Department of Mechanical and Aerospace Engineer, University of California, Los Angeles
David E. Parekh	Georgia Tech Research Institute

Publications

"Jet Mixing Enhancement by High Amplitude Fluidic Actuation," J. B. Freund and P. Moin, in preparation.

Awards Received

-

Transitions

-

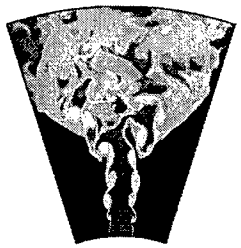

Figure 1. Snapshot of the scalar concentration for a jet actuated with dual-frequency forcing and $St_\alpha = 0.66$, $St_h = 0.31$, $A_\alpha = 0.025$, $A_h = 0.075$.

Figure 2. The averaged centerline scalar concentration for the flapping, bifurcating and standard jet, Re = 1500.

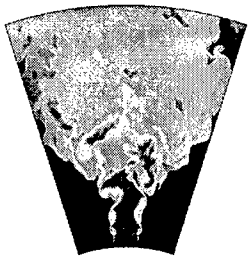

Figure 3. Snapshot of the scalar concentration for a jet at Re = 6000, $St_\alpha = 0.79$, $St_h = 0.36$, $A_\alpha = 0.025$ and $A_h = 0.075$.

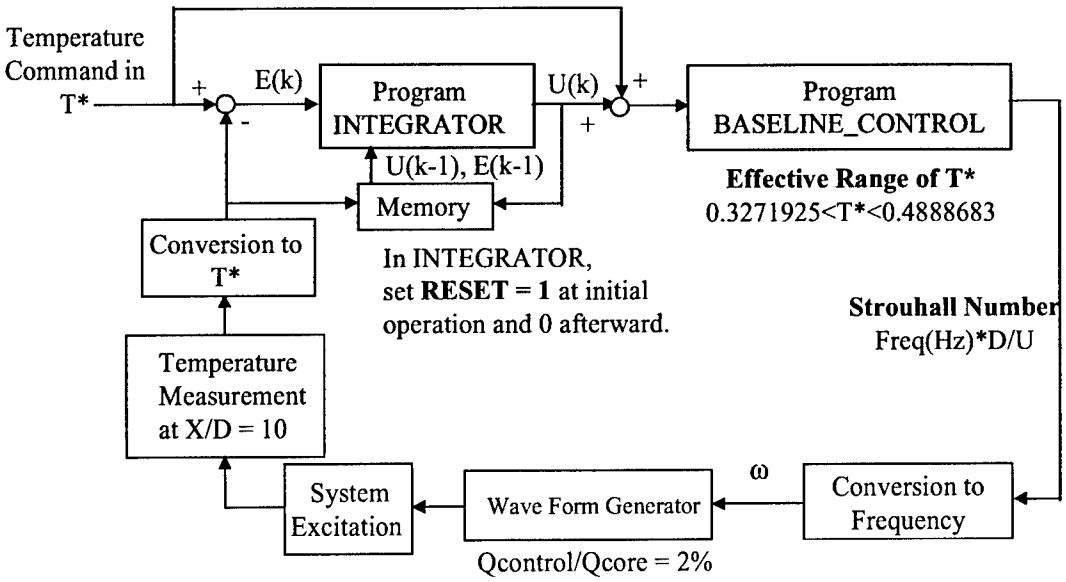

Figure 4. Control architecture for real-time feedback control of mixing in a heated jet

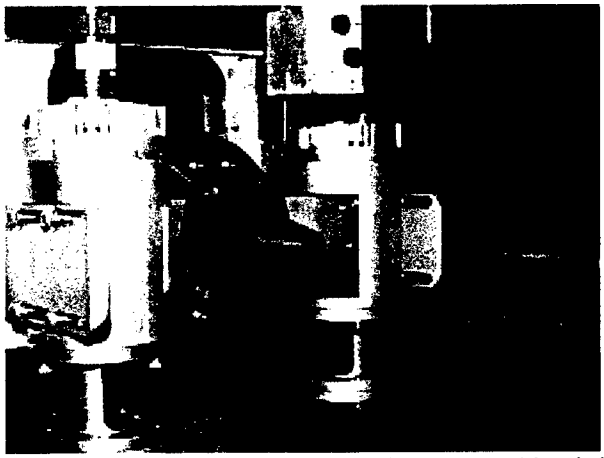

Figure 5. GTRI laboratory configuration using the RAM 750 miniature engine for demonstration of turbulent jet mixing control

EXPERIMENTAL INVESTIGATION OF HIGH-SPEED BOUNDARY LAYERS WITH WALL ROUGHNESS

F49620-98-1-0038

Dr. Rodney D. W. Bowersox
Department of Aerospace Engineering and Mechanics
The University of Alabama

Abstract

The focus this year was on both analyzing the supersonic data and performing the subsonic experimental research. Detailed investigations of the mean and turbulent scaling were performed for the supersonic test conditions, and the Mach 0.22 test condition was completed this July and the data analyses are in-progress. This abstract presents an overview of this work.

Introduction

Compressibility and surface roughness produce complex turbulent boundary layers, which have important practical Air Force applications. For example, *New World Vistas*[1] has identified viscous drag reduction and increased engine efficiency as enabling technologies for future Air Force war fighting capabilities. A key technological challenge that is important to all of the components of vehicle propulsion and aerodynamic systems is the quantification of the of effect surface roughness on turbulent boundary layer characteristics (e.g., skin friction, heat transfer, Reynolds shear stresses, boundary layer growth, etc.). A second Air Force applications is access to space, where for example research for the Space Shuttle program indicated that vehicle control effectiveness was significantly influenced by roughness on the control surface and the forebody ahead of the control panel.[2]

Current predictions of high-speed flow over surfaces with roughness are founded in heuristic extrapolations of the incompressible low-speed database, and the development of engineering prediction methods and turbulence models suitable for high-speed flow over rough surfaces is hindered by a scarcity of experimental data.

Objective

The principal objective of this research program is to experimentally investigate the combined influence of compressibility and surface roughness on the mean and turbulent flow characteristics of high-speed high Reynolds number turbulent boundary layer flow to further understanding and predictability.

Approach

A comprehensive experimental program that uses both traditional and laser diagnostic techniques is currently being performed. To provide information that will be useful to a broad range of applications and to quantify compressibility effects, three high Reynolds number flow conditions are being tested: incompressible (M = 0.22), compressible

subsonic (M = 0.67), and supersonic (M = 2.8). To better isolate compressibility effects, for each flow condition, the Reynolds number is matched (Re/m = 20 x 10^6) and the same six flow models (described in the next paragraph) are being tested.

Five rough wall models and a smooth wall case, for comparison purposes, are being tested to examine roughness height and blockage effects. The roughened wall models consist of three random sand-grain and two uniformly distributed roughness topologies. The 2-D distributed roughness model has rectangular elements (0.56 x 0.56-mm^2) that span the width of the test section with a wavelength of 2.18-mm. The 3-D distributed plate has cubic pillars (0.56 x 0.56 x 0.56-mm^3) also with a wavelength of 2.18-mm. The surface topology of each model was accurately (to within 4.0%) documented with a confocal laser scan microscope.

Along with the detailed experimental studies, a companion numerical investigation is being performed primarily to quantify the strengths and weaknesses of current turbulence models. In-house boundary layer and parabolized Navier-Stokes solvers with a variety of popular algebraic models are being used. van Driest first established a simple modification of his near wall damping function for rough-wall flow.[3] Since then, numerous other formulae based on the mixing length method followed. The two additional models investigated here, namely those of Cebeci-Chang[4] and Kragstad[5], also involve modifying the van Driest damping function. These models were compared to the experimental data acquired in this study.[6]

Table 1: Roughness Parameters

Model	Mean height (mm)	Std. Dev. (mm)	Blockage (mm^2/mm)	K_s^2 (μm)	k_s^{+2}
Smooth[1]	0.007	0.005	0.00	N/A	N/A
80 Grit	0.53	0.17	0.53	0.44	104
36 Grit	0.90	0.34	0.90	1.42	395
20 Grit	0.83	0.50	0.82	1.98	572
3D Distrib.	0.56	0.024	0.14	0.91	241
2D Distrib.	0.56	0.024	0.56	1.09	289

[1]For k = 0.007mm, k^+ = 1.1 (aerodynamically smooth).
[2]Equivalent sand grain calculated with the method of Schlichting[1] for the Mach 2.8 data plotted with van Driest scaling.

Progress

Detailed further analyses of the mean and turbulent scaling of the supersonic test condition was completed this year. The Mach 0.22 flow condition was also mapped, and the Mach 0.67 condition is in progress, and will be completed in early August.

Results

Due to space limitations a brief sample of the results for the Mach 0.22 and 2.8 results are presented here. Further descriptions of the supersonic results and the methods are presented in Refs. [6-11].

Table 2 compares the boundary layer properties for incompressible and supersonic test conditions. Both the momentum and skin friction coefficients for the incompressible

rough wall cases were roughly 2.0 times those for the supersonic test condition, which based on previous studies [Liepmann and Goddard (1957)] was the expected result. Figure 1 shows the present mean flow incompressible results with outer and inner scaling. The results compare well with the conventional theoretical curves. Figure 2 presents a preliminary raw data comparison between the incompressible and supersonic test conditions. Qualitatively, the figures between the two test conditions look very similar, however more detailed comparisons will be performed with the compressible data plotted with the usual van Driest scaling [van Driest (1951)].

Shown in Fig. 3 are example results from the scaling analysis performed on the supersonic data, where the kinematic and full thermodynamic turbulent shear stresses with inner scaling are shown. Collectively, the results indicate that those turbulence properties with thermodynamic dependence scale differently than the kinematic properties. Latin and Bowersox (2000) present a very detailed description of the results.

Table 2 Comparison of Mach 0.22 and Mach 2.8 Boundary Layer Parameters

	Incompressible			Compressible		
Plate	δ (mm)	θ (mm)	C_f	δ (mm)	θ (mm)	C_f
Smooth	10	1.4	0.0021	12	0.8	0.0016
2-D	17	2.6	0.0075	17	1.3	0.0036
3-D	13	2.2	0.0064	16	1.3	0.0035
80 Grit	13	2.1	0.0062	15	1.1	0.0030
36 Grit	14	2.4	0.0070	18	1.4	0.0039
20 Grit	15	2.5	0.0073	17	1.5	0.0040

Future Work

The subsonic experimental testing and numerical calculations will be completed this summer and the final report will be submitted to AFOSR.

Personnel

Rodney Bowersox is the lead PI. Student support has/is provided by Capt. Robert M. Latin (PhD student, completed 6/98), Mr. Huaiguo Fan (MS student, completed 9/98 - *Best MS Thesis, College of Engineering and Department of Aerospace Engineering*), and Victor Pritchett (PhD student, in-progress).

Publications

- Latin, R., *Influence of Surface Roughness on Supersonic High Reynolds Number Turbulent Boundary Layer Flow*, Air Force Institute of Technology PhD Dissertation AFIT/DS/ENY/98M-02, March, 1998.
- Latin, R. and Bowersox, R., "Influence of Surface Roughness on the Mean and Turbulent Flow Properties of Supersonic Boundary Layer," AIAA-99-1017, AIAA 37th Aerospace Sciences Meeting, Reno, NV, Jan. 1999.
- Latin, R. and Bowersox, R., "Flow Properties of a Supersonic Turbulent Boundary Layer with Wall Roughness," In-Print, *AIAA J.*

- Latin, R. and Bowersox, R., "Influence of Surface Roughness on Supersonic Boundary Layer Turbulent Flow Structure," *14th International Symposium on Airbreathing Engines (XIV ISABE)*, Florence, Italy, Sept. 5-10, 1999.
- Fan, H., *Numerical Analysis and Turbulence Modeling of High-Speed Turbulent Flow Over Rough Surfaces*, The University of Alabama MS Thesis, September 1998. Recipient of Department and College of Engineering Best Thesis Award.
- Fan, H. and Bowersox, "Numerical Analysis of High-Speed Flow over Rough Surfaces," AIAA-99-2381, 35th AIAA/ASME/SAE/ASEE Joint Propulsion Conference, Los Angeles CA, June 1999.

Technology Transitions

In addition, this work is directly related to many of the goals listed in the *New World Vistas* [e.g., drag reduction and improved engine efficiency (IHPTET) for hypersonic missiles, global reach aircraft and access to space].

Acknowledgement/Disclaimer

This work was sponsored in part by the Air Force Office of Scientific Research, USAF, under the grant/contract number F49620-98-1-0038. The views and conclusions contained herein are those of the author and should not be interpreted as necessarily representing the official policies or endorsements, either expressed or implied, of the Air Force Office of Scientific Research or the U.S. Government.

References

1. USAF Advisory Board, *Aircraft and Propulsion Technologies, New World Vistas Air and Space Power for the 21st Century*, USAF, 1995.
2. Christoph, G. H., "Prediction of Rough-Wall Skin Friction and Heat Transfer," *AIAA Journal*, Vol. 21, No.4, 1983, pp. 509-515.
3. van Driest, E.R., "On Turbulent Flow Near a Wall," *Journal of Aerospace Science*, Vol.23, Nov.1956, pp. 1007-1011.
4. Cebeci, T. and Chang, K.C. "Calculation of Incompressible Rough-Wall Boundary-Layer Flows," AIAA Journal Vol. 16, No.7, 1978, pp. 730-735.
5. Kragstad, P., " Modification of the van Driest Damping Function to Include the Effects of Surface Roughness," *AIAA Journal* Vol.29, No. 6, 1990, pp. 888-894.
6. Fan, H. and Bowersox, "Numerical Analysis of High-Speed Flow over Rough Surfaces," AIAA-99-2381, 35th AIAA/ASME/SAE/ASEE Joint Propulsion Conference, Los Angeles CA, June 1999.
7. Latin, R., *The Influence of Surface Roughness on Supersonic High Reynolds Number Turbulent Boundary Layer Flow,* PhD Dissertation, AFIT/DS/ENY/98M-02, March 1998.
8. Latin, R. and Bowersox, R., "Influence of Surface Roughness on the Mean and Turbulent Flow Properties of Supersonic Boundary Layer," AIAA-99-1017, AIAA 37th Aerospace Sciences Meeting, Reno, NV, Jan. 1999.
9. Latin, R. and Bowersox, R., "Influence of Surface Roughness on Supersonic Boundary Layer Turbulent Flow Structure," *14th International Symposium on Airbreathing Engines (XIV ISABE)*, Florence, Italy, Sept. 5-10, 1999.

10. Bowersox, R., "Experimental Investigation Of High-Speed Boundary Layers with Wall Roughness," Proceedings from the 1998 AFOSR Turbulence and Internal Flows/Unsteady Aerodynamics and Hypersonics Conference, Annapolis MD, August 1998, pp. 31-36.
11. Bowersox, R., "Experimental Investigation Of High-Speed Boundary Layers with Wall Roughness," Proceedings from the 1999 AFOSR Turbulence and Rotating Flows, Albuquerque, NM, August 18-19, 1999.
12. Liepmann, H. and Goddard, F., "Note on Mach Number Effect Upon Skin Friction of Rough Surfaces," *J. Aero/Space Sciences*, Vol. 24, No. 10, 1957, pp. 784.
13. Van Driest, E., "Turbulent Boundary Layers in Compressible Fluids," *J. Aeronautical Science*, Vol. 26, No. 3, 1951, pp. 287-319.
14. Latin, R. and Bowersox, R., "Flow Properties of a Supersonic Turbulent Boundary Layer with Wall Roughness," In-Print, *AIAA J*, 2000.

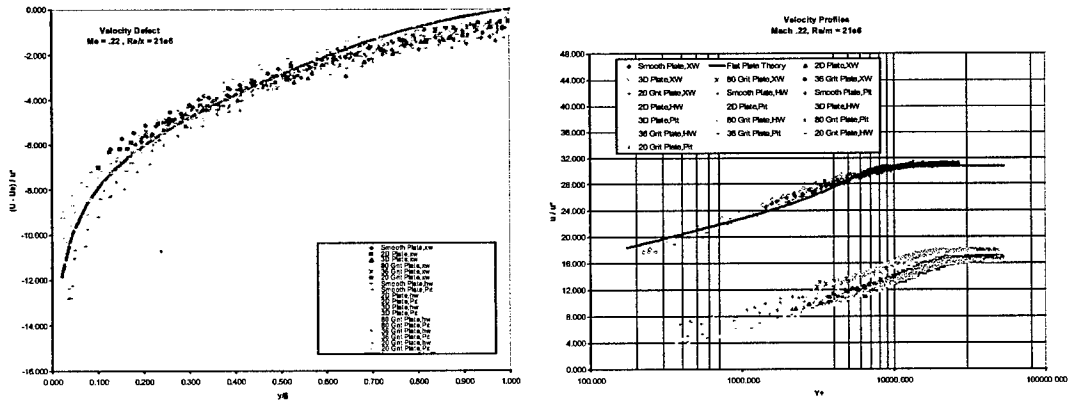

Fig. 1 Subsonic (M = 0.22) Defect Law and Law of the Wall Plots (Pitot Pressure and Hot/Cross-Wire).

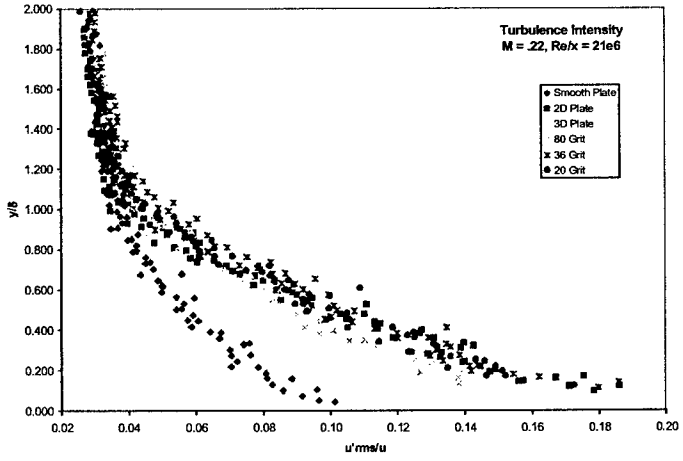

(a) Hot-Wire Turbulence Intensity

fluid dynamic codes for difficult conditions. However, refraction of light beams can distort the views, introduce positioning errors and block measurements in some desired regions. A solution to these difficulties is to match the indices of refraction of the model and the fluid so that light rays are not deflected. While the INEEL MIR flow system has the refractive matching advantage that permits measurements that would otherwise be impossible, its innovation and technical significance is its large size. It is considerably larger than other systems using the MIR technique; consequently, it provides significantly better spatial and temporal resolution at a given Reynolds number, typically by an order-of-magnitude.

The MIR flow system employs a light mineral oil as the working fluid. The current test section is two feet square and nine feet long. Maximum design flow rate is about 5500 gpm. Current instrumentation includes a two-component fiber optics LDV, a computer-controlled three-directional traversing mechanism, hot-film anemometers, a MacIntosh data acquisition system with LabView software and typical temperature, pressure and velocity sensors. A parallel auxiliary flow loop with an electric heater and a heat exchanger is employed with feedback control from a MacIntosh system in order to maintain a selected, steady temperature in the system.

Maximum velocity in the current test section is about two meters per second. Qualification measurements with hot film sensors and with the LDV showed the freestream velocity profile to be uniform to within one per cent and the freestream turbulence level was 0.5 to 0.8 per cent without tripping. Fluid temperature is maintained to within 0.01 C to control its refractive index.

We expect to obtain a grid of measurements of mean and turbulence quantities within the viscous layer and near wall region of a boundary layer over each real surface model. For the near wall region, the key to correct modeling is to match the non-dimensional parameters in terms of wall scaling and to have the same range of dimensionless pressure gradients plus the proper scaled geometry. The test section inlet section would be modified to induce elevated freestream turbulence, to simulate gas turbine conditions, and the streamwise pressure gradient would be adjusted to match operating conditions appropriately. Measurements would be conducted with a 2-component fiber optics LDV system. The locations where near-wall data are obtained would be fabricated of fused quartz having the same refractive index as the oil in the MIR Facility. This approach will allow for high signal-to-noise measurements even within the part of the viscous layer that is buried in the terrain of the roughness elements. In addition, it will provide for improved spatial and temporal resolution compared to typical experiments in wind or water tunnels.

Progress to Date

1. A Ph.D. candidate and an undergraduate student have been selected and have started to work on the project. The Ph.D. candidate has completed a laser safety course and a LDV short course. He is currently receiving training on the operation of the MIR Facility.

THE BOUNDARY LAYER OVER TURBINE BLADE MODELS WITH REALISTIC ROUGH SURFACES

AFOSR Grant Number: F49620-00-1-0265

Ralph S. Budwig
Department of Mechanical Engineering
University of Idaho
rbudwig@uidaho.edu

July 14, 2000

Introduction

This extended abstract is written to summarize the objectives, approach, progress to date, and future plans of a new project funded through the DEPSCoR Program. The start date of the project was April 15, 2000 and the duration is three years.

Objectives

Surface roughness is known to have a significant impact on turbine heat loads and performance. As the exposure history of turbine flow path components is increased, many of the external surfaces become rougher, which results in the increase of heat loads and friction losses. While there have been several investigations that included surfaces with uniform or two dimensional roughness patterns there is now a clear need to measure the influence of *real surface* roughness on turbine blade flow and heat transfer.

The objective of the proposed investigation is to conduct measurements that will reveal the influence of *real surface* roughness on the boundary layer. The test surface will be a large-scale version of rough surfaces that are specified by the Air Force Research Laboratory/Propulsion Directorate. That is, geometric models of real surfaces would be employed but in much larger size so we can obtain high quality velocity and turbulence data in the near wall region, including the viscous layer. Thus, the measurements obtained would be related to convective heat transfer from the surface. Since the near wall region is still subsonic in a transonic boundary layer, such detailed measurements should be valuable to assess and guide development of computational fluid dynamics models proposed for predictions of flows over realistic surfaces in gas turbine passages at engine operating conditions.

Approach

The measurements will be conducted in the Matched-Index-of-Refraction (MIR) Facility at the Idaho National Engineering and Environmental Laboratory (INEEL), the largest MIR Facility in the world. Optical flow measurement techniques, such as laser Doppler velocimetry (LDV) and Particle Tracking Velocimetry, permit flow field determination without locating transducers in the flow. By using transparent models, complex flow fields can be studied and the results can be used to assess the validity of computational

fluid dynamic codes for difficult conditions. However, refraction of light beams can distort the views, introduce positioning errors and block measurements in some desired regions. A solution to these difficulties is to match the indices of refraction of the model and the fluid so that light rays are not deflected. While the INEEL MIR flow system has the refractive matching advantage that permits measurements that would otherwise be impossible, its innovation and technical significance is its large size. It is considerably larger than other systems using the MIR technique; consequently, it provides significantly better spatial and temporal resolution at a given Reynolds number, typically by an order-of-magnitude.

The MIR flow system employs a light mineral oil as the working fluid. The current test section is two feet square and nine feet long. Maximum design flow rate is about 5500 gpm. Current instrumentation includes a two-component fiber optics LDV, a computer-controlled three-directional traversing mechanism, hot-film anemometers, a MacIntosh data acquisition system with LabView software and typical temperature, pressure and velocity sensors. A parallel auxiliary flow loop with an electric heater and a heat exchanger is employed with feedback control from a MacIntosh system in order to maintain a selected, steady temperature in the system.

Maximum velocity in the current test section is about two meters per second. Qualification measurements with hot film sensors and with the LDV showed the freestream velocity profile to be uniform to within one per cent and the freestream turbulence level was 0.5 to 0.8 per cent without tripping. Fluid temperature is maintained to within 0.01 C to control its refractive index.

We expect to obtain a grid of measurements of mean and turbulence quantities within the viscous layer and near wall region of a boundary layer over each real surface model. For the near wall region, the key to correct modeling is to match the non-dimensional parameters in terms of wall scaling and to have the same range of dimensionless pressure gradients plus the proper scaled geometry. The test section inlet section would be modified to induce elevated freestream turbulence, to simulate gas turbine conditions, and the streamwise pressure gradient would be adjusted to match operating conditions appropriately. Measurements would be conducted with a 2-component fiber optics LDV system. The locations where near-wall data are obtained would be fabricated of fused quartz having the same refractive index as the oil in the MIR Facility. This approach will allow for high signal-to-noise measurements even within the part of the viscous layer that is buried in the terrain of the roughness elements. In addition, it will provide for improved spatial and temporal resolution compared to typical experiments in wind or water tunnels.

Progress to Date

1. A Ph.D. candidate and an undergraduate student have been selected and have started to work on the project. The Ph.D. candidate has completed a laser safety course and a LDV short course. He is currently receiving training on the operation of the MIR Facility.

2. The PI, collaborators, and students have met to complete the conceptual design for the project approach. This conceptual design is illustrated in figure 1.

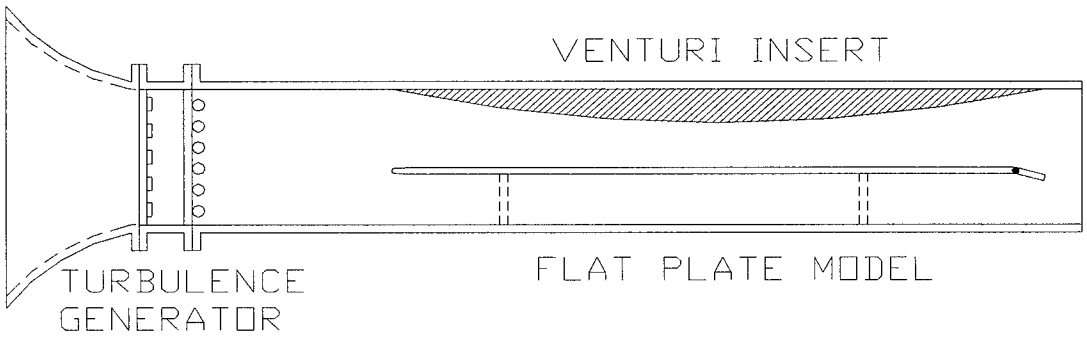

Figure 1. Schematic diagram of MIR Facility test section to illustrate conceptual design of the project approach.

(a) **Freestream turbulence**: Experiments will be conducted with low and high freestream turbulence levels. A grid and/or jet grid located at the inlet to the test section will be used to generate the high turbulence level condition.
(b) **Pressure Gradient**: The experiments will be conducted with a streamwise pressure gradient distribution that is scaled to simulate a typical turbine blade distribution. We will establish this pressure gradient distribution along the surface of the flat plate with a specially designed venturi insert. The insert will be secured to the top wall of the MIR Facility test section.
(c) **Flat Plate Models:** The flat plate models will extend a maximum length of the MIR Facility test section to attain a maximum Reynolds number ($Re_x \cong 300{,}000$). The models will be constructed of a combination of aluminum and fused quartz. The locations where near-wall data are obtained would be fabricated of fused quartz. Experiments will be conducted with three models - a smooth surface model, a distributed roughness (sand-grain roughness) model, and a model with realistic surface roughness.

3. The PI and Ph.D. candidate have met to formulate an overview plan for all three years and a detailed plan for year one. These plans are summarized below in the Future Plans section.

4. The PI has had telephone meetings with Dr. Richard Rivir of AFRL to discuss the appropriate conceptual design for modeling surface roughness.

employed to study the fluid/MEMS interactions from both a fundamental fluid dynamics perspective and from a control theory viewpoint. Our test configuration is shown in Figure 2. This configuration consists of a "macro" scale vibrating piezo flap for actuation and a MEMS based shear sensor array for reattachment detection. As discussed below, we are using this configuration to quantify the MEMS actuation requirements, to develop our MEMS sensing capabilities and to provide a test case for development of model based and neural network control strategies for the non-linear system.

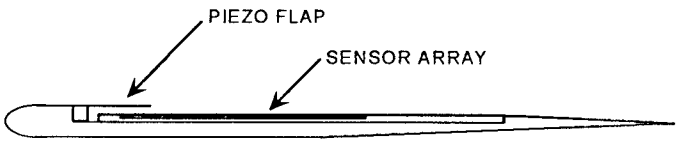

Figure 2. Test Geometry for quantitative determination of actuation requirements.

Progress

Results for several aspects of this project have been reported in the literature and will only be summarized here for brevity. Our computational algorithms were checked against experimental results and shown to yield sufficient accuracy.[1] The CFD results were then used to develop neural network control. Using radial basis functions, we have successfully trained neural networks to map the flow characteristics (i.e., C_L/C_D as a function of angle of attack and Reynolds number) for viscous flow around a two dimensional airfoil.[2] Building on the success of these studies, inverse plant models based on neural network mappings are being developed and will be used in feedforward compensators. The impact of leading edge blowing on the low Reynolds number flow field was also investigated numerically.[3] These computational techniques are currently being applied to the test geometry of Figure 2 as a complement to the experimental results presented below.

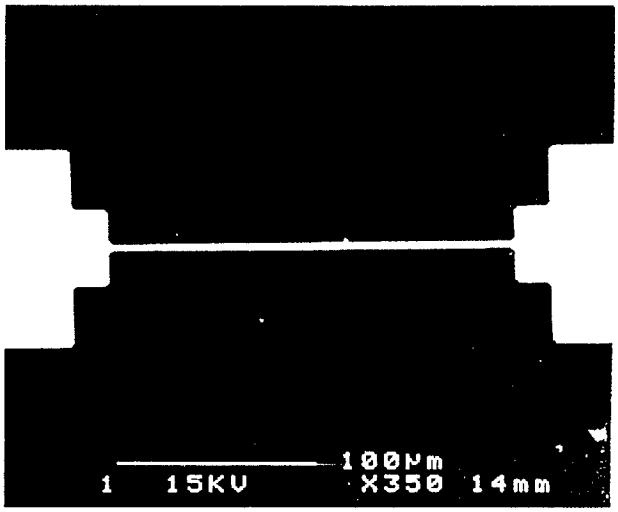

Figure 3. SEM image of MEMS shear sensing element.

Our main experimental investigation for this reporting period has made use of the test geometry in Figure 2. An elliptical leading edge profile was used to ensure the laminar boundary layer remains attached until separation at the at the trailing edge of the piezo flap. The piezo flap actuator design was based on a similar design by Dr. Louis Cattafesta.[4] The deformation of the piezo actuator was measured with a scanning laser vibrometer. A transfer function for the actuator tip was determined and is presented in Figure 4. A linear array of MEMS shear sensors is being used to detect the reattachment location on the upper surface. Figure 3 shows a SEM image of a single shear stress sensor

USE OF MEMS FOR MICRO AIR VEHICLES

AFOSR GRANT F49620-97-1-0507

Bruce Carroll, Norman Fitz-Coy, Andrew Kurdila, Mark Sheplak, and Wei Shyy
Department of Aerospace Engineering, Mechanics & Engineering Science
University of Florida

Toshikazu Nishida
Department of Electrical and Computer Engineering
University of Florida

Abstract

This is a three-year, multidisciplinary effort to investigate the application of MEMS to the control of low Reynolds number flows about Micro Air Vehicles (MAVs). The specific goals of this investigation are to develop a quantitative and qualitative understanding of microelectromechanical systems (MEMS) based sensor and actuator interactions with low Reynolds number flows found on MAVs, resulting in improved aerodynamic performance and mechanisms for active and passive flight control.

Approach

A dominant aerodynamic feature of MAVs is the lower lift-to-drag ratio and much reduced stall margin, which leads to a precipitous decline in aerodynamic efficiency as Reynolds number is lowered. The amplification of small-scale MEMS control inputs into large-scale effects via fluid dynamic instability and growth mechanism are being investigated. Figure 1 shows a low Reynolds number (Re < 100,000), laminar separation followed by transition of the separated shear layer and reattachment. Mild actuation of the boundary layer near the separation location is expected to trigger a quicker transition of the separated shear layer, providing a mechanism for control of the reattachment location. We are also considering MEMS induced and controlled vortical structures, originating with small perturbations at the leading edge of the MAV wing to enhance the lift. A third possible mechanism is to utilize flexible membrane wing panels as an additional amplification mechanism for the MEMS actuation. While Figure 1 describes our ultimate goal for an improved MAV airfoil, simpler geometries are being

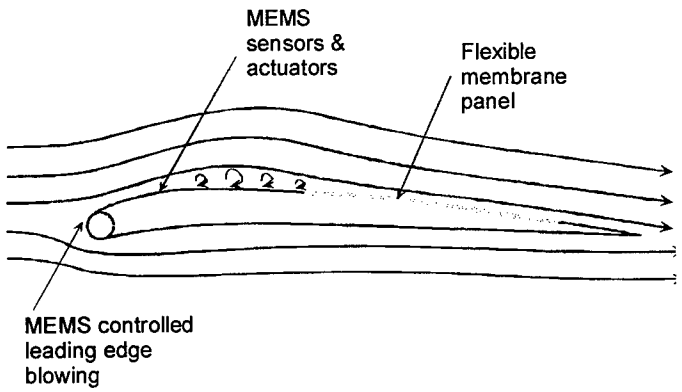

Figure 1. Illustration of actuation and sensing strategies

employed to study the fluid/MEMS interactions from both a fundamental fluid dynamics perspective and from a control theory viewpoint. Our test configuration is shown in Figure 2. This configuration consists of a "macro" scale vibrating piezo flap for actuation and a MEMS based shear sensor array for reattachment detection. As discussed below, we are using this configuration to quantify the MEMS actuation requirements, to develop our MEMS sensing capabilities and to provide a test case for development of model based and neural network control strategies for the non-linear system.

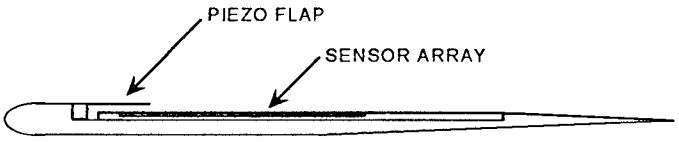

Figure 2. Test Geometry for quantitative determination of actuation requirements.

Progress

Results for several aspects of this project have been reported in the literature and will only be summarized here for brevity. Our computational algorithms were checked against experimental results and shown to yield sufficient accuracy.[1] The CFD results were then used to develop neural network control. Using radial basis functions, we have successfully trained neural networks to map the flow characteristics (i.e., C_L/C_D as a function of angle of attack and Reynolds number) for viscous flow around a two dimensional airfoil.[2] Building on the success of these studies, inverse plant models based on neural network mappings are being developed and will be used in feedforward compensators. The impact of leading edge blowing on the low Reynolds number flow field was also investigated numerically.[3] These computational techniques are currently being applied to the test geometry of Figure 2 as a complement to the experimental results presented below.

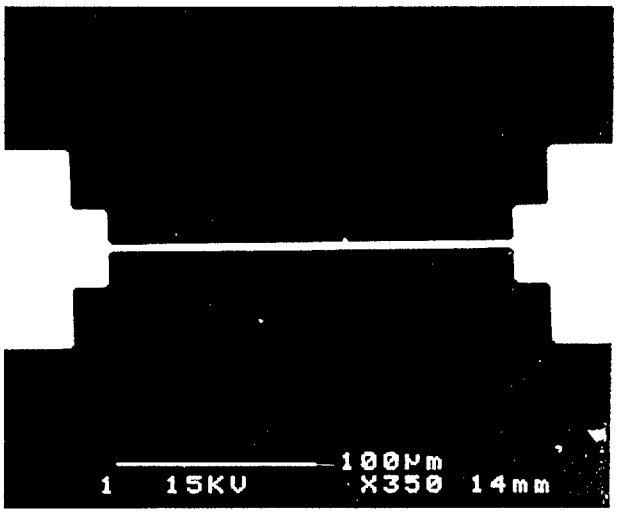

Figure 3. SEM image of MEMS shear sensing element.

Our main experimental investigation for this reporting period has made use of the test geometry in Figure 2. An elliptical leading edge profile was used to ensure the laminar boundary layer remains attached until separation at the at the trailing edge of the piezo flap. The piezo flap actuator design was based on a similar design by Dr. Louis Cattafesta.[4] The deformation of the piezo actuator was measured with a scanning laser vibrometer. A transfer function for the actuator tip was determined and is presented in Figure 4. A linear array of MEMS shear sensors is being used to detect the reattachment location on the upper surface. Figure 3 shows a SEM image of a single shear stress sensor

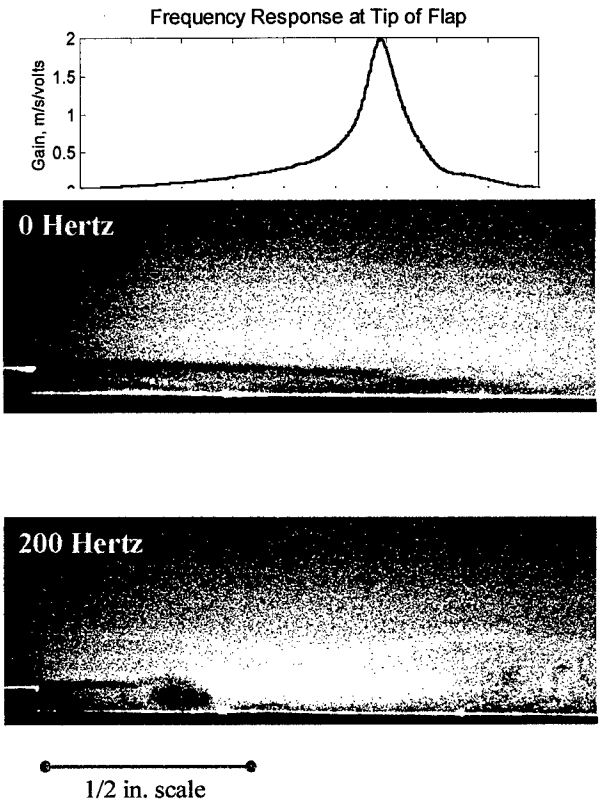

Fig. 6 Flow visualization using the PIV system. Top picture shows flow without excitation, bottom picture shows vortex structure generated at 200 Hz excitation.

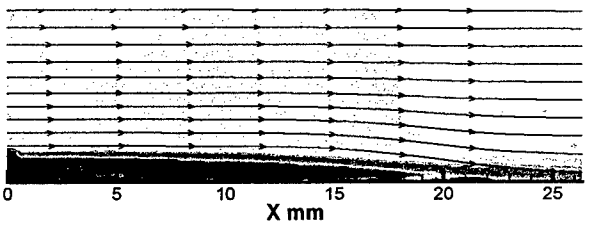

a) no excitation (0 Hz)

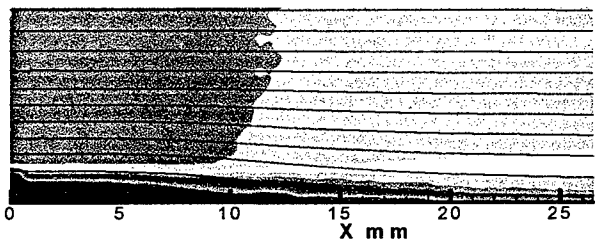

b) 200 Hz excitation

Fig. 7 Mean velocity profiles downstream of sudden expansion. Random phase shifts between realizations. The reattachment location is seen to move forward with excitation but time dependent flow structures are obscured

that was fabricated using a wafer bond/etch-back process at MIT. The sensing element is a platinum thin film deposited on a 1500Å-thick silicon nitride diaphragm over a 10μm-deep sealed vacuum cavity. The sensor is packaged on a milled printed circuit board flush mounted on the surface of the airfoil.

A series of preliminary experiments with a low speed impinging jet verified the operation of the shear sensor array. Before useful measurements on the current test geometry can be performed, we deemed it necessary to obtain a detailed characterization of the shear experiments have been performed to (TCR) for platinum thin film sensing icated a TCR = .0027 $°C^{-1}$ with 2.7% . Extensive current-voltage testing of a the experimentally determined TCR, trical biasing conditions. Mean shear

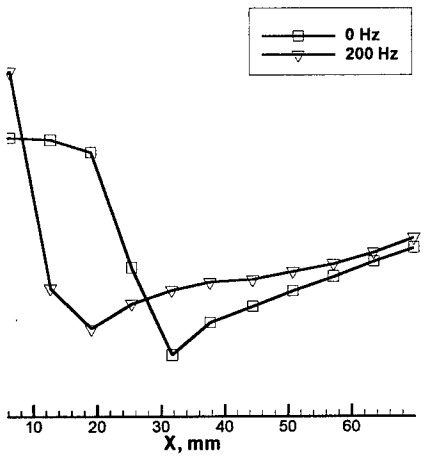

. Mean surface pressure distributions l upper surface without excitation and Hz excitation.

from zero to 500 Hz. Representative

3.* Shyy, W., He, X. and Thakur, S. "Jets and Free Stream Interaction Around a Low-Reynolds Number Airfoil Leading Edge," Numerical Heat Transfer, Part A, Vol. 35, (1999) pp.891-902.

4. Cattafesta, L. N., III, Garg, S., and Washburn, A. E., "Piezoelectric Actuators for Fluid-Flow Control," Proceedings of the SPIE, Vol. 3044, pp. 147-157, March, 1997.

5.* V. Chandrasekaran, A. Cain, T. Nishida, M. Sheplak, "Dynamic Calibration Technique for Thermal Shear Stress Sensors with Variable Mean Flow," To be presented at the AIAA Winter Annul Meeting, Jan. 10-13, 2000, Reno Nevada.

6.* A. J. Kurdila, B. F. Carroll "Reduced Order Modeling for Low Reynolds Number Flow Control," Smart Structures and Materials Conference, Technical Conference 3667 Mathematics and Control in Smart Structures, SPIE Paper no. 3667-07, Proceedings of SPIE Vol. 3667, Newport Beach, CA, Mon.-Thurs. 1-4 March 1999.

7.* Carlos Fuentes, Xiong He, Bruce Carroll, Yongsheng Lian, and Wei Shyy, "Low Reynolds Number Flows Around an Airfoil with a Movable Flap – Part 1: Experiments" AIAA 2000-2239, Denver, CO, June 2000.

*Indicates a publication resulting from this grant.

vortex. The convective speed of the vortex structures is approximately 2.0 m/s. Noting that the free stream velocity is 8.4 m/s, we see that the convective speed is approximately 24% of the free stream velocity.

Future Work

This work is continuing on an unfunded basis as new funding is secured. Phase locked PIV imaging will be continued for other flow conditions. This data will then be used to refine the computational algorithms, especially the transition model. A scanning vibrometer is being used to perform a 3-D characterization of actuators under load. This information is critical to provide accurate boundary conditions to the numerical simulations and to provide specifications of actuation requirements for future MEMS actuator development.

Personnel

Faculty and graduate assistants from two departments are collaborating on this research effort. The work is subdivided into three main subject areas: Aerodynamics, MEMS, and Controls, although considerable overlap and coordination between areas exists. The personnel in each subject area are listed in the following table:

Subject Area	Faculty	Graduate Assistants
Aerodynamics	Bruce Carroll (AeMES) Wei Shyy (AeMES)	Carlos Fuentes Xiong He
MEMS	Toshikazu Nishida (ECE) Mark Sheplak* (AeMES)	Anthony Cain
Controls	Norman Fitz-Coy (AeMES) Andrew Kurdila* (AeMES)	Nilay Papila Jing Li

*Drs. Sheplak and Kurdila are new members of our faculty and were not listed on the original proposal. However, they have been making substantial contributions to the project and are now listed as Co-PI's.

Acknowledgment/Disclaimer

This work was sponsored by the Air Force Office of Scientific Research, USAF, under grant/contract number F49620-97-1-0507. The views and conclusions contained herein are those of the authors and should not be interpreted as necessarily representing the official policies or endorsements, either expressed or implied, of the Air Force Office of Scientific Research or the U. S. Government.

References

1.* Shyy, W., Klevebring, F., Nilsson, M., Sloan, J., Carroll, B. and Fuentes, C. "A Study of Rigid and Flexible Low Reynolds Number Airfoils," Journal of Aircraft, Vol. 36, (1999) pp.523-529.

2.* Papila, N., Shyy, W., Fitz-Coy, N. and Haftka, R.T., "Assessment of Neural Net and Polynomial-Based Techniques for Aerodynamic Applications," AIAA 17th Applied Aerodynamics Conference, Paper No. 99-3167 (1999).

3.* Shyy, W., He, X. and Thakur, S. "Jets and Free Stream Interaction Around a Low-Reynolds Number Airfoil Leading Edge," Numerical Heat Transfer, Part A, Vol. 35, (1999) pp.891-902.

4. Cattafesta, L. N., III, Garg, S., and Washburn, A. E., "Piezoelectric Actuators for Fluid-Flow Control," Proceedings of the SPIE, Vol. 3044, pp. 147-157, March, 1997.

5.* V. Chandrasekaran, A. Cain, T. Nishida, M. Sheplak, "Dynamic Calibration Technique for Thermal Shear Stress Sensors with Variable Mean Flow," To be presented at the AIAA Winter Annul Meeting, Jan. 10-13, 2000, Reno Nevada.

6.* A. J. Kurdila, B. F. Carroll "Reduced Order Modeling for Low Reynolds Number Flow Control," Smart Structures and Materials Conference, Technical Conference 3667 Mathematics and Control in Smart Structures, SPIE Paper no. 3667-07, Proceedings of SPIE Vol. 3667, Newport Beach, CA, Mon.-Thurs. 1-4 March 1999.

7.* Carlos Fuentes, Xiong He, Bruce Carroll, Yongsheng Lian, and Wei Shyy, "Low Reynolds Number Flows Around an Airfoil with a Movable Flap – Part 1: Experiments" AIAA 2000-2239, Denver, CO, June 2000.

*Indicates a publication resulting from this grant.

ACTIVE CONTROL OF SELF-SUSTAINED OSCILLATIONS IN THE FLOW PAST A CAVITY

AFOSR GRANT F49620-98-1-0095

Tim Colonius
Division of Engineering and Applied Science
California Institute of Technology
Pasadena, CA 91125

Abstract

Recently, several investigators have used open and closed-loop active flow control to reduce resonant oscillations in subsonic and transonic flows over open cavities, e.g. [1, 2, 3]. Closed-loop control has been shown to produce reductions in tonal noise with lower power input compared to open-loop control. In these studies, control strategies used on the cavity have been relatively simple, typically gain/phase/delay controllers with notch filters, or adaptive controllers which are not model-based. These have been successful at attenuating oscillations at certain frequencies, but if one wants to improve these results by making use of more sophisticated control strategies, it is necessary to have an accurate model of the flow physics.

Generally, our research is aimed at computation and the development of accurate dynamical models of the resonant oscillations for the purpose of bifurcation analysis and control. We have performed an extensive set of Direct Numerical Simulations of resonant oscillations in two-dimensional flow at freestream Mach numbers from 0.2 to 0.8 [4]. The simulations provide the data used to derive and evaluate models. Based on the method of Proper Orthogonal Decomposition (POD) and Galerkin projection, we have obtained low-order models (from 6 to 60 states). In this report we briefly discuss the methodology used (full details may be found in ref. [5]) and we examine the extent to which these capture the dynamics of the cavity oscillations by comparing with the original DNS data. We close by mentioning related work which is also being carried out in our effort to compute, model and control cavity oscillations.

We have previously reported on the development and validation of the DNS code which solves the fully compressible, unsteady Navier-Stokes equations for rectangular cavities with laminar upstream boundary layers [4]. This report focuses mainly on two-dimensional simulations used for the purpose of developing low order models. The following parameters may be independently varied in code: the length of the cavity relative to the initial boundary layer thickness at the cavity leading edge, L/θ ; the Reynolds number, Re_θ, based on the freestream velocity, U, and the ambient kinematic viscosity; the Mach number of the freestream, M; and the cavity length to depth ratio, L/D .

POD/Galerkin Projection Based Models

The Proper Orthogonal Decomposition (POD) is a commonly used tool for extracting coherent structures from data, either experimental or computational[6, 7]. Given a set of data, represented as a function of space and time, the POD determines a basis set of orthogonal functions of space which span the data optimally in the L^2 sense. In practice, the data is usually discretized in both space and time, in which case finding

the POD modes reduces to a standard eigenvalue problem, and in the common case where the number of snapshots in time is smaller than the number of grid points, the POD modes are most easily computed using the method of snapshots.
POD modes can be defined for a vector quantity, which might represent all the dependent variables of the calculation, for example, or for scalar quantities, resulting in individual modes for each variable treated. For the present modeling, we have computed scalar POD modes for the velocity components, enthalpy, and vorticity. The vorticity modes are useful for visualization but are not used in the Galerkin projection.
We perform a Galerkin projection of the modes onto the original system of PDE from which the snapshots were taken. This generates a system of Ordinary Differential Equations; we then truncate this system to low numbers of modes and examine the extent to which the system captures the correct dynamics of the DNS. In the present case, we also make several simplifications to the full compressible equations that are appropriate for the cold flow considered here (such as the neglect of variations of the kinematic viscosity with temperature, and of viscous dissipation and heat conduction in the energy equation).
Several of the parameters we are interested in (here, M and L/θ) do not appear in the governing equations, but result from initial and boundary conditions (L). This is undesirable because there is no clear way to include parameters in the Galerkin equations unless they appear directly in the governing PDEs. We can partially resolve this difficulty by appropriately nondimensionalizing the equations, such that the relevant parameters do appear. This idea of rescaling the equations is a special case of a more general idea of mapping different domains (geometries) into a canonical geometry [8]. It is not possible to perform such a mapping for the final parameter, L/D, but based on our previous DNS results (and a result shown below), it appears to be less critical to overall dynamics than the others.
We computed POD modes from three of the DNS runs that are discussed in ref [4], using the method of snapshots, and taking between 51 and 101 snapshots over 5–10 periods of the cavity oscillation. The Mach number is 0.6 for these cases, and $L/D = 2$ for runs A and B, and 4 for run C. The values of L/θ are similar (53, 58, and 60 for runs A,B, and C, respectively), and Re_θ is 57, 69, and 59 for runs A,B, and C respectively. In all cases discussed here, we took the snapshots after the initial transients had settled out, and the mean of all the snapshots is subtracted before the POD modes are computed.

Results

We first examine the structure of the POD modes for Run A in Figure 1, which shows v-velocity contours of the mean and POD modes. The modes are typical of the runs considered here, and show disturbances in the shear layer that correspond very closely with linear stability eigenfunctions corresponding to the first two resonant (Rossiter) frequencies (the linear stability results may be found in ref [4]). The structure of the modes show even better agreement with discrete Fourier transform (in time) of the DNS results at the two resonant frequencies. This result shows that capturing the low order dynamics with the POD models is very promising. The POD modes for

Run B (not shown) look similar, although the first two modes shown in Figure 1 are not present, because in Run B the cavity is oscillating primarily in Rossiter mode 2, while in Run A the cavity oscillates in Rossiter modes 1 and 2. In general, the higher POD modes show finer and finer spatial scales. Figure 1 also shows the percent of the fluctuating energy ($\|q - \bar{q}\|^2$) captured in each mode, for Runs A and B. The first 4 modes capture a total of 50% of the energy in Run A, and 76% in Run B. The difference between the two runs is to be expected, since Run A has more complicated behavior. The higher modes still capture a significant amount of energy, but since this energy is at the smaller spatial scales, it is likely that they will be unimportant for modeling the overall global behavior of the cavity, as is shown below.

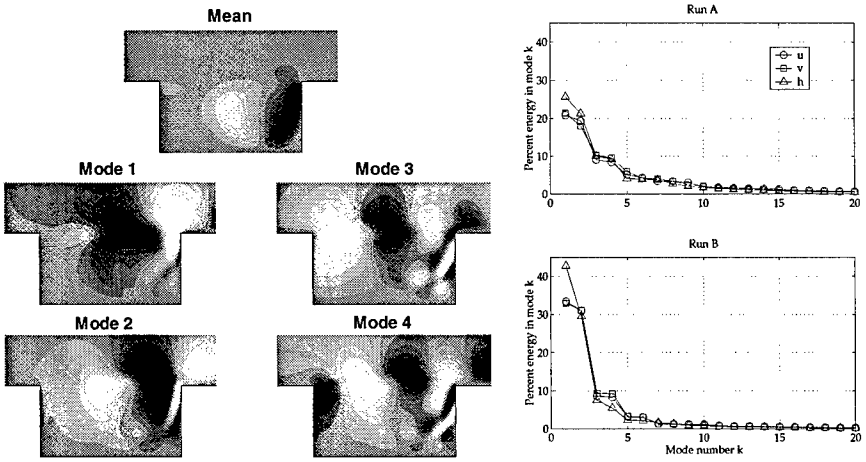

Figure 1: LEFT: Mean and first four POD modes for Run A (Contours of v-velocity.) RIGHT: Percent energy in the fluctuations captured by POD modes for u, v, and h, for two different run conditions. In Run A, the cavity is oscillating in Rossiter modes 1 and 2, and in Run B, the cavity is in Rossiter mode 2.

We now discuss low-order models for the cavity that are determined by severely truncating the Galerkin projection of the POD modes onto the governing PDEs. We consider Run B, which is oscillating primarily in the second Rossiter mode. The initial conditions for all the low-order models discussed here were obtained by projecting a snapshot of the DNS run onto the POD modes. Figure 2 shows how the models behave as we increase the number of modes retained from 2 to 4 to 20. (These correspond to ODEs with 6, 12, and 60 states, respectively, since modes for u, v, and h are taken separately.) Initially, all of the models track well for the first three or four periods. Though it is not apparent in the figure, the 20-mode case follows the DNS the closest for the first period, but later the 2-mode case actually performs best of all. The bottom plot of Figure 2 shows the same data, for a longer time interval, and here it is clear that none of the models correctly predict the amplitude of the oscillation, although the 2-mode model comes closest. This result is disappointing, but is not surprising, since the theory guarantees only that the projected Galerkin system will track the full system for arbitrarily small times, and says nothing about

the global behavior of the low-order model. Also, it is worth pointing out that for many control purposes it is not necessary to have a model which correctly predicts long-time behavior.

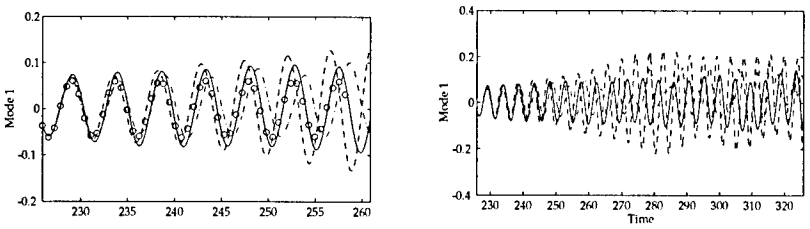

Figure 2: The left plot shows time traces of the first POD mode for u-velocity: Galerkin simulations 2 modes (——), 4 modes (----), and 20 modes (—·—), and projection of DNS (o). Note that only a small region of the DNS near the cavity is used (the computational domain for the DNS extendes to much larger distance from the cavity). The right plot is identical, but for longer time.

We have also investigated how well the model performs at early times when the cavity oscillations are still developing, and have not yet saturated. Since the POD modes were taken after the transients had died out, we would not expect this region of phase space to be as well captured by the projection. We find that the model still tracks the DNS results reasonably well for short times (comparable times to the tracking in figure 2, demonstrating that even though the Galerkin model is accurate only locally in time, it is valid over a relatively large portion of phase space.

A possible reason why the long-time behavior is not better predicted can be understood on physical reasoning. As oscillations grow in amplitude, the mean flow will change, spreading the shear layer, and therefore reducing the growth rate of disturbances. Such an effect is not present in our model, since the spatial shape of the mean and the POD modes is fixed by the snapshots used for the POD. Thus this saturation mechanism (spreading the shear layer) may not be present in our model, and may explain why the model over predicts the final amplitude of the limit cycle. Future work will involve using larger numbers of snapshots taken during transient runs, to attempt to capture those dynamics.

Other important issues to be addressed include closer examination of the effects of the parameters in the equations (particularly L/θ and M). We show here an interesting result that we believe will allow us to exploit the scaling discussed in the last section. Figure 3 shows the mean and first POD mode for runs B and C, which had similar L/θ but L/D different by a factor of 2. The contour levels are identical in the two cases and it can be seen that the modes are quite similar. This behavior is also seen for the other variables, and for the first few POD modes.

Related Work

We briefly mention some related work on cavity oscillations undertaken during the past year. We had previously reported on a transition in the cavity oscillations be-

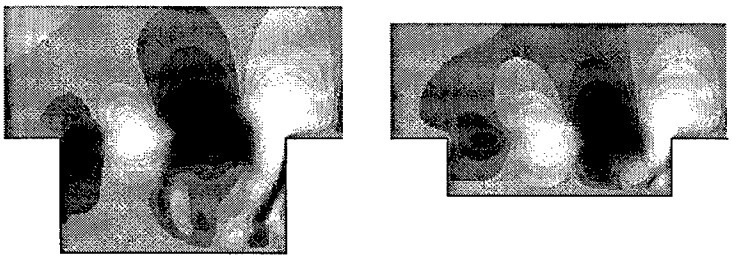

Figure 3: The first POD mode for Runs B with $L/D = 2$ (LEFT) and Run C with $L/D = 4$ (RIGHT). (Contours of v-velocity.)

tween a shear layer mode, which is characterized by acoustic feedback and convective shear layer instabilities, and a wake mode, which is characterized instead by large-scale vortex shedding at a Strouhal number, based on cavity length and freestream velocity, that is independent of Mach number. It appears that the wake mode is the result of a transition from convective instability in the shear layer to absolute instability. The absolute instability arises because for sufficiently large disturbances in the shear layer, a significant flow is induced in the cavity. When this flow is directed upstream in the portion of the cavity near the leading edge, the shear layer may be absolutely unstable. Thus the onset of wake mode should occur under situations where the two-dimensional disturbances in the shear layer grow beyond some critical amplitude. This idea is borne out in detail by predictions we have made based on linear stability theory and a simple model for the acoustic feedback [4]. It appears that at higher Reynolds numbers, and in three-dimensional flow, the shear layer disturbances grow to much lower amplitude (there is much greater spreading of the layer due to smaller scales) than they do in the low Reynolds number 2D flow, and we suspect this is the reason why wake mode has only been observed experimentally at very low Reynolds number. Further details may be found in ref. [4]. Preliminary results that we have obtained for a Large Eddy Simulation of the three-dimensional flow, show that shear layer mode is maintained at much longer L/θ than it is for the corresponding two-dimensional flow [9]. Although turbulence and three-dimensionality serve to suppress the wake mode, we believe that it may still be possible for it to arise in applications (for example in cavities place very near the leading edge). As the drag and internal cavity flow and pressure fluctuations are significantly larger in wake mode, efforts should be made to avoid this parameter regime in design.

Additional Information

Personnel at Caltech supported in part under this grant:

1. Dr. Tim Colonius, Principal Investigator, Asst. Prof. of Mechanical Engineering,
2. Dr. Greg Hernandez, Postdoctoral Scholar
3. Mr. Clarence W. Rowley, Graduate Research Assistant,

Publications resulting from this grant (9/1/99-8/31/00):

1. Rowley, C.W., Colonius, T. and Murray, R.M., "POD Based Models of Self-Sustained Oscillations in the Flow Past an Open Cavity", *AIAA Paper 2000-1969*, 2000.

2. Rowley, C.W. and Colonius, T., "Discretely Nonreflecting Boundary Conditions for Linear Hyperbolic Systems", *Journal of Computational Physics*, **157**, 500-538, 2000.

3. Colonius, T., Basu, A.J., and Rowley, C.W., "On self-sustained oscillations in two-dimensional compressible flow over rectangular cavities", *Submitted to Journal of Fluid Mechanics*, 1999.

Acknowledgment/Disclaimer. This work was sponsored (in part) by the Air Force Office of Scientific Research, USAF, under grant/contract number F49620-98-1-0095. The views and conclusions contained herein are those of the authors and should not be interpreted as necessarily representing the official policies or endorsements, either expressed or implied, of the Air Force Office of Scientific Research or the U.S. Government.

References

[1] Leonard Shaw. Active control for cavity acoustics. AIAA Paper 98-2347, 1998.

[2] L. N. Cattafesta III, S. Garg, M. Choudhari, and F. Li. Active control of flow-induced cavity resonance. AIAA Paper 97-1804, June 1997.

[3] David R. Williams and Drazen Fabris. Closed-loop control in cavities with unsteady bleed forcing. AIAA Paper 2000-0470, January 2000.

[4] Tim Colonius, Amit J. Basu, and Clarence W. Rowley. On self-sustained oscillations in two-dimensional compressible flow over rectangular cavities. *Journal of Fluid Mechanics*, submitted, 1999.

[5] C. W. Rowley, T. Colonius, and R. M. Murray. Pod based models of self-sustained oscillations in the flow past an open cavity. AIAA Paper 00-1969, June 2000.

[6] Philip Holmes, John L. Lumley, and Gal Berkooz. *Turbulence, Coherent Structures, Dynamical Systems and Symmetry.* Cambridge University Press, 1996.

[7] Lawrence Sirovich. Turbulence and the dynamics of coherent structures, parts I–III. *Quarterly of Applied Mathematics*, XLV(3):561–590, October 1987.

[8] A. I. Khibnik, S. Narayanan, C. A. Jacobson, and K. Lust. Analysis of low dimensional dynamics of flow separation. *Notes in Computational Fluid Dynamics*, submitted, 1998.

[9] K-J. Oh and T. Colonius. Large eddy simulation of the compressible flow over an open cavity. Technical Report, July 2000.

Laboratory Annual Task Report FY 00

LRIR:92PR10COR

Title: **Turbomachinery Fluid Mechanics**

Lab Task Manager: **Dr. William W. Copenhaver**

Commercial Phone: 937-255-7163 DSN: 785-7163 FAX: 937-255-1790

Mailing Address: AFRL/PRTF Bldg 18,1950 Fifth St., Wright Patterson AFB OHIO 45433-7251

Email Address: william.copenhaver@wpafb.af.mil

AFOSR Program Manager: **Dr. Thomas Beutner**

Research Objectives: Develop fundamental understanding of the physics of complex turbomachinery flows and their impact on performance, stability and reliability, specifically:

- Quantify and develop flow control strategies for unsteady aerodynamic phenomena, which cause viscous loss, blade vibrations and structural fatigue in transonic compressor rotors.
- Identify and quantify the impact of far field blade rows in multistage compressor configurations involving complex interactions between, passage shocks and blade boundary layers on entropy rise, stability and secondary flows.
- Using computational and experimental methods, formulate and refine theoretical models for blade row interactions that represent the flow phenomena, which cause losses, flow blockage and instability in turbomachinery.
- Refine model improvements through computational studies and experimentation.

Progress for FY 00: The experimental studys of our transonic blade row interaction research have been completed. We have obtained detailed instantaneous velocity field measurements between the IGV and the transonic rotor blade for various IGV/rotor spacings. In addtions we have obtained the rotor exit total pressure and total temperature field. These results confirm a drop in total pressure and efficiency as IGV/rotor spacing decreases. Computational investigations are underway with both steady and unsteady NS solvers to help establish the cause for the reduction in stage performance. One steady solver APNASA and three different unsteady codes are being implemented: MSU Turbo, TSUM3D, and TFLOW by AFRL, NASA Glenn and Stanford respectively. The unsteady solutions have yet to be completed, however the steady results from the APNASA code do demonstrate the same trends as seen in the experiments. The computational results suggest that the additional losses can be attributed to the interaction of the transonic rotor bow wave with the upstream IGV. When spacing is large this interaction is minimal, however when spacing is reduced the influence is substantial. The steady solution shows a 5% increase in power loss at the IGV exit and a 10% increase at the rotor exit when the spacing is reduced.

In addition we have begun to explore the potential for flow control to increase loading capability for short chord stators in compressors. Through a Phase II SBIR we have designed a highly loaded stator blade row with flow control that has a 30% reduction in chord length over conventional designs. The stator was designed using the 3D N/S solver ADPAC developed for NASA at Allison Engine Company. ADPAC has the ability to simulate suction and blowing on the surface of the airfoil, through injections or extractions of mass across predefined grid regions. Cascade studies are underway to validate the computational tools prior to completion of the final design.

In our HCF research, through collaboration with NASA Glenn and Virginia Tech, we have demonstrated the influence of wake filling on downstream rotor structural response. Wakes were filled with an external mass flow source utilizing less than 1% of the core flow, resulting in a reduction of the first torsional resonant response of the rotor of 70%. In addition the acoustic signature of the compressor was measured to establish the potential for active rotor response control utilizing the acoustic signature as a feedback mechanism.

We have also re-iniated a joint effort with the French Government to explore the potential for high response total pressure probe measurements.

Forecast for FY00: We will continue with our stator flow control efforts, with plans to measure the instaneous flow field around our flow controlled stators with the PIV technique developed last year. Design modifications are underway to accommodate the PIV system for use during the flow control experiment. Our goals are to quantify the velocity field around the flow-controlled stator and thereby establish improved design methods for stators with flow control. In addtion, as part of our High Impact Technology program we will begin to explore alternative methods for high-pressure (overall pressure ratio 120) toping systems. The intial investigation will involve acoustic compression methods.

Use of Funds (FY 00, $K):

In House	Capital Equipment	On Site Contractor	Contracts/Grants
115	33 – Experimental/Computational Apparatus	11 Comp. Spec.	
		85 Advanced Diagnostics	10 UTC

Funding Profile:	FY00	FY00	FY01
	$254K	$230	

Appendix A: In-House Activities

- **Task Support**

Air Force Employees

Name	Degree	Discipline	Involvement
William W. Copenhaver	Ph.D.	Internal Aerodynamics and Experimental Methods	30%
Steve Gorrell	Ph.D. Candidate	Internal Aerodynamics and Experimental Methods	50%
David Car	MS	Computational Analysis	10%

On-Site Contractors

Dr. Jordi Esdevadeordal	Diagnostics Expert	100%
Jeff Edwards	Computer Specialist	10%

Visitors

Professor Albin Bölcs	Professor	Laboratory Director EPFL	July 00
Todd Bailey (Virginia Tech)	Ph.D. Candidate	Mechanical Engineer	00-01
Steven Ray (Wright State)	M.S. Student	Mechanical Engineer	99-00
David Clark (Wright State)	M.S. Student	Mechanical Engineer	99-00
Tim Leger (Wright State)	M.S. Student	Mechanical Engineer	99-00
Daniel Atkins (University Dayton)	M.S. Student	Mechanical Engineer	99-00

- **Publications:**

Journal Publication

"Variations in Upstream Vane Loading with Changes in Back Pressure in a Transonic Compressor," D. Probasco, J. Wolff, W. Copenhaver, R. Chriss, ASME Journal of Turbomachinery, July 2000.

"Transonic Compressor Influences on Upstream Surface Pressures with Axial Spacing," P. Koch, D. Probasco, J.Wolff, W. Copenhaver and R. Chriss, AIAA Journal of Propulsion and Power, Vol. 19 No. 5, Sept. 2000.

Kobayashi, H., Leger, T. J., and Wolff, J. M., "Experimental and Theoretical Frequency Response of Pressure Transducers for High Speed Turbomachinery," International Journal of Turbo and Jet Engines, Vol. 17, No. 2, 2000, pp. 153-160.

Articles Accepted for Journal Publication

"Axial Spacing Effects in a Transonic Compressor on the Upstream Vane Loading," D. P.Probasco, J. M.Wolff, W. W.Copenhaver, and R. Chriss, International Journal of Turbo and Jet Engines, June 1999.

"3-D Inlet Guide Vane Generated Vortical Forcing Functions," P. J. Koch, J. Moran, and J. M. Wolff, International Journal of Turbo and Jet Engines, Sept 1999.

Symposium/Conference Papers

"Study of Flow-Field Interactions in a Transonic Compressor Using DPIV", J. Estevadeordal, S. Gogineni, L. P. Goss,W. Copenhaver and S. Gorrell, AIAA-00-0378, January 2000.

"Wake-Filling and Reduction of Rotor HCF Using Stator Trailing Edge Blowing," S.T. Bailie, W.F. Ng, R.A. Burdisso, W.W. Copenhaver, and C.M. Blackwell, AIAA Paper 00-3377, 36th AIAA/ASME/SAE/ASEE Joint Propulsion Meeting, Huntsville, Alabama, July 17-19, 2000.

Three-dimensional structure of turbulent scalar fields with applications in aerooptics

AFOSR Grant F49620-00-1-0036

Paul E. Dimotakis
Aeronautics and Applied Physics
California Institute of Technology, Pasadena, CA 91125

Christopher Martin
Physics
California Institute of Technology, Pasadena, CA 91125

Abstract

This research is focused on fundamental investigations of the three-dimensional structure of scalar fields in turbulent flows and its applications to aerooptics and the propagation of light beams through a turbulent medium, in general. This effort begun in January 2000 with a first task targeting ground-based astronomical observations and optical propagation through atmospheric turbulence. A first set of experiments was undertaken on the Caltech Palomar 5 m telescope, in May 2000. The work is comprised of several related investigations. Key to these is high framing rate digital imaging; an essential component of the instrumentation for all investigations part of this research.

The Palomar experiments

In an attempt to obtain diffraction-limited images with ground-based telescopes, astronomers have developed both active and passive systems. Active correction techniques broadly fall into the category of adaptive optics, which is enjoying intensive current research. However, adaptive optics faces some hurdles before its techniques migrate to visible wavelengths. Passive systems can themselves be divided into pupil-plane interferometry and focal-plane interferometry. Focal-plane interferometry, particularly speckle interferometry, is relatively simple to implement. However, traditional speckle interferometry suffers from a need for frequent calibration and unquantifiable systematic effects. Non-redundant speckle masking eliminates many systematic errors, but only uses a small fraction of the light-collecting power of the telescope. Pupil-plane interferometry has the capacity for diffraction-limited images in visible light, using the entire telescope pupil, without the need for external calibration.

Previous experiments in pupil-plane interferometry have not achieved these goals, owing to a variety of shortcomings. Most pupil-plane interferometers have been rotation-shearing interferometers, where two copies of the telescope pupil are rotated relative to one another and recombined. The resulting interferogram intensity depends on the amplitudes, visibility modulus, and phase difference of the combined pupil locations. Some previous experiments introduced a phase gradient (tilt) in the interferogram, and

interpreted deviations from a sinusoidal signal as phase differences. Others have introduced a modulated phase term over the entire pupil (piston), and obtained a full quadrature phase measurement by combining sets of 4 measurements. The phase-gradient interferometers cannot distinguish amplitude fluctuations from visibility and phase differences. Path-length-modulated interferometers are unreliable when the modulation frequency is less than the frequency set by atmospheric motions. These shortcomings have pointed to the need for an instantaneous measurement of the full complex visibility (amplitude, visibility modulus, and phase difference).

A 180-degree rotation shearing pupil-plane interferometer was implemented, that measures the full complex visibility over the entire pupil in a single exposure. Two important developments were employed. The first is a Mach-Zender arrangement, rather than a Michelson arrangement, for the beam-combining optics. Regardless of the geometry of the beam combiners, there are two complementary interferograms, whose phase differences differ by 180 degrees. This is ensured by conservation of energy; where one interferogram is brighter due to interference, the other interferogram is fainter. In a Michelson arrangement, one of these two interferograms is reflected back out through the telescope. In a Mach-Zender arrangement, both interferograms are available to be imaged. Having both interferograms permits their summation to determine the amplitude of the incident wavefronts, independent of any interference effects. Another way to visualize the difference between arrangements is to recognize that the maximum efficiency of a Michelson arrangement is 50%, while a Mach-Zender arrangement can achieve 100%.

The second development is to introduce a quarter-wave phase shift in half of each interferogram. Since 180-degree rotational shear is used, each interference pair appears twice on each interferogram. For every point in an interferogram, the diametrically opposed point is produced by interfering the same two points in the pupil, in the opposite sense, *i.e.*, comparing Point B with Point A instead of Point A with Point B. Since the intensity of an interference pair is a commutative function with respect to the pair of operands, the intensity of diametrically opposed points in an interferogram is identical. This redundancy is exploited by introducing a path-length-difference of one quarter-wave in half of each interferogram. In this fashion, diametrically opposed points in an interferogram are no longer identical; rather, they differ in phase by 90 degrees. Since the two interferograms differ in phase by 180 degrees, and each interferogram displays each interference pair with both 0 and 90 degrees of phase shift, we have a full quadrature-phase measurement (*i.e.*, 0, 90, 180, 270 degrees of path-length-difference) for every interference pair in the pupil. An attempt to render the optical geometry of the instrument is depicted in Fig. 1.

There are several limitations in this instrument. The two most serious limitations are spectral coherence and temporal coherence. To see interference over large atmospheric phase differences, the spectral bandwidth must be small. For instance, assuming an r_0 of 10 cm across the Palomar 5 m pupil, the rms phase difference between the most-distant interference pairs is $[6.88\ (D/r_0)^{5/3}]^{1/2}$ radians = 11 waves. This means that the fractional bandwidth must be less than 1/11 to maintain coherence at the interferogram edges.

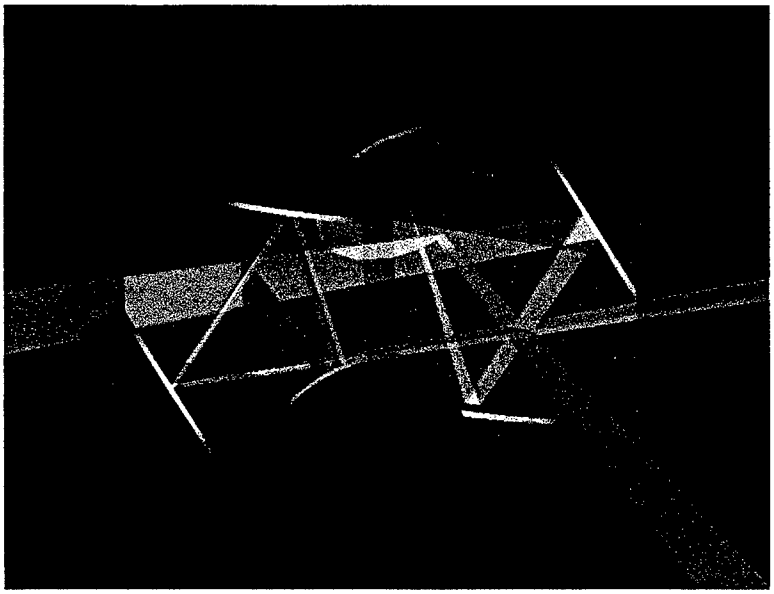

Fig. 1 Shearing interferometer optics

To avoid smearing as the atmosphere moves its "phase screen" across the telescope pupil, exposure times must be kept short, $t < r_0/U$, where U is the wind velocity. An r_0 of 10 cm and U = 10 m/s imply a maximum exposure time of 10 ms. In practice, the spatial resolution in the interferogram is better than r_0, so, to maintain that resolution, even shorter exposure times are needed. We operated at both 50 Hz and 100 Hz, with a 50% duty cycle, corresponding to 10 ms and 5 ms exposure times to permit comparisons.

In addition to the two interferograms, a simultaneous (aberrated) in-focus image was also recorded. This allows two things: it facilitates target acquisition and guiding, and allows monitoring of the wave-front reconstruction. A good measurement of the wave-front phase distribution permits checking that the point-spread function associated with that distribution matches what is measured in the in-focus image. To the best of our knowledge, this has not been done in any previous rotation shearing interferometers.

To record the two interferograms and the in-focus image simultaneously, the active (1024×1024)-pixel area of the CCD is divided into 4 quadrants, each of 512×512 pixels (one quadrant is unused). An image mask 4 arcsec in diameter is used, to avoid corrupting the interferograms with light from the in-focus image. In readout, on-chip binning is employed to reduce the effective number of pixels to 256×256 per quadrant, yielding an interferogram resolution of 2 cm/pixel on the Palomar 5 m telescope, and an in-focus image scale of 16 milli-arcsec/pixel.

With the quadrature-phase interferograms and the in-focus images, the visibility phase of our diffraction-limited images is obtained by integration of phasor gradients. As a result of an interferogram resolution better than r_0 (2 cm/pixel relative to a ~10 cm r_0), neighboring pixels do not suffer from phase wrapping (phase differences comparable to 2□). By averaging phasor gradients over many frames, the atmospheric contribution to the phasor gradients disappears, leaving only the phasor gradients of the diffraction-

limited image. The amplitude and visibility modulus are recorded unambiguously in each individual frame.

The interferometer, as described, operates as a standard stellar interferometer, observing stellar discs and close binary stars, with some capacity to observe circumstellar environments (protoplanetary discs, young stellar objects). There are two immediate descendents of this interferometer, which greatly expand the available science goals. The first will incorporate a standard spectral dispersion element and a lenslet array, which will enable it to cross-correlate broad emission lines in active galactic nuclei and measure the physical size of the broad-line region. The other direction planned for a second-generation interferometer incorporates a lenslet array and a novel refractive chromatic dispersive lens, to obtain wide-field (~10 arcsec) diffraction-limited images, enabling the use of a natural guide star to measure atmospheric phase aberrations, while observing a fainter science object. This interferometer can function as a replacement for adaptive optics in the visible, obtaining wide-field diffraction-limited images of faint (V ~ 21-25) objects.[1] The Palomar experiments were performed in May 2000. Acquired image-data required several hundred Gigabytes of storage. Their processing is in progress.

Digital-imaging instrumentation

Experiments in progress rely on two digital-imaging systems. The first is a moderate framing rate camera (10-20 fps), dubbed the Cassini camera, developed in collaboration with JPL, which relies on a CCD developed for NASA's Cassini mission, completed four years ago. The second is the recently completed kilo-frame per second system, dubbed the KFS system, which uses a high-speed multi-channel CCD (KFS CCD), also developed in collaboration with JPL. Both systems rely on 1024^2 CCD focal-plane arrays. System design and integration for both systems was by Daniel Lang. The first (raw) images obtained (December 1999), using the KFS system, are depicted in Fig. 2.[2]

The KFS CCD is a full-frame CCD.[3] Its 32 output channels allow it to acquire up to 1000 full-resolution images per second. In the Palomar experiments, low readout noise is of paramount concern. The system was operated at both 50 and 100 fps. 2×2 binning was employed for a (512×512)-pixel resolution.

---

[1] The interferometer and associated image-forming/-acquisition system was designed and implemented by Brian Kern, in collaboration with Christopher Martin and Paul Dimotakis. The optical system was developed with support by NSF Grant AST9618880 and the present AFOSR Grant, F49620-00-1-0036.

[2] The KFS digital-imaging system was developed in collaboration with JPL, under sponsorship by a DURIP Grant F49620-95-1-0199 and completed under sponsorship by AFOSR Grants F49620-98-1-0052 and F49620-00-1-0036, and NSF Grant AST9618880.

[3] The KFS CCD was developed by Mark Wadsworth, in collaboration with S. A. Collins and S. T. Elliott at JPL, and Daniel Lang, Paul Dimotakis and Chris Martin at Caltech, following a preliminary design by James Janesick while he was at JPL.

For the Palomar experiments, time aperture was provided with a chopper wheel in the light path to block off light during the readout interval. The chopper wheel has a 50/50 on/off duty cycle and was synchronized to the CCD timing controller using a phase-locked loop which also provided a variable offset between the chopper sync signal and the CCD readout sequence. The beam diameter is approximately 2% of the blade arc so the readout time was set to be less than 0.48 of the chopper period. A readout time of 8 ms was used at 50 fps, and a 4 ms readout time was used at 100 fps.

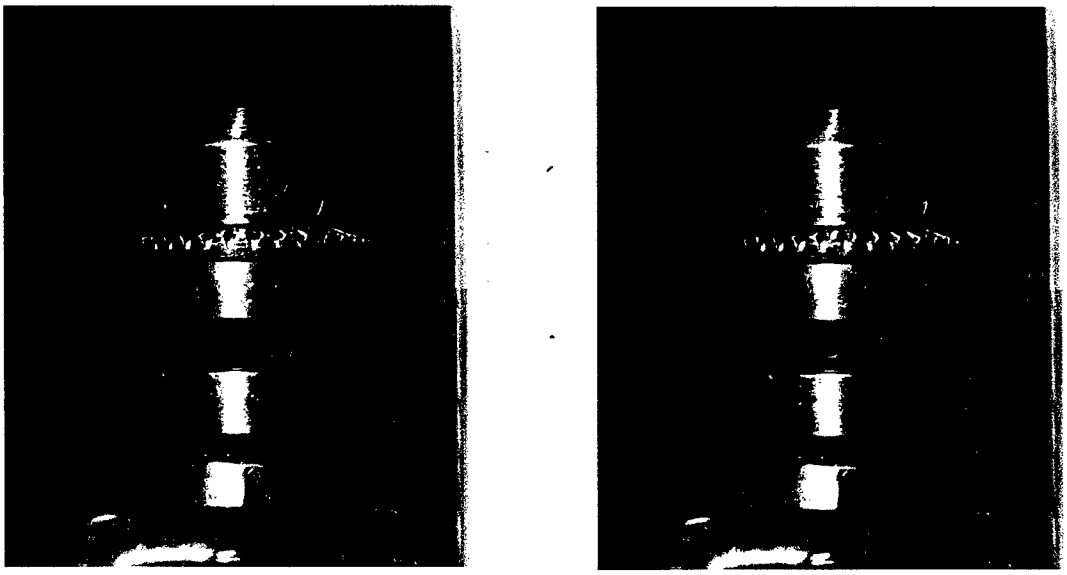

Fig. 2 First KFS-CCD images of spinning drill chuck. Synchronized strobe-light illumination, 1024^2-pixel frames, 12-bits/pixel, 50 frames/s (raw CCD data).

The camera head contains local voltage regulators and 32 output amplifiers, one for each output channel.[4] The camera head is attached to a LN2 dewar and the entire assembly is evacuated. The CCD is cooled using a copper spring foil that attaches to a rod going to the LN2 dewar.[5] A temperature of 0 °C was sufficient to reduce dark current noise to negligible values at these frame rates. A readout noise of, approximately, 30 e's/pixel was achieved at these frame rates.

The image-data acquisition system is a follow-on of the acquisition system used for the Cassini camera and. It was designed and implemented by Daniel Lang, in collaboration with Paul Dimotakis. It consists of a PC controlling a VXI crate with the CCD power controller, CCD timing controller, and eight 4-channel A/D converter boards, each capable of 40 MHz sampling rate, for a total of 32 channels and an aggregate data-acquisition rate in excess of 10^9 samples/s. The CCD power controller provides power to the CCD camera and controls the mechanical shutter. The CCD timing controller provides timing signals for the CCD camera head, the A/D converter, and the chopper

[4] The camera-head housing was designed by Pavel Svitek, in collaboration with Daniel Lang, Paul Dimotakis, and Brian Kern.

[5] The camera-housing cooling system was designed by Brian Kern, in collaboration with Pavel Svitek and Daniel Lang.

wheel phase-locked loop. The 4-channel A/D converter boards include programmable gain, offset, low-pass filters, and correlated double-sampling (CDS). The CDS stage samples the CCD outputs after the outputs have been reset and again after the charge signal has been transferred and takes the difference of the two. The CDS stage eliminates the CCD reset noise and reduces the effect of $1/f$ noise. The signals are then digitized by 12-bit 40-MHz A/D converters (4 per board), compressed using lossless real-time compression algorithm, and stored in high-speed Dynamic RAM (DRAM). Each A/D board contains 512 Megabytes of DRAM for a total of 4 Gigabytes of DRAM. This allows approximately 20,000 (512×512) frames to be recorded in real-time.

The PC provides overall control of the experiment, displays acquired images, and records the acquired data to disk. Since the data acquisition runs can by fairly long (20,000 frames at 50 fps = 400 seconds), some means must be provided to ensure that the telescope properly tracks the target star during the Palomar measurements. The attendant data rate is too high for the PC to process in real-time. To get around this problem, the PC takes a snapshot of the A/D boards and reads in the most recently acquired image. It then processes and displays the image. This cycle is repeated, displaying approximately one out of 50 frames, at approximately 1 fps.

Other work

Other work in progress is focusing on the 2- and 3-D structure of scalar fields derived from transverse jets in a cross flow as well as in turbulent flow behind a grid. Their primary emphasis is on mixing and the resulting spatial-spectrum behavior. They are conducted in water flow facilities and rely on laser-induced fluorescence (LIF) techniques and the Cassini and KFS digital-imaging systems.

Acknowledgment/Disclaimer

This work was sponsored (in part) by the Air Force Office of Scientific Research, USAF, under grant number F49620-00-1-0036. The views and conclusions presented are of the authors and do not necessarily represent official policies or endorsements, expressed or implied, of the Air Force Office of Scientific Research, or the U.S. Government.

Personnel

Paul E. Dimotakis	J. K. Northrop Prof. of Aeronautics and Prof. of Applied Physics
Brian Kern	Graduate student, Physics
Susan L. Kolden	Administrative Assistant, Aeronautics
Christopher Martin	Professor of Physics
Daniel B. Lang	Engineer, Aeronautics
Murphy Wang	Graduate Research Assistant, Aeronautics

All personnel supported part time.

AEROSPACE TURBOMACHINERY FLOW PHYSICS

AFOSR Grant F49620-00-1-0014

A.H. Epstein, E.M. Greitzer, G.R. Guenette, J.L. Kerrebrock, J. Paduano, C.S. Tan,
R. Keogh, A. Khalak, D. Vo
Gas Turbine Laboratory,
Massachusetts Institute of Technology

1.0 Abstract

The primary barriers to achieving increased quality of aerospace turbomachinery devices are linked to local phenomena, which are inherently three-dimensional and/or unsteady. The objective of this multi-investigator program is to address issues associated with unsteady and three-dimensional flow phenomena in the following technical areas:

1) Stall flutter in aircraft engine compressors and forced excitations at the high pressure of rocket turbopump turbines.

2) Tip clearance flow effects in axial and centrifugal turbomachines.

3) Physics of coolant/main flow interactions in advanced aircraft/rocket turbines.

4) Use of an active rotor to delineate parametric dependence of aerodynamic damping.

Progress made during the period October 1, 1999 to June 31, 2000 is described in Section 2.0 entitled "Parametric Dependencies of Aeroengine Flutter for Flutter Clearance Applications", Section 3.0 entitled "Influence of Film Cooling on the Aerodynamic Performance of Fully Scaled Turbine Stage", and Section 4.0 entitled "Unsteady Phenomena in Axial Turbomachinery Endwall Flows: Role of Blade Passage Flow Structures in Axial Compressor Rotating Stall Inception."

2.0 Parametric Dependencies of Aeroengine Flutter for Flutter Clearance Applications

Successful aeroengine designs must be free from turbomachinery flutter under all operating conditions. Flutter is a vibrational instability of the rotor blades, which can rapidly promote High Cycle Fatigue (HCF) failure. If not caught during testing, flutter problems have the potential to impact Air Force readiness on a fleet-wide basis [1].

The current work addresses the problem of constructing a rational testing procedure to insure flutter clearance, throughout the operational flight regime of a turbomachine. In so doing, a new set of similarity parameters has been developed for operability assessment. This set consists of four parameters: (m_c, N_c, K_0*, g/ρ*), where the first two parameters are the corrected mass flow, m_c, and corrected rotor speed, N_c, and the latter two parameters are new, which we term the compressible reduced frequency, K_0*, and the reduced damping, g/ρ*.

The reduced damping, g/ρ*, combines the mechanical damping, g, and the mass ratio, μ, into a single non-dimensional parameter, useful for linear stability purposes. This

parameter, is defined as

$$\frac{g}{\rho^*} = \frac{gm_0}{c^2\rho_0} = \frac{4}{\pi}g\mu$$

where m_0 is the modal mass (per unit length), c is the chord, and ρ_0 is the inlet density. The g/ρ^* label emphasizes the dependence upon inlet density. For cases with frictional damping (*e.g.* inserted blades), the reduced damping is order 1 and has a significant impact on flutter stability.

The compressible reduced frequency, K_0^*, is defined as $\omega_0 c/(\gamma RT)^{1/2}$, where ω_0 is the blade natural frequency at rest, and $(\gamma RT)^{1/2}$ is the inlet speed of sound (which varies with inlet temperature, T). The K_0^* parameter comes out from a decoupling of corrected performance effects from purely aeroelastic effects. Roughly speaking, for a constant structure (*i.e.* constant $\omega_0 c$) the parameter K_0^* varies with the temperature, a parameter for which the performance is "corrected."

The first two parameters of the set, m_c and N_c, account for the corrected performance, as normally measured for high speed turbomachines. For constant structural parameters, the latter two parameters, K_0^* and g/ρ^*, span the inlet temperature and density. These can be related to the flight conditions in terms of flight Mach number and altitude. An implication of this four-parameter viewpoint is that the flutter clearance of a machine depends not only upon corrected performance point, but also upon the flight envelope of the aircraft of intended use.

These parameters were applied to the analysis of full-scale test data provided by the Volvo Corporation. Figure 1 shows the trends with K_0^* and g/ρ^*. Both increasing K_0^* and increasing g/ρ^* (at constant m_c and N_c) have stabilizing effects upon flutter stability. We propose that these trends hold generally. The trend with g/ρ^* is analytically based in

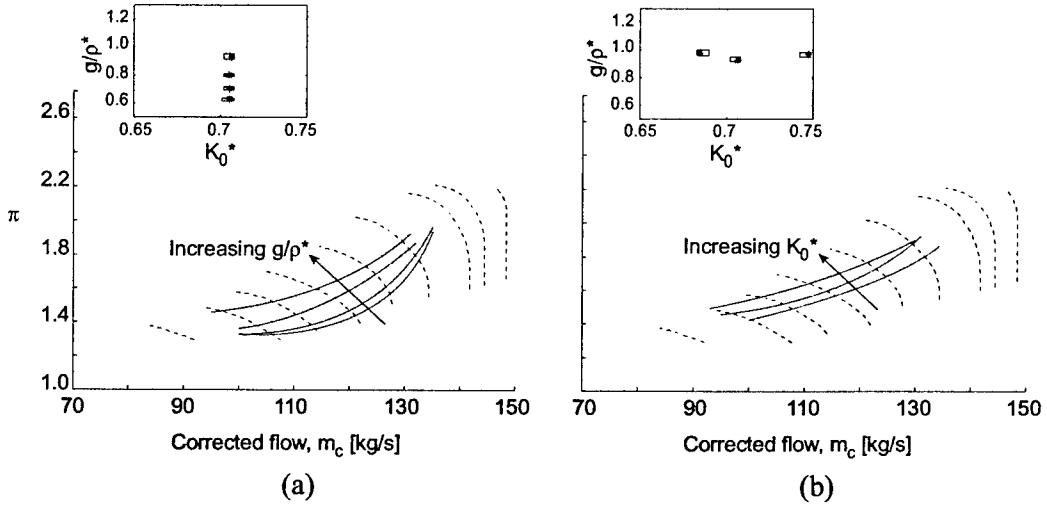

Figure 1: Trends of performance map flutter boundary with changes in K_0^* and g/ρ^* from full-scale engine data. Figure (a) shows the effect of varying g/ρ^*, and (b) shows the effect of varying K_0^*. Increases in both K_0^* and g/ρ^* are stabilizing.

the equations of motion, and is equivalent (by similarity) to the statement that increasing the mechanical damping is stabilizing. The trend with K_0* is ultimately empirical, but it is supported by several previous studies and is equivalent (by similarity) to the widely-held design principle that increasing the natural frequency stabilizes flutter.

With the relevant similarity parameters spanning a four-dimensional space, the range of comprehensive testing is vast. The proposed trends with K_0* and g/ρ*, however, suggest a way to simplify the requirements for comprehensive testing. Since increasing K_0* and increasing g/ρ* are both stabilizing, it follows that the worst case at a particular (m_c, N_c) are the minimum values of K_0* and g/ρ*. Thus, clearance for the engine at the minimum K_0* and g/ρ* imply clearance throughout the entire flight regime.

3.0 Influence of Film Cooling on the Aerodynamic Performance of Fully Scaled Turbine Stage

This section outlines the results of an experiment to measure the influence of film cooling on the performance of a fully scaled high-pressure turbine stage. The goal of the experiment was to measure the influence of film cooling on the isentropic efficiency and corrected mass flow of a high-pressure turbine stage. A baseline turbine stage without film cooling was tested over a range of operating conditions (corrected speeds and pressure ratios). The stage was then modified to incorporate vane, blade, and casing film cooling. The turbine stage was then tested to measure the performance changes that can be attributed to film cooling. The film-cooled stage was tested over a range of operating conditions and coolant flow conditions. The coolant was varied from 4% to 12% of the inlet mass flow for mainstream-to-coolant temperature ratios of 1.6 and 1.1.

A representative result in Figure 2 elucidates the change in isentropic efficiency as a function of coolant-to-mainstream mass flow ratio; at the design coolant mass flow ratio of 10% the isentropic efficiency of the stage is reduced by 2%. Measurements also indicate that the change in performance due to film cooling is strongly dependent on the

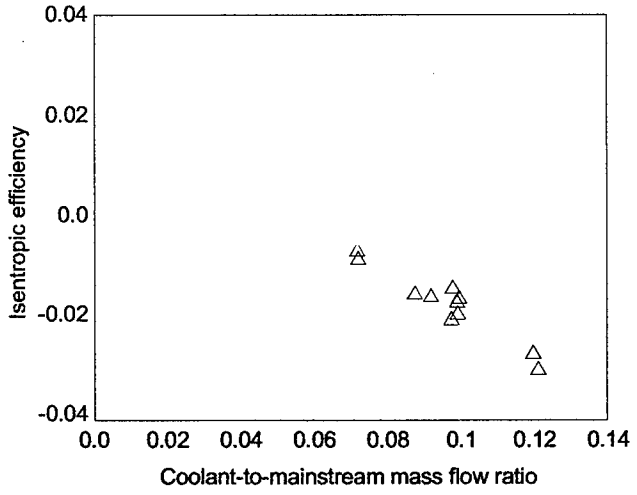

Figure 2: Change in isentropic efficiency as a function of coolant-to-mainstream mass flow ratio.

turbine operating point. Specifically, at high-corrected speeds the loss due to film cooling is significantly reduced, whereas at high-pressure ratios the loss due to film cooling is increased.

The results of the experiments are currently being analyzed to give a detailed breakdown of the loss mechanisms that contribute to the observed change in performance between the baseline and film-cooled measurements. A major issue being addressed is the degree to which non-cooling losses are changed as a result of film cooling. Film cooing increases the reaction of the stage, which in turn will reduce the stage profile and endwall losses. This will offset some of the loss due to the mixing of the mainstream and coolant, and the cooling system pumping losses.

4.0 Unsteady Phenomena in Axial Turbomachinery Endwall Flows: Role of Blade Passage Flow Structures in Axial Compressor Rotating Stall Inception

A key objective here is to establish the link between blade passage flow events (particularly the tip clearance flow and the casing boundary layer) and rotating stall inception to enable the quantitative delineation of the physical parameters that control rotating stall. Recently, three-dimensional single and multi-bladed computations of an isolated compressor rotor (E3 blading) by Hoying [2] showed that the central feature of the flow associated with the development of short length-scale (spike) stall inception was the tip clearance vortex moving forward of the blade leading edge. Vortex kinematics arguments were used to provide a physical explanation of this motion and also to explain why the tip vortex trajectory at the leading edge of the compressor sets compressor stability. However, the generic nature of the deduction/hypothesis based on these computed results has been challenged by experimental and computational data on the Whittle Laboratory low speed compressor [3], which show that the tip vortex trajectory is not at the rotor leading edge at (spike) stall inception. In the past year the research effort has been focused on addressing this difference and examining conditions for which other blade passage flow event (different from that based on tip leakage vortex trajectory at the leading edge) could set the stall inception.

Additional single blade passage calculations have been carried out for the same compressor rotor but with tip clearance varying from 0.6% to 2.0% axial chord. Post processing of the newly computed results and further interrogation of Hoying's computed results (for single blade passage as well as multi-blade passage) indicated that at stall inception, the tip leakage vortex is not at the leading edge but rather it is the front edge of the vorticity field associated with the tip clearance flow (*i.e.* the interface demarcating the tip clearance flow and incoming flow) that is at the blade tip leading edge. In addition, the stability criteria based on tip leakage vortex trajectory at the leading edge is valid only for relative flow axial to the rotor, which is normally not the case for compressor.

For the newly computed results the interface between the tip clearance flow and the incoming flow reaches the rotor tip leading edge plane at the lowest flow coefficient for which a steady state solution can be obtained (for tip clearance size ranging from 0.6 % to 2.0 % of blade chord). Other data supports this observation. Among them are experimental casing oil flow field from a low-speed compressor exhibiting spike stall inception and its corresponding cascade by Saathoff *et al.* [4]. Computational results of high-speed rotors by Hoeger *et al.* [5] and Adamczyk *et al.* [6] also point to the incoming/tip clearance flow interface being at the leading edge plane at the lowest flow

coefficient for which a steady state solution is possible. If the throttle is closed past the lowest flow coefficient, our computations shows tip clearance flow spillage on the pressure side towards the adjacent blade passage, as evidenced in cascade casing oil flow from Saathoff *et al.* [4] and in a computational tip flow field in a low speed rotor at short length-scale stall inception by Hah *et al.* [7]. Representative result from the present calculation, from the flow visualization in [4] and from the computations in [7] is shown in Fig. 3; they indicate the incoming/tip clearance flow interface at the leading edge plane (at the lowest flow coefficient for which a steady state solution is possible or at spike stall inception).

These observations lead to a flow breakdown criteria based on the incoming flow/tip clearance flow interface being at the rotor tip leading edge plane on the blade passage pressure side. The hypothetical explanation behind the criteria is that any flow reduction causes spillage, thus increasing the incidence and loading on the blade tip, intensifying the tip clearance flow and leading to further flow spillage. This is hence an unstable flow situation.

However, a computational case with large tip clearance indicates a flow breakdown without the incoming/tip clearance flow interface reaching the rotor leading edge plane. In contrast to the smaller clearance situations, there is a large rate of increase in tip blockage with respect to mass flow reduction at or near lowest flow coefficient for which a steady state solution is possible. This could possibly implicate tip blockage as playing a role in setting the flow breakdown.

The above observations and hypothesis, while plausible, have to be put on a rigorous and quantitative basis. To do so we need to implement the following research tasks: (1)

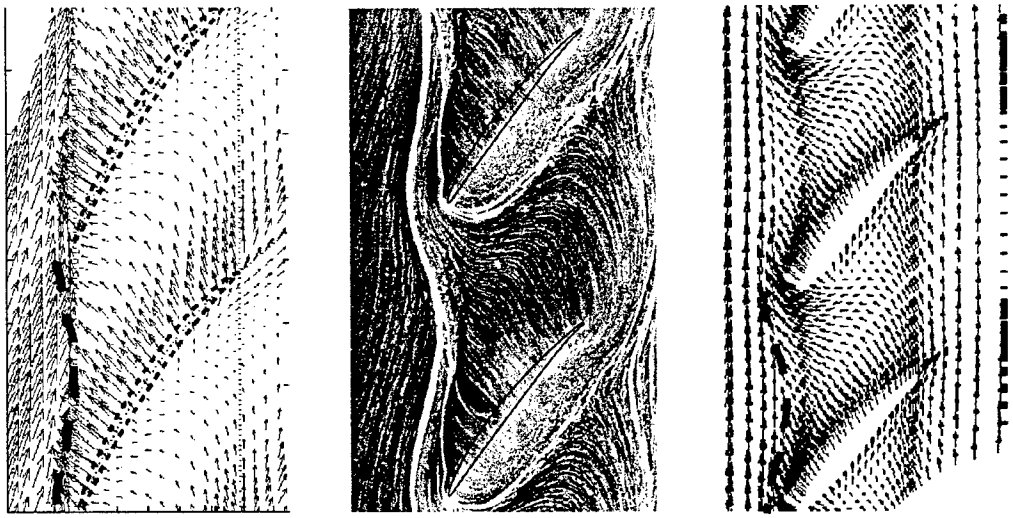

Figure 3: Tip clearance flow past the last steady solution in our computation (left) compared to those for highest pressure rise point in cascade [4] (center) and initial spike disturbance formation in full rotor computations [7] (right); dashed lines indicate estimated incoming/tip clearance flow interface.

Contrast single-blade passage results against multi-blade passage results and establish the utility of single-blade passage calculation for stall inception prediction; (2) Interpret/ explain the instability of incoming/tip clearance flow interface at leading edge plane on a physical basis; (3) Establish the generic nature of hypothesis with respect to tip clearance size and compressor characteristics; and (4) Ascertain the role of blockage due to tip leakage flow on stall inception, specifically the conditions for which this is the case.

Acknowledgement/Disclaimer

This work was sponsored (in part) by the Air Force Office of Scientific Research, USAF, under grant number F49620-00-1-0014. The views and conclusions contained herein are those of the authors and should not be interpreted as necessarily representing the official policies or endorsements, either expressed or implied, of the Air Force Office of Scientific Research or the U.S. government.

References

1. S.E. Kandebo, F100-PW-229 Failures Affect F-15E Readiness, *Aviation Week and Space Technology*, June 27 1994.

2. D.A. Hoying, C.S. Tan, H.D. Vo and E.M. Greitzer, Role of Blade Passage Flow Structures in Axial Compressor Rotating Stall Inception, *ASME Journal of Turbomachinery*, Vol. 121, 1999, pp. 735-742.

3. P. Seitz, Private Communication, Whittle Laboratory, Cambridge University, UK, 1999.

4. H. Saathoff and U. Stark, Tip clearance Flow Induced Endwall Boundary Layer Separation in a Single-Stage Axial Low-Speed Compressors, *ASME Paper 2000-GT-0501*, 2000.

5. M. Hoeger, G. Fritsch and D. Bauer, Numerical Simulation of Shock-Tip Leakage Vortex Interaction in a HPC Front Stage, *ASME Journal of Turbomachinery*, Vol. 121, 1999, pp. 456-468.

6. J.J. Adamczyk, M.L. Celestina and E.M. Greitzer, The Role of Tip Clearance in High Speed-Fan Stall, *ASME Journal of Turbomachinery*, Vol. 115, 1993, pp. 28-39.

7. C. Hah, R. Schulze, S. Wagner and D.K. Hennecke, Numerical and Experimental Study for Short Wavelength Stall Inception in a Low-Speed Axial Compressor, Paper ISABE 99-7033, presented at 14th ISABE, Florence, Italy, 1999.

Personnel Supported

Graduate Students: A. Khalak, R. Keogh, D. Vo

Faculty and Research Staff: A. Epstein, E. Greitzer, J. Guenette, J. Kerrebrock, J. Paduano, C. Tan

Administrative Support Staff: H. Anderson, L. Martinez, D. Park, J. Proudman

Publications

"Aerodynamic Performance Measurements of a Fully-Scaled Turbine in a Short Duration Facility," R.C. Keogh, G.R. Guenette, and T.P. Sommer, ASME paper 2000-GT-0486, 2000.

NUMERICAL INVESTIGATION OF THE CONTROL OF SEPARATION FROM CURVED AND BLUNT TRAILING EDGES USING DNS AND LES

AFOSR Grant Number F49620-00-1-0069

Abstract

by

Hermann F. Fasel
Department of Aerospace and Mechanical Engineering
The University of Arizona
Tucson, AZ 85721

Submitted to

The Air Force Office of Scientific Research

July 2000

NUMERICAL INVESTIGATION OF THE CONTROL OF SEPARATION FROM CURVED AND BLUNT TRAILING EDGES USING DNS AND LES

AFOSR GRANT F49620-00-1-0069

Hermann F. Fasel
Department of Aerospace and Mechanical Engineering
The University of Arizona, Tucson

Abstract

In a numerical/theoretical effort, we are investigating the control of separation using periodic excitation. Extensive experimental research by Wygnanski and co-workers (Wgynanski 1997) has provided considerable evidence that periodically forced wall jets (tangential oscillatory blowing) may be an effective method for the control of separation of flows over single-element or segmented airfoils (including flaps). However, many of the fundamental mechanisms that are responsible for the often striking effect of periodic excitation on separating flows are still not understood. In particular, experiments have shown that wall curvature, both convex and concave, as well as tangential blowing (or local suction), may have a puzzling effect on the efficiency of periodic excitation; in certain instances the effect of periodic excitation may be enhanced while in other situations it can be diminished. Therefore, in close collaboration with on-going and planned experimental efforts by Wygnanski and co-workers, we are performing direct numerical simulations (DNS), large-eddy simulations (LES), and unsteady Reynolds-Averaged Navier-Stokes calculations (URANS) for some key configurations that are prototypical for the use of active flow control in future practical applications. Examples for which the present and future investigations will be relevant are airplanes and rockets at large angles of attack where, without separation control, massive separation would occur. The work described is a continuation of a research effort funded previously by AFOSR, where the major emphasis has been on separation prevention for a flat plate geometry using steady and pulsed tangential blowing (weak wall jet). The focus of the present research is on curved wall geometries with the objective to determine the influence of wall curvature on the generation and development of the large coherent structures in the forced flow.

Over the past decade, a great amount of experimental work has been performed by Wygnanski and coworkers (Wygnanski 1997) which clearly demonstrates the effectiveness of using pulsed wall jets for delaying separation. In Figure 1, four of their experiments are illustrated that we are considering for our numerical investigations. In the slotted flap experiment by Seifert et al. 1993 (Figure 1a), separation control is achieved by steady wall blowing (weak wall jet), and the effectiveness was significantly improved by additional periodic forcing. This flow geometry is very complex, since effects of adverse pressure gradient and curvature are present simultaneously. In contrast, curvature effects do not play a role for a flat trailing edge flap (Figure 1c) as investigated by Seifert et al. (1993). In the experiments by Neuendorf and Wygnanski (1999) on a Coanda cylinder (Figure 1b), the effect of curvature on a forced wall jet was studied separately. As these experiments have convincingly shown, longitudinal

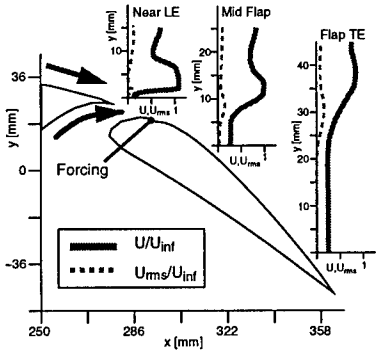

a) Experiment by Seifert et al. (1994)

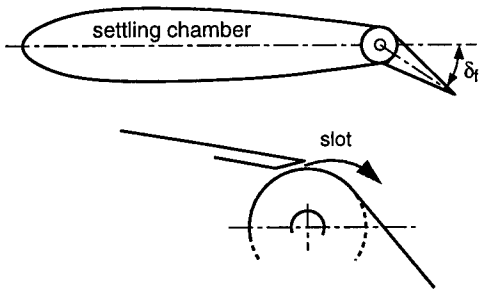

b) NACA 0015 airfoil with slotted flap from experiments by Seifert et al. (1993)

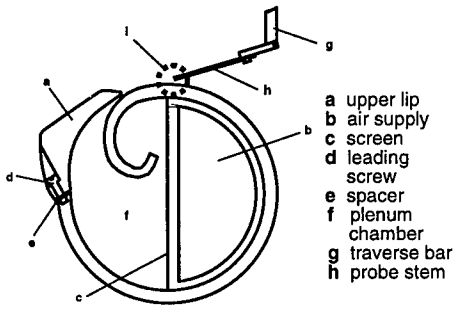

c) Schematic of Coanda cylinder experiment by Neuendorf and Wygnanski (1999)

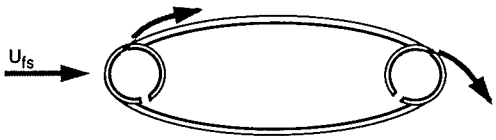

d) Schematic of experiment by Wygnanski and coworkers, currently in preparation

Figure 1: Experiments on active separation control by Wygnanski and coworkers considered for planned numerical investigations.

vortices of the Görtler type arise in the flow by virtue of a centrifugal instability mechanism. This 3-D mechanism can compete with the 2-D instability of the outer shear layer and therefore reduce the efficiency of 2-D periodic forcing. A new experiment by Wygnanski and coworkers that is currently being set up (Figure 1d) incorporates Coanda cylinders into the leading and the trailing edge of an elliptical airfoil. This enables to systematically investigate the effects of curvature as well as the actuator location on control efficiency.

The goal of the present numerical research effort is (with the aid of the findings from the experiments shown in Figure 1) to uncover the governing physical mechanisms responsible for the striking effect of oscillatory blowing on separation, and thus provide the physical understanding required to further develop this technique for practical use. Towards this end we are performing simulations using simplified model geometries, as shown in Figure 2, that allow us to isolate the relevant competing mechanisms in this complex flow problem. During the previous research project funded by AFOSR (until November 1999) we have focussed on turbulent weak wall jets on a flat plate without and with a free stream pressure gradient (Figure 2a). In the straight flap geometry shown in Figure 2b, the geometry effect of the flap deflection is included without introducing instability mechanisms due to wall curvature. This extension will enable us to match closely the straight flap experiments from Figure 1b. The effect

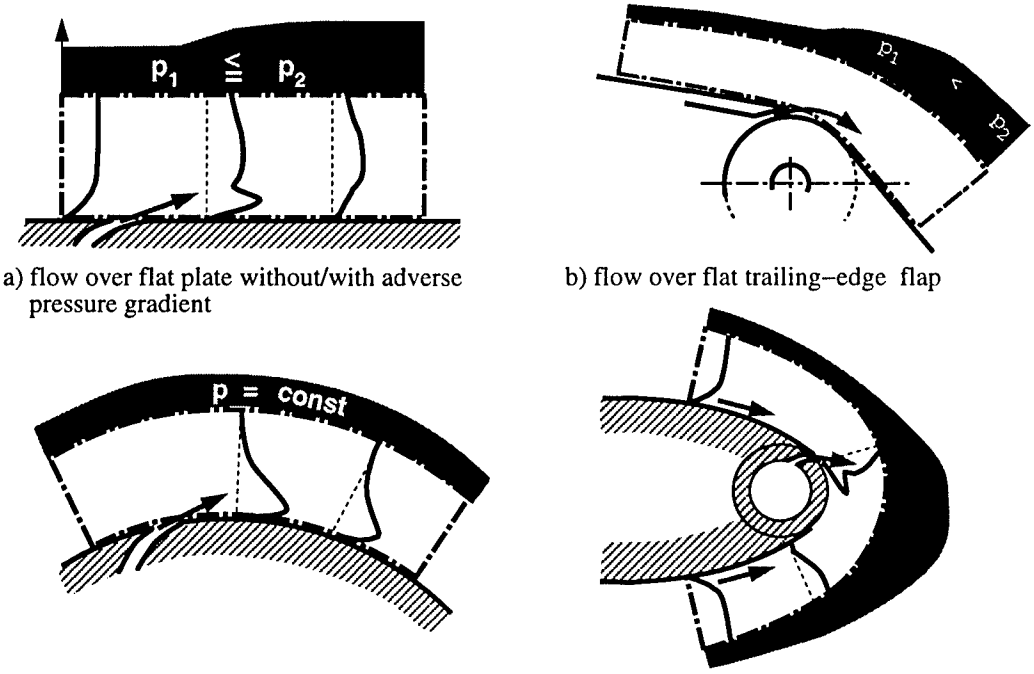

a) flow over flat plate without/with adverse pressure gradient

b) flow over flat trailing–edge flap

c) flow over curved wall (Coanda cylinder)

d) flow over trailing edge of elliptical airfoil

Figure 2: Generic wall jet configurations for investigating different aspects of the flow over a slotted flap.

of curvature is studied separately for a strong wall jet over a curved wall geometry with constant curvature (Figure 2c) where reliable experimental data are available for comparison (Neuendorf and Wygnanski, 1999). Finally, in close collaboration with the experiments by Wygnanski, we will study the flow over the trailing edge of an elliptical airfoil.

The Navier-Stokes code employed for our numerical investigations was originally developed in our research group for boundary layer transition (Meitz and Fasel, 2000). In this code, the complete incompressible Navier-Stokes equations are solved in vorticity-velocity formulation. For the time integration, a fourth-order Runge-Kutta method is employed. For the spatial discretization in the streamwise and the wall-normal directions, fourth-order accurate compact differences are used, while the spanwise direction is treated pseudo-spectrally. Our Navier-Stokes code has since been adapted to curved wall geometries and was employed for the DNS of a Stratford ramp (e.g. Zhang et al. 1999a,b). Over the past few years, in cooperation with C. Speziale of Boston University (Speziale 1998) we have developed and tested a new Flow Simulation Methodology (FSM) that is consistent with DNS for fine grid resolution and with URANS calculations for coarse grid resolution, and represents an LES between those limits. The subrid-scale model that is incorporated for this FSM into our Navier-Stokes code is based on the algebraic stress model (ASM), developed originally by Gatski and Speziale (1993). For the FSM, the model also includes a contribution function for the subgrid-scale stress that depends on the local grid resolution compared with the Komolgorov length scale. A detailed discussion of the FSM for boundary layer flow without and with adverse pressure gradient is given by Zhang et al. (2000).

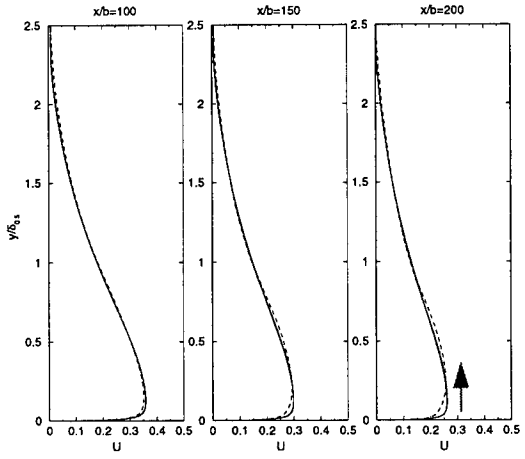

a) Effect of large scale structures on the mean u–velocity profile. — unforced, --- forced.

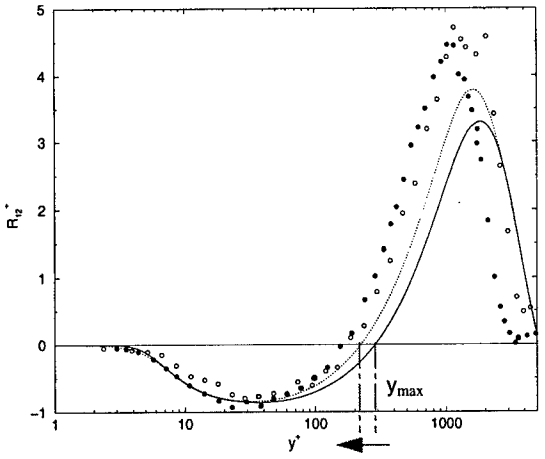

b) Turbulent stress $\tau_{12}=R_{12}+\overline{u'v'}_{coherent}$ at x/b=200 in wall–coordinates. — unforced, ····· forced, • & ○, experiment.

Figure 3: URANS calculation of strong wall jet forced with large amplitude. From Seidel and Fasel (2000).

For further testing of the FSM and as a reference case for the Coanda flow we have computed a forced strong wall jet along a flat plate using our new FSM in the URANS limit. Our computation was set up to closely match the experiment of a forced strong wall jet with $R_j = 10000$ by Katz et al. (1992). We were able to capture the major features observed in the experiment, e.g. a significant skin friction reduction in the forced flow due to the presence of large amplitude disturbances. This is indicated in Figure 3a which shows the streamwise mean flow profiles at three downstream location for the unforced and for the forced flow. As in the experiment, forcing causes a significant shift away from the wall of the velocity maximum and the entire inner region, but hardly effects the outer region of the wall jet. A most interesting feature of the wall jet, that is often pointed out in the literature, is the displacement of the zero of the Reynolds stress from the location of the velocity maximum towards the wall ($y_{R_{12}=0} \approx 0.6 y_{max}$). Any equilibrium RANS model based on the Bousinesq assumption fails to capture this displacement. In our URANS calculation of the forced wall jet, despite the use of an equilibrium ASM for the Reynolds stress, we observe this displacement in the total turbulent stress $\tau_{12} = R_{12} + \overline{u'v'}_{coherent}$. This is illustrated in Figure 3b. From this result, we conjecture that large coherent structures in the turbulent wall jet provide a major contribution to this displacement in the turbulent stress.

Recently we have started with RANS calculations for the Coanda flow (Figure 2c). Some preliminary results for the constant pressure region of the flow are presented in Figure 4. Shown is the effect of the radius of the wall curvature, R, (radius of the Coanda cylinder) on the spreading rate of the half width (Figure 4a) and on the decay of the velocity maximum (Figure 4b). As a reference, the plane wall jet with jet exit Reynolds number $R_j = 10000$ from experiments by Katz et al. (1992) is also

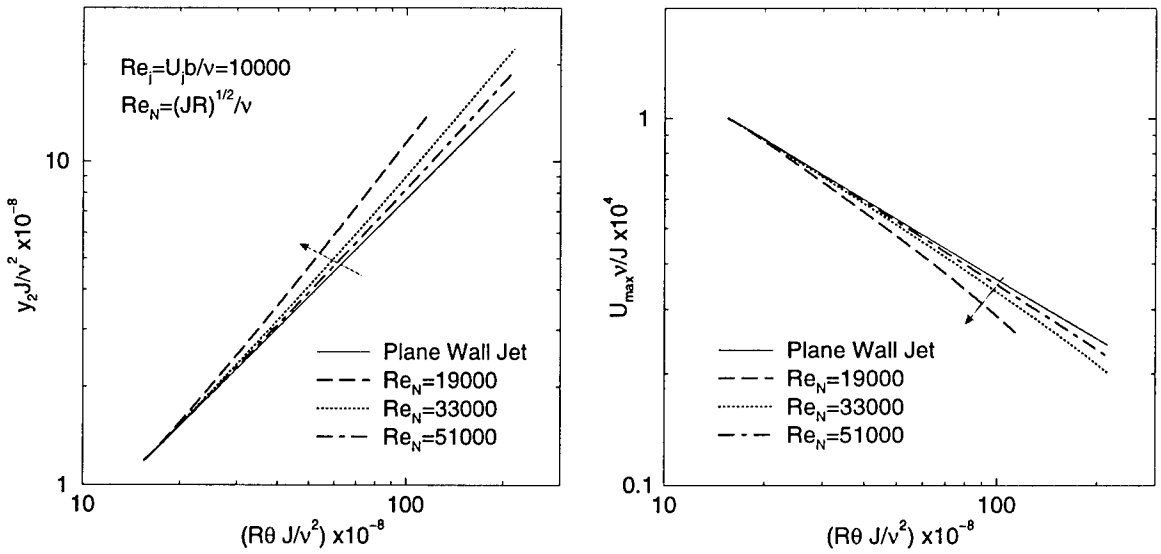

a) spreading rate of half width b) decay of maximum velocity

Figure 4: RANS calculation of Coanda flow. Influence of cylinder radius R on spreading rate and decay of maximum velocity.

shown. The calculation show that the smaller the Radius of the wall curvature is, the faster the wall jet spreads and the faster its mean velocity decays.

Future Work

During the next year we plan to study the Coanda flow in detail, including the adverse pressure gradient region and the separated flow region. We will match as closely as possible the experiments by Neuendorf and Wygnanski (1999) with our numerical simulations (FSM used as an LES and in the URANS limit). Of great interest will be how well we can capture the longitudinal vortices that develop in the shear layer region of the wall jet due to a centrifugal (Görtler-type) instability of the flow. We will then determine the effect of forcing on the development of the flow. Using our curved wall code, we will also investigate the straight trailing-edge flap (Figure 1b, 2b) and compare with our earlier findings for the flat plate with adverse pressure gradient (Figure 2a).

Acknowledgement/Disclaimer

This work was sponsored by the Air Force Office of Scientific Research, USAF, under grant number F49620-00-1-0069 and was also supported in part by a grant of HPC time from the DoD HPC Shared Resource Center, NAVO. The views and conclusions contained herein are those of the author and should not be interpreted as necessarily representing the official policies or endorsements, either expressed or implied, of the Air Force Office of Scientific Research or the U.S. Government.

References

Gatski, T. and Speziale, C., 1993, "On Explicit Algebraic Stress Models for Complex Turbulent Flows," *J. Fluid Mech.* **254**, 59-78.

Katz, Y., Horev, E., and Wygnanski,I., 1992, "The Forced Turbulent Wall Jet," *J. Fluid Mech.*, **242**, 577-609.

Meitz, H.L. and Fasel, H.F., 2000, "A Compact-Difference Scheme for the Navier-Stokes Eqnations in Vorticity-Velocity Formulation," *J. Comp. Phys.*, **157**, 3721-403.

Neuendorf, R. and Wygnanski, I., 1999, "On a Turbulent Wall Jet Flowing Over A Circular Cylinder," *J. Fluid Mech.* **381**, 1-25.

Seifert, A., Bachar, T., Koss, D., Shepshelovich, M., and Wygnanski, I., 1993, "Oscillatory Blowing: A Tool to Delay Boundary-Layer Separation," *AIAA J.* **31**, 2052-2059.

Seifert, A., Darabi, A., Sokolov, M., and Wygnanski, I., 1994, "The Use of Oscillatory Blowing for Managing the Flow Around a Slotted Airfoil at Low Reynolds Numbers," Euromech Colloquium 328, Management and Active Control of Turbulent Shear Flows, Technical Univ. Berlin, Oct. 1994.

Seidel, J., and Fasel, H., 2000, "Numerical Investigation of Forced Turbulent Wall Jets," AIAA Paper 2000-2317.

Speziale, C., 1998, "Turbulence Modeling for Time-Dependent RANS and VLES: A Review", *AIAA J.* **36**, 173-184.

Wygnanski, I., 1997, " Boundary Layer and Flow Control by Periodic Addition of Momentum (invited)," AIAA Paper 97-2117.

Zhang, H.-L. and Fasel, H., 1999a, "Numerical Investigation of the Evolution and Control of Two-Dimensional Unsteady Separated Flow Over a Stratford Ramp," AIAA Paper 99-1003.

Zhang, H.-L. and Fasel, H., 1999b, "Direct Numerical Simulation of the Turbulent Flow over a Stratford Ramp", AIAA Paper 99-3359.

Zhang, H.-L., Bachman, C.R., and Fasel, H.F., 2000, "Application of a New Methodology for Simulations of Complex Turbulent Flows," AIAA Paper 2000-2535.

Personnel

Hermann F. Fasel, Professor, principal investigator
Stefan Wernz, graduate student

Presentations at Conferences

Wernz, S. and Fasel, H., 1999, "Numerical Investigation of Resonance Phenomena in Wall Jet Transition", IUTAM Symposium on Laminar-Turbulent Transition, Sedona, Az, September 13-17, 1999.

Seidel, J., and Fasel, H., 2000, "Numerical Investigation of Forced Turbulent Wall Jets," AIAA-Fluids 2000, Denver, Co, June 19-22.

UNSTEADY AERODYNAMICS & AEROMECHANICS OF MULTI-STAGE TURBOMACHINERY BLADING

AFOSR GRANT F49620-97-009

Sanford Fleeter
School of Mechanical Engineering
Purdue University
West Lafayette, Indiana 47907-1288

Abstract

The overall objective of this research is to develop the technology needed to predict significant blade row forced response in a multistage environment, thereby providing accurate predictions of HCF. Specific objectives include: (1) development of a benchmark standard multistage transonic research compressor; (2) a quantitative understanding and predictive capability for multi-stage blade row forced response; (3) address the inherently small damping of complex higher order modes, investigating techniques to control the flow induced vibrations; (4) consider the issue of robustness including the role of such issues as variability and flight maneuvers, nonlinearities, and fluid-structure interactions.

This multidisciplinary research program requires an integrated experiment-theory approach, accomplished through collaboration between Pratt & Whitney, Duke University, and Purdue University. Task 1 is directed at a benchmark standard multistage transonic research compressor. In cooperation with Pratt & Whitney, the Purdue High Speed Axial Research Compressor will feature new IGV, rotor, and stator rows representative of the front stages of modern Pratt-designed high-pressure compressors. In Task 2, a quantitative understanding and predictive capability for multistage blade row forced response will be developed. In addition, Duke will develop a new unsteady aerodynamic analysis of multistage flows in turbomachinery - especially flows associated with flutter and forced response. The method will be computationally much more efficient than the current generation of time-domain codes. Task 3 addresses the inherently small damping of complex higher order modes, investigating techniques to control the flow induced vibrations. Task 4 addresses the issue of robustness.

The advanced-design IGV, rotor and stator rows have controlled diffusion airfoil (CDA) profiles and have been fabricated and instrumented. The IGV's and stators have a 4.45 cm (1.75 in.) chord and a constant 7% thickness and feature variable stagger angles and adjustable axial spacings. The rotor is a blisk having 18 controlled diffusion blades with a 2.0 in. chord and a thickness distribution varying linearly from 8% chord at the root to 4% at the tip.

Unsteady Blade Row Interactions: A transonic rotor operates with a supersonic relative velocity with a subsonic axial component. Shocks thus form near the leading edges that can propagate upstream. These propagating shocks represent a significant forcing function to the upstream vane row. The rotor also generates an unsteady forcing function to the downstream stator row. The reduction in the relative velocity in the wake causes a decrease in the absolute velocity as

well as a change in incidence to the downstream stators. This produces a fluctuating lift and moment that can result in large vibratory stress.

The new IGV's and stator vanes were utilized in conjunction with the existing rotor to investigate IGV-rotor interactions. Experiments have been performed at both design and part-speed operating conditions and include measurements of the rotor generated unsteady aerodynamic forcing functions to the upstream IGV and downstream stator, the resultant IGV and stator unsteady aerodynamic response, and PIV measurements of the instantaneous IGV and stator vane-to-vane flow fields at several time instants over one interaction cycle.

Transonic rotor-IGV interactions resulted in a highly unsteady IGV flow field, with the rotor leading edge shocks reflected by the vane pressure surface and diffracted by the suction surface. The reflected shock segment traveled across the vane passage as it propagated upstream, interacting with the incident shock of the adjacent rotor blade before it eventually impacted the suction surface of the upper vane in the leading edge region. This interaction resulted in a time-dependent wave pattern being established in the upstream vane passage. The unsteady aerodynamic loading generated by these transonic interactions was very significant, with the maximum peak-to-peak static pressure fluctuations over the aft region of the vane as large as 60% of the inlet total pressure.

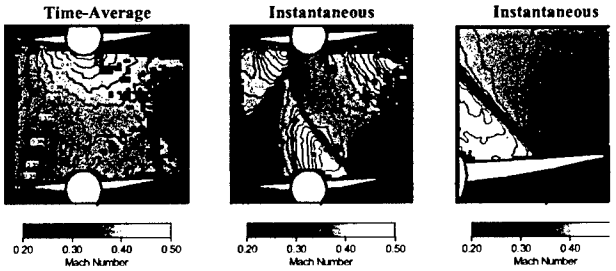

IGV flow field at 20,000 rpm

The downstream stators periodically chop the rotor wakes, with the low momentum wake fluid drifting across the stator passage and accumulating on the pressure surface as the chopped wake segments are transported downstream. This intra-stator wake transport generates high levels of unsteady loading on the pressure surface at the transonic operating condition.

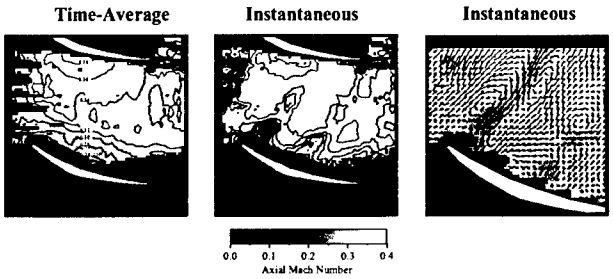

Stator flow field at 20,000 rpm

Multistage Unsteady Aerodynamic Analysis: We have continued to develop a computational analysis of unsteady multistage flows in turbomachinery. For a given multistage fan or compressor, we first generate a computational mesh for each blade row. The steady multistage flow is then computed using conventional computational fluid dynamic (CFD) techniques, with so-called "mixing planes" used to couple together the solutions computed in the individual blade rows. Having computed the steady flow, we then solve several unsteady time-linearized problems on each computational grid. Each solution is identified with one of a set of discrete "spinning modes," each with a different frequency and interblade phase angle. These unsteady flow problems are solved in parallel, using time-linearized CFD techniques that have been developed in the last ten years for isolated blade rows. At each iteration of the flow solver, information is exchanged among the various spinning mode solutions at the inter-row computational boundaries. This iteration procedure is continued until a converged solution is obtained.

We have continued to develop a computational analysis of unsteady multistage flows in turbomachinery that can be used to model these more complex flow features. The outline of the approach is as follows. For a given multistage fan or compressor, we first generate a computational mesh for each blade row. The steady multistage flow is then computed using conventional computational fluid dynamic (CFD) techniques, with so-called "mixing planes" (the inter-row computational boundaries of the computational grid) used to couple together the solutions computed in the individual blade rows. Having computed the steady flow, we then solve several unsteady time-linearized (frequency domain) problems on each computational grid. Each solution is identified with one of a set of discrete "spinning modes," each with a different frequency and interblade phase angle. These unsteady flow are problems are solved in parallel, using time-linearized CFD techniques that have been developed in the last ten years for isolated blade rows. At each iteration of the flow solver, information is exchanged among the various spinning mode solutions at the inter-row computational boundaries. This iteration procedure is continued until a converged solution is obtained.

We have refined the three-dimensional analysis technique considerably. Specifically, we can now compute the aerodynamic damping of a rotor embedded in a multistage machine. As an example, consider the unsteady aerodynamic analysis of a front stage compressor and inlet guide vane. Within a single passage of each blade row, a computational grid is generated. Only a single passage of each blade row is used in the computational analysis, regardless of the blade count or interblade phase angle of the excitation, dramatically reducing the computational cost.

For this steady flow condition, the unsteady aerodynamic response of the rotor was calculated for a bending vibration of the rotor blades at a reduced frequency of 1.0. For each case, the unsteady aerodynamic pressure on the surface of the airfoil was integrated to obtain the aerodynamic damping of the system. These calculations were computed for the rotor alone, and also for the rotor in the presence of the upstream inlet guide vane and downstream stator. For the latter case, the calculations were computed using one spinning mode and seven spinning modes.

The aerodynamic damping computed using the rotor alone differs substantially from the aerodynamic damping computed using the multistage analysis. These results confirm that

multistage effects are indeed important, and that the results obtained from unsteady aerodynamic analyses that do not account for neighboring may not be reliable. Also, over most of the interblade phase angle range, the one mode and seven mode results are virtually identical. This implies that the dominant coupling between blade rows is due to a single spinning mode. Note that using two levels of multigrid, the unsteady multistage analysis required just 40 minutes of CPU time on a single processor Silicon Graphics workstation, making the method useful for aeromechanical design applications.

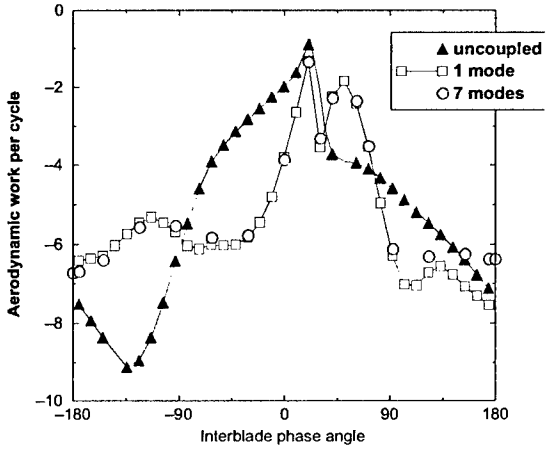

Work per cycle for bending vibration of rotor blades

Robustness & Fluid-Structure Interactions: Flow induced vibration in turbomachine blade rows is a coupled fluid-structure problem. Thus, instead of utilizing separate fluid and structural models, a coupled interacting fluid-structures analysis is needed. To begin to address this need, the finite element code ALE3D (Arbitrary-Lagrangian-Eulerian-3D) that solves the three-dimensional Euler equations is being extended to address the unsteady aerodynamics of turbomachine blade rows. For each time step, a Lagrangian calculation is performed, the mesh relaxed, and new flow quantities are found via an advection calculation. The outer portion of the mesh is relaxed to its original position, while the inner portion is relaxed to reduce mesh skewness due to blade motion. Only one blade passage is analyzed and a Fourier series decomposition is used at the periodic boundaries for non-zero interblade phase angles. Thus, in TAM-ALE3D (Turbomacheinery-Aero-Mechanics-Arbitrary-Lagrangian-Eulerian-3D), the same finite element model is applied to both the blading and the fluid, resulting in consistency between the fluid and structure. Hence the exchange of energy and momentum across the fluid-structure boundary is not prone to phase-lagging errors that tend to act as energy sources or sinks at the fluid-structure boundary.

The TAM-ALE3D coupled interacting fluid-structure analysis enables the vibratory stress to predicted. This was demonstrated though a simulation of the blade row interaction generated flow and vibration phenomena in the IGV row of the Purdue Transonic Compressor. Specifically, at the part-speed rotor operating condition, the downstream rotor potential field excited the trailing edge flapping mode of the upstream IGV's. This HCF problem was analyzed through an IGV-rotor TAM-ALE3D simulation. The IGV row unsteady aerodynamics generated by the downstream rotor were predicted first. A TAM-ALE3D fluid-structure interaction

simulation was then performed, with the aerodynamically induced cyclic stress on the IGV's predicted. The airfoils are modeled as rigid while the flow field is established. The IGV's are then allowed to move freely in response to the flow. At this point the time step of the simulation is reduced by an order of magnitude to capture the short time scale response of the metal vanes. The aerodynamics and response of the IGV's are simulated for 100 milliseconds, which requires approximately 9 days on two SGI RS10000 processors running in parallel.

Two part-speed rotor-operating conditions are considered, 14,000 and 15,000 rpm, which correspond to excitation frequencies on the IGV of 4,433 Hertz and 4,750 Hertz that are close to the 4,024-Hertz natural frequency of the IGV trailing edge flapping mode. The 15,000 rpm condition is especially important since the machine was run at this speed while data was acquired. The dynamic response of the IGV's is presented for points at 95% chord at hub and tip.

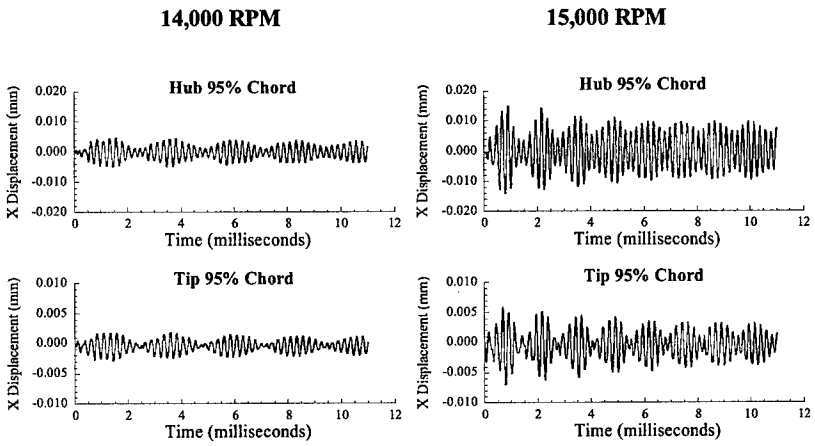

IGV displacement at hub and tip at 95% chord

At each operating condition, the hub experiences more displacement than the tip. The beating pattern shows that the 14,000 rpm condition is closer to the excited mode natural frequency since it has fewer beats. However, the hub and tip displacements are over two times greater at 15,000 rpm. Although the 14,000 rpm condition is closer to the trailing edge flapping mode natural frequency, the 15,000 rpm condition results in a larger stress amplitude in the IGV's.

This unexpected result is explained by consideration of magnitude of the unsteady aerodynamic forcing. The modal forcing amplitude for the trailing edge flapping mode due to unsteady aerodynamic excitation reveals that the aerodynamic forcing increases by a factor of four as the rotor speed increases from 14,000 rpm to 15,000 rpm, thereby resulting in the larger IGV cyclic stresses at 15,000 rpm.

Acknowledgement/Disclaimer

This work was sponsored (in part) by the Air Force Office of Scientific Research, USAF, under grant/contract number F49620-97-009. The views and conclusions contained herein are those of the authors and should not be interpreted as necessarily representing the official policies or

endorsements, either expressed or implied, of the Air Force Office of Scientific Research or the U.S. Government.

Personnel Supported

Purdue University	Duke University
Sanford Fleeter, Distinguished Professor	Kenneth C. Hall, Professor
Patrick Lawless, Associate Professor	Earl H. Dowell Professor
Ronnie McGuire, Research Engineer,	Natalia Smelova, Graduate Research Assistant
John Papalia, Graduate Research Assistant	Dimitro Voytovich, Graduate Research Assistant
Adam Plant, Graduate Research Assistant	
Steve Szczap, Graduate Research Assistant	

Publications

Sanders, A.J. and Fleeter, S., "An Experimental Investigation of IGV-Rotor Interactions in a Transonic Axial-Flow Compressor," *AIAA Journal of Propulsion and Power*, Vol. 38, No. 2, February 2000, pp. 284-291.

Sanders, A.J. and Fleeter, S., "Unsteady Blade Row Interactions in a Transonic Multistage Compressor," *5th National Turbine Engine High Cycle Fatigue Conference*, March 2000.

Richman, M., and Fleeter, "Simulation and Correlation of Rotor-IGV Interactions In A Transonic Compressor," *5th National Turbine Engine High Cycle Fatigue Conference*, March 2000.

Gottfried, D. A. and Fleeter, S. "A New Approach for Aerodynamic Damping Predictions In Blade Rows," *5th National Turbine Engine High Cycle Fatigue Conference*, March 2000.

Gottfried, D. and Fleeter, S., Turbomachine Blade Row Interaction Predictions With A Three-Dimensional Finite Element Method," *AIAA Paper 2000-3226*, July 2000.

Richman, M.S., and Fleeter, S., "Navier-Stokes Simulation Of IGV-Rotor-Stator Interactions in a Transonic Compressor," *AIAA-2000-3379*, July 2000.

Awards Received

Sanford Fleeter: Fellow, American Institute of Aeronautics and Astronautics, (Awarded 2000).

Sanford Fleeter: 2000 International Society of Rotating Machinery Research Award (ISORMAC) Award, (Awarded 2000).

ASME Joint Propulsion Best Paper: Sanders, A., Papalia, J. and Fleeter, S., "A PIV Investigation of Transonic IGV-Rotor Interactions, *AIAA Paper 99-2674*, June 1999.

Kenneth C. Hall was elected Fellow of the American Society of Mechanical Engineers.

Transitions

The IGV experimental data, including vane surface steady and unsteady pressures and PIV data, have been sent to Pratt & Whitney - North and are being utilized to validate their HCF unsteady aerodynamic codes. Point of Contact: Gary Hilbert.

Beginning in June 1998, Duke University began work under contract with General Electric Aircraft Engines under their University Strategic Alliance (USA) program. One of the main goals

is to transfer technology developed under government grants, and apply it to industrial problems. During this reporting period, Duke University used the multistage analysis developed under this program to analyze the flutter stability of a GE compressor.

A COMPUTATIONAL INVESTIGATION OF MEMS

AFOSR GRANT F49620-98-1-0027

David B. Goldstein
Center for Aeromechanics Research
Department of Aerospace Engineering & Engineering Mechanics
The University of Texas at Austin
Austin, TX 78712-1085

Abstract

Flow control may be achieved by using MEMS to alter the fine scale flow structures within a boundary layer. In the present work, a direct numerical simulation of a turbulent boundary layer is coupled with an immersed boundary method to simulate the detailed effects of an array of synthetic jet MEMS. Initial results show that the inactive MEMS devices have a weak effect on the boundary layer from their mere physical presence. Time averaged data show how the jet arrays affect the coherent structures of the boundary layer when activated in different combinations while instantaneous data show the formation of the three-dimensional jets in detail.

Background

A turbulent boundary layer may seem to contain random fluctuations of velocity and pressure but in reality those fluctuations are associated with coherent vortical structures that arise, evolve and decay in a quasi-periodic fashion. Of particular interest are the streamwise vortices that originate from the formation and stretching of horseshoe vortices. These vortices lead to the formation of low speed streaks which are believed to be responsible for the breakdown and eruption of the wall layer – a key mechanism in the production of new vortical structures and the increase in shear stress at the wall. Recent advances in both construction and testing have allowed experimentation with microjet MEMS (Micro Electronic Mechanical Systems) for reducing shear stress over a flat plate [1] and for controlling flow over airfoils and cylinders [2,3]. A reduction in wall shear stress has also been observed in direct numerical simulation (DNS) of turbulent channel flow subjected to an opposition control scheme [4,5] that does not include detailed actuator simulation. Although the potential of synthetic jets for flow control and viscous drag reduction has been suggested experimentally, a full DNS involving turbulent flow and the detailed physics of the jets has yet to be attempted. Simulating the internal structure of the devices is important since previous numerical studies show that the resulting synthetic jets are highly dependent on both the flow parameters and geometric parameters of the particular device [6].

Objectives

The current objectives are to expand our previous study [6] to examine the performance of 3-D slot jets and their impact on a turbulent boundary layer. In particular, we aim to: (1) incorporate an array of actuators in the DNS of a turbulent channel flow, (2) model the impact of several actuator combinations involving changes in magnitude, direction,

pulsing order and frequency on boundary layer coherent structures and (3) examine the usefulness of combining actuators and sensors with passive surface texturing to determine optimum density, operation and placement of the devices. We report here on preliminary results from work on items (1) and (2).

Force Field Model in a Spectral Method

The spectral method used was initially developed to study turbulent channel flow [7]. This method expands the spatial variables of the incompressible Navier-Stokes equations with Fourier and Chebyshev polynomials. The equations are solved with a Chebyshev-tau method with cosine grid clustering in the wall-normal direction. Time stepping is done with an Adams-Bashforth scheme for the non-linear terms and Crank-Nicholson for the viscous terms. Spectral representations make this method attractive for DNS of turbulence due to the low computational cost of fast transform methods and for the accuracy of results in smooth flows. A localized force field method [8] is used to simulate stationary and moving boundaries that make up the internal mechanism of the actuators. This approach has already been validated against experiments and other simulations for a number of turbulent flows [8-10].

Actuator Modeling

The domain consists of a rectangular channel with mean flow in the x-direction. Flow is periodic in both the x and z directions while the horizontal y-planes are defined as the channel boundaries. The actuators are constructed by inserting a virtual surface containing four slots *8* gridcells above the bottom of the channel (fig. 1(a)). In the space between the plate and the lower channel wall, dividing walls spanning the length of the domain are placed to create the jet cavities such that each actuator unit consists of two slot jets powered by a common membrane. Hence, each jet pair is coupled *180* degrees out of phase (fig. 1(b)). The dividing walls are defined as shear-free surfaces that allow parallel fluid motion but no penetration in the z-normal direction – a necessity to reduce "ghost" impressions of the internal geometry above the plate created by Gibbs phenomena. The actuators themselves are rectangular sections of the shear-free wall spanning the height of the cavity and measuring two slot lengths long. The devices use the force field method to impose a time-varying velocity in the z-direction at the driver section of the wall. To simulate the membrane motion, the magnitude of the specified z-velocity is shaped as a sine^2 surface. Since the fluid is incompressible and the domain periodic in the x-direction, only spanwise sub-surface flow can create net mass fluxes in and out through such slots.

A fully developed turbulent channel flow was used as the starting point of the simulations. The new geometry with the virtual plate and internal structure was inserted abruptly into the flow and the simulation was allowed to run for *25,000* time steps to stabilize once more with no actuation applied by the membrane. Instantaneous contours of normalized Ω_y vorticity at a level $4\ l^*$ above the virtual surface (fig. 2) show faint traces of the presence of the slots. These traces are believed to be a result of the turbulent boundary layer spawning separated flow at the sharp edges of the slots. Flow properties were then averaged over the next *20,000* time steps and the results show essentially no long term effect of the presence of the inactive slots in the flow.

Steady and Single Actuation

Two forms of actuation are tested. In the first case ("–++–"), the devices are operated such that there is blowing out of the two center slots and suction down into the two outer slots. The second case is the opposite actuation ("+––+"), with suction down the center and blowing out of the edges. The pumping force is set to produce a jet with average normal (v) velocity $1.5\ u^*$ at the slot plane. Actuation is done with a step function that abruptly starts the membrane motion. Figure 3 shows instantaneous contours of streamwise velocity on a zy-plane cutting through the slots for both test cases. It can be seen that in both cases, fluid sucked into the cavity retains some of its streamwise momentum below the surface while ejected fluid comes out with negligible streamwise momentum. This suggests that modeling actuators with simple wall-normal boundary suction/blowing is not adequate. Time averaged data for a steady blowing case are shown in figure 4 as iso-surfaces of streamwise velocity corresponding to $u^+ = 4$. The "+" jets present themselves as "shark fins" deformed by convection and shearing of the mean flow. For the "–++–" case, fig. 4(a) shows the formation of two pairs of low speed streaks: a narrow and weak pair along the inside of the two outer slots and another more pronounced pair located just outside of the two outer slots. In contrast, the "+––+" case (fig. 4(b)) only shows the presence of a three wide low speed streaks. The instantaneous effects of the steady jets *35* viscous time units after the sudden start are illustrated by the iso-surfaces of Ω_x vorticity shown in fig. 5. The "–++–" case (fig. 5(a)) shows very few vortical structures on the outside of the slots but considerable vorticity production along the center. In comparison, the "+––+" case (fig. 5(b)) shows a more even distribution of vorticity throughout the channel. Preliminary results of a single short "–++–" *pulse* (rather than simply turning the jets on) are illustrated in figure 6 as instantaneous iso-surfaces of normalized Ω_x vorticity and streamwise velocity. Figure 6(a) shows the resulting flow at peak blowing: the center jets are seen as raised bumps on the streamwise velocity surface. Figure 6(b) shows the resulting flow half a period after the jets were turned off. Two vortical structures can be seen lifting off as a result of the previous action of the blowing jets and the raised streamwise velocity surface continues to grow in the wall-normal direction as it starts to deform in a manner similar to that seen in figure 4.

Future Work

In the immediate future, we will continue to study the impact of the actuator arrays on the boundary layer. The focus will be on the impact of the actuators on selected structures or events as we vary parameters such as number of pulses, magnitude of the jet, pulsing period and order. We expect to present detailed results on this work at the Reno 2001 AIAA Aerospace Sciences Meeting. We will then integrate the actuators with sensors and other passive elements as we seek to reduce viscous drag.

Acknowledgement/Disclaimer

This work was supported by the Air Force Office of Scientific Research, grant F49620-98-1-0027. The views and conclusions contained herein are those of the authors and should not be interpreted as necessarily representing the official policies or endorsements,

either expressed or implied of the Air Force Office of Scientific Research or the U.S. Government.

References

1. K. S. Breuer, K. Amonlirdviman, R. Rathnasingham, "Adaptive Feed-Forward Control of Turbulent Boundary Layers," paper AIAA 98-1025, 36th AIAA Aerospace Sciences. Meet., Reno, NV, 1998.
2. D. Smith, M. Amitay, V. Kibens, D. Parekh, and A. Glezer, "Modification of Lifting Body Aerodynamics Using Synthetic Jet Actuators," paper AIAA 98-0209, 36th Aerospace Sciences Meet., Reno, NV, 1998.
3. A. Crook, A. M. Sadri, and N. J. Wood, "The Development and Implementation of Synthetic Jets for the Control of Separated Flow," paper AIAA 99-3176, 17th Applied Aerodynamics Conf., 1999.
4. H. Choi, P. Moin, and J. Kim, "Active Turbulence Control for Drag Reduction in Wall-Bounded Flows," 1994, *J. Fluid Mech.*, vol. 262, p75-110.
5. P. Koumoutsakos, T. Bewley, E. P. Hammond, and P. Moin, "Feedback Algorithms for Turbulence Control - Some Recent Developments," paper AIAA 97-2008, 1997.
6. C. Y. Lee and D. B. Goldstein, "Two-Dimensional Synthetic Jet Simulation," paper AIAA 2000-0406, 38th Aerospace Sciences Meet., Reno, NV, 2000.
7. J. Kim, P. Moin and R. Moser, "Turbulent statistics in fully developed channel flow at low Reynolds number," 1987, *J. Fluid Mech.*, vol. 177, p133-166.
8. D. B. Goldstein, H. Handler and L. Sirovich, "Modeling a No-Slip Boundary with an External force Field," 1995, *J. of Comp. Physics*, vol. 105, p354.
9. D. B. Goldstein, H. Handler and L. Sirovich, "Direct numerical simulation of turbulent flow over a modeled riblet covered surface," 1995, *J. Fluid Mech.*, vol. 302, p333-376.
10. D. B. Goldstein and T.-C. Tuan, "Secondary flow induced by riblets," 1998, *J. Fluid Mech.*, vol. 363, p115-151.

Personnel Supported

Conrad Y. Lee Graduate Student, The University of Texas at Austin

Publications / Presentations

See Ref. [6], also submitted for review to the AIAA Journal
Presentation at TEXMEMS I, Texas A&M University, 1999
Presentation at TEXMEMS II, Southern Methodist University, 2000
C. Y. Lee and D. B. Goldstein, "DNS of MEMS for Turbulent Boundary Layer Control," Abstract sent to Reno 2001 AIAA Aerospace Sciences Meeting

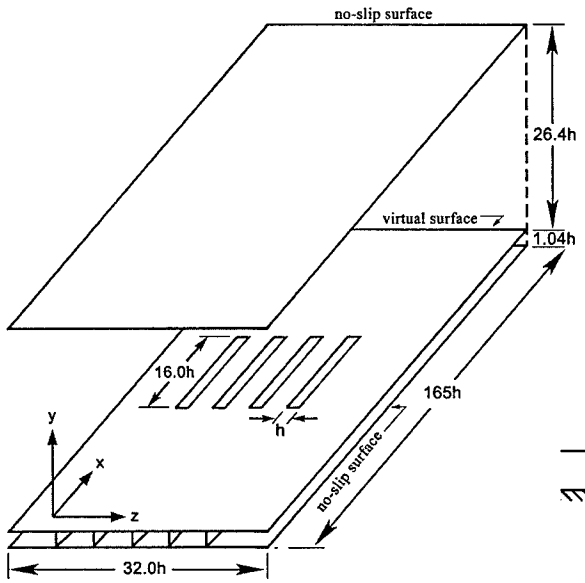

Figure 1(a): Schematic of channel and actuators

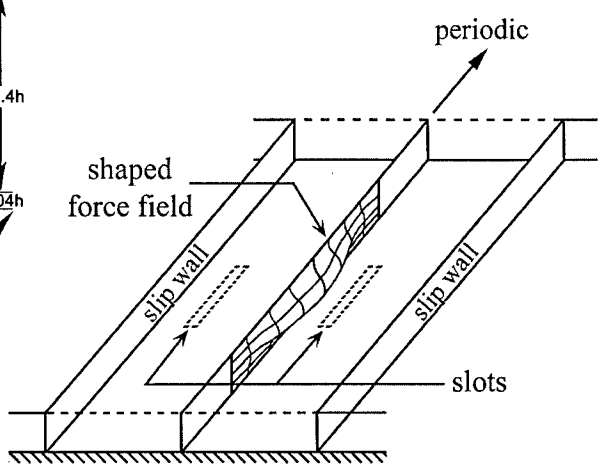

Figure 1(b): Schematic of single actuator array and sample force field shape for membrane deformation

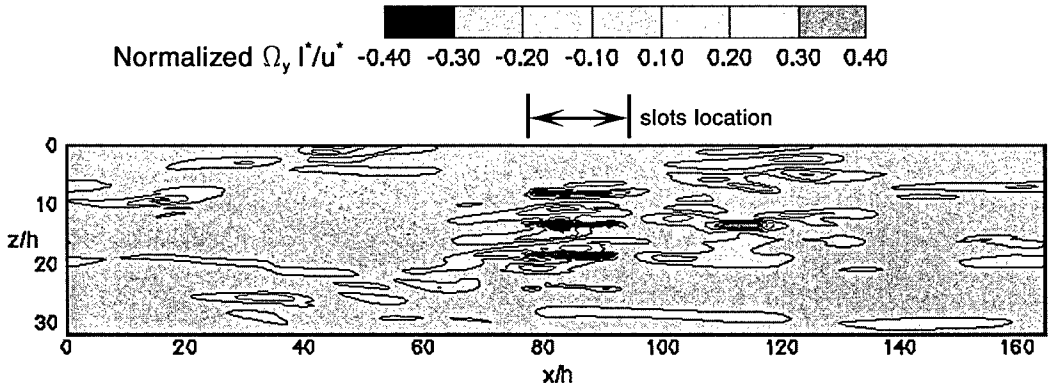

Figure 2: Contours of normalized vorticity 4 wall units above the plate (no actuation)

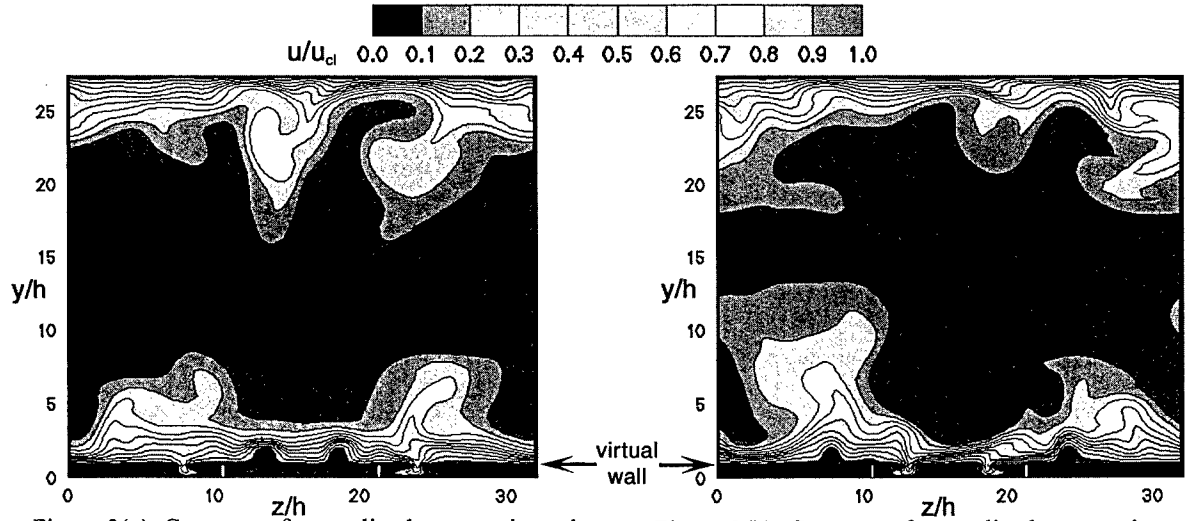

Figure 3(a): Contours of normalized streamwise vel. on zy-plane through actuators for "-++-" actuation (black = virtual solid walls, white = actuator)

Figure 3(b): Contours of normalized streamwise vel. on zy-plane through actuators for "+--+" actuation (black = virtual solid walls, white = actuator)

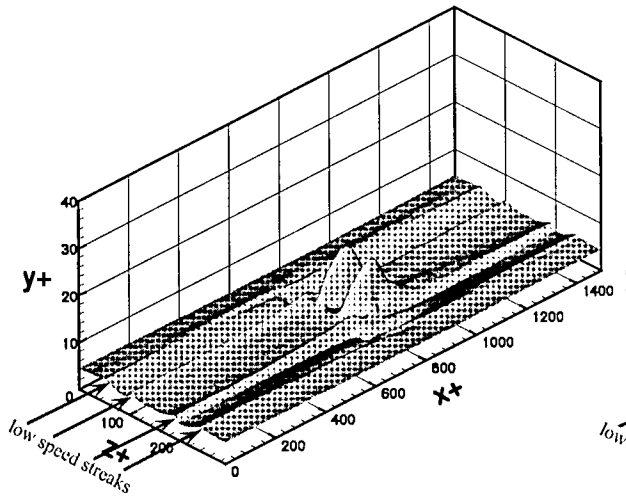

Figure 4(a): Contours of average streamwise velocity for $u^+ = 4$ ("-++" actuation)

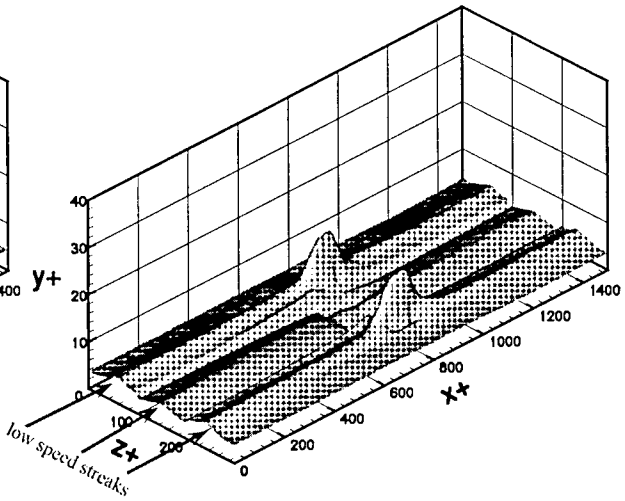

Figure 4(b): Contours of average streamwise velocity for $u^+ = 4$ ("+--+" actuation)

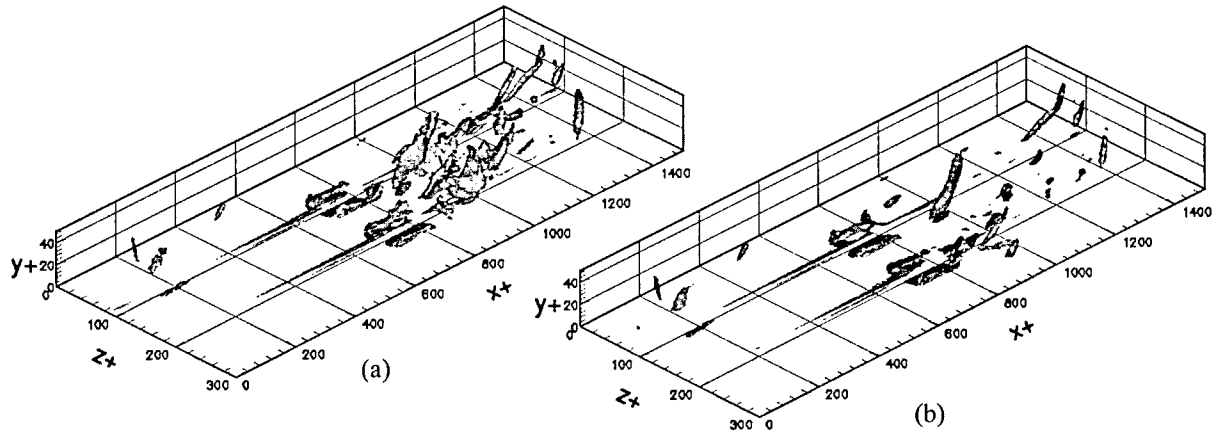

Figure 5: Contours of instantaneous normalized vorticity ($\Omega_x l^*/u^* = \pm 0.8$) taken 35 t^* after sudden start of steady jets for (a) "-++-" case and (b) "+--+" case

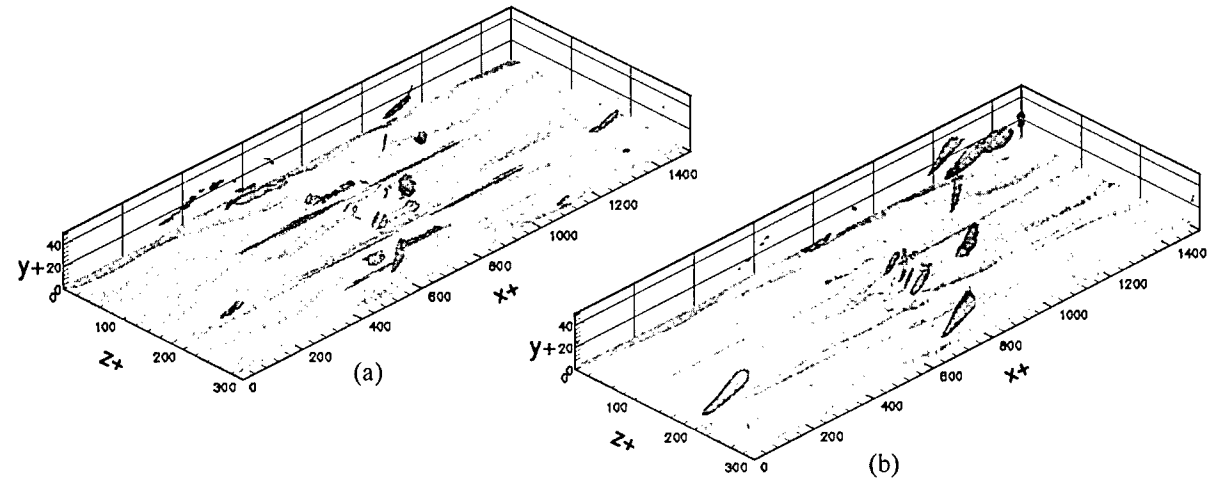

Figure 6(a): Contours of normalized vorticity ($\Omega_x l^*/u^* = \pm 0.8$) and streamwise vel. ($u^+ = 4$) for single pulse case at peak actuation for (a) "-++-" case and (b) "+--+" case

FLOWFIELD MIXING ENHANCEMENT AND NOISE CONTROL USING FLEXIBLE FILAMENTS

AFOSR GRANT No. F49620-96-1-0378

Ephraim Gutmark
Department of Aerospace Engineering and Engineering Mechanics
880 Engineering Research Center
University of Cincinnati
Cincinnati, OH 45221-0070
(513)-556-1227

Abstract

The subject research program seeks to explore a novel method for achieving passive flow field control, with applications to mixing enhancement and noise reduction, through the interaction of the flow with flexible filaments. Figure 1 shows how a centerbody device is used to hold and align the filament along the centerline of the flow. A small knot is tied near the end of the filament in order to stabilize it in the flow.

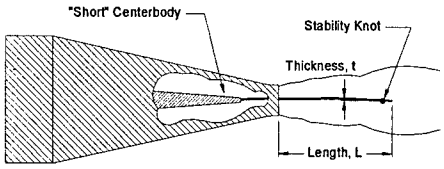

Figure 1: Attachment of Filament Using Centerbody Device

The primary purpose of the filament is to modify the large-scale structures within the flow. These structures consist of the vortex formation in subsonic flow and the shock structure in supersonic flow. This flow control can result in improved mixing, lower noise, and a more stable flow. Detailed acoustical measurements using this arrangement have shown that it can significantly reduce the acoustical emissions (up to 32 dB) from both subsonic and supersonic jet flows, especially at screech conditions[1]. Additionally, preliminary experiments indicated that significant mixing enhancement and flow control can be obtained using this configuration. The primary objective of this research program is to expand on these results to fully develop this unique approach to flow field modification.

Objective

The main goal of the subject research program is to thoroughly investigate the use of flexible filaments for flow control applications. Specifically, the program seeks to achieve the following objectives:

1) *Understand the physical mechanisms governing the filament/flow interaction.* Developing an understanding of the mechanisms responsible for the filament induced flow modifications is crucial for exploiting the full potential of this concept.

2) *Determine the optimal filament configuration(s) for achieving the desired flow control.* There are numerous parameters associated with the filament including its material properties, geometry, size, attachment location, and the number of filaments used. Each of these parameters may influence the extent of flow field modifications. The impact of these parameters will be investigated as part of the project.
3) *Quantify the attainable flow enhancements/modifications.* The potential benefits of the filaments for noise control and mixing enhancement will be investigated to document the extent of the enhancements achievable.
4) *Identify additional applications for this concept.* During the course of the research program, efforts will be made to identify additional applications for this concept.

Approach

To execute the subject research program, a jet flow facility capable of producing both subsonic and supersonic flows was constructed. The facility is capable of producing primary flow Mach numbers up to approximately 2.0. Also, the primary flow may be heated to a stagnation temperature of 500°F. In order to facilitate accurate acoustical measurements, an anechoic chamber has also been constructed with a lower cutoff frequency of approximately 400 Hz. The chamber is fully instrumented with an array of high frequency condenser microphones. In addition, a traversing mechanism is available for complete mapping of the sound field. The layout of the microphone array as well as two separate areas covered by the sound pressure mapping is shown below in Figure 2.

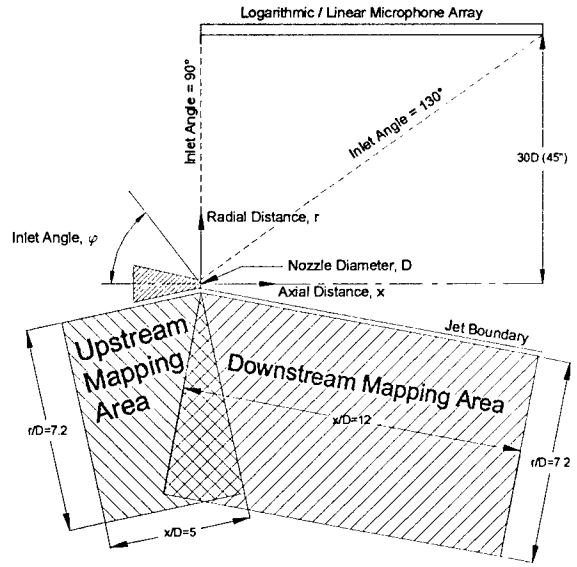

Figure 2: Layout of Microphone Arrays and Mapping Areas

Progress

During the past year, extensive acoustical testing of the jet has continued. Initially, tests were conducted in order to identify an optimal filament configuration. The two primary filament parameters of length and thickness were systematically varied to allow an optimal filament configuration for noise suppression to be identified. Both the filament length, L, and thickness, t, were defined as a ratio to the primary nozzle diameter, D. Referring back to Figure 1, note that since the centerbody tip is actually upstream of the

nozzle exit plane, it is possible to have filaments with negative L/D. The results of these tests indicated that the filament effectiveness was much more sensitive to variations in length than to variations in thickness. Once an optimal filament configuration was identified, detailed acoustical measurements were made over a range of jet operating conditions in order to fully quantify the effect of the filament. This included collection of acoustical data at jet temperatures up to 500°F in an effort to determine what effect jet temperature might have on the filament effectiveness. Results of these tests proved very promising. Specifically, they showed the filament performance to actually improve with increasing temperature. Finally, a PC controlled traversing mechanism was used to obtain a complete mapping of the jet near field. This data was used to better understand and quantify the overall spatial effect of the filament on the jet near field.

Results

In order to systematically determine the optimal filament configuration, a series of tests were performed with the jet operating at Mach 1.3 with no heating. Filament L/D ratios were varied from -0.75 to 10 in an effort to identify both a critical length required for any suppression and a length for optimal suppression. Figures 3 and 4 show the narrowband spectra for selected filament lengths obtained with microphones at a radial distance of 30 primary diameters and inlet angles of 90° and 130° respectively. While the dramatic suppression attainable with the longer filaments is clearly evident, note that some small attenuation can be observed with an L/D ratio of 0 (i.e. coincident with nozzle lip). Figure 5 summarizes the results of the length optimization for both inlet angles tested. While reductions as high as –22dB are observed with an L/D=8, the filament effectiveness begins to flatten out beyond L/D of approximately 3 to 4. This is particularly apparent at the downstream location where the filament effectiveness is more limited due to the absence of high screech amplitudes. For practicality reasons, the optimal filament length was determined to be approximately L/D=3. However, it should be noted that additional attenuation is attainable with longer filaments if the length can be accommodated. To complete the filament optimization, the length was held constant at L/D=8 while the thickness was systematically varied. As Figure 6 shows, the filament performance was not nearly as sensitive to variations in thickness as it was to variations in length. Basically, there is a minimum allowable thickness beyond which the filament becomes acoustically invisible. This threshold can be seen in Figure 6 to occur at about t/D=0.04. In most applications, the selection of the appropriate thickness would be made on the basis of strength requirements. Next, tests were performed in order to observe any changes in the jet spectra with elevated temperatures. Specifically, acoustical data was collected with the jet at a Mach number of 1.3, with no filament attached over a range of temperatures from ambient to 500°F. These tests confirmed the previous findings of Massey and Ahuja, which indicated that the peak noise level of the jet should increase as temperature ratios are increased from 1.0 to approximately 1.8^2. Next, these tests were repeated with an "optimal" filament of L/D=6 and t/D=0.08 attached in order to quantify the filament performance at elevated temperatures. The results of these tests as well as the baseline temperature effect tests are summarized below in Figure 7. The upper two curves show the baseline (no filament) peak SPL of the jet for inlet angles of 90° and 130° as the temperature increases. The two lower curves show the peak SPL of the jet for the same inlet angles when the optimal filament is attached. Notice the filament effect in

the 90° direction. The filament reduces the peak SPL to approximately 97 dB and the dependence of this peak level on temperature appears to have been eliminated. This results in reductions of peak SPL ranging from 19 dB at ambient to an incredible 32 dB at a temperature of 425°F. While not this dramatic, the filament also provides effective attenuation in the downstream direction ranging from 8 dB at ambient to 17 dB at 500°F. These results prove that increasing jet temperatures does not mitigate the filament effectiveness and to the contrary, may actually improve it. Figure 8 shows a comparison of the baseline and optimal filament spectra obtained from the 90° microphone for the jet operating at M=1.3, T=425°F. The dramatic effect of the filament can be fully appreciated from this figure. In addition to complete suppression of all screech tones, the SPL is attenuated across the entire frequency range with no crossover observed.

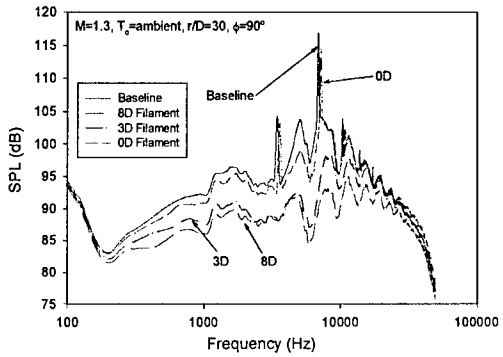

Figure 3: Spectra for Various L/D, ϕ= 90°

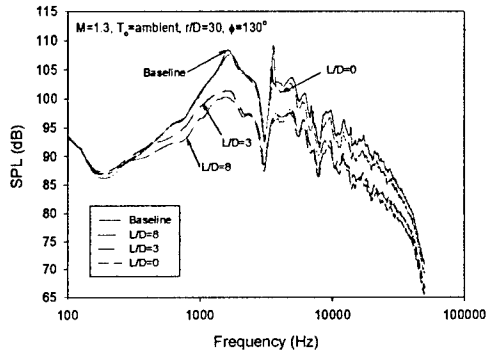

Figure 4: Spectra for Various L/D, ϕ= 130°

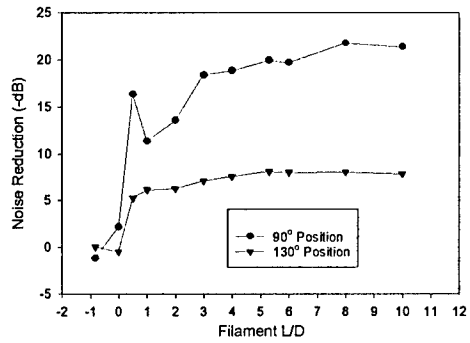

Figure 5: Filament Length Optimization Summary

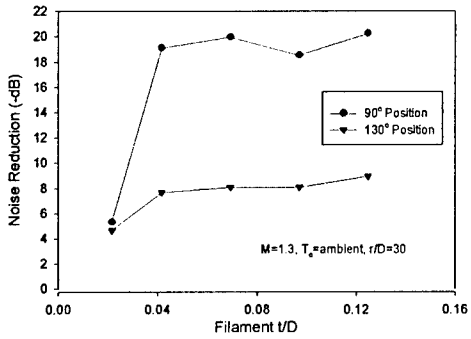

Figure 6: Thickness Optimization Summary

Finally, a complete mapping of the overall sound pressure level (OASPL) in the near field was completed in order to better understand the spatial effect of the filament on the overall sound pressure field. Refer back to Figure 2 for an explanation of the upsteam and downstream mapping areas. The baseline mappings for the cold jet at M=1.3, shown in Figures 9 and 10 exhibit the expected directional characteristics[3]. The fundamental screech tone is clearly evident in Figure 9 as it propagates in the upstream direction and the harmonic can be identified in Figure 10. Introduction of the optimal filament results in a much smoother sound field as seen in Figures 11 and 12. The peak OASPL observed is reduced by 16 dB from 151 dB in the baseline case to 135 dB with the optimal filament attached. In addition to this, the range of observed OASPL is reduced by the filament. In the baseline case, the sound field covered a range of approximately 20 dB from the peak near the nozzle lip to the lowest observed near the edge of the mapping areas. However,

with the optimal filament attached, this range between maximum and minimum observed OASPL is reduced to only 8 dB. The conclusion drawn from the mapping is that the filament is effective across the entire sound field in addition to the discrete inlet angle previously studied.

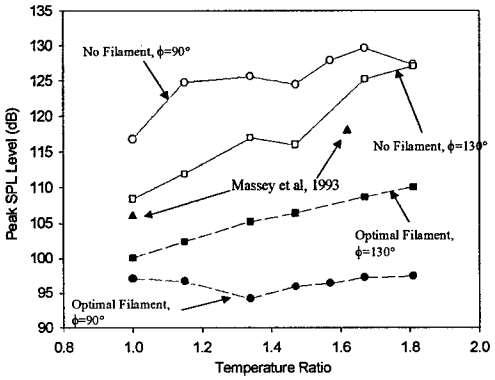

Figure 7: Summary of Temperature Effects

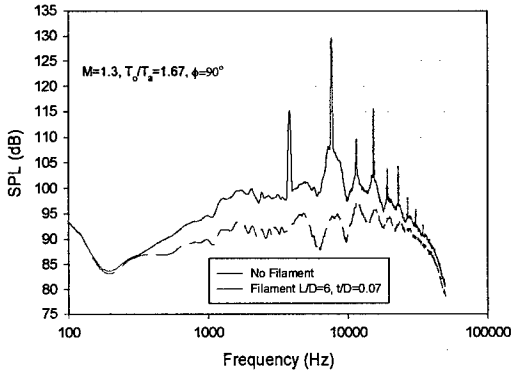

Figure 8: Spectra Comparison at 425°F

Technology Transfer

In addition to the results obtained at Louisiana State University, experiments were also conducted at the Boeing INTF to evaluate the ability of the filament to suppress noise. These tests focused primarily on the filament effect on high subsonic cold flow jets. While not as dramatic as for the supersonic case, the results indicate that the filament still produces substantial noise reduction (3-6 dB) over the entire frequency range[4].

Future Plans

The work described above concludes the third and final year of grant/contract number F49620-96-1-0378. It is the opinion of the investigators involved that the work can be considered a success as all of the initial objectives were achieved. This work will be continued at the University of Cincinnati as a joint venture with General Electric Aircraft Engines.

Acknowledgement / Disclaimer

This work was sponsored (in part) by the Air Force Office of Scientific Research, USAF, under grant / contract number F49620-96-1-0378. The views and conclusions contained herein are those of the authors and should not be interpreted as necessarily representing the official policies or endorsements, either expressed or implied, of the Air Force Office of Scientific Research or the U.S. Government.

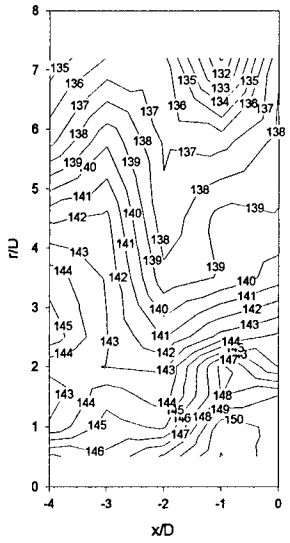

Figure 9: Upstream Baseline Mapping

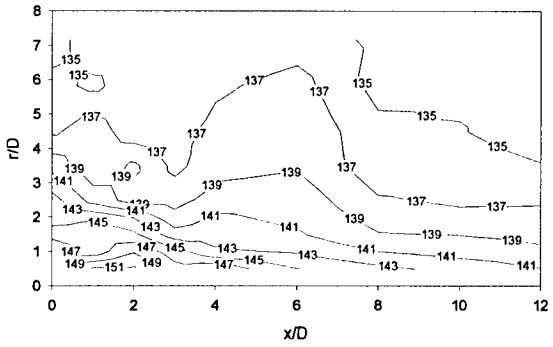

Figure 10: Downstream Baseline Mapping

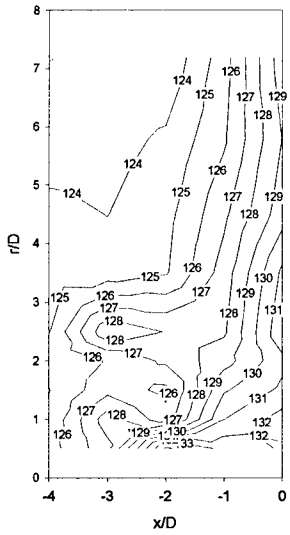

Figure 11: Optimal Filament Upstream

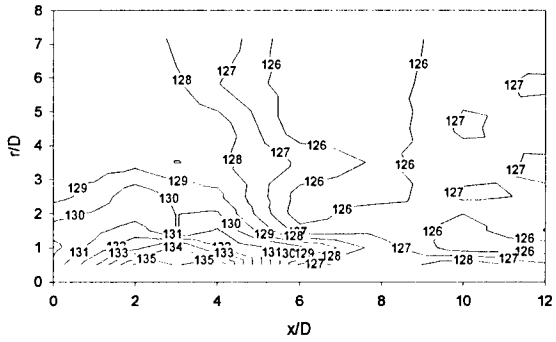

Figure 12: Optimal Filament Downstream

References

1) Callender, B., Gutmark, E, "Reduction of Underexpanded Jet Noise by Flow/Filament Interaction", AIAA 2000-0082.
2) Massey, K.C., Ahuja, K.K., Jones, R.R., C.K.W. Tam, "Screech Tones of Supersonic Heated Free Jets", AIAA 93-0141.
3) Tam, C.K.W. "Supersonic Jet Noise". Annual Review of Fluid Mechanics Vol 27, pp.17-43, 1995
4) Anderson, B., Wygnanski, I., Gutmark, E., "Noise Reduction by Interaction of Flexible Filaments with an Underexpanded Subsonic Jet", AIAA 99-1921, January 1999.

Personnel Supported

Bryan Callender	Graduate Student, Louisiana State University
Dr. Ephraim Gutmark	Professor, Louisiana State University

Velocity Measurements in a Synthetic Jet

MIPR number 985203029

Yair Guy, Julie A. Morrow and Thomas E. McLaughlin
Department of Aeronautics
USAF Academy, CO 80840

Abstract

Detailed measurements of the velocity field in a synthetic jet emanating from a piezoelectric actuator are conducted. A two-dimensional, steady, turbulent jet is synthesized from the ambient air by periodically deflecting a piezoelectric-driven disk, enclosed in a cavity. The cavity is sealed all around, with only a two-dimensional slot, 0.5 mm wide and 30 mm long, on one side. The actuator is excited with square and sinusoidal waveforms, and the time-dependent velocity is measured with a hot-film anemometer over a wide range of excitation frequencies and spatial locations. Time-averaged values and useful statistics are then computed from these data.

The need to improve fighter aircraft and missile maneuverability has inspired extensive study of the flow past wings and of methods to enhance its performance. In recent years, the efficacy of active control by oscillatory flow excitation with zero net mass flux and non-zero momentum flux has been shown[1-8]. It is more effective for delaying separation from a lifting surface, relative to steady blowing traditionally used for this purpose. This concept has been proven for basic configurations[1, 2], airfoils[3, 4] and delta wings[5-8]. However, in all these cases, the mechanism used to generate the velocity oscillations needed for zero-mass-flux flow control was hardware-intensive. An alternative is to use a synthetic jet. To use the synthetic-jet actuator to its capacity, it is imperative that its performance be fully known. The actuator should be characterized in terms of its response to frequency and input voltage, and the velocity field it produces. The present investigation is focused at studying the characteristics of the synthetic jet and their dependence on the frequency and the spatial location.

The synthetic jet actuator is comprised of a cavity, a small orifice connecting the cavity to the ambient fluid, and a flexible metal diaphragm that constitutes one side of the cavity (see Figure 1). In the current design, the cavity was cylindrical and communicated to the ambient fluid through a rectangular orifice, 0.5 mm wide and 30 mm in length. The actuator disk consisted of a thin, steel disk on which a piezoelectric ceramic disk (Barium-Titanate) was bonded. The diameter of the steel disk was D=30 mm and its thickness was t=0.2 mm. The diameter of the piezoelectric disk was 20 mm.

It may be expected that velocity output from the actuator is highest when it is excited at its resonant frequency. The vibrating disk can be modeled as a circular plate, rigidly clamped at its edge. The solution to this problem is well documented[11, 12], and the first two resonance frequencies, $f_{1,2}$, are given by:

$$2\pi f_{1,2} = K_{1,2}\sqrt{\frac{4Et^3}{3(1-\nu^2)m_a D^4}} \qquad (1)$$

D = exit-slot width, E = Young's modulus, t = thickness of actuator disk, ν = Poisson's ratio, and m_a= mass per unit area of actuator disk. $K_{1,2}$=10.2 and 21.3, respectively. The first two resonance frequencies of the actuator were computed using equation (1), based on the mechanical properties of the steel disk alone. They are f_1=584 Hz. and f_2=1218 Hz.

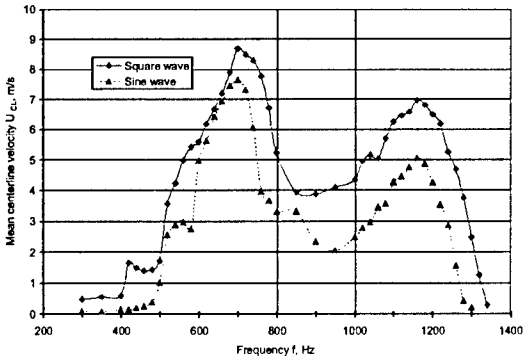

Figure 1: Schematic drawing of the actuator.

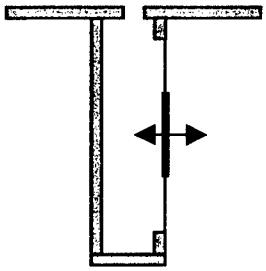

Figure 2: Mean centerline velocity at a distance of X/d=12 from the slot exit.

The centerline velocity at distance of X/d=12 from the slot exit was measured at various values of the excitation frequency. Note that X = axial distance away from slot and d = exit-slot width. The results are presented in Figure 2, where the time-averaged (mean) velocity is plotted with respect to the excitation frequency, for square and sinusoidal waves. Two resonance frequencies of f_1=700 Hz. and f_2=1160 Hz. are easily identified. These measured resonance frequencies are close to the computed values, indicating that the actuator may indeed be modeled as a clamped, circular plate. The discrepancy from the computed values (especially at the lower resonance frequency) may be attributed to interference introduced by the large piezoelectric disk that was bonded at the center of the steel disk. Young's modulus of the piezoelectric is about one half of that of steel, hence a lower resonance frequency relative to the computed value should be expected.

The mean velocity is higher when the actuator is excited with a square wave, relative to the sinusoidal excitation, throughout the entire frequency range (Figure 2). This results from the more abrupt deflection of the disk when excited with a square wave. The mean velocity close to the slot exit peaks when the actuator is excited at its resonance frequency, as may well be expected. The maximum mean velocity at an excitation frequency of f_1=700 Hz. is 8.7 m/s when the actuator is excited with a square wave, and 7.0 m/s when excited with a sinusoidal wave. It is important to note that the actuator produced fairly high velocities even when operated off-resonance. A mean velocity of 2.0 m/sec was obtained when the actuator was excited with a square wave at 500 Hz, and 1.0 m/sec when excited with a sinusoidal wave at the same frequency.

Spectral analysis of the centerline velocity was performed with a TSI-supplied FFT routine. The results are for excitation with a square waveform at 660 Hz. Figures 3 and 4 show that, close to the slot-exit, spectral peaks exist and their amplitudes decrease as the axial distance from the slot-exit increases. At the slot-exit, the high frequency forcing of the actuator results in spectral peaks at the fundamental frequency of 660 Hz and its higher harmonics (Figure 3). This confirms the fact that at the slot-exit the flow is dominated by velocity fluctuations induced by the oscillating membrane. A similar pattern exists up to an axial distance of X/d=12 (Figure 4), but a reduced energy content at the high harmonics can be observed. As mentioned in the previous section, this is the approximate location where the velocity fluctuations induced by the oscillating membrane subside, and a steady jet is formed.

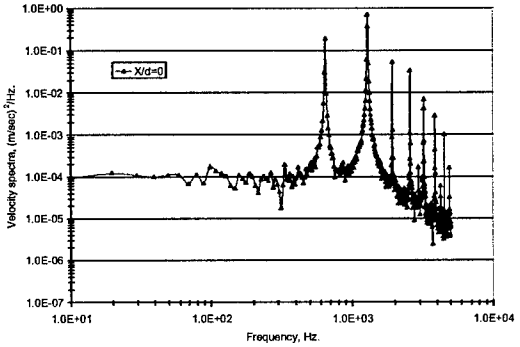

Figure 3: Power spectra of the centerline velocity at an axial distance of X/d=0.

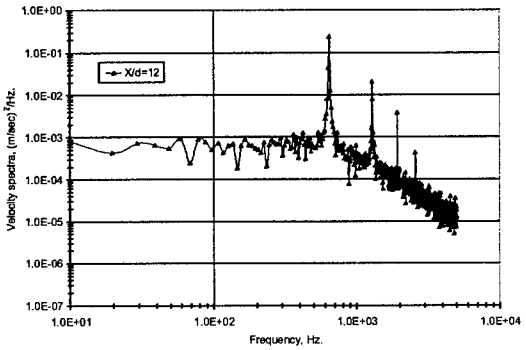

Figure 4: Power spectra of the centerline velocity at an axial distance of X/d=12.

Velocity Profiles Across the Jet

Velocity profiles across the jet were measured at several axial distances perpendicular to the axis of the slot, ranging from X/d=3 to X/d=80. The actuator was excited with a square wave at a frequency of 660 Hz. A sample of the experimental results is presented in Figures 5 and 6, where the nondimensional mean velocity, U/U_{CL}, is plotted with respect to the nondimensional similarity coordinate $Y/Y_{½}$. U = time averaged (mean) velocity at a given spatial location and U_{CL}= time averaged (mean) centerline velocity at a given spatial location. Y = lateral distance across slot or jet. Y=0 at the slot-exit center and $Y_{½}$ = lateral distance where U/U_{CL}=0.5. Several theoretical methods to compute the velocity distribution across a steady, two-dimensional, turbulent jet exist, and are well documented[11, 14]. Two of these methods are used here for the sake of comparison. The computed results from Equations (2) and (3) are included in Figures 5 and 6.

$$\frac{U}{U_{CL}} = \sec h^2\left(\frac{7.67\,Y}{X}\right) \qquad (2) \qquad\qquad \frac{U}{U_{CL}} = \cos^2\left(\frac{\pi\,Y}{4\,Y_{1/2}}\right) \qquad (3)$$

Figure 5 shows the measured and the computed velocity profiles at axial distances of X/d=3, 6, 9, and 12, namely before the formation of a steady jet. A fair agreement between the computed and the measured results exists up to a lateral distance of $Y/Y_{½}$=1

only. Beyond this point, the velocity profile spreads over a wider lateral distance, relative to what might be expected in a steady jet. As mentioned in the previous section, these locations are in the region where the jet is just being formed; hence a discrepancy from the theoretical values is to be expected. The experimental results presented in Figure 5 confirm this statement. The discrepancies increase as the lateral distance from the center of the jet increases. However, it should be noted that at a given lateral location $Y/Y_{½}$, the discrepancy between the measured and the computed results decreases as the axial distance from the slot increases. This is consistent with the fact that increasing the axial distance means getting closer to the point where a steady jet is formed. The computed results are only valid for a fully developed jet. Figures 6 shows the measured and the computed velocity profiles at axial distances of X/d=30 and 40. These locations are within the steady, fully developed jet; hence a good correlation with the theoretical values is expected. Indeed, Figure 6 indicates a good correlation with the results computed by Equation (2), over most of the transverse range. The results computed with Equation (3) seem to underpredict the width of the jet.

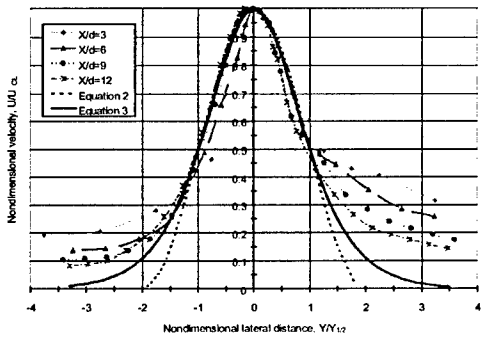

Figure 5: Transverse profile of the mean velocity. Axial distances X/d=3, 6, 9, 12.

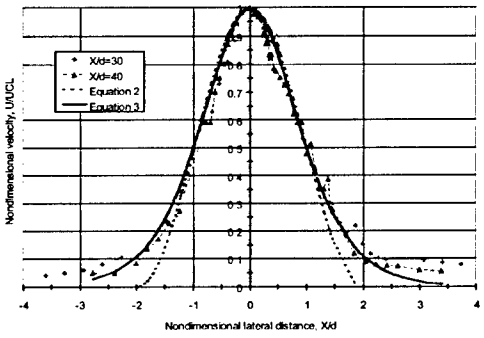

Figure 6: Transverse profile of the mean velocity. Axial distances X/d=30, 40.

Synthetic jets are a viable means of active flow control. At present, the effects of synthetic jet actuator geometry on actuator performance are being tested at the US Air Force Academy for a two dimensional airfoil. Tests will also be conducted on a delta wing within a few months. Preliminary results indicate the jet-velocity and the operating (resonance) frequency are dependent on the geometry of the actuator. In order to optimize the output of an actuator, the dependence of its performance on the major geometric parameters should be determined. This will enable users to maximize the output velocity, i.e. maximize the momentum imparted to the flow and to tailor the actuator to the desired operating frequency.

Measured results of the velocity field in a synthetic jet emanating from a piezoelectric actuator were presented. The actuator was excited with square and sinusoidal waveforms, and the resulting velocity was measured over a wide range of excitation frequencies and distances. Time-averaged values and useful statistics were computed from the reduced data and sample results were presented. It was shown that two regions exist in the flow-field created by the actuator. Close to the slot-exit, the flow is unsteady, and is dominated by large velocity fluctuations induced by the oscillating

membrane. At axial distances larger than approximately 12 slot-widths, the flow pattern changes. Downstream of this location it appears as a steady jet, where the flow is no longer affected by the oscillating membrane. This jet exhibits properties that are indicative of a fully developed, two-dimensional, turbulent jet.

The centerline velocity close to the slot exit was measured at various excitation frequencies. The results showed the existence of two resonance frequencies at which the mean exit velocity was maximized. The measured resonance frequencies were 700 Hz and 1160 Hz, and agreed well with theoretical computations. The mean velocities at the two resonance frequencies were 8.7 m/sec and 7.0 m/sec, when the actuator was excited with a square wave. When excited with a sinusoidal wave, the actuator produced mean velocities of 7.7 m/sec and 5.0 m/sec, at the same frequencies.

Acknowledgements

The authors wish to thank SSgt. B. Johns for his assistance in performing the experiments, and Prof. Douglas R. Smith of the University of Wyoming for providing the synthetic jet actuator. Special thanks are extended to Prof. Israel ("Wygy") Wygnanski for the efforts undertaken to make this research possible.

References/ Published Works

1. Greenblat, D. and Wygnanski, I., "Dynamic Stall Control by Oscillatory Forcing", AIAA Paper 98-0676, 1998.

2. Nishri, B. and Wygnanski, I., "On the Flow Separation and its Control", Computational Methods in Applied Science, 1996.

3. Seifert, A., Darabi, A. and Wygnanski, I., "Delay of Airfoil Stall by Periodic Excitation", AIAA Journal of Aircraft, Vol. 33, No. 4, 1996.

4. Wygnanski, I. and Seifert, A., "The Control of Separation by Periodic Oscillations", AIAA Paper 94-2608, 1994.

5. Guy, Y., Morrow, J. A. and McLaughlin, T. E., "Velocity Measurements on a Delta Wing with Periodic Blowing and Suction", AIAA Paper 2000-0550.

6. Guy, Y., Morrow, J. A. and McLaughlin, T. E., "Parametric Investigation of the Effects of Active Flow Control on the Normal Force of a Delta Wing", AIAA Paper 2000-0549.

7. Guy, Y., Morrow, J. A. and McLaughlin, T. E., "Pressure Measurements and Flow Field Visualization on a Delta Wing with Periodic Blowing and Suction", AIAA Paper 99-4178.

8. Guy, Y., Morrow, J. A. and McLaughlin, T. E., "Control of Vortex Breakdown on a Delta Wing with Periodic Blowing and Suction", AIAA Paper 99-0132.

9. Blevins, R. D., "Formulas for Natural Frequency and Mode Shape", Krieger, Malabar, FL, 1984.

10. Young, W. C. "Roark's Formulas for Stress & Strain", McGraw-Hill, New York, 1989.

11. Schlichting, H., "Boundary Layer Theory", McGraw-Hill, New York, 6^{th} Edition, 1968.

12. Bradshaw, P., Cebeci, T. and Whitelaw, J. H., "Engineering Calculation Methods for Turbulent Flow", Academic Press, 1981.

13. Rathnasingham and R. Breuer, K. S., "Coupled Fluid-Structural Characteristics of Actuators for Flow Control", AIAA Journal, Vol. 35, No. 5, May 1997, pp. 832-837.

14. White, F. M., "Viscous Flow", McGraw-Hill

Distributed Turbulent Flow Control by Neural-Networked MEMS

F49620-93-1-0332

Principal Investigator

C. M. Ho
Mechanical and Aerospace Engineering Department
University of California, Los Angeles
Los Angeles, California 90095

Phone: 310-825-9993 Fax: 310-206-2302
E-mail: chihming@seas.ucla.edu

Co-Principal Investigators

R. Goodman **J. Kim** **Y. C. Tai**

Abstract

The work to develop the complete M3 system for active control of the turbulent boundary layer is ongoing. Significant progress has been made, especially in the area of CFD simulations and electronic design of the neural network. Whereas previous simulations have concentrated on the case of an incline plane at different angles to the flow, recent efforts have resulted in the successful simulation of an oscillating plane in the flow. This provides invaluable insight to the effects of actuation of the microflap on shear and drag. Specifically, it allows for the study of the physical mechanisms by which the microflap interacts with the flow. Implementation of the neural network algorithm onto an electronic circuit has also moved closer to fruition. Several issues have been overcome to allow for a perturbative neural network scheme to be laid out in circuitry. In the experiment aspect of the project, a previously undetected flaw in the experimental procedure was corrected. Experimental studies of the effects of continuous microflap actuation have been made. The real-time controls system setup will be re-employed in order to determine the proper logic for the neural network.

CFD

Direct simulation of low-Reynolds-number turbulent channel flow has been a tool in our investigation of MEMS boundary layer control. A pseudo-spectral method with a periodic channel is used which accurately calculates the flow's turbulent fluctuations at much lower cost than other methods. Simulations with blowing/suction actuation at the channel wall showed such actuation could reduce skin friction by 20%. The simulations showed further that the actuation could be properly controlled by a neural network using

shear stress at the wall as its input. The effective action of the neural network seems to be to identify near-wall streamwise vortices, and produce transpiration flow that weakens them and hence diminishes turbulent transport of momentum to the wall.

With those results established, the attention was directed to simulation of the flap actuators. These actuators add to the complexity of control and simulation. In comparison to the blowing/suction actuation, the action of the flaps is not instantaneous; at least one whole cycle of the flap's rise and fall is involved. The boundary conditions involved in simulating a fine moving structure with edges, corners and flow on both sides of its surface are more complicated than the relatively simple prescription of normal velocity at the flow domain boundary needed for blowing/suction simulation. An immersed boundary method was developed for the task. The effects of the flaps are modeled by including a body force term in the fluid dynamics momentum equation. This body force is constructed so that the no-slip condition at the flap surface is met. With this method, the fluid dynamics computations are still performed using the smooth-walled channel as the flow domain, taking advantage of simplicity and efficiency for the equation solvers developed for this simple, regular geometry.

Our immersed boundary method has been tested against published viscous flow results that have similarities with the flow around our flaps. The simulation results have also been checked against results from our wind tunnel testing. Simulations of an early 4 mm square version of the flap actuator oscillating at a slow 40 Hz elucidated the mechanisms by which the flap was modifying the flow over it. Raising the flap into higher speed fluid above it created a high shear layer. This zone was further enhanced by the motion of fluid being sucked underthe flap to fill the opening space there. The shear layer then rolled up into a vortex which moved downstream from the flap and induced motion of near wall fluid away from the wall. Tip vortices generated on the edges of the flap contributed to this induced motion of low speed fluid away from the wall. The movement of low speed fluid away from the wall was seen in wind tunnel tests of the flaps. The simulations clarified the mechanisms involved by providing velocity data at locations inaccessible to hot wire anemometers. It also showed that the effect of the flap was most pronounced not at the flap itself, but rather a short distance downstream after a small delay.

Simulations of an array of flaps have been performed. The same control strategy that was used to control the blowing/suction actuation has been repeated with the flap actuators. Another neural network control has also been tried that predicts high-shear streaks and actuates a flap when one is predicted. The flaps we are modeling in these simulations are the newer types being produced which are 2 mm long and 1 mm wide and designed to oscillate at 3 kHz. For the test conditions in the wind tunnel, in terms of near-wall scaling, the flaps are 70 wall units long and 35 wall units wide. Their oscillation period is 5 wall units. For the wind tunnel test conditions, the Reynolds number based on friction velocity and channel half height is about 400. Simulations are performed at a Reynolds number of 180. This is high enough far the near-wall region of our actuators to behave as it does in higher Reynolds number flows. The flow modification produced by these fast, slender flaps is different than that seen with the square flaps. The effect of the

flaps' downstroke dominates over the upstroke producing downwelling fluid downstream of the flap instead of upwelling fluid. So far these simulations have not shown a long-time drag reduction resulting from the flap actuation.

Experimental

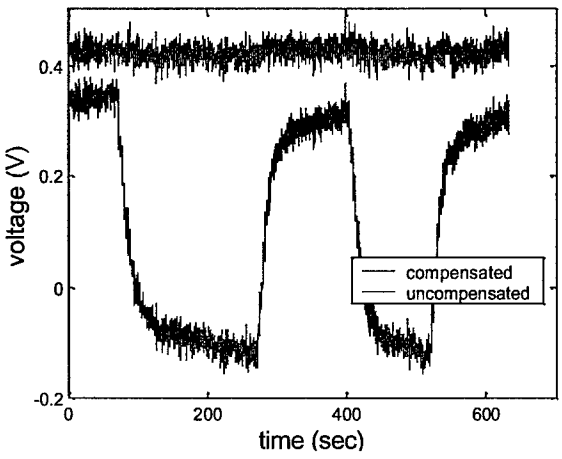

Figure 1 Shear stress sensor output with power applied to microflap actuator

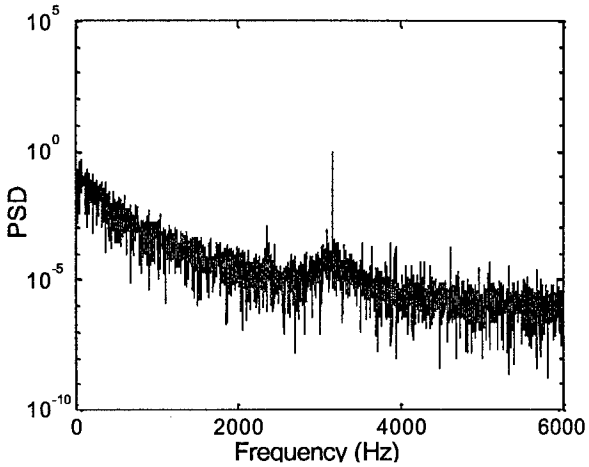

Figure 2 Power spectrum density of shear stress measurement with continuous microflap actuation

Recent efforts have been concentrated on ascertaining the validity of the shear stress measurements. It was found that the previous attempts to use on-chip temperature compensation contained inaccuracies due to a flawed calibration process. In the previous calibration process, instead of directly correlating the on-chip temperature sensor output with the shear stress sensor output, the temperature sensor output was first correlated with a thermocouple measurement in the free stream. It was assumed that as there was no external source of heating during the calibration process, the temperature on the surface of the sensor would be the same as the free stream. However, it turned out that even in this case, there is a discrepancy between the two temperatures and that this discrepancy is large enough to be responsible for the apparent shear reductions that we have previously measured. In the current measurements, this flaw in the calibration process is corrected.

A comparison of the shear stress sensor output with and without the appropriate on-chip temperature compensation is shown in Figure 1. In the case shown, the shear stress sensor is located immediately downstream of the actuator. Power was supplied to the microflap actuator but its deflection should be minimal, as there was no magnet provided to generate the magnetic force necessary for full actuation. The actuator was placed in a flow field of 10 m/s. The dips in the voltage in the uncompensated case are due to power to the actuator being switched on and off. As can be seen, the current temperature compensation scheme can very effectively correct the disturbances caused by the heating effects of the actuator.

The effects of continuous actuation of the microflap in a flow field were also investigated. From the average of the shear stress measurements, the effects of a

continuously actuated microflap in a flow field of 10 m/s are not very apparent. However, examination of the power spectrum density reveals that a large peak exists at the actuation frequency of the microflap. This peak does not appear when the microflap is not actuated. From this, it can be seen that the motion of the microflap does indeed impart an effect on the flow. Further research will be done to investigate the correlation between the position of the microflap during actuation to the effects on the shear stress. Furthermore, the real time control system mentioned in the previous report will be set up again to develop the neural network logic.

Circuitry

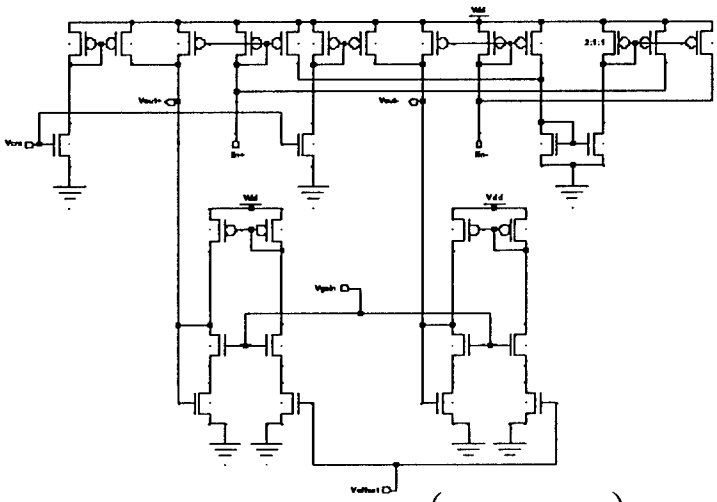

$$\Delta V_{out} \approx R \cdot \Delta I_{in} = R \cdot \left(\sum_i \left(I_{weight_i} \cdot \Delta V_{in_i} \right) \right)$$

$$\text{where } R \approx \frac{1}{2K(V_{gain} - V_T)}$$

Figure 3 Neuron Circuit

Efforts continue toward a single chip solution to implement the fully adaptive neural network and training algorithm. A new neuron circuit (Figure 3) has been developed which addresses several shortcomings of the previous design. The old design had a very limited linear range and saturated quickly. This proved to be a problem when the neuron was receiving inputs from many synapses. The effective resistance of the new neuron is much easier to control and has a wider range. This is achieved by cascade biasing a transistor into its linear region. This region is then used to obtain lower effective resistance values.

The neural network is to be trained by using the perturbative weight update rule. The perturbative technique requires generating random weight increments to adjust the weights during each iteration. A conceptually simple technique of generating random perturbations would be to amplify the thermal noise of a diode or resistor. Unfortunately, the extremely large value of gain required for the amplifier makes the amplifier susceptible to crosstalk. Any noise generated from neighboring circuits would also get amplified. Since some of this noise may come from clocked digital sections, the noise

would become very regular, and would likely lead to oscillations rather than the uncorrelated noise sources that we desire. Therefore, another technique is required. Instead, the random weight increments are generated with linear feedback shift registers (Figure 4) that produce a long pseudo-random bit sequence. These random bits are used as inputs to a counter that stores and updates the weight. The counter outputs go directly to the D/A converter inputs of the synapses. If the weight updates led to a reduction in error, the update is kept. Otherwise, an inverter block is activated which inverts the counter inputs. This has the effect of restoring the original weights. A block diagram of the full neural network circuit function is provided in Figure 6.

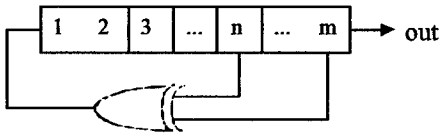

Figure 4 Linear feedback shift registrar

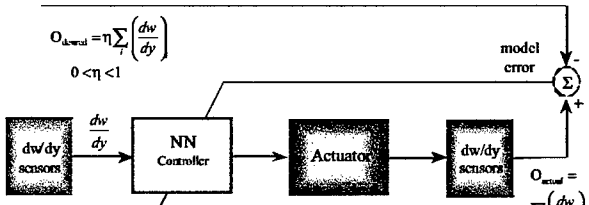

Figure 5 Direct perturbative control scheme

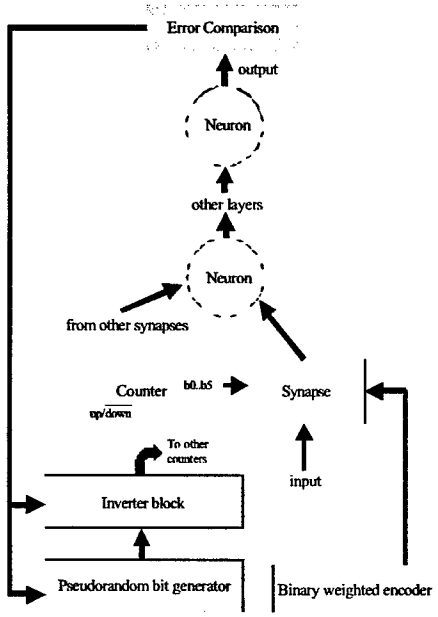

Figure 6 Neural network block diagram

The above neural network circuits were sent out for fabrication and have recently been received. Testing is ongoing to measure their functionality. After testing the function of the chip on certain test training patterns such as parity function (XOR) learning, the network will be used for training with wind tunnel sensor measurements. The final goal will be to use the chip for direct perturbative control in the wind tunnel (Figure 5). In this scheme, inputs from upstream sensors go through the neural network to control the actuator. Downstream sensors are used to determine the effect of the actuator. If the drag decreases, the weight perturbation is kept, otherwise it is thrown away. This should lead to a gradual decrease in drag.

M^3 System

As previously reported, the efforts of this project have already resulted in the successful fabrication of a M^3 system, whereby micro-sensors, actuators, and electronics were integrated onto a single chip. In addition, a rudimentary edge detector was also included to serve as the neural network logic. The components of this system have been tested in wind tunnel experiments and have to shown to be fully functional, the results of which

were already reported. The fabrication process of the M^3 system has since then been moved from a 4" wafer to a 6" wafer. In the upcoming M^3 system, electronic circuitry based on the neural network logic developed from CFD results will also be integrated. It is expected that the new wafers containing all the components will be ready in 2 months with the final release of the sensors and actuators being ready a month afterward. Wind tunnel testing will be carried out then.

Acknowledgment/Disclaimer

This work was sponsored by the Air Force Office of Scientific Research, USAF, under grant/contract number F49620-93-1-0332. The views and conclusions contained herein are those of the authors and should not be interpreted as necessarily representing the official policies or endorsements, either expressed or implied, of the Air Force Office of Scientific Research or the U.S. Government.

Personnel Supported

John Mansfield	Postdoc, University of California, Los Angeles
James Lew	Graduate Student, University of California, Los Angeles
Zhigang Han	Graduate Student, Caltech
Vincent Koosh	Graduate Student, Caltech

DRAG CONTROL IN TURBULENT BOUNDARY LAYERS USING LARGE-SCALE PASSIVE MANIPULATORS

(July, 2000)

AFOSR GRANT NUMBER F49620-98-1-0150

Fazle Hussain
Department of Mechanical Engineering
University of Houston, Houston Texas 77204-4792

ABSTRACT

1. OBJECTIVE

Recent direct numerical simulations (Schoppa & Hussain 1998, 2000) reveal a new large-scale control scheme for suppressing the generation of drag-enhancing streamwise vortices from streaks. This demonstrates that a significant drag reduction is achievable via a large-scale steady control flow, requiring no sensor, actuator, or instantaneous flow information. The control flow suppresses the streak instability (actually, transient growth of otherwise stable streaks) — responsible for (re)generating drag-enhancing near-wall (buffer-layer) streamwise vortices and thereby significantly reduces drag (and hence turbulent heat transfer).

Our objective was to first demonstrate the drag reduction via proof-of-concept experiments in a small air channel flow facility at low Re_θ values using Large-scale Passive Manipulators (LPM) that generate the control flow of weak counter-rotating streamwise vortices over one wall.

2. APPROACH

Experiments were performed in an air channel flow facility (45cm long x 49cm wide x 5 cm high) using its bottom (Plexiglas) wall as the test plate. The test plate is allowed to float freely on a liquid bath (figure 1). Note that the length of the test (floating) plate is necessarily kept small so that the flow is a flat plate TBL, not a turbulent channel flow.

The floating plate is set flush with the fixed upstream plate, with the air flow turned off. Turbulence generator (a saw-tooth blade; base width = 4mm and height =1.5mm) is used to trip the boundary layer for it to become fully turbulent (Hussain & Clark 1977). For drag control, we used a spanwise row of 42 LPMs mounted on the flat plate at a downstream distance of 13 cm from the turbulence generator. A single LPM is a half-delta winglet (2mm high and 4mm long) aligned alternately at + α -- the angle of

incidence with the flow direction-- such that the LPMs produce alternate clockwise and anti-clockwise largescale streamwise vortices. We varied α over the range + 6 – + 12 degrees and $\alpha = +8^{\circ}$ provided the best result within the velocity range we examined (about 12 m/sec –14 m/sec).

The downstream motion of the floating plate is opposed by a cantilever beam fitted with a strain gauge. Static balance of forces on the plate is thus achieved, and the strain gauge measures the net drag (including form and skin-friction drag due to the LPMs) on the plate. Since there is no motion in the liquid bath, all drag experienced by the plate is due to the air flow. The strain gauge can measure force with a resolution of 0.5 milligram, which corresponds to the measurement of a change in drag to within 0.03% even at a fairly low free-stream velocity (say 3m/s). The accuracy is expected to be higher at higher air velocities.

3. PROGRESS

Originally, we started measuring drag on the plate by hanging the test plate with two long

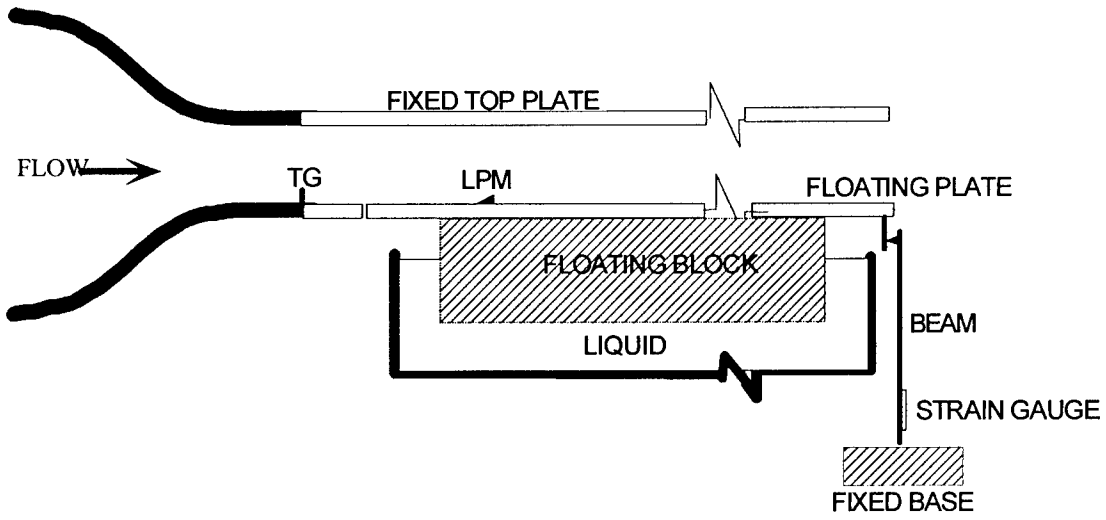

Figure 1. Schematic showing the side cross-sectional view of the channel flow facility. TG: Turbulence Generators; LPM: Large-scale Passive Manipulators.

strings. For a given velocity, the hanging plate deflected downstream by the drag, and the plate was forced back to its original position using counterweights. To keep the plate vertical under flow condition, we had to arrest the plate's transverse motion using bearings. Because of poor measurement resolution and bearing friction, we developed the floating plate measurement technique. This technique has one problem; at speeds higher than about 25m/sec the plate becomes unstable and force measurement is not possible. At lower speeds, the streamwise motion of the test plate is smooth and stable.

We are currently considering a new system to improve further the drag measurement resolution by an order of magnitude and at a much higher Re_θ values (see section 5) .

4. RESULTS

For drag control (as discussed in section 2) we used 42 (21 pairs) of LPMs such that each alternate winglets are oppositely inclined (yawed) to the streamwise direction and generate swirls of opposite signs. The near-wall control flow is thus like alternating spanwise wall-jets superimposed on the TBL. The z-separation of wall-jet collision (streamwise) lines, being much larger than the average streak spacing (z^+=100), enables control of many streaks by each control flow vortex (swirl). The streaks are squeezed together in one-half of a swirl and spread apart in the other half. Both effects cause weakening of the streaks, making their flank slope fall below the instability limit: cross-diffusion or planar reconnection in the first case and flattening (or swatting) of streaks in the second case.

In our experiments, LPM height roughly equals four times the displacement thickness (δ^* about 0.5mm in the velocity range of 12 m/sec to 25m/sec), and their spanwise spacing is chosen to be a few times the streak spacing

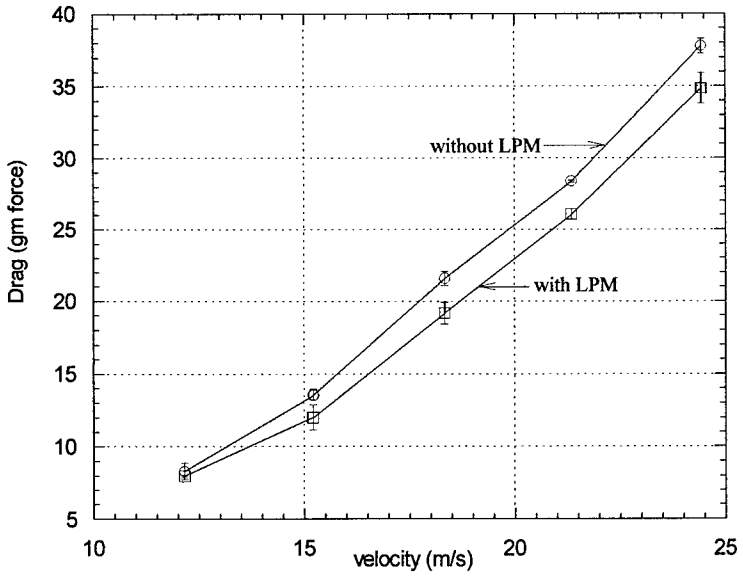

Figure 2. Total drag on the floating plate without and with LPM control.

With the current measurement system using one strain gauge (which is not temperature compensated compared to 2 or 4 strain gauge system) the net drag reduction shows some

variation from experiment to experiment which is about 4% to 11%. This variation is perhaps because of change in temperature and inaccurate angular setting of the LPMs.

Figure 2 shows one set of our results indicating noticeable drag reduction. For example, drag reduction are about 11%, 11.5% and 8% for U= 15.25, 18.25, and 24.5 m/sec respectively.

5. FUTURE PLAN

(a) Currently, we are considering a few options to measure TBL drag directly using: (i) full bridge-strain gauge system (i.e. four strain gauges: two in tension and two in compression) which are temperature compensated and have high resolution. (ii) Differential Variable Reluctance Transducer (DVRT) which can measure displacement with a resolution of 10 nanometer. This system will require properly calibrated springs – low spring constant for low velocities and high spring constant for high velocities to utilize the full stroke length of the DVRT.

(b) Use miniature step motors to set LPM angles accurately via remote control without disturbing the test plate. Alternate LPMs can be connected to a worm grear driven by a single motor so that inclination angles of these alternate LPMs can be changed simultaneously and identically. Another worm gear will connect the other set of the alternate LPMs.

(c) Once the drag reduction is conclusively established with a single spanwise row of LPMs, we will systematically vary for a single Re_θ the LPM parameters, viz. the angle of attack of the half-delta winglets (which affects the circulation and streamwise extent of the swirling control flow, as well as device drag), their spanwise spacing (which determines the number of streaks influenced by a single LPM), and their height (which is expected to crucially influence both device drag penalty and the transverse location of the center of the control flow swirl). The height of the LPMs will be selected from the measured local displacement thickness (δ^*). We will use two LPM heights, viz. $8\delta^*$ and $4\delta^*$.Two transverse spacing of LPMs will be used, viz 25 and 50 streak spacing. These spacing will be estimated from the measured wall units.

(d) To measure drag as well as shear stress, experiments will be performed in a low-noise in-house (1m wide x 1.6m high x 7m long test section) wind tunnel. A carefully designed and machined floating plate setup similar to the one used in the channel flow facility will be built

(e) This tunnel will facilitate hot-wire measurements within the sublayer. The estimated sublayer thickness near the end of the tunnel is about 0.25mm and hot-wire measurements will provide about 8 data points within the sublayer, allowing an accurate estimate of the wall shear stress (τ_w) employing Clauser cross plot method.

(f) Hot-wire (single wire) measurements will be performed at three transverse locations: at the z-plane between a pair of LPMs and other two in the z-planes through the trailing edge of the LPMs. For each transverse location, boundary layer

characteristics (viz. U(y), u'(y)) will be measured at a few streamwise locations. These data will indicate the drag reducing effect of the first row of LPMs and will dictate the placement of the next row of LPMs. The second row of LPMs will be placed at the streamwise location where τ_w, determined from near-wall U(y) data, will reach within 90%of the equilibrium value. Direct drag measurements will be carried out with two rows of LPMs over a range of Re_θ (3000-8000) to delineate the range of effectiveness of this scheme.

ADDITIONAL FUTURE PLAN

(a) Develop code for prediction for flow around LPMs and for drag reduction.

(b) Educe CS structures in LPM wake using a cross-wire rake, compare with numerical predictions and improve code.

(c) Study feasibility for heat transfer control by measuring local heat transfer behind LPMs with heated air/wall.

(d) Study the feasibility of applying LPM in aircraft for drag reduction.

6. ACKNOWLEDGEMENT/DISCLAIMER

This work was sponsored by the Air Force Office of Scientific Research, USAF, under grant number F49620-98-1-0150. The views and conclusions contained herein are those of the authors and should not be interpreted as necessarily representing the official policies or endorsements, either expressed or implied, of the Air Force Office of Scientific Research or the U.S. Government

7. REFERENCES

1. Schoppa, W. & Hussain, F., "A Large-scale Strategy for Drag Reduction in Turbulent Boundary Layers," The Physics of Fluids, Volume 10, pp.1049-1051 (1998).

2. Schoppa, W. & Hussain, F., "Coherent Structure Dynamics in Near-wall Turbulence," Fluid Dynamics. Research, volume 26, pp. 119-139 (2000a).

3. Hussain, A.K.M.F. & Clark, A. R., "Upstream Influence on the Near Field of a Plane Turbulent Jet," The Physics of Fluids, Volume 20, pp.1416-1426 (1998).

8. RESEARCH PERSONNEL

Fazle Hussain, Professor, Mech. Eng, Dept., Univ. of Houston.
Hyder Husain, Research Associate Professor, Mech. Eng, Dept., Univ. of Houston.

A COORDINATED COMPUTATIONAL and EXPERIMENTAL STUDY
of GAS TURBINE BLADE COOLING WITH DYNAMICAL SYSTEMS
SUBGRID-SCALE MODELS for LARGE-EDDY SIMULATION

F49620-00-1-0258

Jamey Jacob and James McDonough
Department of Mechanical Engineering
University of Kentucky, Lexington, KY

Abstract

The project herein has as its goal the general enhancement of physical understanding of gas turbine blade cooling via internal cooling flows. The research to be undertaken during the three-year study consists of the following inter-related projects: i) specific, well-coordinated laboratory experiments to produce new gas turbine blade cooling data, including effects of rotation, ii) detailed investigation of subgrid-scale (SGS) models for large-eddy simulation (LES) based on use of "synthetic" SGS velocity (and temperature) fields constructed from discrete dynamical systems, and iii) experimental/computational studies of novel geometries believed to hold significant advantages for internal blade cooling heat transfer.

The overall goals of the project are first to generate new experimental data sets to improve physical understanding of turbine blade heat transfer in the presence of rotation; second, to produce LES SGS models suitable for use with efficient, flexible finite-difference (-volume) methods, and thus applicable to practical engineering problems involving complex geometries (e.g., internal cooling air circuits of turbine blades), and if necessary, "tuned" to gas turbine blade heat transfer problems, and finally, to quantitatively investigate the effectiveness of some recently-proposed novel cooling air circuit geometries.

The experimental portion will deliver measurements of flow within a rotating duct with turbulators. It will include full field instantaneous 2- and 3-D turbulent velocity profiles within the cooling passages and over turbulators; pressure and temperature measurements will be made along the wall stations using surface mounted probes. The primary goals are to extend the complexity of past and current experimental studies to truly realistic conditions and to use this data to validate and provide initial and boundary conditions to serve as initialization data for numerical computations. In the former goal, the effect of rotation will be included. By using both stationary and rotating set-ups, we can determine rotational effects on the flow field and heat transfer rates. Various turbulence enhancing geometries will also be tested to determine their effects on pressure drops and heat transfer. In the latter goal, the data obtained from this study will be used to validate the computational results, specifically the turbulence models.

There are intended to be two principal results from the theoretical/computational research to be undertaken in this project. The first will be a deeper, more thorough understanding of the details of using dynamical systems to construct synthetic-velocity SGS models as proposed herein. This is a new approach, and one that will probably lend itself to fruitful research for a number of years yet; we would expect during this project to lay the groundwork for understanding both theoretical and implementational aspects of this new approach to

turbulence modeling. The second is the computer code that will result from implementing the new models. As we have emphasized throughout, the 2-D code is already in existence, and we have provided sample results from it. The 3-D code is now under development with support from the GE Aircraft Engines Combustor Group. The dynamical systems SGS models developed during this project will be tuned (if necessary) to the internal cooling-air circuit problem and inplemented in this code, thus providing an efficient LES-like tool for turbine blade cooling analyses.

Research Plan

The research being proposed for this three-year project is intended to be a closely coordinated experimental and computational effort expected to yield improved physical understanding of turbine blade internal cooling air circuit heat transfer under realistic conditions and reliable, efficient subgrid-scale models for LES-like flow field and heat transfer calculations.

The experimental portion of the study will include novel measurements of the flow within a turbine blade cooling air circuit. The experiments will focus on the effect of rotation on the flow field, specifically the turbulent flow characteristics which have a large impact on the rate of cooling by heat transfer. The effects of rotation will be investigated by repeating experiments in identical setups without and with rotation. A primary goal is to determine when rotational effects become a dominant force in the channel flow. As a key element of this proposal, we also seek to measure the efficiency of various turbulence generating devices (turbulators) used to enhance the heat transfer rate. Using surface temperature and pressure measurements, various geometries such as rods, blocks and dunes will be analyzed. This is critical since though many researchers have focused on turbulator efficiency, it has been without the effects of rotiation. The proposal includes modern non-intrusive measurement techniques that measure the instantaneous (unsteady) 2D and 3D flow field within a plane or volume of the channel. Unlike typical PIV measurements, algorithms specifically developed for high-gradient vortical flow fields will be utilized (see Sholl and Savaş, 1998). This will allow accurate measurements within the primary regions of interest, such as behind a turbulator or the corner areas of a serpantine duct.

The computational portion of the study will involve constructing such models specifically in the context of cooling-air circuit flows in gas turbine blades. As already noted, universality of SGS models in general, and of those to be studied here in particular, has not been demonstrated, so we would prefer to first guarantee high-quality results for the specific problem at hand and investigate other problems in the future. As will be evident below, one of the key parts of the class of models proposed for development is a nonlinear discrete dynamical system used to create discrete time series that locally (in space) exhibit qualitative behavior in accord with corresponding physical small-scale phenomena (velocity and temperature in the present case) and at the same time generate correct statistical quantifications. We have previously shown that these requirements can be met for physical data sets (see Mukerji et al., 1998) using techniques developed by the Co-PI of this proposal (McDonough et al., 1998b). Thus, we are already prepared to make use of experimental data as soon as they are available, but moreover, because we have detailed understanding of the model construction process we will use this to guide the specific nature of the laboratory experiments.

Experimental Portion

The experimental studies planned for the project focus on turbine blade air cooling circuit dynamics. In this case, the nature of the cooling system precludes making measurements in an actual turbine blade system; thus, it is necessary to effectively model the system in the laboratory under the constraint that the boundary conditions (inlet, exit, wall conditions) should be identical to that of a real duct. In an effort to minimize effects of probe interference and to acquire the most data possible, velocity field measurements will be made using optical techniques. Temperature and pressure measurements will be made at the walls and heat fluxes and pressure losses respectively will be determined accordingly. Further, we note that if rotational effects are neglected, a fairly simplistic system is adequate. Inclusion of these effects is one of the novel features of this proposed study, however, and thus leads to an elaborate experimental setup, as discussed below.

The primary method of velocity measurement will be optical in nature. Optical measurements are desirable for several reasons. The measurements are non-intrusive in the classical sense, requiring only adequate seeding of the fluid medium. This avoids contamination of the flow from probe interference and the required seeding volumetric ratio is such that the effects on the flow physics are negligible (Somerscales, 1974; Agui and Jimenez, 1987). Also, the measurements result in instantaneous full field data rather than field data constructed from avearged point measurements. This allows a complete description of the flow field and prevents misleading conclusions from ambiguous collections of point-to-point data, thus the method records unsteady (instantaneous) flow field data rather than steady (time-averaged) data.

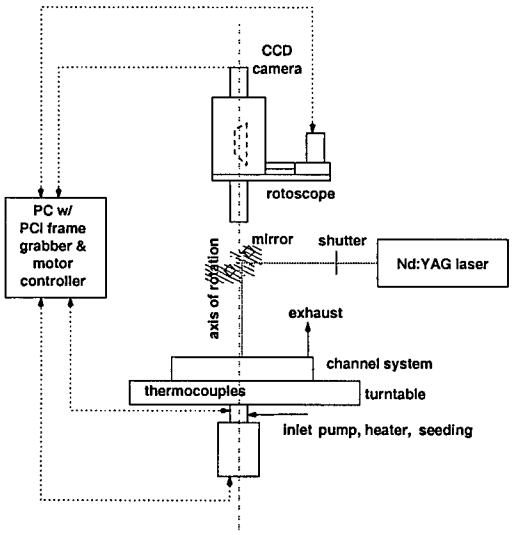

Figure 1. Test-bed schematic.

A turbine blade cooling circuit apparatus will be constructed for the proposed experimental measurements.The goal of the first phase is to take baseline measurements within a stationary (non-rotating) channel. The emphasis here will be on the velocity measurements but temperature and pressure measurements will be made on the surface as well. The efficacy of standard turbulator geometries and bleed holes will also be assessed. The goal of the

second phase is to examine a single channel of simple geometry and determine the effects of rotation on the velocity field and wall temperatures. In designing this setup, it is important to match several appropriately scaled parameters of the actual turbine blade cooling system as given in the previous section. These include the inlet and exit conditions (mass flow, temperature, pressure), the wall surface conditions of the duct, such as dimensionless heat flux. The duct models will consist of duct flow segments with heat transfer enhancing geometries, viz., ribs, pin-fins, impingement cooling cells, and various turbulators (including dunes). Heating coils will be used to heat the incoming flow to scaled temperatures, and a high pressure blower will be used to drive the flow. The channels will include optical windows for velocity and temperature measurements.

Computational Portion

The computational studies performed during the course of this project will be associated with constructing and testing synthetic-velocity SGS models for the LES-like methods described below. We will present this as follows. To begin, we will provide a summary description of the overall proposed method, first for velocity fields and then for passive scalars, and present some sample results already obtained. We will note specific areas of this technique known to need further development, and then describe our proposed methods for carrying this out.

The new approach to be considered here is one stemming from work by the Co-PI of this proposal on what has been termed additive turbulent decomposition (ATD). This approach was envisioned as a highly-efficient and parallelizable form of LES intended to ameliorate deficiencies of both filtering and SGS modeling when it was first introduced by McDonough et al. (1984a, 1984b) in the guise of "large-scale/small-scale decomposition." Developments along these lines continued with the work of McDonough and Bywater (1986, 1989), Yang and McDonough (1992), McDonough and Saito (1994), McDonough and Wang (1995) and Mukerji and McDonough (1996), the latter two of which pertain specifically to parallelization efforts. Two main features of this approach are use of unfiltered large-scale equations and local small-scale DNS as SGS models.

It has become clear through these studies, however, that in order to apply this to practical problems during the next decade it will be necessary to model the small-scale portions of the flow, rather than to directly compute them as had been the original intent. A detailed analysis of an approach whereby this can be done is presented in Hylin and McDonough (1994), with preliminary computed results in 2-D reported in McDonough et al. (1995) and McDonough (1997). Recently Hylin and McDonough (1996,1999) provided a refined analysis of their earlier approach.

There are four key ideas employed in the construction of the ATD approach that distinguish it from other forms of LES. First, the equations of motion are neither averaged (as in RANS methods) nor filtered (as in usual LES). Formally, an additive splitting of the governing equations into large- and small-scale parts is employed as is also done in the nonlinear Galerkin (NLG) and multi-level procedures of Temam and co-workers (cf., Marion and Temam, 1989; Temam, 1996). The main consequence of this is that there is no subgrid-scale stress tensor T_{ij} to be modeled. Hence, need for the Boussinesq hypothesis is removed, and interaction of large- and small-scale contributions to the solution take place through the nonlinear advection terms of the N.-S. equations, as occurs physically.

The second notion used in our proposed method is to filter solutions (rather than equations) in order to remove aliasing that arises from under resolution, and at the same time define the resolved-scale portion of the solution. This is similar to what is typically done in LES (and it serves the same purpose), but it is more straightforward because T_{ij} no longer appears, and because the solution can be viewed simply as a "signal" to which sophisticated and efficient signal processing/image processing techniques can be applied to extract the true discrete solution from the computed aliased one.

The third key aspect of this version of LES is associated with the form of the models of small-scale flow behavior, i.e., the SGS models. We have already observed that T_{ij} no longer appears, but the dependent variables are still decomposed into large- and small-scale parts as

$$u_i(\boldsymbol{x},t) = \overline{u}_i(\boldsymbol{x},t) + u_i^*(\boldsymbol{x},t), \quad i = 1,2,3 \qquad \text{and} \quad p(\boldsymbol{x},t) = \overline{p}(\boldsymbol{x},t) + p^*(\boldsymbol{x},t). \quad (1)$$

It should be clear that $\overline{\boldsymbol{u}}$ is analogous to the resolved scale of LES, and $\boldsymbol{u}^*$ is the unresolved, SGS, part of the solution. The governing equations are thus formally solved for $\overline{u}_i$ and $\overline{p}$, the large-scale velocity and pressure fields, and the u_i^*, p^* fields are modeled via methods employing discrete dynamical systems, as described in detail in Hylin and McDonough (1994,1996,1999). In general, as alluded to above, this constitutes a synthetic velocity method for subgrid-scale LES models.

The final distinguishing aspect of this approach is the manner in which the modeled quantities are applied. In particular, they are utilized to construct the "complete" solutions (32) rather than for deriving either turbulent stresses or eddy viscosities. This of course implies that accurate models must be constructed in order for the complete quantities to be accurate representations of actual physics. But it should be clear that since these models represent measurable quantities, and there are significantly fewer of them than in previous modeling approaches, this does not appear to be an insurmountable task. In fact, most of this has already been accomplished in the formal sense (Hylin and McDonough, 1996,1999; McDonough et al., 1998b) and successfully applied to experimental data by Mukerji et al. (1998). Furthermore, this direct use of small-scale quantities leads to the viewpoint that they can be interpreted as corrections to the (deliberately) under-resolved large-scale quantities. This is similar to the philosophy underlying multi-level methods (see Temam, 1996), and we will subject it to rigorous investigation during the proposed research.

REFERENCES

J. C. Agui, J. Jimenez (1987). *J. Fluid Mech.*, **185**, 447–468.

E. C. Hylin, J. M. McDonough (1994). *University of Kentucky, Mech. Engr. Report*, **CFD-01-94**.

E. C. Hylin, J. M. McDonough (1996). *University of Kentucky, Mech. Engr. Report*, **CFD-02-96**.

E. C. Hylin, J. M. McDonough (1999). *Int. J. Fluid Mech. Res.*, **26**, 539-567.

M. Marion, R. Temam (1989). *SIAM J. Numer. Anal.* **26**, 1139–1157.

J. M. McDonough (1995). *Int. J. Fluid Mech. Res.* **22**, 27–55

J. M. McDonough (1997). In *Parallel Computational Fluid Dynamics: Algorithms and Results Using Advanced Computers*, Schiano, et al. (Eds.) Elsevier Science B. V. Amsterdam, 92–99

J. M. McDonough, R. C. Bywater (1986). *AIAA J.* **24**, 1924–1930.

J. M. McDonough, R. C. Bywater (1989). In *Forum on Turbulent Flows–1989.* Bower, Morris (Eds.), *ASME-FED* **76**, ASME, NY, 7–12.

J. M. McDonough, J. C. Buell, R. C. Bywater (1984a). ASME Paper 84-WA/HT-16,

J. M. McDonough, R. C. Bywater, J. C. Buell (1984b). AIAA Paper 84-1674.

J. M. McDonough, S. Mukerji and S. Chung (1998b). *Appl. Comput. Math.* **95**, 219–243.

J. M. McDonough, K. Saito (1994). *Fire Sci. and Tech.* **14**, 1–18.

J. M. McDonough, D. Wang (1995). In *Parallel Computational Fluid Dynamics: New Algorithms and Applications.* N. Satofuka et al. (Eds.), Elsevier Science B. V. Amsterdam, 129–136.

S. Mukerji, J. M. McDonough, M. P. Mengüç, S. Manickavasagam and S. Chung (1998). *Int. J. Heat Mass Transfer* **41**, 4095–4112.

M. J. Sholl, Ö. Savaş (1997). AIAA Paper 97-0493.

E. F. C. Somercales (1974). In *Flow: Its Measurement and Control in Science and Industry*, **1**, Instrument Society of America, 795–808.

R. Temam (1996). *J. Comput. Phys.* **127**, 309–315.

Y. Yang, J. M. McDonough (1992). In *Bifurcation Phenomena and Chaos in Thermal Convection.* Bau et. al. (Eds.). *ASME-HTD* **214**, ASME, NY, 85–92.

Personnel Supported

Jamey D. Jacob	Professor, University of Kentucky
James M. McDonough	Professor, University of Kentucky
James Poncer	Graduate Student, University of Kentucky
Stewart Bible	Undergraduate Student, University of Kentucky

Publications

N/A.

Awards Received

N/A.

Transitions

N/A.

NONEQUILIBRIUM TURBULENCE STUDY USING HOLOGRAPHIC PARTICLE IMAGE VELOCIMETRY

AFOSR Grant No. F49620-98-1-0414

Byron Jones and Hui Meng*
Department of Mechanical & Nuclear Engineering
Kansas State University
Manhattan, KS 66506

*Mailing Address: Dept. of Mechanical & Aerospace Eng,, SUNY, Buffalo, NY 14260

Abstract

The objective of this project was to develop a three-dimensional flow field measurement tool, viz. holographic particle image velocimetry (HPIV), for applications in turbulent and complex flows. While the basic prototype based on off-axis holography has been established, challenges remain in the following areas:

- Measurement accuracy calibration
- Processing speed improvement, elimination of wet chemical processing of the hologram and eventually realization of time-series measurement
- Capability of measuring flows of *various* volumes and spatial resolutions
- Capability of obtaining discrete-phase information

The approach we have taken is simultaneous development of HPIV technology and pilot investigation using PIV. The latter, being a more mature technique, helps us to pave the way for HPIV application. In FY2000, we have accomplished the following:

1. HPIV measurement accuracy

Validation of the HPIV measurement of velocity fields on a 3D grid is accomplished through examination of continuity equation. In the example shown in Fig. 1, it is found that the divergence has a mean value of $0.51s^{-1}$ and a standard deviation of $6.63s^{-1}$. To estimate the relative error, we evaluate the net flux $\Delta Q = \iiint_{CV} \nabla \cdot \mathbf{u} dV$ entering an arbitrary control volume $CV=\Delta x\Delta y\Delta z$, divided by the total flux $Q = U \cdot \Delta y \Delta z$ passing through the control volume: $\eta = \frac{\Delta Q}{Q}$. For an estimation of the worst case, we choose the 95% coverage divergence value and the smallest control volume size (the grid size), it is found from the experimental data that $\eta \sim$ 4.7%. Hence, continuity is satisfied reasonably well.

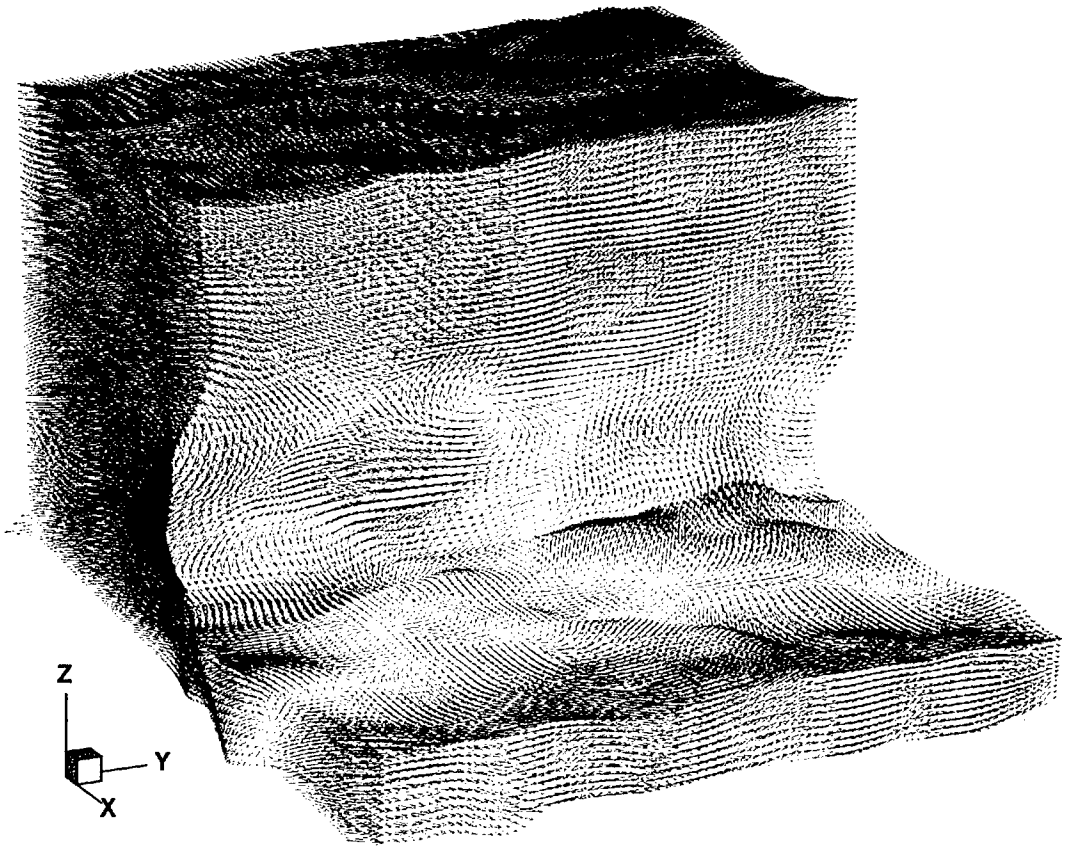

Figure 1. HPIV measurement of flow passing a trapazoidal mixing tab mounted in a water channel flow, showing hairpin vortex structures. The instantanous 3D velocity field is found to satisfy the continuity equiation rather well.

2. Parallel HPIV Data Processing Platform

Based on a single Pentium PC and a simple thresholding centroid extraction, we have achieved a data processing speed of 7 hours for one hologram (120 GB raw image data) giving 3D velocity field. To improve processing speed, two candidate data processing platforms were compared: an FPGA-based hardware implementations of our algorithms (based on hardware parallelism) and a distributed processing systems. Considering the flexibility, scalability and development cost, we have built our new processing system based on a distributed system model. At the center of the design is an eight-port Myrinet network switch working at 1.28Gbps full duplex communication bandwidth on each port, which connects the acquisition computer (acquisition node) to three processing computers (processing nodes, two Pentium workstations and one dual Pentium server). We decouple the acquisition from the processing (displacement or velocity extraction, namely CCC). The acquisition node is responsible for image data acquisition only and simply dispatches the image data to the processing nodes. The network infrastructure is critical for this application, since the huge amount of image data demands high communication bandwidth. Keeping in mind that our ultimate design goal is to adapt a large 4K×4K 12-bit format (currently a 1K×1K 8-bit format is used) digital camera at 30 frames per second (FPS), the required

bandwidth on the acquisition node is approximately 768Mbps, which can be well fit into the bandwidth capacity of the Myrinet. We have also included a 180GB RAID (Redundant Array of Inexpensive Disks) into the system. This RAID system serves as a temporary storage space for experimental image data. A high-capacity tape backup (70GB each cartridge) is also attached to the system for archiving the image data. Because of the high bandwidth of the RAID device, image acquisition can be potentially performed at full speed of the camera (assuming without on-line processing), which is about 15 times faster than before. The system is also capable of storing PIV image data at real-time with nearly no capacity limit, greatly improving our overall experiment capability. The new data processing system is being tested.

3. HPIV Application to Particulate Flow

Extension of the HPIV technique for multiphase flow applications has been explored, such that the measurements provide not only the flow velocity field on a 3D grid, but also 3D information of *individual* particles – including the position and velocity. Our original off-axis HPIV system is found suitable for this purpose. Unlike most other PIV or HPIV systems where velocity is obtained from correlations and hence spatially averaged over a group of particles, our HPIV system retains the individual particle information. The key to extracting a 3D particle image from a hologram is to correctly identify the 3D image (elongated and possibly split), which requires effective 3D edge detection. A volume-rendering algorithm is developed, referred to as Particle Reconstruction by Edge Detection (PRED). The method extracts the continuous exterior surface of a particle image and guarantees to pick up all the above-the-threshold pixels that are connected, and hence it preserves the 3D particle images much better than the previous simple pixel clustering. From the extracted particle images, the centroid locations of the particles and the displacements of them over the double exposure are extracted, giving 3D particle position distribution and velocity distribution. The procedure of HPIV measurement of a particulate flow is illustrated in Fig. 2.

As a pilot study for the application of HPIV to particulate flows, 2D PIV has been applied to particle suspension in an isotropic turbulent flow in an enclosed chamber driven by 8 fans at controllable speed. The algorithms for characterizing the particles will allow us to separate the discrete phase and the tracers for the continuous phase when both phases are present. So far we have tested mono-dispersed cases. On the PIV snapshots, we applied particle centroid finding based 2D edge detection and hence obtained particle locations. From a large number of realizations we were able to obtain the particle Radial Distribution Function (RDF), $g(r/\sigma)$ evaluated in 2D, where r is inter-particle distance and σ particle diameter. We also obtained PDF of the particle velocities. With well-resolved PIV images, the measured RDF for St = 2.94 at small r/σ values is seen to *increases* drastically as r decreases. This measurement result demonstrates significant preferential distribution (agglomeration of particles).

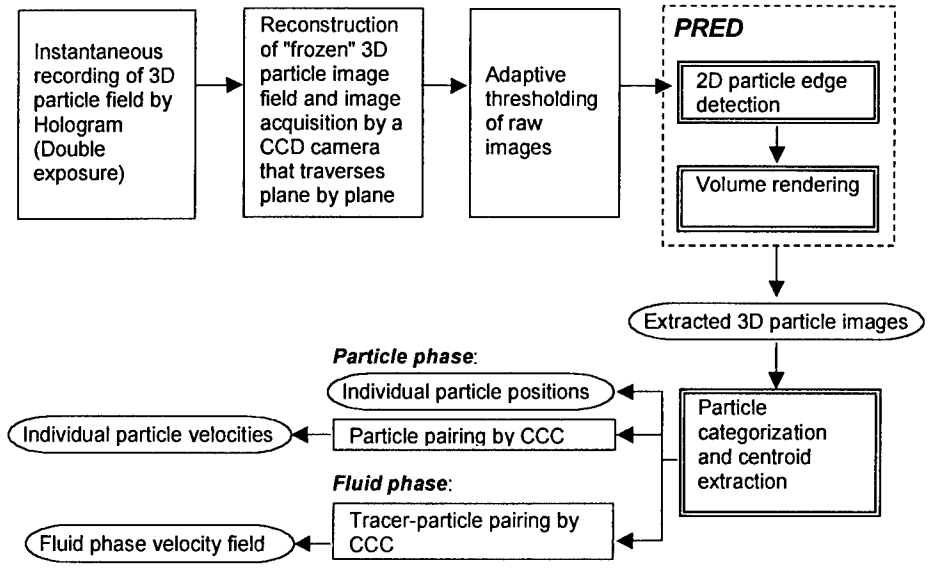

Figure 2: Procedure of HPIV measurement of a particulate flow.

3. Combined Experimental and DNS Study of Flow Past a Surface-Mounted Mixing Tab

To complement HPIV application, time-series digital particle image velocimetry (PIV) has been applied in the wake of a surface-mounted, trapezoidal tab. The purposes of this study are: (1) to provide detailed, high-accuracy 2D PIV data to validate the planned HPIV measurements and direct numerical simulations (DNS) in the same flow; (2) to understand the vortex dynamics and thus, the mechanics of vortex-enhanced mixing and rational of the design of the mixer as well as possible control mechanisms using the tab.

From over 22,000 time-series, high-resolution PIV realizations obtained in the streamwise wall-normal planes, streamwise spanwise planes and cross-stream planes in multiple locations downstream of the tab, we were able to virtually build the 3D model for the wake structures and investigate the evolution and interaction of the structures. Moreover, we were able to use the 3D structures model derived from the PIV data to guide the HPIV experiment under the same flow conditions. We intend to use the tab wake as a benchmark flow to quantitatively evaluate the success of our HPIV technique. This study also provided some insight on the industry application, e.g. mixing point of view. From the large amount of PIV data, we further computed turbulence statistics, such as Reynolds stress, turbulent kinetic energy, turbulent kinetic energy dissipation rate, etc, and used them to evaluate the turbulent mixing.

We conducted DNS of this tab flow at $\mathrm{Re} = 600$, the same Reynolds number as in the recent PIV measurements and compared the simulation results with the PIV measurements in terms of flow statistics and wake vortex structures. The mean flow profiles from the simulation and the PIV measurements show close resemblance and comparable quantitative values. The simulation produces similar wall stress distribution as the experiment. The simulation also produces the three-dimensional topology of the hairpin vortex structures and the pair of counter-rotating vortices in the wake of the tab. Both DNS and PIV show that the wake of a surface-mounted mixing tab is dominated by hairpin vortices; the pressure-induced counter-rotating vortex pair is

taken over by hairpin vortices after a short distance after the tab. Tab wake vortex lines, vorticity magnitude iso-surfaces and pressure iso-surfaces (from DNS) all indicate that the legs of hairpin vortices intertwine with one another and demonstrates braiding patterns. In the near-tab wake region the intertwining legs of hairpin vortices stem from the pair of counter-rotating vortices. Streamwise vortices (intertwining hairpin legs) provide prominent cross-stream mixing, evident from Fig. 9, which shows PIV measurement of a hairpin passage period. DNS (not shown here) provides the same dynamical sequence.

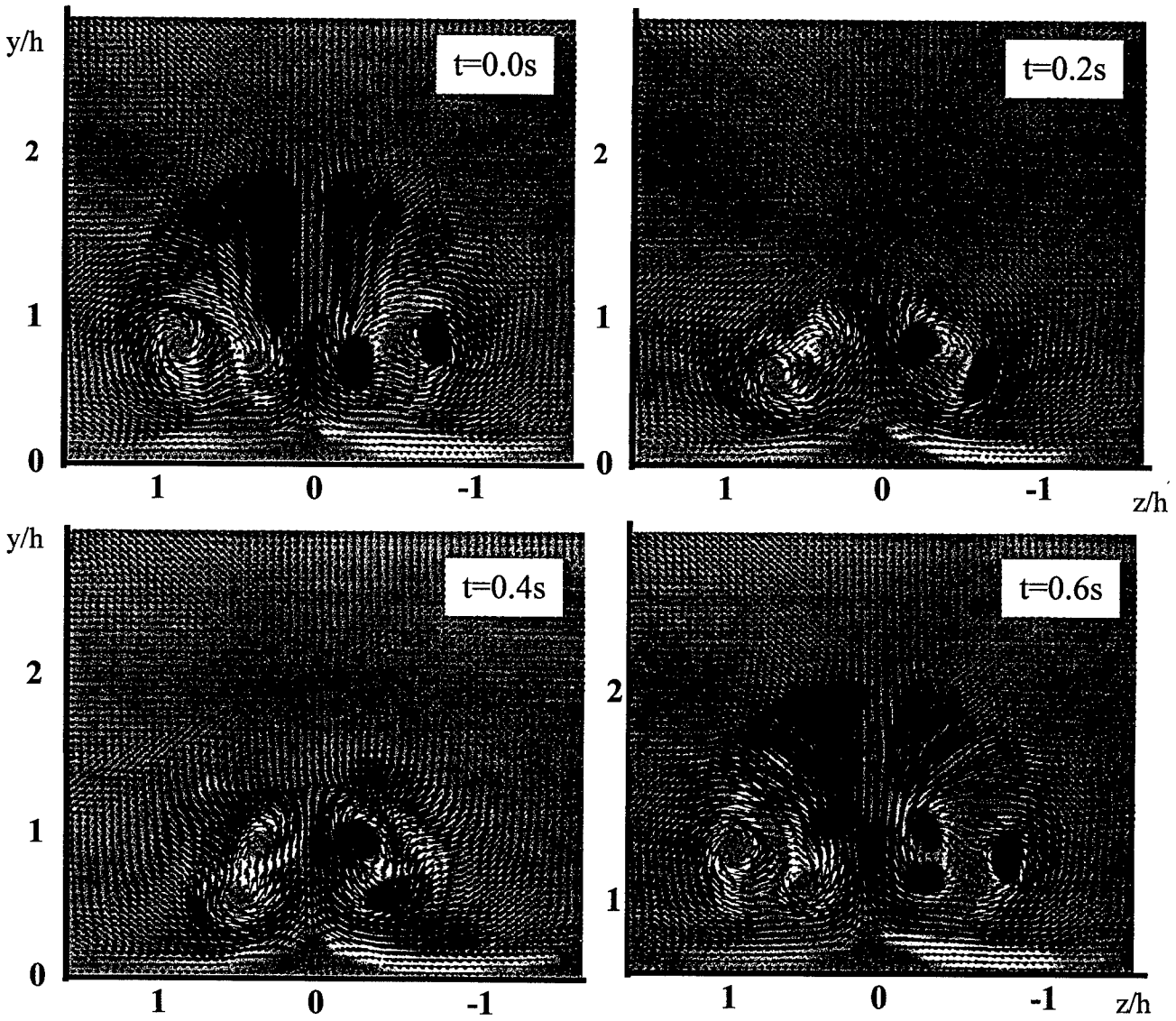

Figure 3. A time sequence of PIV measured velocity and vorticity field in the cross-stream plane, over a hairpin passage period.

Future Plans

1. Complete the upgrade of the off-axis HPIV system in both the data processing platform and expansion of optical access capability (using imaging lenses and larger reference beams).
2. Apply the upgraded HPIV system to the mixing tab flow and other complex flows.
3. Investigate new holographic recording materials and digital HPIV reconstruction.
4. From our HPIV/PIV/DNS study of the tab flow develop flow control mechanisms using flapping tabs, which could benefit the Air Force.

Acknowledgement/Disclaimer

This work was sponsored (in part) by the Air Force Office of Scientific Research, USAF, under No. F49620-98-1-0414. The views and conclusions contained herein are those of the authors and should not be interpreted as necessarily representing the official policies or endorsements, either expressed or implied, of the Air Force Office of Scientific Research or the U.S. Government.

References

1. Y. Pu, X. Song and H. Meng, "Holographic PIV for Diagnosing particulate Flows", Proceedings of the Third Int'l Workshop on PIV'99, Santa Barbara, September 16-18, 1999.

2. Y. Pu, X. Song and H. Meng, "Studying Particulate Flows Using Holographic PIV", The 52nd Annual Meeting of DFD, American Physical Society, New Orleans, LA, Nov. 21-23, 1999.

3. W. Yang and H. Meng, "Dynamics of Tab-Wake Vortices", The 52nd Annual Meeting of DFD, American *Physical Society,* New Orleans, LA, Nov. 21-23, 1999.

4. S. Dong and H. Meng, "A Direct Numerical Simulation of the Flow Past a Surface-Mounted Mixing Tab", The 52nd *Annual Meeting of DFD, American Physical Society,* New Orleans, LA, Nov. 21-23, 1999.

Personnel Supported

Matthieu Delahaya Graduate Student, Kansas State University, Manhattan, KS

Publications

Pu, Y. and H. Meng, "An advanced off-axis holographic particle image velocimetry system", Experiments in Fluids, 29, 184-197 (2000).

Elavarasan, R. and H. Meng, "Flow visualization study on the role of coherent structures in a tab wake", Fluid Dynamics Research 27, 183-197 (2000).

Sheng, J., H. Meng, and R. O. Fox, "A large eddy PIV method for turbulence dissipation rate estimation", to appear in *Chemical Engineering. Science.* (2000).

FLUID-OPTIC INTERACTIONS III
(Adaptive-Optic Correction)

F49620-00-1-0025

Eric J. Jumper
Department of Aerospace and Mechanical Engineering
University of Notre Dame, Notre Dame, Indiana

Abstract

Background

Since Notre Dame's initial efforts in 1993 (Fluid-Optic Interactions, F49620-93-0163, and Fluid-Optic Interactions II, F49620-97-1-0489), we have moved the understanding of aero optics from a statistically-based, averaged, optical-path-difference (OPD) approach, based on statistical, fluid-mechanical measurements, to a formal, cause-and-effect understanding of optical propagation through compressible shear layers [1] [2]. Once we were able to identify the physics of the flow responsible for aberrating the optical wavefront, it became clear that adaptive-optic correction for optical propagation through compressible shear layers was possible through a combination of high-speed wavefront sensing, flow control, and reduced-order data compression. This grant-research effort is directed specifically toward fleshing out the subcategories of the physics that will eventually lead to an adaptive-optic correction demonstration.

Objectives

The overall objective of this research effort is to mature our understanding of the physics of three technical areas that are crucial to an eventual, real-time, adaptive-optic correction for optical propagation through a compressible, free shear layer.

The three areas on which we are concentrating are as follows:

- Objective A: Experimental verification of the aberration physics of the distorting flow field in a weakly-compressible, free shear layer (high-speed layer at Mach 0.8, low-speed layer at Mach 0.1);
- Objective B: Exploration of a low-order representation of the aberrated wavefront associated with propagation through the shear layer for the purpose of quick, conjugate-wavefront construction, including the ability for oblique viewing through the shear layer;
- Objective C: Demonstration of control (i.e., forcing) of the most-unstable, shear-layer modes in our newly-developed, compressible shear layer facility.

Approach

Objective A: In our previous grant, we had demonstrated that the aberrating mechanism for a weakly-compressible shear layer was the mechanical balance of the swirling, coherent, velocity patterns in the flow with their concomitant pressure wells that must be present to accomodate the turning radii associated with the structures [2]. In the present work, a free-shear-layer facility is being designed and constructed at Notre Dame for the experimental verification of this aberrating mechanism. The shear layer will ultimately be a controlled, two-dimensional layer (see Objective C, below). Once controlled, the optical, static-pressure, and velocity fields will be phase-locked to build up time-resolved velocity and concomitant pressure fields, along with the integrated index-of-refraction field (i.e., density field) in a plane normal to the flow and shear-layer-span direction.

Objective B: Critical to a real-time, adaptive-optical demonstration will be the anticipation, or "estimation" of the aberrating flow as it convects downstream across the viewing aperture, based on a simple, upstream, "reduced-order" measurement. Earlier studies, using rigorous, Fourier-optics methods, indicate that this estimation process, even in the case of the lower-speed jet, must be very fast, and the optimum correction must be applied without significant delay, in order for the correction to be effective [3]. If the wavefront is changing over the viewing aperture in uncorrelated ways, then the upstream sensor will be unable to predict the downstream aberration; however, if the flow is at least partially controlled, then a simple, upstream sensor should be sufficient to predict the wavefront over the entire viewing aperture, so that real-time correction becomes possible.

Objective C: At the time of writing our proposal for the present grant, we had assumed that we would be controlling the free shear layer with some sort of mechanical or piezo-electric devices located at the shear-layer splitter plate. This control is not only needed to address Objective A, above, but also to eventually make adaptive-optic corrections possible. Based on recent advances and flow-control successes using phased plasma arrays (PPA) for excitation of instability modes in high-speed flows [4], we have adapted this PPA technology to the flow-control problem. We will initially test the use of these devices on a $7m/s$, low-speed, heated-jet facility [5], requiring actuation at about $500Hz$. We will design the actuators to have a bandwidth to $2000Hz$, anticipating the forcing frequency of the high-speed, shear-layer facility to be approximately $1500Hz$.

Progess, Results, Future Plans

Objective A: Toward the end of our last grant, the optical-wavefront data we had obtained from the free-shear-layer facility at AEDC was used to study the impact of a weakly-compressible flow on an otherwise unaberrated wavefront [6]. Although the AEDC experiments remain significant in their presentation of time-resolved measurements for wavefront propagation through a compressible shear layer, the work has served to raise additional questions that must be answered. Experimentation in

the AEDC facility is impossible, due both to the presently-inoperative state of the facility and the associated cost of operation, even if it were operational. A more-pragmatic approach involves the modification of an existing, transonic, wind tunnel to allow for testing at the University of Notre Dame's Hessert Center for Aerospace Research. One of our three in-draft tunnels, powered by up to three, $3310cfm$, Allis-Chalmer vacuum pumps, will be used to drive the shear-layer facility we are presently developing. The facility will have an optically-transparent test section mated with existing nozzle and diffuser sections. This combination will create a free-shear layer by using two flow sources. For the high-speed side (roughly 0.8 Mach), the flow will pass through an approximately $30:1$ contraction nozzle, which will be somewhat adjustable. The low-speed side (roughly 0.1 Mach) will be fed from a large settling tank, which will be fitted with a valve to room pressure, so that sufficient pressure drop can be created by the valve to allow for the static pressures between the two flows to be matched. Optical access will be available in directions both normal to the shear layer (along the aero-optical path), and parallel to the shear layer (in the splitter-plate direction). Such optical access will allow for the creation of Schlieren photographs, capturing the layer's roll-up phenomena, and for use of laser-Doppler velocimetry (LDV), which will be used to extract information about the related velocity fields. Hot-wire-anemometry techniques will also be used. A schematic of the Notre Dame facility is shown in Figure 1.

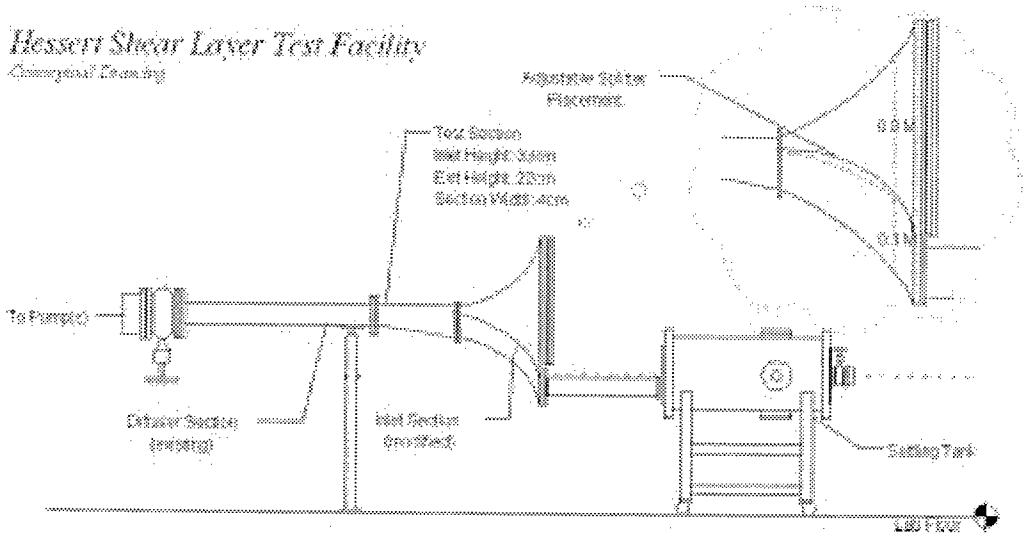

Figure 1: Notre Dame's Shear-Layer Facility, Under Construction

Objective B: Earlier work at Notre Dame has involved the generation of adaptive-optic, spatio-temporal, design requirements, based on time-resolved, wavefront-error measurements, and Fourier-optics tools [3]. This work is presently being extended to the case of the compressible shear-layer optical data from AEDC (discussed above), and the required, adaptive-optic, deformable-mirror update rate is expected to be on the order of tens of kilohertz, depending on Strehl-ratio requirements. Such a system response can only be achieved through a combination of flow control with a sparse-data, upstream, optical sensor, and a low-order representation of the wavefront error.

Recently Proper Orthogonal Decomposition (POD) has been applied to CCA data acquired from Notre Dame's low-speed, heated jet facility. The analysis indicates that the index-of-refraction mapping can be reconstructed by a small number of eigenmodes, where each mode represents an OPD contribution. Time-dependent, modal coefficients have been generated to allow for wavefront reconstruction, and we are considering using these modal coefficients as a fast, direct means for manipulating a deformable-mirror correction. Further, it has been shown that while the OPD contributions of the modes vary with viewing angle, as shown in Figure 2, the modal coefficients do not, and so the total OPD can be easily reconstructed, independent of viewing angle. The relationship between the application of the POD to the two-dimensional, index-of-refraction mapping, and the application of the POD to the one-dimensional OPD signal, is presently being studied.

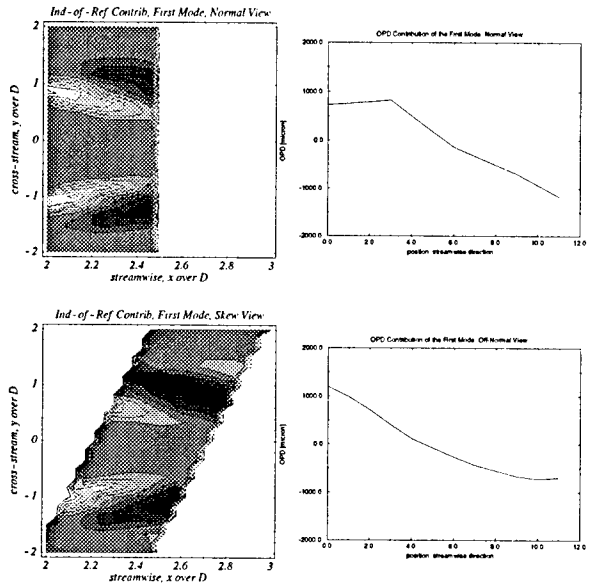

Figure 2: Normal and Off-Normal Viewing through Index-of-Refraction Mapping, with OPD Contributions, for First Mode, φ_1; 2DJT, Forced Flow ("Compensated")

Objective C: Shear-layer control will be crucial if our "real-time," adaptive-optic scheme is to be applied to a compressible shear layer. As such, a number of shear-layer control schemes have been investigated. Unlike low-speed shear and boundary layers, high-speed shear layers are known to be more difficult to "lock" with forcing. Several forcing methods have been considered [5]. The most-promising design concept at this time involves the PPA's, discussed above. An array of plasma actuators are presently being developed for both the new shear-layer facility, and the heated-jet facility.

Personnel

Three researchers have worked on this project over the past year. Dr. Eric J. Jumper has been the Principal Investigator. James M. Cicchiello, a graduate-research assistant, has worked primarily on Objective B. Mitchell A. Chouinard, a graduate-

research assistant, has worked on Objective A, and will be working on Objective C in the coming year.

Publications

During this reporting period, two journal articles [7] [8] have been accepted for publication and should appear in the near future, and two, technical-meeting papers [9] [10] have been presented, as follows:

- Hugo, R.J., and Jumper, E.J. "Applicability of the Aero-Optic, Linking Equation to a Highly-Coherent, Transitional Shear Layer," *Applied Optics*, accepted for publication as of January, 2000, #AO14210.
- Fitzgerald, E.J., and Jumper, E.J. "Two-Dimensional, Optical-Wavefront Measurements Using a Small-Aperture-Beam-Technique, Derivative Instrument," *Optical Engineering*, accepted for publication as of June, 2000, #OE990291.
- Fitzgerald, E.J., and Jumper, E.J. "Aperture Effects on the Aero-Optical Distortions Measured for a Compressible Shear Layer," AIAA paper 2000-0991, January, 2000.
- Fitzgerald, E.J., and Jumper, E.J. "Scaling Aero-Optic Aberrations Due to Propagation Through Compressible Shear Layers," AIAA paper 2000-2354, June, 2000.

Awards

There have been two awards this past year. First, the AIAA, paper presentation of Fitzgerald and Jumper [2] received the AIAA, Plasmadynamics and Lasers, Best Paper Award for the period $1999-2000$ (the award was presented in June, 2000). Second, the Principal Investigator, Dr. Eric J. Jumper, was selected for a Distinguished Visiting Professorship, Department of Aeronautics, United States Air Force Academy, for the academic year beginning in August, 2000.

Technology Transitions

A STTR grant has been awarded to the research team [11], to develop a commercially-viable, high-speed wavefront sensor, based on the research supported by the AFOSR grant.

Acknowledgment/Disclaimer

This work was sponsored by the Air Force Office of Scientific Research, USAF, under grant/contract number F49620-00-1-0025. The views and conclusions contained herein are those of the authors and should not be interpreted as necessarily representing the official policies or endorsements, either expressed or implied, of the Air Force Office of Scientific Research, or the U.S. government.

References

[1] Jumper, E.J. "Recent Advances in the Measurement and Analysis of Dynamic, Aero-Optic Interactions," (Invited Review Paper) AIAA paper 97-2350, 1997 (a version of this paper will be published, with E.J. Fitzgerald, in *Progess in Aerospace Sciences*).

[2] Fitzgerald, E.J., and Jumper E.J. "Further Consideration of Compressibility Effects on Shear-Layer, Optical Distortion," AIAA paper 99-3617, June, 1999 (a version of this paper has been submitted to *Journal of Fluid Mechanics*).

[3] Cicchiello, J.M., and Jumper, E.J. "Far-Field, Optical Degradation Due to Near-Field Transmission Through a Turbulent, Heated Jet," *Applied Optics*, Vol 36, **25**, September, 1997, pages 6441-6452.

[4] Corke, T.C., and Matlis, E. "Phased Plasma Arrays for Unsteady Flow Control," AIAA paper 2000-2323, 2000.

[5] Hugo, R.J., and Jumper, E.J. "Constant-Current Anemometry Applied to Aero-Optical Measurements," AIAA paper 99-3616, 1999.

[6] Hugo, R.J., and Jumper, E.J., Havener, G., and Stepanek, C. "Time-Resolved Wavefront Measurements Aberrated by a Compressible Shear Layer," *AIAA Journal*, Vol 35, **4**, pages 671-677, 1997.

[7] Hugo, R.J., and Jumper, E.J. "Applicability of the Aero-Optic, Linking Equation to a Highly-Coherent, Transitional Shear Layer," accepted for publication in *Applied Optics.*

[8] Fitzgerald, E.J., and Jumper, E.J. "Two-Dimensional, Optical-Wavefront Measurements Using a Small-Aperture-Beam-Technique-Derivative Instrument," accepted for publication in *Optical Engineering.*

[9] Fitzgerald, E.J., and Jumper, E.J. "Aperture Effects on the Aero-Optical Distortions Measured for a Compressible Shear Layer," AIAA paper 2000-0991, 2000.

[10] Fitzgerald, E.J., and Jumper, E.J. "Scaling Aero-Optic Aberrations Due to Propagation Through Compressible Shear Layers," AIAA paper 2000-2354, 2000.

[11] Cheung, K.C., and Jumper, E.J. "High-Temporal-Bandwidth, Optical-Wavefront-Sensor Technologies," STTR Proposal F003-0400, Phase I, to commence August, 2000.

PROPAGATING POTENTIAL DISTURBANCES IN TURBOMACHINERY

F49620-99-1-0251

Eric J. Jumper
Department of Aerospace and Mechanical Engineering
University of Notre Dame, Notre Dame, Indiana

Abstract

Background. This joint project between the University of Notre Dame and the Air Force Institute of Technology investigates the unsteady forced response of vanes in compressible-flow cascades, where the vanes are forced by unsteady, upstream-propagating potential disturbances. The investigation is geared toward providing a better understanding of high-cycle fatigue (HCF) failures in turbomachinery, particularly in terms of compressor stage-to-stage aerodynamic interactions. The work further examines aerodynamic phenomena identified in joint studies between Notre Dame and the Air Force Academy, performed under the Air Force Science and Technology (S&T) HCF program.

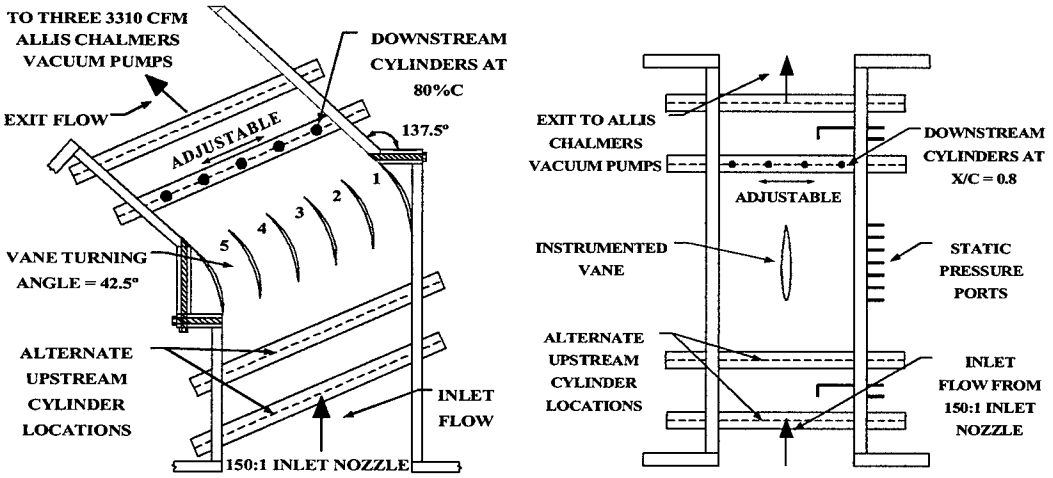

(a) Previous Cascade (b) Current Tunnel

Figure 1: Top-View Schematic of Fabian *et al.*[1,2] Cascade and Current Tunnel Section.

As part of the previous S&T studies, Fabian *et al.*[1,2] examined the unsteady surface-pressure response of a rearward-forced transonic cascade, where unsteady forcing was produced by upstream-propagating potential disturbances generated from a row of five cylinders placed 0.80 vane-chords downstream, as shown in Figure 1a. From this investigation, the fundamental-frequency surface-pressure response was found to systematically increase toward the vane-row trailing edge, as shown in Figure 2, suggesting the possible existence of a trailing-edge "singularity." Additionally, the first-harmonic surface-pressure response exhibited greater amplitude than the fundamental near the leading edge, and less amplitude at the trailing edge. The thin cascade vanes used by Fabian *et al.* unfortunately limited the trailing-edge pressure-tap locations, making inferences regarding the pressure-response behavior beyond $x/c = 0.80$ purely speculative.

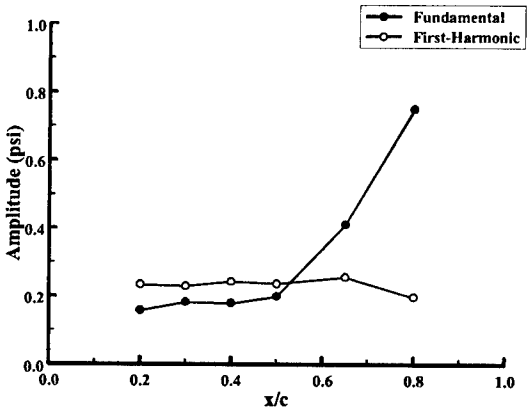

Figure 2: Cascade Pressure Amplitude: $M_\infty = 0.43$, $k = 4.3$, Five-Cylinder Forcing.[1,2]

In light of the Fabian *et al.* results, the current investigation attempts to characterize the unsteady pressure response over the aft half chord of a subsonic, rearward-forced, sharp-trailing-edge, unloaded, initially-isolated airfoil. The investigation repeats the experiments of Fabian *et al.*, but in a simpler, initially single-vane configuration (Figure 1b), allowing the airfoil to be unloaded and instrumented to locations reaching $x/c = 0.93$.

Experimental Parameters. A NACA 16-0012 airfoil, or vane, was tested in a 3.85 in. × 3.95 in. transonic tunnel (Figure 1b). This vane was instrumented with eight, surface-mounted ultra-miniature transducers located along the mid-span region from $x/c = 0.54$ to 0.93. Unsteady forcing was established through von Karman vortex shedding from a row of cylinders placed 0.80 vane chords downstream, where the cylinders were aligned parallel to the vane span. No active shedding control was used; however, the character of the shedding was monitored via surface-mounted transducers on the cylinders. Two-hundred data sets were collected at each transducer for four free-stream tunnel Mach numbers, M_∞, ranging from 0.33 to 0.51, two reduced frequencies, k, of 5.6 and 7.5, and two forcing configurations (four and two-cylinder forcing). The collected data were phase-locked via one of the pressure transducers embedded in the forcing cylinders.

Cylinder Vortex Shedding. Unlike the results of Fabian *et al.*,[1,2] the relative phase of the vortex-shedding across the current cylinder row forcing cylinders depended heavily upon M_∞, k, and configuration. Moreover, the shedding relative phase was found to play an essential role in the vane pressure response. For example, out-of-phase shedding produced anomalous pressure-response results, while in-phase shedding produced data comparable in some ways to that of Fabian *et al.* Only data from in-phase shedding were amenable to analysis; limiting our investigation to four flow and forcing conditions.

The character of the trigger signals also differed from that of Fabian *et al.* The Fabian *et al.* triggers showed no signs of harmonic content,[1] while the current trigger data exhibited significant harmonic content under most conditions. Figure 3 shows representative trigger signals from the current investigation. Note that under certain flow conditions the signals show significant harmonic content, while at other conditions they do not. The effect of this harmonic content, in terms of vane pressure response, is unclear at this time; however, we consider the harmonic content to be undesirable.

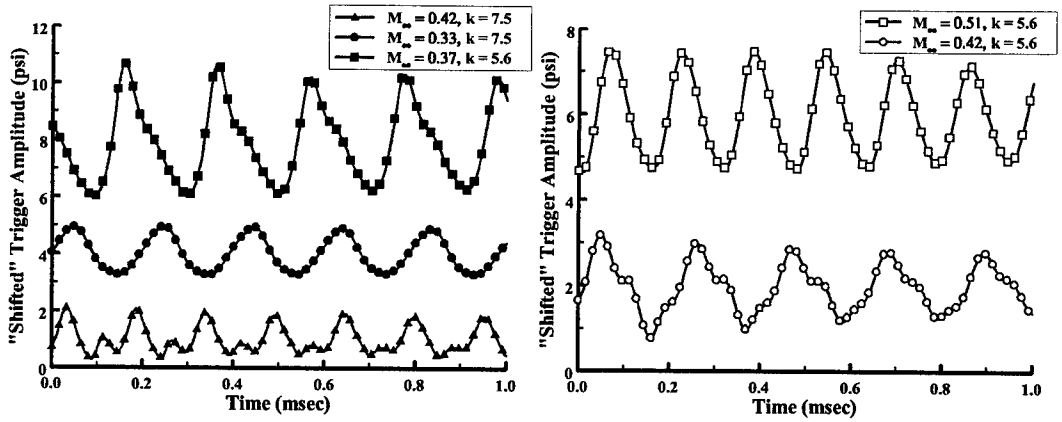

(a) Four-Cylinder Forcing (b) Two-Cylinder Forcing

Figure 3: Vertically-Shifted Trigger Signals: Four-Cylinder and Two-Cylinder Forcing.

Relative Phase. The relative-phase data from each pressure-response frequency component were compiled and compared to a phase model developed by Fabian *et al.*[2] This comparison showed good agreement between the measured phase data and the Fabian *et al.* model, implying two important results. First, the measured disturbances on the vane propagated upstream. Second, the disturbance propagation speed was acoustic, confirming potential forcing from the downstream cylinders.

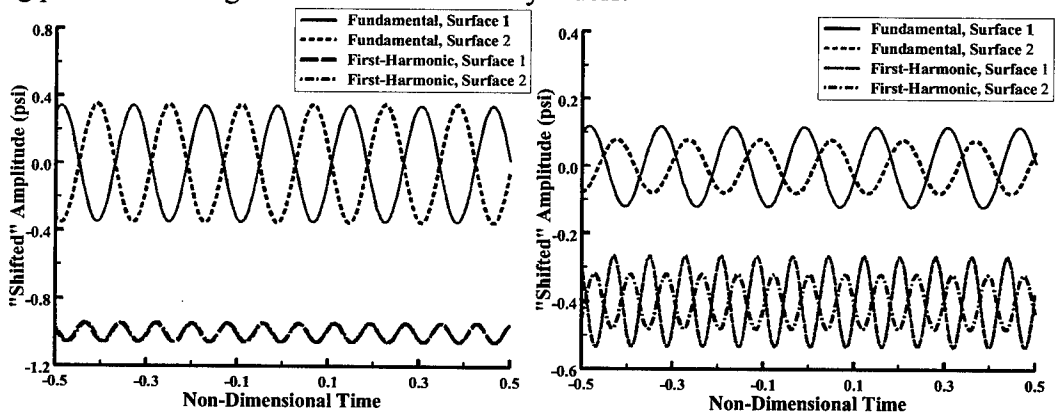

(a) $x/c = 0.592$ (b) $x/c = 0.872$

Figure 4: Decomposed Amplitudes: $M_\infty = 0.51$, $k = 5.6$, Two-Cylinder Forcing.

Figure 4 shows the fundamental and first-harmonic components of the response measured on opposing vane surfaces at $x/c = 0.592$ and 0.872. In Figure 4a, the fundamental components are π out of phase, while the first-harmonic components are in phase; consistent with the vane pressure-response measured by Fabian *et al.*[2] Conversely, both the fundamental and first-harmonic components are out of phase in Figure 4b. The reason for this change is unknown; however, it may be related to harmonic amplitude variation.

Fundamental Amplitude. The fundamental amplitudes for the four and two-cylinder forcing configurations are given in Figure 5, from which several observations can be made. First, no increase in amplitude occurs beyond $x/c \approx 0.75$, unlike that of Fabian *et al.* (Figure 2). Second, the amplitudes are large, reaching as high as 1.0 psi peak-to-peak

amplitude for the $M_\infty = 0.37$, $k = 5.6$ case (approximately 50% of the tunnel static pressure). Finally, the amplitudes are of similar order to those measured by Fabian *et al.*

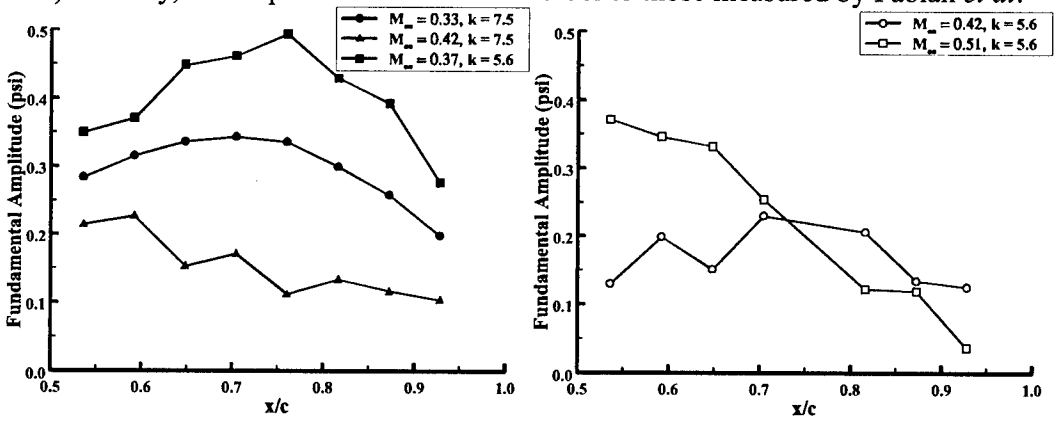

(a) Four-Cylinder Forcing (b) Two-Cylinder Forcing

Figure 5: Fundamental Amplitudes: Four-Cylinder and Two-Cylinder Forcing.

Normalized First-Harmonic Amplitude. The normalized, first-harmonic amplitudes corresponding to the data of Figure 5 are shown in Figures 6 and 7 (absent the $M_\infty = 0.33$, $k = 7.5$ case); Figures' 6 and 7 amplitudes are normalized by their respective fundamental values at each x/c position. For four-cylinder forcing, the $M_\infty = 0.37$, $k = 5.6$ first-harmonic demonstrates little variation up to the $x/c \approx 0.816$ location, increasing near the trailing edge; also, the first-harmonic never exceeds the fundamental. In contrast, the $M_\infty = 0.42$, $k = 7.5$ first-harmonic not only exceeds the fundamental, but also exhibits a systematic increase along the vane. Moreover, comparison of the $M_\infty = 0.42$, $k = 7.5$ data between Figures 5a and 6b suggests that a continuously-increasing first-harmonic may correlate to a continuously-decreasing fundamental. Similarly, the approximately-constant, then increasing, trend of the $M_\infty = 0.37$, $k = 5.6$ first-harmonic in Figure 6a may be associated with an increasing, then decreasing, fundamental.

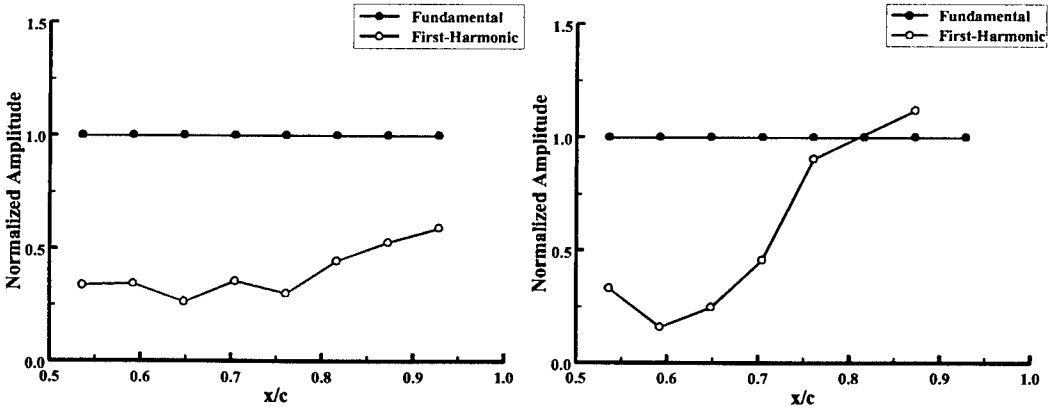

(a) $M_\infty = 0.37$, $k = 5.6$ (b) $M_\infty = 0.42$, $k = 7.5$

Figure 6: Normalized Amplitudes for Four-Cylinder Forcing.

This association is also suggested in the normalized first-harmonic amplitudes for two-cylinder forcing. As shown in Figure 7a, the first-harmonic at $M_\infty = 0.42$, $k = 5.6$ shows little change, varying only slightly near the trailing edge. Comparing this behavior with

the concomitant data in Figure 5b, the nearly-constant first-harmonic correlates with an increase in the fundamental (the first-harmonic trailing-edge rise corresponds to a drop in the fundamental). Similar comparisons for the $M_\infty = 0.51$, $k = 5.6$ case show a first-harmonic increase along the chord to be associated with a decrease in the fundamental. In the Fabian *et al.* case the normalized first-harmonic (Figure 2) decreases continuously over the vanes, correlating to a continuous increase in the fundamental. Therefore, the proposed correlation between the fundamental and first-harmonic is consistent for the Fabian *et al.* data, as well as the current four and two-cylinder forcing data.

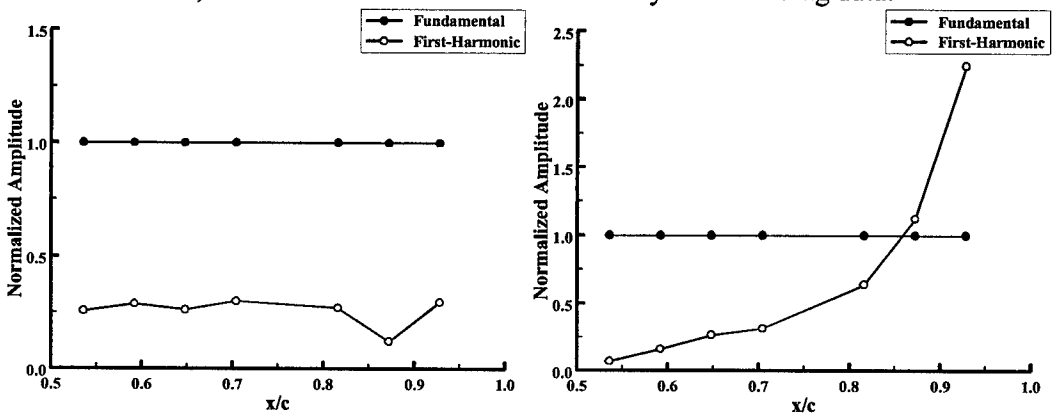

(a) $M_\infty = 0.42$, $k = 5.6$ (b) $M_\infty = 0.51$, $k = 5.6$

Figure 7: Normalized Amplitudes for Two-Cylinder Forcing.

Discussion and Conclusions. To date, our characterization of vane trailing-edge response due to rearward forcing has produced more questions than answers. What we can conclude is that rearward forcing produces significant unsteady pressure response; however, a possible trailing-edge singularity, as suggested by Fabian *et al.*, cannot be substantiated. On the other hand, we cannot rule out the possibility of singularity-like behavior under different forcing conditions. The first-harmonic dependence on flow and forcing conditions, and its relation to the fundamental, suggests that, at least in the trailing-edge region, the first-harmonic may influence the overall pressure-response more than originally suspected. In fact, certain first harmonic characteristics may indicate poor forcing conditions. Our difficulty in obtaining clean, in-phase forcing may also contribute to the response character, as well as influence the first harmonic.

Our relative inability to produce robust in-phase forcing and a clean trigger, as compared to Fabian *et al.*,[1,2] is somewhat perplexing, but may be due to several configuration differences. For example, the previous cascade was forced from five cylinders, and the physical distance between the vanes and cylinders, while 0.80 vane chords downstream, was shorter than the current configuration. The Fabian, *et al.* cascade vanes were also heavily loaded, and formed five equally-spaced flow passages, allowing flow periodicity. Moreover, Wade *et al.*[3] recently examined the unsteady potential field upstream of an isolated cylinder, as well as multiple cylinders, in a compressible-flow tunnel; finding the unsteady aerodynamic environment to be extremely complicated, consisting of disturbances propagating not only from the cylinders, but also the cylinder images. Thus, the current forcing environment may have also consisted of multiple cylinder-image sources, vane-image reflections, and possibly new vane-response mechanisms.

Future Plans

The current investigation represents only an initial attempt at the trailing-edge pressure-response problem. Future tunnel configurations are being constructed to incorporate three vane passages, five forcing cylinders, active cylinder-shedding control, and shorter forcing distances.

Acknowledgement/Disclaimer

This work was sponsored by the Air Force Office of Scientific Research, USAF, under grant/contract number F49620-99-1-0251. The views and conclusions contained herein are those of the authors and should not be interpreted as necessarily representing the official policies or endorsements, either expressed or implied, of the Air Force Office of Scientific Research or the U.S. Government.

References

1. M. K. Fabian and E. J. Jumper, "Rearward Forcing of an Unsteady Compressible Cascade," *Journal of Propulsion and Power*, 1999, 15 (1): 23-30.

2. M. K. Fabian, E. A. Falk and E. J. Jumper, "Upstream-Propagating Acoustic Waves Interacting With A Compressible Cascade," *Journal of Propulsion and Power*, 2000, to be published.

3. Wade, P.C., P. I. King, D. R. Hopper, E. J. Jumper and A. Asghar, "Velocity Fields Upstream of Rods Used for Forcing Unsteady Compressible Cascades," AIAA paper 00-3229, July 2000.

Personnel Supported

Eric J. Jumper	Professor, Principal Investigator
Eric A. Falk	Graduate Research Assistant
Asad Asghar	Graduate Research Assistant
Aleksander Šekularac	Graduate Research Assistant

Publications

"Upstream-Propagating Potential Disturbances Interacting with a Compressible Cascade," M. Fabian, E. Falk, E. Jumper, accepted for publication in *Journal of Propulsion and Power.*

"Upstream-Propagating Potential Disturbances in the F109 Turbofan Engine Inlet Flow," E. Falk, E. Jumper, M. Fabian, J. Stermer, accepted for publication in *Journal of Propulsion and Power.*

"A Conformal Mapping Analysis of Cascade Trailing-Edge Flows," A. Šekularac, E. Falk, E. Jumper, B. Haven, AIAA paper 00-0229, January 2000.

"Unsteady Pressure Response on a Rearward-Forced Isolated Compressible-Cascade Vane," A. Asghar, E. Falk, E. Jumper, D. Hopper, P. King, AIAA paper 00-3228, July 2000.

STRUCTURE-BASED TURBULENCE MODELING

GRANTS: F49620-95-0145, F49620-95-0357, F49620-98-0138

S. C. Kassinos and W. C. Reynolds
Department of Mechanical Engineering
Stanford University

1. Motivation and Objectives

Turbulence modeling is a critical element of modern CFD codes for flow analysis. Models must be fairly simple and computationally affordable to be useful in repetitive engineering calculations, yet they must be sufficiently representative of the physics to capture the important flow features controlled by turbulence, such as flow separation, skin friction, and heat and mass transfer. There is particular need for improved models that are robust and accurate in rotating flows, which are important in aerospace propulsion systems. Advanced aerospace power and propulsion systems employing magnetohydrodynamics (MHD), and possible schemes for control of electrically-conducting external flow on aerospace or marine vehicles, also require turbulence models superior to those presently available.

The objective of this effort is the development of a new type of one-point turbulence modeling for engineering analysis. The goal is to incorporate information about the structure of turbulence which plays a key role in the transport of the turbulence stresses, particularly in flows with strong mean or frame rotation, streamline curvature, and in MHD flows.

2. Approach and Recent Developments

The needed structure information is carried by new one-point tensors whose definitions and transport equations were obtained in the initial phase of this project Kassinos, Reynolds, and Rogers [1]. The first important development was the construction of a structure-based one-point model of the rapid distortion (RDT) of homogeneous turbulence Kassinos & Reynolds [2,3], hereafter denoted by KR. Extensions of this model for flows with weak mean deformations followed in a later stage. An equally important product of this initial effort is the two-point Interacting Particle Representation Model (IPRM), an emulation of the turbulent field by fictitious particles carrying key properties, that predicts the response of homogeneous turbulence to both rapid and slow deformations with impressive accuracy.

Recent developments in structure-based modeling include the construction of a one-point differential structure-based model, the **Q**-model, based on the differential transport equation for the stropholysis tensor. This rather complex model provides a proof-of-concept validation for the basic modeling approach, but is too expensive for engineering use.

The structure-based modeling approach has matured to the point where it is now possible to initiate formulation of simplifications for routine engineering use. One of the important recent developments, is the formulation of an algebraic two-equation structure-based model, which is simple enough for engineering use, but captures the essential features of more complex models developed under this project.

In the past year, our efforts were focused in three key areas: (1) development and validation of the differential **Q**-model for wall-bounded flows with and without system rotation; (2) formulation and initial development of an algebraic two-equation structure-based model

for engineering use; (3) formulation and implementation of structure-based modeling for homogeneous MHD turbulence. These developments are described in more detail below.

3. Stropholysis Modeling

KR have shown that mean or frame rotation breaks the reflectional symmetry, present in the spectrum of homogeneous turbulence that had previously been only irrotationally strained. The breaking of reflectional symmetry, a dynamically crucial effect, is not reflected in one-point statistics like the Reynolds stresses, but it is reflected in a third-rank fully symmetric tensor, the stropholysis tensor $\mathbf{Q}^*$, for which KR have derived an exact evolution equation. Recently, we formulated a new one-point model, the **Q**-model, which is based on our understanding of the stropholysis effects. For irrotational deformations of homogeneous turbulence the **Q**-model produces excellent results for both rapid and slow mean deformations. For flows with combinations of strong mean rotation and strain, the **Q**-model produces good results, and in some key flows, captures features that are completely missed by standard Reynolds Stress Transport (RST) models.

During the past year, the formulation of the **Q**-model was extended to inhomogeneous flows with the addition of gradient diffusion transport in the model equations. Wall blocking is accounted through an adaptation of the elliptic relaxation scheme developed originally by Durbin [6] for RST models. For example, the predictions of the one-point **Q**-model for the case of turbulent flow through a straight cylindrical pipe with and without axial rotation are shown in Figure 1 (as lines). The effect of increased axial rotation on the axial mean velocity profile is shown in Figure 1(a) for fully developed pipe flow at a Reynolds number of $Re_o = 20,000$ based on the pipe diameter and axial velocity at the pipe centerline. The model captures the effect of axial rotation correctly and agreement with the experimental result of Imao *et al.* [7] is excellent. Here the rotation number $N = U_{\theta,\text{wall}}/U_o$ is the ratio of the circumferential wall velocity to the mean axial velocity at the pipe centerline. The effect of the axial rotation rate on the shear stress $\langle vu \rangle$, normalized with twice the turbulent kinetic energy k, is shown in Figure 1(b). Again agreement with experiments is good. An important parameter often reported for rotated pipe flow is the the damping coefficient $d = \langle u^2 \rangle(N)/\langle u^2 \rangle(N = 0)$, which gives the ratio of the axial Reynolds stress component normalized by its value for the non-rotating case. The development of $d(x)$ along the pipe centerline in the initial pipe section, where the turbulence is still developing, is a challenging prediction for standard turbulence models. As shown in Figure 1(c) for the case $Re_o = 40,000$, the one-point **Q**-model captures this initial development quite well.

4. Algebraic Structure-Based Turbulence Model (ASBM)

Until recently, our research efforts have been focused on complex turbulence models that incorporate more physics than conventional Reynolds transport models. From this work we have learned a great deal about the kinematics and dynamics of turbulence under both slow and rapid mean distortion. In the past year, we started incorporating this insight into a turbulence model that is sufficiently simple to be affordable for engineering computations. The model uses algebraic equations to determine tensor, vector, and scalar parameters of the turbulence structure, and from these determines the turbulent stresses. The only partial differential equations involved are the transport equations for two turbulence scales (k-ε or k-ω). The algebraic equations produce states consistent with rapid distortion theory for

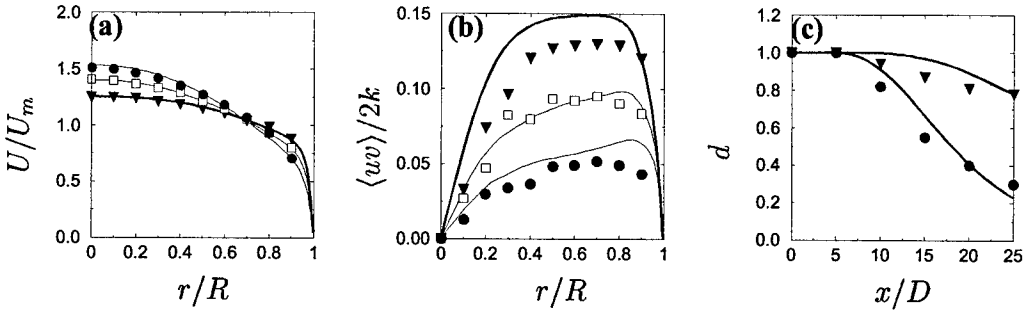

Figure 1: Turbulent pipe flow with axial rotation. (a)-(b) Fully developed pipe flow at $Re_o = 2\text{x}10^4$; **Q**-model predictions (lines) vs. experimental data (symbols) by Imao *et al.* [7] for the axial mean velocity profile and structural parameter. (c) Developing pipe flow at $Re_o = 4\text{x}10^4$; **Q**-model predictions (lines) vs. experimental data (symbols) by Zaets *et al.* [8] for the evolution of the damping coefficient. In cases (a) and (b) symbols correspond to: (▾) N=0, (▫) N=0.5, and (•) N=1. In case (c) symbols correspond to: (▾) N=0.15 and (•) N=0.6. Here the rotation number is defined as $N = U_{\theta,\text{wall}}/U_o$.

rapidly distorted turbulence, and in good agreement with experimental data and numerical simulations for moderate distortion rates. The correct kinematic and dynamic effects of mean or frame rotation are captured, making the model particularly advantageous for turbomachinery flows and flows with strong rotation. The model is the only two-equation model to display material indifference to rotation for two-dimensional turbulence having its axis of independence aligned with the axis of rotation (see [4]).

Under certain conditions, homogeneous turbulence subjected to shear in a rotating frame can attain an equilibrium state in which the normalized stresses $r_{ij} = R_{ij}/R_{kk}$ remain constant, while the energy k and dissipation rate ε grow and the time scale τ remains fixed. We consider the case where the frame rotation is aligned with the mean rotation and the mean velocity gradient in the frame is $U_{i,j} = \Gamma\delta_{i1}\delta_{j2}$. Figure 2. shows the fixed-point states of $\varepsilon/\Gamma k$ as a function of $\eta = -\Omega^f_{12}/\Omega_{12}$ that are predicted by the ASBM (using the standard ε model equation). Here η is the ratio of the frame rotation rate to the mean rotation rate and is positive when the frame counter-rotates relative to the mean rotation. Note that fixed-states with non-zero $\varepsilon/\Gamma k$ are obtained only over a limited range of η. Outside this range the fixed-state value of $\varepsilon/\Gamma k$ is zero.

Near a wall the structure and stress need to be adjusted for wall blockage. At a wall, the eddies must all lie in the plane of the wall and all must be fully jetal (motion along eddy axis). We accomplish this with a procedure resembling elliptic relaxation. However, unlike the elliptic relaxation formulation for RST models, which is based on purely mathematical considerations, the wall blockage scheme in the ASBM is based on physical arguments about the effect of wall blockage on the turbulence structure. Figure 2(b) shows a test of this idea for channel flow. Here $U_1(x_2)$, k and ϵ from the DNS by Moser *et al.* [9] were used to determine $S_{12}\tau$, and the ASBM was used to predict the r_{ij} using a model for the blockage. Note that the agreement of the stresses with the DNS is quite good, except very near the channel centerline where the mean strain rate and mean rotation rate both vanish locally but the stresses are not quite isotropic because of non-local influence by the

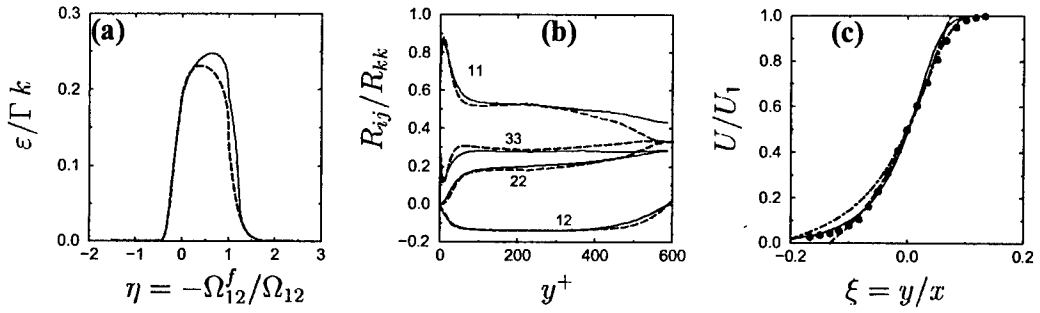

Figure 2: (a) Bifurcation diagram of the ASBM (using standard ε equation) for homogeneous shear flow in a frame rotating about the spanwise axis. (b) Apriori test of ASBM in fully developed channel flow at $Re_\tau = 590$, showing the validity of the blocking concept: (——) DNS by Moser *et al.* [9]; (– – – –) ASBM. (c) Mean velocity profile in a self-similar turbulent mixing layer: (– – – –) standard k-ε model; (—·—) standard k-ω model; and (——) ASBM using k-ω equation; (•) experiments by Liepmann & Laufer [10].

surrounding turbulence.

We have used provisional versions of the ASBM to examine the effects of frame rotation on the self-similar turbulent mixing layer. Figure 2(c) shows the mean velocity field predicted by using the standard k-ϵ and k-ω models and the ASBM with the standard ω equation. Note that the ASBM does well matching experimental data. We are currently making calculations for the mixing layer in a frame rotating about the streamwise axis. The ASBM predicts a thinning of the shear layer as a result of the shear stress reduction brought about by the frame rotation. Experimental or DNS results for mixing layers with streamwise frame rotation would be very useful for assessing these predictions.

5. Structure-Based Modeling of MHD Flows

The response of magnetohydrodynamic (MHD) turbulence to an externally applied magnetic field is of importance in propulsion systems design as well as in the control of electrically conducting flows. The objective of this effort is to incorporate MHD effects in the structure-based family of turbulence models. Structure-based models are well suited for capturing MHD effects because the structure plays a key role in the evolution of MHD turbulence as has been shown by Kassinos & Reynolds [5].

The formulation of structure-based models for homogeneous MHD turbulence is based on the same approach that has proved successful in the past for the formulation of one-point structure-based turbulence models. The additional effects are first incorporated with minimal assumptions in the non-local (two-point) Interacting Particle Representation Model (IPRM). Then a formal averaging procedure is applied to the IPRM governing equations to produce the corresponding one-point model. Additional modeling provides closure at the one-point level while maintaining realizability. This formalism provides a rigorous foundation for the one-point formulation (Kassinos & Reynolds [5]).

The extended IPRM and extended one-point **Q**-model have been evaluated for the case of decaying homogeneous turbulence in a conductive fluid. At a time $t = t_1$ the turbulence is exposed to a uniform magnetic field $B_i = B\delta_{i1}$ which is maintained active till a later time

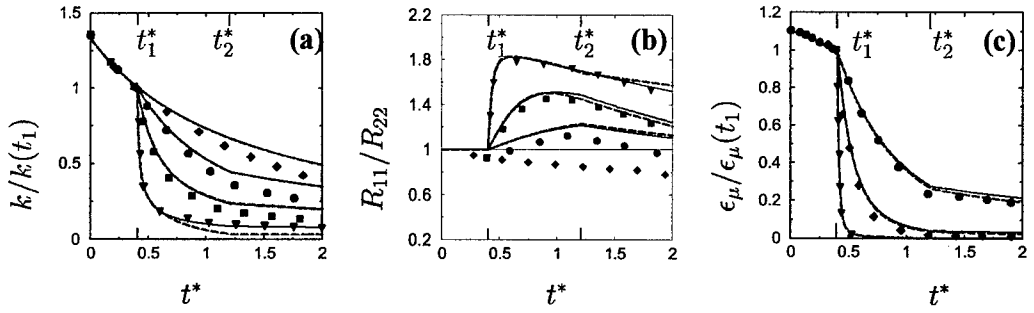

Figure 3: Effect of the magnetic interaction number N on the time evolution of (a) the normalized turbulent kinetic energy, (b) the ratio of R_{11} (Reynolds stress component parallel to applied the magnetic field) to R_{22} (Reynolds stress component normal to the applied magnetic field), and (c) total Joule dissipation. (——) IPRM; (– – – –) Q-model. Symbols: DNS by Schumann [11] (♦ $N = 0$; • $N = 1$; ■ $N = 5$; ▼ $N = 50$).

t_2. The turbulence is allowed to evolve for an additional time interval (t_2 to t_3) under no magnetic field. The test case and conditions have been chosen to match as closely as possible those used in the DNS of Schumann [11]. Figure 3a shows the evolution of the turbulent kinetic energy normalized with its value $k(t_1^*)$ at activation time t_1^*. Following Schumann's choice, evolutions are shown in terms of the dimensionless time t^*, based on the turbulence time scale at activation time. Four different magnetic interaction numbers ($N = 0, 1, 5,$ and 50) are considered. The case $N = 0$ corresponds to pure decay of homogeneous isotropic turbulence for the entire time interval $t^* = (0, t_3^*)$. The discrepancy between the DNS and model predictions for the rate of decay at large times (for $N = 0$) can partly be attributed to the quite limited resolution of the DNS (see [5],[11]). For the remaining cases the magnetic field is active in the time interval $t = (t_1^*, t_2^*)$ and this is reflected in the enhanced rate of decay of the turbulent kinetic energy due to Joule dissipation. The predictions of the IPRM and one-point model are in good agreement with each other and with the DNS results. Except for $N = 50$, the models tend to predict a somewhat lower decay rate than what is found in the DNS. Figure 3b shows the time evolution of the ratio R_{11}/R_{22} (i.e. the ratio between the Reynolds stress components in the directions parallel and normal to the magnetic field), and Figure 3c shows the evolution of the total magnetic (Joule) dissipation (see [5]). In both cases model predictions agree quite well with the DNS results.

Acknowledgment/Disclaimer

This work was sponsored by the Air Force Office of Scientific Research, USAF, under grants number F49620-95-0145, F49620-95-0357, and F49620-98-0138. The views and conclusions contained herein are those of the authors and should not be interpreted as necessarily representing the official policies or endorsements, either expressed or implied, of the Air Office of Scientific Research or the U.S. Government.

References

1. S. C. Kassinos, W. C. Reynolds and M. Rogers, One-Point Turbulence Structure Tensors. Resubmitted for publication to the *J. Fluid Mech.*, 2000.

2. S. C. Kassinos and W. C. Reynolds, A Structure-Based Model for the Rapid Distortion

of Homogeneous Turbulence. Report TF-61, Thermosciences Division, Department of Mechanical Engineering, Stanford University, Stanford, 1994.

3. W. C. Reynolds and S. C. Kassinos, One-Point Modelling of Rapidly Deformed Homogeneous Turbulence. Proceedings of the Royal Society of London, 1995, **A,451**, 87-104.

4. W. C. Reynolds, S. C. Kassinos, C. A. Langer, and S. Haire, New directions in turbulence modeling. Third International Symposium on Turbulence, Heat, and Mass Transfer. Nagoya, Japan April 3-6, 2000.

5. S. C. Kassinos and W. C. Reynolds, "Structure-based modeling for homogeneous MHD turbulence". *Annual Research Briefs 1999*, CTR, NASA Ames/Stanford, 301-315.

6. P. Durbin, Separated Flow Computation with the k-ε-v^2 model. *AIAA J.*, 1995, **33**, 659.

7. S. Imao, M. Itoh, and T. Harada, Turbulent Characteristics of the Flow in an Axially Rotating Pipe, *Int. J. Heat and Fluid Flow*, 1996, **17**(5), 444-451.

8. P.G. Zaets, N. A. Safarov, and R. A. Safarov, Experimental study of turbulent flow characteristics in a pipe rotating about its longitudinal axis (in Russian). *Modern Problems of Continuous Medium Mechanics*, Moscow Physics and Techniques Institute, 1985, 136.

9. R. D. Moser, J. Kim, and N. N. Mansour, Direct numerical simulation of turbulent channel flow up to $Re_\tau = 590$. *Phys. Fluids*, 1999, **11**(4) pp. 943-945.

10. H. W. Leipmann and J. Laufer, *Investigations of Free Turbulent Mixing*, NACA TN **1257**, 1946.

11. U. Schumann, Numerical simulation of the transition from a three- to two-dimensional turbulence under a uniform magnetic field, *J. Fluid Mech.*, **74**, 1976, 31-58.

Personel Supported

William C. Reynolds	Professor, Stanford University, California.
Stavros C. Kassinos	Research Associate, Stanford University, California.
Mr. Scot Haire	Graduate Student, Stanford University, California.
Mr. Carlos Langer	Graduate Student, Stanford University, California.

Publications

S. C. Kassinos, C. A. Langer, S. Haire, and W. C. Reynolds, Structure-based modeling for wall-bounded flows. To appear in a special issue of the *Int. J. Heat and Fluid Flow*, October 2000.

W. C. Reynolds, S. C. Kassinos, C. A. Langer, and S. Haire, New directions in turbulence modeling. Third International Symposium on Turbulence, Heat, and Mass Transfer. Nagoya, Japan April 3-6, 2000.

S. C. Kassinos and W. C. Reynolds, "Structure-based modeling for homogeneous MHD turbulence". *Annual Research Briefs 1999*, CTR, NASA Ames/Stanford, pp. 301-315.

S. C. Kassinos and W. C. Reynolds, Insights for LES from Structure-based Turbulence Modeling. In Lecture Notes in Physics: Industrial and Environmental Applications of Direct and Large-Eddy Simulation, Springer, 1999.

Awards Received

Honorary Doctorate of Engineering from the University of Manchester Institute of Science and Technology (UMIST) awarded to Professor William C. Reynolds on June 14, 2000.

TURBULENCE AND COMPLEX FLOW PHENOMENA IN AXIAL TURBOMACHINES

AFOSR GRANT # F49620 – 97 – 1 – 0110

Joseph Katz & Charles Meneveau
Department of Mechanical Engineering
The Johns Hopkins University
Baltimore, MD 21218

Abstract

The objective of this project is to measure the unsteady flow structure in axial turbomachines and use the data to address turbulence and complex flow modeling issues in complicated geometries. This report has two sections. The first briefly describes our progress in developing our new two-stage axial turbomachine test facility. The second section introduces a new model of deterministic stresses for passage averaged RANS that accounts for interactions between the non-uniform outfulx from one blade row with the complex blade geometry of the neighboring blades. Deterministic stresses calculated using this model are compared to measured distribution of deterministic stresses using data obtained in a centrifugal pump with a vaned diffuser (Sinha et al., 2000a, b). The model successfully reproduces the correct magnitude of deterministic stresses occurring due to unsteady leading-edge separation on the diffuser vanes.

Axial Flow Facility

The axial turbomachine test facility has been constructed in order to perform detailed velocity measurements within an entire stage including the rotor, stator, gap between them, inflow into the rotor and the wake structure downstream of the stator. Sketches of the system were included a previous report. The facility provides unobstructed view for 2-D PIV and 3–D holographic PIV measurements within the entire stage. Using acrylic rotor and stator and a fluid (water with NaI) with optical index of refraction that matches that of the acrylic facilitates this unlimited access. In addition to the AFOSR grant mentioned above, support for constructing this facility has also been provided by ONR. The blades have outside and hub diameters of 30 and 21.6 cm, respectively. The design flow rate is 0.195 m^3/s and the system is driven at 900 rpm by a 25 HP motor. The test loop has a temperature control system and provides flexibility in installing other devices including pressure transducers, honeycombs and grids as well as modifying the blade rows. Construction of the facility and performance measurements (that confirmed the design parameters) have been completed. Integration of a precision shaft encoder and an electronic control system for synchronizing our PIV system with the rotor phase have also been completed. Using a recently awarded AFOSR DURIP grant we have also purchased a 2048x2048 $pixels^2$, 15

frames/second "cross-correlation" digital camera and integrated it with a high speed mass data acquisition system that has a sustained acquisition rate of 60 MB/s and capacity of 250 GB. This camera will be used for high-resolution PIV measurements in the axial turbomachine facility.

Addressing Turbulence Modeling Problems in Turbomachines

Due to practical constraints, numerical simulations of flows within an entire multistage turbomachine cannot be performed using unsteady RANS on a routine basis. Using RANS on each blade row separately presents difficulties in matching boundary conditions. In the "passage-averaged" approach (Adamczyk, 1985) unsteady effects caused by neighboring rows are averaged out and accounted for through "deterministic" stresses. We have used PIV data generated in a centrifugal pump facility with a vaned diffuser to examine the Reynolds and Deterministic stresses caused by rotor-stator interactions (Sinha et al., 2000a, b; also briefly in the FY 99 report). The experiments have been performed in a transparent pump that enables PIV measurements within the impeller and the stator. The deterministic stresses are obtained from the difference between phase-averaged and passage averaged velocity. The facility is sketched in Figure 1a and the measured deterministic kinetic energy is shown as a reference in Figure 1b. Our data agrees with conclusions of previous studies (e.g. Rhie et al., 1995) that deterministic stresses can be of similar or higher magnitude than the Reynolds stresses, especially in regions of boundary layer separation and in near wakes. In this abstract we introduce a new deterministic stress model and compare the results to our experimental data.

The measured deterministic stresses show strong tangential variations which by construction are not included in the "swept wake" model of Adamczyk et al. (1990). In that model the wake profile obtained from steady calculation in the preceding blade row is swept circumferentially over the domain, and deviations from the mean are averaged to calculate the modeled deterministic stresses. This process eliminates any tangential variations of the stress field. Conversely, a substantial part of the measured deterministic stresses are caused by the unsteady response of the flow around the stator blades, particularly the boundary layers and the wakes, to non-uniform pressure and velocity distributions at the exit of the impeller. These observations motivate the presently proposed "bimodal deterministic stress model, as described below.

The proposed model is based on the expectation that the phase-averaged, time-varying outflow from a blade row is reasonably well correlated with sweeping an accurately computed passage-averaged outflow from the same blade row (computed in the frame of reference of this blade row). To clarify this point using the centrifugal pump data, Figure 2a shows the measured angle α between the velocity at a point P (P is shown in Figure 2b) and the circumferential direction, as function of rotor orientation angle θ (for definitions, see Figure 1). The solid circles show α obtained form the measured phase-averaged velocity fields at various rotor orientations. A jet-wake like phenomenon is evident: For $\theta < 210^0$, when point P is in the pressure side of the impeller blade, the radial velocity at the exit from the rotor increases and the circumferential

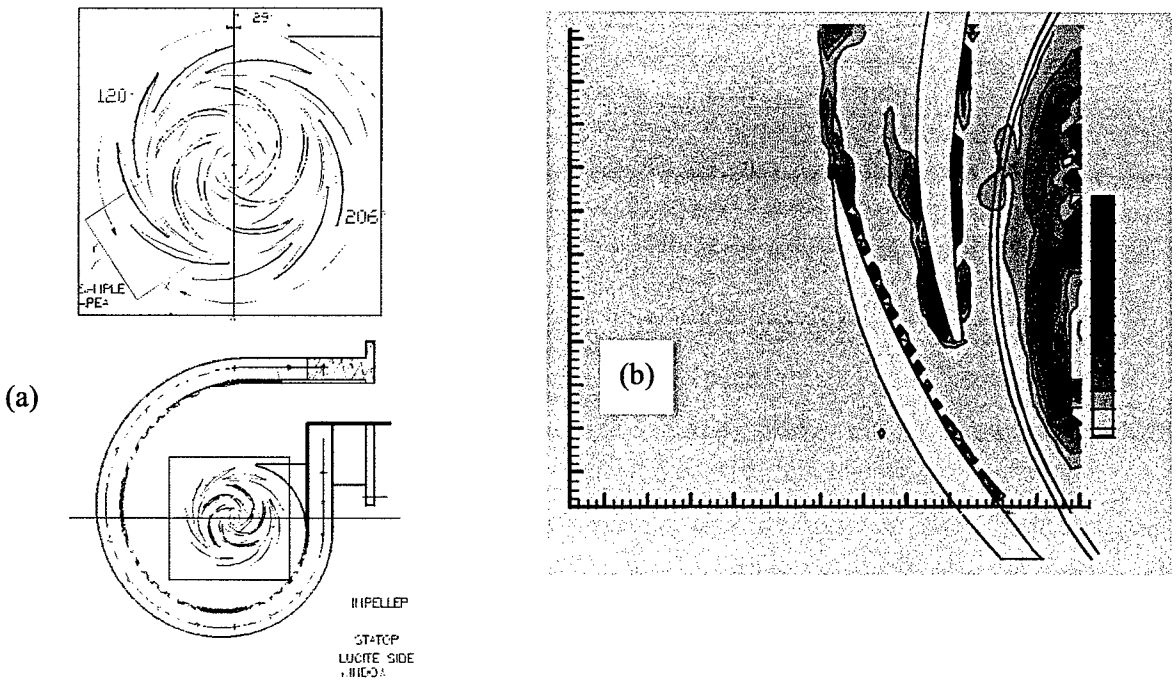

Figure 1: (a) The geometry of the centrifugal pump with a vaned diffuser showing the sample area; (b) Measure d distribution of deterministic kinetic energy, k^{*det} (Sinha et al., 2000a, b).

velocity decreases. Consequently, the angle of incidence of the flow at the entrance to the stator blade row increases, as compared to the lower angle during the rest of the cycle. As discussed in Sinha et al. (2000a, b) this incidence angle change causes phase-dependent leading edge separation in the diffuser and high deterministic stresses. These phase-averaged results (solid circles) are unknown during passage-averaged simulations of the flow within the stator and the rotor, and therefore they cannot be used as input into a model. However, the non-uniform outflux from the impeller can be deduced from the passage averaged simulations of the flow within the rotor. As an illustration, the solid line in Figure 2a is the same angle, when the steady velocity field is rotated and plotted at the same phase as the phase-averaged values. This data would be available during a passage-averaged simulation and can be used as input to a model. This comparison shows that sweeping the rotor passage-averaged velocity distribution appears to give a reasonably accurate indication of the time-varying inflow angle into the stator row.

As opposed to the swept wake model, the rotated passage-averaged field is used only as a boundary condition for steady flow calculations in the stator domain. The presently introduced bimodal (or multimodal in other cases) deterministic stress model is based on performing two (or more, n) simplified steady RANS calculations of the flow inside the downstream blade-passage (B_d), for two (or more) representative phases of the upstream blades (B_u). For these calculations the computational domain D_d only covers the blade-row B_d. For each calculation k (k=1,2,..,n), the inlet condition into the domain D_d is the passage-averaged velocity $\mathbf{v}^{\text{pass-k}}(x_{\text{in}})$ of B_u at

positions x_{in}, which coincide with the inlet boundary of D_d. To each rotor outflow structure, we assign a weight w_k (k=1,2,..,n), equal to the fraction of time for which that condition is valid.

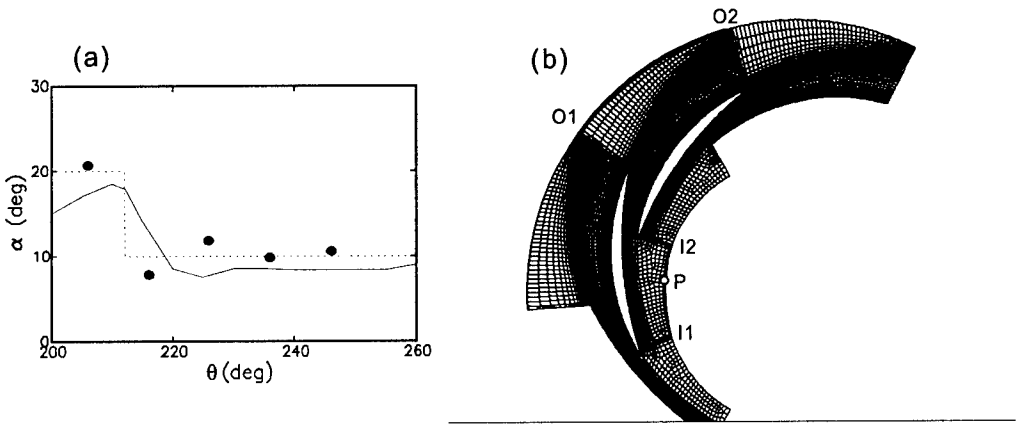

Figure 2: (a) The measured angle formed by the velocity and the tangential direction, at a point P shown in (b). Solid circles: Angle of the phase-averaged velocity as function of rotor phase. Solid line: angle obtained by sweeping the measured passage-averaged velocity in the rotor frame past point P, as function of blade orientation. Dotted line: The bimodal approximation; (b) Mesh and domain (dark contour) used in the FLUENT™ computations. Cyclic periodic boundary conditions are used and two repetitions are shown for clarity. The inlet of the computational domain is the segment I1-I2 and the outlet is O1-O2.

Suppose that each of the n simplified calculations yields a velocity field $\mathbf{u}^k(\boldsymbol{x})$, with $\boldsymbol{x}$ pertaining to D_d and with $\mathbf{u}^k(\boldsymbol{x}_{in}) = \mathbf{v}^{pass\text{-}k}(\boldsymbol{x}_{in})$. The deterministic stresses are then evaluated as:

$$\tau_{ij}^{det} = -\frac{1}{n}\sum_{k=1,n} w_k \left(u_i^k\right)' \left(u_j^k\right)'$$

where $(u_i^k)'$ is the deviation of the kth velocity field from the mean velocity over all the n simplified simulations,

$$\left(u_i^k\right)' = u_i^k(\boldsymbol{x}) - \frac{1}{n}\sum_{k=1,n} W_k u_i^k(\boldsymbol{x})$$

The summations approximate a time-integration over a period equal to a rotor passage. To illustrate and test the approach, we choose the case shown in Fig. 2a. In this case the rotor is the upstream blade row, and the stator is the downstream row, B_d. This cycle is reasonably well represented by two different inlet conditions (i.e. n=2). The first is a velocity of 2.2 m/s at an angle α_1=20^0, and the second is a velocity of 4.3 m/s at α_2=10^0 (see dotted line in Figure 2a). Since it appears that the first angle occurs for about 20% of the rotor passage, the assigned weights are w_1=1/5 and w_2=4/5. To perform the two simplified steady RANS calculation in the stator domain, we apply FLUENT™ in a 2-D domain with cyclic periodic boundary conditions. Both standard k-ε with a wall-function, and RNG k-ε models are used with little difference between them. Consequently, only results of the RNG k-ε model are shown. Figure 2b shows the grid that reproduces exactly a 2-D section of the stator. The mesh has a very good resolution of

the near-wall and wake regions. The inlet condition is applied at the inlet at the segment *I1-I2* (corresponding to the set of points x_{in}). Outlet boundary conditions are applied at *O1-O2*.

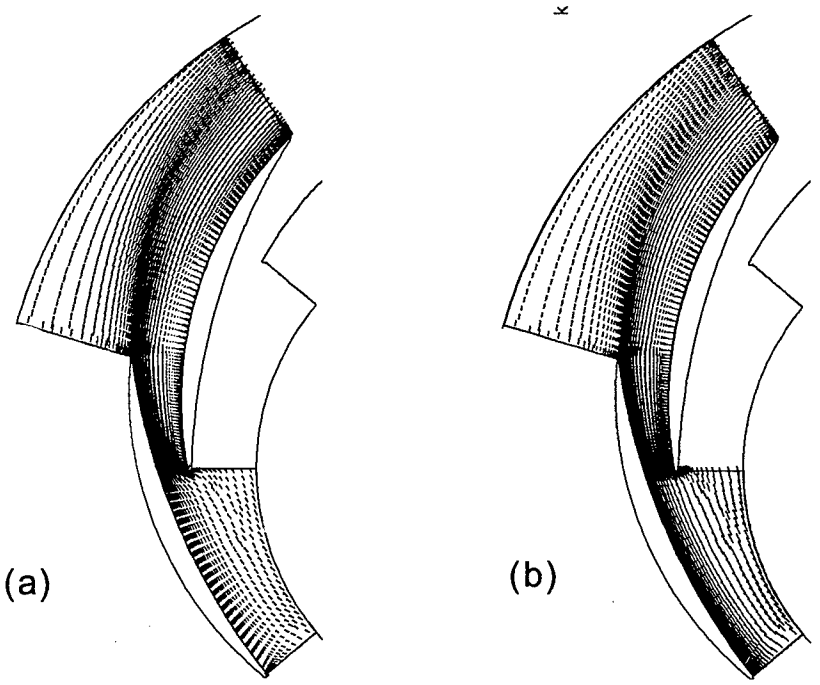

Figure 3. Velocity fields computed for different inlet conditions. (a) k=1 - the high inlet angle of 20^0 case; (b) k=2 - the low inlet angle of 10^0 case. The flow in (a) exhibits leading edge separation, while the flow in (b) remains attached.

The calculated velocity fields are shown in Figures 3a and b, for k=1 and 2, respectively. In agreement with the experimental data, boundary layer separation occurs at the leading edge of the stator for the k=1 case. The flow remains attached for the k=2, lower incidence angle (10^0), case. This "flip-flopping" between attached and separated flows produces strong deterministic stresses and kinetic energy, as shown in Figure 4. A comparison Figure 1b shows that the peak region around the leading edge, and even the peak magnitudes, are well described by this model.

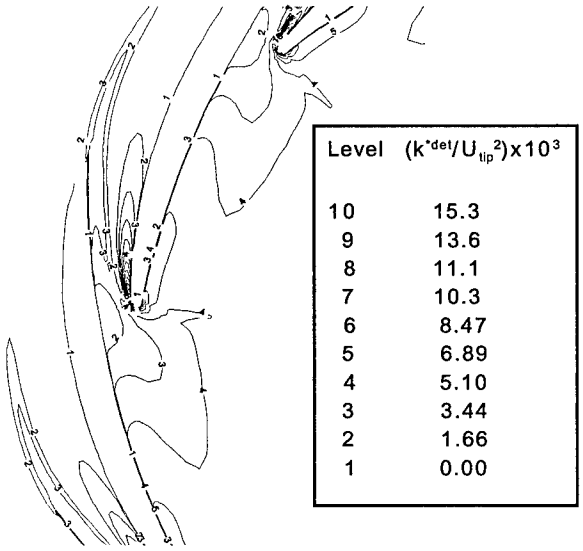

Figure 4: Deterministic kinetic energy ($-\tau_{ii}^{det}/2$), as calculated from the bimodal model. Peak values occur near the separated flow region and agree with the experimental data in Figure 1b. The values in the stator wake fall below the measured values.

However, problems still remain in predicting the deterministic kinetic energy in the stator wake, which is higher in the measured distributions. The experimental data also shows phase dependent mid-vane separation on the suction side (which causes meandering of the wake) whereas the calculated field remains attached. Additional work is required to find out how much additional information is needed at the inlet in order to reproduce this mid-vane separation.

The practicality of the model relies on our ability to represent the entire cycle using a few representative inlet conditions, requiring only a few steady RANS calculations. In general these calculations should be performed in 3-D, but in the present example 2-D calculations are sufficient, due to the mainly 2-D nature of the flow in the pump diffuser. It is unlikely that such 2-D flow would exist in the axial flow facility. Clearly, this model development is in its infancy and needs substantial additional work, refinement and further tests. Future evaluations will be performed based on the experimental results that will be generated in the axial flow facility.

Acknowledgement/Disclaimer

This work was sponsored by the Air Force Office of Scientific Research, USAF, under grant number F49620-97–1-0110. The views and conclusions contained herein are those of the authors and should not be interpreted as necessarily representing the official policies or endorsements, either expressed or implied, of the Air Force Office of Scientific Research or the U.S. Government.

References

Adamczyk, J.J., 1985, "Model Equation For Simulating Flows In Multistage Turbomachinery." *ASME paper No.* 85-GT-226.

Rhie, C.M., Gleixner, A.J., Spear, D.A., Fischberg, C.J., Zacharias, R.M., 1995, "Development And Application Of A Multistage Navier-Stokes Solver. Part A: Multistage Modeling Using Body Forces And Deterministic Stresses," *ASME Paper No.* 95-GT-342.

Sinha, M., Katz, J., (2000), "Quantitative Visualization of The Flow in A Centrifugal Pump with Diffuser Vanes, Part A: On Flow Structure and Turbulence," Journal of Fluids Engineering, Vol. 122, No. 1, pp. 97-107.

Sinha, M., Katz, J., Meneveau, (2000), "Quantitative Visualization of The Flow in A Centrifugal Pump with Diffuser Vanes, Part B: Addressing Passage Averaged and LES Modeling Issues in Turbomachinery Flows," Journal of Fluids Engineering. Vol. 122, No. 1, pp. 108-116.

Supported Personnel

Faculty members: Joseph Katz and Charles Meneveau (0.25 months each);
Post Doctoral Fellow: M. Guin (30%); Graduate Student: Guang Chen (50%)
Mechanical Engineer; Y. Ronzhes (10%)

Publications:

Two journal papers, Sinha et al. (2000a, b) have been published – see full references above.
A paper by Meneveau and Katz (2000) describing the present model is presently in preparation.

PROPAGATING POTENTIAL DISTURBANCES IN TURBOMACHINERY

QAF185005203207
Paul I. King
Department of Aeronautics and Astronautics
Air Force Institute of Technology
Wright-Patterson Air Force Base, OH 45433

ABSTRACT

Introduction

Periodic disturbances in a uniform flow field can be created through potential disturbances propagated from circular rods shedding Von Karman vortices. Fabian et al.[1] showed that upstream propagation from circular rods shedding vortices forces unsteady pressures of high amplitude near the trailing edges of a vane in cascade and result in a near-singularity at the trailing edge. The Air Force Institute of Technology and the University of Notre Dame are collaborating[2,3] on controlling the periodicity of such disturbances to force a periodic field upstream on a stationary cascade of loaded compressor blades and determine the unsteady pressures. The first part of AFIT's investigation is concerned with the measurement of the velocity field absent the blades, via hot film and split film probes.

Facilities and Methods

Testing was conducted in the compressor cascade test facility at the Air Force Institute of Technology.[4] A 40-hp (30 kW) centrifugal blower rated at 3000 cfm, 1.6 psig total head provides airflow for the tunnel. For this preliminary research, tunnel speed was approximately 65 m/s. Later, higher speeds will be introduced to study compressibility effects. The test section is rectangular, 2 inches by 8 inches. The walls slide in the streamwise (longitudinal) direction allowing the cylinder to be shifted with the probe fixed. The cylindrical rods were 3/16 inch diameter aluminum stock, designed to shed vortices at a frequency of approximately 2.6 kHz at 0.2 Mach number. Miniature Kulite differential pressure transducers were mounted at the 90 deg point (transverse to flow) of the cylinders.
Velocity data were taken with either miniature x-hot film or split film probes operating in constant temperature mode. Hot films were TSI model 1240-20, inserted from the side of the tunnel to measure at the tunnel centerline for various vertical cylinder locations. Excitation, amplification, low-pass filtering (30 kHz) and voltage offset were provided by Dantec model 90C10 CTA Modules. Analog voltages passed through a National Instruments SCB-68 shielded connector box connected to a National Instruments AT-MIO-16E-1 A/D board with 8 sequential, differential inputs sampled at a total rate of 1.25×10^6 samples/s.

Phase Locked Data Collection

Data collection was triggered by a pressure peak on one cylinder. 250 sets of pressure and velocity signals were collected and ensemble averaged. Ensemble averaged voltages were low-pass filtered using the Matlab® filtfit command which uses a forward and reverse digital filtering procedure to minimize phase distortion. With a fourth order low pass Butterworth filter set at a cutoff frequency of 6 kHz, a comparison of filtered and unfiltered velocity waves at the fundamental frequency showed phase agreement within 0.01 rad. Since a split film sensor is rather insensitive to turbulence effects a filtering routine was not required. Finally,

truncation endpoint transients in the filtered data were minimized with the use of a Hanning window, a half-cosine wave with the peak value of unity centered on the data string. Averaged and filtered voltages were converted to velocities and fitted to a two-frequency sinusoidal function using the Matlab® function fminsearch. The frequency, phase and amplitude were modeled in the form,

$$W(t) = A_f \sin(\omega_f t + \phi_f) + A_h \sin(\omega_h t + \phi_h) \tag{1}$$

and coefficients determined by a least squares method similar to simulated annealing used by Fabian et al.[5] The pressure signal contained only a single frequency sine wave for all data sets.

Model for Fixed Probe, Single Cylinder

A modified potential flow model was developed for the tunnel centerline velocity (fixed probe) due to varying cylinder locations. It was expected that with superposition this model would account for the velocity field of an array of cylinders. (This turned out not to be the case and at this point in the project a model for multi-cylinders has not been obtained.) The model superposes the potential solution for a uniform flow over a doublet, which simulates a cylinder in cross flow, with a vortex of sinusoidally varying strength which models the alternating bound circulation due to shedding from the cylinder. The resulting expression for arbitrary time and space is[6]

$$\vec{V}(r,\theta,t) = \left\{U_\infty \cos\theta\left(1-\frac{R^2}{r^2}\right)\right\}\hat{r} \quad - \quad \left\{U_\infty \sin\theta\left(1+\frac{R^2}{r^2}\right)+\frac{\Gamma\sin(\omega_f t)}{2\pi r}\right\}\hat{\theta} \tag{2}$$

where U_∞ is the freestream velocity, θ is the angle measured counterclockwise from the downstream side of the cylinder, r is the distance from the center of the cylinder and R is the cylinder diameter. The last term in Eqn. 2 is the perturbation potential (Γ) at the fundamental frequency, ω_f. The propagation time relative to a reference results in a phase lag, ϕ, in the sine term of Eqn. 2. For an arbitrary point in the flow, the propagation speed is vector sum of acoustic speed and freestream velocity: c = a*sqrt(1+2Mcosθ+M^2). This results in the following generalized expression for velocity:

$$\vec{V}(r,\theta,t) = \left\{U_\infty \cos\theta\left(1-\frac{R^2}{r^2}\right)\right\}\hat{r} \quad - \quad \left\{U_\infty \sin\theta\left(1+\frac{R^2}{r^2}\right) \quad +\frac{\Gamma}{2\pi r}\sin\left(\omega_f t - \frac{r\omega_f}{a\sqrt{1+2M\cos\theta+M^2}}\right)\right\}\hat{\theta} \tag{3}$$

In our data both x and y velocity waves exhibit amplitudes at the fundamental frequency for $\theta = \pi$, a result not predicted from the above model. Our results also lacked a harmonic in the x (drag) direction though this could be due to small perturbations of a single cylinder. It is presumed that an array of cylinders shedding in phase would create substantially larger perturbations. The model suggested by Eqn. 3 suggests radial symmetry. The results of our experiment, however, suggest a weak dependence on the x coordinate and thus for the most part a better fit to the phase and amplitude data was produced by considering x and y as separate perturbations and not as components of a single circular perturbation.

Reflected Cylinder Model

Because of the moving cylinder the tunnel walls present a boundary not present in the infinite field potential model. In potential theory wall reflection is modeled with virtual cylinders symmetrically located on the opposite side of the wall from the real cylinder. A new model

included the real cylinder and two virtual cylinders on either side of endwalls. (Added virtual cylinders did not improve the model). The resultant effect of the three waves was modeled as:

$$A_c \sin(\omega t + \phi_c) = A_1 \sin(\omega t + \phi_1) + A_2 \sin(\omega t + \phi_2) + A_3 \sin(\omega t + \phi_3) \quad (4)$$

The subscript c in Eqn. 4 indicates the combined wave, and the subscripted numbers indicate the component waves. The three amplitude terms ($A_{1,2,3}$) and three phase terms ($\phi_{1,2,3}$) are of the same form (k/r^n) used in the previous single cylinder model. The three component waves are modeled at the same frequency, but due to reflections the virtual cylinders are 180 degrees out of phase with the real cylinder. After some trigonometric manipulation, Eqn. 4 becomes

$$A_c \sin(\omega t + \phi_c) = \sqrt{B^2 + C^2} \sin(\omega t + \delta) \quad (5)$$

where

$$B = A_1 \cos\phi_1 + A_2 \cos\phi_2 + A_3 \cos\phi_3$$

$$C = A_1 \sin\phi_1 + A_2 \sin\phi_2 + A_3 \sin\phi_3$$

and δ is given by $\tan^{-1}(C/B)$. The combined amplitude was modeled in the form

$$A_c = k\sqrt{\left(\frac{\cos\phi_1}{r_1^n} + \frac{\cos\phi_2}{r_2^n} + \frac{\cos\phi_3}{r_3^n}\right)^2 + \left(\frac{\sin\phi_1}{r_1^n} + \frac{\sin\phi_2}{r_2^n} + \frac{\sin\phi_3}{r_3^n}\right)^2} \quad (6)$$

The amplitudes of all three cylinders were considered to be the same at their source locations, so the constant k was factored out of the expression. Similarly, the combined phase was modeled as

$$\phi_c = \phi_{shift} + \tan^{-1}\left(\frac{\sin\phi_1/r_1^n + \sin\phi_2/r_2^n + \sin\phi_3/r_3^n}{\cos\phi_1/r_1^n + \cos\phi_2/r_2^n + \cos\phi_3/r_3^n}\right) \quad (7)$$

The combined phase was allowed to shift by an arbitrary amount, as in the single cylinder model. Each phase term was calculated individually over a range of tunnel locations, and the combined phase and amplitude obtained from Eqn.'s 6 and 7. Because the inverse tangent calculation is not quadrant specific, sharp jumps in the combined phase model were common. Multiples of π were added to the combined phase as necessary to smooth the curve. Notice that the phase and amplitude of the combined model are a function of the phase, amplitude and position of the individual cylinders. Thus, the phase and amplitude models are not independent.

Results

Perturbation amplitudes and phases were measured at 5 (upstream) locations. One location, 1.25 inches upstream of a single cylinder is shown in Fig.'s 1. and 2, where phase in radians and amplitude are plotted for various y locations of the cylinder. It is convenient to examine the results in the x-y coordinate system rather than in the usual cylindrical coordinates used in potential theory. Y-velocity phase is nearly symmetrical about y = 0 and increases sharply by π between y = $\pm$1.25 in and $\pm$ 2 in. Data taken at smaller y intervals (not shown) verified this observation. The y-phase at other x locations all had a sharp jump at the same y location. As shown later this jump was due to wall effects. The x-velocity phase unexpectedly was not symmetrical and steadily increased with y.

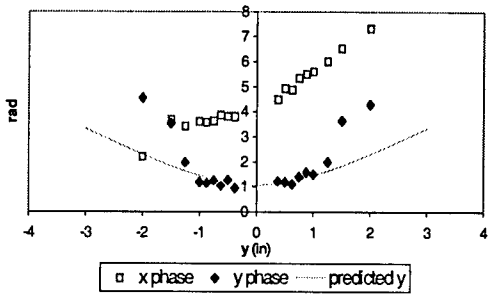

Fig. 1. Perturbation phase at x = 1.25 in

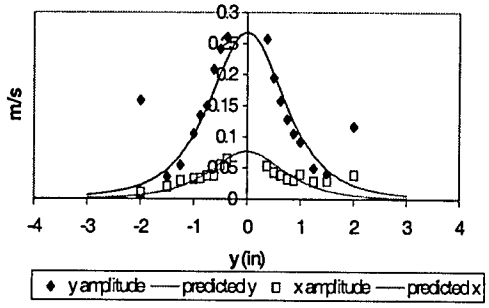

Fig. 2. Perturbation amplitude at x = 1.25 in

Shown in Fig. 2 are the amplitudes of the unsteady x and y velocities, which were also determined from the curve fit to the 250-set ensemble averaged velocities. The amplitude distributions are fairly symmetrical about the tunnel centerline, but the y-velocity has a sharp attenuation at the location of the phase jumps seen in Fig. 1. The model for y-perturbations in Eqn. 3 is compared to the experimental data. For the points nearest the cylinder, the model gives a fairly good description of the changing phase in y. Beyond approximately 1 inch in either direction, however, the prediction does not follow the jump in the data. Additionally, at different x locations, different phase shifts were required to make the prediction fit the data. This seemed to indicate that the waves were propagating in a manner not fully described by a single cylinder model. Although the single cylinder model for x phase is the same as that for the y phase, the shape of the x data is clearly not predicted by a similar curve. The amplitude was modeled using k/r^n, a form similar to the amplitude term of Eqn. 3. k was chosen to be an arbitrary constant and n an arbitrary power. In Fig. 2 a match to the x-y perturbation amplitudes was achieved with n = 4 and k = 0.2, significantly different results from the usual model with n = 1. A portion of the y-velocity amplitudes was matched with k = 0.7, but the sharp attenuation is not captured by the model.

Virtual image model

In all figures in this section the modeled exponent, n, is equal to 0.04, an unexpectedly small positive power and due to the minimal falloff of amplitude with x at the centerline of the tunnel. Phase and amplitude models are shown in Fig.'s 3 and 4, with the constant k equal to 0.025. For the most part, the model captures the essence of the amplitude data except for the slight asymmetry in the x amplitude distribution at the outer y location.

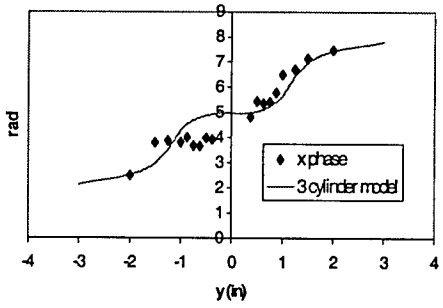

Fig. 3 Three-cylinder phase model for x= 1.5in

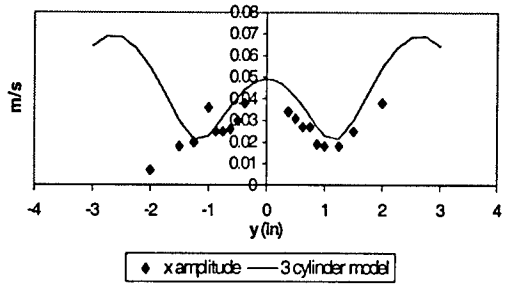

Fig. 4. Three-cylinder amplitude model for x = 1.5in

A pronounced asymmetry is seen in the x phase data in Fig. 3. Upon examination of the physical characteristics of the data, the model (shown) was inverted on the left hand side, a

result that closely approximated the behavior of the data. Both the data and model match the asymmetry about y = 0. The inversion to the left-hand side of the x phase model in Fig. 3 was made by taking the negative of the quantity inside the brackets of equation 7. In equation form this would be expressed $\tan(-\delta) = \tan(\pi-\delta)$. The inverted portion of the curve was then shifted by a phase constant to align it with the right hand portion of the curve. The arbitrary phase shift, φ_{shift}, varied somewhat, but showed no particular trend with x distance. The shift magnitude was selected by aesthetically matching the curve to the data at a particular x location without regard to other x locations.

Y Phase and Amplitude Fits

Fig.'s 5 and 6 show the fit of the three-cylinder model to the phase and amplitude of the y perturbation data, respectively. As in the fit of the model to the x perturbation data, the power n is 0.04.

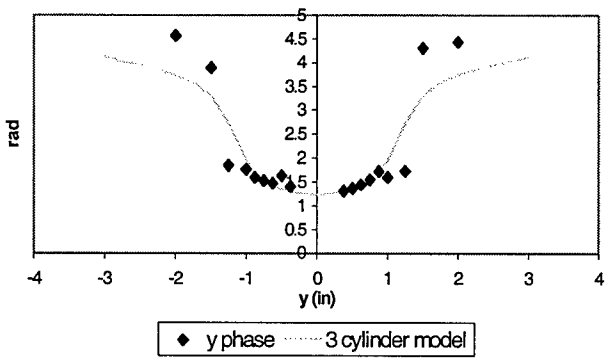

Fig. 5. Three-cylinder model for y phase, x = 1.5

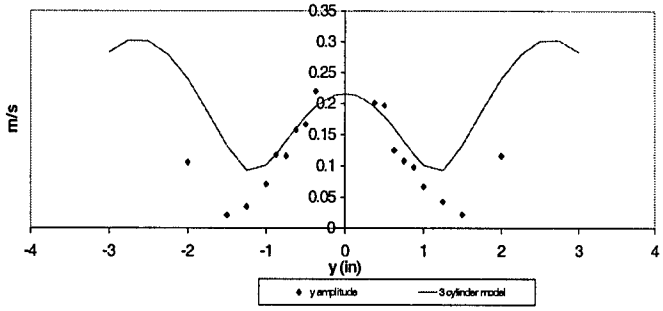

Fig. 6. Three-cylinder model for y amplitude, x = 1.5 in

The y phase model in Fig 5 matches the basic characteristics of the data including the jump in phase. This modified wall model reinforces the notion that wall effects are the cause of the phase jump. In the center portion of the curve, the model accurately predicts the phase. Toward the more extreme y locations the prediction displays the proper trend, but does not completely follow the data. The constant k determined for the y amplitude estimates showed more variation than for x. The value of k varies from 0.1 to 0.14 for different x locations. The very low attenuation exponent, n, was indicative of almost no decay in y amplitude with x distance, requiring an increase in k.

The upper portion of the y amplitude prediction in Fig. 6 fits the data reasonably well. The location and the magnitude of the minimum amplitude are not well predicted, however. The point of minimum amplitude on either side of the model is where the disturbances propagating from real and virtual cylinders combine to produce the greatest wave cancellation.

Multi-Cylinder preliminary results

It was expected that with the insertion of multiple cylinders into the test section either synchronous or asynchronous shedding would occur. For the cases of 5 cylinders of 1.6 in spacing or 10 cylinders of 0.8 in spacing a repeatable pattern of shedding phasing among the

cylinders was observed, but the pattern was rather random, neither synchronous nor asynchronous. Amplitudes of y-velocity perturbations for one, five and ten cylinders, as with the single cylinder, experience attenuation at about 1.25 inches above the centerline. All magnitudes increase with y in a similar fashion, with those for the five-cylinder case being the largest, and the 10 cylinder configuration surprisingly the smallest. The phases all exhibit a π shift at the location of amplitude attenuation.

Conclusions

The velocity flow field upstream of a single and multiple rods in a planar array was measured. Results from x-hot film and split film measurements in a low speed wind tunnel show that the flow field is extremely influenced by the tunnel wall reflections. The velocity field does not fall off radially as in unbounded potential flow and amplitudes of velocity perturbations experience cancellation between the cylinder and tunnel wall. Modeling with simple 1-D unbounded potential flow theory and virtual images captures the wall reflection effects.

The use of a multi-cylinder array does not necessarily result in coherent in-phase or out-of phase vortex shedding. More work is needed to determine the influence of Mach number and upstream components on synchronous vortex shedding.

Acknowledgements

This research effort is jointly sponsored by the Air Force Office of Scientific Research under QAF185995203036, and the Air Force Institute of Technology Department of Aeronautics and Astronautics.

References

1. Fabian, Michael K. and Eric J. Jumper. "Rearward Forcing of an Unsteady Compressible Cascade," Journal of Propulsion and Power, Nov-Dec 1998.

2. Wade, P.C., King, P.I., Hopper, D.R., Jumper, E.J. and Asghar, A., "Velocity Field Upstream of Rods used for Forcing Unsteady Compressible Cascades," AIAA 2000-3229, 36th Joint Propulsion Conf., 17-19 July 2000, Huntsville, AL.

3. Asghar, A, Kalk, E.A., Jumper, E.J., Hopper, D.R. and King, P.I., "Unsteady Pressure Response on a Rearward-Forced, Isolated Compressible Cascade Vane," AIAA 3228, 36th Joint Propulsion Conf., 17-19 July 2000, Huntsville, AL.

4. Hopper, David R. "Measurements of the Effects of Tunnel Wall Proximity on the Velocity Field Upstream of a Rod With Vortex Shedding in Low-Speed Flow,". MS Thesis, Air Force Institute of Technology, 2000.

5. Falk, Eric A., Eric J. Jumper, and Brenda A. Haven. "Upstream-Propagating Potential Waves Elicited from the Stator Row Downstream of a Fan," AIAA paper number 99-2805, 1999.

6. Karamcheti, Krishnamurty. Principles of Ideal-Fluid Aerodynamics, 376-389. New York: John Wiley and Sons, Inc., 1966.

DEVELOPMENT OF DOPPLER GLOBAL VELOCIMETER (DGV)
AFOSR/DEPSCoR Grant F49620-98-0068

John Kuhlman, PI
West Virginia University
Mechanical and Aerospace Engineering Department
Morgantown, WV 26506-6106

Abstract

A two-component Doppler Global Velocimeter (DGV) system has been developed, along with a two-component Point Doppler Velocimeter (PDV) system. Velocity measurements have been obtained for both systems to quantify accuracy. Results have been obtained for velocity distributions over the surface of a rotating wheel, and for several simple flows such as fully-developed turbulent pipe flow, a circular jet, an annular jet, a swirling jet, and the flow over a NACA 0012 airfoil model.

Based upon rotating wheel data, PDV data linearity is ± 0.5 % (i.e., ± 0.3 m/sec, out of 57 m/sec). PDV data for the flow over a NACA 0012 airfoil show mean velocities that agree with hot wire data to within ±2-3 m/sec, while the RMS data agree to within ±0.5-0.7 m/sec. Also, recent results in a series of three turbulent jet flows generally show similar mean velocity agreement between PDV and hot wire data. The PDV RMS data differ from hot wire RMS results by 1-2 m/sec.

Accuracy of the DGV system has also been investigated. For rotating wheel results, RMS noise levels are ±1 m/sec out of 58 m/sec, while total velocity range errors are ±1-2 m/sec. Fully turbulent pipe and jet flow mean velocity measurements agree with pitot probe traverse data. DGV RMS data do not agree with hot wire measurements, as expected.

Introduction

Several non-intrusive whole field velocimetry techniques are currently under development that provide velocity data in a plane, which can thus reduce the time required to map out a complex flow field. This project is exploring the accuracy of DGV, a nonintrusive, planar imaging, Doppler-based velocimetry technique, as well as the accuracy of related PDV. DGV techniques use an iodine vapor cell to determine the Doppler shift, and hence the velocity, of small seed particles in a flow field, as these particles pass through a two-dimensional sheet of laser light. The same portion of the light sheet is viewed through a beamsplitter by a pair of video cameras, with the iodine cell placed in the optical path of one of the cameras. The laser wavelength and iodine absorption line are matched such that flow velocities of interest yield Doppler shifted frequencies in the linear part ("edge") of the absorption line of the cell. The ratio of scattered light intensities collected by two corresponding pixels viewing a point in the flow yields a normalized signal that is proportional to the particle velocity at that point. Point Doppler Velocimetry (PDV) is a related technique, where photodiodes are used in place of video cameras, along with front lenses and pinholes, to collect scattered light from a single point in a seeded flow.

A two-channel non-scanned point PDV system has been developed (Kuhlman, et al., 1997), along with a two-channel planar imaging DGV system (Naylor and Kuhlman, 1998, 1999). The accuracy limits of both systems are being systematically explored and improved, through a series of measurements in relatively simple, unheated flows such as fully-developed turbulent pipe flow, a series of three circular jets (uniform, annular, and swirling), and the flow over an airfoil. A rotating wheel is also being used as a velocity standard. While current DGV systems lack the accuracy of conventional LV or PIV, DGV has proven in a short time to be a very flexible whole-field velocimetry technique.

Apparatus and Procedure

The present systems closely follow the basic DGV technologies originally developed by Meyers, et

al. (1991). For PDV, photodiodes have been used, along with front lenses and pinholes, to collect scattered light from a single point in a seeded flow. Kuhlman, et al. (1997) and James (1997) have described the PDV system in detail. A reference iodine cell has been used to compensate for laser frequency drift. Calibration of the iodine cells has been accomplished in situ, using a continuous scan of the mode structure of the cw Argon ion laser, by mechanically altering the tilt of the etalon through about 10-20 mode hops (James, 1997); see Fig. 1 for examples of typical calibration curves.

The DGV system hardware has been described in Naylor and Kuhlman (1998, 1999, 2000), and in more detail in Naylor (1998). Most of this hardware is similar to that used for the PDV system. Eight-bit Hitachi KP-M1 CCD cameras and a Matrox Genesis frame grabber have been used to capture images for the DGV system. All four cameras are read simultaneously using sync pulses from the Genesis board. Nikon 35-135mm, f3.5-4.5 zoom lenses have been used with the CCD cameras. Polarizing filters have been placed in front of the beam splitters to minimize effects due to polarization sensitivity of the beam splitters. Image processing software has been developed, as described by Naylor (1998), which closely follows the image processing methods developed by Meyers (1992, 1996). Flow seeding for DGV and PDV measurements is provided by a commercial fog machine, which feeds a large plenum to dampen pulsations in the smoke output.

During the past year, 2-component PDV data have been obtained using a continuous "strip chart" data recording method for three different jet flows: a standard uniform exit jet, an annular jet, and a swirling jet (Kuhlman and Collins, 2000), each at a Reynolds number of 10^5. More recently, conventional time series at fixed locations in these flows have been obtained, where at each location data have been obtained at a sampling rate of 10 kHz, in 8 k blocks, corresponding to 0.8192 sec time records. From these time series, mean and RMS velocities, as well as time autocorrelation coefficients and power spectra have been computed for both PDV and hot wire data, to assess the accuracy of the PDV system for turbulence measurements.

Results

Recent analysis of a mean velocity offset error has indicated that it was largely due to the random, uncorrelated variations in the stem temperatures of the original iodine cells. This stem temperature variation has been observed to vary with a short term RMS of 0.1 degrees C (Naylor, 1998). This has been found to correspond to an error in the computed Doppler shift frequency of 7 MHz, which then corresponds to a mean velocity error of from 2 to 10 m/sec, depending on the geometry and viewing direction of the PDV system (Naylor and Kuhlman, 2000). This level of velocity error is consistent with the observed mean velocity offset error. This error has been eliminated through use of vapor limited iodine cells.

Comparisons of the recent PDV jet data with hot wire data are shown in Figs. 2-4; see Collins (2000). Fig. 2 compares the PDV axial velocity data with hot wire results at the exit of the standard jet. Similar comparisons for centerline axial velocity profiles and radial profiles at x/D = 6 are shown in Figs. 3 and 4, respectively. PDV mean velocities are repeatable to within 2-4 m/sec, out of a total range of 60 m/sec. PDV RMS results generally repeat to within 0.5-1 m/sec. However, there are some regions where the PDV mean velocities differ from the hot wire data by as much a 7 m/sec, while the PDV RMS results differ from hot wire data by as much as 1.5-2 m/sec on the jet centerline (Fig. 3). Higher PDV RMS values are measured for the more recent results, which have used higher sampling rates and longer time records, along with a smaller PDV sampling volume. This has reduced the effects of spatial averaging in reducing the RMS, but at the same time it has increased the effects of multiple scattering, since more seed material is then required. PDV correlation coefficients generally agree well with hot wire correlation coefficients, but PDV power spectra show a larger amount of noise at frequencies above about 3 kHz.

Conclusions and Future Plans

The WVU two-component point Doppler velocimeter system has been significantly improved through the use of vapor-limited iodine cells that are not sensitive to temperature variations. Also, use of a smaller measurement volume has improved the RMS results. Two-component velocity measurements have been obtained for a uniform circular jet flow at a nominal exit velocity of 60 m/sec, corresponding to a Reynolds number of 10^5. Similar results have also been obtained for an annular jet and a swirling jet. These data runs have been duplicated to judge the repeatability of these measurements, and also have been compared with hot wire anemometer data for the same flow conditions. Point Doppler velocimeter mean velocity results are generally repeatable to within approximately 1-2 m/sec; the RMS velocity results are repeatable to within about 0.5 m/sec. Exit profiles of mean axial velocity data generally agree with hot wire anemometer results to within about 2-4 m/sec. However, the RMS velocity results are consistently lower than the hot wire results (by as much as 1.5-2 m/sec), everywhere but at the exit of the standard jet. This is believed to primarily be due to spatial averaging for the point Doppler velocimeter results. At the jet exit the PDV RMS is too high; the measured RMS of 1-2 m/sec is indicative of the resolution of the current instrument.

Further improvements to the PDV system are planned for the remaining grant period. Calculations have shown that the primary limitation to the current system is the resolution of the A/D board. This board will be replaced with a true 16-bit board; it is expected that this will have the potential to improve resolution from about 1 m/sec (at present), to about 0.2-0.3 m/sec. Also, avalanche photodiodes (APDs) will be used, which will allow use of lower seeding levels and reduce the effects of secondary scattering.

Personnel

Four MS students and one PhD student have completed their degrees while working on this project, as listed below.

Senthilkumar Ramanath	MSME, 1997.
Kelly James	MSME, 1997.
Steve Naylor	PhD, 1998.
David Webb	MSME, 1999.
Patrick Collins	MSME, 2000.

In addition, one MS student (Tom Scarberry) and one PhD student (Dawn Wu) are currently working on the project. Several undergraduate students have also worked on the project.

Transitions

The new iodine cell calibration procedure developed as part of this work (Fig. 1) has been evaluated by the NASA Langley research team for use with their Argon ion laser DGV system. Negotiations are currently underway with Dr. Cecil Hess of Metrolaser to further refine the accuracy of the point system as described above.

Acknowledgements/Disclaimer

The present work has been supported under AFOSR/DEPSCoR Grants F49620-94-1-0434 and F49620-98-1-0068, Dr. James M. McMichael, Dr. Mark Glauser, and Dr. Tom Beutner, technical monitors, as well as NASA Langley Research Center Grants NAG-1-1892 and NAGW-4464. The views and conclusions contained herein are those of the author and should not be interpreted as necessarily representing the official policies or endorsements, either expressed or implied, of the Air Force Office of Scientific Research or the U.S. Government.

References

Collins, P., "Point Doppler Velocimetry (PDV) Measurements in Circular Jets," MS Thesis, West Virginia University, MAE Department, 2000.

James, K., "Determination of the Accuracy of a Two-Component Point Doppler Velocimetry System," MS Thesis, West Virginia University, MAE Department, 1997.

Kuhlman, J. M., Naylor, S., James, K., and Ramanath, S., "Accuracy Study of a 2 — Component Point Doppler Velocimeter (PDV)," paper AIAA-97-1916, presented at AIAA 28th Fluid Dynamics Conference, June 29-July 2, 1997, Snowmass, CO.

Kuhlman, J., "Development of Doppler Global Velocimeter," Final Report for AFOSR/DEPSCoR Grant F49620-94-1-0434, May, 1998.

Kuhlman, J. M. and Webb, D. L., "2-Component Point Doppler Velocimetry (PDV) Measurements of Turbulent Flow over an Airfoil," paper AIAA-99-3517, presented at AIAA 30th Fluid Dynamics Conference, June 28-July 1, 1999, Norfolk, VA.

Kuhlman, J. and Collins, P., "Circular Jet 2-Component Point Doppler Velocimetry (PDV) Velocity Data," paper AIAA-2000-2296, presented at AIAA 21st Aerodynamic Measurement Technology and Ground Testing Conference, June 19-22, 2000, Denver, CO.

Meyers, J. F., Lee, J. W., and Cavone, A. A., "Signal Processing Schemes for Doppler Global Velocimetry," 14th International Congress on Instrumentation in Aerospace Simulation Facilities, Oct. 27-31, 1991, Rockville, MD.

Meyers, J. F., "Doppler Global Velocimetry, The Next Generation?," paper AIAA-92-3897, presented at AIAA 17th Ground Testing Conference, July 6-8, 1992, Nashville TN.

Meyers, J. F., "Evolution of Doppler Global Velocimetry Data Processing," 8th Int'l. Symp. On Applications of Laser Techniques to Fluid Mechanics, July 8-11, 1996, Lisbon, Portugal.

Naylor, S., "Development and Accuracy Determination of a Two-Component Doppler Global Velocimeter (DGV)," PhD Dissertation, West Virginia University, MAE Department, 1998.

Naylor, S. and Kuhlman, J., "Accuracy Studies of a Two-Component Doppler Global Velocimeter (DGV)," paper AIAA-98-0508, AIAA 36th Aerospace Sciences Meeting, Jan. 12-15, 1998, Reno, NV.

Naylor, S. and Kuhlman, J., "Results for a Two-Component Doppler Global Velocimeter (DGV)," paper AIAA-99-0268, AIAA 37th Aerospace Sciences Meeting, Jan. 11-14, 1999, Reno, NV.

Naylor, S. and Kuhlman, J., "Results for a Two-Component Doppler Global Velocimeter," AIAA Journal, Vol. 38, No. 5, May, 2000, pp.835-842.

Ramanath, S., "Development of a Point Doppler Global Velocimeter (DGV)," MS Thesis, West Virginia University, MAE Department, 1997.

Webb, D. W., "Development of and Measurements using a Point Doppler Velocimetry (PDV) System," MS Thesis, West Virginia University, MAE Department, 1999.

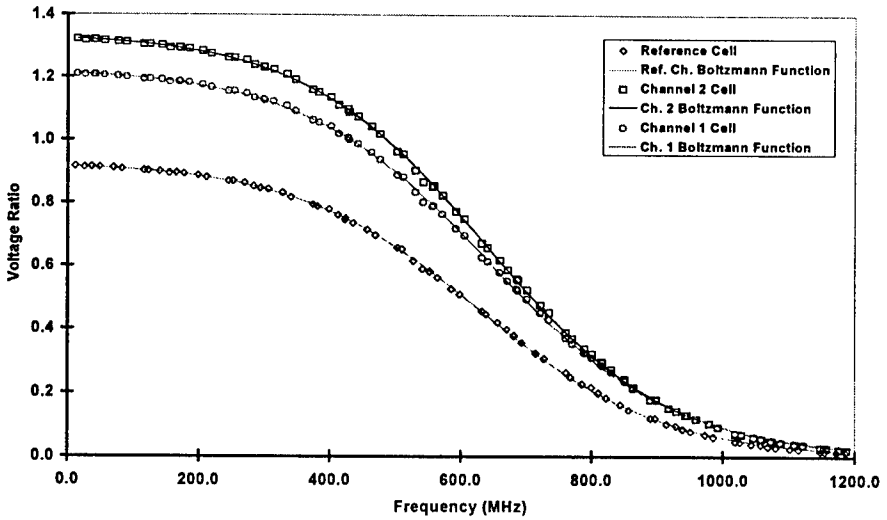

Fig. 1 Example of iodine cell calibration data and Boltzmann function curve fits

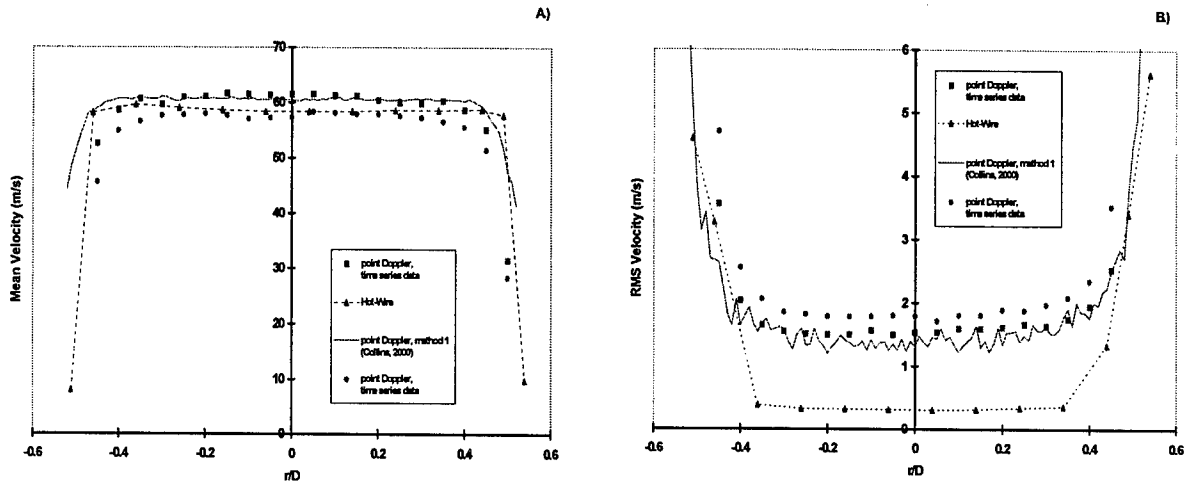

Fig. 2 Comparison of point Doppler velocimetry and hot wire results: standard jet - axial velocities at exit

a.) mean velocities

b.) RMS velocities

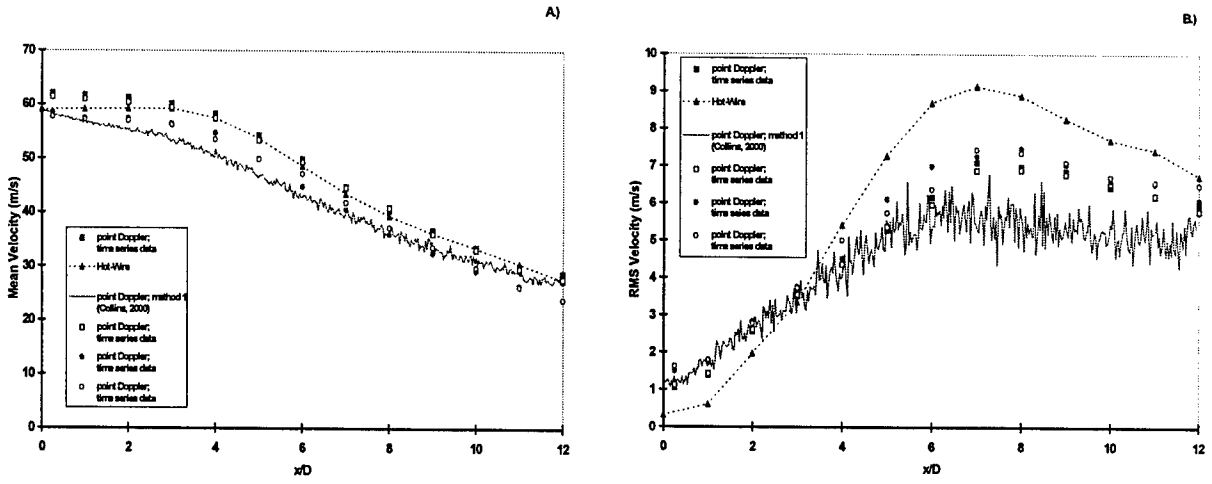

Fig. 3 Comparison of point Doppler velocimetry and hot wire results: standard jet - axial velocities along centerline

a.) mean velocities

b.) RMS velocities

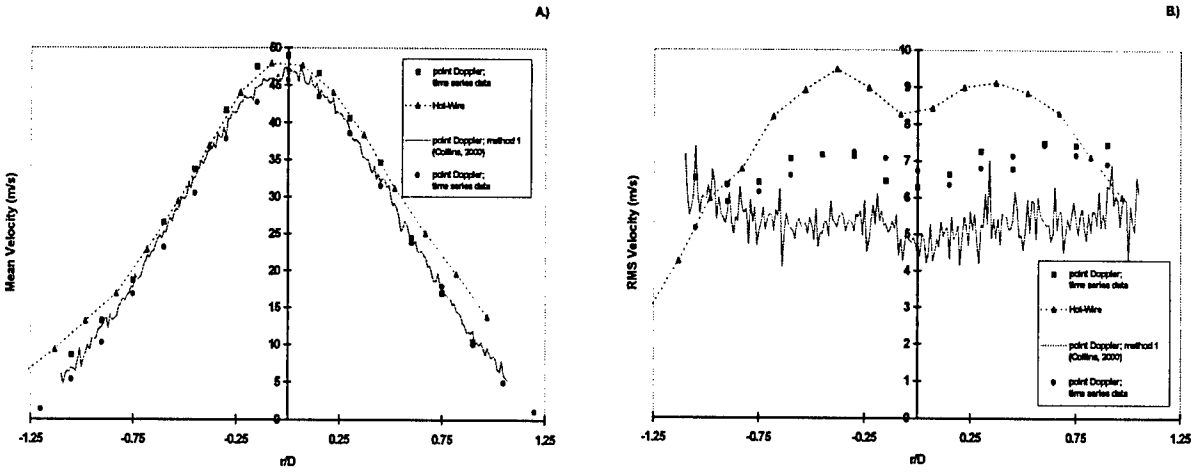

Fig. 4 Comparison of point Doppler velocimeter and hot wire results: standard jet - axial velocities at x/D = 6

a.) mean velocities

b.) RMS velocities

LARGE EDDY SIMULATION FOR HEAT TRANSFER PREDICTION UNDER FREE-STREAM TURBULENCE

Progress Report for the period 7/1/99 through 6/30/00

Sponsored by AFOSR under grant No. F49620-97-1-0047

Sanjiva K. Lele
Dept. of Mechanical Engineering and Dept. of Aeronautics and Astronautics
Stanford University, Stanford, CA 94305-4035.

Summary

The primary objective of this research is to develop large eddy simulations (LES) as a tool for heat transfer prediction over a turbine blade immersed in a hot stream containing free-stream turbulence (FST). The research consists of developing and validating the LES methodology on a series of test problems, before it can be applied to the turbine blade problem. These test problems are chosen to allow a detailed validation of the elements critical to heat transfer prediction on a turbine blade. These are (in order of increasing complexity/realism) :

(1) Simulation of realistic free-stream turbulence with intensity and length scale appropriate for turbine blade heat-transfer and its interaction with blade leading edge region
(2) Simulation of the disturbed turbulent boundary layers over an idealized blade surface in presence of free-stream turbulence
(3) Simulation of boundary layer heat-transfer under free-stream turbulence in presence of film-cooling jets on an idealized blade surface
(4) Simulation of realistic turbine blade heat-transfer under free-stream turbulence.

Research under the present grant is focussed on items (1) and (2) while items (3) and (4) are subjects for future work.

Progress

Several major improvements were made to the new LES code being developed in this project. The improved code is being used to study turbine blade heat-transfer near the leading-edge region under free-stream turbulence. The work completed in FY 00 has focussed on numerical algorithm improvements (fully-implicit scheme with dual time-stepping), refinement of boundary conditions (inflow turbulence specification scheme) and the validation of the LES tool. One graduate student (Andy Xiong) is carrying out his dissertation research under this project. A summary of the key research results will be given first and is followed by a discussion of our future plans.

LES Code Improvements

A computer code recently developed for a different project (Collis and Lele, 1997) which combines high-order finite-difference schemes on curvilinear coordinates with implicit time advancement was adapted to perform the LES calculations of heat transfer under free-stream turbulence. This extension of the original code required progress in the following major areas: grid-generation, boundary conditions, the solution algorithm for three-dimensional flows, and the incorporation of suitable subgrid-scale models for LES. In our previous work the spatial discretization was based on fourth-order central difference schemes in two directions and the

Fourier-spectral scheme in the spanwise direction. This combination of schemes made it very difficult to treat the spanwise direction implicitly. Our LES tests highlighted the need for an implicit treatment of the spanwise direction. To achieve it, the discretization scheme in the spanwise direction was changed to a fourth-order central difference scheme. A combination of approximate factorization and dual-time stepping were used to obtain a fully-implicit, three-dimensional, fourth-order accurate LES solver. The gain in numerical stability was much larger than any reduction in spanwise resolution. In the present implementation the sub-grid flux terms are treated with a mixed implict-explicit scheme. The subgrid-scale turbulent viscosity, evaluated by the dynamic procedure, is treated explicitly but the strain-rate and temperature gradient are treated implicitly. The new code is also well suited for efficient execution on a variety of parallel machine platforms. The parallelization is based on the message passing interface (MPI). The speed up observed on a 32 node machine is nearly ideal for the problem sizes of interest.

The grid/mesh requirements for conducting LES studies of turbine-blade heat-transfer are very different from a RANS approach. The need to respresent the large-scale energy-containing eddies of free-stream turbulence limits the grid stretching which can be used away from the body, and care must be taken to ensure that the grid in nearly isotropic in the free-stream. In previous year's progress report this and other grid generation issues and appropriate boundary conditions which model the experimental wind-tunnel situation (blocking) while permitting the imposition of desired inflow were detailed. Some further refinements to the boundary conditions were made. These allow accurate imposition of desired unsteady inflow disturbance while maintaining the imposed non-uniform mean-flow. In figure-1 an example which demonstrates the accuracy of the inflow-treatment is shown. In this test case a Taylor vortex (of zero net circulation) was imposed as the inflow disturbance. The contour plot of velocity components and vorticity shows that the vortex-structure is accurately preserved by the inflow scheme. As the vortex moves closer to the body, it is distorted by the mean-strain and as it passes over the leading-edge region it affects the boundary layers on the body. Well behaved solutions are obtained throughout the interaction. Details of the numerical scheme and quantitative results will be reported in an upcoming conference paper (Xiong and Lele, 2001). For the example shown the Reynolds number $Re \equiv \rho_\infty U_\infty D/\mu_\infty = 10^4$, $T_w/T_{0,\infty} = 1.075$, $V_{swirl}/U_\infty = 0.1??$, and $M_\infty = 0.15$. Note the reference length scale is taken to be the leading-edge diameter, D. The laminar solutions compare very well with boundary layer theory (Reshotko and Beckwith, 1958). Analytical modeling of unsteady effects, relevant to the turbomachinery environment will be developed in future.

Most heat-transfer experiments on the effects of free-stream turbulence have been carried out at low-Mach number, and the range of Reynolds number Re is 10^5 to 10^6. Turbine blade flows, however, are in low-transonic range and their Reynolds number (based on chord) varies from 10^5 to 10^7 (depending on the turbine stage and altitude). The current code is expected to provide accurate solutions over the low-transonic range, but before such flows are computed it is necessary to validate the LES capability in the low-Mach number range for which detailed experimental data is available. This assessment is carried out in two steps as discussed below.

Specification of Free-stream Turbulence

In heat-transfer experiments controlled free-stream turbulence is often introduced via a turbulence-generating grid. With a proper design, the generated turbulence is nearly-

isotropic and homogeneous. Further downstream this turbulence interacts with the test-surface. This controlled experiment provides a good benchmark to validate the simulations. However, it is necessary to establish that the turbulence being fed into the computational domain is physically realistic and the inflow-algorithm does not deteriorate this property. Inflow turbulence was provided using a precomputed LES of isotropic turbulence. Significant testing of the LES method was also carried out on the isotropic decaying turbulence. In our LES the subgrid terms are evaluated using the standard dynamic procedure (Moin et. al. 1991), however since the numerical scheme used is different and we use non-density-weighted filtering (Boersma and Lele, 1999) a detailed validation was necessary. Test-filters for the dynamic procedure were based on box-filter using Simpson's rule. The LES results were compared to low-Reynolds number DNS data and excellent agreement was found. Further comparisons were then made with higher Reynolds number experiments of Comte-Bellot and Corrsin at Taylor microscale Reynolds number $Re_\lambda = 65$. Comparison of the computed turbulent kinetic energy with the experimental data is very good. Results from such tests were reported previously and will not be repeated for brevity. New work was undertaken to ensure that the inflow-data being fed is not time-periodic. A new algorithm was developed which uses several planar samples of the data in a periodic-cube to generate a non-periodic inflow signal. The sampling planes traverse the cube at speeds which are not related to each other by a rational number. The variance of the signal is preserved by the algorithm. The frequency-spectra have some distortion but the small jitter introduced ensures temporally-decorrelated signal after a correlation time has passed. Figure 2 show the inflow data obtained from a periodic box of turbulence, and its rearragement by the new inflow algorithm. The temporal auto-correlation of the two signals is also plotted in these figures. Evidently the improvement is dramatic. An additional step beyond this an accurate interpolation of the inflow data to the curved inflow boundary. We carry out a fourth-order B-spline interpolation of the periodic box data to the curved inflow boundary. Now using multiple curved sampling surfaces we get the inflow data needed. LES of the leading-edge region heat-transfer with the FST specification using the new inflow scheme is described later.

Disturbed Boundary Layers with Organized Disturbances

An efficient solution algorithm for LES with free-stream turbulence has been developed and implemented. A study of the leading-edge heat-transfer under organized disturbances was undertaken. The disturbances considered were spanwise non-uniformities of the impinging flow which get stretched over the leading-edge region to form streamwise vortices. Our computational results verified the existance of a specific length scale, λ_s, for the largest enhancement of heat-transfer. Such a scale was observed previously in our work on a planar stagnation-point flow (Bae, Lele and Sung, 2000). For $\lambda > \lambda_s$, the heat-transfer augmentation decreased with λ. Our numerical results on the augementation levels compare well with experimental observations. Figure 3a shows a summary of data extracted from the 'organized-disturbance' test cases. The enhancement of heat-transfer rate at selected streamwise stations is plotted against the wavelength, λ, of the inlet disturbance. Evidently, for $\lambda/D > 0.1$ the enhancement decreases with the lengthscale. The most-amplified scale $\lambda_s/D \approx 0.1$. The contour plots shown in the figure 3b represent isotherms. Evidently, when λ is near λ_s significant vorticity enhancement due to mean-strain (Sutera, 1965) creates significant cross-plane velocity components which result in the 'mushroom-shaped' isotherms. In the region where the cross-plane flow is directed away from the wall, the boundary-layer thickens but this is

more than offset by the increased heat-transfer in the region away from the vortex-pair's center where the flow directed towards the wall and a thinner boundary layer results.

LES of Leading-edge Heat-Transfer under Free-stream Turbulence

The LES code is currently being used to simulate leading-edge heat-transfer under free-stream turbulence on idealized blade geometry (Von Fossen et. al. 1995). Preliminary results are shown in figures 4 and 5. The case shown corresponds to inflow FST with $u_{rms}/U_\infty = 0.07$ and $L/R = 0.2$, where L is the integral scale, and R is the leading-edge radius of curvature. Inflow data is specified at a distance $x/R = -5$ upstream from the leading edge as in the experiment. The case simulated corresponds to a maximum model width of $6R$ which is 33% of the wind-tunnel width. The computational domain extends up to $x/R = 10$. The LES calculation used a mesh of $383 \times 192 \times 32$ points. The spanwise domain width is $W/R = 2$. Grid points are clustered in the boundary layer to keep about 20 points within the boundary layer at the leading edge. Inflow data was specified using a precomputed isotropic turbulence calculation on a cubic domain with the same spanwise width, and transformed according to the algorithm described earlier. The grid size at the inflow plane gives $\Delta x = \Delta y = \Delta z$ in the region surrounding the stagnation streamline. Significant amplification of vorticity can be observed as the flow approaches the stagnation point. The strongest vorticity locally resembles the situation obtained with organized disturbances. In the regions close to the strongest vortices, largest heat-transfer rates are observed. Statistical analysis of the data is currently underway and will be reported in the conference paper.

Acknowledgement/Disclaimer

This work was sponsored by the Air Force Office of Scientific Research, USAF, under grant number F49620-97-1-0047. Work described under the ASSERT grant F49620-98-1-0355 was also (in part) supported by this parent grant. The views and conclusions contained herein are those of the author and should not be interpreted as necessarily representing the official policies or endorsements, either expressed or implied, of the Air Force Office of Scientific Research or the U.S. Government.

REFERENCES

Van Fossen, G. J., Simoneau, R. J. and Ching, C. Y. (1995) *J. Heat Transfer*, v. 117, pp. 597-603.

Sutera, S. P. (1965) *J. Fluid Mech.*, v. 21, pp. 513-534.

Collis, S. S. and Lele, S. K. (1997) Report No. TF-71, Flow Physics and Computation Division, Department of Mech. Eng., Stanford Univ.

Moin, P., K. Squires, W. Cabot, and S. Lee (1991) *Phys. Fluids A*, v. 11, pp. 2746-57.

Boersma, B. J. and Lele, S. K. (1999)*AIAA/CEAS Paper* AIAA-99-1874, AIAA/CEAS Aeroacoustics Conference, Seattle.

Reshotko, E. and Beckwith, I. E. (1958) NACA Tech. Rep. 1379.

Xiong, Z. and Lele, S. K. (2001) *AIAA Paper*, Numerical study of leading edge heat transfer under free-stream disturbance, Submitted for presentation at AIAA Aerospace Sciences Meeting, Reno, 2001.

Bae, S., Lele, S. K. and Sung, H. J. (2000) Influence of inflow disturbances on stagnation-region heat transfer. To appear in *J. Heat Transfer.*

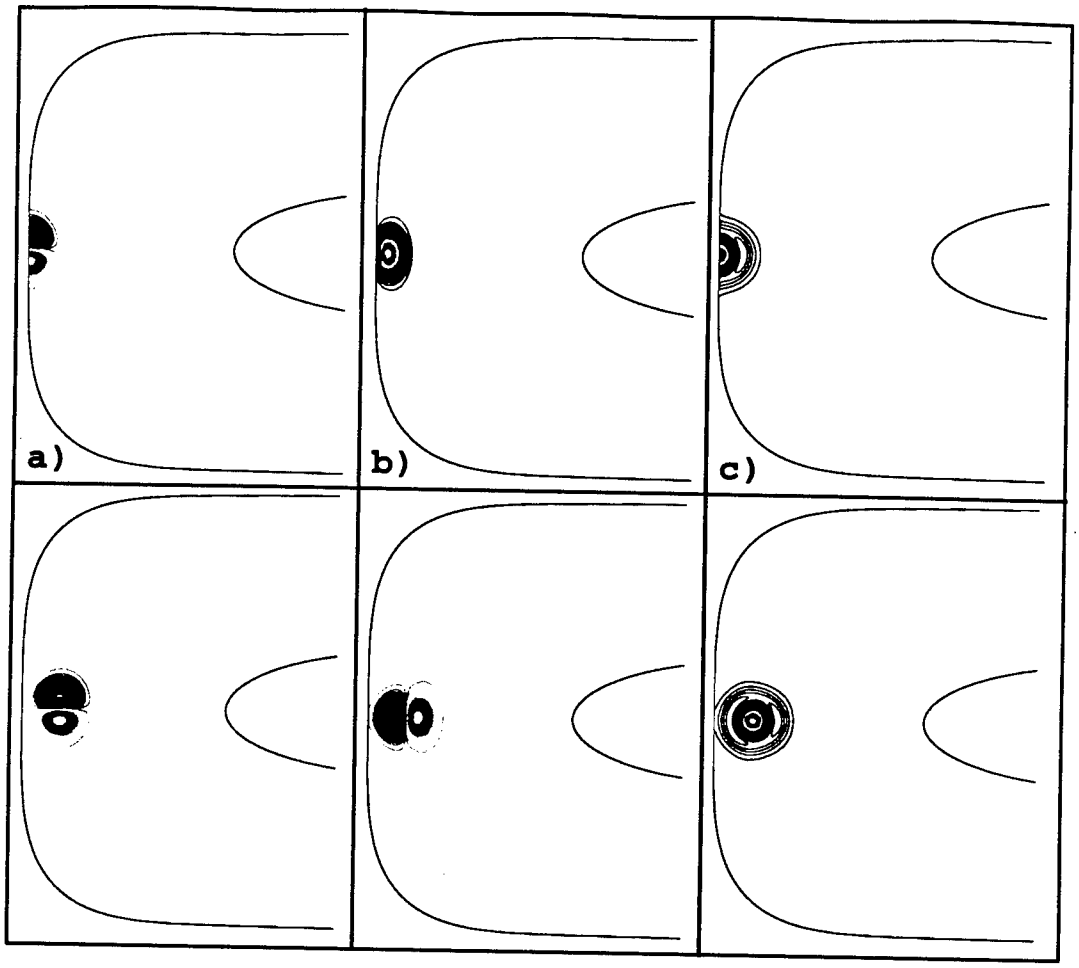

Fig 1. Taylor vortex passing at inflow, upper row t=1.18, lower row t=2.35. a) streamwise velocity, b) transverse velocity, c) spanwise vorticity

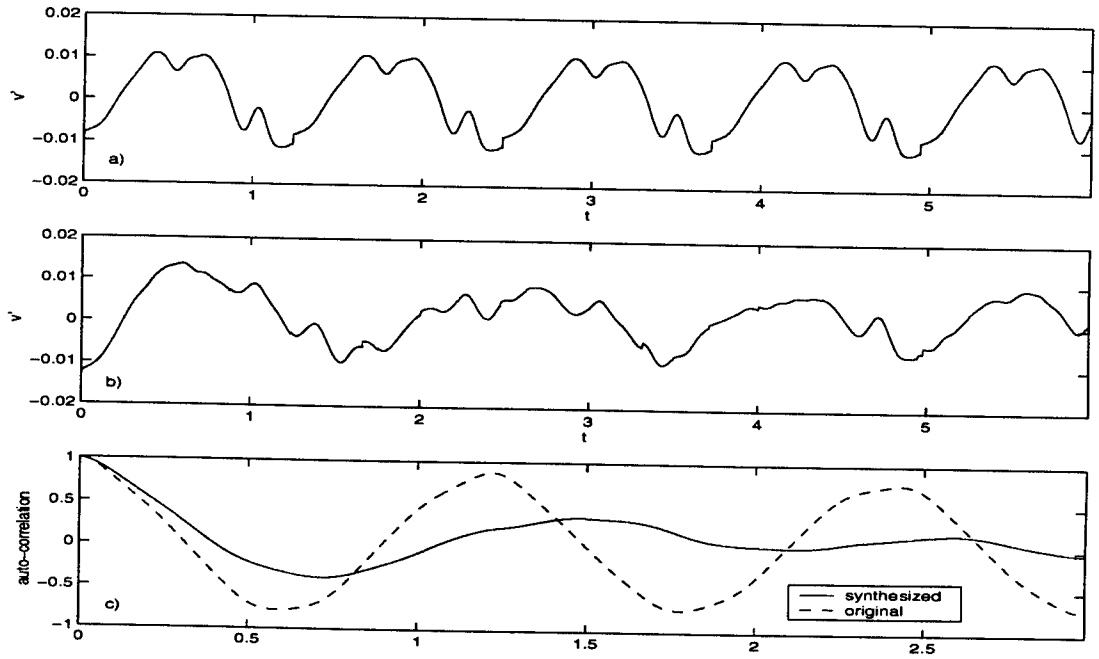

Fig 2. Generation of non–periodic inflow signal. a) original signal, b) synthesized signal, c) autocorrelation

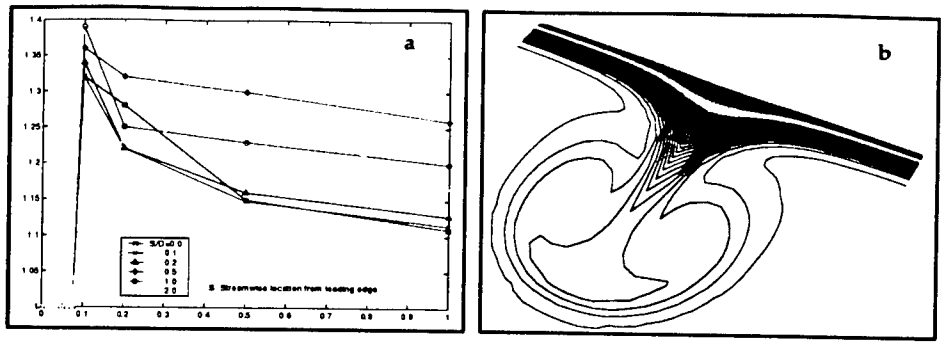

Fig 3. a) Increase of heat transfer vs. spanwise wavelength at different streamwise locations on body surface,
b) Temperature contour projected on streamwise stagnation plane

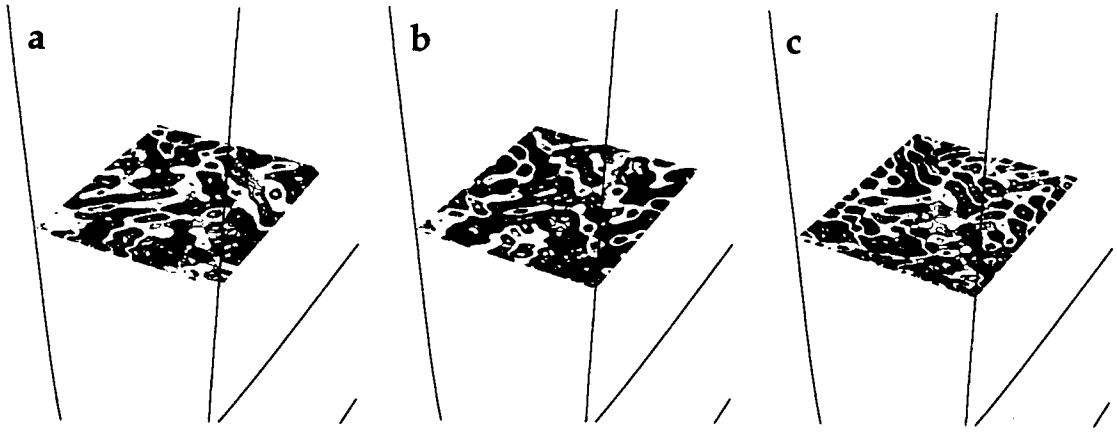

Fig 4. Passing isotropic homogeneous turbulence . a) ω_x, b) ω_y c) ω_z on inflow plane.

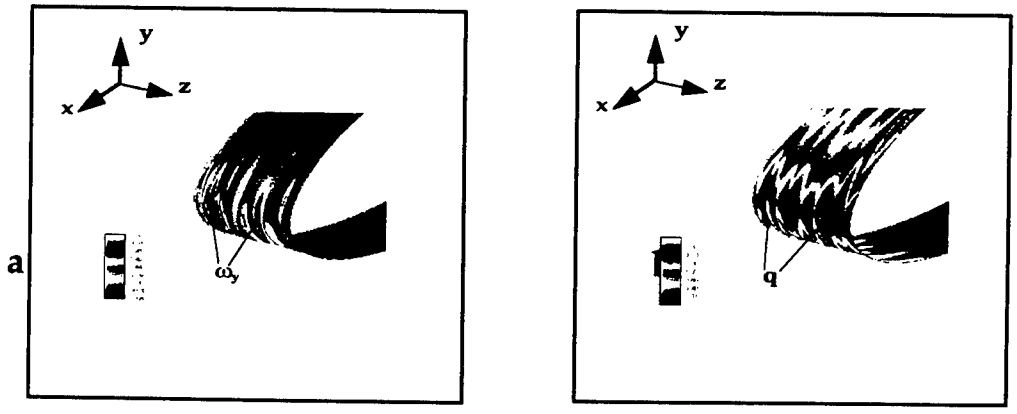

Fig 5. a) Vorticity stretching at leading edge. b) local heat transfer rate under free stream turbulence.

NUMERICAL SIMULATION OF TURBULENT HIGH SPEED JETS

AFOSR Grant F49620-98-1-0035
Progress report on work conducted under AASERT grant
during 7/1/99 through 6/30/00

Sanjiva K. Lele
Department of Mechanical Engineering
and
Department of Aeronautics and Astronautics
Stanford University, Stanford, California

Abstract

Suppression of high speed jet noise is of critical importance to the design of future generations of military and civilian aircraft. Supersonic jet screech is a type of supersonic jet noise which is a primary source of acoustic fatigue in aft structures of fighter aircraft. The objectives of this research are to gain a fundamental understanding of the components of screech, create a simulation database to aid in development of predictive models of screech, and develop methods to control screech.

Supersonic jet screech has been known to be governed fundamentally by a feedback cycle since the pioneering work of Powell [1]. The elements of this feedback cycle include: 1) the amplification of instability waves in the jet, 2) the interaction of vortical disturbances with the shock-cell structure in the jet, 3) the back propagation of the acoustic disturbance to the nozzle lip, and 4) the conversion of acoustic disturbances into instability waves at the nozzle lip, *viz.* receptivity which ultimately closes the feedback loop. In the screech cycle, noise is generated in the second element. The model problem which provides a framework for studying the shock-cell noise generation process is shown in Figure 1. A two-dimensional unsteady shear layer interacts with a single jet shock or compression wave, radiating sound. If the shear layer were turbulent, the generated noise would be broadband.

Results of direct numerical simulations (DNS) of this flow were reported in [2] and [3]. Findings from DNS strongly suggest that the sound generation process can be regarded as the scattering of an incident oblique stationary wave disturbance by the unsteady motion of the mixing layer. This motivated further calculations using a set of linearized Euler equations. The disturbance quantities are linearized about an unsteady base flow obtained from DNS. The "shock", or compression wave, is imposed as an incident disturbance in the form of a boundary condition. It and the resultant scattered sound make up the perturbed, or solution, field.

Highlights of the linearized Euler simulations with a Gaussian compression wave, or "G-wave," are given here. The amplitude and wave form of the radiated acoustic

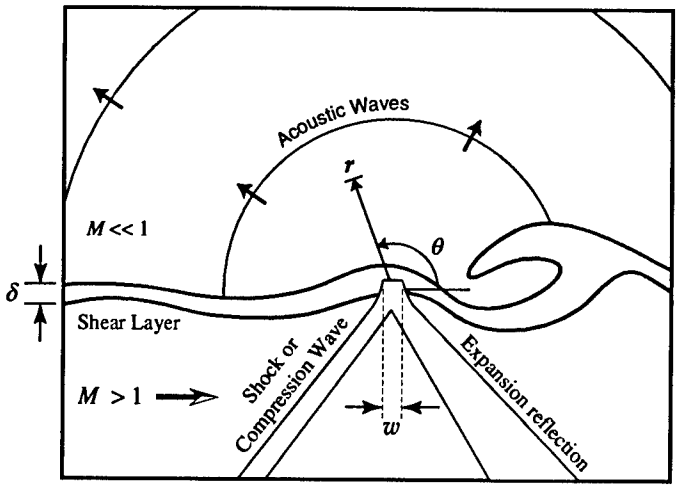

Figure 1: Schematic of the shock-vortex interaction computation.

field is a function of the strength of the instability wave at the location where the compression wave intersects the shear layer. Radiated acoustic amplitude is plotted against the instability wave amplitude $K \equiv \sqrt{\int_{-\infty}^{+\infty} \frac{\overline{u'^2}+\overline{v'^2}}{2} dy}$ in Figure 2 . Acoustic amplitude is found to scale linearly with K for small K. Beyond this linear region lies an "exponential" region, so named because the acoustic amplitude varies exponentially with K. At still higher K, the acoustic amplitude reaches a peak, then decreases slightly before increasing again. The peak in acoustic amplitude is associated with the point where the shear layer vortex "rolls over." This third region is termed the "saturation" region. The acoustic wave form changes significantly between the three regions as shown in Figure 3. Here x_{src} refers to the downstream location at which the incident compression wave interacts with the shear layer, so a greater x_{src} corresponds to a higher value of K. Within the exponential region, the acoustic wave form undergoes a fundamental transition. The pressure trace acquires the shape of the incident Gaussian compression wave at the upper extremes of the region and this shape is maintained throughout the saturation region. However, as x_{src} or K are decreased, the Gaussian bump is absorbed into a more sinusoidal wave-form. We believe the compact wave form of the saturated region is associated with the "feedback shock" observed in the flapping mode of the rectangular screeching jet [4].

Further progress has been made in describing the sound generation process using geometric acoustics. With this approach, the incident shock is modeled as a thin plane wave, oriented at the Mach angle in the supersonic stream so that it remains stationary in the steady case. This standing wave is composed of a family of acoustic rays of different phase. A further simplification is made by prescribing a Stuart vortex mixing layer as the base flow. The strength of the vortices is given by a non-dimensional parameter A. For small A the shear layer has uniform vorticity, which clumps into strong vortices as A is increased. Acoustic ray paths are obtained by integrating the Eikonal equation along the characteristics. Figure 4 shows the refracted rays that are transmitted through the mixing layer for a particular Stuart vortex strength. Figure 5 shows the fraction of rays which are transmitted versus the

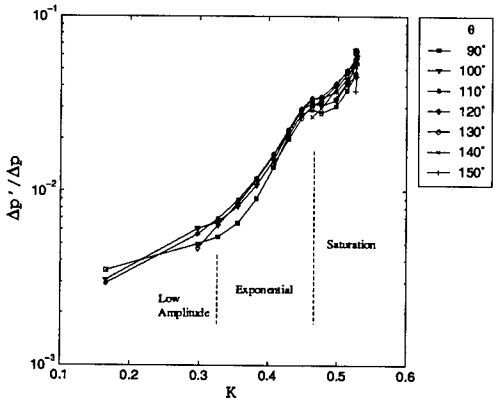

Figure 2: Radiated acoustic pressure amplitude versus instability wave amplitude K. Acoustic amplitude is taken as mean-to-peak amplitude $\Delta p'$ normalized by G-wave amplitude Δp. Sampled at $r/\delta = 30$.

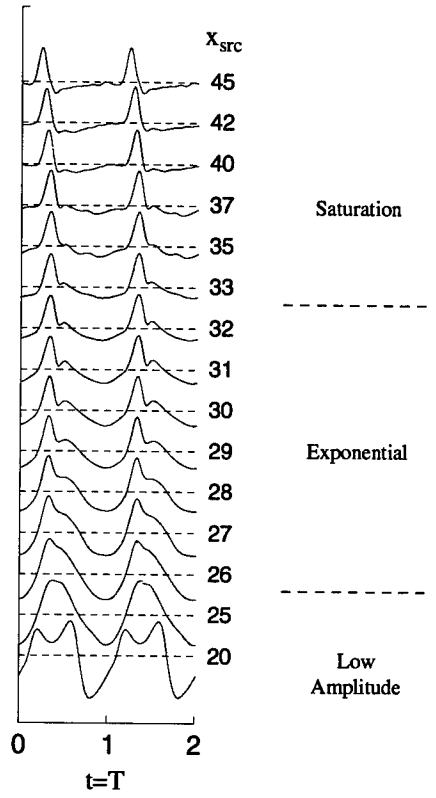

Figure 3: Acoustic pressure traces normalized to respective mean-to-peak amplitude. Sampled at $r/\delta = 30$ and $\theta = 90°$. The mean-to-peak amplitude is plotted in Figure 2.

strength of the vortices A. There is apparently a critical value of the vortex strength below which no rays are transmitted through the layer. This is analagous to the onset of the region of saturation noted in the linearized Euler simulations. However, geometric acoustics predicts a sudden onset of transmission, with no parallel to the exponential growth region seen in the linearized Euler computations.

The primary focus of the research effort has now shifted to study of the receptivity element of jet screech. There are linear theoretical models which describe the receptivity process in shear layers with and without the presence of a thin semi-infinite plate, see [5] and [6]. There is currently no model available which takes into account both finite thickness shear layers and the presence of a trailing edge. There is also some question as to the extent of the region over which the receptivity process occurs, and the precise role of the nozzle lip in the transfer of energy to instability wave disturbances.

A computational model problem is used here to study trailing-edge receptivity.

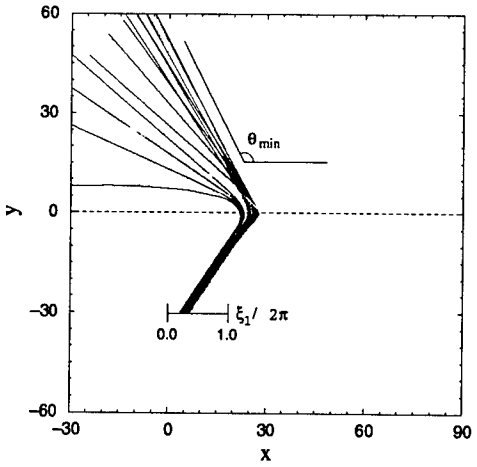

Figure 4: Transmitted rays representing standing plane wave(s) incident on Stuart vortex mixing layer of magnitude $A = 0.650$. Initial condition phase parameter varies from $\xi_1/2\pi = 0.199$ to 0.365.

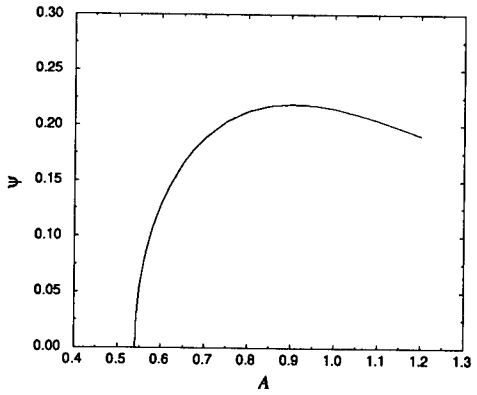

Figure 5: Fraction ψ of all possible rays (representing an oblique incident standing wave) which pass through Stuart vortex mixing layer.

The model problem considered is a two dimensional supersonic half-jet issuing from below a thin, rigid nozzle lip. An acoustic source simulating discrete-tone shock noise is placed downstream of the lip. The acoustic feedback at and near the nozzle lip creates instability waves in the shear layer.

The Navier-Stokes code required to study this problem has been developed, but some further refinements are necessary to handle numerical difficulties associated with maintaining accuracy near the lip trailing edge. Numerical artifacts near the lip trailing edge are currently controlled by means of artificial dissipation applied throughout the entire domain, which dampens non-physical short wave components of the solution. Our new code is portable to parallel computers via the MPI interface.

Results of a sample calculation obtained recently are shown in Figure 6. A compact, harmonic acoustic source is prescribed downstream of the nozzle lip trailing edge. A Mach 1.2 boundary layer is present on the lower side of the lip, simulating a supersonic jet exit profile. The lip width is approximately 40 percent of the boundary layer momentum thickness. The refractive effect of the shear flow on the acoustic field is evident in the visualization. In this case the frequency of the source is higher than the unstable bandwidth of the shear layer, so excited vortical disturbances are not present. Other low frequency cases are in progress which will illuminate the receptivity process.

In related work, a parallel linear stability analysis of compressible wake-shear layer profiles has been completed. The profiles considered are representative of velocity profiles observed downstream of supersonic jet nozzle lips. Results from this study will guide parameter choices in the numerical simulations and will aid in interpreting simulation results.

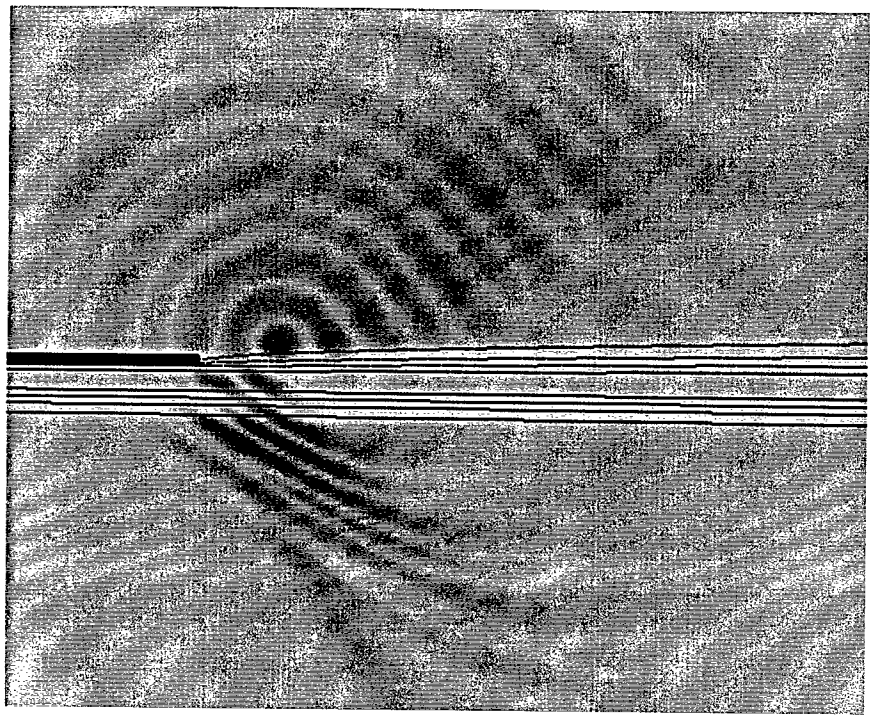

Figure 6: Visualization of the DNS of a compact time harmonic acoustic source placed near the trailing edge of a supersonic jet nozzle lip. The smooth contours are dilatation and the solid contour lines are vorticity. The jet issues from below the lip at a Mach number of 1.2. The wavelength of the acoustic disturbance is $\frac{\lambda}{\theta_{bl}} = 10.0$, where θ_{bl} is the boundary layer momentum thickness on the jet side of the lip.

Personnel Supported

Sanjiva K. Lele	Professor, Stanford University
Ted A. Manning	Graduate Student, Stanford University
Matthew F. Barone	Graduate Student, Stanford University

Publications and Awards

Recent publications arising from the work supported by this grant include [7], [8], and [9]. Work reported in [3] received the R.T. Knapp Best Paper award from the ASME Fluids Engineering Division.

Acknowledgment/Disclaimer

This work was sponsored by the Air Force Office of Scientific Research, USAF, under grant number F49620-98-1-0035 with Dr. Steve Walker as the program monitor. In its initial phase, this work was partially supported under AFOSR grant F49620-97-1-0047. The views and conclusions contained herein are those of the authors and should not be interpreted as necessarily representing the official policies or endorsements, either expressed or implied, of the Air Force Office of Scientific Research. This grant

supported the Ph.D. dissertation work (now completed) of Ted A. Manning and continues to support the Ph.D. dissertation work of Matthew F. Barone.

References

[1] A. Powell. On the Mechanism of Choked Jet Noise. *Proc. Phys. Soc. (London)*, 66(pt. 12, no. 408B):1039–1056, December 1 1953.

[2] T. A. Manning and S. K. Lele. Numerical Simulations of Shock Vortex Interactions in Supersonic Jet Screech. AIAA Paper 98-0282. Reno, Jan. 1998. 36th AIAA Aerospace Sciences Meeting and Exhibit.

[3] T. A. Manning and S. K. Lele. Numerical Simulations of Shock Vortex Interactions in Supersonic Jet Screech: an Update. In *Proceedings of FEDSM '98*, number FEDSM-5238, Washington, DC, June 1998. ASME Fluids Engineering Division Summer Meeting.

[4] A. Krothapalli, Y. Hsia, D. Baganoff, and K. Karamcheti. The role of screech tones in mixing of an underexpanded rectangular jet. *J. Sound and Vibration*, 106(1):119–143, 1986.

[5] C. K. W. Tam. Excitation of instability waves in a two-dimensional shear layer by sound. *Journal of Fluid Mechanics*, 89:357–371, 1978.

[6] E. J. Kerschen. Receptivity of shear layers to acoustic disturbances. AIAA Paper 96-2135. New Orleans, LA, June 17-20 1996. 1st AIAA Theoretical Fluid Mechanics Meeting.

[7] T.A. Manning. *A Numerical Investigation of Sound Generation in Supersonic Jet Screech.* Ph.D. thesis, Stanford University, November 1999.

[8] T. A. Manning and S. K. Lele. A numerical investigation of sound generation in supersonic jet screech. AIAA Paper 2000-2081. Maui, Hawaii, June 12-14 2000. 6th AIAA/CEAS Aeroacoustics Conference.

[9] T. A. Manning and S. K. Lele. A mechanism for the generation of shock-associated noise. To appear in Proceedings of The 20th International Congress of the International Union of Theoretical and Applied Mechanics (IUTAM), Chicago, September 2000.

DEVELOPMENT OF MICRO-RESOLUTION PIV AND ANALYSIS OF MICROTHRUSTERS FOR SMALL-SCALE AIRCRAFT AND SPACECRAFT

AFOSR GRANT NO. F49620-97-1-0515

Carl D. Meinhart & Marin Sigurdson
Department of Mechanical and Environmental Engineering
University of California

I. Summary

A Particle Image Velocimetry system has been proposed to measure velocity fields of high-speed air flows in 300 μm thick 2-D silicon-micromachined nozzles. The technique has been successfully demonstrated by measuring liquid flows, and progress has been made on several fronts to adapt the technique to gas flow. The higher speeds and accelerations of the airflow dictate more stringent requirements in particle size and density and in temporal resolution, and therefore in imaging. Additionally, the seeding of the flow with tracing particles, while straightforward in liquid flows, presents major challenges in gas flows. The solution proposed here uses reflective Differential Interference Contrast (DIC) microscopic imaging to record images of small (50 – 100 nm.) particles appropriate for air flow, and an aerosol generator to seed the flow with these particles.

II. Liquid Velocity Measurements in Micronozzle

As reported in Meinhart (1999c), measurements of flow through a micronozzle were conducted using water as the fluid medium to determine the conditions in which PIV measurements could be obtained in the relatively deep micronozzles. The liquid flow was seeded with relatively large 700 nm dia. fluorescently-labeled polystyrene particles. The particles were imaged using a NA = 0.6, 40x objective lens, and an epi-fluorescent imaging system similar to that described by Meinhart *et al.* (1999a). The flow was illuminated by a frequency doubled, Q-switched Nd:YAG laser with pulse width of 5-7 ns. The images were recorded using a 1300 X 1030 pixel X 12-bit interline-transfer, cooled CCD camera. The interline-transfer feature of the camera allows for the acquisition of two back-to-back images within 500 ns. A flow rate of 4 ml hr^{-1} was delivered to the nozzle by a syringe pump.

The velocity fields were calculated using a standard cross correlation algorithm. Both interrogation windows were 64 × 20 pixels, or 10.9 × 3.4 μm in the x and y directions, respectively. The interrogation spots were overlapped by 50%, yielding a velocity-vector spacing of 5.44 μm in the streamwise direction and 1.7 μm in the spanwise direction.

III. Additional Constraints Posed by Gaseous Flow:

While the PIV technique has been demonstrated successfully by measuring liquid flows, the measurement of high-speed air flows through micronozzles remains difficult, in part because we would like to measure gas velocities and accelerations much higher

than those measured in liquid flows. This translates into a requirement for particles of small size and mass, such that can faithfully follow the flow. Higher resolution in time will also be necessary to capture details of high-speed flow, as will shorter exposure times to prevent streaking. These requirements were discussed and quantified in Meinhart (1999c).

Imaging Solution: DIC

In Meinhart (1999c), the optical method of Differential Interference Contrast (DIC) was proposed as a solution to the problem of imaging very small (50 – 100 nm) particles necessary for airflow PIV in micronozzles. The reflective DIC system consists of a linear polarizer, a mirror, an adjustable Wollaston prism, and a DIC analyzer. The DIC system is described in detail in Meinhart (1999c), where there are also images shown of 50 nm silicate particles, not visible without the aid of DIC.

While DIC has been found to be quite successful in imaging small particles using white light, the use of DIC with laser illumination has not yet been optimized. Because of the coherence of the laser beam, a "laser speckle" diffraction pattern is produced when the DIC system is used with the Nd:YAG laser. There are various methods used to reduce laser speckle. Examples of these include: counter-rotating glass diffusers (Partlo, and Oldham, 1991), modified fiber array (Dingel, 1993), and illumination with a fluorescent beam produced by a laser dye.

Seeding the Gas Flow

In addition to the restrictions placed on the airflow PIV system by the higher speeds and accelerations, there is also the problem of seeding the flow, that is, developing and maintaining a sufficiently disperse aerosol of solid or liquid particles in the gas stream. There are at least four commonly used methods for suspending such an aerosol.

A powder disperser uses a gas stream, either aimed at a powder sample or bubbled up through the powder to create a powder cloud, or blown through a venturi to suck powder up into the throat. The particles dispersed in the gas stream are normally clumps of several individual particles (Melling, 1997); indeed it is very difficult to distribute a completely deagglomerated aerosol. Reducing moisture in the gas stream and in the powder sample may help in dispersion efficiency by reducing hydrostatic coagulation forces, but this must be balanced with the effect of electrostatic forces, which increase with dryness (Melling). Particle size and material also play a part in agglomeration. TSI (St.Paul, MN) quotes their powder dispersers as able to disperse powders larger than 500 nm; anything smaller is not effectively deagglomerated. Rough, soft particles are more difficult to disperse than smooth, hard particles (Melling, 1997).

An atomizer avoids the problem of deagglomerating cohesive powders. A pressure difference across a nozzle pulls liquid through the nozzle, creating a polydisperse liquid aerosol. If the liquid is a suspension of (monodisperse) solid particles, the aerosol can be dried, leaving a (monodisperse) dilute aerosol of solid particles. Alternatively, if the liquid is a solution (saline is common), the aerosol can be dried, leaving a solid aerosol of solute crystals.

A condensation aerosol generator allows a vaporized medium to condense on a tiny nucleus. If this is done at constant temperature, as in a Sinclair-LaMer type generator, a monodisperse aerosol is attained, though it is relatively low in concentration.

An electrospray aerosol generator, such as the one developed by TSI, Inc., uses an electric field to pull uniform tiny liquid droplets off the end of a capillary tube. The resulting aerosol is monodisperse and nearly comparable in concentration to that of the atomizer, the droplet size is 150 nm. If these droplets are a saline solution, final solid particle size can be as large as 50-100 nm. While this coincides with the ideal size for airflow seeding particles, it is necessary to be able to produce larger (easily seen) particles as well during the optimization of the imaging and flow systems.

Coagulation

As soon the aerosol is generated, it unfortunately begins to recoagulate. As particles move relative to each other by Brownian motion, turbulence, or body forces, they collide and coalesce. Theoretical treatments of coagulation begin by assuming perfect collision efficiency, that is any particles which come into contact will stick (Green, 1964, Fuchs, 1964, and Reist, 1993 all present details on coagulation.) If particles that collide do not stick together, they will, because of proximity, have an increased probability of another collision, thus raising the "effective" collision efficiency. If a monodisperse aerosol is moving only through Brownian motion, the number concentration n as a function of time may be described as

$$\frac{1}{n} = \frac{1}{n_o} + Kt$$

where K is the coagulation constant. K can be derived theoretically for the above case, and turns out to be 4.0×10^{-10} cm^3/s for 200 nm particles in air at STP (Fuchs, 1964), but additional complications of our system such as polydispersity and turbulence, may affect this number by orders of magnitude. Nevertheless, some interesting observations may be made about this process. First, for a high coagulation constant, and an observation point a finite time after t = 0 (tenths of seconds perhaps), increasing the initial concentration is meaningless: the particles will immediately coagulate. There is therefore, a limit to the concentration of an aerosol that can be generated and maintained. Second, for high initial concentrations, it is important for the observation point to be as soon as possible after t = 0 so as not to allow the aerosol to coagulate. This translates for us into a short as possible run between the aerosol generator and the test section. We keep these practical limitations in mind as we search for a flow seeding method.

IV. Airflow Velocimetry Experiments

Although it is common to use aerosol generators of the aforementioned type for seeding gas flow for PIV, most experiments have been done on much larger scale. A reduction in scale not only necessitates a reduction in particle size, but also an increase in particle number concentration. Our needs, therefore, push the limits of what has been used, what is available, and perhaps what is possible. If a 40X, N.A. 0.6 objective lens is used, depth of field, taken from Meinhart *et al.* (2000), is 10 μm, and resolution of the

camera is taken to be 6.8 μm / pixel, the image volume is 3.74 X 10^{-7} cm^3. If 15 particles are needed per interrogation volume and interrogation windows of 64 X 20 pixels are used as in Meinhart (1999c) corresponding to a resolution of 5.44 X 1.7 μm, then it is desirable to have about 4.5 X 10^5 particles per image volume. Ensemble averaging techniques for steady flow can reduce this nearly an order of magnitude (Meinhart *et al.*, 1999b), but that still leaves a desirable aerosol concentration of 2 X 10^{10} particles / cm^3. Specified maximum number concentrations on commercially available aerosol generators run in the 10^6 to 10^8 range, so dispersion of a highly concentrated aerosol becomes one of the limiting system criteria.

Shallow Channel Design

In order to ignore for the moment the problems associated with high speed flow, and to increase the overall volume flow rate, which generally increases aerosol generation, a new channel was designed for testing the airflow PIV system, shown in Figure 1. The channel is wide, increasing the flow rate, and shallow, keeping the illuminated depth to a minimum to reduce noise from out-of-focus particles. Additionally, because the channel is quickly made on a mill rather than using micromachining techniques, there is more flexibility than with the micronozzle. For example, the bottom of the channel was colored black to improve image quality. In another design, the channel and manifold were made from acrylic, to allow illumination from behind the channel. The intent is to use the less restrictive shallow channel to get a PIV system working. The system can then be fine-tuned for the more restrictive micronozzle.

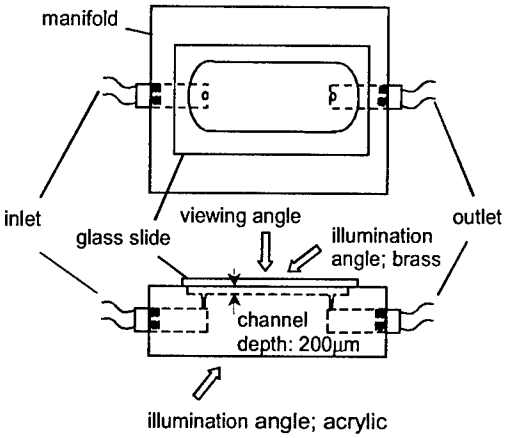

Figure 1. Shallow Channel Design

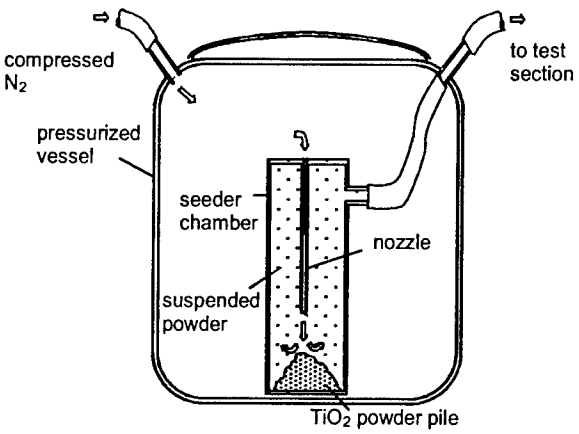

Figure 2. Powder Dispersion Seeder

Powder Dispersion Seeder

The first aerosol generation system used was a powder dispersion seeder designed and built in-house, diagrammed in Figure 2. Nitrogen is the working gas; TiO_2 was chosen as the powder because of its availability in a range of appropriate sizes and its low density (compared with metals). A gas stream impinges on a pile of powder, creating a cloud of powder. The pressure differential between the cloud chamber and the outside causes the cloud to be sucked through the channel.

This seeder was not effective in producing observable particles in the flow stream. Because there was clearly powder exiting the test section, the absence of particles in any images could be traced to either of two problems: first, the imaging system was not capable of detecting such small particles; or second, the seeder was distributing such a low concentration (and given the observed powder mass flow, large particle size) of particles, the chances of one falling in the exposure window were quite low. Because various sizes of TiO_2 particles were used (200 – 700 nm average diameter), which were easily imaged when captured on a glass slide, and because finally one large (~5 μm) particle entrained in the flow was captured in an image, it seems more logical that the problem is with the agglomeration of the powder and therefore the low number concentration of the aerosol. There was also obvious loss of aerosol to tubing walls, which were coated with powder at the end of each experiment. Special conductive flexible tubing was tried, with no measured improvement in results.

Atomizer

A TSI, Inc. Atomizer (Model 3076) was used in the airflow velocimetry system. Using simply water as a working liquid, an aerosol of water droplets was produced. The shallow channel quickly became waterlogged, that is, enough water quickly deposited on the viewing window so as to prevent imaging. Therefore, for evaluation of the atomizer as an aerosol generator, the channel was removed, and the flow was simply aimed at a glass slide through which the flow was observed. In this configuration, a droplet was captured in an image about every third frame. From this, an aerosol concentration can be inferred of around 10^5 particles/cc of particles larger than the smallest detectable size. TSI's specifications for this instrument quote 10^8 particles/cc with a mean diameter of 3.0 μm and a geometric standard deviation of less than 2.0. From the image pairs gathered of the droplets in external flow, a uniform velocity of 1.2 m/s was calculated.

V. Thick layer experiments

In addition to the study of micronozzles, gas flow micro-PIV can be used to study high-Reynolds number boundary-layer flows, where it is desirable to know details of the flow field close a surface. One difficulty in such investigation is the illumination and imaging of this thin layer to the exclusion of the rest of the flow. In macro-PIV a laser light sheet is often used to selectively illuminate the flow. The thickness of the light sheet is chosen to be smaller than the optical depth-of-field so that all illuminated particles are in focus. In micro-PIV, a very thin (1-10 μm) light sheet would be desirable to restrict the plane of measurement. Such a thin light sheet, however would be difficult to create and nearly impossible to align with focal plane of the optics. Instead, we choose to illuminate the entire flow field while limiting the depth of the flow to a few hundred microns. With greater depth, or with a conventional laser light sheet of millimeter thickness in deep flow, out of focus particles contribute to unacceptably high background noise. We seek to overcome this problem in order that a laser light sheet (~ 1mm) may be used to illuminate boundary layer flow and micro-PIV be performed to measure the flow field. Toward this end, we have performed liquid-flow thick-layer experiments in an open channel, 1.9 mm deep. To minimize background noise from out-of-focus particles,

we use very low particle concentrations in the flow (0.01 to 0.001% volume concentration). To achieve high resolution with low concentration, it is necessary to analyze many images in steady state flow and use an ensemble averaging technique to combine the information; see Meinhart *et al.* (1999b). By adjusting the focal plane within the flow, velocity fields can be measured at several depths in the thick layer. Figure 3 shows a velocity profile near the bottom of the channel derived from velocity field measurements at each depth.

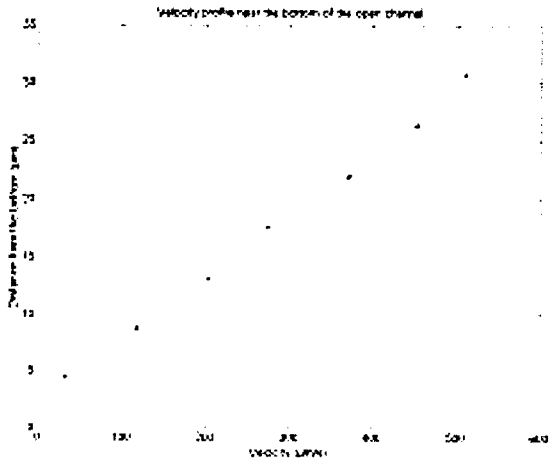

Figure 3. Velocity profile near the bottom of the open channel. The profile shows a nearly linear profile that is reasonable close to the bottom of the channel.

VI. Conclusion

Although we have demonstrated that micron-resolution velocity measurements can been obtained for liquid flows in micronozzles, significant challenges must be overcome for successful measurements of high-speed gas flows at the microscale. These challenges are discussed in detail, and solutions are proposed. The method of reflective Differential Interference Contrast (DIC) imaging, combined with a laser coherence reduction technique, is proposed to record images of very small particles desirable for air flow PIV in micronozzles. It is also necessary to choose an optimum aerosol generator that can produce a highly dispersed aerosol as required for airflow PIV in micronozzles.

Acknowledgment/Disclaimer

This work was sponsored (in part) by the Air Force Office of Scientific Research, USAF, under grant/contract number F49620-97-1-0515. The views and conclusions contained herein are those of the authors and should not be interpreted as necessarily representing the official policies or endorsements, either expressed or implied, of the Air Force Office of Scientific Research or the U.S. Government.

References

Dingel, B., Kawata, S. & Minami, S. 1993. Speckle reduction with virtual incoherent laser illumination using a modified fiber array. *Optik.* **Vol. 94**, pp. 132-136.

Fuchs, N. A. 1964. *The Mechanics of Aerosols*. Pergamon Press, New York.

Green, H. L. and Lane, W.R. 1964. *Particulate Clouds: Dusts, Smokes and Mists, 2nd ed.* E. & F. N. Spon Ltd., London.

*Meinhart, C. D., Wereley, S. T. & Santiago, J. G. 1999a. PIV Measurements of a Microchannel Flow. *Exp. in Fluids* **Vol. 27**, pp.414-419.

*Meinhart, C. D., Wereley, S. T. & Santiago, J. G. 1999b. A PIV Algorithm for Estimating Time-Averaged Velocity Fields. *Proceedings of Optical Methods and Image Processing in Fluid Flow, 3rd ASME / JSME Fluids Engineering Conference,* July 18-23, San Francisco, CA.

*Meinhart, C. D., Gray, M. H. B. & Wereley, S. T.,1999c. PIV measurements of high-speed flows in silicon-micromachined nozzles. American Institute of Aeronautics and Astronautics, AIAA-99-3756

*Meinhart, C. D., Wereley, S. T. & Gray, M. H. B. 2000. Volume illumination for two-dimensional particle image velocimetry. *Meas. Sci. Technol.* **Vol. 11,** pp. 809-814.

Melling, A. 1997. Tracer particles and seeding for particle image velocimetry. *Meas. Sci. Technol.* **Vol. 8**, pp. 1406-1416.

Partlo, W. N. and Oldham, W. J. 1991. Reducing coherence in a fith-harmonic YAG source (213 nm) for use in microlithography. *J. Vac. Sci. Technol. B.* **Vol. 9**, pp. 3126-3131

Reist, P. C. 1993. *Aerosol Science and Technology, 2nd ed.* McGraw Hill, New York.

Supported Personnel

Marin Sigurdson – Associate Laboratory Engineer
Derek Tretheway – Postdoctoral Researcher
Mike Gray – Graduate Student Researcher
Yang Lu – Graduate Student Researcher

* Publications resulting from supported research.

PULSED INJECTION FOR NOZZLE THROAT AREA CONTROL

AFOSR No. F49620-98-C-0016

Daniel N. Miller, Patrick J. Yagle
Propulsion Systems
Lockheed Martin Aeronautics Co.

Erich E. Bender, Brian R. Smith
Computational Fluid Dynamics
Lockheed Martin Aeronautics Co.

Peter J. Vermeulen
Mech. Engr. Dept.
University of Calgary

Ahmad D. Vakili
Mech. & Aerospace Engr. Dept.
Univ. of Tennessee Space Institute

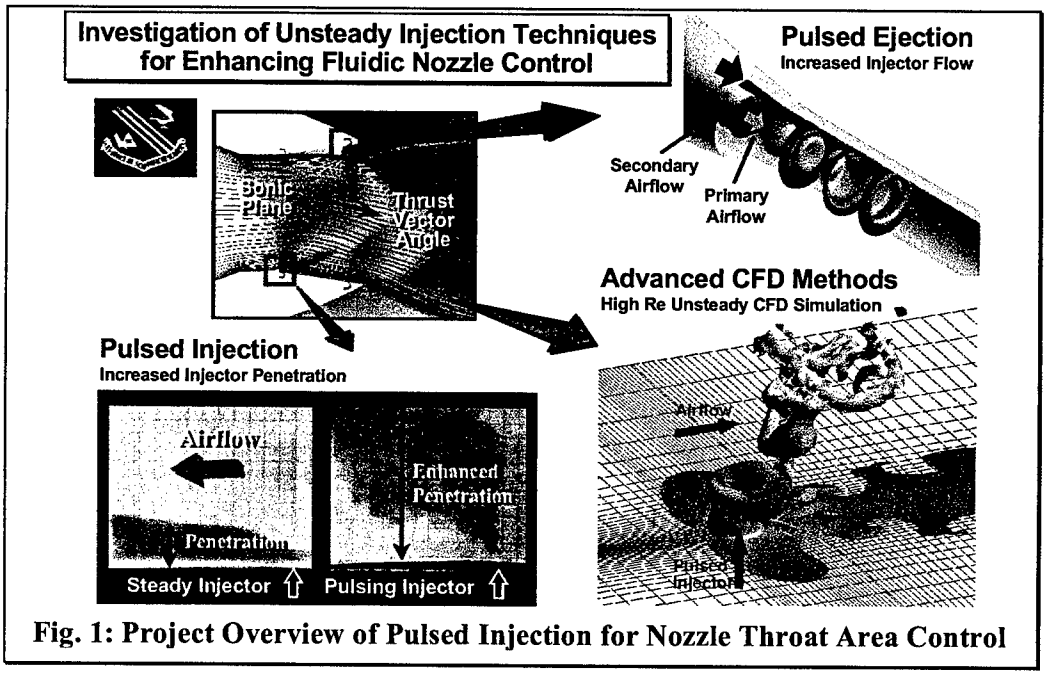

Fig. 1: Project Overview of Pulsed Injection for Nozzle Throat Area Control

Overview

Fluidic injection is of interest to provide internal flowpath shape variation for jet control in structurally-fixed nozzles, and holds the promise of reducing the weight and complexity of future exhaust systems by eliminating mechanical flowpath actuation[1,2,3]. On-going work with *steady injection* has shown that, by introducing an injector into the exhaust stream near the throat or the exit, the injector plume can produce a stable fluidic obstruction[2,3]. By metering injector flow, the size of this obstruction, and hence, the internal flowpath shape can be actively modified to control both jet area and thrust vector angle. This research effort is investigating two unsteady injection techniques for increasing the fluidic blockage produced by an injector blowing into an internal, compressible cross flow (Fig. 1). If greater blockage can be obtained by pulsed injection, the mass flow required for nozzle jet control can be reduced. Reducing injector flow (bled from the engine) is desired to achieve the peak system performance. The first technique, denoted *pulsed injection*, addresses the periodic modulation of an injector stream into a cross flow to increase stream penetration, diameter, and blockage relative to steady

injection[4,5]. The second technique, denoted *pulsed ejection*, exploits the nature of a periodically modulated primary stream for increasing the entrainment of a co-annular, secondary flow. The combined stream will provide greater mass flow and blockage to the injector without requiring additional compressor air. This technique may also be applied to boost the pumping efficiency of aircraft ejector systems (e.g. nacelle ventilation). A Computational Fluid Dynamics (CFD) simulation and modeling methodology is being developed and used to investigate the two described techniques in a compressible flow regime. An experimental study of actuators suitable for pulsed injection is also underway.

Objectives

The overall objective of this research effort is to investigate basic, unsteady injection techniques for enhancing fluidic nozzle control. Specific objectives in the project are to:

1) Develop a CFD Simulation Methodology for Pulsed Injection

Simulations are required to provide detailed understanding of a 3-D, unsteady flow field.

2) Explore Basic Schemes Using Pulsed Injection to Increase Fluidic Blockage

The general relationship between injector-jet structure, penetration, entrainment, and blockage is sought for both pulsed injection and pulsed ejection concepts.

3) Identify Fundamental Issues for a Higher Speed Pulsed-Injection System

Basic issues need to be explored with simulations of pulsed injection into a compressible flow and compared with the characteristics of an available pulsing actuator for injection.

4) Develop a Rapid Analysis Method

An efficient CFD modeling method for pulsed injection is required for design studies.

Approach/Progress/Future Plans

The approach, progress and future plans for this effort are outlined below for the following tasks: 1) CFD Simulation Methodology, 2) Pulsed-Injection Investigation, 3) Pulsed-Ejection Investigation, 4) Simplified CFD Model, and 5) Pulsed-Injection Test.

1) CFD Simulation Methodology

A systematic study of CFD simulations for pulsed and steady injection into a cross-flow was completed. This work was recently detailed in a technical publication.[1] The resulting methodology showed the effects of grid resolution, turbulence model, and

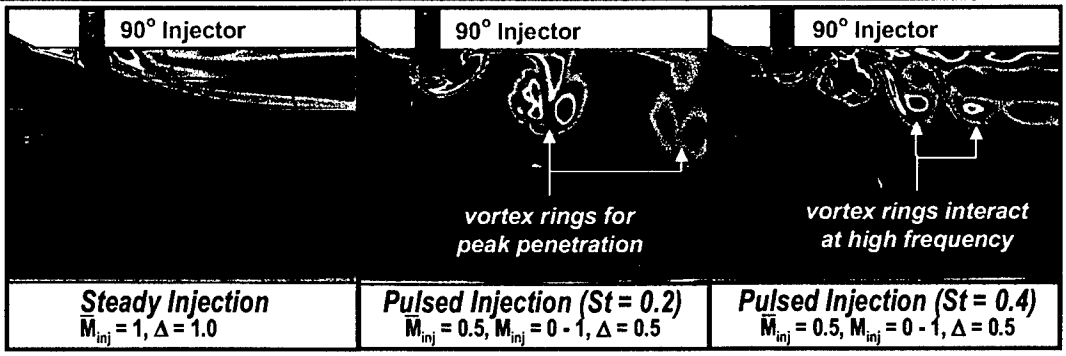

Fig. 2: Effect of Pulse Freq. on Jet Structure/Penetration in a Crossflow (*CFD Vorticity Contours: Red-High, Injector Conditions: St = fD_{inj}/V_{inj}, M = Mach No., Δ = Duty Cycle)*

numerical discretization on accuracy with comparison to test data. The pulsed jet simulations were shown to be more sensitive to grid resolution than a steady jet of equal mass flow. The use of a two-equation Reynolds-Averaged Navier Stokes (RANS) turbulence model was shown to be inadequate for pulsed jet simulations, while Large Eddy Simulation (LES) models gave good results. The pulsed jet solutions were shown to be sensitive to the order of accuracy and the flux limiters of the upwind discretization of the compressible CFD code.

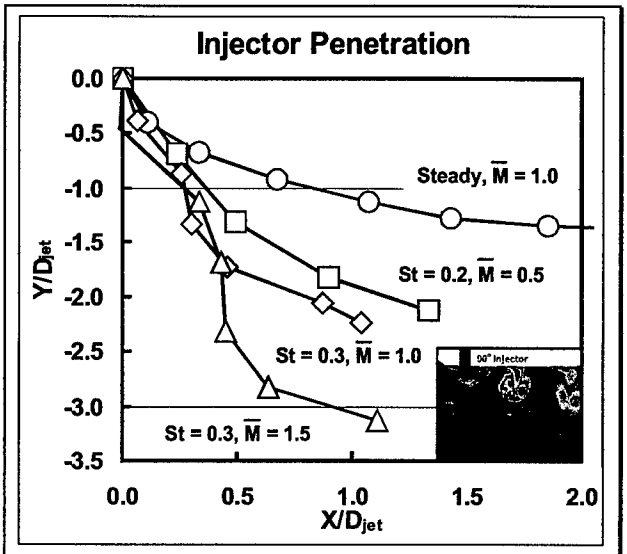

Fig. 3: Effect of Injector Frequency and Mach Number on Jet Center Penetration (from CFD)

2) Pulsed Injection Investigation

The first basic scheme investigated in this project (denoted *pulsed injection*) involved the periodic modulation of an injector stream into a nozzle cross flow to increase stream penetration and blockage relative to steady injection (Fig. 2). The 3-D simulation methodology described above was used to explore the effects of injector pulsing frequency, strength, angle, and area distribution on jet trajectory, penetration, diameter, and blockage. Highlights are discussed in the following and are summarized in Figs 2-4. Simulations were run with cold air issuing from an injector into a transonic nozzle crossflow using a time-averaged injector/nozzle mass flow ratio of 0.05 and a total pressure ratio of 2. Pulsing the injector in the compressible regime produced a measured increase in jet penetration and diameter over a steady injector. Previous work established this relationship for incompressible flow.[4,5] The basic mechanism governing this enhanced penetration is believed to be the appropriate formation, spacing, and strength of vortex rings generated at the injector exit. The effect of pulsing frequency (f) or Strouhal No. ($St = fD_{inj}/V$) on injector jet structure and penetration is illustrated in Figs. 2 and 3. The pulsing frequency determines the spacing between injector vortex rings. Peak penetration was achieved with a St of 0.3. Higher frequency pulsing ($St > 0.4$) produced very close vortex ring spacing, which decreased penetration. The injector Mach No. set the relative strength of the vortex rings. The

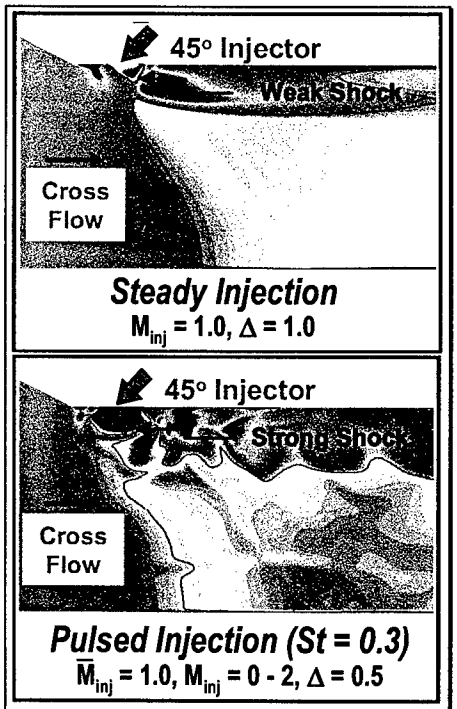

Fig. 4: Effect of Compressibility (*CFD Mach Contours: Red-High*)

injector was fully modulated with a 50% duty cycle to produce a time-averaged Mach No. (M_{inj}) of 0.5, 1, or 1.5. Increasing M_{inj} produced gains in jet penetration (Fig. 3) and blockage. Maximum jet blockage with pulsing was obtained when the injector was angled upstream into the crossflow with a M_{inj} of 1.5 (78% increase over a steady transverse jet). Conditions for peak penetration did not always produce increased blockage. The injector vortex rings entrained the crossflow at certain conditions, which decreased the jet blockage. Gains in penetration using pulsing were smaller than observed in previous incompressible studies. The additional momentum imparted during pulsing may be partially dissipated in the compressible regime because of increased injector jet shock strength (Fig. 4). A paper detailing these findings is planned for the AIAA 2001 fluids conference.

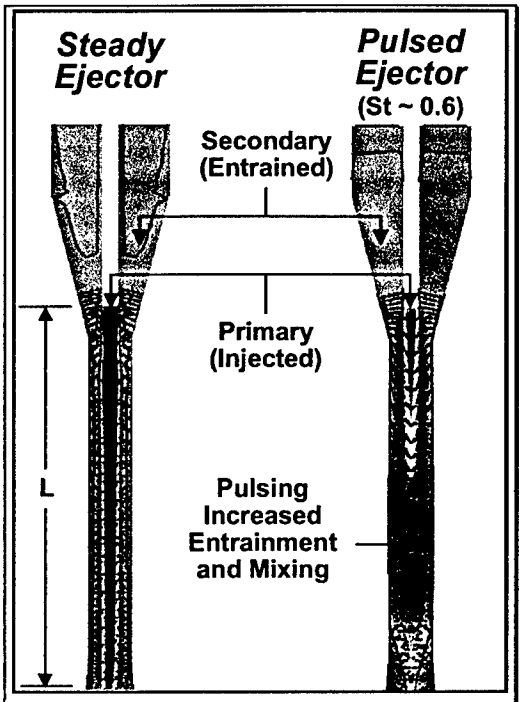

Fig. 5: Effect of Pulsing on Ejector Entrainment/Mixing (*CFD P_t Contours*)

3) Pulsed Ejection Investigation

The second basic scheme, currently under investigation (denoted *pulsed ejection*), uses a pulsed high-pressure primary stream to boost the entrainment of a co-annular, secondary flow (Fig. 5). The combined stream from this device will provide greater mass flow and, therefore, fluidic blockage[2] to the injector jet without requiring additional primary flow (e.g. compressor bleed air). Sources for the secondary stream include ambient or engine fan air. CFD simulations are being used to investigate the effects of the following governing parameters on ejector pumping efficiency: primary jet pulsing frequency or Strouhal No. (St=fL/V), pulsing strength, primary/secondary area and pressure ratio, and ejector mixing tube length (L). Preliminary highlights are described below and are summarized in Figs. 5-7. Simulations were run with cold primary air issuing into a co-annular stream using a primary/secondary area ratio of 1/3 and an average total pressure ratio of 1.5. The primary jet Mach No. was fully modulated between a value of 0 and 1. Results from a 3-D simulation

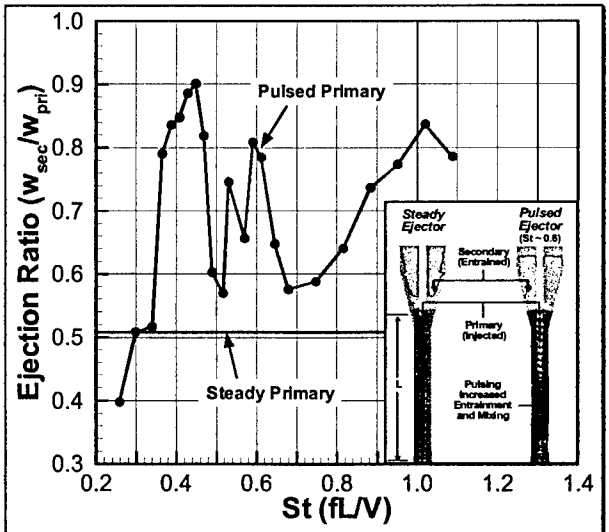

Figure 6: Effect of Pulsing Frequency on Ejector Pumping Efficiency (from CFD)

using a fine grid resolution and 3rd order solver predicted a 100% increase in entrainment over that of a steady primary stream (steady jet solutions were run using both LES and RANS turbulence models). Comparison of total pressure contours taken from CFD revealed the dramatic increase in mixing and entrainment using a pulsed over a steady primary jet (Fig. 5). Ejector efficiency (entrainment ratio) exhibited a large variation with primary jet pulsing frequency (Fig. 6). The pulse wave front of the primary jet has a pronounced acoustic interaction with both the secondary flowpath and mixing tube. The primary jet pulsing frequency has a strong effect on this acoustic interaction (Fig. 7). Future work includes a systematic study to more fully characterize this technique.

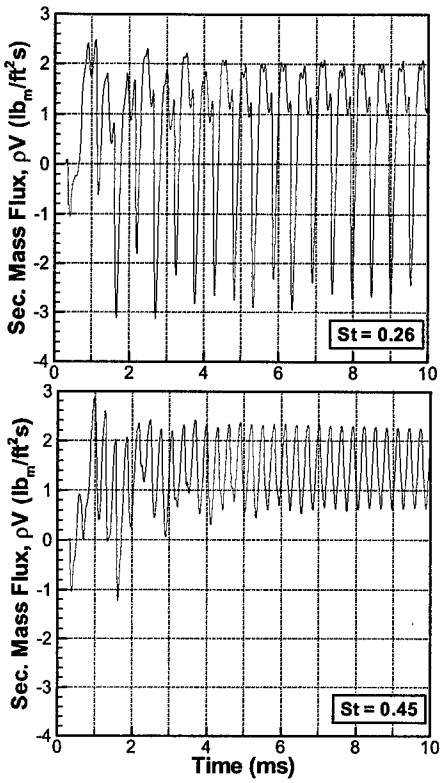

Fig. 7: Effect of Pulsing Frequency on Ejector Waveform (from CFD)

4) Simplified CFD Model

Many solutions will be required to optimize parameter settings, when evaluating injection techniques for flow control in a design environment. Simulation of pulsed injection is computationally intensive and for applications with multiple injectors, large grids will be required for adequate resolution. For such cases, simulation is too costly. Future work includes development of a simplified CFD model of the pulsed injected stream that will capture its essential effect, without the need of a highly resolved simulation.

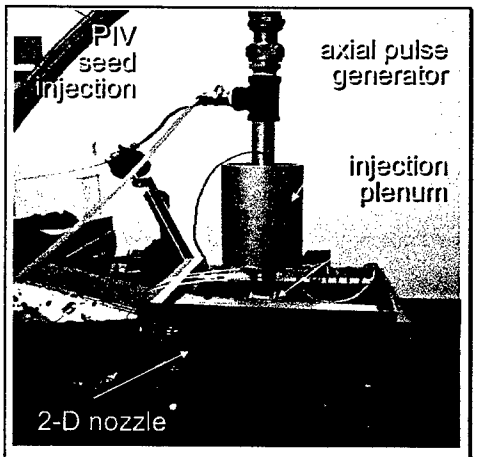

Fig. 8: Test Setup for Pulsed Injection in a Nozzle Crossflow

5) Pulsed-Injection Testing

An investigation of pulsed injection actuators is being conducted at the University of Tennessee Space Institute (UTSI).[4] In this task, two actuators are being evaluated for injector-jet penetration and blockage in a compressible, confined cross flow. The airflow of an injector issuing into a 2-D nozzle is visualized through a side-view window (Fig. 8). Particle imaging velocimetry (PIV) is being used to measure the jet structure and velocity. A Honeywell fluidic diverter valve was first evaluated. This actuator creates pulses by switching the injector stream between two exit ports. Maximum frequency was limited to 200 Hz. Problems with actuator hardware and PIV measurement did not allow an

adequate examination. High-response pressure data taken near the injector exit revealed that the actuator generated a quasi-periodic pulse front. PIV images taken at the injector exit did not reveal any distinct vortical structures. A plenum was used to integrate the actuator and nozzle. The volume of the plenum may have acted as a low-pass filter, attenuating the pulse strength. Future work includes evaluation of an axial, acoustic pulse generator (developed at UTSI) capable of operation at higher frequencies (~2600 Hz). PIV measurements are being taken at the injector exit using a very small plenum volume.

Acknowledgment/Disclaimer
This work was sponsored (in part) by the Air Force Office of Scientific Research, USAF, under contract number F49620-98-C-0016. The views and conclusions contained herein are those of the authors and should not be interpreted as necessarily representing the official policies or endorsements, either expressed or implied, of the Air Force Office of Scientific Research or the U.S. Government.

References
1. Bender, E., Miller, D., Smith, B., Yagle, P., Vermeulen, P.,Walker, S., "Simulation of Pulsed Injection in a Crossflow Using 3-D Unsteady CFD," 2000, AIAA No. 2000-2318.

2. Yagle, P., Miller, D., Ginn, K., Hamstra, J., "Demonstration of Fluidic Throat Skewing for Thrust Vectoring in Structurally Fixed Nozzles," 2000, ASME No. 2000-GT-0013.

3. Miller, D., Yagle, P., Hamstra, J., "Fluidic Throat Skewing for Thrust Vectoring in Fixed-Geometry Nozzles," 1999, AIAA No. 99-0365.

4. Vakili, A., Sauerwein, S., Miller, D., "Pulsed Injection Applied to Nozzle Internal Flow Control," 1999, AIAA No. 99-1002.

5. Vermeulen, P., Ramesh, V., "NOx Measurements for Combustor with Acoustically Controlled Primary Zone," 1996, ASME No. 96-GT-129.

Publications
"Simulation of Pulsed Injection in a Cross Flow Using 3-D Unsteady CFD," Bender, E., Miller, D., Smith, B., Yagle, P., Vermeulen, P.,Walker, S., 2000, AIAA No. 2000-2318.
"Pulsed Injection Applied to Nozzle Internal Flow Control," Vakili, A., Sauerwein, S., Miller, D., 1999, AIAA No. 99-1002.
"Fluidic Throat Skewing for Thrust Vectoring in Fixed-Geometry Nozzles," Miller, D., Yagle, P., Hamstra, J., 1999, AIAA No. 99-0365.

Awards Received
AIAA Best Paper Award, 35th Joint Propulsion Conference, Los Angeles, CA.
Title: "Fluidic Throat Skewing for Thrust Vectoring in Fixed-Geometry Nozzles"
Invention Disclosure Award, Lockheed Martin Corporation.
AIAA Poster Award, Art of Flow Control Session, Fluids 2000 Conference, Denver, CO.

Transitions
The CFD methodology developed in this project has been used in development of fluidic nozzle technology in the AFRL Internal Flow Control program (point of contact at Lockheed Martin: Brant.Ginn@lmco.com, 817.935.1033) and in development of actuation techniques in the AFRL Active Weapons Bay Noise Suppression program (point of contact at Lockheed Martin: Brian.R.Smith@lmco.com, 817.935.1124).

BOUNDARY CONDITIONS FOR THE LARGE EDDY SIMULATION OF WALL-BOUNDED TURBULENT FLOWS

AFOSR Grant F49620-00-1-0111

Principle Investigator:
Parviz Moin, Stanford University

Co-investigators:
Javier Jiménez, Jeffrey Baggett, Franck Nicoud

Period: 8/1/99 – 7/21/00

Objectives and Approach

The application of large eddy simulation (LES) to attached turbulent boundary layers is limited to low Reynolds numbers because the characteristic dimension of the energy containing structures scales with the distance from the wall. The goal of this research is to develop approximate "wall-boundary conditions" so that the near-wall flow need not be resolved. This will allow the computational grid to be chosen in terms of outer scales (e.g. boundary layer thickness) instead of Reynolds number dependent inner scales, thus permitting the application of LES at much higher Reynolds numbers for engineering applications. Our general methodology is to combine empirical analyses of near-wall behavior in existing experimental and numerical simulation databases, theoretical analysis of highly anisotropic near-wall flow, and ideas from optimal control theory to develop and improve wall models which will be tested in select large-eddy simulations of attached and separated flows.

Summary of Previous Work

To do a proper LES in which all of the energy containing structures are captured outside of the viscous region requires $N \sim O(\mathrm{Re}_\tau^2)$ grid points [3] which is only slightly better than direct simulation for which $N \sim O(\mathrm{Re}_\tau^{9/4})$. The only way to alleviate this Reynolds number dependence is to restrict the grid refinement to distances away from the wall which are fixed fractions of the outer flow scale. In attached flows this means that the last grid point would be in the logarithmic layer and that a boundary condition must be supplied to model the unresolved region adjacent to the wall. The main results for the current generation of wall models are:

- "Off-Wall" Approximate Boundary Conditions — applied to velocity field at some height above wall
  - Sensitive to structural information representing the near-wall region.
  - Velocity boundary conditions produce spurious boundary layer and anamolous pressure fluctuations that contaminate the flow.

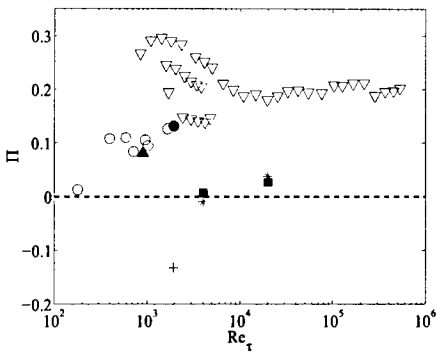

Figure 1: Wake component of mean velocity profiles. ○ , smooth channels; ▽ , smooth and rough pipes. Solid symbols are LES of channels. ■ , 'dynamic' boundary condition, finite differences [4]; ∗, same, but with modified boundary viscosity. ▲ , resolved boundary, B-splines [9]; +, resolved boundary, finite differences filtered at $2\Delta x$ [10]. ● , same, filtered at $3\Delta x$. This figure is adapted from [4].

- Wall Stress Approximate Boundary Conditions — provide viscous stresses in the first grid volume that cannot be calculated from outer flow.
  - Simple algebraic wall stress models work fine in low to moderate Reynolds number attached flows.
  - Differential wall stress models (e.g. boundary layer equations) improve predictions in separated regions.
  - Wall stress models degrade in high Reynolds number attached flows due to near-wall SGS modeling and numerical errors.

Due to space limitations, the wide variety of approximate boundary conditions are not presented here. A recent review was prepared under this contract and is given in [4].

Progress & Results

Sensitivity of outer flow to approximate boundary conditions

In [8] it was argued that in the expected logarithmic mean velocity profile in an attached turbulent boundary layer

$$u^+ = \kappa^{-1} \log y^+ + A, \tag{1}$$

the logarithm itself and probably the Kármán constant κ depend only on universal properties of turbulence, but that the additive constant A is determined by a near-wall layer where (1) no longer applies. This suggest that, if we use the wrong wall boundary condition for the LES equations, most of the flow, except for the first few grid points close to the wall, and for the additive constant in the mean velocity profile, might be correct.

Unfortunately the issue is clouded by numerical effects. In the first place, except for very high order numerical schemes, the solution in the first few points near the wall are wrong in any case, because the effective resolution of the numerical methods is never better than a few grid points. Numerical errors get confused with modeling inadequacies. Consider the pipes and channels summarized in Figure 1. The velocity profiles away from the wall can be characterized by the magnitude of their wake parameter Π [7]. The open symbols in Figure 1 are results either from experiments or from direct simulations. The wake parameters of pipes decrease from relatively high values at low Reynolds numbers to an

asymptote above $Re_\tau \approx 10^4$. Those of channels increase from near zero at low Reynolds numbers to converge with those of the pipes at about the same Re_τ.

The solid triangle, which agrees with experiments, is a LES using a high-order numerical method and a zonal grid which resolves the near-wall layer. The two solid squares use second-order finite differences, and a fairly sophisticated wall boundary condition; they have incorrect wake parameters consistent with a lower Reynolds number. That the problem is not with the boundary conditions is suggested by the asterisks, which use the same code but a fairly different boundary condition, and still have the same incorrect profiles.

Performance of empirical or physical wall stress models

In [4, 5], we show that there is little difference, with respect to the mean velocity, between algebraic wall stress models and wall stress models based on the thin boundary layer equations in simulations of turbulent channel flow at high Reynolds numbers. We found that the slope of the mean velocity profile was always too low for the first several grid points resulting in an under-prediction of the mass flux for the predicted skin friction.

This is because these physically based wall stress models can do little to compensate for the inaccuracies in the subgrid scale model and numerical errors on the coarse near-wall grid. It was argued that the dynamically determined Smagorinsky eddy viscosity was incorrect for the first few grid points and instead we extrapolated the model constant from the interior of the flow. This increased the near-wall eddy viscosity and the increased dissipation resulted in a nearly correct mean velocity profile.

Optimal Control Based Wall Modeling

At high Reynolds numbers, the wall stresses not only have to predict mean characteristics such as the average drag, they also have to provide boundary conditions for the fluctuating velocities that can compensate for the numerical and subgrid scale modeling errors associated with the coarse near-wall grid. At low to moderate Reynolds numbers the flow is evidently able to compensate for these errors, but at high Reynolds numbers wall stress models based on first order quantities such as the mean stress balance are inadequate. To find the proper and apparently non-intuitive wall stresses that work we have turned to optimal control theory.

The problem of finding approximate boundary conditions to approximate the effects of the near-wall region can be regarded as a control problem in which the objective is for the coarse-grid, outer LES to yield good low-order statistics, and the unknown controls are the wall stress boundary conditions. The mathematical framework for optimal control in fluid mechanics is well established [1], but this application to LES is new. This approach has the potential to generate approximate boundary conditions that can account for the numerical and SGS modeling errors that are intrinsic to the near-wall region.

Using a second order finite difference code with the plane averaged dynamic Smagorinsky model and a 32^3 uniform grid we have conducted several LES's at $\mathrm{Re}_\tau = 4000 (\mathrm{Re}_C \approx 10^5)$. At each time step an objective function

$$J(\phi) = \sum_{i=1,3} \alpha_i J_{i,\mathrm{mean}}(\phi) + \sum_{i=1,2,3} \beta_i J_{i,\mathrm{rms}}(\phi) + \sum_{i=1,2,3} \gamma_i J_{i,\mathrm{cost}}(\phi) \tag{2}$$

is minimized with respect to the control parameter ϕ which consists of the streamwise and spanwise wall stresses, as well as wall-normal transpiration velocity. The fact that the control is optimized at each time step results in a suboptimal control [6]. The first term in (2) measures the deviation of the plane-averaged mean flow from a reference profile, in this case a logarithmic profile. The second term measures the deviation of the plane-averaged r.m.s. velocity fluctuations from reference profiles taken

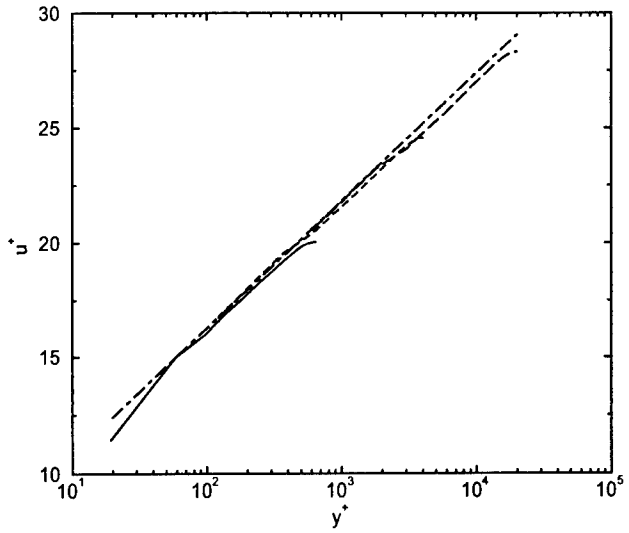

Figure 2: Mean velocity profiles from LES's with the LSE model on uniform 32^3 grid: ——: $\mathrm{Re}_\tau = 640$; ---- : $\mathrm{Re}_\tau = 4000$; ——— : $\mathrm{Re}_\tau = 20000$; —·— : $< u >^+ = 2.41 \ln y^+ + 5.2$

from an LES simulation with a zonal grid that was refined in the near-wall region [9]. The third term is a penalty term that regulates the strength of the control.

An adjoint method is used to find the gradient of the objective function with respect to the control parameters and a steepest descent algorithm is applied to minimize the functional in (2). Details of the algorithm may be found in [11, 12].

In [12], the wall-normal transpiration velocity portion of the control was set to zero and the objective function (2) contained no contribution from the velocity fluctuations, that is $\beta_i = 0$. It was found that the suboptimal control approach produced wall stress approximate boundary conditions that yielded a much improved mean streamwise velocity profile than other wall stress models. However, the streamwise velocity fluctuations are too high. Even when the objective function contains the second term ($\beta_i \neq 0$) that targets the velocity fluctuations, the results do not improve significantly.

To better capture the velocity fluctuations, we are now including a wall-normal transpiration velocity as part of the control parameter ϕ; see [11]. Preliminary results indicate that the mean velocity profile is further improved by the incorporation of the transpiration velocity as part of the suboptimal boundary condition (when $\beta_i = 0$ in (2)). We are currently testing the effect of the inclusion of transpiration velocity on the velocity fluctuations and results will be presented at the meeting.

While the suboptimal control approach could be used as a wall model, provided a target mean velocity profile is known at least for the near-wall region of interest, the cost of the simulation with the suboptimal control is about 20 times greater than that with a simple algebraic wall model. Fortunately, the suboptimal control approach provides a set of reference data that can be used to derive new wall models. The wall stresses produced by the suboptimal procedure (with only the mean flow targeted no transpiration velocity) were correlated to the local velocity field by a linear regression scheme, Linear Stochastic Estimation (LSE), similar to [2]. The resulting algebraic wall model based on a LSE correlation coefficients nearly exactly reproduced the suboptimal simulation at a cost only slightly higher

than running the simulation on a coarse grid with no wall model. Furthermore, the same coefficients yielded good mean flow predictions over a large range of Reynolds numbers (from 180 to 20000 based on the shear velocity); see Figure 2 and on a variety of uniform grids ranging from size 24^3 to 64^3.

Future Plans

We will continue to explore the derivation of improved wall models using the optimal control / linear stochastic estimation framework. In particular, the suboptimal control mentioned above, in which the control was optimized so that the best mean flow was obtained at each time step should be extended to find the best wall stresses over a longer time horizon. The same approach will also be used to attempt to find an improved SGS model for the first several grid volumes adjacent to the wall and to attempt to find improved "off-wall" boundary conditions.

The robustness of the LSE wall model coefficients produced by optimal control/LSE framework will be tested by incorporating the new wall models in simulations of different flows and with different numerical methods.

Finally, since it seems likely that different approximate boundary conditions will be needed in different flow regimes, we will also begin examining the problem of determining how and where to switch between different wall models including switching to no wall model in regions that are dominated by large scale eddies such as in separated zones.

Acknowledgement/Disclaimer

This work was sponsored by the Air Force Office of Scientific Research, USAF, under grant numbers F49620-00-1-0111. The views and conclusions contained herein are those of the authors and should not be interpreted as necessarily representing the official policies or endorsements, either expressed or implied, of the Air Force Office of Scientific Research or the U.S. Government.

References

[1] F. Abergal and R. Temam. On some control problems in fluid mechanics. *Theoret./ Comput./ Fluid Dynamics*, 1:303–325, 1990.

[2] R.J. Adrian, B.G. Jones, M.K. Chung, Y. Hassan, C.K. Nithianandan, and A. Tung. Appoximation of turbulent conditional averages by stochastic estimation. *Phys. Fluids*, 1:992–998, 1989.

[3] J.S. Baggett, J. Jiménez, and A.G. Kravchenko. Resolution requirements in large-eddy simulations of shear flows. In *Annual Research Briefs*, pages 51–66. Center for Turbulence Research, 1997.

[4] W. Cabot, and P. Moin. Approximate wall boundary conditions in the large-eddy simulation of high Reynolds number flow. *Flow, Turbulence, and Combustion*, 63:269–291, 1999.

[5] W. Cabot, J. Jiménez, and J.S. Baggett. On wakes and near-wall behavior in coarse large-eddy simulation of channel flow with wall models and second-order finite-difference models. In *Annual Research Briefs*, pages 343–354. Center for Turbulence Research, 1999

[6] H. Choi, P. Moin, and J. Kim Active turbulence control for drag reduction in wall-bounded flows. *J. Fluid Mech.* 262:75–110,1994.

[7] R.B. Dean. A single formula for the complete velocity profile in a turbulent boundary layer, *ASME J. Fluids Engng.*, 98:723-727, 1976.

[8] J. Jiménez. Some open computational problems in wall-bounded turbulence. In Proc. of the 8th European Turbulence Conference.

[9] A.G. Kravchenko, P. Moin, and R. Moser. Zonal embedded grids for numerical simulations of wall-bounded turbulent flows. J. Comp. Phys., 127:412–423, 1996.

[10] T.S. Lund and H.J. Kaltenbach. Experiments with explicit filtering for LES using a finite-difference method, *CTR Ann. Res. Briefs*, Stanford Univ. 91–106, 1995.

[11] F. Nicoud, J. Baggett. On the use of the optimal control theory for deriving wall models for LES. In *Annual Research Briefs*, pages 329–341. Center for Turbulence Research, 1999

[12] F. Nicoud, J.S. Baggett, W. Cabot, and P. Moin. LES wall-modeling based on optimal control theory. Accepted in *Physics of Fluids*, 2000.

[13] N.V. Nikitin, F. Nicoud, B. Wasishto, K.D. Squires, and P.R. Spalart. An approach to wall modeling in large-eddy simulations. *Phys. Fluids*, 12:1629–1632, 2000.

[14] U. Piomelli, J. Ferziger, P. Moin, and J. Kim. New approximate boundary conditions for large eddy simulations of wall-bounded flows. *Phys. Fluids*, 1:1061–1068, 1989.

Personnel Supported

The following personnel have been supported from this grant in this period: Parviz Moin; Javier Jiménez as a senior research fellow of the Center for Turbulence Research at Stanford University; and William Cabot as a senior research associate of the Center for Turbulence Research at Stanford University. Jeffrey Baggett and Franck Nicoud as research associates of the Center for Turbulence Research at Stanford University. Graduate student Jeremy Templeton was added to the program in July 2000.

Publications

The publications, [4, 5, 8, 11, 12, 13], listed in the bibliography appeared, or were accepted, during the current period.

Interactions/Transitions

- Jeffrey Baggett and Franck Nicoud presented results based on this research at the 52nd Meeting of the Fluid Dynamics Division of the American Physical Society in New Orleans in November 1999.
- In July 2000 the wall models developed and validated under this contract were incorporated in an LES code used by United Technologies, Inc. Additionally, a major portion of this LES code was also developed with support from AFOSR's Turbulence and Rotating Flows program and was delivered to UTC in September 1999.

TOWARDS OPTIMUM FORMULATIONS OF LARGE EDDY SIMULATION OF TURBULENCE

NSF-CTS-9616219

R. D. Moser, S. Balachandar and R. J. Adrian
Department of Theoretical and Applied Mechanics
University of Illinois, Urbana-Champaign

Motivation and Objectives

One of the most promising techniques for the prediction of turbulent flows is that of Large Eddy Simulation (LES), in which an under-resolved representation of the turbulence is simulated numerically by modeling the effects of the unresolved small-scales on the simulation. Such simulations have been applied in several flows with reasonable success. However, there are several outstanding problems that need to be addressed before LES can fulfill its promise as a tool for turbulence prediction in engineering flows. The most serious problems limiting the usefulness of LES is the representation of turbulence near walls and other strong inhomogeneities. Other difficulties include the dependence of models on the filter and/or numerical discretization, the treatment of inhomogeneous filters and the lack of understanding of the modeling errors and their impact.

Our objective in this research is to address these issues and develop a rigorous framework in which to develop and analyze LES models and simulations. The basis for this analysis is an optimum LES formulation discussed below.

Approach

The starting point for the development of LES is the definition of a spatial filter $\tilde{\cdot}$, which can be applied to the Navier-stokes equations to obtain an equation for the filtered velocity $\tilde{u}_i$:

$$\frac{\partial \tilde{u}_i}{\partial t} = -\frac{\partial \tilde{u}_i \tilde{u}_j}{\partial x_j} - \frac{\partial \tilde{p}}{\partial x_i} + \frac{1}{\mathrm{Re}} \frac{\partial^2 \tilde{u}_i}{\partial x_j \partial x_j} + M_i, \tag{1}$$

Where M_i is the sub-grid model (force) term, which includes the divergence of the sub-grid stress as well as terms that arise when the filter does not commute with differentiation. The problem in LES of course is to model M_i. A very important result of our research (Langford & Moser, 1999) is that an LES w will match the one-time statistics of filtered turbulence $\tilde{u}$ if and only if the model $m_i(w)$ of M_i is given by

$$m_i(w) = \langle M_i(u) | \tilde{u} = w \rangle \tag{2}$$

This model also minimizes the difference between M_i and m_i (in the mean-square sense), and so this model has all the properties that one could ask of a sub-grid model. We therefore call it the ideal sub-grid model.

Unfortunately, the conditional average in (2) cannot practically be determined, since the conditions are that the entire filtered velocity field match the entire LES field. However, it can be estimated using stochastic estimation (Adrian et al, 1989) which is a well-established technique for estimating conditional averages. To perform stochastic estimation one requires large quantities of two-point correlation data. For example, in linear estimation one needs $\langle \tilde{u}_j(\mathbf{x}') \tilde{u}_k(\mathbf{x}'') \rangle$ and $\langle M_i(\mathbf{x}) \tilde{u}_k(\mathbf{x}'') \rangle$.

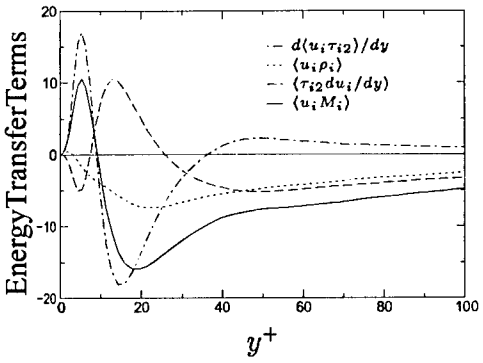

Figure 1: Energy transfer ($\langle u_i M_i \rangle$) to and from the large-scales, and contributions from terms on the right hand side of (3).

To obtain the required data, we resort to direct numerical simulation (DNS), which is limited to low Reynolds numbers, and experimental velocity field measurements, which are currently limited to two-dimensional measurements. These data sources are used together to overcome the weaknesses in each. Estimation data is being gathered for several simple model flows (channel flow and cylinder wakes are reported here) so that the flow-specific optimal models can be synthesized into generally applicable models.

Turbulent Channel Flow

Results of applying the optimal LES approach to isotropic turbulence suggest that a simple model that respects the detailed energy transfer from resolved to subgrid scales is sufficient to produce excellent LES results (Langford, 2000). In applying optimal LES to the channel flow, we seek the generalization of this observation. That is, what properties of the subgrid term must the model respect to produce good LES results?

To answer this, the turbulent channel flow DNS data of Moser, Kim & Mansour (1999) at $Re_\tau = 590$ were used to apply the optimal LES procedure. The filters used for the following results is a Fourier cut-off filter in the streamwise and spanwise directions, with no filter in the wall-normal direction.

The mean energy transfer to/from the resolved scales ($\langle u_i M_i \rangle$) is shown in figure 1. Note that there is a large positive peak near the wall at about $y^+ = 8$, which represents a large energy addition to the resolved scales at that location. There is also a large energy drain further from the wall. An optimal LES model using velocity event data that is local in y can be shown to respect this energy transfer at each y-location. However, this is not sufficient to produce an LES with good mean velocity or rms velocities, as is shown in figure 2. As is common with most LES of wall-bounded turbulence, the peak rms streamwise velocity is much larger (18%) than the filtered DNS.

One of the reasons for the discrepancy can be understood by decomposing the energy transfer term $\langle u_i M_i \rangle$ as follows:

$$\langle u_i M_i \rangle = \frac{\partial \langle u_i \tau_{i2} \rangle}{\partial x_2} + \left\langle \tau_{i2} \frac{\partial u_i}{\partial x_2} \right\rangle + \langle u_i \rho_i \rangle, \qquad \rho_i = \frac{\partial \tau_{i1}}{\partial x_1} + \frac{\partial \tau_{i3}}{\partial x_3}. \tag{3}$$

where τ_{ij} is the subgrid stress. The first term on the right of (3) is interpreted as the subgrid contribution to wall-normal energy transport, while the other two terms combine to give

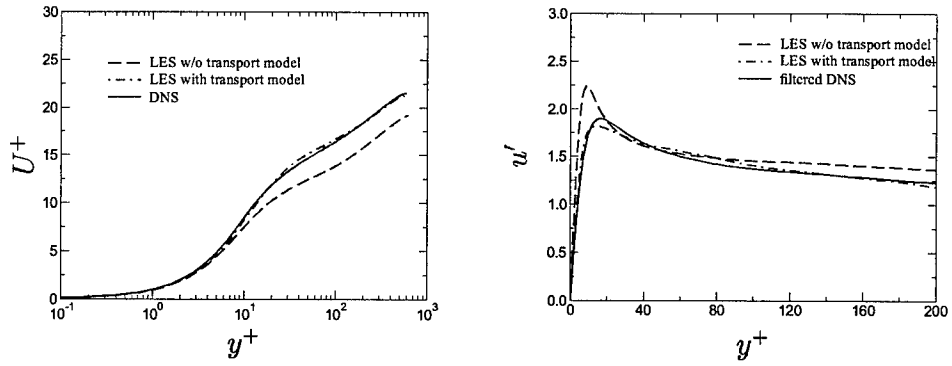

Figure 2: Mean velocity (a) and rms streamwise velocity in the channel flow at $Re_\tau = 590$. Shown are results from DNS and LES using optimal models that do and do reproduce the subgrid contribution to large-scale energy transport in y.

energy transfer between large and small scales. These terms are also shown in figure 1. Notice that the near-wall positive peak in $\langle u_i M_i \rangle$ is due entirely to the transport term. While the local optimal model discussed above reproduces $\langle u_i M_i \rangle$, it does not respect the y transport component. A reformulated version of the optimal model does reproduce each of the terms in (3) so that the transport term is treated as a transport term. This is accomplished by developing optimal representations for τ_{i2} and ρ_i separately in terms of both local (in y) velocity and its y derivatives. When this reformulated model is used, both the mean velocity profile and the rms streamwise velocity fluctuations are much better, though some improvement is still possible (see figure 2).

This result along with others not discussed here indicate that there are several properties of the LES model term for channel flow and presumably other wall bounded flows, that must be reproduced by the model. These properties are: 1) Subgrid contribution to the mean Reynolds stress, 2) Subgrid contribution to wall-normal transport of resolved $u_i u_j$, 3) Exchange of energy (or $u_i u_j$) with the subgrid, and 4) Subgrid contribution to intercomponent exchange of of resolved-scale energy. These are not automatically reproduced by the linear estimates used here because they are local in y. If a truly global linear estimate were used, the subgrid terms in the equation for the two-point correlation tensor would be reproduced by the optimal model, and presumably the results shown in figure 2 would be further improved upon.

Bluff Body Wakes

One of the significant challenges in the development of large eddy simulation is how to handle dynamically significant regions of small scale. The classical example is the near wall region, as in the channel flow discussed above. Here we address the question of modeling dynamically significant thin shear-layers off the wall in the interior of the flow. The classic example is the free-shear layers in the wake of a bluff body in cross flow. Although the wake at large has a wide range of length and time scales the dynamics are critically controlled by the thin shear layers that separate from either side of the bluff body. This poses interesting challenges to accurate implementation of large eddy simulation since it is not clear how these shear layers could be be filtered while their dynamical effect on the wake is preserved.

A rational approach to low-dimensional projection (as in LES) is to reduce the geometric dimensionality of the problem, say from a three-dimensional flow to a two-dimensional or

axisymmetric projection of that flow. This is particularly attractive for plane wakes which dominated by large, spanwise coherent structures. The LES modeling problem is then to model the effects of the missing three-dimension perturbations. Optimal modeling for a two-dimensional projection is applied to a flow over a flat plate held normal to a cross-flow at $Re = 250$ (based on plate height and free-stream velocity). The required data base was obtained from a high resolution three-dimensional direct simulation.

We start with the two-dimensional, span-averaged spanwise vorticity equation:

$$\frac{\partial \bar{\omega}_z}{\partial t} + \frac{\partial \bar{u}_j \bar{\omega}_z}{\partial x_j} = \frac{1}{Re} \frac{\partial^2 \bar{\omega}_z}{\partial x_j \partial x_j} + M \qquad j = (1,2) \tag{4}$$

where the over-bar indicates an average over the spanwise direction and the coordinates x_1 and x_2 correspond to the streamwise and cross-stream directions. In the above equation M accounts for all the three-dimensionality and can be expressed in terms of the three-dimensional spanwise vorticity flux, T_j, as

$$M = \frac{\partial T_j}{\partial x_j} \quad \text{where} \quad T_j = \overline{\omega_j w} - \overline{u_j' \omega_z'} \tag{5}$$

and primes indicate three-dimensional perturbation away from the span-average. The spanwise vorticity flux is analogous to the Reynolds stress term or the subgrid scale momentum flux in the large eddy equations. To close this system, we consider different optimal estimates of M or T_j.

Some important outcomes of this investigation are as folows: 1) The contribution of three-dimensional flux to two-dimensional dynamics is significant. Without appropriate closure Karman vortex dynamics and the resulting lift and drag forces will be significantly over predicted. 2) Gradient diffusion type models are inadequate for predicting the dynamics of the two-dimensional projection. 3) The optimal formulation is challenging in flows with multiple directions of inhomogeneity. Limited statistical sample in such flows results in a problem known as "over generalization" in which the estimates reproduce the statistical fluctuations in the limited sample. This problem was overcome by limiting the number of estimation events, either in terms of a few POD modes, or a few points in the neighborhood of the estimation point. 4) Even with the optimal closure the normalized error in the term to be modeled is quite high at 69%, suggesting that M is largely stochastic, in agreement with findings in isotropic turbulence and turbulent channel flow. 5) The improvement of quadratic closure over the linear closure is not significant.

To support optimal LES development, a spectrally accurate code has been used to produce a DNS data base of the three-dimensional wake of a circular cylinder. The simulation has been performed for a Reynolds number of $Re = 1500$ using a grid of up to 150x300x140 points along the radial, circumferential and spanwise directions. Simulation time covers about 5 shedding cycles in the fully saturated three-dimensional regime. Particular care has been taken to make sure that all features of the attached boundary layer, the separated shear layers and the wake are adequately resolved, since these are of primary concern in the LES modeling. The data acquisition will also continue over the next year, concurrent with post-processing of the data. For the several filters being considered, the term to be modeled is being computed and projected on the requisite divergence-free space. Based on this data the requisite two-point correlations will be computed. Subsequently we plan to employ the optimal closure procedure to develop optimal filters and subgrid models suitable for wake flow simulations.

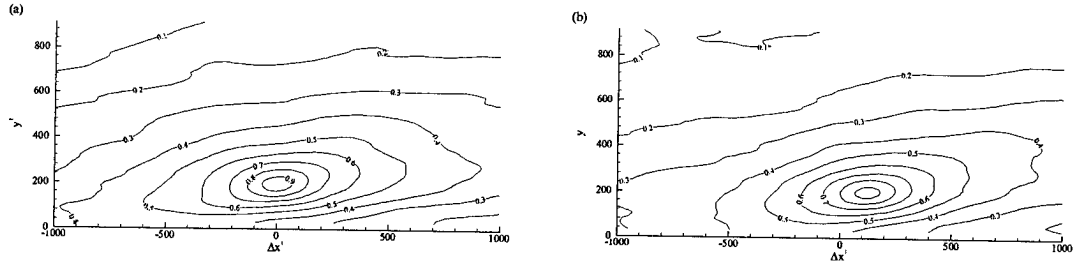

Figure 3: Two-point correlations of streamwise velocity fluctuations in the streamwise/wall-normal plane for $y_r^+ = 200$. (a) $R_{uu}(\Delta x^+, y^+; \tau^+ = 0)$; (b) $R_{uu}(\Delta x^+, y^+; \tau^+ = 6.7)$.

High Reynolds Number Correlations

The DNS discussed above are limited to relatively low Reynolds number. To reach the high Reynolds numbers needed to pursue LES development, an experimental effort to measure small time-delay space-time correlations is under way. First, using stochastic estimation, the conditional average (2) can be approximated from the time-derivative of the velocity space-time correlation. Thus, the velocity space-time correlation tensor for small time-delay must be measured and interpreted. Additionally, the issue of Reynolds-number scaling of velocity space-time correlations in wall turbulence has not been adequately addressed heretofore. This is also a crucial aspect of performing accurate large eddy simulations of turbulence. Therefore, a careful experimental effort has been undertaken to measure these velocity correlations over a modest range of Reynolds numbers.

To this end, large ensembles of two-dimensional particle-image velocimetry (PIV) velocity fields are acquired in the streamwise/wall-normal plane of fully-developed turbulent channel flow at $\mathrm{Re}_\tau = 594$, 1202, and 1817 using a two-CCD-camera arrangement. The cameras are focused on the same field of view; however, the acquisition of the second is delayed in time so that space-time correlations for small time-delay can be determined from the velocity data.

Two-point correlations for both zero and non-zero time-delay are calculated for small time-delay. As an example, $R_{uu}(\delta x, y_r, y, \tau)$ for $y_r^+ = 200$ and $\tau^+ = 0$ and 6.7, are shown in Figure 3 for $Re_\tau = 1202$. In both cases, the longitudinal correlation function is inclined away from the wall at an angle of approximately 13° and persists for over 1000 viscous wall units in the streamwise direction. This is consistent with the notion that the log-layer of wall turbulence is populated by coherent packets of hairpin-like vortices that coherently convect in the streamwise direction. Currently, the derivative of the various correlation functions with respect to τ is being computed, along with the convective derivative of the instantaneous velocity fields. Together, this information will provide a means of assessing the accuracy of LES models in simulating higher Reynolds number wall turbulence. Additionally, the scaling of the correlation functions and the temporal derivative of the correlation functions is being addressed as a means of properly scaling LES models to higher Reynolds numbers.

Other Information

Supported under this grant in whole or in part over the last year have been Stefan Volker, Jacob Langford, John Wu, Ken Christensen and Arup Das graduate students in the MIE

(Volker) and TAM departments at the University of Illinois, and Dr. Zi-Chao Liu, a research scientist in the TAM department. The work supported here was presented at the 1997, 1998 and 1999 meetings of the Division of Fluid Dynamics of the American Physical Society, the 1998 Canadian Congress on Applied Mechanics (Hamilton Ontario), and the Second AFOSR International Conference on DNS and LES (Rutgers University) and several papers have been produced (Moser & Adrian, 1998; Jimenez & Moser, 1998; Langord & Moser, 1999; Moser, Langford & Volker, 1999; Najjar & Balachandar, 1999, Balachandar & Najjar, 1999; Adrian & Balachandar, 1998; Tomkins, Adrian & Balachandar, 1998; Adrian, 1999; Liu & Adrian 1999, Langford, 2000, Langford & Moser 2000)

Acknowledgment/Disclaimer

This work is jointly sponsored by the National Science Foundation and the Air Force Office of Scientific Research, USAF, under grant/contract number NSF-CTS-9616219. The views and conclusions contained herein are those of the author and should not be interpreted as necessarily representing the official policies or endorsements, either expressed or implied, of the Air Force Office of Scientific Research or the U. S. Government.

References

Adrian, R. J. 1999 On the physical space equation for large-eddy simulation of inhomogeneous turbulence. TAM Report No. 915. UILU-ENG-99-6017. Department of Theoretical and Applied Mechanics, University of Illinois at Urbana-Champaign.

Adrian & Balachandar 1998 Vortex packets and the structure of turbulence. Proceedings of the International Symposium on Seawater Drag Redcuction; Newport, RI, 33-38.

Adrian, R. J., Jones, B. G., Chung, M. K., Hassan, Y., Nithianandan, C. K. & Tung, A. 1989 Approximation of turbulence conditional averages by stochastic estimation. *Phys. of Fluids* **1**, 992-998.

Balachandar, S. and Najjar, F. M. 1999 Optimal two-dimensional projections of wake flows, In preparation for *J. Fluid Mech.* Submitted to *Phys. of Fluids.*

Jimenez, J. & Moser, R. D. 1998 LES: Where Are We and What can We Expect, AIAA 98-2891, 29th AIAA Fluid Dynamics Conference, June 15-18, Alburquerque, NM (invited), also to appear in *AIAA J.*

Langford, J. A. 2000 Toward Ideal Large-Eddy Simulations, Doctoral Thesis, Department of Theoretical and Applied Mechanics, University of Illinois at Urbana-Champaign.

Langford, J. A. & Moser, R. D. 1999 Optimal LES formulations for isotropic turbulence. *J. Fluid Mech.* **398**, 321-346.

Langford, J. A. & Moser, R. D. 2000 Breakdown of continuity in finite volume large-eddy simulations, submitted to *Phys. of Fluids.*

Liu, Z.C. & Adrian, R. J. 1999 Evidence for hairpin packet structure in DNS channel flow, in Turbulence and Shear Flow Phenomena -1: First Int'l Symposium, Sept 12-15, 1999, Santa Barbara, CA, eds. S. Banerjee and J. Eaton, (Begell House, New York) pp. 609-614.

Moser, R. D. & Adrian, R. 1998 Turbulence Data for LES Development and Validation, ASME paper FEDSM98-5092, ASME Fluids Engineering Division Summer Meeting, June 20-25, Washington, DC, (invited).

Moser, R. D., Kim, J. & Mansour, N. N. 1999 Direct numerical simulation of turbulent channel flow up to $Re_\tau = 590$, *Phys. of Fluids* **11**, 943-945.

Moser, R. D., Langford, J. A. & Volker, S. 1999 Optimal LES: How Good Can and LES Be? *Proceedings of the Second AFOSR International Conference on DNS and LES*, June 7-9, Rutgers Univeristy (invited).

Najjar, F. M. & Balachandar, S. 1998 Low-frequency unsteadiness in the wake of a normal flat plate, *J. Fluid Mech.* **370**, 101-147.

Tomkins, Adrian & Balachandar 1998 The structure of vortex packets in wall turbulence. AIAA 98-2962, 1-13.

WEAKLY COMPRESSIBLE DESCRIPTIONS OF TURBULENCE IN COMPRESSIBLE FLOWS

F49620-97-1-0089

Robert D. Moser
Department of Theoretical and Applied Mechanics
University of Illinois, Urbana-Champaign

Motivation and Objectives

A large fraction of the effort in turbulence research, including numerical simulations, experiments, theory and modeling, has been directed toward incompressible turbulence. This is largely due to the simplifications that the incompressible assumption allows, and to the belief that turbulence is in essence an incompressible phenomenon. However, many of the flows of technological interest are compressible (e.g. external aerodynamics, propulsion systems) leading to the requirement that our understanding of incompressible turbulence be translated to these compressible flows. An example of this is that most commonly used turbulence models for compressible flows are modifications of models developed for incompressible flows (e.g. the k-ϵ model).

Fortunately, in many flows the small-scale turbulence is nearly incompressible, albeit with non-constant density, even though the flow itself is highly compressible. For example, in much of the literature on compressible boundary layers (see the review by Spina et al., 1994), differences relative to an incompressible boundary layer (up to $M = 5$, say) are understood as being caused by variations in the mean density across the layer. This has long been appreciated and is the basis of the Van Driest (Van Driest 1951, 1956) transformation and the Morkovin hypothesis (Morkovin 1961).

These observations suggest that a formulation based on low Mach number asymptotics, in which the turbulence is treated as weakly compressible while the mean is considered to be fully compressible, would provide a good description of the boundary layer to quite large Mach numbers, and a rational basis for the development of compressible turbulence models. Aided by direct numerical simulation data, the research under this grant is aimed at developing and evaluating such weakly compressible descriptions of compressible turbulence.

Approach

The starting point for the analysis required for the development of our weakly compressible turbulence description is the asymptotic analysis of Zank & Matthaeus (1991). However, examination of DNS fields, indicates that in fact the Zank & Matthaeus formulation is inadequate for analysis of the boundary layer, and presumably compressible shear layers in general. To generalize, we consider a representation of the compressible fields as follows:

$$\mathbf{u} = \mathbf{u}_I + \varepsilon(\mathbf{u}_t + \mathbf{u}_a), \tag{1}$$

$$p = 1 + \varepsilon^2(p_I + p_a), \tag{2}$$

$$T = \frac{\gamma}{\gamma - 1} + \varepsilon T_t + \varepsilon^2 T_a, \tag{3}$$

$$\rho = 1 + \varepsilon\rho_t + \varepsilon^2\rho_a; \tag{4}$$

where subscript 'I' denotes the nontrivial incompressible part, subscript 't' denotes the variable temperature (thermal) part and subscript 'a' denotes the acoustic part. This along with the assertions that the incompressible velocity is divergence free, and that the compressible components vary on a time scale a factor of ϵ shorter than the non-acoustic variables, allow the compressible Navier-Stokes equations to be decomposed into equations for acoustic and non-acoustic variables.

For example, the governing equations for the nonacoustic part of the flow are:

$$\frac{\partial \rho_n'}{\partial t} + \left(u_{nj}\frac{\partial \rho_n'}{\partial x_j}\right)' + u_{nj}'\frac{\partial \overline{\rho}}{\partial x_j} + \left(\rho_n\frac{\partial u_{nk}'}{\partial x_k}\right)' = 0, \tag{5}$$

$$\frac{\partial u_{ni}'}{\partial t} + \left(u_{nj}\frac{\partial u_{ni}'}{\partial x_j}\right)' + u_{nj}'\frac{\partial \overline{u}_i}{\partial x_j} = -\left(\frac{V_n}{\gamma Ma^2}\frac{\partial p_n'}{\partial x_i}\right)' + \frac{2}{Re}\left(V_n\frac{\partial \mu_n s_{nij}}{\partial x_j}\right)' \tag{6}$$

$$\gamma\overline{p}\frac{\partial u_{nj}'}{\partial x_j} = \frac{\gamma-1}{Pr\,Re}\frac{\partial}{\partial x_k}\left(\mu_n\frac{\partial T_n}{\partial x_k}\right)', \tag{7}$$

$$\rho_n' = \frac{\gamma}{\gamma-1}\left(\frac{\overline{p}}{T_n}\right)', \tag{8}$$

where $\mathbf{u}, \rho, T, p$ are velocity, density, temperature, and pressure respectively, over-bar denotes Reynolds average, prime denotes fluctuation, V is a specific volume, and subscript 'n' denotes nonacoustic part of a variable. Note that these equations are autonomous, i.e. the evolution of nonacoustic quantities is unaffected by the presence of acoustic waves in the flow. The most important issue in turbulence modeling is how the mean flow is affected by turbulence, through the Reynolds stress. For the compressible boundary layer, the acoustic fluctuations do not contribute significantly to the Reynolds stress. Thus, in boundary layer flows, one only has to be concerned with modeling of the nonacoustic part of the flow, and the set of equations (5)–(8) can be used for this purpose.

Similarly, a set of equations for the acoustic part of the flow can be written, which are similar to the equations for linear acoustics in a nonuniform medium. The major subtlety to this analysis is that the acoustic and nonacoustic equations are only decoupled to a certain finite order. At this order, coupling terms are present, and these terms can not be sensibly assigned to either acoustic or nonacoustic equations.

To make use of this result in analyzing compressible turbulence, one must be able to actually determine the acoustic and non-acoustic portions of a compressible turbulent field. A numerical decomposition procedure is used to do this for fields obtained from Direct Numerical Simulation (DNS). DNS is an ideal source of data for this purpose, since virtually any quantity of interest can be determined from the simulation fields. The resulting decomposition can then be used as a basis for analysis and modeling of compressibility effects in turbulence.

To address the observed differences in the effects of compressibility on wall-bounded and free shear flows, the analysis and evaluation of DNS data is performed for two compressible turbulent shear layers, the flat-plate boundary layer and the mixing layer. Since not all

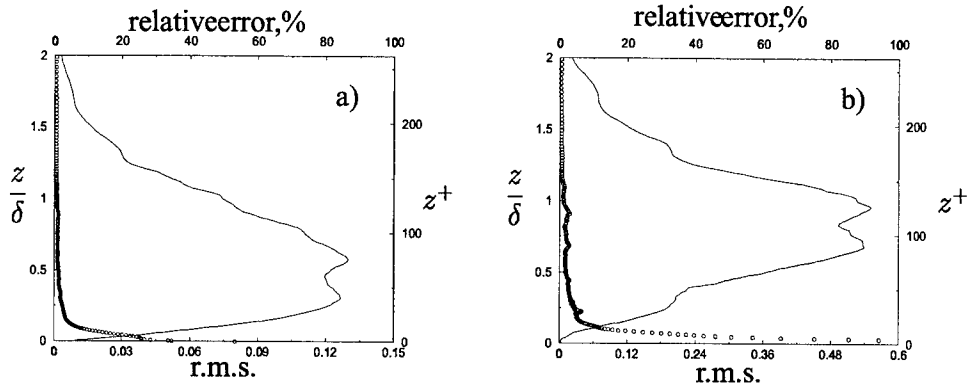

Figure 1: The r.m.s. profiles of the time derivatives of a) nonacoustic velocity fluctuations $\mathbf{u}_n'$ and b) nonacoustic density fluctuations ρ_n' calculated from: the governing equation (——), two subsequent in time data fields (·····), the difference between them (- - - -), and the relative error (oooo) for $Ma = 6$.

the required simulations are currently available, particularly for the mixing layer, some simulations have been and will be performed as part of this effort. The code used to perform the required simulations is based on a Fourier/B-Spline representation, which provides a high-order, high resolution non-dissipative numerical approximation to the Navier-Stokes equations.

Decomposition of Turbulent Fields

A numerical procedure to decompose a turbulent compressible boundary layer field into nonacoustic and acoustic parts has been developed. The decomposition is based on the requirement that the decomposed fields satisfy the decoupled governing equations as closely as possible. The starting point is the relation (7) between nonacoustic velocity divergence and nonacoustic heat flux. In addition to the thermal component, nonacoustic temperature and density also include a higher order pseudosound component, which is a linear response of the system to the nonacoustic (incompressible) pressure fluctuations. The pseudosound is assumed to obey isentropic relations. Being a higher order effect, pseudosound is not expected to play a major role in (7), so the nonacoustic heat flux on the right hand side of (7) can be computed based on the thermal part of the nonacoustic temperature, which is simply written as $T_n = T - p'/\bar{\rho}$. Given nonacoustic velocity divergence from (7), acoustic fluctuating velocity divergence can be obtained by difference, and with the assumption that acoustic velocity is irrotational acoustic, and then nonacoustic velocity can be obtained. Next, nonacoustic pressure p_n' can be computed by taking the divergence of (6) and solving a Poisson-like equation, with time derivative of nonacoustic velocity divergence determined by time differentiating (7), consistent with our goal to obtain a nonacoustic field satisfying its governing equations as closely as possible. Finally, density and temperature can be decomposed using an isentropic equation of state for the acoustic fluctuations.

It should be noted here that the assumption of irrotationality of an acoustic field can lead to significant errors in regions of strong mean gradients, such as in the near wall region of a compressible boundary layer.

The decomposition procedure has been applied to the DNS data of Maeder & Adams (2000),

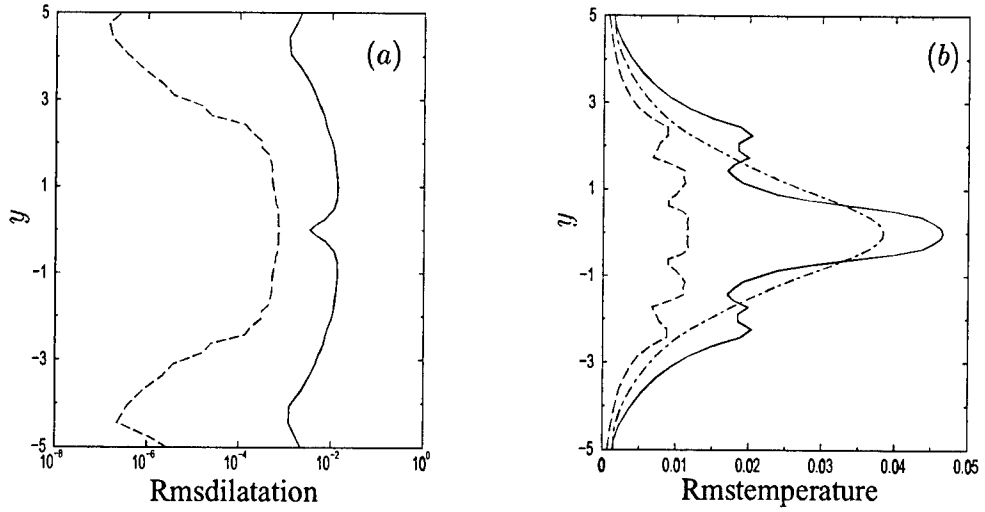

Figure 2: Rms of a) velocity divergence and b) temperature fluctuations in a two-dimensional $Ma_c = 0.4$ mixing layer. Shown are ——total, - - - -, nonacoustic and - · - · -acoustic contributions

with stream Mach numbers 3, 4.5 and 6. Resulting acoustic and nonacoustic fields have been checked by comparing the time derivatives of nonacoustic velocity and density obtained from two subsequent in time decomposed fields and from corresponding governing equations (5)–(6). The time derivatives are presented in figure 1.

The error in satisfying nonacoustic governing equations is less then 5% except near the wall ($y^+ < 30$), where it becomes large because of invalidity of irrotationality assumption for acoustic fluctuations in the regions of strong mean gradients, as expected.

The results of this decomposition are now being applied to investigate the nature of compressibility effects in the boundary layer. Two primary routes are being pursued. First a statistical analysis of the decomposition fields is being performed to provide input for modeling efforts. For example, it is clear from the asymptotic analysis and the decomposition data that the pressure dilatation term in the energy equation is not significant in this flow. Secondly, the decomposed fields can be used to directly evaluate the coupling between turbulent and acoustic fluctuations. This is complicated by the fact that the coupling is so weak, and that it is likely to be strongest near the wall, where strong mean gradients make the decomposition results questionable. For these reasons, the analysis of coupling may be better suited to the mixing layer discussed below.

Compressible Mixing Layers

Free shear layers, such as the mixing layer are known to exhibit much stronger compressibility effects than boundary layers at similar free-stream Mach numbers. They are thus of great interest in investigating the coupling of acoustic fluctuations with turbulence. A decomposition analysis similar to that for the boundary layer is being applied to the mixing layer.

To acquire data for this purpose, DNS of compressible mixing layers are being performed.

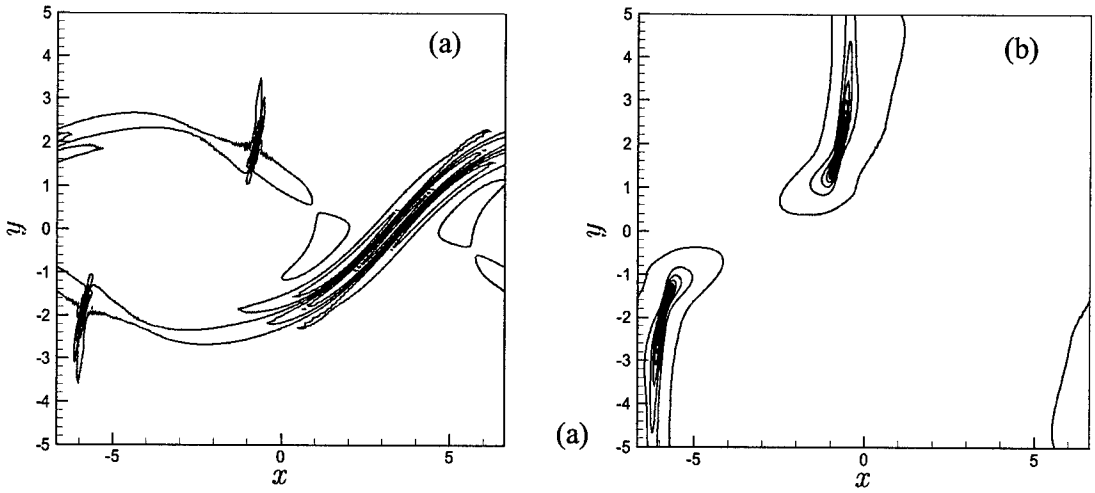

Figure3: Contours of velocity divergence in a $Ma = 0.8$ mixing layer. Shown are a) the contribution from thermal fluctuations, and b) the contribution from acoustic fluctuations. The shock is clearly visible in b).

Such simulations pose a strict demand on computational resources and numerical methods. A DNS code has been developed for this purpose. It incorporates a highly accurate B-spline collocation numerical technique. B-spline collocation methods offer consistent and high resolution regardless of grid distribution. Also, the functional expansion nature of spline methods provides an easy formulation procedure (Kwok & Moser, 2000).

Two-dimensional mixing layer simulations with convective Mach number of 0.4 and 0.8 were carried out to provide input for both the theory development and planned three dimensional simulations. In particular, the simulations provide critical information on the relative importance of incompressible, acoustic and thermal parts of the velocity, temperature, pressure and density fields. For a mixing layer with equal free-stream temperatures, we expect the thermal fluctuations to be less important than in the boundary layer, since the mean temperature gradients are small. Indeed, for a mixing layer with $Ma_c = 0.4$, the thermal velocity dilatation is much smaller than the acoustic dilatation, and the thermal and acoustic temperature fluctuations are of the same magnitude (Figure 2). Thus in this case, the thermal component of the flow is one order higher than shown in (1-4) for the boundary layer. This requires minor adjustment to the decomposition procedure.

The acoustic and nonacoustic dilatation and temperature fluctuations were determined as in the boundary layer starting from equation (7). This is remarkably successful, even at quite high Mach numbers. For example at $Ma_c = 0.8$, where in the two-dimensional mixing layer, eddy shocklets appear, this decomposition correctly isolates the shock dilatation in the acoustic field (Figure 3).

The primary interest is in the application of this analysis to three-dimensional mixing layers. New simulations to support this analysis are just beginning. To avoid problems associated with the extreme sensitivity of the mixing layer to initial conditions, and to facilitate detailed comparisons to incompressible mixing layers, the simulations are being started from fully turbulent initial conditions taken from the incompressible direct numerical sim-

ulations of Rogers & Moser (1994).

The decomposition procedure allows us to determine the turbulent and acoustic components of the flow, as well as the coupling terms that dynamically couple these two components together. After determining the decomposed fields, one can evaluate and visualize the coupling terms and their relation to the structures in the turbulent flow field. This will provide new (and possibly definitive) information on the mechanisms responsible for the observed reduction in growth rate of the mixing layer with increasing compressibility. By understanding the mechanisms of interaction, one will be able to make better approximations in developing models and turbulence prediction techniques, and contribute to the knowledge needed to develop turbulence modification technologies.

Other Information

Supported under this grant have been Stanislov Borodai and Wai-Yip Kwok, both graduate students in the TAM department at University of Illinois. The work supported here was presented at the 1997, 1998 and 1999 meetings of the Division of Fluid Dynamics of the American Physical Society, and three papers have resulted from this work (Borodai & Moser, 2000, Kwok, Moser & Jimenez, 2000, Guarini et al., 2000).

Acknowledgment/Disclaimer

This work is sponsored by the Air Force Office of Scientific Research, USAF, under grant/contract number F49620-97-1-0089. The views and conclusions contained herein are those of the author and should not be interpreted as necessarily representing the official policies or endorsements, either expressed or implied, of the Air Force Office of Scientific Research or the U. S. Government.

References

S. Borodai and R. D. Moser 2000 The decomposition of compressible boundary layer turbulence into acoustic and variable density parts, Submittd to *Theo. Comp. Fluid Mech.*

S. E. Guarini, R. D. Moser, K. Shariff & A. Wray 1999 Direct numerical simulation of a supersonic turbulent boundary layer at $M = 2.5$. To appear in *J. Fluid Mech.*

W. Y. Kwok, R. D. Moser and J. Jimenez 1999 A critical evaluation of the resolution properties of B-spline and compact finite difference methods. Submttedc to *J. Comput. Physics.*

T. Maeder, N. A. Adams, and L. Kleiser 2000 Direct simulation of turbulent supersonic boundary layers by an extended temporal approach. Submitted to *Journal of Fluid Mechanics.*

M. V. Morkovin 1961 Effects of compressibility on turbulent flows. In *Mecanique de la Turbulence,* ed. A. Favre, 367-380.

M. M. Rogers and R. D. Moser 1994 Direct simulation of a self-similar turbulent mixing layer, *Phys. Fluids A*, **6**, 902-923.

E. Spina, A. Smits, and S. K. Robinson 1994 The Physics of Supersonic Turbulent Boundary Layers. Ann. Rev. Fluid Mechanics, **26**, 287.

E. R. Van Driest 1951 Turbulent Boundary Layer in Compressible Fluids. J. Aeronaut. Sci., **18**, 145.

E. R. Van Driest 1956 On Turbulent Flow Near a Wall. J. Aeronaut. Sci., **23**, 1007.

G. P. Zank and W. H. Matthaeus 1991 The equations of nearly incompressible fluids. 1. Hydrodynamics, turbulence and waves. Phys. Fluids A, **3**, 69-82.

EFFECTS OF SHOCKS ON THE UNSTEADY HEAT TRANSFER IN A FILM-COOLED TRANSONIC TURBINE CASCADE

F49620-00-1-0024

Wing F. Ng
Professor of Mechanical Engineering
Virginia Tech, Blacksburg
(540) 231-7274
wng@vt.edu

Tom Diller
Professor of Mechanical Engineering
Virginia Tech, Blacksburg
(540) 231-7198
tdiller@vt.edu

Abstract
A research program is continued to study the effects of unsteady shock impingement on the film cooling heat transfer in transonic turbine blades. Fundamental physical understanding is gained of how these unsteady phenomena affect the heat transfer with and without film cooling. Thermal and aerodynamic conditions are set to simulate engine conditions. The experimental program is being conducted in the Virginia Tech heated, transonic turbine cascade wind tunnel. A shock wave is generated in a shock tube and passes into the cascade upstream of the blade row to simulate the interaction of a shock emerging from the trailing edge of an upstream nozzle guide vane on the downstream rotating blade row. A simple model has been developed based on new physical understanding of the unsteady process.

Progress
Tests were run using a blade instrumented with six *Vatell* HFM-7/L Heat Flux Microsensors, six high speed *Kulite* Pressure Transducers and six surface thermocouples. The steady-state values of both the Heat Transfer Coefficient and the Film Cooling Effectiveness were determined for all six measurement locations on the suction surface during each experimental run. Heat exchangers were used to heat the mainstream air and cool the film cooling flow to maintain realistic temperature ratios. Details of the blade instrumentation and film cooling hole design are shown in Figure 1 and Figure 2.

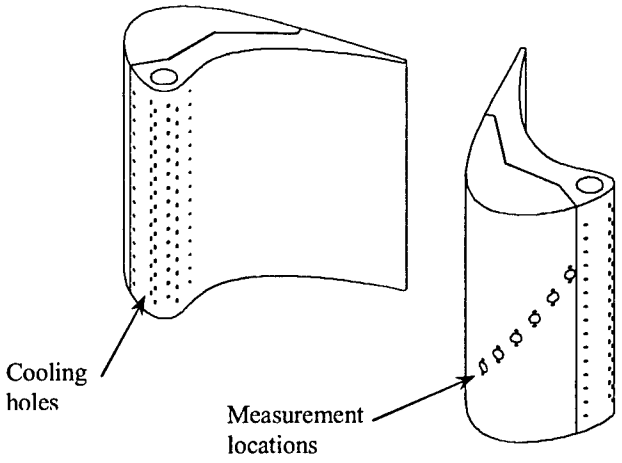

Figure 1: Fully Instrumented Blade Showing Sensors and Showerhead Film Cooling Configuration

The coolant scheme was inspired by a generic General Electric design. This film cooling scheme consists of six rows of coolant holes. The holes are 10.4 mm (0.041 inches) in diameter with a 91.4 mm (0.360 inch) spacing (an 8.78 s/D ratio). The coolant locations from suction side to pressure side are referred to as Suction Gill (SG), Suction Nose 2 (SN2), Suction Nose 1 (SN1), Nose (N), Pressure Nose (PN), and Pressure Gill (PG). The locations and descriptions are shown in Figure 2. In order to keep the coolant film layer from lifting off the surface of the blade, the coolant holes at locations SN1, SN2, N, and PN are all angled in the spanwise direction by 30°. The coolant holes at locations SG and PG are not angled in the spanwise direction but angled in the streamwise direction by 45° to the surface.

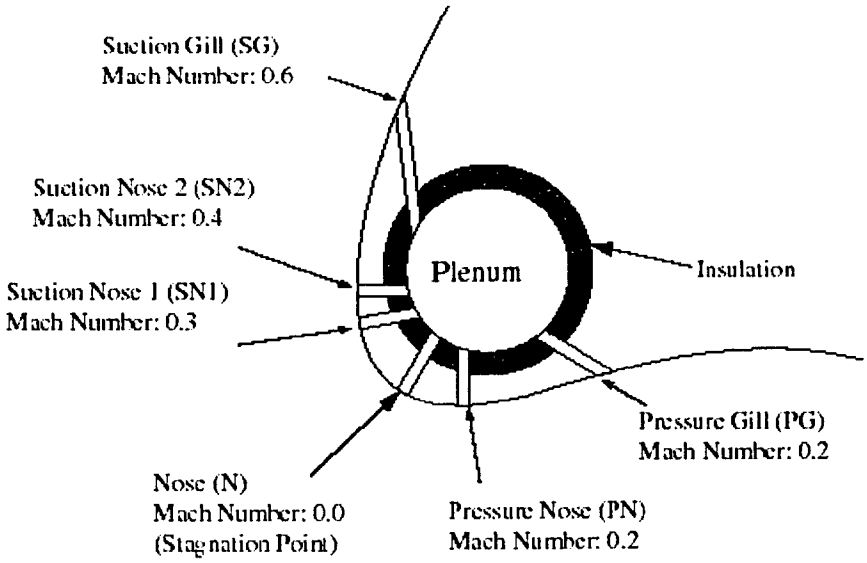

Figure 2: Details of Film Cooling Configuration

A wide variety of parameters were varied (shock strength, coolant pressure, initial level of heat flux) in order to determine the effect of the passing shock on the heat transfer coefficient and the film effectiveness. The shock strength was varied between a pressure ratio of 1.23 and 1.32, film cooling blowing ratios ($p_{coolant}/p_{mainstream}$) were varied between 1.04 and 1.2, and the initial level of heat flux was varied by changing the initial temperature of the flow for a single run in the range of 100°C and 35°C. By comparison of different traces it was found that the heat transfer coefficient is not influenced strongly by the passing shock. The majority of the effect of the shock is a transient change in the fluid temperature.

The heat transfer data was compared to different predictive models published in the literature. Of all the models evaluated, the best agreement could be found for a model assuming a constant heat transfer coefficient and predicting the heat transfer from a temperature variation induced by isentropic compression:

$$q_M = h \cdot T_M \quad \text{with} \quad T_M = T \cdot \left[\left(\frac{p + p'}{p} \right)^{\frac{\gamma-1}{\gamma}} - 1 \right]$$

where q_M is the predicted change in heat flux, h is the steady-state heat transfer coefficient, T_M is the predicted change in temperature, and p is the measured change in pressure due to the shock.

Figure 3 presents a comparison of heat flux data with results from this model. The prediction matches the measured heat flux in terms of magnitude and shape, although it slightly underpredicts the initial peak. The contribution of the variation of the heat transfer coefficient to the overall unsteady heat flux proves to be small compared to the unsteady heat transfer caused by the variation of temperature induced by the passing shock. Conversely, if the thermal boundary layer is assumed to be renewed by the shock, the initial peak in heat flux is overpredicted.

Additional tests were performed to determine whether a stronger shock would have any different effect on the boundary layer and heat transfer. The shock strength was increased from a pressure ratio of 1.23 to a pressure ratio of approximately 1.50, the maximum attainable with the current shock tube arrangement. Flow shadowgraphs showed no disturbance of the boundary layer and suction surface heat flux data showed no unexplained effects.

The next phase of this project will investigate the effects of high freestream turbulence on film cooling and blade heat transfer. An actively blown turbulence grid is being designed in an attempt to match engine combustor exit turbulence intensity and length scale. Time-resolved surface heat transfer and passage velocity measurements will be performed to investigate and quantify the effects of high intensity, large length-scale turbulence on surface heat transfer and to correlate velocity fluctuations with heat transfer.

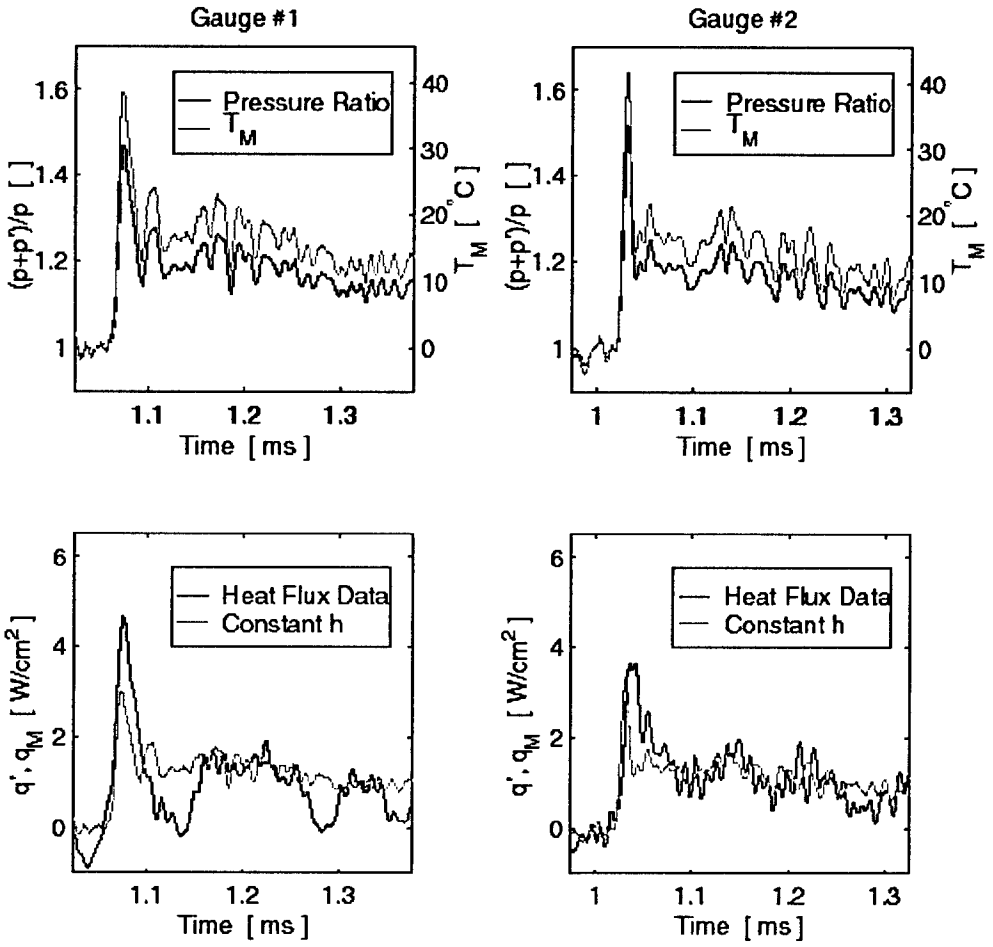

Figure 3: Comparison of Heat Flux Data with Moss' Assumption of a Constant Heat Transfer Coefficient (Experiment With Film Cooling).
Left Column: Gauge #1
Right Column: Gauge #2
Top Row: Pressure and Temperature Time Histories
Bottom Row: Comparison of Predicted and Measured Heat Flux

Transitions

Vatell Corp.

As part of the Virginia Tech research project from AFOSR, Vatell Corporation has press-fit Heat Flux Microsensors directly into the aluminum gas turbine blade models. The sensors measure both heat flux and temperature at the blade surface using sputtered thin films. Heat Flux is measured using the output of 300 thermocouple pairs arranged as a differential thermopile across a thin thermal resistance layer. Surface temperature is measured with an adjacent thin-film resistance element.

Testing, modeling and designing new sensors is being done cooperatively with Vatell Corp. A joint effort evaluating new calibration methods is continuing. Vatell Corporation markets Heat Flux Microsensors produced in its Thermateq facility in Blacksburg, VA. They continue to modify their production line to increase capacity and quality.

General Electric Aircraft Engines (GEAE)

Interaction with GEAE has continued with research discussions. The film cooling hole pattern was designed by GEAE based on their experience on state-of-the-art film cooling hole pattern on aircraft engine blades.

Wright Laboratory

Discussions have continued with Wright Laboratory personnel. Topics included measurement technology, film cooling experimentation and turbulence effects.

Personnel

Principal Investigators: Wing Ng and Tom Diller

Graduate Students:

Name	Degree	Source of Funding
Andrew Nix	PhD	ASSERT
John Evans	BS	AFOSR

Publications

Chapters of Books, Editor of Books or Proceedings

Diller, T. E., "Heat Flux," Ch. 15, in Mechanical Variables Measurement, Solid, Fluid, and Thermal, Ed. J. G. Webster, CRC Press, Boca Raton, Florida, 1999, pp. 15.1-15.15.

Conference Papers

Smith, D. E., Bubb, J. V., Popp, O., Diller, T. E., and Hevey, S. J., "A Comparison of Radiation Versus Convection Calibration of Thin-Film Heat Flux Gauges," in Proceedings of the ASME Heat Transfer Division -- 1999, HTD-Vol. 364-4, ASME, NY, 1999, pp. 79-84.

Smith, D. E., Bubb, J. V., Popp, O., Grabowski III, H. Diller, T. E., Schetz, J. A., and Ng. W. F., "An Investigation of Heat Transfer in a Film Cooled Transonic Turbine Cascade, Part I: Steady Heat Transfer," ASME Paper 2000-GT-202, 2000.

Popp, O., Smith, D. E., Bubb, J. V., Grabowski III, H. Diller, T. E., Schetz, J. A., and Ng. W. F., "An Investigation of Heat Transfer in a Film Cooled Transonic Turbine Cascade, Part II: Unsteady Heat Transfer," ASME Paper 2000-GT-203, 2000.

Publications Submitted

Holmberg, D. G. and Diller, T. E., "Simultaneous Heat Flux and Velocity Measurements in a Transonic Turbine Cascade," submitted to the ASME Journal of Turbomachinery.

Awards

Tom Diller · Fellow of the American Society of Mechanical Engineers
Who's Who in Science and Engineering, 5th Ed., 2000
International Directory of Distinguished Leadership, 2000 Ed.
Lexington Who's Who 1999/2000 Millenium Ed.

Acknowledgement/Disclaimer

This work was sponsored by the Air Force Office of Scientific Research, USAF, under grant/contract number F49620-00-1-0024. The views and conclusions contained herein are those of the authors and should not be interpreted as necessarily representing the official policies or endorsement, either expressed or implied, of the Air Force Office of Scientific Research or the US Government.

TURBINE ENGINE CONTROL USING MEMS FOR REDUCTION OF HIGH-CYCLE-FATIGUE

F49620-97-1-0521

Wing F. Ng
Chris Kraft Professor of Engineering
Virginia Tech, Blacksburg VA
(540) 231-7274
wng@vt.edu

Ricardo A. Burdisso
Professor of Mechanical Engineering
Virginia Tech, Blacksburg VA
(540) 231-7355
rburdiss@vt.edu
August 2000

Abstract
The High-cycle-fatigue (HCF) of compressor components is due to blade vibration and the accumulated damage of the fatigue stress cycle. One major source of such fatigue stress cycles is the forced response of the blade from unsteady aerodynamic excitation. In particular, the unsteady effect on the rotor blade loading due to the movement of the rotor through disturbances from the stationary wake of an upstream stator or inlet guide vane (IGV) had been shown to have a major effect on the HCF of compressor blades and the first stage fan rotor.

This research program uses trailing edge blowing (TEB) for wake-filling to minimize disturbances seen by the downstream rotor blades. The main objective is to experimentally demonstrate in realistic environments the potential of the active flow control system to re-energize the wakes to improve the HCF life of fan rotors. Because the flow is 3D and non-uniform along the blade span, the amount of TEB air must be carefully tailored, from the hub to the tip on the stator blade, to achieve the desired effect of minimizing the stator wake velocity defect along the entire blade span. To accomplish this, MEMS-based micro-valves are used to control the blowing of each individual hole at the trailing edge.

Progress
The experimental efforts are being performed on three unique facilities. The first facility consists of a small high-speed turbofan simulator, which is used to test active flow control concepts. The second setup is a turbofan engine experiment, which is used to study TEB in a realistic environment. The third facility is a high speed single stage compressor at the Wright Laboratory, which is used to investigate the effect of the TEB on the blade HCF life.

Simulator Experiments: Active Control of Wake Filling Using Microphone Error Sensors
The active flow control experiments were performed in the high-speed turbofan simulator shown

in Fig. 1. The first set of experiments consisted of using as error signal the differences between a Pitot-Static probe measuring the free stream flow and Pitot-Static probes measuring the wake velocities. Complete filling of the wakes resulted in a reduction in sound power level of 4.4 dB. These experimental tests demonstrated the potential of using active control for optimum re-energizing of the wakes. The drawback of this sensing is that it is an intrusive sensor that generates wakes in itself. Thus, one of the key tasks undertaken was to develop non-intrusive acoustic sensing to infer the filling of the wakes by monitoring the noise due to the strut wake-rotor interaction effect. The acoustic sensing approach consisted of placing microphones flush mounted on the casing of the simulator in between each strut and the rotor as shown in Fig. (1). The microphones sense the acoustic signature as the blades pass and cut the wakes from the struts generating strong tonal components at the BPF and its harmonics. Minimizing the BPF signals from the microphones will result in the optimum re-energizing of the wakes. Two active control schemes were developed in conjunction with the microphone sensing approach.. In the first control scheme only the magnitude of the BPF tone was used to generate the error signal for an optimal controller. However, this approach has a main drawback, which is the slow system response (> 40 seconds to converge). The second control scheme consisted of using both the magnitude and phase of the BPF tone to implement a PID feedback controller to overcome the slow convergence problem. This control approach was tested in the simulator. The time histories of the control and the magnitude of the error signals were recorded and they are shown in Fig. (2). This figure shows the convergence process after the system is

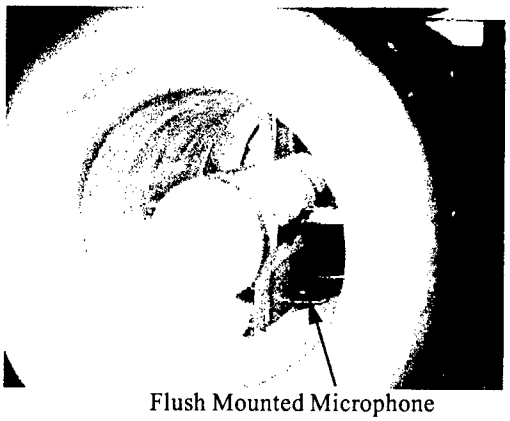

Figure (1): High-speed turbofan simulator with four struts used in active flow control experiments.

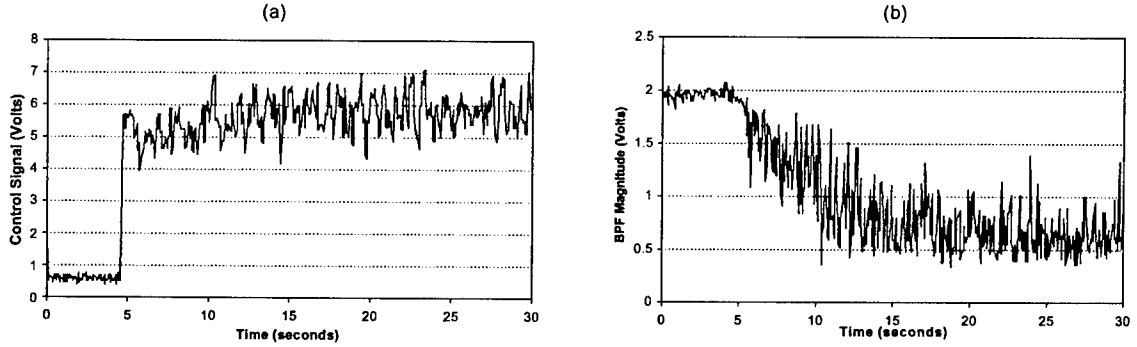

Figure (2): Time histories of (a) control signal and (b) BPF tone magnitude.

turned on at about 5 second. It can be found that the control signal converges to the steady state of 5.5 Volts in about 4 ~ 5 seconds. The BPF power is significantly reduced in about 4 seconds while completed minimization is achieved in 10 seconds. The sound power level was reduced by 4.9 dB which is very close to the 4.4 dB obtained using Pitot probe as error sensors. Based on the comparison of the results using Pitot probes and the microphone sensors, it was demonstrated

that the feasibility of the acoustic sensing approach to eliminate the need for intrusive flow sensors to successfully fill the wakes and, thus, reduce the unsteady loading experienced by the blades.

Engine Experiments: Setup: Wake Filling Experiments on a Turbofan Engine

The simulator is an excellent test bed to efficiently evaluate, in terms of cost and time, concepts for wake management. However, this setup is not realistic in terms of the characteristics of the wakes. A series of experimental investigations were conducted to determine if the use of TEB in inlet guide vanes (IGV) could eliminate the low pressure and velocity regions (deficits) in the viscous wakes shed by the vanes for axial locations of practical stator-rotor spacing. Steady state and unsteady aerodynamic measurements were performed in a running Honeywell F109 turbofan engine (Fig. 3). The vane was designed without camber to avoid an off-design condition of the F109 engine. The vanes have practical chord and thickness relative to the fan blades. The trailing edge of the vane contains discrete holes at the axial centerline, from tip to hub, for flow control.

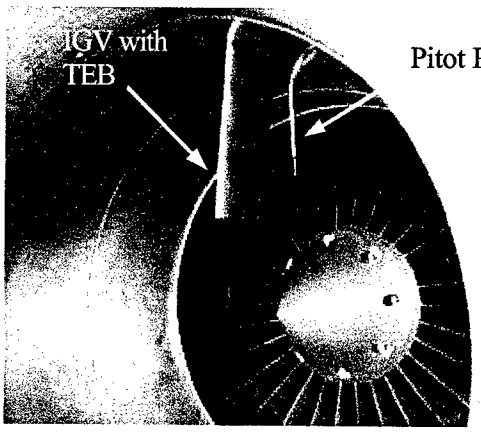

Figure (3): Honeywell F109 turbofan engine and single IGV with TEB.

The steady-state experiments were conducted with the IGV 3.5 rotor chords upstream of the rotor in order to eliminate unsteady flow interactions. Pitot-static surveys were taken at axial locations between 0.1 to 0.75 IGV chords downstream of the vane for both the no blowing and trailing edge blowing cases. Experiments were performed at fan speeds between 65% and 100% maximum speeds. Results show that complete span and pitchwise wake filling is obtained at and above 0.5 chord lengths downstream of the vane, near complete filling is obtained at less than 0.5 chords. The mass flow requirement for complete span and pitchwise wake filling is only 0.03% of the engine mass flow per IGV for each fan speed tested. These results show that the use of TEB is effective and feasible in reducing the viscous forcing function of upstream stators.

The unsteady experiments were conducted with the IGV placed 0.45 fan chords upstream of the fan. A high-frequency total pressure probe was placed between the IGV and rotor and indexed circumferentially to acquire the unsteady wake profile. Experiments were performed for both subsonic and transonic fan speeds. No blowing results show that the potential flow field propagating upstream from the subsonic fan reduces the mean IGV wake compared to the steady experiments where the IGV was isolated, see Fig. 4(a). This proved to have a beneficial effect on flow control by reducing the required mass flow by 20% for complete wake filling, Fig. 4(b).

No blowing results for transonic fan speeds show that the IGV wake is adversely affected by the shocks propagating upstream of the rotor, Fig. 5(a). The IGV and fan shock interaction causes the boundary layer on the IGV to separate further upstream when compared to subsonic fan

speeds. However, TEB results showed that complete wake filling could be achieved with only a 10% increase in required mass flow when compared to the steady results, Fig. 5(b).

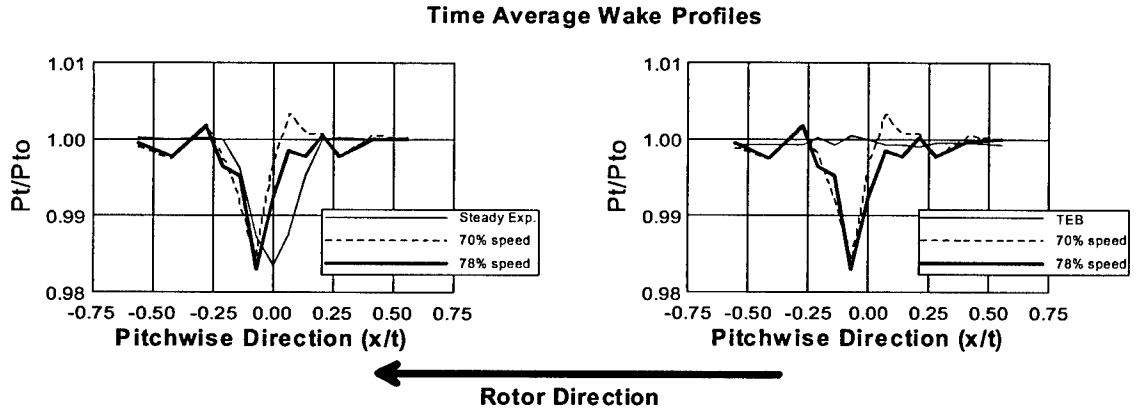

Figure (4). Unsteady Subsonic Fan Results

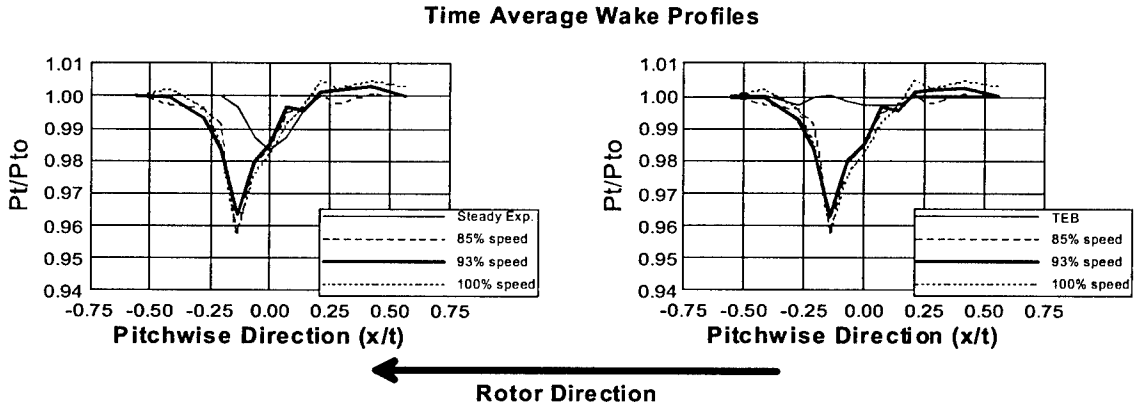

Figure (5). Unsteady Transonic Fan Results

These experiments show that the use of TEB to reduce unsteady stator-rotor interaction is effective for both subsonic and transonic rotor speeds at practical component spacing. Furthermore, the mass flow required for complete wake filling is only 0.03% of the engine mass flow per IGV.

Compressor Experiments: Wake Filling-Rotor Strain Measurement

The previous research tasks addressed critical issues for the practical implementation of the active TEB technique. However, the main goal of the technique is to reduce the HCF damage due to the wake induced unsteady forcing function on the blades. Thus, experiments were conducted to monitor the strain on the blades of a compressor with and without TEB. The facility for these experiments is the high-speed compressor at the Wright Laboratory in the Compressor Aero Research Lab (CARL). This highly loaded transonic compressor rig at CARL is representative of modern compressor design and features on-rotor strain measurement capability. A configuration with 12 IGVs was chosen with an IGV-to-rotor spacing of 0.26 IGV chords. Flow to seven blowing holes per IGV was controlled by four independent lines (see Fig. 6). A rig-mounted manifold array ensured that the flow from each of the four lines was distributed equally among all 12 IGVs.

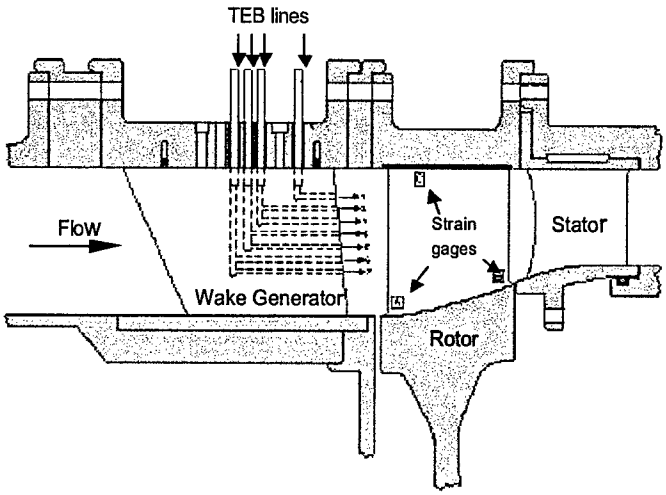

Figure (6): Flowpath of transonic compressor configured for wake generator TEB and rotor strain measurement.

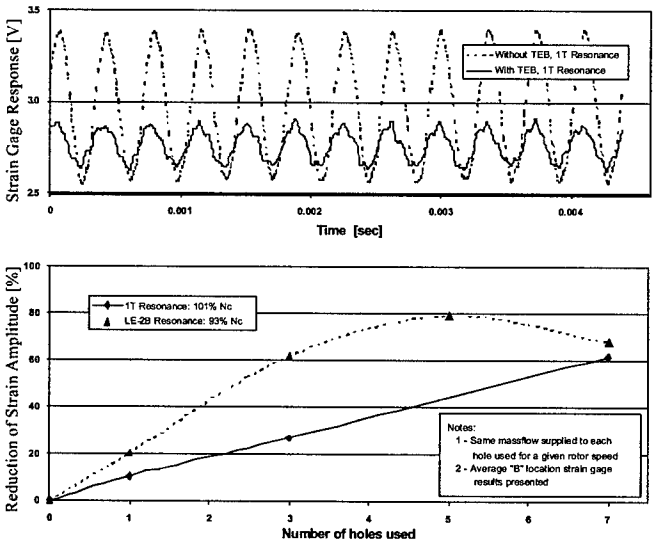

Figure (7): Reduction of resonant rotor response using trailing edge blowing for ensemble-average of 25 revolutions.

Experiments were conducted at the CARL facility in April of 2000. Data was collected with and without uniform full-span TEB at three rotor speeds, two of which excited rotor vibration modes at resonance. In addition, the effect of partial-span TEB was evaluated by selectively shutting off sectors of blowing holes by means of the four independent lines. The primary unsteady measurements, recorded by a high-speed analog tape system, included the rotor strain gage signals and acoustic data from four casing-mounted microphones. Steady measurements of the compressor's aero performance and the four TEB line massflows were recorded.

Substantial reductions of the rotor blade vibration were achieved at several compressor operating conditions by applying TEB. Though the 12 IGVs caused a strong resonance of the first torsional (1T) mode at 13,630 rpm (101% Nc), the average peak-to-peak rotor strain amplitude was reduced by over 60% with full-span TEB applied (see Fig. 7). The total TEB massflow used for this case was less than 0.8% of the compressor core flow (0.06% per IGV). The second leading edge bending (LE-2B) mode, excited by a 12-IGV harmonic at 12,550 rpm (93% Nc), was reduced by nearly 80% using less than 0.6% of the core flow for TEB. In addition, preliminary evaluation of the casing microphone data suggests that the devices may be useful as non-intrusive sensors for an active TEB control system.

While large reductions of rotor vibration were achieved in a modern transonic compressor using TEB, limitations of the available air supply prevented optimization of the TEB line flow rates. Each line flow rate was scaled according to results of the steady wind tunnel experiments mentioned above. Since the flow rates were not optimized in the unsteady compressor

environment, which includes strong IGV-rotor interaction and shock effects, further reductions in rotor vibration may be achievable. Future work may include such optimization of the TEB line massflows, and their distribution, at one or more compressor operating conditions.

Future efforts will also focus on the development of an active TEB control system, capable of automatically optimizing TEB for a wide range of compressor operating conditions, using non-intrusive error sensors such as the casing microphones.

Technology Transitions

Extensive interaction between the Virginia Tech team and personnel at the Wright Laboratory in the Compressor Aero Research Lab (CARL) was held to coordinate the rotor strain measurement effort. Numerous technical discussions were held with Dr. Copenhaver of the CARL to define the experiments performed.

Personnel

Principal Investigators:	Ng, Rappaport, Burdisso
Ph.D. Students (5):	J. Feng, J. Kozak, T. Bailie, C. Kontogeorgokis, B. Song
MS Student:	N. Rao, C. Carter

Publications

1. N. Rao, J. Feng, R. Burdisso, and W. Ng, "Experimental Demonstration of Active Trailing Edge Blowing Control to Reduce Unsteady Stator-Rotor Interaction." (Accepted).
2. J. Feng, R. Burdisso, and W. Ng, "Active Flow Control Using Microphone Sensors to Reduce Fan Noise," 6th AIAA/CEAS Aeroacoustics Conference, AIAA-00-1993, Mauni, Hawii, 12-14 June 2000.
3. T. Bailie, W. Ng and W. Copenhaver, "Wake-Filling and Reduction of Rotor HCF Using Stator Edge Blowing," 36th AIAA/ASME/SAE/ASEE Joint Propulsion Conference, AIAA-00-3101, Huntsville, Alabama, 7 July, 2000.
4. J. Kozak and W. Ng, "Investigation of Unsteady IGV and Transonic Fan Interactions on Trailing Edge Blowing Flow Control", 4th ASME International Gas Turbine, New Orleans, LA, Submitted for review, July 2000.
5. J. Kozak and W. Ng, "Investigation of Unsteady Stator/Rotor Interactions on Stator Trailing-Edge Blowing in a F109 Turbofan Engine", 36th AIAA/ASME/SAE/ASEE Joint Propulsion Conference, AIAA-00-3103, Huntsville, Alabama, 7 July 2000.
6. J. Kozak and W. Ng, "Investigation of IGV Trailing-Edge Blowing in a F109 Turbofan Engine", 36th AIAA/ASME/SAE/ASEE Joint Propulsion Conference, AIAA-00-0224, 38th Aerospace Science and Exhibit, Reno, NV, January 2000.

Acknowledgement/Disclaimer

This work was sponsored by the Air Force Office of Scientific Research, USAF, under grant/contract number F49620-97-1-0521. NASA Glenn RC, NSF, and the Department of Mechanical Engineering at Virginia Tech also provided partial support. The views and conclusions contained herein are those of the authors and should not be interpreted as necessarily representing the official policies or endorsements, either expressed or implied, of the Air Force Office of Scientific Research or the US Government.

TURBULENCE MODELING USING TURBULENT POTENTIALS

F49620-00-1-0033

Blair Perot
Department of Mechanical & Industrial Engineering
University of Massachusetts, Amherst

Abstract
The objective of this work is to continue the development of the turbulent body-force potential model. The turbulent potential model (Perot, 1999) is a new type of RANS model which has a cost comparable to two equation models but a predictive accuracy closer to Reynolds Stress Transport models. Of particular interest in this work is the model's abilities to predict rotating flows and the transition to turbulence.

ROTATION

Like Reynolds stress transport models, the turbulent body-force potential model has the attractive property of explicit production-like terms that depend on the system rotation rate. These terms are sufficient to make the model predict the right qualitative behavior in rotating channel flow, however the predictions are not quantitatively accurate. The deficiency lies in the fact that system rotation has secondary effects on turbulence that must be accounted for. In particular, rotation reduces the rate of turbulence dissipation, and enhances return to isotropy. The plan is to alter the dissipation equation, and return to isotropy model to account for these secondary rotation effects. This will be done by comparing the model with DNS simulations of isotropic decaying turbulence and sheared homogeneous turbulence in the presence of rotation. The model will then be applied to rotating channel flow and swirling pipe flow.

The effect of system rotation on the dissipation rate is accounted for in the turbulent potential model by altering the destruction of dissipation term. This is the only term that can be changed in rotating isotropic decaying turbulence. The model constant in that term is now made a function of the non-dimensional frame-invariant rotation rate, $C_{\varepsilon 2} = C^0_{\varepsilon 2}(1.0 + A_1 \hat{W}\frac{k}{\varepsilon})/(1.0 + A_2 \hat{W}\frac{k}{\varepsilon})$ where $\hat{W} = |\omega + 2\Omega|$ is the frame indifferent rotation rate. The constant A_1 is set to 0.04, which matches the model of Bardina *et. al.* and the experimental data of Wigeland & Nagib, at low rotation rates. The constant A_2 is set to 0.025, which increases $C_{\varepsilon 2}$ to a value of 3.0 at very high rotation rates. Note that this model change also affects non-rotating flows through the vorticity in the frame indifferent rotation rate. Tests of non-rotating channel flow showed little difference due to this model enhancement. The effect of this model enhancement on isotropic decaying turbulence subject to rotation is shown in figure 1. This figure shows the decay of turbulent kinetic energy as a function of time. The symbols are DNS data taken from the paper of Speziale, the solid line is the present model prediction, and the dashed line is standard model prediction with no rotation adjustment.

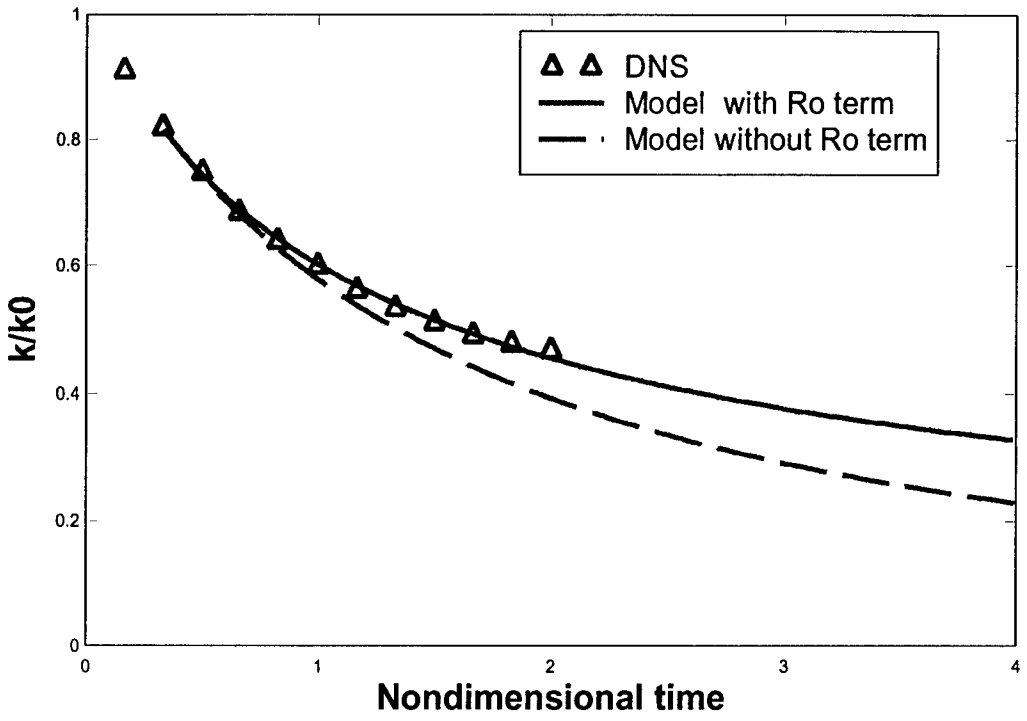

Figure 1. Decay of isotropic rotating turbulence. $\mathrm{Ro} = \varepsilon/\Omega k = 0.014$, $\mathrm{Re} = k^2/(\nu\varepsilon) = 260$. Symbols are DNS data from Speziale. Solid line is the proposed model. Dashed line is the standard epsilon equation without any modification for rotation.

The model predictions for rotating homogeneous shear flow (with a shear rate S) are shown in Figure 2. This figure shows the turbulent kinetic energy as a function of time for three different rotation rates, Ω. Symbols are the LES data of Bardina, Ferziger & Reynolds for $\Omega/S = 0.5$ and $\Omega/S = -0.5$, and the DNS data of Matsumoto *et. al.* for the case of homogeneous shear with no rotation. The lines are the model predictions. The model agreement is quite good and demonstrates the model's ability to predict both stable and unstable solutions at different rotation rates. The stability boundaries of the model are very close to the theoretical stability boundaries of $-0.5 < \Omega/S < 0.5$. The form of the return to isotropy model was not altered to obtain these results, but the modified rotation rate, $\hat{W} = |\omega + 2\Omega|$, was used where vorticity normally appears in the model. This has the added benefit of making the model frame indifferent.

The next tasks will be to look at the model's behavior in rotating channel flow where rotation is aligned with the vorticity, and swirling pipe flow where the rotation is perpendicular to the vorticity. It is anticipated that these two test cases will provide significant insight into the models ability to predict practical rotating flows.

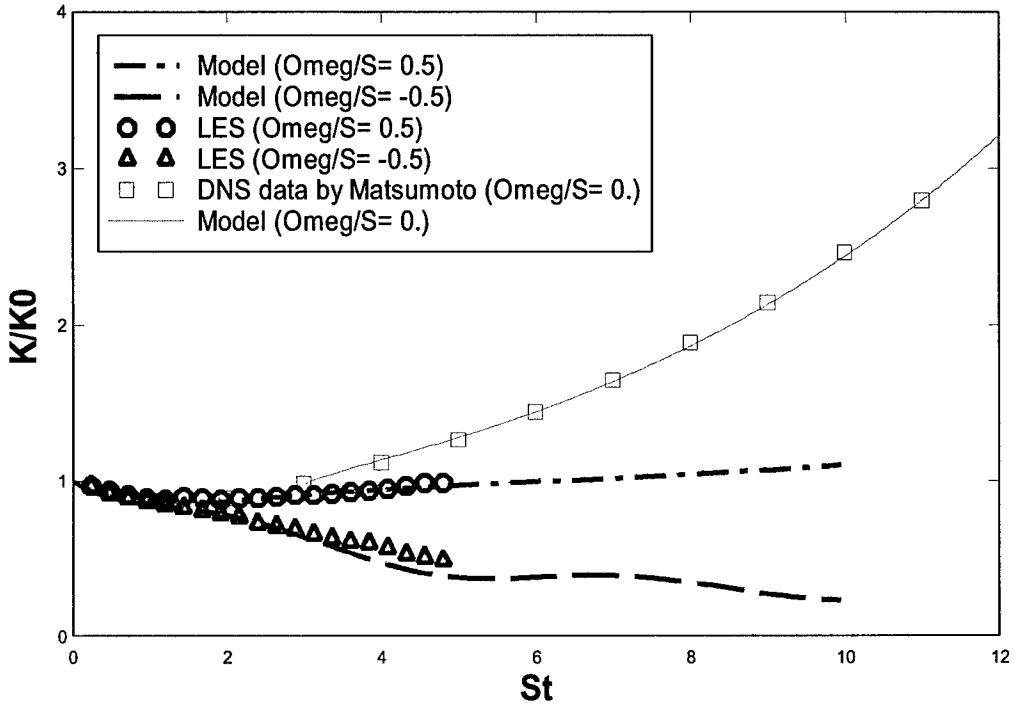

Figure 2. Rotating homogeneous shear flow for three different rotation rates. Turbulent kinetic energy as a function of time. Symbols are DNS and LES data, and lines are the model predictions. From top to bottom $\Omega/S = 0, 0.5, -0.5$.

TRANSITION

A very desirable property for one-point closures is the ability to predict both natural and bypass transition. While transition is a very different phenomena from fully developed turbulence, it is possible for RANS models to predict behavior qualitatively similar to bypass transition. Far fewer RANS models can "transition" from very low levels of initial turbulence (so called natural transition). Initial test of the turbulent potential model shown the ability to qualitatively reproduce natural and bypass transition and also relaminarization. More importantly, and unique to turbulent potential model, is the ability to externally control those transition processes through a constant in the model. This aspect of the project focuses on determining what is the appropriate value for the transition constant in various flow situations, and determining to what extent the constant is affected by external flow conditions such as geometry, viscosity, and free-stream turbulence levels.

Figure 3 shows the models predictions of natural transition in a zero-pressure gradient boundary layer. The figure shows the coefficient of friction as a function of the Reynolds number based on downstream position, Re_x. Both the laminar theory ($Cf = 0.664/Re_x^{1/2}$) and the turbulent correlation $Cf = 0.027/Re_x^{1/7}$ are plotted. The turbulent correlation assumes that the turbulent boundary layer starts at the transition Reynolds number of $3x10^6$. The symbols are the transition data of Schubauer & Klebanoff for a free-stream turbulence intensity of 0.03% (natural transition) extracted from the paper of Abu-Ghannam & Shaw. The lines show the model predictions for the coefficient of friction for three different values of the transition constant. A value of 0.008 appears to give good predictions. The model shows some overshoot in the coefficient of friction as the flow becomes fully turbulent. This is thought to be due to the use of the boundary layer approximation for these tests. Nearly parallel shear flow is probably not a very good approximation during the later stages of transition to turbulence where the boundary layer grows very quickly.

Future work will evaluate the model's ability to predict bypass transition and relaminarization. It will also look at bypass transition in favorable and adverse pressure gradient boundary layers, and the natural transition of planar wakes and jets.

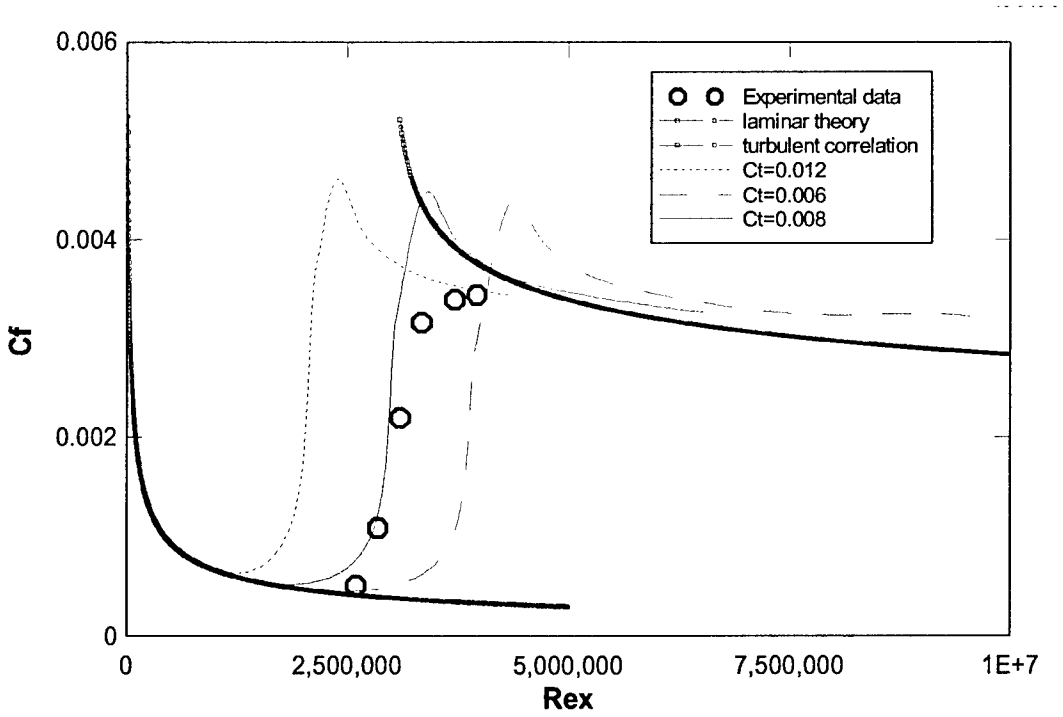

Figure 3. Natural transition to turbulence in a zero pressure-gradient boundary layer. Symbols are the data of Schubauer and Klebanoff. Thick lines are the laminar theory and turbulent correlation. Thin lines are the turbulent potential model predictions for various values of the transition constant.

Acknowledgement/Disclaimer
This work was sponsored by the Air Force Office of Scientific Research, USAF, under grant number F49620-00-1-0033. The views and conclusions contained herein are those of the authors and should not be interpreted as necessarily representing the official policies or endorsements, either expressed or implied, of the Air Force Office of Scientific Research or the U.S. Government.

References

1. B. J. Abu-Ghannam and R. Shaw, Natural Transition of Boundary Layers – the Effects of Turbulence, Pressure Gradient, and Flow History. International Journal of Mechanical Engineering Science, 1980, 22 (5), 213-228.

2. J. Bardina, J. H. Ferziger and W. C. Reynolds, Improved Turbulence Models Based on Large Eddy Simulation of Homogeneous, Incompressible Turbulent Flows, Stanford University Tech. Report TF-19, 1983, Stanford University, CA.

3. J. Bardina, J. H. Ferziger and R. S. Rogallo, Effect of Rotation on Isotropic Turbulence; Computation and Modelling. Journal of Fluid Mechanics, 1985, **154**, 321-336.

4. A. Matsumoto, Y. Nagano, and T. Tsuji, Direct Numerical Simulation of Homeogeneous Turbulent Shear Flow, 5th Symposium on Computational Fluid Dynamics, Tokyo, 1991, 361-364.

5. J. B. Perot, Turbulence Modeling Using Body Force Potentials, Physics of Fluids, 1999, **11** (9), 2645-2656.

6. G. B. Schubauer and P. S. Klebanoff, Contributions on the Mechanics of Boundary-Layer Transition, NACA Tech. Report 1289, 1955, 853-863.

7. C. G. Speziale, Turbulence Modeling in Noninertial Frames of Reference, Theoretical and Computational Fluid Dynamics, 1989, **1**, 3-19.

8. R. A. Wigeland and H. M. Nagib, Grid Generated Turbulence With and Without Rotation about the Streamwise Direction. Illinois Institute of Technology Fluids and Heat Transfer Report 78-1, 1978, Illinois Institute of Technology, Chicago, IL.

Personnel Supported

Blair Perot	Professor, University of Massachusetts, Amherst
Amitahb Bhattachayra	Graduate Student, University of Massachusetts, Amherst

Awards Received

College Outstanding Advisor Award – May 2000.

APPLICATION OF LARGE EDDY SIMULATION TO COOLING AND FLOW PROBLEMS IN AEROPROPULSION SYSTEMS

AFOSR GRANT F49620-00-1-0229

Richard H. Pletcher
Department of Mechanical Engineering
Iowa State University

Introduction

Better methods are needed for predicting features of turbulent flows in certain critical components of gas turbine engines. With the present state of computer hardware, design codes are usually restricted to the use of relatively simple turbulence models. Unfortunately, flows in gas turbine engines are not simple and an accurate turbulence model for film cooling flows and flows undergoing transition, in particular, have been very illusive.

Earlier work has led to the development of a capability to do large-eddy simulations of compressible flows with significant heat transfer. It is now proposed to apply this capability based on a compressible form of the filtered Navier-Stokes equations to flows in configurations characteristic of those occurring in critical turbine components of aeropropulsion systems. The objective of the research is to expand the capabilities of LES technology to contribute to the solution of urgent problems in propulsion systems and to contribute to the physical understanding of such flows. The long-term goal is to advance LES technology to the point where it is effective for computing realistic flows in a rotating, multistage turbomachine. First, however, some building block simulations need to be carried out for a single blade element.

The first task will be to address cooling flows in turbines, both the film cooling of external blade surfaces and the complex flows in internal passages. The design goals of high specific power and thrust and low specific fuel consumption have been reached, in part, by an increase in turbine inlet temperature. Present performance has been enabled by efficient cooling schemes for turbine blades. Future improvements in engine efficiency will place even greater demands on blade cooling procedures. Accurate numerical prediction schemes for film cooling and turbine flows in general have been very elusive, particularly under conditions of high levels of freestream turbulence.

Approach

The numerical formulation used in the research is based on a finite volume discretization of the Favre-filtered compressible Navier-Stokes equations. Significant levels of heat transfer occur in the gas flows of interest and the compressible formulation enables the effects of property variations to be taken into account. The scheme solves for the primitive variables of velocity, pressure, and temperature in a fully coupled manner. Two codes have been used recently. One employs the LU-SGS implicit scheme [1,2] and has been optimized for parallel implementation using the message passing interface (MPI). The other employs a vectorized version of the strongly implicit procedure (SIP) [3,4].

Central difference representations have been favored although an option to use an upwind scheme exists in the SIP code. Low Mach number preconditioning [5] is used to enable solutions to be obtained efficiently at the low Mach numbers arising in many applications of interest.

Progress to Date

The project will consider both blade external film cooling as well as cooling flows in internal blade passages. Work has been initiated on both configurations. Propulsion systems usually contain rotating components and the rotation can exert significant influences on the structure of turbulence and, consequently, transport processes in rotating components. Large eddy simulations are underway to assess the scope of these influences, particularly as they influence heat transfer. Flows with rotation present a considerable challenge to solution methods based on the Reynolds-averaged Navier-Stokes equations. Experimental measurements are also more difficult to obtain due to the rotation.

The simplest rotating flow geometry that bears a resemblance to applied configurations occurs in a straight channel. Several investigators have applied DNS and LES to a rotating channel containing an incompressible, constant property flow (see especially [6]), but less is known about the influence of rotation on heat transfer. Figure 1 shows the geometry being considered for the rotating channel flow. The channel is rotating counterclockwise about the z direction. The upper surface becomes the destabilized (pressure) surface and the lower wall becomes the stabilized (suction) surface. The conservation equations were solved in a reference frame rotating with the channel by adding a term accounting for the Coriolis force. The centrifugal force associated with the rotation was absorbed into the pressure term. The results to follow were obtained for a rotation number ($Ro = 2\Omega\delta/U$) of 0.144 where δ is the channel half-height and U is the bulk velocity. The Reynolds number was 11,200 based on the hydraulic diameter and bulk velocity, and uniform heat flux heating and cooling was employed. The simulations were run with a domain size of $2\pi \times 2 \times \pi$ with a grid that contained $48 \times 64 \times 48$ control volumes in the x, y, and z directions, respectively. Earlier work indicated that without rotation this grid provided results in good agreement with DNS and experimental data. The grid point closest to the wall was generally located at $y^+ < 1$.

When property variations are taken into account, flows with heating or cooling do not attain a fully developed state. However, experiments show that far downstream of the entry region, a slowly evolving quasi-developed state exists. Earlier work [2] demonstrated that for laminar flow with uniform heat flux conditions, results using step periodic boundary conditions can match flow conditions that evolve from variable property developing flow. The step periodicity is based primarily on the use of streamwise periodicity of the mass flux, and the imposition of a step in temperature between inflow and outflow based on an energy balance that utilizes the heat flux imposed and the mass flow rate.

Calculations were performed for four different cases: no heat transfer, low heating, high heating and high cooling. The isothermal results for the mean velocity are compared

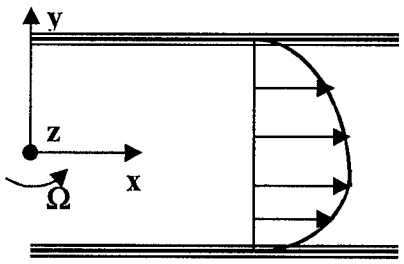

Figure 1: Coordinate system for rotating channel flow.

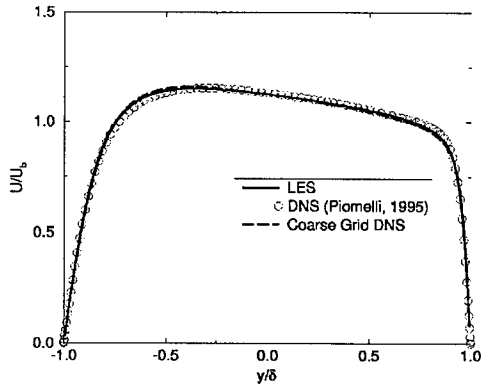

Figure 2: Streamwise velocity distribution, rotating channel flow.

with the DNS results of Piomelli and Liu [7] in Fig. 2. The simulations were obtained with the dynamic SGS model (labeled LES) and with no model (labeled coarse grid DNS). For the mean velocity plotted in global coordinates, the use of a SGS model had little effect. Two key features of flows with rotation are the skewing of the velocity distribution toward the stabilized wall due to the Coriolis force and the enhancement and suppression of turbulence on the destabilized and stabilized sides, respectively. Alteration of the turbulence structure is accompanied by large-scale vortical structures.

Figure 3 shows profiles of streamwise velocity for various heating conditions. The velocity has been nondimensionalized using the average of the friction velocity on both walls. The curves are labeled LH for low heating, HH for high heating and HC for high cooling. Wall temperature differences are given in Table 1. The bulk temperature was approximately 293K. Use of density scaling would reduce the spread in the curves significantly. Figure 4 shows the distribution of the streamwise rms velocity. Notice that the peaks near the upper (destabilized) wall are 2-3 times larger than near the lower (stabilized) wall. The ratio of the two peak values is seen to be larger for the high heating case than the high cooling case. The distribution of the v rms velocity is shown in Fig. 5. Here we observe a single peak value skewed toward the pressure side. The resolved Reynolds stress distributions are shown in Fig. 6. These turbulent stresses are seen to be much larger near the top wall than near the bottom wall. In fact, the stresses near the top wall are on the order of 5 times larger than near the bottom wall. A distinct tendency to for the flow to laminarize near the stabilized wall can be observed. Figure 7 shows the distribution of the resolved Reynolds heat flux. Compared to the resolved stresses, the resolved heat flux distribution is more nearly symmetric about the channel centerline, the ratio of the magnitudes of the peaks near each wall being approximately a factor of 2. A summary of several wall parameters including skin-friction coefficient and Nusselt number are given in Table 1. It is interesting that the ratio of the Nusselt numbers for the two walls is larger (on the order of 3) than the ratio of the skin-friction coefficients (on the order of 2.5).

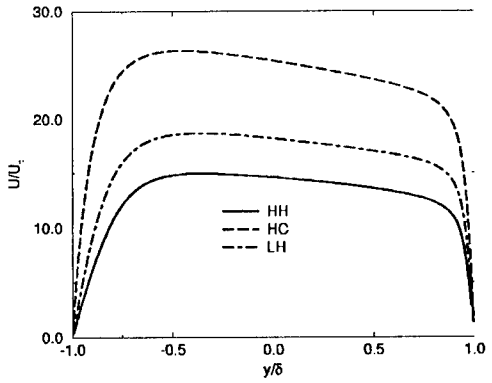

Figure 3: Streamwise velocity distribution, rotating flow with heating and cooling.

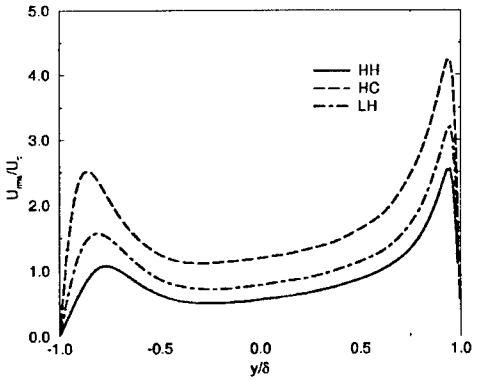

Figure 4: Distribution of u_{rms}, rotating flow with heating and cooling.

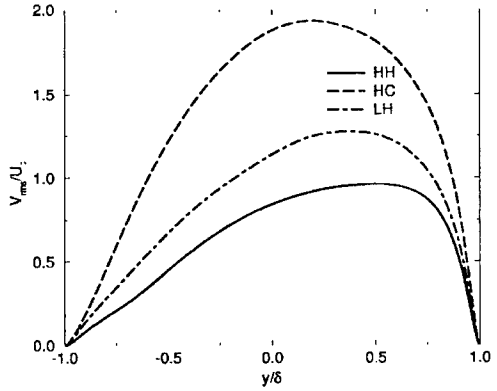

Figure 5: Distribution of v_{rms}, rotating flow with heating and cooling.

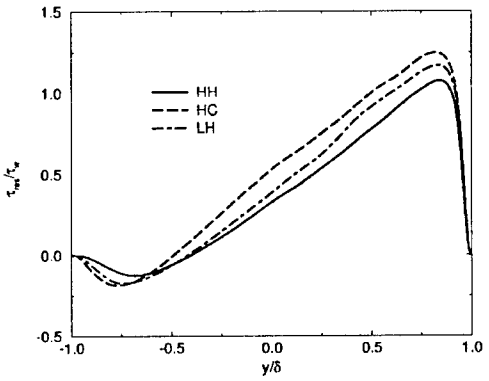

Figure 6: Distribution of resolved stress, rotating flow with heating and cooling.

Table 1. Summary of Wall Parameters, Rotating Flow

Case	$u_{\tau,top}$	$u_{\tau,bot}$	$\frac{\Delta T}{T_b}$	Nu_{top}	Nu_{bot}	$C_{f,top}$	$C_{f,bot}$
Low Heating	0.0701	0.0470	0.0585	60.04	20.70	0.00551	0.00228
High Heating	0.0889	0.0759	0.594	66.29	18.47	0.00587	0.00279
High Cooling	0.0686	0.0263	0.471	62.14	18.57	0.00544	0.00212

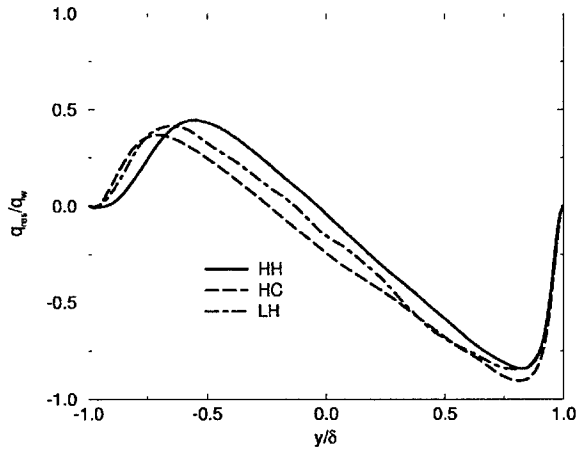

Figure 7: Distribution of resolved Reynolds heat flux, rotating flow with heating and cooling.

Future Plans

The evaluation of rotation effects, particularly as they influence cooling in internal blade passages, will continue and will include channels with rib-roughened walls. Additional rotation rates will be considered in order to assess trends and to determine if the simulations are able to predict complete suppression of turbulence on the stabilized wall as observed experimentally. The LES of film cooling configurations at realistic temperature levels will be a major part of future research. Challenges include treatment of multiple fluid streams, complex geometry, and high levels of freestream turbulence. Comparisons will be made with available experimental data (for example, [8-12]).

Acknowledgment/Disclaimer

This work was sponsored in part by the Air Force Office of Scientific Research, USAF, under grant number F49620-00-1-0229. The views and conclusions contained herein are those of the authors and should not be interpreted as necessarily representing the official policies or endorsements, either expressed or implied, of the Air Force Office of Scientific Research or the U. S. Government.

References

1. L. D. Dailey and R. H. Pletcher, "Evaluation of Multigrid Acceleration for Preconditioned Time-Accurate Navier-Stokes Algorithms," *Computers and Fluids*, Vol. 25, No. 8, pp. 791-811, 1996.

2. L. D. Dailey and R. H. Pletcher, Large Eddy Simulation of Constant Heat FluxTurbulent Channel Flow with Property Variations, AIAA Paper No. 98-0791, 1998.

3. K.-H. Chen and R.H. Pletcher, "Primitive Variable Strongly Implicit Calculation Procedure for Viscous Flows at All Speeds," *AIAA J.* Vol. 29(4), 1241-1249,1991.

4. W.-P. Wang and R. H. Pletcher, On the Large Eddy Simulation of a Turbulent Channel Flow with Significant Heat Transfer, *Physics of Fluids* 8(12): 3354-3366, 1996.

5. R. H. Pletcher, and K.-H. Chen, On Solving the Compressible Navier-Stokes Equations for Unsteady Flows at Low Mach Numbers, AIAA Paper 93-3368-CP, 1993.

6. R. Kristoffersen and H. L. Andersson, Direct Simulations of Low-Reynolds-Number Turbulent Flow in a Rotating Channel, *Journal of Fluid Mechanics* 256: 163-197, 1993.

7. U. Piomelli and J. Liu, Large-Eddy Simulation of Rotating Channel Flows using a Localized Dynamic Model, *Physics of Fluids*, 7: 839-848, 1995.

8. J. P. Bons, C. D. Mac Arthur, and R. B. Rivir, The Effect of High Free-Stream Turbulence on Film Cooling Effectiveness, *J. Turbomachinery*, 118: 814-825, 1996.

9. J. P. Bons, R. B. Rivir, C. D. MacArthur, and D. J. Pestian, The effect of Unsteadiness on Film Cooling Effectiveness, AIAA Paper 95-0306, 1995.

10. S. P. Gogineni, D. D. Trump, R. B. Rivir, and D. J. Pestian, PIV Measurements of Periodically Forced Flat Plate Film Cooling Flows with High Free Stream Turbulence, ASME Paper 96-GT-236, 1996.

11. S. W. Burd, R. W. Kaszeta, and T. W. Simon, Measurements in Film Cooling Flows: Hole L/D and Turbulence Intensity Effects. ASME Paper 96-WA/HT-7, 1996.

12. S. W. Burd, and T. W. Simon, The Influence of Coolant Supply Geometry on Film Coolant Exit Flow and Surface Adiabatic Effectiveness. ASME Paper 97-GT-25, 1997.

Personnel Supported

Steven Sass	Graduate Student, Iowa State University
Ning Meng	Graduate Student, Iowa State University

Publications

N. Meng and R. H. Pletcher, Large Eddy Simulation of Rotating Channel Flows with and without Heat Transfer, Proceedings of the International Mechanical Engineering Congress and Exposition, November, 2000.

MEMS-BASED PROBES FOR VELOCITY AND PRESSURE MEASUREMENTS IN UNSTEADY AND TURBULENT FLOWFIELDS

AFOSR GRANT NUMBER: F49620-98-1-0162

Othon K. Rediniotis, Lance W. Traub and Espen S. Johansen
Department of Aerospace Engineering, Texas A&M University, College Station, Texas

Thomas R. Tsao
United Micromachines, El Monte, California

ABSTRACT

This work presents our progress in the development of MEMS (Micro-Electro-Mechanical Systems)-based, high-performance, fast-response, multi-sensor pressure probes of miniature size for velocity and pressure measurement in unsteady and turbulent flow fields. The fabrication and calibration of a MEMS-based, miniature 5-sensor, hemispherical-tip probe, are discussed. The development of an unsteady calibration rig is presented. Additionally, an analytic method is presented which allows prediction of the instantaneous pressures on the hemispherical tip of the 5-sensor probe. This methodology in turn is used in a correction algorithm that enables the prediction of the instantaneous velocity components from the instantaneous 5 pressures measured by the probe.

PROBE DESIGN AND FABRICATION

Figure 1 is an exploded view of the probe, showing the various components as they are assembled. The tip, sealing tubes, and mounting stage are fabricated by the Miniaturization Laboratory, as well as tools to facilitate final assembly. The MEMS pressure array has been fabricated by United Micromachines and its design and fabrication have been discussed in previous years' reports.

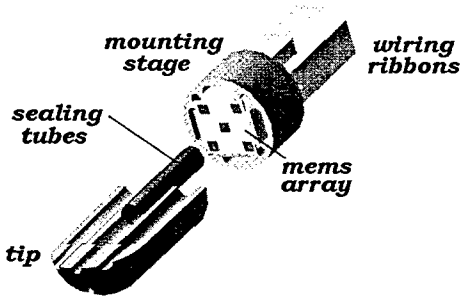

Figure 1. Exploded view of the MEMS 5-sensor probe.

The mounting stage is the most difficult piece to fabricate, as it has features requiring the smallest of tools and the highest precision of location. A fixture, referred to as the "sealer", is used to accurately position the tubes on the MEMS array, so that epoxy can be placed around the outside diameter of each tube. A picture of the first-generation fabricated sealer is shown in figure 2 against an adult's fingerprints to illustrate its size. After the epoxy has cured, the tip is fitted over the ends of the tubes and new epoxy is placed around the outside of each tube before completing the joint. Figures 3 and 4 present probe pictures at different stages of assembly. Figure 3 shows the MEMS sensor array installed in the stage, while the figure 4 shows the assembly after the sealer is installed. The five MEMS pressure sensors can be seen through the openings of the sealer. Finally, in order for the reader to perceive the size of the probe, figure 5 presents pictures of the MEMS-probe on a quarter and figure 6 shows the probe between an adult's thumb and index fingers. Figure 7 shows a typical miniature probe tip.

CALIBRATION FACILITY

One of the difficulties in the development of an unsteady probe is the design of a rig, which allows generation of a clean, controllable, and repeatable fluctuating velocity flow field. A solution has been developed in the form of the flow pulsator shown in Fig. 8. The pulsator is connected to a custom designed jet facility, built for this application. Through the use of carefully located screens, the turbulence intensity of this facility has been determined from hot wire measurements to be $\approx 0.3\%$. The flow angularity of the jet was also measured using a nulling technique. The maximum angularity was determined to be < 0.2 deg for all frequencies of flow pulsation. The concept of the pulsator is to continuously vary the jet exit dimensions, and from continuity the exit flow velocity must vary accordingly. The exit diameter of the pipe is 1.5", and

two square blocks are used to partially choke the flow through the pipe. These blocks are rotating, driven by two electric motors and are synchronized using gears. The peak-to-peak diameter of the blocks is 2" and they are placed 2.75" apart. This results in a maximum open area (minimum flow restriction) of 96% and a minimum open area (maximum flow restriction) of 61%, yielding a total area change of 36%. An optical encoder measures the rotation of the flow pulsator. The pulsator is capable of producing flow oscillations from 0 to 2500 Hz.

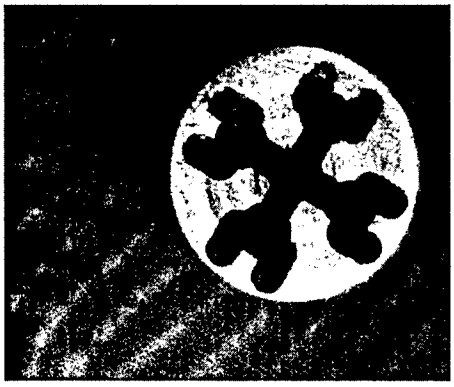

Figure 2. First-generation fabricated sealer shown against an adult's fingerprints.

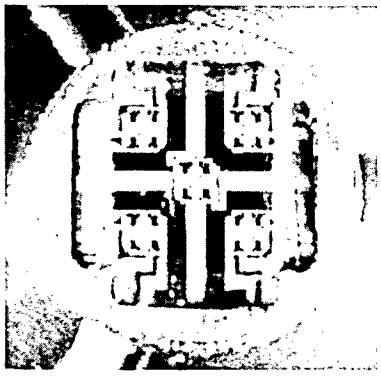

Figure 3. MEMS sensor array installed in the stage.

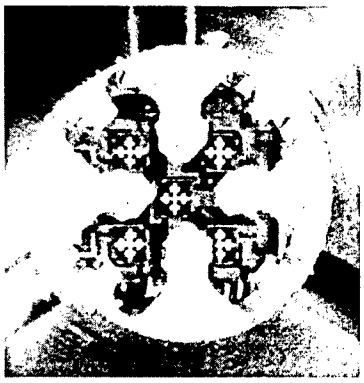

Figure 4. Assembly after the sealer is installed (sensors seen through the openings).

Figure 5. MEMS Sensor housing on a quarter.

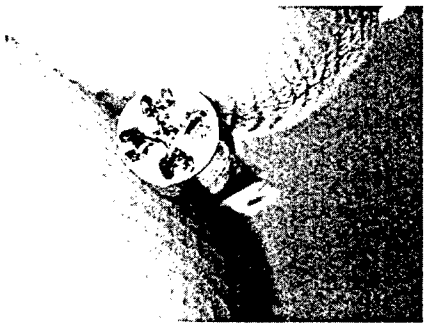

Figure 6. Probe between thumb and index finger.

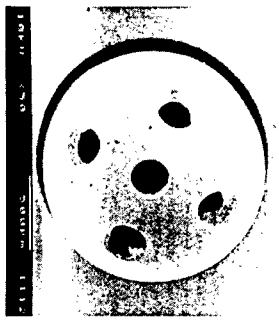

Figure 7. Typical probe tip.

Experimental optimization with the facility has shown that the optimal probe placement is approximately 0.5" downstream of the pulsator center (centerline of the two rotating blocks). At this location the governing equation is the unsteady Bernoulli equation given by:

$$H(t) = 1/2\rho v(t)^2 + p(t) + \rho\frac{\partial\phi}{\partial t} \qquad (1)$$

where H(t) is the instantaneous stagnation pressure, v(t) and p(t) the instantaneous velocity and static pressure. The differential is the inertial term. Thus for measurements to be useful, it is necessary to measure v(t) and p(t). The velocity was measured using a hot wire anemometer, which was located such that interference with the probe was minimized, and p(t) was measured using a surface flush mounted fast response pressure transducer. All the measurements are at the same axial location. Equation (1) then allows direct estimation of the inertial term as re-arranging gives:

$$\rho\frac{\partial\phi}{\partial t} = H(t) - 1/2\rho v(t)^2 - p(t) \qquad (2)$$

where all the terms on the RHS of Equation (2) are measured (the center port of the 5-hole probe measures H(t) when the probe is aligned with the flow). A sample of measurements from this facility is shown in Fig. 9. Presented are the instantaneous velocity (hot wire converted to dynamic pressure), static pressure (flush

mounted wall sensor), instantaneous stagnation pressure (front port on the probe), and a lateral port on the probe. The data was acquired at a mean free stream velocity of 70 m/s. The flow fluctuation frequency was 1350Hz. As may be seen, he facility is capable of generating a high quality fluctuating flow essential to fast response probe development.

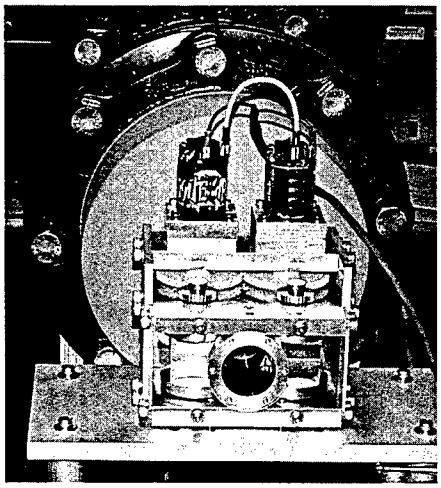

Figure 8. Flow pulsator mounted on nozzle.

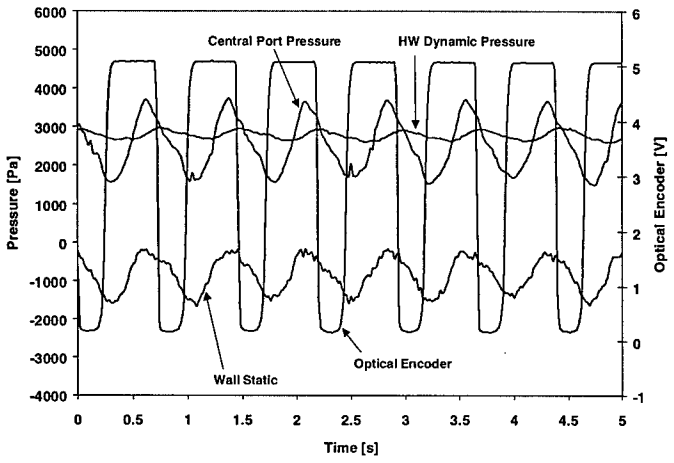

Figure 9. Flow pulsator dynamic pressure oscillations.

UNSTEADY PREDICTION METHOD

The calibration of MEMS-based probes is complicated by the equation governing the potential unsteady fluid flow. Generally, with a fluctuating flow, the pressure measured at a port consists of an instantaneous and an inertial/apparent mass component, which corresponds to the $\partial\phi/\partial t$ term in the unsteady Bernoulli equation. The inertial effect is generally small at low frequencies (< 400 Hz), allowing the use of steady calibration algorithms; at higher frequencies this is no longer the case. Therefore, calibration of such a probe (depending on the method adopted) would require estimation of the inertial term. The time dependence of the potential, ϕ, may be estimated using potential prediction methods, i.e. axial or surface singularity methods as detailed below (geometric parameters defined in figure 10).

The unsteady flow around a probe may be considered to contain apparent mass/inertial, circulation-induced lift, dynamic stall as well as dynamic boundary layer effects. In the present implementation, dynamic flow behaviour is assumed to be dominated by inertial or apparent mass effects (Humm et al.[1]); these are accounted for. We decompose the pressure measured at each port on the probe into a steady and an inertial term, where the steady term was determined from a static calibration, and the inertial term was estimated using inviscid theory as follows from the unsteady Bernoulli equation (ignoring rotations of the body coordinate system) i.e., $\frac{\Delta P}{\rho} = -\frac{1}{2}\nabla^2\phi - V_\infty.\nabla\phi - \frac{\partial\phi}{\partial t}$, where the first two terms on the right hand side constitute the steady component, and the third term, the unsteady component. The solution methodology to account for the inertial effect has been described in a previous progress report

Naturally, in the implementation of the correction procedure, accurate determination of the potential on the probe face is essential. Matsunaga et al[2], used a distribution of singularities (doublets) along the axis to model the hemisphere-cylinder representation of the probe. However, for this type of body, an axial distribution of singularities does not yield an accurate representation of the flow, essentially due to a discontinuous second derivative of the surface. In the present study, the surface singularity method was used to model the flow despite a significant increase in complexity and computational expense (effects of singularity type selection shown in figure 11). As Laplace's equation is linear, the perturbation potential due to axial flow and that due to transverse flow can be decomposed and solved independently. To reduce the computational cost, different methods were used for the axial and transverse flow solutions.

The axial flow over the probe (considered an axisymmetric hemisphere cylinder) was solved using the method of Landweber[3], as presented by Albone[4]. Landweber has shown that by applying Green's theorem to the solution of the boundary value problem for ϕ, an integral expression for surface velocity may be obtained. This method is more rapid than other surface singularity methods, but yields velocity on the body surface only. Within the user prescribed tolerance, the method is exact. The perturbation potential was found by integrating the perturbation velocity, using cubic splines to describe the velocities.

The transverse flow was solved using the more general, but computationally more expensive method of Lotz[5]. This method uses an axial distribution of source/sink rings in combination with the no penetration boundary condition to determine the source strengths. The method is complicated by the behaviour of the kernel or core functions that are singular when the effect of the element on itself is evaluated, requiring careful implementation of suitable limits. The source strength at each fixed-point location is found using a power series of rising powers of π. These allow determination of the perturbation potential at any point in the flow field. Although tedious, the method does yield essentially exact solutions.

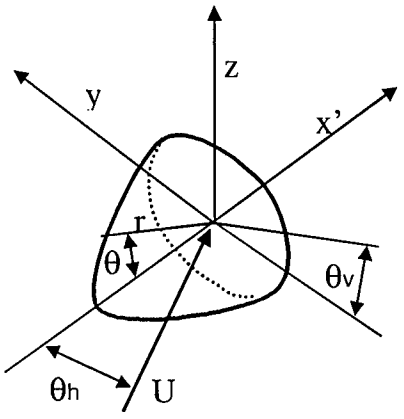

Figure 10. Definition of geometric parameters.

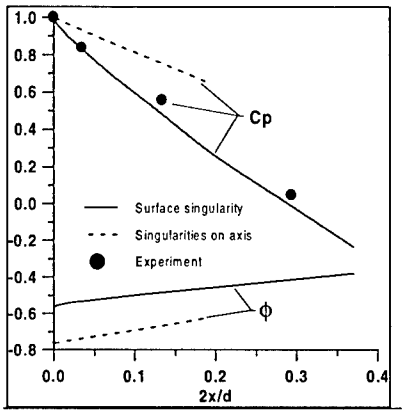

Figure 11. Effects of singularity selection on predicted Cp and potential over a hemisphere cylinder.

Figure 12 shows comparisons between the present method and the results of Vandrey[6], who used a surface source ring method. Predictions of the surface pressure measured over a hemisphere cylinder at zero incidence using Landwebers method are shown in Figure 13. Agreement with experiment is seen to be good.

Using the axial and transverse perturbation potentials determined using the surface singularity methods above allows the determination of the attached flow surface pressures at any location on the hemisphere as outlined below. As mentioned prior, the contributions of the axial and transverse flow can be determined separately due to the linear nature of Laplace's equation.

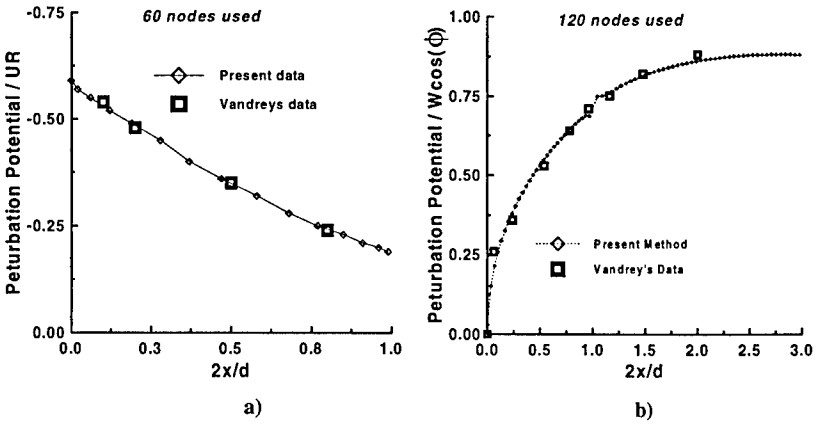

Figure 12. Comparison of present method with Vandreys data for the perturbation potential over a hemisphere cylinder, a) axial potential and b) transverse potential.

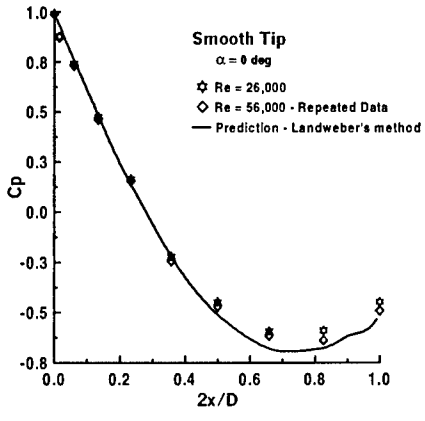

Figure 13. Comparison of Landweber's method with exper. data for the surface pressure over a hemisphere cylinder.

VELOCITY DUE TO AXIAL FLOW

A least squares curve fit of the perturbation potential in Fig. 12a yields (where x'=x-r)

$$\phi' = Ur\cos(\theta_h)\left(-0.5854 + (x/r)0.5478 - (x/r)^2 0.1502\right) \tag{3}$$

The tangential velocity is then : $V_\theta = \frac{1}{r}\frac{\partial \phi_{tot}}{\partial \theta}$ (4)

where ϕ_{tot} is the freestream plus perturbation potential. Noting that for the present geometry x/r=1-cos(θ), evaluation yields

$$V_\theta = U\cos(\theta_h)\left(1.2478\sin\theta) + 0.3\sin(\theta)\cos(\theta)\right) \tag{5}$$

VELOCITY DUE TO TRANSVERSE FLOW

The calculation of the induced velocities due to the transverse component of the decomposed freestream is straightforward but contains a subtlety. The transverse flow induces two velocity components on the hemisphere surface: one lateral and one axial such that it opposes the velocity due to axial decomposition of the freestream. It is this component that is responsible for the rearward movement of the stagnation point with incidence.

Using the numerical data in Fig. 12b gives a transverse perturbation potential of:

$$\begin{aligned}\phi' = {} & \mathrm{Ur}\sin(\theta_h)\cos(\theta_v)[0.0328 + 3.5127(x/r) - \Lambda \\ & -16.7795(x/r)^2 + 49.9447(x/r)^3 - \Lambda \\ & -79.5651(x/r)^4 + 63.3577(x/r)^5 - 19.832(x/r)^6]\end{aligned} \tag{6}$$

The lateral velocity component is found using $w1 = \frac{1}{r}\frac{\partial \phi_{tot}}{\partial \theta_v}$ (7)

where ϕ_{tot} is the freestream plus perturbation potential. Evaluation yields

$$\begin{aligned}w1 = {} & -U\sin(\theta_h)\sin(\theta_v)[0.0328 + 3.5127(x/r) - 16.7795(x/r)^2 + 49.9447(x/r)^3 \\ & -79.5651(x/r)^4 + 63.3577(x/r)^5 - 19.832(x/r)^6]\end{aligned} \tag{8}$$

The axial component w2 is determined using: $w2 = \frac{1}{r}\frac{\partial \phi_{tot}}{\partial \theta}$ (9)

using x/r=1-cos(θ), evaluation of w2 gives:

$$\begin{aligned}w2 = {} & U\sin(\theta_h)\cos(\theta_v)[3.5127\sin(\theta) - 33.559(1-\cos(\theta))\sin(\theta) + 149.834(1-\cos(\theta))^2 \\ & \sin(\theta) - 318.26(1-\cos(\theta))^3\sin(\theta) + 316.789(1-\cos(\theta))^4\sin(\theta) - \\ & 118.992(1-\cos(\theta))^5\sin(\theta) + \cos(\theta)]\end{aligned} \tag{10}$$

The surface pressure coefficient is then found using: $Cp = 1 - \left(\frac{(V_\theta - w2)^2 + w1^2}{U^2}\right)$ (11)

Figure 14 shows a typical prediction using the equations above with the experimental data of Hoang[7]. The methodology presented then allows straightforward prediction of instantaneous pressures as the potential is known allowing estimation of $\partial\phi/\partial t$.

COLLABORATIONS, TECHNOLOGY TRANSITION AND FUTURE PLANS

We have worked closely with Dr. Avi Seifert and Bill Sellers group at NASA Langley, as well as Aeroprobe Corp. on the experimental calibration of the probe. Also, we are in the process of licensing the developed technology, through Texas A&M, to Aeroprobe Corp. Preparation of patent applications are also in process. The experience we have acquired through this project combined with our collaboration with Aeroprobe Corp. has resulted in many commercial probes that are currently being used in many universities, companies and federal labs. An extensive description of our success stories is available upon request. In terms of future plans, once the 5-sensor probe is completed, we will proceed with the development of a MEMS-based, spherical, omni-directional pressure probe that will overcome the angularity limitations of the 5-sensor probe.

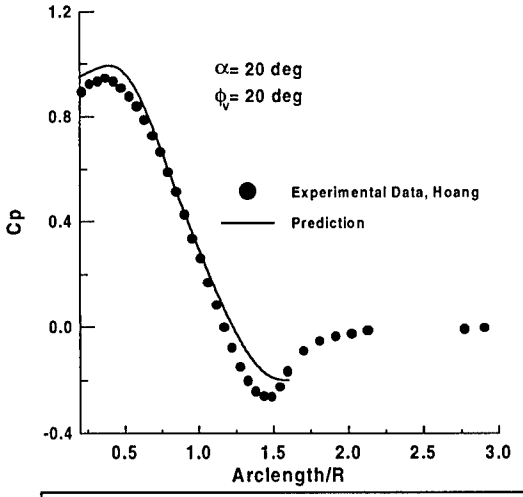

Figure 14. Comparison of Hoang's hemisphere-cylinder data and present prediction.

ACKNOWLEDGEMENT/DISCLAIMER

This work was sponsored by the air force office of scientific research, USAF, under the grant/contract number F49620-98-1-0162. The views and conclusions contained herein are those of the authors and should not be interpreted as necessarily representing the official policies or endorsements, either expressed or implied, of the air force office of scientific research or the u.s. government.

REFERENCES

1 Humm, H.J., Gossweiler, C.R. and Gyarmathy, G., "On Fast-Response Probes: Aerodynamic Probe Design Studies," *presented at the International Gas Turbine and Aeroengine Cogress and Exposition,* The Hague, Netherlands, June, 1994.

2 Matsunaga, S., Ishibashi, H., and Nishi, M., "Measurement of Instantaneous Pressure and Velocity in Nonsteady Three-Dimensional Water Flow by Means of a Combined Five-Hole Probe," *Transaction of the AME J. of Fluid Engineering*, Vol. 102, 1980, pp. 196-202.

3 Landweber, L., "The Axially Symmetric Potential Flow About Elongated Bodies of Revolution, "Rep. Taylor Model Basin, Washington, No. 761, 1951.

4 Albone, C. M., "Fortran Programmes for Axisymmetric Potential Flow Around Closed and Semi-Infinite Bodies," A.R.C., C.P. 1216, London, 1972.

5 Lotz, I., "Calculation of Potential Flow Past Airship Bodies in Yaw," NACA TM 675, D.C., 1932.

6 Vandrey, F., "A Method for Calculating the Pressure Distribution of a Body of Revolution Moving in a Circular Path Through a Perfect Incompressible Fluid," A.R.C. R&M 3139, Dec. 1953.

7 Hoang, N. T., Rediniotis, O. K. and Telionis, D. P., "Symmetric and Asymmetric Separation Patterns Over a Hemisphere-Cylinder at Low Reynolds Number and High Incidence," Journal of Fluids and Structures, Vol. 11, pp. 793-817, 1997.

DEVELOPMENT AND CALIBRATION OF WALL-SHEAR-STRESS MICROSENSOR SYSTEMS

AFOSR GRANT F49620-96-1-0482

Eli Reshotko
Department of Mechanical and Aerospace Engineering
Case Western Reserve University
Cleveland, Ohio

Mehran Mehregany
Department of Electrical Engineering and Applied Physics
Case Western Reserve University
Cleveland, Ohio

Abstract

The long term objective of this program is to develop the requisite technologies for integrating different sensors and actuators in desired combinations with electronics and telemetry on the same substrate. This is a multi-year program. We are now completing the program

Our concentration has been on wall-shear-stress sensors. We have produced and calibrated floating element wall-shear-stress sensors, both active and passive. We have developed a calibration channel and a calibration procedure based on continuum isothermal compressible channel flow. We have also developed and tested a wall-shear-stress sensors with integrated electronics initially based on the Analog Devices Inc. (ADI) airbag accelerometer circuitry, and more recently on one developed at CWRU.

This past year's work continued the emphasis on the accuracy of the calibration process. We are trying to reduce the uncertainty of measurement from the past estimate of 5% to a goal of 1%. Our results are reported in a M.S Thesis recently completed. A journal manuscript is in preparation.

Past Work

Prior to the start of this grant, we built a new calibration channel satisfying the requirements for non-leakage, non-choking, and having appropriate pressure and temperature measurements. The pressure measurements are required to evaluate the shear stress and the temperature measurements are to assure the isothermal character of the flow. It has been shown in our past work that in order to separate shear forces on the sensor element from pressure forces on the edge of the element, it is necessary to know the pressure gradient in the flow at the sensor location both during calibration and in operation.

Current Work

1. Improving accuracy of the calibration process

In an effort to improve the accuracy and reduce the uncertainty in the calibration process, each element of the procedure was investigated in detail. The basic calibration relationship is

$$\tau = - (b/2)(dp/dx)(1- \gamma M^2)$$

where b is the height of the channel, dp/dx is the measured pressure gradient at the sensor location, γ is the ratio of specific heats of the test gas (nitrogen) and M is the Mach number at the sensor location. We have had our rotameters recalibrated by the manufacturer so that our Mach number determination is within 1%. The pressure measuring circuits have been cleaned out and now give reliable readings. Since it is the pressure *gradient* that is required, the absolute value of pressure is of lesser importance, but we are trying to get an independent verification of the pressure transducer calibration. The largest inaccuracy is in the measurement of the channel height, b. Since this height is if the order of 200 μm, it is not measurable within 1% by any standard means. It is difficult to bring a microscope to the channel or vice-versa.

We have instead used the microwave technique called "Microstrip" (Pozar, David M.: Microwave Engineering, 2nd Ed., Wiley, 1998, pp.160 ff). A gold microstrip line is printed on the glass cover plate of the channel. The metal bottom of the channel is grounded. The transmission frequency that minimizes the reflected signal is directly related to the gap between the glass and the metal. Our measurements indicate a sensitivity of about ± 3μm which is about ±1.5% for a channel height of 200 μm. We believe our overall uncertainty now to be about ± 2%.

These results are presented in the M.S. Thesis of Mr. Mehul Patel entitled "Development of MEMS Wall Shear Stress Calibration System."

Personnel

The work on this grant in the past year has been carried out by Mr. Mehul Patel under the supervision of Prof. Reshotko.

Honors and Awards

Dr. Reshotko received the 1999 Otto Laporte Award for Research in Fluid Dynamics, American Physical Society, "For lasting contributions and leadership to the understanding of transition to turbulence in high-speed flows and non-homogeneous flows."

Acknowledgement/Disclaimer
This work was sponsored (in part) by the Air Force Office of Scientific Research, USAF, under grant number F49620-96-1-0482. The views and conclusions contained herein are those of the authors and should not be interpreted as necessarily representing the official policies or endorsements, either expressed or implied, of the Air Force Office of Scientific Research or the U.S. Government.

Publications and Presentations over the period of this grant

Mehregany, M., DeAnna, R.G. and Reshotko, E.: "Microelectromechanical Systems for Aerodynamics Applications," AIAA Paper 96-0421, Jan. 1996

Reshotko, E., Pan, T. Hyman, D. and Mehregany, M.: "Characterization of Microfabricated Shear Stress Sensors," Eighth Beer-Sheva International Seminar on MHD Flows and Turbulence, Jerusalem, Israel, Feb. 1996

Reshotko, E., Mehregany, M. and Bang, C.: "MEMS Applications in Aerodynamic Measurement Technology,": AGARD-CP-601, May 1998, pp. 35-1 to 35-10. (Invited paper presented at RTO/AGARD FDP Symposium on Advanced Aerodynamic Measurement Technology, Seattle, Sept. 1997)

Reshotko, E., Pan, T., Hyman, D. and Mehregany, M.: "Characterization of Microfabricated Shear Stress Sensors," in H. Branover and Y. Unger, eds. *Progress in Fluid Flow Research: Turbulence and Applied MHD,* Progress in Aeronautics and Astronautics, vol. 182, chapt. 22, AIAA, 1998, pp.335-351

Pan, T., Hyman, D., Mehregany, M., Reshotko, E. and Garverick, S.: "Microfabricated Shear Stress Sensors, Part I: Design and Fabrication," AIAA Journal, vol. 37, no.1, Jan.1999, pp.66-72

Hyman, D., Pan, T., Reshotko, E. and Mehregany, M.: "Microfabricated Shear Stress Sensors, Part II: Testing and Calibration," AIAA Journal, vol. 37, no. 1, Jan. 1999, pp.73-78

Patel, Mehul: "Development of MEMS Wall Shear Stress Calibration System," M.S. Thesis, Department of Mechanical & Aerospace Engineering, Case Western Reserve University, May 2000

July 2000

RECTANGULAR SUPERSONIC JETS MODIFIED FOR MIXING ENHANCEMENT AND NOISE REDUCTION

F49620-97-1-0493*

M. Samimy
Department of Mechanical Engineering
The Ohio State University

Abstract

Trailing-edge modifications in the form of simple cutouts in a rectangular Mach 2 nozzle with an aspect ratio 3 was used to explore passive mixing enhancement capabilities of these modifications in various flow regimes. Earlier results revealed that the trailing edge modifications, that are in the plane of the nozzle, do not affect the thrust force, the spanwise surface pressure gradient set up by the trailing edge modifications in the underexpanded flow regimes is the main source of streamwise vorticity in these flows, and by proper design and arrangement of trailing edges, one can change the level and rate of mixing and thus perhaps the level, directivity, and frequency content of generated noise (Kim and Samimy, 1999). In the previous results, the cutouts were on either splitter plate of a half nozzle or on the extension plate of a full nozzle. In the practical cases, the cutouts would be on the nozzle block itself. Sample results will be presented here for this case, which indicate the effectiveness of the cutouts in generating streamwise vortices even in the ideally expanded flow regime (Kim and Samimy, 2000).

Introduction

Extensive research has been conducted over the past few years on mixing enhancement using trailing edge modifications in supersonic rectangular jets. In the previous work, the trailing edge modifications (or cutouts) were either on the splitter plate in a half nozzle (Samimy et al., 1998) or on the nozzle extension in a full nozzle (Kim and Samimy, 1999). The use of trailing edge modifications of this type resulted in significant mixing enhancement in the underexpanded flow regime, moderate enhancement in the overexpanded regime, and no significant mixing enhancement in the ideally expanded flow regime (Samimy et al., 1998 and Kim and Samimy, 1999). It is noteworthy that the mixing enhancement was achieved without thrust loss in these experiments. Through a detailed investigation of the physics of the vortex generation mechanism, Kim and Samimy (1999) concluded that the spanwise pressure gradient on the modified trailing edge surfaces is the major source of streamwise vorticity.

The reason for the use of the trailing edge modifications on the splitter plate or on the nozzle extension in a full nozzle was to simplify the problem so that the physics of the streamwise vorticity generation mechanism could be identified. However, in the practical applications, the cutouts would be located on the nozzle blocks, i.e., before the expansion in the nozzle diverging section is completed. Therefore, some experiments were carried out to show that a cutout on the contoured nozzle block is effective in mixing enhancement in all flow regimes, including the ideally expanded regime.

*The work is jointly sponsored by NASA Glenn Research Center (NAG-1986)

Experimental Facility and Techniques

The air delivery system to the nozzle is similar to the one used by Kim and Samimy (1999) with additional flow conditioning screens installed in the stagnation chamber. As in the previous experiments (Kim and Samimy, 1999), the nozzle exit measures 2.86 cm wide and 0.95 cm high, with an equivalent diameter ($D_{eq}=(4A_{exit}/B)^{1/2}$) of 1.86 cm. The schematic of the baseline nozzle and the types of cutouts on the nozzle block are shown in Fig. 1. Contrary to the previous trailing edge modifications, in which the cutouts were either on the splitter plate (Samimy et al. 1998) or on the nozzle extension in a full nozzle (Kim and Samimy, 1999), the cutouts are located on the contoured nozzle blocks. These contoured nozzles are designed to generate uniform flows at the nozzle exit, which operated at the design conditions. The nozzle block has a cutout of either Rectangular type on the Side (RS), shown in Fig. 1 (b), or Rectangular type at the Center (RC), shown in Fig. 1 (c). The cutouts on the nozzle block are more representative of practical applications. This is the only major difference between the present nozzles and the previous nozzles. The cutout dimensions are the same as those used in the previous experiments. The wall thickness at the cutout edge in the present case is gradually decreased from 4.5 mm at the beginning of the cutout to 1 mm at the nozzle exit, while it was 1 mm in the previous cases.

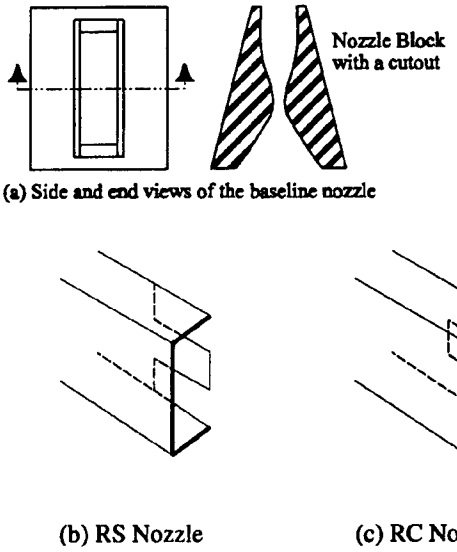

Fig. 1 Schematic of nozzle configurations.

As in previous work, the instantaneous cross-sectional images were acquired by the laser sheet illumination technique. The visualizations of the jet cross-section were performed at four downstream locations, i.e., $x/D_{eq}=1$, 2, 4, and 8. The jet was operated at three fully expanded jet Mach numbers of 1.75, 2.0 (design Mach number), and 2.5.

Results

From the average and instantaneous jet cross-sectional images at four downstream locations, the jet evolution and overall mixing were investigated. As in the previous experiments, the pair of counter rotating streamwise vortices generated by each cutout dictates the cross-sectional development and mixing characteristics of the jet. The mixing area at a given downstream

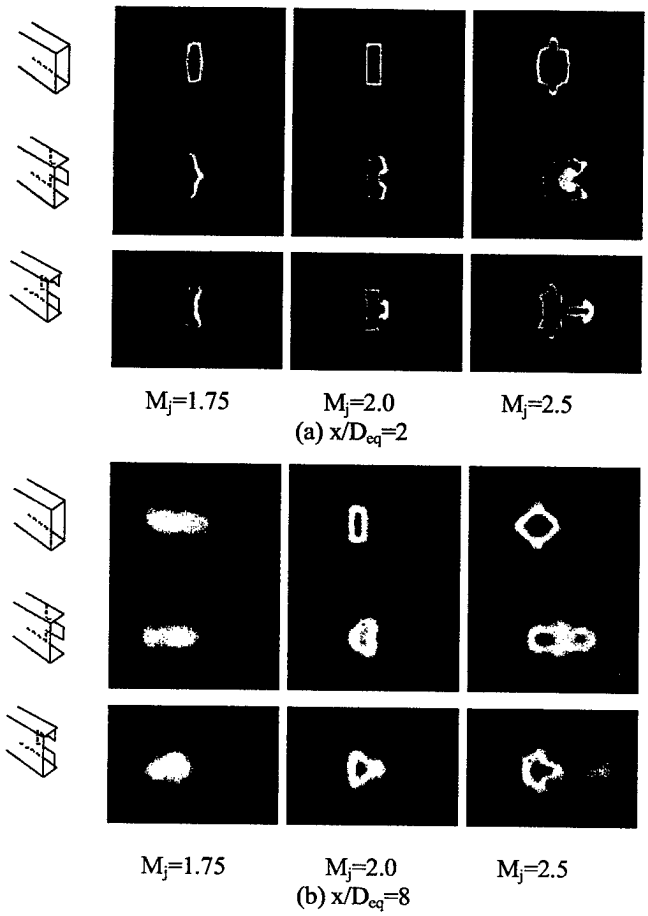

Fig. 2 Average cross-sectional images. The physical dimensions of each image are 116.4 mm ($6.3D_{eq}$) wide and 77.6 mm ($4.2D_{eq}$) high for (a); and 178.5 mm ($9.6D_{eq}$) wide and 119.0 mm ($6.4D_{eq}$) high for (b).

location was calculated and normalized with a reference mixing area. The reference mixing area for each nozzle was acquired at $M_j = 2.0$ (ideally expanded) using the baseline nozzle after flow visualizations for the nozzle operated at three flow conditions were performed. The average jet cross sectional images of 50 instantaneous frames at x/D_{eq}=2 and 8 are shown in Fig. 2. The image distortions due to the angle between the camera axis and the jet axis were corrected using image processing.

Underexpanded case ($M_j = 2.5$)

As shown in the images of Fig. 2 and discussed in the previous experiments (Kim and Samimy, 1999), two types of counter-rotating streamwise vortices were observed in this flow regime: a kidney type by nozzle RS and a mushroom type by nozzle RC. It is believed that the spanwise pressure gradient on the nozzle block surface around the cutout is the major source of streamwise vorticity in the underexpanded case. In the underexpanded flow regimes for the base nozzle, the effects of corner vortices can be easily seen in Fig. 2 (Samimy et al., 1998).

The jet cross-sectional development for nozzles with cutouts on the contoured nozzle block is quite similar to that for nozzles with cutouts on the splitter platel or on the nozzle extension. Even though M_j is the same in this and the previous experiments, the degree of underexpansion in the present case is higher, since the ratio of static pressure at the beginning of the cutout to the ambient pressure is 5.3, in comparison with 2.3 in the previous case. The increased underexpansion generates stronger pairs of counter-rotating streamwise vortices and in turn results in more energetic mixing. As in the previous cases, the vortex pairs interact in nozzle RS at x/D_{eq}=2. This interaction results in reduced growth rate after the interaction as shown in Fig. 3(a). In the underexpanded flow regime, the mixing areas of nozzle RS at x/D_{eq}=2 and 8 show 30% and 25% increases over that of a nozzle with the same cutout located on the splitter plate (Samimy et al., 1998).

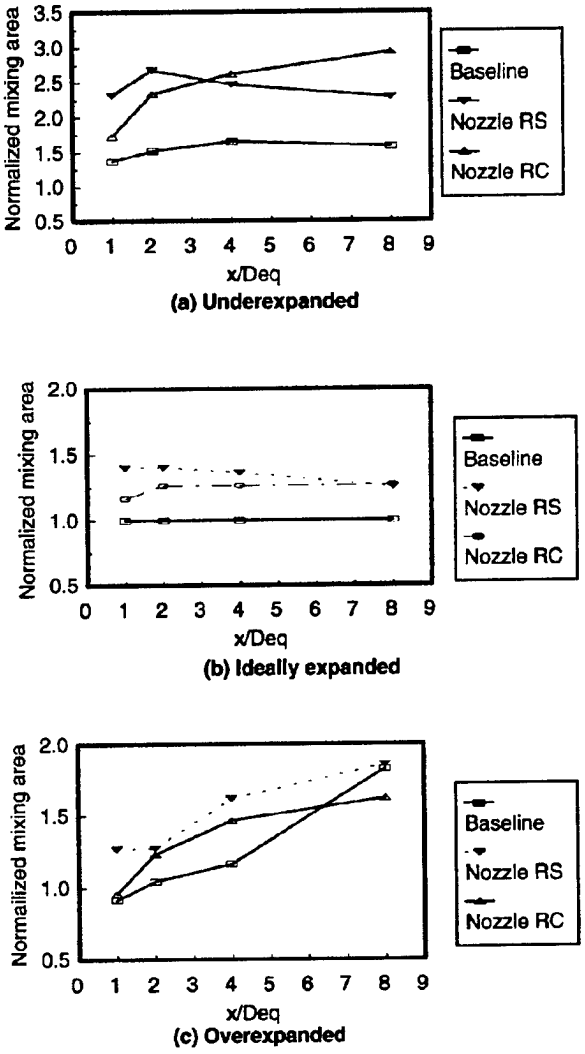

Fig. 3 Normalized mixing regions with downstream location.

For nozzle RC, a mushroom type pair of streamwise vortices rolls up farther away from the jet center when compared to that of a nozzle with the same cutout located on the splitter plate. At

both x/D_{eq}=2 and 8, the normalized mixing area of nozzle RC was increased about 20% over that of a nozzle with the same cutout located on the splitter plate. The increased spanwise pressure gradient on the contoured nozzle block with a cutout, seemed to generate a stronger mushroom type pair of counter-rotating streamwise vortices. By the pumping action of this pair of vortices, a significant ejection of the jet air into the ambient air was observed at all downstream locations. Similar to previous work (Kim and Samimy, 1999), this favorable pumping action of mushroom type vortices resulted in a continuous increase in mixing as shown in Fig. 3(a). As in the previous experiments, nozzle RS, which generates a kidney type pair of streamwise vortices, showed better mixing in the near field, while nozzle RC, which generates a mushroom type pair of streamwise vortices, showed better mixing at farther downstream locations as shown in Fig. 3(a).

Ideally expanded case (M_j = 2.0)

Significant jet cross-sectional development is observed for this flow condition by the cutout on the contoured nozzle block. With this nozzle configuration, the jet cross-sectional developments with downstream location for nozzles RS and RC are similar to those in the underexpanded flow regime of M_j=2.2 with similar cutouts in previous experiments. This is expected since the ratio of the static pressure at the beginning of the cutout to the ambient pressure is 2.4, in comparison with 1.0 in the previous cases with cutouts on the splitter plate or on the nozzle extension. This underexpansion generates a surface pressure gradient around the cutout, which is a necessary condition for streamwise vorticity generation. The two pairs of counter-rotating streamwise vortices are similar to those in the M_j=2.5 case, although not strong enough to deform the jet cross-section dramatically.

Mixing areas at x/D_{eq}=2 and 8 increased about 20% when they are compared with those for nozzles with similar cutouts on the splitter plate. Nozzle RS shows better mixing in the near field as in the M_j=2.5 case.

Overexpanded case (M_j = 1.75)

With the cutout on the contoured nozzle block, the jet cross-sectional development is significantly altered for far downstream locations. The jet cross sections of nozzle RS and RC show an axis switching, as in the baseline nozzle, by x/D_{eq}=8 location for the present cases. On the other hand, only the baseline nozzle showed an axis switching by this location in the previous cases (Samimy et al., 1998). From the instantaneous images, the degree of flapping motion of mixing layers can be inferred. In the previous cases (Kim and Samimy, 1999), most of the cutouts significantly reduced the flapping motion. However, the present cutout did not significantly change the flapping motion. The unaltered flapping motion is most likely responsible for the enhanced mixing.

Nozzle RS shows approximately 60% increased mixing at x/D_{eq}=8 when compared with that of a nozzle with a similar cutout on the splitter plate, although it shows a little reduced mixing at x/D_{eq}=2. Nozzle RC shows reduced mixing level at x/D_{eq}=2 and about the same mixing level at x/D_{eq}=8, when it is compared with that of a nozzle with a similar cutout on the splitter plate.[1] Contrary to the previous cases, the growth rates of mixing area for both nozzles RS and RC are positive all the way up to x/D_{eq}=8. As mentioned earlier, the unaltered jet flapping motion is most likely related to the enhanced mixing.

Summary

Rectangular nozzles with cutouts on the contoured nozzle blocks showed higher mixing levels than previous experiments with the cutouts either on the splitter plate in a half nozzle or on the extension plates in a full nozzle. Except for the increased mixing level, the overall development of jet cross sections with downstream location and the role of streamwise vortices remained similar to those of previous experiments with the cutouts on a splitter plate or a nozzle extension plate. The role of streamwise vortices in the jet development of the ideally expanded case seemed to be similar to those in the underexpanded case.

In the overexpanded flow regime, the present nozzle with a cutout on a contoured nozzle block showed about the same level of flapping motion as the baseline nozzle, while nozzles with cutouts on the splitter or on the extension in the previous experiments showed reduced flapping. The unaltered flapping motion of nozzles with a cutout resulted in positive growth rates all the way up to $x/D_{eq}=8$, while the growth rates of nozzles with cutouts on nozzle extensions were negative at far downstream locations. Therefore, a nozzle with a cutout on a contoured nozzle block would perform better in mixing at all flow conditions. It should be noted, that in the previous experiments with the cutouts either on the splitter plate in a half nozzle or on the nozzle extension in a full nozzle, there was no thrust loss associated with the cutouts. However, no thrust measurements were performed for the present cutouts.

Acknowledgment/Disclaimer

This work was sponsored in part by the Air Force Office of Scientific Research, USAF, under grant/contract number F49620-97-1-0493. The views and conclusions contained herein are those of the authors and should not be interpreted as necessarily representing the official policies or endorsements, either expressed or implied, of the Air Force Office of Scientific Research or the U.S. Government.

References

Samimy, M., Kim, J. -H., Clancy, P. S., and Martens, S., "Passive control of supersonic rectangular jets via nozzle trailing edge modifications," AIAA Journal, Vol. 36, No. 7, 1998, pp. 1230-1239.

Kim, J.-H and Samimy, M., "Mixing Enhancement via Nozzle Trailing Edge Modifications in a High Speed Rectangular Jet," Physics of Fluids, Vol. 11, No.9, 1999, pp. 2731-2742.

Kim, J.-H. and Samimy, M., "On Mixing Enhancement via Nozzle Trailing Edge Modifications in High Speed Jets," AIAA Journal, Vol. 38, No.5, 2000, pp. 935-937.

CONTROL OF TRANSITION IN SWEPT WING BOUNDARY LAYERS USING MEMS DEVICES AS DISTRIBUTED ROUGHNESS

AFOSR GRANT F49620-97-1-0520

William S. Saric and Helen L. Reed
Mechanical and Aerospace Engineering
Arizona State University, Tempe, AZ 85287-6106
saric@asu.edu

Abstract

Previous experiments at the ASU Unsteady Wind Tunnel on stability and transition in swept-wing boundary layers have shown that, under certain flow conditions, the use of micron-sized subcritically spaced artificial roughness elements applied near the leading-edge can significantly delay transition. These experiments used roughness elements for which amplitude and shape could not be dynamically changed and were, therefore, suitable for only one particular set of flight conditions. Current efforts use surface-mounted polyester tape, which covers holes aligned in the spanwise direction to form a variable-amplitude roughness array. Applying pressure to a chamber beneath the polyester tape alters the amplitude of these roughness elements. Previous experiments accomplished transition control under laboratory conditions for a highly polished surface with low distributed (random) roughness levels. The advantage of the current roughness arrays is that the setup allows for reproduction of realistic flight conditions. Flight vehicles experience changing surface roughness conditions in operation. Micron-sized debris deposited on the vehicle causes necessary changes in the spacing and amplitude of the roughness elements to achieve transition control. For this reason, practical implementation of this control mechanism will require development of a suitable active feedback control system. The pressure driven system is being supplemented with a spanwise array of glow-discharge units.

Project Goals

Vary the surface roughness conditions and freestream turbulence levels to determine the effective limits of artificial roughness elements in controlling transition. Determine an appropriate active feedback control system that is practical for flight vehicles.

Approach

Transition to turbulence in swept-wing boundary layers has shown sensitivity to both freestream conditions and 3-D roughness. The basic idea in current research is to examine transition for purely crossflow dominated swept-wing boundary layers. The 45-deg swept wing in current use in experiments at the ASU Unsteady Wind Tunnel is mounted at a small negative angle of attack such that a favorable pressure gradient is produced which causes considerable crossflow while also suppressing Tollmien-Schlichting (TS) waves.

The transition process, for most configurations, can be divided into three distinct phases. The first phase is the process by which disturbances are introduced into the boundary layer (i.e. receptivity). What the research reveals is that once the stationary mode

saturates the boundary layer has achieved a new stable laminar configuration and that breakdown to turbulence is via some mechanism besides the primary instability. Two experiments have been completed in the past year that explore the possibility that breakdown of the laminar boundary layer is due either to a high-frequency secondary instability or to an absolute instability. For the current research, receptivity will be explored in greater detail. We are interested in understanding how initial conditions (i.e. surface roughness and freestream turbulence) affect the production and development of instabilities within the boundary layer. The experiments consist of performing spanwise hot-wire scans at constant height and discrete chord locations. The amplitudes of the instability modes present are determined using Fourier analysis of the mean data acquired during the spanwise scans. The fluctuation data are simultaneously acquired during the spanwise scans because the spatial distribution of the fluctuations relative to the underlying mean-flow is critical in detecting the onset of the secondary instability which leads to transition.

Current Work

Secondary Instability. The high-frequency secondary instability has been detected in several previous experiments and computations, but prior to the just-completed Unsteady Wind Tunnel experiments, had never been conclusively shown to be responsible for breakdown. What the new results show is that once the primary instability provides sufficient distortion of the steady boundary-layer flow, the shear layer in the wall-normal direction is inflectional and undergoes a Rayleigh-type instability while the shear in the spanwise direction becomes unstable to a Kelvin-Helmholtz-type instability. These instabilities appear with a most-amplified frequency between 2 and 4 kHz for the Reynolds numbers investigated. Multiple instability modes are detected at various positions within stationary vortex structure and all these modes are found to have growth rates well above the growth of the most-amplified primary instability. The details of the mean flow's configuration appear to be important not only for determining the growth rate of the secondary instability modes but also for selecting which type of mode, spanwise or wall-normal, is dominant. In all cases, breakdown is observed within several percent chord of where the secondary instability is first observed, and when turbulence first appears it is spatially correlated with the position of the secondary instabilities. The conclusion is that the secondary instability is responsible for breakdown to turbulence.

Absolute Instability. The absolute instability experiment consists of using the variable roughness insert to change the leading-edge roughness configuration during a continuous wind-tunnel run. This provides a means of determining whether the flow is insensitive to initial conditions, a symptom of an absolute instability. An absolute instability is defined as an instability mode whose group velocity goes to zero while the temporal growth rate is positive. This provides a situation where a disturbance wave packet generated by a very-short-duration input can grow to arbitrarily large amplitude and cause breakdown for all future times, even after the initial disturbance source has been removed. Whether or not such an instability exists for swept-wings is of fundamental importance for the prospect of transition suppression, because if an absolute instability exists, it means that occasional failures to maintain control of the initial roughness would render the boundary layer turbulent for all subsequent time. The experiment begins by starting with very low amplitude roughness and determining the transition location using the fast hotwire

scanning technique developed for this experiment. Next, the roughness amplitude is increased and transition is observed to move forward on the wing. If an absolute instability were present it would now be active in this configuration. Finally, the roughness amplitude is reduced to its initial low-amplitude state. In all cases tested, the transition location moves back to its initial position, indicating that the transition mechanism is not an absolute instability. If it were, the instability and breakdown to turbulence would persist at the same location regardless of the initial roughness amplitude. This result emphasizes that it is the secondary instability that is solely responsible for breakdown of swept-wing crossflow boundary layers.

Roughness Measurements. A confocal-laser displacement sensor has been utilized to obtain accurate measurement of both the artificial roughness element amplitude and shape at discrete applied pressures. These measurements recorded the height at specific grid points using a 3-D traverse system. Figure 1 shows the shape of the roughness element for a specific applied pressure.

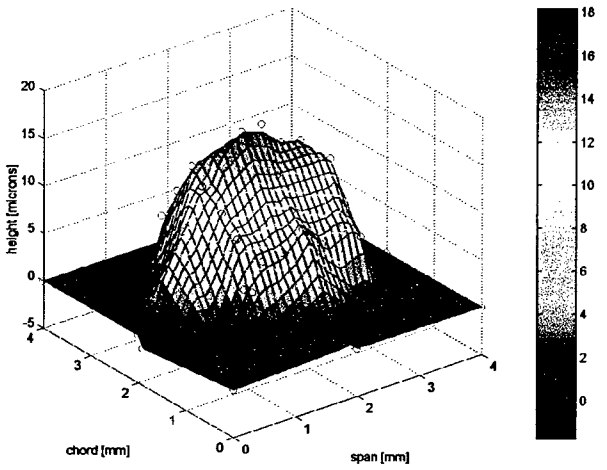

Figure 1. Shape and Amplitude of roughness actuator at 1.45 psi, center 18 μm.

Although the resolution of the 3-D traverse system was sufficient for measuring the amplitude and shape of the roughness element, it is inadequate for measurement of surface roughness amplitude and spectra. Preliminary experiments using nominal background roughness have shown promising results and indicate that the system is capable of producing good quality data.

Although infrequent, flight vehicles do experience higher freestream turbulence conditions where traveling waves dominate the transition process. Previous research has shown that these waves dominate transition when the freestream turbulence intensity, defined by $Tu = [\frac{1}{3}(u'^2+v'^2+w'^2)]^{1/2}$, exceeds 0.0015. In order to achieve these flow conditions, a turbulence-generating device has been designed and installed within the contraction cone of the tunnel. Figure 2 shows a sketch of this device.

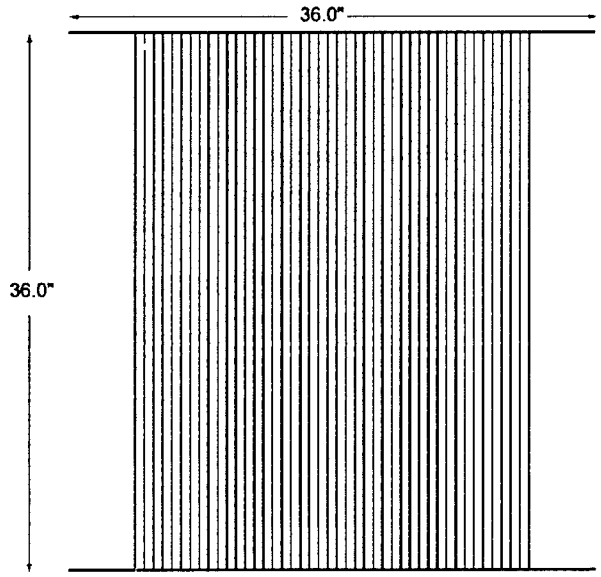

Figure 2. Freestream turbulence generator.

Future Plans

Roughness Actuators. Two techniques for initiating spanwise disturbances will be tried. The first is to use distributed electrical resistive heaters at the surface and the second is to use glow-discharge elements following Corke and Matlis[1] and Roth et al[2].

Experiments. Multiple surface roughness/freestream turbulence configurations need to be tested using the roughness actuators. As discussed above, the primary objective will be to define the effective limits of the artificial roughness elements in controlling transition. These results will be used to benchmark the necessary elements required for implementation of an active feedback control system applicable to flight vehicles. Specific questions include the ability of the system to accommodate Reynolds number as well as angle of attack changes that determine necessary spacing and amplitude of the roughness elements.

Acknowledgement/Disclaimer

This work was sponsored (in part) by the Air Force Office of Scientific Research, USAF, under grant/contract number F49620-97-1-0520. The views and conclusions contained herein are those of the authors and should not be interpreted as necessarily representing the official policies or endorsements, either expressed or implied, of the Air Force Office of Scientific Research or the U.S. Government.

References

1. T.C. Corke and E. Matlis, "Phased Plasma Arrays for Unsteady Flow Control" AIAA Paper no. 2000-2323.
2. J.R. Roth, D.M. Sherman and S.P. Wilkinson, "Boundary-layer control with a one-atmosphere uniform glow discharge surface plasma," AIAA Paper No. 98-0328.

Personnel Supported

William Saric	Professor, Arizona State University
Helen Reed	Professor, Arizona State University
Danny Clevenger	Technician, Arizona State University
Edward White	Graduate Student, Arizona State University
Pierre Gabet	Graduate Student, Arizona State University
Robert Gladden	Graduate Student, Arizona State University

Publications

"A Validation of the Parabolized Stability Equations for Three-Dimensional Boundary Layers" (invited) H. Reed, W.S. Saric, *ASME Paper No. FEDSM2000-11345.*

"Application of Variable Leading-Edge Roughness for Transition Control on Swept Wings" E. White and W. Saric, *AIAA paper No. 2000-0283.*

Talks and Lectures

"A Validation of the Parabolized Stability Equations for Three-Dimensional Boundary Layers" (invited paper) W.S. Saric, *ASME Paper No. FEDSM2000-11345,* June 11-15, 2000.

"Stability and Transition in 3-D Boundary Layers" (invited lecture) W.S. Saric, C.I.R.A. (Centro Italiano Ricerche Aerospaziali) 3rd ERCOFTAC SIG 33 Workshop, New and Emerging Techniques for Transition Prediction, Ravello, Italy, April 27-28, 2000.

"Application of Variable Leading-Edge Roughness for Transition Control on Swept Wings" E. White, 38th AIAA Aerospace Sciences Meeting and Exhibit, Reno, NV. January 10-13, 2000.

"The Need for Remote Real-time Measurements of MEMS Actuators in a Transition-Control Experiment" W. Saric,. Vibra*Scan* Annual Scanning Laser Vibrometer Users Meeting, San Jose, CA. June 8, 1999.

"Crossflow-Dominated Breakdown in Swept-Wing Boundary Layers" E.B. White, 16th Arizona Fluid Mechanics Conference, Tempe, AZ. February 25-26, 2000.

"Crossflow Transition Control using Variable Leading-Edge Roughness Arrays" Edward B. White, American Physical Society's 52nd Annual Meeting of the Division of Fluid Dynamics, New Orleans, LA. November 21-23, 1999.

"Transition in 3-D Boundary Layers at Elevated turbulence Levels" William S. Saric, Edward B. White, Robert Gladden. Minnowbrook III Workshop on boundary Layer Transition and Unsteady Aspects of Turbomachinery Flows, Blue Lake Mountain, NY. August 20-23, 2000.

"Transition on Swept Wings" Edward B. White and William S. Saric, ICAS (International Council of the Aeronautical Sciences) 2000 Congress, 29 August 2000, Harrogate, United Kingdom

PULSED-SOUND MEASUREMENTS OF THE INFLUENCE OF HIGH-AMPLITUDE NOISE ON BOUNDARY LAYER TRANSITION TO TURBULENCE

AFOSR GRANT F49620-00-0075

William S. Saric and Helen L. Reed
Mechanical and Aerospace Engineering
Arizona State University, Tempe, AZ 85287-6106
saric@asu.edu
http://wtsun.eas.asu.edu

Abstract

Although there has been significant experimental progress in understanding the transition process, researchers are still unable to predict transition. Arguably the most important yet least understood phase of transition is the process by which freestream disturbances are introduced into the boundary layer (i.e. receptivity). Understanding of receptivity provides the essential initial amplitudes and other characteristics of the resulting instabilities, which can be used to validate both theoretical and numerical models. For this reason, current experimental work being conducted at the Arizona State University Unsteady Wind Tunnel focuses on the receptivity of a 20:1 super-ellipse leading-edge subjected to pulsed planar acoustic waves.

Project Goals

Determine leading-edge receptivity coefficients using pulsed acoustic forcing. Use these results to resolve the present conflict that exists between numerical models and experimental results obtained using constant acoustic forcing. Determine an active control system in order to obtain longer sample times that will provide more finely resolved spectral information characterizing the instability.

Approach

The pulsed acoustic forcing technique is used to generate leading-edge receptivity coefficients. The acoustic disturbances are introduced via an array of nine McCauley Sound speakers located upstream of the test section. These acoustic freestream disturbances are used to excite Tollmien-Schlichting (TS) waves within the boundary layer. The input acoustic wave is measured using a hot-wire placed in the freestream. Another hot-wire placed within the boundary layer measures a Stokes wave associated with the acoustic disturbance along with the lagging TS wave. The Stokes wave is observed first since it travels at sonic speed whereas the observed TS wave, according to linear theory, travels at a maximum of one-third the freestream velocity.

The pulsed technique eliminates many of the problems associated with previous experiments that used continuous acoustic forcing. For example, reflected waves caused by the diffuser downstream of the test section can be separated through the use of an input window. Detection and separation of these reflected waves is important since it is believed that the receptivity of the leading-edge is greater for reflected waves (upstream-traveling) than for the input (downstream-traveling) waves.

One of the disadvantages associated with the pulsed acoustic forcing technique is that the spectral information obtained, which characterizes the disturbance, has inherently poor frequency resolution. In the spectral domain, frequency resolution increases with sampling length. The poor frequency resolution is unavoidable since the input signal occurs only for a short time in order to avoid including detrimental effects from reflected waves.

Multiple constraints prevent direct measurement of the instability characteristics at the leading-edge. For example, physical constraints prevent placement of the hot-wire within the boundary layer at this location. Furthermore, the amplitude of the TS waves are not distinguishable given the noise present within the acquisition system. Given these constraints, the amplitude of the TS waves are measured further downstream and linear theory is used to determine the corresponding receptivity coefficients.

Current Work

In order to perform the sensitive receptivity measurements, background turbulence levels should be extremely low. This ensures that the only freestream disturbance present is that introduced by the input sound. For this reason, current efforts include placement of new screens within the tunnel to reduce low-frequency turbulence. Measurements are underway which will define the effectiveness of these screens. The high-frequency turbulence is dissipated in the settling chamber and, therefore, no active means of control need to be implemented.

As explained above, one of the difficulties associated with acoustic forcing is the unwanted reflected waves caused by the diffuser downstream of the test section. Preliminary work has been initiated to determine an active control system that will eliminate these detrimental reflected waves. The control system will use a speaker placed downstream of the diffuser to achieve cancellation. Even nominal success in this area will provide sample times with spectral information containing three times the resolution currently attainable. Experiments using multiple hot-wires mounted in the streamwise direction between the input sound source and the downstream side of the diffuser are underway. These measurements will define the propagation of the acoustic signals as they travel through the plenum, contraction cone, test section, and diffuser. A schematic of the Arizona State University Unsteady Wind Tunnel is shown in Figure 1.

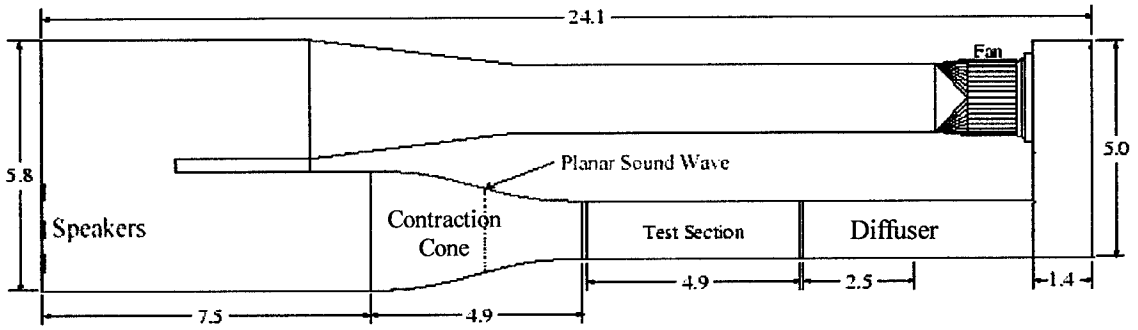

Figure 1. Diagram of the ASU Unsteady Wind Tunnel. All dimensions in meters.

The contraction cone and diffuser are of specific interest because these areas produce the unwanted reflected waves.

Future Plans

As discussed previously one of the near term challenges is the understanding the acoustic properties of the tunnel as well as the development of a robust active control system. Long term goals include the determination of leading-edge receptivity coefficients at higher freestream velocities. At this higher velocities the TS frequency band of interest allows for an increase in spectral resolution.

It is expected that a catalog of receptivity coefficients will be developed that will provide a target for DNS validation at higher Reynolds numbers.

Acknowlegement/Disclaimer

This work was sponsored (in part) by the Air Force Office of Scientific Research, USAF, under grant/contract number F49620-00-0075. The views and conclusions contained herin are those of the authors and should not be interpreted as necessarily representing the official policies or endorsements, either expressed or implied, of the Air Force Office of Scientific Research or the U.S. Government.

Personnel Supported

William Saric	Professor, Arizona State University
Pierre Gabet	Graduate Student, Arizona State University
Robert Gladden	Graduate Student, Arizona State University

Publications

"Boundary Layer Receptivity to Freestream Disturbances and its role in Transition" (invited) E.B. White, *AIAA Paper No. 99-3788,* June 28 – July 1, 1999.

"Leading-Edge Acoustic Receptivity Measurements Using a Pulsed-Sound Technique" Edward B. White, William S. Saric, Ronald Radeztsky, Jr. *To appear Laminar-Turbulent Transition, Volume V. Eds. W. Saric and H. Fasel, in press, Springer-Verlag, 2000.*

"Boundary-Layer Receptivity to Freestream Disturbances," William Saric, Helen Reed and Edward Kerschen, *Ann. Rev. Fluid Mech. Vol. 32*, to appear.

"Direct Numerical Simulation of Leading-Edge Receptivity to Sound" David Fuciarelli, Helen Reed and Ian Lyttle, AIAA Journal, Vol. 38, No. 7, 2000, pp 1159-1165.

Talks and Lectures

"Boundary Layer Receptivity to Freestream Disturbances and its role in Transition" (invited) E.B. White, 30th AIAA Fluid Dynamics Conference, Norfolk, VA. *AIAA Paper No. 99-3788,* June 28 – July 1, 1999.

"Validation of an Acoustic-Receptivity Experiment Using a PSV" E. White. Vibra*Scan* Annual Scanning Laser Vibrometer Users Meeting, San Jose, CA. June 8, 1999.

"Leading-Edge Acoustic Receptivity Measurements Using a Pulsed-Sound Technique" Edward B. White, IUTAM Symposium on Laminar-Turbulent Transition, Sedona, AZ. September 13-17, 1999.

SHOCK WAVE AND BOUNDARY LAYER CONTROL FOR AERO-OPTIC APPLICATIONS

AFOSR GRANT F-49620-00-1-0319

Alexander J. Smits
Department of Mechanical and Aerospace Engineering
Princeton University, Princeton NJ

Richard B. Miles
Department of Mechanical and Aerospace Engineering
Princeton University, Princeton NJ

Abstract

We have recently demonstrated the strong stabilizing effects of low levels of helium injection into a Mach 8 transitional boundary layer (Etz 1998, Erbland *et al.* 1997). The experiments appeared to show that helium injection delays transition indefinitely. Interestingly, injection of air at the same location with the same momentum flow rate had no significant effect. While the phenomenon was far from understood, it was speculated that the injection of helium effectively reduces the Reynolds number near the wall (the kinematic viscosity of helium is a factor of 8 higher than that of air at the same temperature). It appeared that transition was delayed, and turbulent mixing was inhibited. In support of this conjecture, sodium fluorescence images clearly showed the presence of a relatively thin, highly stable helium layer near the wall.

Here we present more detailed studies of this phenomenon. In particular, FRS and a new MHz imaging system was used to study the three-dimensional character of the flow field affected by the helium. These results permit a more complete understanding of the effects of helium injection on hypersonic boundary layers, and its possible use in aero-optics. The complete results were presented by Auvity *et al.* (2000) at the recent AIAA Fluids 2000 Meeting in Denver. Only a summary is given here.

Figure 1 presents three planform views of the boundary layer for the three different stagnation conditions with helium injection using FRS. According to Erbland (2000), the strong contrast in greyscales are a good indication of the boundary between the relatively hot boundary layer fluid (dark) and the external freestream fluid (bright). The laser sheet is located 4.5 mm away from the surface, where the undisturbed boundary layer thickness is about 8 mm. The helium injection greatly affects the structure of the boundary layer downstream of the injection location. Here, J is the ratio of the jet momentum to the freestream fluid momentum. Conditions 1. 2 and 3 correspond to unit Reynolds numbers of 11×10^6, 14×10^6, and 16×10^6, respectively. The corresponding local Reynolds number Re_θ was about 4000 for all conditions. A dark area of relatively constant width marking the helium injection is clearly seen in the middle of every image in figure 1, surrounded by undisturbed boundary layer fluid. The width of this region is slightly larger than the width of the injection slot, and it is about the same for the three images presented in figure 1. It appears that very little lateral diffusion of helium takes place and it remains confined to a region of constant width.

Spanwise views give insight into the structure of the boundary layer downstream of the injection slot. In figure 2, three spanwise views obtained for the same stagnation conditions as in figure 1 are presented. The grey line show on each image represents the lateral location of the injection slot and is drawn on the plate surface.

Figure 1. Planform views of the boundary layer with helium injection for different stagnation conditions. (a) Condition 1, J = 0.16; (b) Condition 2, J = 0.12; (c) Condition 3, J = 0.16. The flow is from the left to the right.

Figure 2. Spanwise view of the boundary layer with helium injection for different stagnation conditions. (a) Condition 1, J = 0.16; (b) Condition 2, J = 0.12; (c) Condition 3, J = 0.16. The flow is out of the page.

The troughs represent a decrease in the boundary layer thickness and appear as bright lines in figure 1 suggesting that the boundary layer structure seen on images in figure 2 is maintained in the streamwise direction. In order to confirm this, an average of about thirty images was formed for Condition 2 with different injection rates (figure 3). The time-averaged images with helium injection show a distinct boundary layer structure, especially at the higher injection rates, whereas the boundary layer without injection presents no such structure. The troughs seen in figure 2 have a stable position on average for all the injection rates presented in figure 3.

The structure of the boundary layer for $J < 0.20$ consists of successive spanwise crests and troughs and can be interpreted as a series of entrained fluid motions toward to the wall alternating with ejected fluid motions outward from the wall. Since the spanwise organization of the boundary layer seems to persist in the streamwise direction, this structure may be attributed to the existence of streamwise counter-rotating vortices in the

boundary layer. The conjectured fluid motions which take place inside the boundary layer with helium injection is presented in figure 4. However, we do not have sufficient evidence to prove that such streamwise vortices are actually present. However, many images strongly suggest that counter-rotating motions are active in the boundary layer. For instance, in figure 2c, a mushroom-shape structure characteristic of streamwise counter-rotating vortices can be seen. Further experimental verification of this conjecture is necessary. For example, surface flow visualization may provide additional evidence.

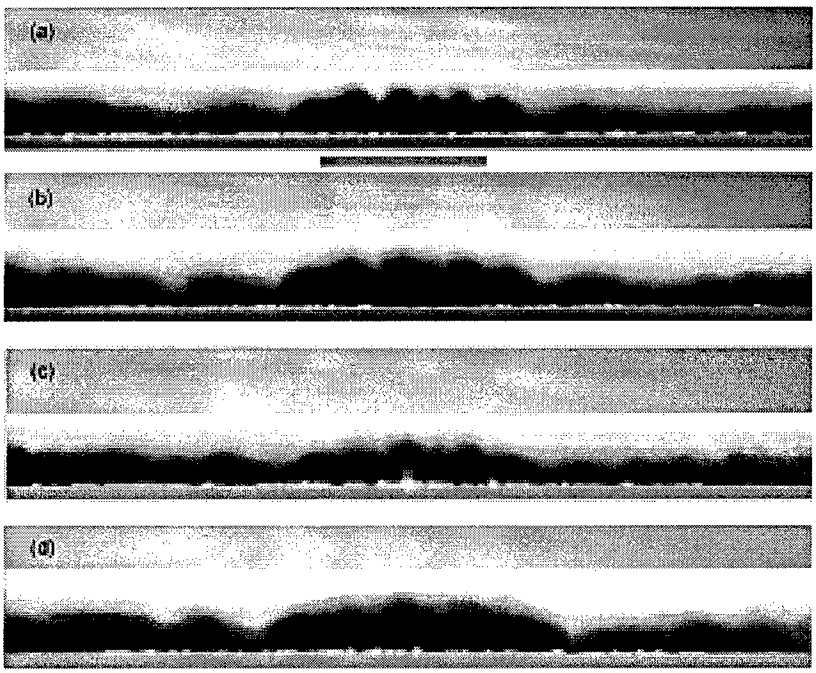

Figure 3. Time-averaged spanwise images of the boundary layer for different injection rates at Condition 2. (a) J = 0; (b) J = 0.07; (c) J = 0.09; (d) J = 0.11; (e) J = 0.13. The flow is out of the page.

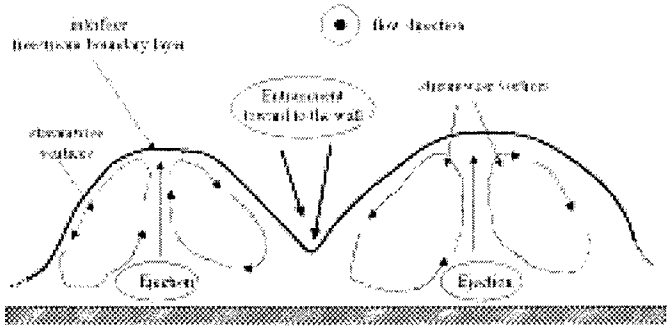

Figure 4. Conjecture on fluid motions inside the boundary layer with helium injection.

If streamwise vortices occur in the boundary layer downstream of slot injection of helium, the appearance of a crest in the averaged spanwise images may correspond to the presence of one pair of counter-rotating vortices. Such streamwise vortices, also called G\"{ortler vortices, have been observed in boundary layers submitted to concave surface curvature. Consequently, the appearance of the streamwise vortices may be associated with concave streamline curvature in the region where the helium is injected.

The new imaging system available in the Gas Dynamics Laboratory uses a "pulse-burst" laser system in conjunction with a high-speed CCD camera. Complete details of the laser system are given in Wu (1998). Briefly, the Nd:YAG laser has the capability of producing a "train" of 30--40 high energy pulses with pulse separation times as shorts as one microsecond. The laser is paired with a novel CCD framing camera recently developed by Princeton Scientific Instruments, Inc. The CCD camera has a 30-image storage buffer built into the image sensor chip itself, and can frame at rates up to 1 MHz. The camera resolution is 180 by 180 pixels. This imaging system can collect a time sequence of 20--30 images. The chosen repetition rate is 500 kHz in order to obtain high laser pulse energy and maximize the sampling window. If the laser sheet is oriented normal to the wall in the spanwise direction, the sequential images can be assembled into a quasi-three-dimensional volumetric image, as long as Taylor hypothesis can be invoked. This requires that the large-scale motions evolve over distances large compared to the boundary layer thickness.

A 30-frame sequence obtained without injection is presented as a volumetric image in figure 5a. The individual images have been stacked in temporal order with the first frame on the right and the last frame on the left. The spacing in the streamwise direction was set using an average convection velocity. In figure 5a, the convection velocity was chosen to equal the freestream velocity (1140 m/s). The convection velocity of the large scale motions is probably slightly lower than that value Huntley (2000). The gap between the frames were filled in by linear interpolation of the greyscales. The surface illuminated in figure 5a is actually the interface between the condensed and sublimated carbon dioxide (nominally the instantaneous boundary layer edge). The interface is made visible by making all the freestream greyscales (the bright region) transparent. The direction of light illumination can be adjusted to create the shadow effect and accentuate the three dimensional nature of the boundary layer.

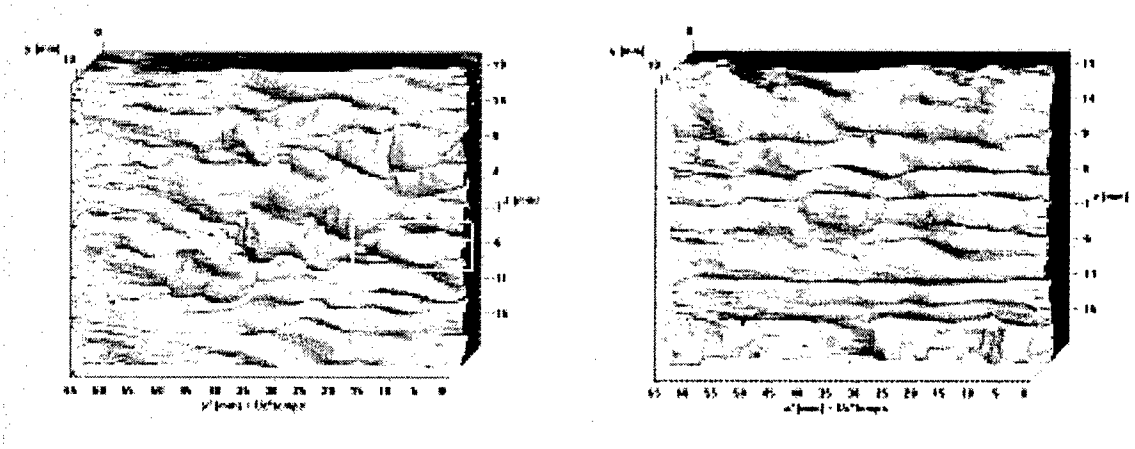

Figure 5. (a) Left: Volumetric reconstruction of the boundary layer without injection. (b) Right: With helium injection, J = 0.09. The flow is from left to right. Stagnation Condition 2.

Figure 5b represents a reconstruction of the boundary layer under Condition 2 with helium injection for J = 0.09. The physical size of the 3D representation is similar to that shown in figure 5a. The spanwise structure of the boundary layer shown in the time-averaged spanwise images can also be clearly in figure 5b. Crests and troughs with a significant streamwise extent are present, in positions similar to that found in the time-averaged images. More smaller-scale disturbances can be observed in the crests for J = 0.13 than for J = 0.09, but the troughs are deeper for J = 0.13.

A key question is how long this stabilizing effect will persist downstream, and if helium injection into a fully turbulent flow will cause the appearance of similar stable streamwise vortices. The phenomenon obviously has important implications for aero-optic applications, flow control and heat transfer to the wall from the external flow. Further studies at higher Reynolds number and lower Mach number are in progress.

Acknowledgment/Disclaimer

This work was sponsored (in part) by the Air Force Office of Scientific Research, USAF, under grant/contract number F49620-00-1-0319. The views and conclusions contained herein are those of the authors and should not be interpreted as necessarily representing the official policies or endorsements, either expressed or implied, of the Air Force Office of Scientific Research or the U.S. Government.

References

Etz M.R. (1998) The effects of transverse sonic gas injection on a hypersonic boundary layer. MSE Thesis, Princeton University.

Erbland P.J., Baumgartner M.L., Yalin A.P. (1997) Development of planar diagnostics for imaging Mach 8 flowfields using carbon dioxide and sodium seeding. AIAA Paper 97-0154.

Erbland P.J. (2000) Filtered Rayleigh Scattering and Homogeneous Nucleation of CO2 in Supersonic Flows. Ph.D. Thesis, Princeton University.

Huntley M. (2000) Transition in Hypersonic Flow over Elliptic Cones. Ph.D. Thesis, Princeton University.

Wu P., Lempert W.R., Miles R.D. and Bromley L. (1998) Tunable pulse-burst laser system for high-speed imaging diagnostics. AIAA Paper 98-0310.

Personnel Supported

Mark Huntley	Graduate Student, Princeton University, Princeton NJ
Pingfan Wu	Graduate Student, Princeton University, Princeton NJ
Alexander J. Smits	Professor, Princeton University, Princeton NJ
Richard B. Miles	Professor, Princeton University, Princeton NJ
Bruno Auvity	Postdoc, Princeton University, Princeton NJ

Publications

Huntley, M. and Smits, A.J. "MHz Rate Imaging of Boundary Layer Transition on Elliptic Cones at Mach 8," AIAA paper #00-0379, 38th AIAA Aerospace Sciences Meeting, Reno, Nevada, January 10-13, 2000.

Huntley, M. and Smits, A.J. "Transition Studies on an Elliptic Cone in Mach 8 Flow Using Filtered Rayleigh Scattering," European Journal of Mechanics B–Fluids, August, 2000.

Auvity, B., Etz, M., Huntley, M., Pingfan Wu and Smits, A.J. "Control of Hypersonic Boundary Layers by Helium Injection," AIAA Paper 2000-2322, Fluids 2000 Conference, Denver, Colorado, June 19-22, 2000.

Awards Received

AIAA Fellow—awarded January 2000 (R.B. Miles)

AIAA Biennial Aerodynamic Measurement Technology Award—January 2000 (R.B. Miles)

Transitions

None.

A NEW APPROACH TO PREDICTION OF AIRCRAFT SPIN

AFOSR GRANT F49620-00-1-0050

Kyle D. Squires
Mechanical and Aerospace Engineering Department
Arizona State University

Abstract

Knowledge of the spin and recovery characteristics of military aircraft is crucial at a variety of levels, e.g., for improving maneuverability, development of control strategies, and ultimately improving future fighter design. Given the often disparate configurations of military aircraft, there is a pressing need for knowledge of their spin characteristics since it cannot be extrapolated from available data.

The long-term objective of this work is development of a Computational Fluid Dynamics tool for prediction and study of aircraft spin. Because of its long moment arm and complex vortex dynamics for bodies at angles of incidence, the major contributor to the spin characteristics of an aircraft is the forebody. The objective of the current research effort is prediction of forebody spin characteristics using Detached Eddy Simulation (DES).

A basis for evaluation of simulation results is provided via comparison to the measurements of Polhamus *et al.* (1959). These investigators measured the forces on a variety of forebody cross-sections and documented the role of the Reynolds number in the type of side force experienced by the forebody. Seven cross sections were considered in the experiments, two of the cross-sections currently being utilized in the simulations are shown in Figure 1: a rounded-corner square and 2:1 aspect ratio ellipse. Freestream flows at an attack angle of 10° (measured with respect to the x axis) and for a Reynolds number range from roughly 1×10^5 to 2×10^6 were considered in the experiments. The measurements show that the side-force (y component in Figure 1) on the rounded square changes sign from the super-critical to the sub-critical regime, with the critical Reynolds number range around $5 \times 10^5 < Re < 6 \times 10^5$. For the 2:1 ellipse, a slight side-force reversal occurs around $Re \approx 5 \times 10^5$.

Simulations performed to date have been used to assess changes in the flow with separation type, i.e., laminar or turbulent boundary layer separation. Solutions of the two- and three-dimensional flows are obtained from the unsteady Reynolds-averaged Navier-Stokes (URANS) equations and using Detached Eddy Simulation. URANS solutions are obtained using the Spalart-Allmaras one-equation model for the turbulent eddy viscosity (Spalart and Allmaras 1994, referred to as S-A throughout). As described below, the primary role of the URANS calculations is to provide an efficient testbed for gauging the effect of separation type on the flow. A simple modification to the S-A model is used to obtain the present DES formulation (e.g., see Nikitin *et al.* 2000).

The calculations are performed on O-type grids generated using the control technique of Hsu and Lee (1991). Grids are generated with the first surface-normal point within

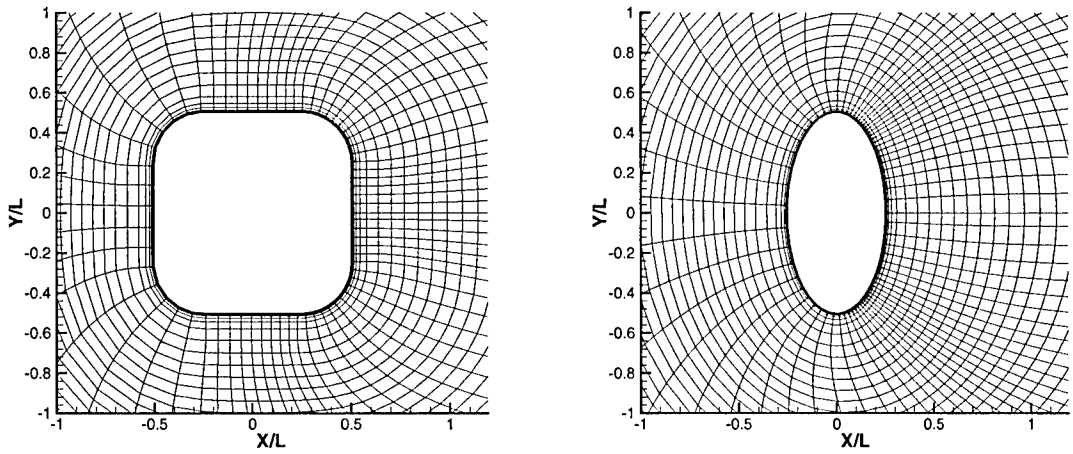

Figure 1: Rounded-corner square and 2:1 aspect ratio ellipse (only every third grid point shown for a subset of the domain). Attack angle of 10° measured with respect to the horizontal (x) axis. Grids generated using control technique of Hsu and Lee (1991).

one viscous unit and a stretching ratio of 1.1 normal to the surface (c.f., Figure 1). Grid sizes for the present simulations are approximately 2.8×10^4 points for two-dimensional simulations and 1.4×10^6 for three-dimensional calculations. A uniform flow at angle of attack 10° is prescribed approximately four body lengths upstream. Convective outflow conditions are employed at the downstream boundary approximately eight body lengths downstream. The timestep, made dimensionless using the freestream velocity and body size, in most of the calculations is 0.01. Studies of the timestep, grid refinement, and domain size are on going.

Simulations performed to date have been used to assess changes in the flow with separation type, i.e., laminar or turbulent boundary layer separation. The laminar separation cases are run using the 'tripless' approach of Shur *et al.* (1996). The turbulence model is zero at the inflow boundary and in the primary boundary layers on the body. Non-zero values of the eddy viscosity convected from downstream activate the model in the separating shear layers. Turbulent boundary layer separation is achieved in calculations in which the inflow eddy viscosity is roughly three times the molecular viscosity. In this case, the turbulence model is activated as soon as fluid enters the boundary layers.

Velocity vectors along the top surface of the box are shown in Figure 2. The vectors shown are from calculations at $Re = 8 \times 10^5$, the vector plots for each case are from the end of the run (last point on the time axis in Figure 3). The laminar boundary layer separation case experiences detachment from the body around $x/L \approx 0.25$, with a clearly different evolution as compared to the turbulent separation case which detaches at $x/L \approx 0.75$

Shown in Figure 3 are time histories of the force coefficients, C_x and C_y, measured

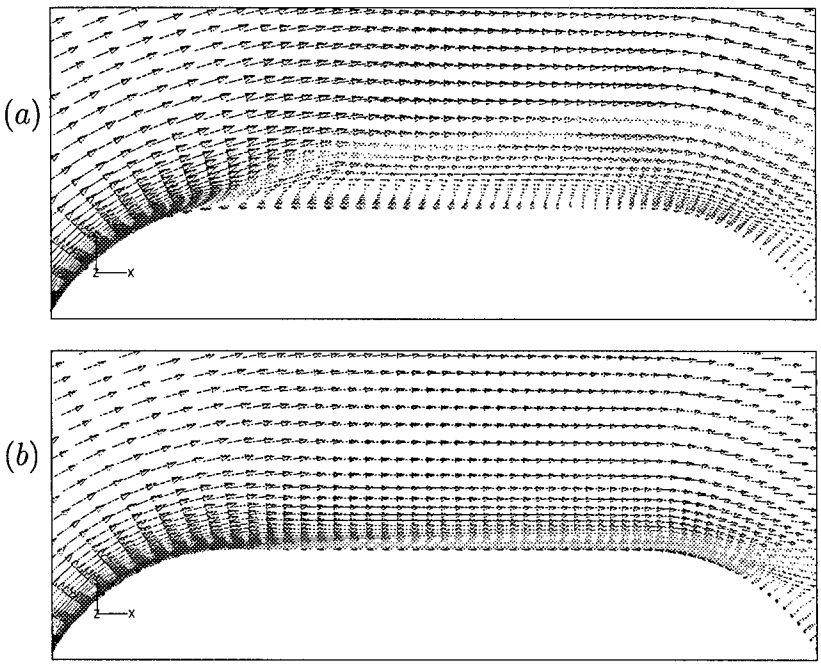

Figure 2: Velocity vectors along top surface of the rounded-corner square, $Re = 8 \times 10^5$. Vectors colored by the value of ν_t/ν. (a) laminar separation case, (b) turbulent separation case.

with respect to the x and y axes, respectively. An initial transient has been excluded from both runs, though the force history from the laminar separation case has not yet reached a temporally periodic variation as has already been established for the turbulent separation case. Apparent in the force histories is the much larger peak-to-peak variation in the forces for the laminar separation case, especially in C_x. The mean values of C_x for the turbulent and laminar separations are 0.78 and 1.54, respectively. The turbulent separation C_x is roughly two times larger than the measured value, while the laminar separation C_x is about 50% larger than the measurements at sub-critical Reynolds numbers of Polhamus *et al.* (1959). The amplitude variations in C_y are also larger for the laminar separation case than for its turbulent separation counterpart. Figure 3*b* shows that the variation in the vertical force for the laminar separation case includes negative values, the maximums of which are approximately as large as the positive values. Force reversal does not occur, however, with the average remaining positive (0.59). The average vertical force coefficient for the turbulent separation case is 0.91, not far from the measured value of approximately 1.0.

The two approaches to separation control considered to date possess the advantage that each is unambiguously defined and each provide limiting cases. Force reversal in C_y is currently being investigated using other separation-control strategies (e.g., tripping the boundary layer on only one side of the box, and then the other side, etc.). Two-dimensional URANS calculations are efficient for gauging the effect of separation type on forces, though three-dimensional DES calculations are required for more refined evaluations and have been initiated. Aspects such as grid refinement and

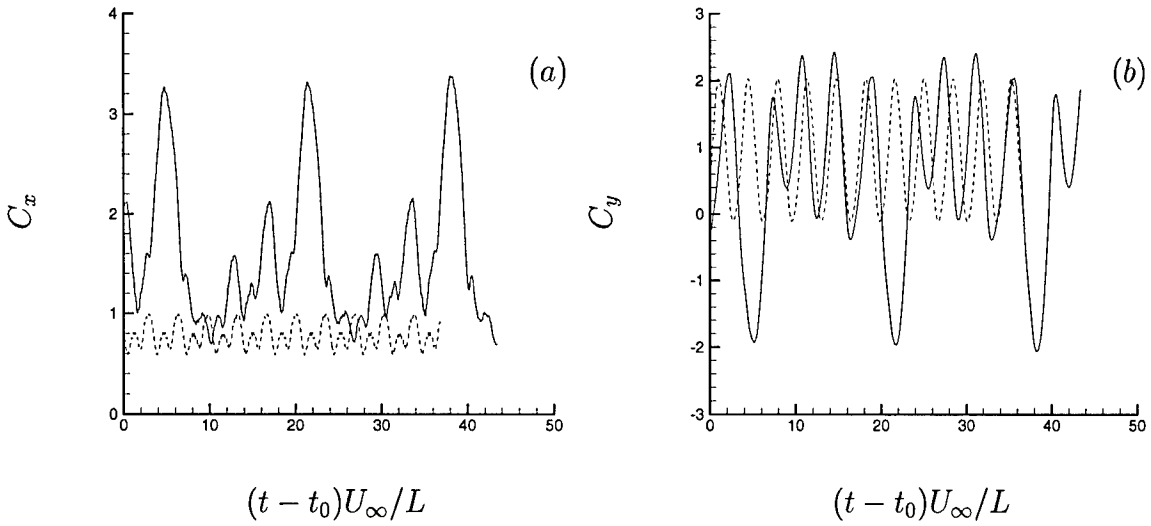

Figure 3: Force coefficient time histories for the rounded-corner square at 10° angle of attack, $Re = 8 \times 10^5$. (a) horizontal-axis force coefficient, (b) vertical-axis force coefficient. —— laminar separation case; ---- turbulent separation case.

influence of the domain size are also currently being studied we intend to summarize these effects prior to the end of Year 1.

Acknowledgments/Disclaimer

This work is sponsored by the Air Force Office of Scientific Research (AFOSR) under grant number F49620-00-1-0050. The views and conclusions contained herein are those of the author and should not be interpreted as necessarily representing the official policies or endorsements, either expressed or implied, of the Air Force Office of Scientific Research or the U.S. Government.

References

1. K. Hsu and S.L. Lee, A Numerical Technique for Two-Dimensional Grid Generation with Grid Control at All of the Boundaries, *Journal of Computational Physics*, 1991, 11:451-469.

2. E.C. Polhamus, E.W. Geller and K.J. Grunwald, Pressure and Force Characteristics of Noncircular Cylinders as Affected by Reynolds Number with a Method Included for Determining the Potential Flow about Arbitrary Shapes", NASA TR R-46, 1959.

3. M.L. Shur, P.R. Spalart, M.Kh. Strelets and A.K. Travin, Navier-Stokes Simulation of Shedding Turbulent Flow Past A Circular Cylinder and a Cylinder with a Backward Splittle Plate, Third Euro. CFD Conf., 1996.

4. P.R. Spalart and S.R. Allmaras, A One-Equation Turbulence Model for Aerodynamic Flows, *La Recherche Aérespatiale*, 1994, 1:5.

Personnel Supported

Kyle D. Squires Professor, Arizona State University

Publications

"An approach to wall layer modeling in Large-Eddy Simulations", N.V. Nikitin, F. Nicoud, B. Wasistho, K.D. Squires and P.R. Spalart, *Physics of Fluids*, vol. 12, no. 7, pp. 1629-1632, 2000.

DYNAMIC MODELING AND FLOW CONTROL STRATEGIES FOR RECTANGULAR JETS: APPLICATION OF POD AND WAVELET ANALYIS

AF-F49620-00-1-0013

Flint O. Thomas
Hessert Center for Aerospace Research
Department of Aerospace & Mechanical Engineering
University of Notre Dame

Abstract

It is widely recognized that coherent vortical structures in turbulent flows are important in processes such as scalar and momentum transport, mixing and noise generation. Despite this generally acknowledged importance, the routine use of the coherent structure concept in turbulence modeling and flow control strategies has not yet been realized. This research effort is focused upon the experimental characterization, modeling and control of coherent structures in a flow of considerable interest in Air Force applications - the rectangular jet. In high performance military aircraft the rectangular jet geometry facilitates thrust vectoring. Further, the larger entrainment rates exhibited by rectangular jets relative to those of comparable axisymmetric jets is of interest from a low observables standpoint (reduced plume signature) as well as for applications demanding enhanced combustion or chemical reaction. These flows are also of interest from a fundamental fluid mechanics point of view since they exhibit major axis switching behavior.

This research effort has as its objectives: the experimental characterization and low order modeling of the coherent structure dynamics of high Reynolds number rectangular jets of low and moderate aspect ratios via a joint application of the proper orthogonal decomposition (POD) and wavelet analysis techniques. This includes the extraction and characterization of the u, v, and w-component POD eigenfunctions and associated eigenvalues. The rectangular jet dynamics (embodied in the POD temporal coefficients) is obtained by projection of the POD eigenfunctions onto instantaneous realizations of the flow field. This projection is performed via wavelet analysis. Similarly, Galerkin projection of a truncated subset of the empirical eigenmodes onto the Navier-Stokes equations is used to develop a low-order dynamical systems model of the rectangular jet flow field. The validity of assumptions associated with the treatment of the truncated modes and their effect on the coherent structure is established by comparing the dynamic behavior resulting from the model ODE's with those from projection of POD modes onto the actual flow. The dynamical system model of the rectangular jet will be utilized for the establishment of rectangular jet flow control strategies. The flow control algorithm will be demonstrated via both the model and laboratory jet flows.

The rectangular jet is an inherently three-dimensional flow and is therefore quite challenging to model since it exhibits no truly homogeneous spatial coordinate. For example, even after invoking the common assumption of treating the streamwise

coordinate as homogeneous (an approach which restricts one to the examination of local flow dynamics), the resulting POD eigenfunctions are still inhomogeneous in the remaining two spatial coordinates. Most previous applications of the POD in turbulent shear flows have been restricted to a single inhomogeneous coordinate. The planar jet (i.e. a rectangular jet in the limit of very large aspect ratio), while geometrically similar to the rectangular jet, is simpler since the spanwise coordinate is homogeneous. Since the successful experimental treatment and modeling of the planar jet flow field seems prerequisite to capturing the dynamics of the presumably more complex low aspect ratio rectangular jet, a significant portion of the first year effort was devoted to developing the experimental techniques and modeling approach in this flow field. Note that the planar jet experiments are viewed as proof-of-concept and are not motivated by any expectation that the flow physics in the planar and rectangular jets will necessarily be similar. The results from the planar jet experiments and modeling effort will be reviewed first.

The large-scale structure in the self-similar region of a planar turbulent jet was experimentally investigated by application of the POD. The work first focused upon the extraction and characterization of the u, v, and w-component POD eigenfunctions and associated eigenvalues. These measurements were performed at several streamwise locations over the range $50 \leq x/D \leq 100$, where D is the nozzle slot width. In addition to being the first implementation of the POD in the planar jet flow field, the measurements were performed in the fully developed part of the flow where visualization by injection of a tracer reveals no evidence of underlying coherent structure. This made an ideal test case to investigate the potential of the method for extracting and modeling flow structure in a complex environment. Twin cross-stream rakes of x-wire probes were used to perform the required cross-spectral measurements with different spanwise separations between the rakes. The reader will find details regarding the measurements procedures and results described in Gordeyev and Thomas [1]. The resulting POD spatial eigenfunctions for each of the three velocity components depend on cross-stream spatial coordinate, Strouhal number, and spanwise wavenumber. Corresponding eigenvalue distributions are obtained in Strouhal number - spanwise wavenumber space. Eigenvalue convergence is demonstrated to be rapid. The results suggest that the flow supports a dominant planar structure aligned in the spanwise direction as well as an essentially three-dimensional structure.

The large-scale structure is reconstructed in physical space by projection of measured u, v, and w-component POD eigenmodes onto instantaneous flow field realizations. The projection is performed by means of a continuous wavelet transform-based technique. The instantaneous flow field realizations are obtained by two methods: (1) a triple x-wire rake arrangement which allows the unambiguous extraction of the planar component of the jet structure and (2) using linear stochastic estimation with three spanwise oriented rakes (i.e. the "complimentary technique" described in [2]). The latter method allows examination of both the planar ($k_z = 0$) and the nonplanar part of the coherent structure. Our results indicate that a dominant planar component of the large-scale structure in the jet consists of two lines of large-scale spanwise vortices arranged approximately asymmetrically with respect to the jet centerline. This planar component of the structure resembles the classic Karman vortex street. There is a strong interaction between

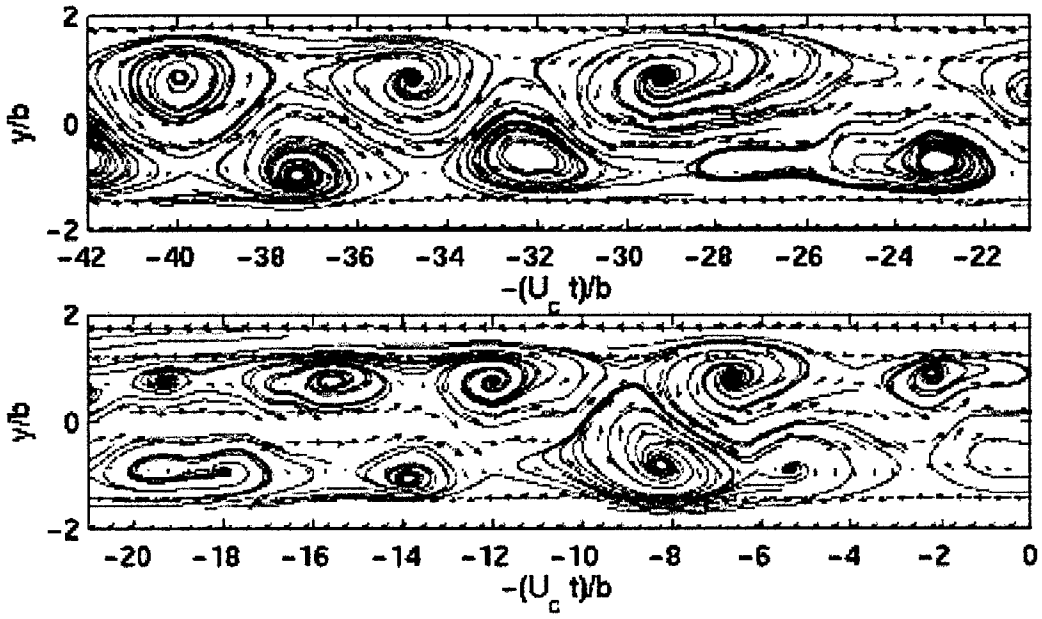

Figure 1. Experimentally determined planar vortical structure in the turbulent jet.

structures on opposite sides of the jet in the form of lateral streaming motions that extend well across the flow. Figure 1 presents a sample of both the velocity vector field and instantaneous streamlines associated with the planar component of the jet coherent structure obtained by superimposing the mean flow and the first three planar POD modes. The velocity data is presented in the frame of reference moving downstream with the constant mean convective speed U_c. Taylor's hypothesis is invoked in order to convert time into a pseudo-spatial streamwise coordinate $x = - U_c t$. All spatial coordinates have been non-dimensionalized by the local mean velocity half-width, b.

Initial examination of the nonplanar modes ($k_z > 0$) shows that their primary effect is to tilt and bend the spanwise vortex tubes. The bending occurs primarily in the streamwise direction. The degree to which the spanwise vortices are distorted varies greatly; in some cases they are nearly streamwise oriented and in others only slight distortion of a primarily spanwise vortex is noted. A few sample realizations from the experiments are shown in Figure 2. This figure shows instantaneous streamline surfaces which wrap around a spanwise vortical structure thereby revealing the flow pattern near the core. Although only a single nonplanar mode has been examined to-date, in reality a continuous spectrum of nonplanar modes $k_z\, b/2\pi < 1$ will distort the spanwise vortices. The result will be similar in overall topology to that presented in Figure 2 but will involve finer scale convolutions of the primary vortex tube.

The POD modes provide a complete set of functions that exhibit optimum convergence. The rapid energy convergence of the POD modes leads to the possibility of building a realistic local low-dimensional model of the planar jet based on the interaction of the

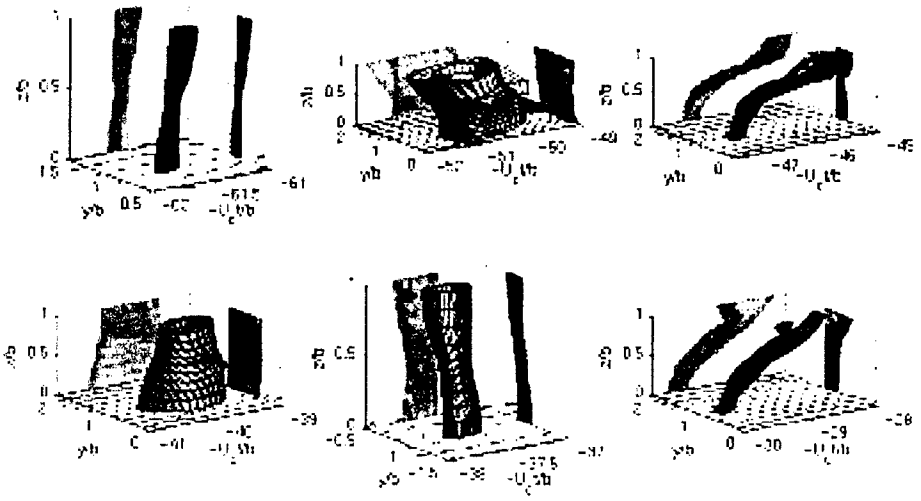

Figure 2. Effect of nonplanar modes on the large-scale spanwise vortices (y and z are the lateral and spanwise spatial coordinates, respectively).

large-scale structures and the mean flow. After the spatial orthogonal modes are extracted, the velocity can be decomposed in the series,

$$u_\alpha(x,y,z,t) = \sum_n \sum_{k_x} \sum_{k_z} c_\alpha^{(n)}(t;k_x,k_z)\, e^{ik_x x}\, e^{ik_z z}\, \varphi_\alpha^{(n)}(y;k_x,k_z) \qquad (1)$$

where $\varphi_\alpha^{(n)}(y;k_x,k_z)$ denotes the n-th α-component POD eigenmode and $c_\alpha^{(n)}(t;k_x,k_z)$ the temporal coefficients which must be determined. This series will be truncated to keep the minimum number N of the most energetic modes. The rest of the modes are considered as a dissipative influence on the large scales. The number of modes kept in the truncation can be varied to investigate the effect of neglected modes. The Galerkin procedure is performed to get a system of equations for the c's. The governing Navier-Stokes equations are symbolically written as

$$NS(\mathbf{u}) = \frac{\partial \mathbf{u}}{\partial t} + L(\mathbf{u}) + Q(\mathbf{u},\mathbf{u}) = 0 \qquad (2)$$

where L and Q are linear and quadratic operators, respectively. We would like to minimize the error after truncating the series by orthogonalizing the N-S equations with the truncated velocity series to the orthogonal basis,

$$(NS(\mathbf{u}^N) \bullet \varphi^{(n)}) = 0 \qquad (3)$$

In terms of temporal coefficients, the system above becomes a finite set of ODE's for the temporal coefficients c_n,

$$\frac{dc_n}{dt} = Bc_n + NL(c_m, c_\lambda) \qquad (4)$$

where B is a matrix and NL is a nonlinear matrix operator on c_n. There still exists an energy transfer from large resolved modes to small unresolved dissipative scales. This interaction can be parametrically described by a simple model, like a Heisenberg spectral

model for isotropic turbulence (see Aubry et al, [3]). This model expresses the Reynolds stress of unresolved modes in terms of the strain rate of the resolved modes and is similar to sub-grid scale modeling in the numerical large-eddy simulation approach. The model introduces a parameter into the system regulating the energy transfer from the large resolved modes to small unresolved ones. Th system (4) is subsequently analyzed by means of dynamical systems theory.

Due to the observed dominance of the first planar component over the nonplanar components, only the first planar POD mode is used in the model. Comparison of the results of the model to experimental data reveals very good agreement. The model correctly predicts both the turbulent spectrum and topology of the large-scale structures. The predictions are found to hold with the number of model equations N as low as 20 equations. This seems quite remarkable for a fully turbulent flow. The planar structural topology resulting from the model is shown in Figure 3. Note the excellent agreement with the experimental realization shown previously in Figure 1.

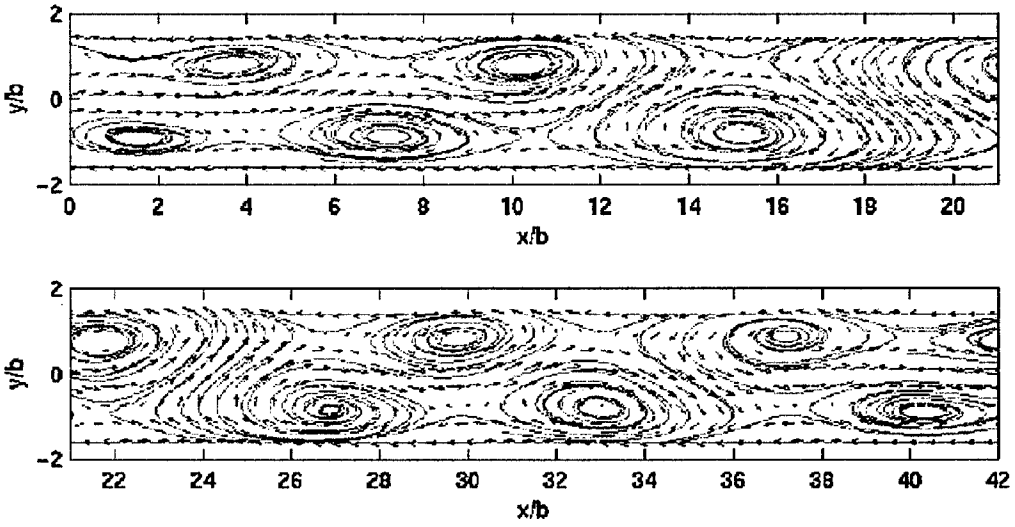

Figure 3. Planar structural topology resulting from the low-order model.

With the expertise gained from the experiments in the planar jet, the focus of the current research is now on a rectangular jet of aspect ratio 7. A nozzle has been fabricated and the base flow documented. The procedure outlined above will be applied in the near field of the rectangular jet. As in the work described above the streamwise coordinate will be taken as homogeneous so that we will be restricted to the examination of local jet dynamics at selected streamwise locations. The resulting POD eigenfunctions will be a function of Strouhal number and the two inhomogeneous cross-stream coordinates. Unlike the experiments described above, the rectangular jet will require a full Cartesian array of x-wire probes laid out in the cross-stream plane. This approach is somewhat reminiscent of that taken by Citrinniti [4] to study the axisymmetric jet at a fixed x location (although in that case only single sensor probes were used). This probe array will also be used for the instantaneous flow field realizations required for projection of the

POD modes and reconstruction of the coherent structure in physical space. This will allow a dynamic reconstruction of the large-scale flow field behavior in each cross-stream plane investigated.

Acknowledgement/Disclaimer
This work is sponsored by the Air Force Office of Scientific Research, USAF, under grant number F49620-00-1-0013. The views and conclusions contained herein are those of the authors and should not be interpreted as necessarily representing the official policies or endorsements, either expressed or implied, of the Air Force Office of Scientific Research or the U.S. Government.

References

1. Gordeyev, S. V. and Thomas, F. O., 'Coherent Structure in the Turbulent Planar Jet. Part 1. Extraction of Proper Orthogonal Decomposition Eigenmodes and their Self-Similarity,' *J. Fluid Mech.*, 414, pp. 145-194, 2000.
2. Bonnet, J. P., Cole, D. R., Delville, J., Glauser, M. N. and Ukeiley, L. S., 'Stochastic Estimation and Proper Orthogonal Decomposition: Complementary Techniques for Identifying Structure,' *Experiments in Fluids*, 17, pp. 307-314, 1994.
3. Aubry, N., Holmes, P., Lumley, J. L., and Stone, E., 'The Dynamics of Coherent Structures in the Wall Region of the Turbulent Shear Layer', *J. Fluid Mech.*, 192, pp. 115-175, 1988.
4. Citrinniti, J., 'Experimental Investigation into the Dynamics of the Axisymmetric Mixing Layer Utilizing Proper Orthogonal Decomposition,' Ph.D. dissertation, SUNY Buffalo, 1996.

Personnel

Flint O. Thomas	Professor, University of Notre Dame
Stanislav V. Gordeyev	Postdoc, University of Notre Dame
R.B. Prabhu (anticipated)	Postdoc, University of Notre Dame

Publications

Coherent Structure in the Turbulent Planar Jet. Part 1. Extraction of Proper Orthogonal Decomposition Eigenmodes and their Self-Similarity, S. V. Gordeyev and F. O. Thomas, *J. Fluid Mech*, vol. 414, pp. 145-194, 2000.

Extraction and Dynamical Modeling of Large-Scale Coherent Structure in the Planar Jet, S. V. Gordeyev and F. O. Thomas, Proceedings of the 20th Int. Congress of the Int. Union of Theoretical and Applied Mechanics, Chicago, 2000.

A Low Order Model of Coherent Structure in a Turbulent Jet, S. V. Gordeyev and F. O Thomas, Bulletin of the APS, vol 44, 8, pp. 35, 1999

Coherent Structure Dynamics in Turbulent Jet Flows via a Joint Application of POD and Wavelet Transform Methods, F. O. Thomas and S. V. Gordeyev, Bulletin of the APS, vol 44, 8, pp. 65, 1999

OPTICAL DIAGNOSTICS FOR TURBULENT FLOWS

AFOSR F49620-97-1-0417 (AASERT) & AFOSR F49620-99-1-0181 (DURIP)

C. Randall Truman
Mechanical Engineering Department
University of New Mexico

Abstract
Flow diagnostic instrumentation to measure turbulent flow in research and instructional wind tunnels has been acquired with a DURIP equipment grant. These instruments include a multi-channel hot-wire anemometer and a recently developed optical analysis system based on a two-dimensional Hartmann sensor. This instrumentation provides the University of New Mexico with the capability to make measurements of turbulent flow similar to that established in the Air Force Phillips Laboratory FOTTOS project. Graduate and undergraduate students will be trained to make turbulent flow measurements with traditional anemometry as well as state-of-the-art optical techniques. With AASERT student support, flow control techniques will be studied for wall-bounded and free shear flows.

Approach
In collaboration with the Air Force Research Laboratory/Phillips Research Site, we previously studied the effect of large-scale (or coherent) structure on optical propagation through a low-Reynolds-number round jet [1-7]. The experiments were carried out at the AFRL/Phillips Research Site in collaboration with the AeroOptics working group led by Dr. Lenore McMackin. An experimental turbulent jet facility was developed at the Phillips Lab in which flow and optical parameters can be measured simultaneously. The Fast Optical Tomography of Turbulent Organized Structures (FOTTOS) system was developed as well as a steering mirror control system for propagation of a thin beam through the jet. Some of these same techniques will be employed in studies at the University of New Mexico.

The wind tunnel to be used in the present work has been loaned by the Air Force Research Laboratory/Phillips Site. It is a subsonic open-circuit tunnel designed and built by Rocketdyne for optical studies of turbulent wall-bounded flow at the AFRL Starfire Optical Range in support of the AirBorne Laser (ABL) program. Nominal design velocity is 18 m/s through the 50 cm (high) by 10 cm (wide) test section. The maximum flow Reynolds number is of the order 10^6 per meter. Silicon rubber heating pads are attached to the aluminum walls in the upstream part of the test section; the temperature of each wall may be controlled separately. Optical-quality windows (13 and 35 cm) are installed in the downstream portion of the test section to allow optical measurement of the flow field. Both thermal anemometry and laser-based diagnostics will be used.

A unique two-dimensional Hartmann wavefront sensor will be used to characterize turbulent flow in the tunnel. Light from an established source (here a laser diode) is passed through the turbulent flow where temperature fluctuations will aberrate the wavefront. This light is focused upon a 2-D array of micro-lenses (or lenslets) that generates a grid of focal spots on a 2-D CCD camera. The wavefront slope over each lenslet is determined from the focal spot

displacements and the wavefront is reconstructed by integrating the slopes. These wavefronts will be analyzed to characterize the turbulent structure. Applications of this sensor include aero-optic measurements in supersonic and hypersonic flow [8-10]. Dr. Dan Neal has established a company, WaveFront Sciences Inc. (Albuquerque), to produce these systems and currently collaborates with AEDC White Oak.

Figure 1 shows a schematic of the wind tunnel with the optical path for the Hartmann sensor. Figure 2 shows the optical components of the Hartmann sensor from the light source to the lenslet array and CCD camera. The relation between the average slope of an aberrated wavefront and the displacement measured in the CCD camera plane is illustrated for one lenslet in Figure 3. Each lenslet in the 2-D array uses a portion of the CCD camera to resolve the displacement of this spot, which is then used to compute the average tilt angle $\theta_{\perp}$ across the lenslet. The two-dimensional distribution of tilt angles across the flow will be related to density (or temperature) gradients in the flow.

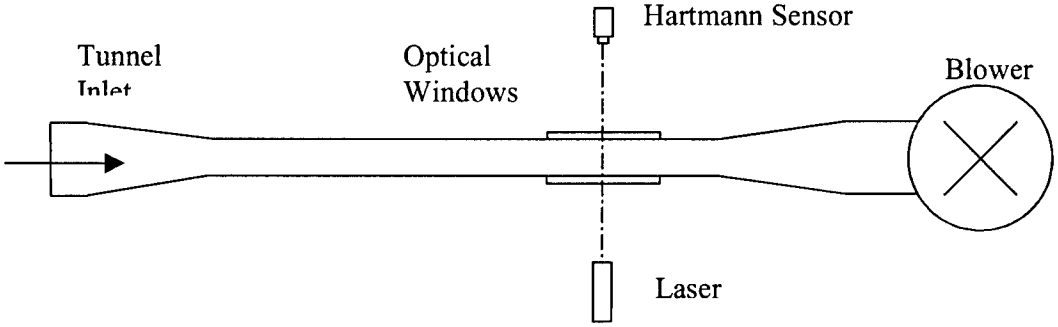

Figure 1. Schematic of wind tunnel with optical path of Hartmann sensor through optical windows in test section

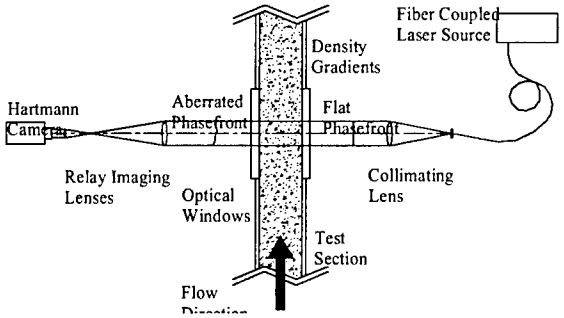

Figure 2. Hartmann sensor components

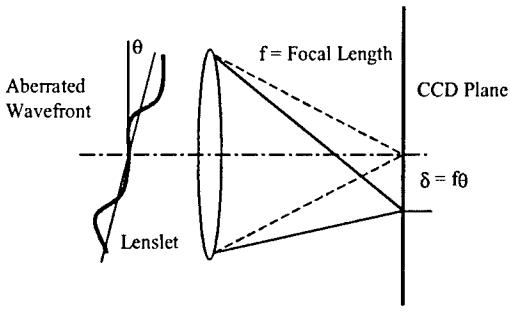

Figure 3 Schematic of Hartmann sensor measurement of average tilt across a lenslet by displacement of focused spot along CCD camera plane

The relay-imaging optics are illustrated in Figure 4. The size of the beam through the flow D1 can be reduced to size D2 into the lenslet array and CCD camera by the magnification factor M=F2/F1, the ratio of focal lengths. This demagnification (for M<1) further serves to increase the phase angle (or tilt) into the lenslet array. Thus it is possible to observe a region of flow larger than the 4 mm x 6 mm aperture of the lenslet array/camera while increasing

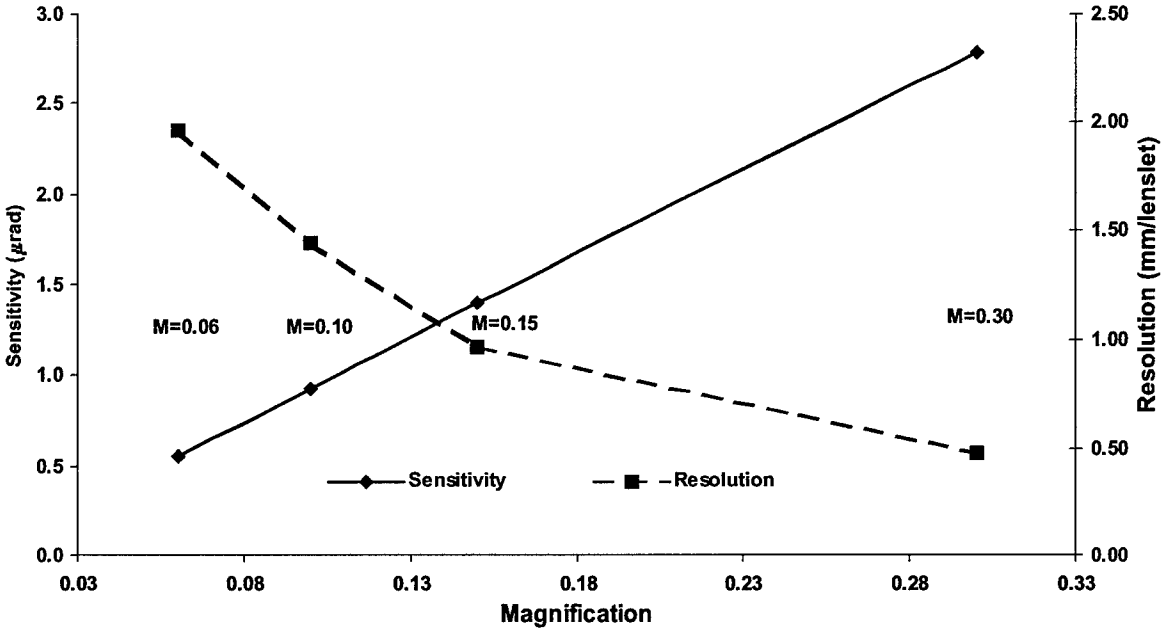

Figure 5 – Sensitivity & Resolution as Function of Magnification for 33 x 44 Lenslet Array

the sensitivity to tilt. Figure 5 shows the trade-off between sensitivity (μrad) and resolution (mm/lenslet) over the field of view as a function of magnification for a 33x44 lenslet array. Sensitivity is the minimum phase angle difference that can be detected by each lenslet. It is beneficial to achieve small spatial resolution and small sensitivity. Several relay imaging lenses were selected so that a range of magnifications from 0.10 to 0.30 could be used. Note that resolutions are on the order of 1 mm/lenslet in the flow, with tilt angles as small as 1 μrad detected.

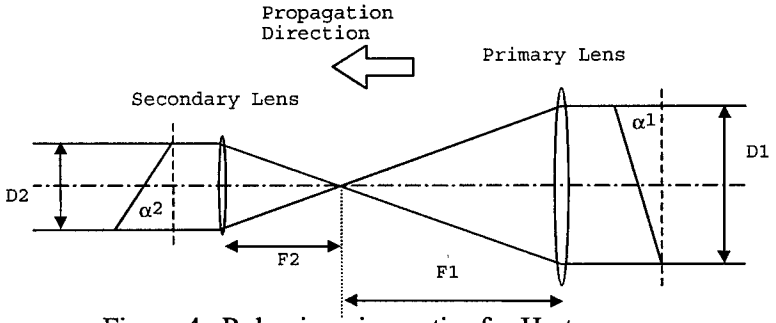

Figure 4. Relay-imaging optics for Hartmann sensor.

A simple test case of a cylinder in cross-flow near a surface will be used to illustrate the measurements. Figure 6 shows a view of the flow normal to the heated surface and along the optical axis of the Hartmann sensor. The wall is heated (up to the window) producing a thermal boundary layer that interacts with the cylinder that is placed perpendicular to and nearly touching the wall. The measured 2-D distribution of tilt angles (Figure 7) and the resulting wavefront (Figure 8) illustrate the presence of temperature gradients in the streamwise and cross-stream directions.

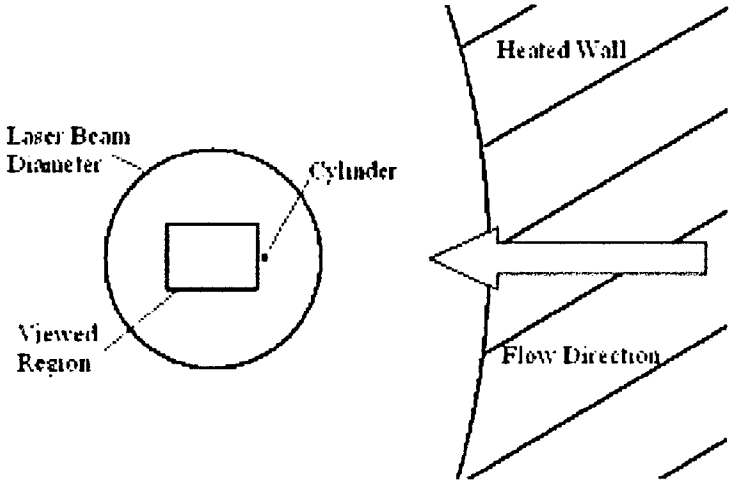

Fig. 6 Cylinder in cross-flow in heated boundary layer; view normal to wall & along optical axis.

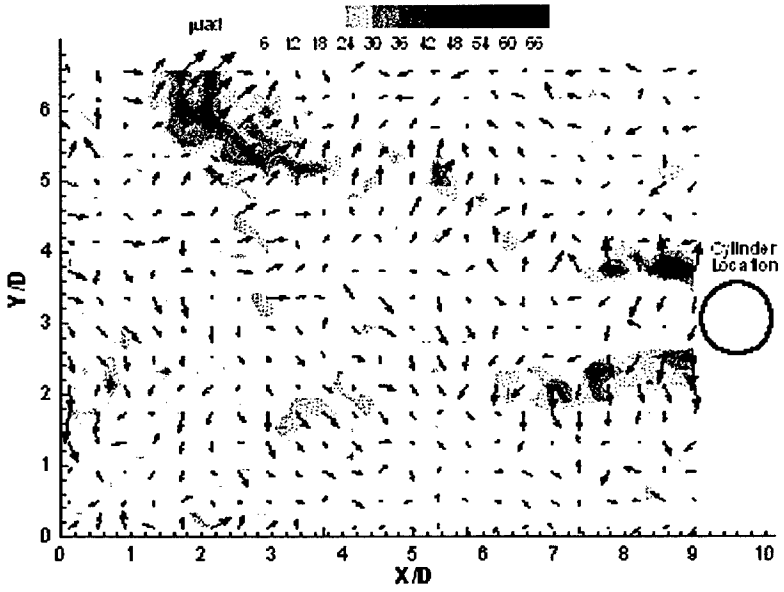

Fig. 7 Optical tilt vectors with contours of tilt magnitude.

For small temperature differences (e.g., 10C) in air, temperature serves as a passive scalar. These temperature gradients can be related to velocity gradients and thus flow structure. The magnification factor M can be increased by changing the relay-imaging lenses to resolve small flow structures. The physical constraint is that the large temperature difference required to produce refractive-index changes for M>>1 may introduce buoyancy effects.

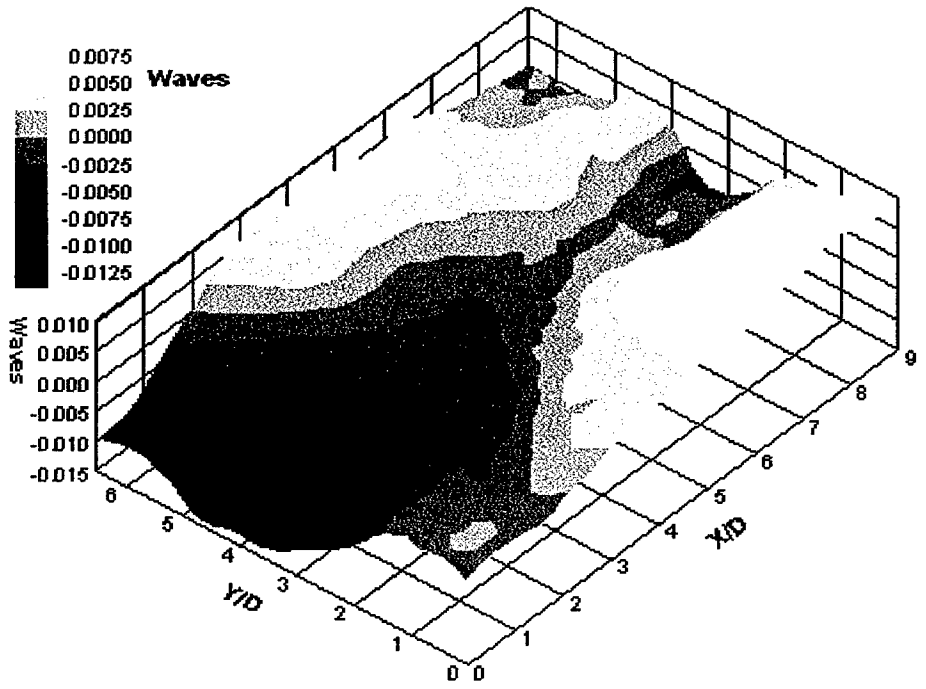

Fig. 8 Wavefront in waves (optical phase error/wavelength of light)

Future Work

The instrumentation will support research in two areas:

1) continued study of optical propagation through turbulent shear flows, and
2) studies of the interaction between deformable surfaces and flow fields, including laminar, transitional and turbulent flows.

The latter includes flow control technologies for aircraft control surfaces and for localized flow control to reduce separation, delay transition or reduce drag. These materials offer the promise of continuous deformable control surfaces with high dynamic response. Ionic polymer-metal composite materials are among those that will be tested in the tunnel, in collaboration with Prof. Mohsen Shahinpoor in Mechanical Engineering at the University of New Mexico.

Acknowledgment/Disclaimer

This work was sponsored (in part) by the Air Force Office of Scientific Research, USAF, under grants AFOSR F49620-97-1-0417 (AASERT) & AFOSR F49620-99-1-0181 (DURIP). The views and conclusions contained herein are those of the authors and should not be interpreted as necessarily representing the official policies or endorsements either expressed or implied, of the Air Force Office of Scientific Research or the U.S. Government.

The assistance of Dr. Dan Neal, Wavefront Sciences Inc., in selecting the optical components to be used with the two-dimensional Hartmann sensor is gratefully acknowledged.

References

1. Luna, T.L., Truman, C.R. & Masson, B.S., 1997, "Linear Stochastic Estimation of Optical Beam Deflection Through a Heated Jet," AIAA Paper 97-0072.
2. McMackin, L., Hugo, R.J., Bishop, K.P., Chen,E.Y., Pierson, R.E. & Truman, C.R., 1997, "High speed optical tomography system for imaging dynamic transparent media," Optics Express, Vol. 1, No. 11 (http://epubs.osa.org/opticsexpress).
3. McMackin, L., Hugo, R.J., Bishop, K.P., Chen, E.Y., Pierson, R.E. & Truman, C.R., 1999, "High speed optical tomography system for quantitative measurement and visualization of dynamic features in a round jet," Experiments in Fluids, Vol. 26, pp. 249-256.
4. Nelson, I.I. & Truman, C.R., 1998, "Identification of Large Scale Structures in a Turbulent Jet Using Optical Techniques," AIAA Paper 98-3016.
5. Sapayo, J. & Truman, C.R., 1997, "Study of Development of Axisymmetric and Helical Modes in Heated Air Jets Using Fast Optical Tomography," AIAA Paper 97-1809.
6. Truman, C. R., Masson, B.S. & McMackin, L., 1996, "Optical Tomographic Study of the Effect of Excitation of a Heated Round Jet," AIAA Paper 96-2323.
7. Truman, C.R., McMackin, L., Pierson, R.E., Bishop, K.P. & Chen, E.Y., 1998, "Open-loop Control of Compensation for Optical Propagation Through a Turbulent Shear Flow," AIAA Paper 98-2832.
8. Neal, D.R., Alford, W.J. & Gruetzner, J.K., 1996, "Amplitude and Phase Beam Characterization using a 2-Dimensional Wavefront Sensor," SPIE Vol. 2870, pp. 72-82.
9. Neal, D.R., Hedlund, E., Lederer, M., Collier, A., Spring, C. & Yanta, W., 1998, "Shack-Hartmann Wavefront Sensor Testing of Aero-Optic Phenomena," AIAA Paper 98-2701.
10. Yanta, W.J., et al., 2000, "Near- and Farfield Measurements of Aero-Optical Effects due to Propagation through Hypersonic Flows," AIAA Paper 2000-2357.

Personnel Supported

Patrocino Chavez	Graduate Research Assistant (Jan. 2000-present), Undergraduate Student (1999; BSME Dec. 1999)
Zachary Smith	Undergraduate Student (1999-2000; BSME May 2000)
Daniel Temer	Undergraduate Student (1999-2000)
Ryan Ebert	Undergraduate Student (summer 2000)
Savanna Garcia	High School Student (summer 2000)

Interactions/Transitions

A project in collaboration with Prof. A. Domaradzki and Dr. Darek Bogucki, University of Southern California, and Dr. Bob Ecke, Los Alamos National Laboratory, was initiated in 1998. This experiment used the optical diagnostics available at the Phillips Lab to study optical propagation through a Rayleigh-Benard cell containing water that simulates turbulent oceanic conditions for velocity and temperature fluctuations. Preliminary results were presented at the 1998 SPIE International Conference on Ocean Optics.

PIV DIAGNOSTICS FOR FLOW CONTROL APPLICATIONS

F49620-00-1-0186

Peter Vorobieff

C. Randall Truman

Jonathan Gallegos
Department of Mechanical Engineering
University of New Mexico

Abstract
The equipment funded by this AFOSR grant is intended to facilitate a wide range of investigations of controlled flows. The diagnostic system will have to be assembled and integrated with the systems producing and controlling the flow. We are implementing the first step of this process as a test case involving perhaps the best-studied problem of hydrodynamics: a cylinder wake. However, the setting of this test case allows us to develop an experimental arrangement integrating the diagnostic system with the computer-controlled flow actuation system. Moreover, the resulting investigation will shed light on an important aspect of cylinder wakes which has not been studied experimentally before.

We will investigate ***the hysteresis of vortex-shedding behind a circular cylinder*** moving through quiescent fluid with periodically varying velocity. We will acquire quantitative information sufficient for a full characterization of the flow in terms of instantaneous velocity field in the plane normal to the axis of the cylinder. The experiment will involve a 3 m horizontal tow tank filled with water, with a belt-drive traverse system providing a prescribed velocity profile for a cylinder model being towed. The experimental diagnostic will be digital Particle Image Velocimetry (DPIV, see Willert and Gharib (1992) for an overview), recovering velocity-field information from the flow at a rate of 30 fields per second. The velocity profile will be selected to vary periodically near the threshold of vortex-shedding. The primary objective of the experiment is to confirm the existence of hysteresis in the onset of vortex-shedding predicted by the stability analysis (Noack and Eckelmann, 1994).

Wakes behind bluff bodies and oscillating loads on bodies immersed in fluid flows have fascinated scientists since antiquity. Specifically, the phenomenon of æolian sounds emitted by a string oscillating in the wind attracted the attention of Aristotle in 4th century b.c.e., but it was not until the works of Bénard (1908) and von Kármán and Rubach(1912) that the flow structure responsible for the oscillation was revealed (Fig. 1).

It is a staggered row of counter-rotating vortices downstream of the body, known as the Bénard-von Kármán vortex street. Vortices shed on the alternating sides of the cylinder cause the oscillation of the flow-induced load on the cylinder. Formation of the vortex

streets and the induced vibrations are vital for a wide variety of applications – from aircraft design to architecture. Cylinder wakes were studied extensively in the following years, but several major issues remain unresolved. Among these is the issue of the hysteresis at the onset of vortex shedding.

Fig. 1: Pattern of counter-rotating, staggered vortices behind a cylinder as observed by Bénard (1908).

The main dimensionless parameter characterizing the cylinder wake is the Reynolds number $Re=u\ D/\ $, where u is the freestream velocity, D is the cylinder diameter and is the kinematic viscosity of the fluid. The vortex shedding does not normally occur until Re exceeds the value of 46. Stability analysis of the flow attributes the onset of vortex shedding to a supercritical Hopf bifurcation (Noack and Eckelmann, 1994). This would imply that the onset should be subject to hysteresis: in the case when the flow velocity increases/decreases past the onset value, there should be a delay in the vortex street formation/destruction. However, despite the fundamental character of the transition and its importance, no experimental observations of the hysteresis exist to date.

We will study the cylinder wake near the onset of vortex shedding. We will tow a Plexiglas cylinder (hollow and thin-walled to minimize refraction) through a free-surface water tank 3 m long, with a depth and width about 50 cm. The cylinder will be mounted on a computer-controlled belt-drive traverse system. The belt drive can sustain horizontal velocities up to 0.5 m/s. The onset Reynolds number Re=46 for a 0.5 cm diameter cylinder will correspond to the towing velocity of about 1 cm/s. We will investigate several velocity profiles oscillating near this onset velocity: sinusoidal, sawtooth-shaped, etc. With the towing velocity changing above and below the onset value, we want to observe a sequence of velocity fields with and without the vortex street. We will illuminate the flow with one or two Nd:YAG lasers producing a vertical pulsed light sheet spanning the length of the tow tank. The water will be seeded with small neutrally-buoyant tracer particles following the flow (polystyrene microspheres). The effective exposure time for the acquisition device will be limited to the laser pulse duration (~5 nanoseconds). A sequence of images of the illuminated section of the flow will show tracer particle motion, which will be quantitatively resolved to velocity field using a Lagrangian particle-tracking code (Sava , 1999).

Figure 2 shows the hardware schematics of the experimental arrangement. The actuation system (Parker Compumotors) is controlled by a personal computer feeding the prescribed motion profile to a Parker 6K4 controller. The controller passes the signals to a stepper drive which in turn rotates the motor attached to the belt. The core of the acquisition system is the digital video camera or camcorder. In Fig. 2, we show a Sony DX-2000 digital camcoder. It is capable of recording and storing 30 frames per second at a resolution of 500 by 1000 pixels. Later it will be replaced by a Kodak Megaplus ES 1.0 digital camera capable of acquiring 15 frames per second with a 2048-pixel square resolution or 30 frames per second with a 1024-pixel square resolution. Each digital

video device sends a strobing signal to a Berkeley Nucleonics digital delay generator BNC-555, which in turn triggers the Nd:YAG Gemini PIV laser. The latter is capable of providing 15 pulse pairs with a variable delay per second, which leads to a flexible setup for measurement of velocities and accelerations at different framing rates, as well as multi-plane velocity measurement involving two lasers. If the Sony digital camcorder is employed, the laser-illuminated flow images are stored on tape and then transferred to the computer via an IEEE 1394 interface board (Canopus DV Raptor). In the case of the Kodak Megaplus camera, images are transferred to the computer in real time through a Bitflow Roadrunner framegrabbing board. Then the sequence of image pairs will be analyzed to produce the field of velocity components in the plane of the laser sheet.

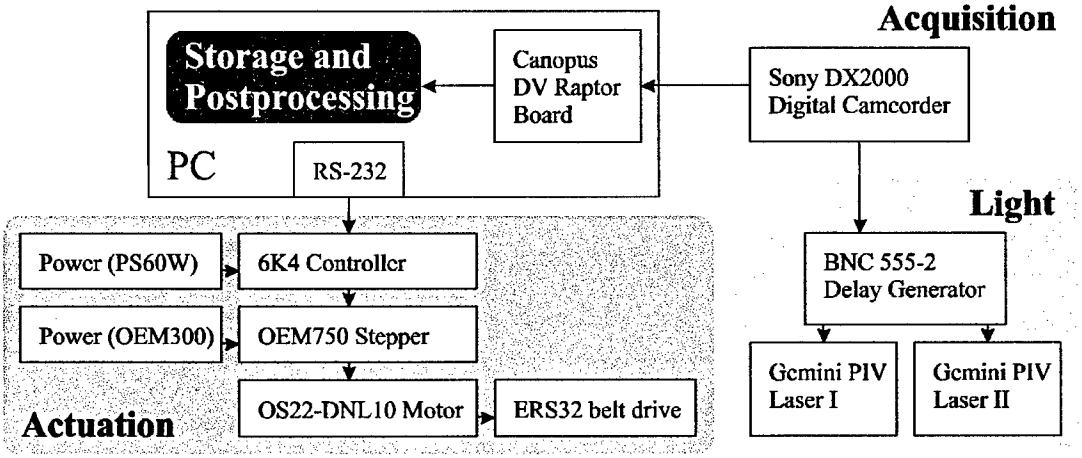

Fig. 2: Scheme of the experimental system.

The overall layout of the experiment is shown in Fig. 3. The computer, Compumotor controller, digital delay generator, laser controls and power supplies are located on and under the optical table in the rear. The tow tank (front) has the belt drive attached to its top. The traversing system is mounted on the belt drive. The cylinder and the camera can travel the length of the tank with a prescribed variable velocity profile. The laser head is positioned under the bottom of the tank. The laser beam passes through a cylindrical lens, producing a vertical laser sheet illuminating a plane in the flow.

Adding a second laser and a second camera will further modify this arrangement, facilitating stereoscopic two-plane PIV. Other future modifications of the tow-tank setup can include adding a second-axis motion and/or rotation actuator to the traversing system, and mounting a model with controllable elements instead of the cylinder.

In summary, the initial stage of building a multi-purpose PIV system for the study of controlled flows will involve developing an integrated setup for a tow-tank cylinder wake study. This study will address the fundamental problem of the hysteresis at the onset of vortex shedding. The resulting actuator control/diagnostics arrangement will be expanded and employed in future water tank/wind tunnel experiments. At present, we are working on the system setup, with all the main components as shown in Fig. 3 already in place.

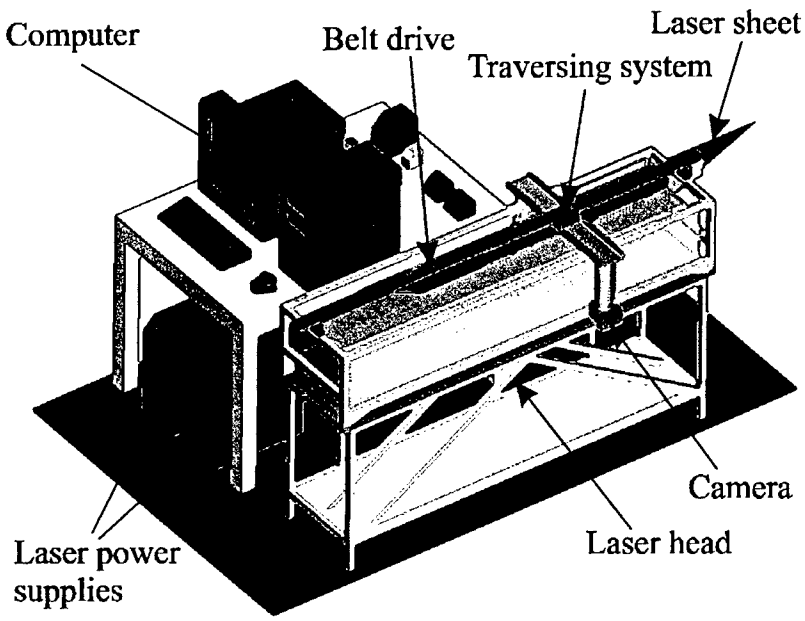

Fig. 3: Experimental layout

Acknowledgement/Disclaimer

This work was sponsored (in part) by the Air Force office of Scientific Research, USAF, under grant/contract number F49620-00-1-0186. It was also partially sponsored by the Oak Ridge Association of Universities. The authors thank Professor Ömer Sava (University of California - Berkeley) for providing a copy of his ALPT code to facilitate velocity-field interrogation. The views and conclusions contained herein are those of the authors and should not be interpreted as necessarily representing the official policies or endorsements, either expressed or implied, of the Air Force Office of Scientific Research or the U.S. Government. No cats were hurt during the preparation of this document.

References

1. H. Bénard, Formation de Centres de Giration à l' Arrière d'un Obstacle en Mouvement. Comptes Rendus, 1908, 147:839-842.

2. Th. von Kármán and H. Rubach, Über den Mechanismus des Flüssigkeits- und Luftwiderstandes. Physikalische Zeitschrift, 1912, 13:49-59.

3. B.R. Noack and H. Eckelmann, A Global Stability Analysis of the Steady and Periodic Cylinder Wake. Journal of Fluid Mechanics, 1994, 270:297-330.

4. C.E. Willert and M. Gharib, Digital Particle Image Velocimetry. Experiments in Fluids, 1991, 10:181-193.

5. Ö. Sava , Advanced Lagrangian Particle Tracking (ALPT) PIV program, 1999.

Personnel supported
None (equipment grant).

Publications
"Hysteresis at the Onset of Bénard-von Kármán Vortex Shedding: An Experimental Study," J. Gallegos, P. Vorobieff, to be submitted to Experiments in Fluids, 2000.

AN EXTREMELY SENSITIVE PZT-BASED MEMS MAGNETOMETER FOR USE AS AN ORIENTATION SENSOR

AFOSR GRANT: F49620-98-1-0500

Dennis K. Wickenden
Applied Physics Laboratory
The Johns Hopkins University, Laurel, MD

William D'Amico
Weapons and Materials Research Directorate
Army Research Laboratory, Aberdeen, MD

Madan Dubey
Sensors and Electronic Devices Directorate
Army Research Laboratory, Adelphi, MD

Program Goals

The overall program goals are to develop an extremely sensitive microelectromechanical (MEMS) magnetometer, based on a resonating xylophone bar,[1] to measure the angular orientation of projectiles with respect to the Earth's magnetic field. The accuracy of this device (due to its inherent sensitivity and the use of multiple sensors on the same structure) and its small size (resonators < 0.5 mm in length) provides a unique capability that surpasses the performance of existing MEMS-based angular rate sensors. Its successful development will revolutionize inertial measurement concepts and applications. Specific goals of the reporting period, covering the period August 1, 1999 to July 31, 2000, include:

- optimizing the polysilicon magnetometer for capacitive readout;
- developing a hybrid magnetometer based on the MCNC (Cronos) SmartMUMPs process;
- developing a fully integrated polysilicon magnetometer;
- developing the packaging for a MEMS-based xylophone magnetometer; and,
- optimizing the PZT processing for a piezoelectric magnetometer.

Progress

Polysilicon Devices

As described in the last report, various polysilicon magnetometers were designed and fabricated on a 1cm square site processed on the MUMPs27 run in September 1998. A schematic diagram of a typical device is shown in figure 1. The lower electrode consists of a 0.5 μm thick poly0 layer patterned on the silicon nitride-coated silicon substrate. The xylophone bar, support electrodes, and mounting pads are fabricated from 2 μm thick poly1 suspended (after release of the sacrificial silicon dioxide) 2 μm above the nitride layer or lower electrode. The mounting pads are attached to the lower electrode by the indicated patterns to provide a rigid anchor that minimizes vibrational coupling with the xylophone

bar.[2] Contact between the xylophone bar and the nitride layer is minimized by having 0.75 μm deep "dimples" in the center and toward the ends of the xylophone bar. An SEM micrograph of a released and mounted 500 x 50 x 2 μm xylophone bar is presented in figure 2. The micrograph clearly displays the anchor pattern, the etch holes, and the topographical evidence of the dimples. It also demonstrates the clean release of the xylophone structure.

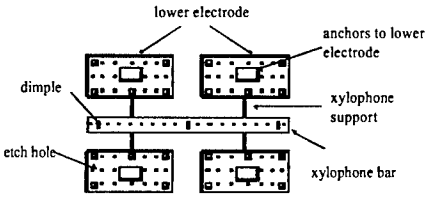

Figure 1. A schematic diagram of a typical polysilicon device.

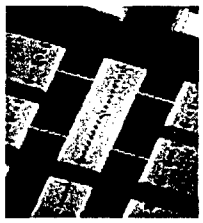

Figure 2. An SEM photograph of a mounted 500x50x2 μm device.

It was deduced that the support arms contribute an increased torsional stiffness to the xylophone bar. This leads to an increased resonance frequency that can be accurately modeled using classical Bernoulli-Euler beam theory. The results of this analysis, depicted as the resonance frequency of a 500x50x2 μm xylophone bar as a function of the width of 45 μm long support arms, is shown in Figure 3. In this figure, the solid line denotes the results of the analysis and the open circles represent the experimental results for devices manufactured on MUMPs 27. The agreement is excellent and well within the manufacturing tolerances of the MEMS processing.

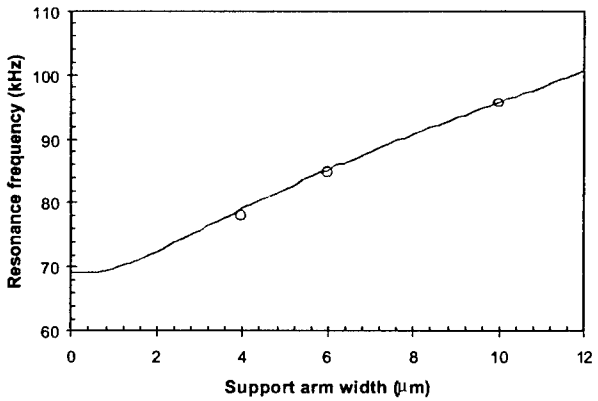

Figure 3. Resonance frequency as a function of support arm width for 500x50x2 μm polysilicon xylophones with 45 mm long support arms.

A plot of the output response of the polysilicon xylophone magnetometer with 4 μm support arm widths as a function of impressed magnetic flux density up to 150 μT is shown in figure 4. The superimposed line is a least-squares fit to the data, and demonstrates that the magnetometer response is linear over the range of magnetic flux density shown. A high

background field originating from a nearby permanent magnetic, housed in a vacuum valve, prevented lower field strengths being characterized. (The valve has since been replaced with a non-magnetic version). The current through the device was limited to 22 μA by the high sheet resistance (10 Ω/square) of the polysilicon. Increasing the current beyond 25 μA led to a degradation in performance of the device.

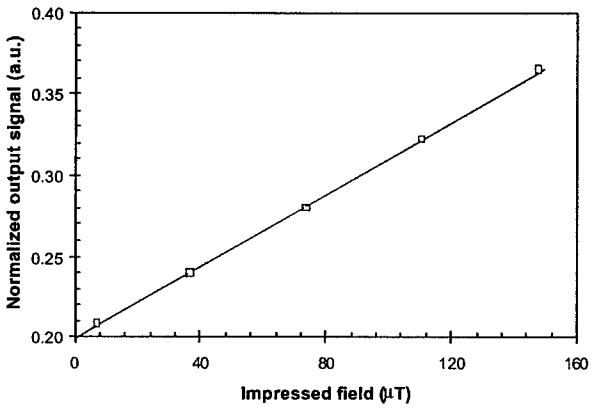

Figure 4. Output response of a 500x50x2 μm xylophone magnetometer as a function of impressed magnetic flux density.

An estimate of the noise floor of the xylophone magnetometer due to thermo-mechanical noise (Brownian motion due to the Langevin force) and, to a lesser extent, Johnson noise (current noise that couples with the magnetic field) yields a value of the order of 100 (pT•A)/√Hz. This limit has been readily achieved using macro-sized conventional (5 x 0.5 x 0.09 mm) devices chemically milled from CuBe foil, and using a drive current of 10 mA.[3] This result and the above noise estimate call out the very important role that the amplitude of the drive current plays in determining the ultimate field sensitivity of xylophone bar magnetometers.

Various designs to decrease the resistance of Cronos polysilicon devices were laid out and manufactured on the MUMPs30 and MUMPs34 runs. In these new designs the drive current to the magnetometer is fed from both sides, giving an immediate doubling of the drive current capability. In addition, magnetometers were manufactured from poly1/poly2 layers and the use of gold stripes deposited on various parts of the xylophone was examined. Also included on the die were various geometries of poly0 and poly2 capacitive plates.

Preliminary characterization of these devices has been undertaken in a new test facility. This facility is evacuated with vane and molecular drag pumps to prevent oil and/or other contaminants depositing on the xylophones and degrading their resonance characteristics. Poly1/poly2 500x50x3.5 μm bars with gold deposited on only the electrodes have resonance frequencies of 165 kHz and Q-factors of between 30,000 and 40,000 at low pressures. The same bars with full gold strips on the support arms have increased resonance frequencies at 168 kHz, due to the increased stiffness of the support arms, and Q-factors

reduced to 10,000. The resonators with the gold strips along the xylophone bar have decreased resonance frequencies of approximately 164 kHz, due either to mass loading of the bar or to the decreased effective Young's modulus, and Q-factors in excess of 10,000. Given the limited data, it is too early to conclude whether the drop in Q-factor observed when gold is deposited on the support arms or along the bar is a limiting effect or not.

Hybrid Magnetometer

The original proposal to develop a hybrid magnetometer was based on the concept of using the Cronos SmartMUMPs foundry. As noted in the last progress report, Cronos is no longer offering SmartMUMPs as a service. However, MicroSensors, Inc. have developed a general purpose, ultra-low noise capacitive readout and control electronics ASIC for MEMS capacitive sensors, Part No. MS3110. This circuit has a capacitance resolution of 0.05 fF with a dynamic range of approximately 100 dB. Engineering samples have been received for evaluation. Programmed 16-pin SOIC circuits will be evaluated using macroscopic (5 mm) magnetometers chemically milled from CuBe foil. Programmed die will be evaluated using a dedicated die produced on the MUMPs34 run. The latter is currently being released and packaged. The MS3110 die will be mounted on the MUMPs chip and wire bonded in place.

Integrated Magnetometer

Work on the integrated magnetometer has concentrated on designing electronics necessary to maintain the magnetometer at resonance. Both analog and digital approaches are being pursued and the initial prototypes are being breadboarded for evaluation.

Packaging

Effort on developing the packaging for the xylophone magnetometer has been postponed until the drive and sense circuit design has been finalized and the real estate requirements are better known.

PZT Processing

Work has continued to develop a process to minimize the residual stress in a Pt/PZT/Pt structure and thus allow the release of an undistorted xylophone bar.[4] In these studies, different layer sequences were deposited on 3" silicon wafers and stress measurements were made using a Tencor FLX-2908 before and after adding each of the layers as well as during and after annealing. In the case of multilayer films, the total thickness of all layers at the given process step was considered. Negative values for stress indicated a compressive stress and positive ones a tensile stress. PECVD oxide and nitride dielectrics were deposited at 250°C and rapid thermal annealed (RTA) annealed at 750°C for 60 sec in nitrogen. Top and bottom metal electrode layers were sputter deposited and either RTA annealed at 700°C for 60 sec or furnace annealed to 700°C (ramped at 15°C/min) under nitrogen. PZT films (250 nm, 500 nm, 1000 nm) were spin coated and the residual stress was measured after crystallization.

The deposition of the bottom electrode layer (20nm Ta/170 nm Pt) onto either dielectric layer did not significantly change the residual stress levels. However, after RTA annealing at 700°C for 60 seconds, the residual stress became tensile at levels of 1070±70

MPa. This effect was examined in more detail by performing an RTA anneal at 750°C after the dielectric deposition and before the electrode deposition. The RTA annealing after oxide deposition changes a compressive stress of -430±50 MPa to a tensile stress of +50±50 MPa. The stress then reverts to compressive after deposition of the bottom electrode, and then becomes tensile upon RTA annealing of the stack. The residual stress decreases with increasing oxide thickness and varies from 200 to 500 MPa – levels significantly lower than when the metal was deposited on unannealed oxide. The behavior of the nitride-coated samples was much more varied and resulted in residual tensile stresses in excess of 100 MPa. It is to be noted that the adhesion of the subsequently deposited PZT improved significantly following annealing.

The cumulative effect on residual stress of the deposition of a 500 nm PZT layer on an RTA annealed bottom electrode, the deposition of a Pt top electrode layer, followed by an RTA anneal at 300°C for 60 seconds in N_2, is illustrated in figure 5. In each case, the deposition of the PZT (including the crystallization process) reduces the residual stress to levels that remain essentially unchanged following the top electrode deposition and RTA anneal.

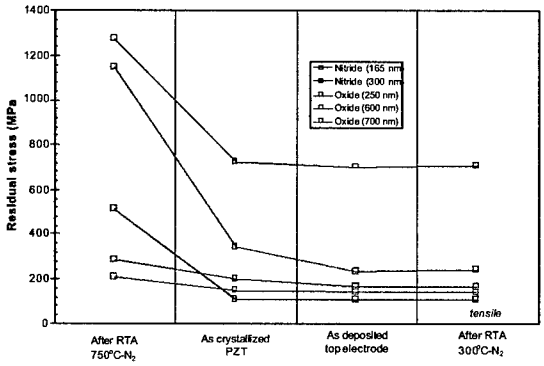

Figure 5. Cumulative residual stress measurements following deposition of PZT and top electrode layers followed by a 300°C RTA anneal in nitrogen.

Comparative studies on annealing the bottom electrode indicated that furnace annealing results in less residual stress than RTA annealing.

Preliminary conclusions from these studies include:

- the variation in residual stress of PECVD oxide-coated wafers is less than for PECVD coated-nitride wafers;
- furnace annealing of the bottom electrode results in less residual stress than RTA annealing;
- annealing the bottom electrode improves the adhesion of the PZT layer;
- the PZT deposition process has the most pronounced effect on the final residual stress levels;
- the final residual stress level of >140±25 MPa tensile is to be compared with a residual stress level of approximately 10 MPa compressive for polysilicon layers; and,

- further work is required to significantly reduce these levels.

Acknowledgment/Disclaimer
This work was sponsored (in part) by the Air Force Office of Scientific Research, USAF, under grant number F49620-98-1-0500. The views and conclusions contained herein are those of the authors and should not be interpreted as necessarily representing the official policies or endorsements, either expressed or implied, of the Air Force Office of Scientific Research or the U.S. Government.

References

1. R.B. Givens, T.J. Kistenmacher, J.C. Murphy, R. Osiander, and D.K. Wickenden, "A xylophone resonator magnetometer with high sensitivity and wide dynamic range," Applied Physics Letters, 1996, 69: 2755-2757.

2. D. Sherman, "An Investigation of MEMS Anchor Design for Optimal Stiffness and Damping," Master's Project, Univ. of Calif., Berkeley, May 1996.

3. R.B. Givens, D.K. Wickenden, D.A. Oursler, R. Osiander, J.L. Champion, and T.J. Kistenmacher, "Heterodyne detection of alternating magnetic fields with a resonating xylophone bar magnetometer," Applied Physics Letters, 1999, 74, 1472-1474.

4. E. Zakar, M. Dubey, R. Polcawich, B. Piekarski, R. Piekarz, J. Conrad, and R. Widuta, "Study of stress in PZT films for MEMS devices", presented at MRS, Boston, 1999.

JHU/APL Personnel Supported

Dennis K. Wickenden	Principal Professional Staff
John L. Champion	Senior Professional Staff
Richard L. Edwards	Senior Professional Staff
Danielle M. Wesolek	Junior professional Staff

Publications

D.K. Wickenden, J.L. Champion, R.B. Givens, T.J. Kistenmacher, J.L. Lamb, and R. Osiander, "Polysilicon xylophone bar magnetometer," SPIE Volume Vol. 3876, Micromachined Devices and Components V, (1999) pp. 267-273.

D.K. Wickenden, B. Davis, and M. Dubey, "An extremely sensitive MEMS magnetometer for use as an orientation sensor on projectiles," Proceedings of the Royal Aeronautical Society Conference on "Nanotechnology and Microengineering for Future Guided Weapons," Royal Aeronautical Society, London, November 1999, pp. 7.1-7.9.

D.K. Wickenden, J.L. Champion, R.B. Givens, T.J. Kistenmacher, J.L. Lamb, and R. Osiander, "Polysilicon xylophone bar magnetometers," Technical Digest of the Solid State Sensor and Actuator Workshop, Hilton Head, June 2000, pp. 150-15.

HIGH PERFORMANCE WOVEN MESH HEAT EXCHANGE

F49620-99-1-0286

Richard Wirtz
Mechanical Engineering Department
University of Nevada, Reno

Abstract

Introduction. In 1955, Kays and London pointed out that a most effective way to increase the performance of a heat exchanger is to increase its surface area-to-volume ratio, β [1]. Small-particle packed beds result in large values of β. Unfortunately, due to the tortuosity effect, the effective thermal conductivity of the solid phase of the packed bed, k_e is relatively small, so that much of the gain in performance obtained by having a large β is lost by having a relatively small k_e.

An anisotropic porous matrix having a large β and a large k_e in a particular direction will result in a very effective heat exchange surface. A woven or braided mesh of heat conducting filaments can be configured to have these characteristics. In order for the technique to be applicable to a wide range of applications, the woven mesh must be structured such that high thermal performance is maintained while coolant pressure drop is held at reasonable levels. This objective can be achieved through careful configuration of the woven structure.

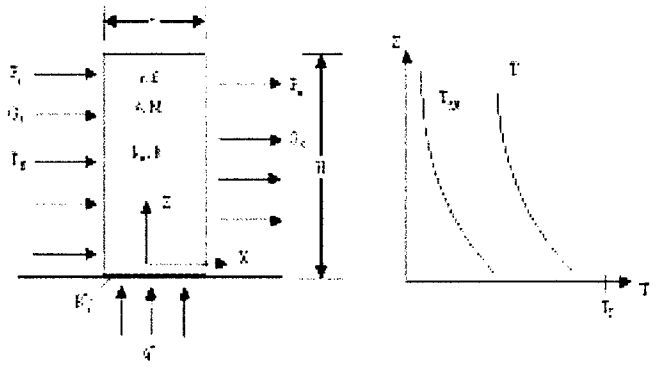

Heat exchangers employing this technology will generally have coolant flowing through a porous woven-mesh of conducting filaments, as shown in Fig. 1, where the mesh element is attached to the heat source at temperature T_s. The mesh element is characterized by its size (t, H) and makeup (porosity, ε; surface area-to-volume ratio, β; filament size and mesh numbers, d, M; thermal conductivity vector $\underline{k}_e$; mesh heat transfer coefficient, h; and, bond thermal resistance at the mesh-surface interface, R_i"). The heat flux into the element is q. The mesh (solid phase) temperature is T(z). Coolant approaches the mesh element at pressure, P_i, superficial mass velocity, G_i and temperature, $T_{f,i}$. It leaves at $P_o(z)$, $G_o(z)$ and $T_{f,o}(z)$. (P_o and G_o will be uniform if t, d and M are uniform.) The mesh thickness in the flow direction (x-direction) is relatively small, dictated by pressure-drop considerations. As a consequence, flow through the mesh is not expected to be fully developed so that thermal equilibrium between the fluid and solid phases cannot be assumed.

Objectives. The overall objective of this work is to develop woven-mesh heat exchanger technology, with particular attention to single-fluid, parallel plate heat exchangers as deployed to cool high-power avionics. The technical approach includes the following elements:

1. Analytical Modeling. Develop analytical thermal/fluid models that can be used to assess the design of woven mesh heat exchangers. Complete parametric studies and document thermal/fluid performance characteristics as a function of mesh configuration.
2. Fabrication Technology. Develop and document fabrication and manufacturing methodology.
3. Weave Characterization. Quantify thermophysical characteristics of woven-filament meshes. Find or develop and verify (through experimental measurement) analytical or empirical models of these quantities.
4. Prototype Testing. Design, construct and test prototype heat exchangers that use this technology. Benchmark analytical models.

Summary of Results

Analytical Modeling – Heat Transfer. We have developed an improved model for heat transfer from a thin porous fin (Fig. 1). A two-energy equation model, it couples one-dimensional steady conduction in the solid phase to an energy balance for one-dimensional flow of coolant through the fin. It is an extension of one proposed by Wirtz [2] in that it contains a better description of the coolant temperature variation across the porous region.

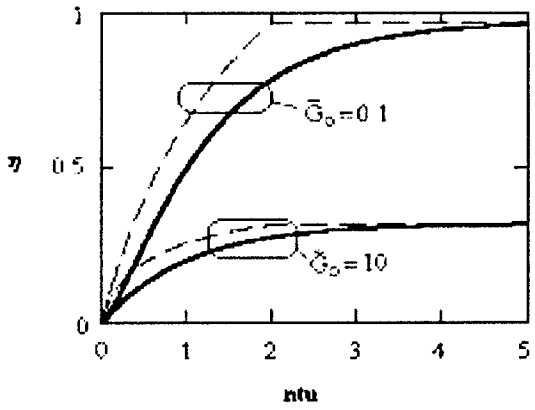

Figure 2 compares the two models for a porous fin of uniform thickness and composition. The figure plots the porous fin effectiveness (analogous to the effectiveness of a solid fin) as a function of the exchange surface Number of Transfer Units, $ntu = \beta t St$ where St is the mesh filament Stanton number. Results are plotted for two representative dimensionless superficial mass velocities, $\bar{G}_o = c_p G_o H^2 / k_{e,z} t$. The figure shows that the new model gives a smooth variation in effectiveness as a function of ntu; it predicts η about 20% lower than the previous model.

Analytical Modeling – Coolant Flow Distribution. It is envisioned that woven-mesh heat exchangers will employ a "finger plenum" configuration, with the woven mesh configured in a serpentine pattern so that the coolant enters through parallel, porous-walled passages, passes through segments of the porous walls, and exits through another set of parallel, porous-walled passages. This configuration, shown in plan view in the

inset of Figure 3, allows for control of coolant pressure drop. A classic problem is that there will be a pressure rise toward the end of each porous entrance passage, and this will result in a non-uniform superficial flow distribution along the length of each segment of the serpentine porous wall.

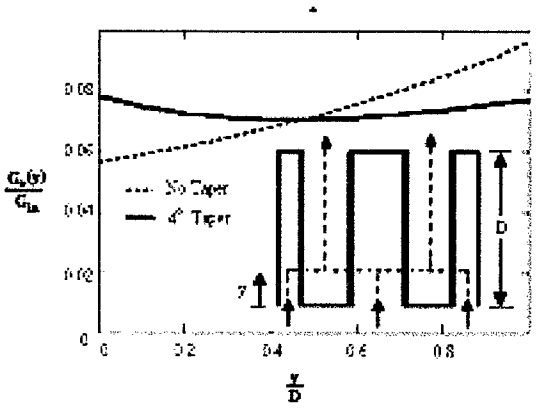

We have developed a one-dimensional flow model that couples the inlet/outlet flows to the porous media flow. The model shows that for a uniform composition and thickness porous wall, a slight taper in the inlet passages (decreasing hydraulic diameter), with a corresponding divergence of the outlet passages will result in an approximately uniform superficial flow distribution. Figure 3 plots the superficial mass velocity normalized by the passage inlet mass velocity as a function of position along a porous wall segment for a typical exchanger configuration. For the case shown ($\varepsilon = 0.39$, $t = 11.3$ mm, water flow), an approximate 4° convergence results in a nearly uniform flow distribution. An interesting added bonus is that the tapered passage results in a 30% reduction in overall pressure drop across the exchanger.

Fabrication Technology – Screen Lay-up. Our original intent was to build up a 3-D mesh by layering 2-D orthogonal weaves (screens) in the x-y plane (Fig. 1). Conducting filaments, with their axes in the z-direction, would then be sewn into the layered screens and the entire system would be bonded to form a rigid 3-D mesh. This approach proved to be infeasible in that the mesh number of commercial screen varies somewhat so that the elements of the layered system become misaligned, preventing the z-axis filaments from being sewn into the composite.

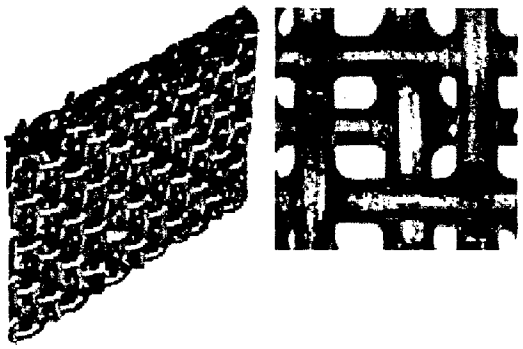

We have found that a simpler, more effective approach is to layer and bond screens in the y-z plane, without particular attention to the alignment of screen filaments. Under these conditions, adjacent screens interlace somewhat, forming a composite with a slightly higher solid fraction ($1-\varepsilon$) and k_e. Bonding of wire filaments can be via diffusion sintering, dip brazing, or re-flow soldering. A commercial equivalent to this is a stainless steel filter material, Rigimesh® [3]. In a subsequent section we show that this structure can have a highly anisotropic effective thermal conductivity. Figure 4 shows a multi-ply prototype formed with copper screen ($d_z = d_y = 0.018$", $M_z = M_y = 16$ in^{-1}). The wire

bonds are re-flow soldiered (Sn/Pb 60/40, k ≅ 55 W/mK). The sample has $\varepsilon = 0.64$, $\beta = 3110 m^{-1}$, $ke_z = 65$ W/mK and $ke_z/ke_x = 3.27$.

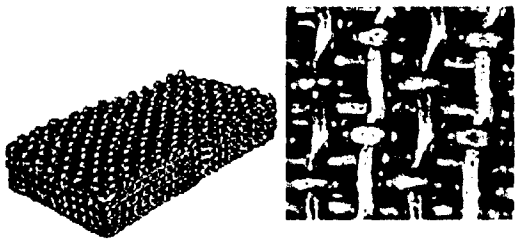

Fabrication Technology – 3-D Orthogonal Weave. An alternative approach is to weave the 3-D mesh directly. The advantage is that a denser structure (higher filament content) having different diameter and pitch filaments running in all three orthogonal directions can be structured. This allows for very wide-ranging possibilities regarding ε, β, k_e, etc. The disadvantage is that commercial weavers do not have much experience weaving 3-D metallic structures; and bonding of the conducting filaments is problematic due to the high density of the composite. An iterative, trial and error development approach has been pursued. We have been working with Fiber Architects Inc., Pittsburgh PA (weave design) in conjunction with T.E.A.M. Inc. Slatersville RI (3-D weaving) for the weave construction. Bonding of filaments is being developed by Vapor Process Engineering, Sacramento CA (diffusion sintering) and Thermo Fusion, Hayward CA (dip brazing). Figure 5 shows a prototype constructed from 0.015 in. diffusion sintered aluminum wire (alloy 1100). The prototype has $\varepsilon \approx 0.5$, $\beta \approx 5400 m^{-1}$.

Mesh characterization. We have developed equations for the physical characterization (ε, β) of Rigimesh®. These are based on existing characterizations of plane weaves [4]. Comparison with existing expressions [5, 6] for 2-D woven screens is excellent.

We have developed a model of the effective conductivity in the y-z plane ($k_{e,z}$ $k_{e,y}$) of a three dimensional Rigimesh® structure. The model, similar to one proposed by Chang [5] for the cross-plane effective conductivity ($k_{e,x}$), is based on network analysis of the equivalent geometric unit cell of the Rigimesh® structure. It includes the effect of wire crimping and screen interlacing. The effect of the wire-bond thermal resistance is included via empirical correlation [5]. The current model, together with Chang's model gives us a complete description of the effective thermal conductivity vector, $\vec{k}_e$.

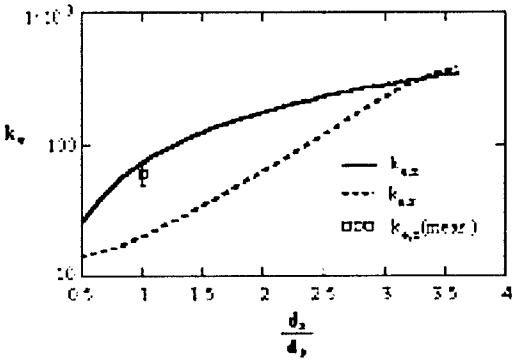

Figure 6 plots k_e for a Sn/Pb bonded copper wire Rigimesh® structure having $d_y = 0.018$ in., $M_z = M_y = 16$ in^{-1}. The Figure shows the current model prediction of $k_{e,z}$ as a function of d_z/d_y together with the cross-plane effective conductivity, $k_{e,x}$ [7]. The figure also shows one of our measurements of $k_{e,z}$ for the case $d_z = d_y$ (sample shown in Fig 4). Both $k_{e,z}$ and $k_{e,x}$ are seen to increase with increasing z-direction wire diameter

(increasing metal content). The effective thermal conductivity anisotropy ratio, $k_{e,z}/k_{e,x}$ is maximum (= 3.32) are dz/dy = 1.2. Additional analysis shows that the anisotropy ratio is generally maximum when $dz/dy \approx 1$.

Future Work

Analytical Modeling.

- Develop an *overall* thermal performance model that can be used to design woven-mesh parallel-plate heat exchanger elements. Link the model to a design optimization algorithm [8].

Fabrication Technology.

- Resolve fabrication issues related to direct 3-D weaving of heat exchange meshes.
    - Identify weave patterns that can be implemented to result in tight, uniform porous wire-meshes.
    - Select the appropriate wire bonding technology for this application.

Weave Characterization.

- Complete characterization of Rigimesh® structures (analytical and experimental verification).
- Develop models of ε, β, $\overset{\perp}{k}_e$, h and Δp of 3-D woven structures. Initiate experimental verification.

Prototype Testing.

- Develop a transient method for the measurement of the effective thermal conductivity components.
- Complete construction of a heat transfer/pressure drop flow loop.

Personnel

Three Mechanical Engineering M.S. candidates have worked on this project: Mr. Dan Fuller, Mr. Jay Park and Mr. Dan Ruch. Mr Jason Erickson, an undergraduate M.E. student also worked on this project. Textile consultant to the project is Ms. Ping Fang.

Acknowledgement/Disclaimer

The Ballistic Missile Defense Organization through the Air Force Office of Scientific Research, USAF, sponsors this work under contract number F49620-99-0286. The views and conclusions contained herein are those of the authors and should not be interpreted as necessarily representing the official policies or endorsements, either expressed or implied, of the Ballistic Missile Defense Organization, the Air force Office of Scientific Research, or the U.S. Government.

References

1. Kays, W. and London, A.L. (1984) Compact Heat Exchangers, Mc Graw Hill.
2. Wirtz, R.A. (1997) "A semi-Empirical Model for Porous Media Heat Exchanger Design", Proc. 32nd National Heat Transfer Conference, ASME HTD-Vol. 349, pp. 155-162.
3. Pall Trinity Micro Corp., Port Washington, NY.
4. Luo, S.L. and Mitra, A. (1999) "Finite Elastic Behavior of Flexible Fabric Composite Under Biaxial Loading", J. Applied Mechanics, Vol. 66, pp. 631-638.
5. Chang, W.S. (1990) "Porosity and Effective Thermal Conductivity of Wire Screens", J. Heat Transfer, Vol. 112, pp. 5-9.
6. Amour, J.C. and Cannon, J.N. (1968) "Fluid Flow through Woven Screens", AIChE J., Vol. 14, pp. 415-420.
7. Koh, J.C.Y. and Fortini, A. (1973) "Prediction of Thermal Conductivity and Electrical Resistivity of Porous Metallic Materials", Int. J. Heat Mass Trans., Vol. 16, pp. 2013-2022.
8. Visual DOC, Vanderplaats Research and Development, Colorado Springs, CO.

MULTI-FUNCTIONAL MATERIALS FOR THERMAL CONTROL OF SENSORS AND ELECTRONICS

F49620-00-1-305

Richard Wirtz
Mechanical Engineering Department
University of Nevada, Reno

Abstract

Novel multi-functional composite materials that combine a thermal energy storage capability with a structural capability are developed. Thermal energy storage is achieved by embedding a phase change material within a conductive metallic or polymer encapsulation that can be formed to suit design requirements. Phase change materials are formulated to undergo "dry" phase transition at temperatures anywhere between 15°C and 200°C. The three-year research program addresses formulation of suitable phase transition materials; fabrication of the resulting composites; and, characterization of their thermal and mechanical characteristics.

Introduction

Many multi-chip modules and sensors are variable power devices. As a consequence, conventional module/sensor coolers must be designed for peak power operation, or an active control system must be incorporated into the cooler to accommodate variations in heat loading. Incorporation of a Thermal Energy Storage (TES) mechanism into the module cooler will allow for a smaller, simpler, less power consuming and more reliable cooling system that is sized for some intermediate heat load. Then, heat is stored in the TES-system during periods of high power operation; and, it is subsequently released from the system during periods of reduced power operation. Phase Change Materials (PCM) formulated to undergo phase transition at key temperatures can provide this load-leveling capability via the latent heat effect.

TES-systems should be such that they add no mass (or volume) to existing systems. Materials having multiple functionality can be used to meet this constraint. For example, TES-composites that combine the heat storage function with a structural function can be formulated. These composites can be incorporated into the system as structural elements (frame members, enclosure skins, shock dampers or acoustical control materials, etc.) while at the same time they are part of the temperature control system.

Hybrid TES-coolers must have steady operating performance that is at least equal to existing systems while at the same time they provide for improved reliability. This requirement can be met by incorporating desirable thermal and mechanical characteristics into the TES-composite.

Phase Change Materials that undergo "dry" phase transition (no liquid phase) are attractive TES-materials since packaging difficulties associated with solid-liquid PCM's are avoided. Furthermore, the absence of a liquid phase eliminates the need for cooling

loops, pumps, and other fluid handling systems. Thus, the TES unit operates passively and is inherently reliable. Since there is no fluid phase, the performance of the unit will be independent of g-loading and system orientation.

"Dry" PCM's are materials that undergo either solid-state phase transition or are encapsulations of solid-liquid PCM's engineered so that the liquid phase is not apparent. An example of the first kind of material is the polyalcohol group, including pentaglycerine (PG) and neopentylglycol (NPG). These materials can be combined to make a material that transitions at temperatures between 24°C and 86°C [1]. The second category of "dry" PCM's (encapsulations of solid-liquid PCM's) has been developed in a variety of formats. For example, Colvin, D.P. and Mulligan have developed a micro-encapsulated paraffin powder.

Two TES-composite systems will be considered:

1. *Macro-encapsulated TES-materials*. The PCM fills a conductive honeycomb or foam structure such as a plate or rod that is then covered with a metallic or elastomer coating. The resulting composite structural elements can be engineered so that they can be formed (bent or hole-punched) and incorporated into a system application.
2. *Micro-encapsulated TES-Materials*. Micro-particles of PCM are either metal coated (via a low temperature coating process such as nickel-carbonyl chemical vapor deposition) or blended into a conductive polymer matrix material. These composites can then be molded to have specified mechanical characteristics.

First Year Work Plan

First year activities will focus on macro and micro-encapsulation of polyalcohol-based TES composites. Proceedures for the formulation of PG/NPG solid solutions will be established; their thermodynamic and thermophysical properties will be documented; and, long term thermal-cyclic testing of transition reversibility will commence. A chemical deposition facility will be established; pleminary experiments on nickel-CVD coating of PG/NPG systems will be initiated. Thermally conductive polymers, including conductivity enhanced thermoplastics, thermosets, polymeric gels and interpenetrating polymer networks will be investigated as encapsulation matrix materials. Their mechanical and thermophysical characteristics will be documented. A low-force testing facility will be established, and near ambient static and cyclic (fatigue) testing will be initiated.

Personnel

The research team includes: R.A. Wirtz (Principal Investigator and Team Leader; Heat Transfer in Electronics), Dhanesh Chandra (Metallurgist and Material Scientist; phase change materials and CVD metal coating), Alan Fuchs (Chemical Engineer; polymer science and engineering) and Yanyao Jiang (Mechanical Engineer; structural analysis, thermal-mechanical fatigue).

Acknowledgement/Disclaimer
The Ballistic Missile Defense Organization through the Air Force Office of Scientific Research, USAF, sponsors this work under contract number F49620-99-0286. The views and conclusions contained herein are those of the authors and should not be interpreted as necessarily representing the official policies or endorsements, either expressed or implied, of the Ballistic Missile Defense Organization, the Air force Office of Scientific Research, or the U.S. Government.

References

1. Chandra, D. and Wei Ding (1991) "Phase Transitions in Plastic Crystals", Journal of The Less Common Metals, Elsevier Sequia, vol.168, 1991, (159-167).
2. Colvin, D.P. and Mulligan, J.C. (1990) "Method of using a PCM Slurry to Enhance Heat Transfer in Liquids", U.S. Patent 4911232.

THE CONTROL OF SEPARATION FROM CURVED SURFACES AND BLUNT TRAILING EDGES.

AFOSR GRANT F 49620-00-1-0070

Israel J. Wygnanski
AME Department
The University of Arizona, Tucson

Abstract

The project initiated last fall encompasses three experiments:

(1) The application of active flow control to an airfoil having a divergent trailing edge (DTE);
(2) A pulsed wall jet over a curved surface in the absence of an external stream;
(3) Pulsation emanating from a circular cylinder in streaming flow at various azimuthal angles with and without transpiration.

Items (1) and (3) required the construction of new apparatus That is currently being calibrated. Therefore, the data related to these items is still exploratory in nature. The present progress report will still focus on item (2) and the massive amount of data that was collected by using a PIV. These experiments endeavor to promote the understanding of the nature of the centrifugal instability in this highly turbulent flow and its interaction with the imposed excitation.

A pulsed wall jet over a curved surface in the absence of an external stream

We attributed the rapid rate of spread of a wall jet over a curved surface (figure 1) to a centrifugal instability that generated streamwise vortices contributing to the transport of momentum across the flow. The existence of such vortices was often inferred from secondary observations rather than from direct measurements of the streamwise vorticity

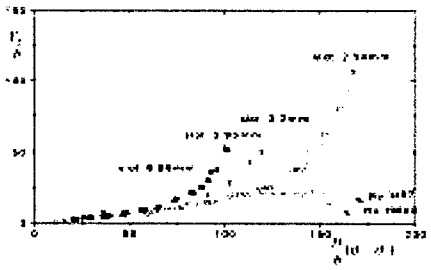

Figure 1: A comparison of local wall jet widths on a cylinder and on a flat surface.

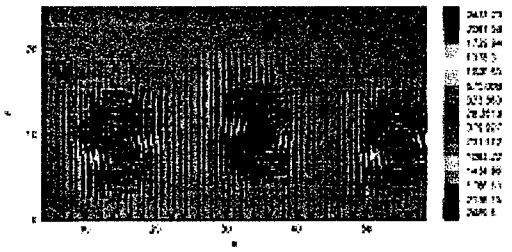

Figure 2 Enhanced, ensemble averaged vorticity contours.

but a PIV coupled with pattern recognition techniques enabled us to map quantitatively a pair ensemble averaged (and thus statistically representative) counter rotating vortices (figure 2). The procedure leading to the eduction of these vortices was described in last year's book of abstracts but the some figures are reproduced here for the sake of completeness.

Hot wire anemometers were used for decades to infer the existence of coherent structures (vortices) in turbulent shear flows. Two point, cross correlation measurements [$G_{33}(\Delta z)$] are often used to educe such structures. However when this technique was used to infer spanwise periodicity in the flow the classical correlation measurements generated less than satisfactory results (figure 3a), although the minimum correlation distance scaled with the width of the jet (figure 3b). The minimum correlation attained by this technique near the surface was: G_{33}=-0.25 implying that the periodicity is rather weak.

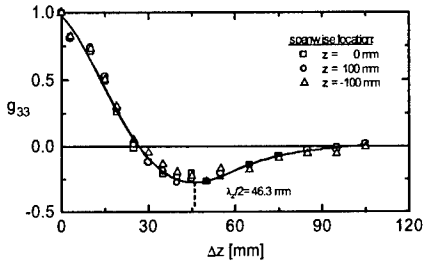

Figure 3a:Cross correlation at θ=160°.

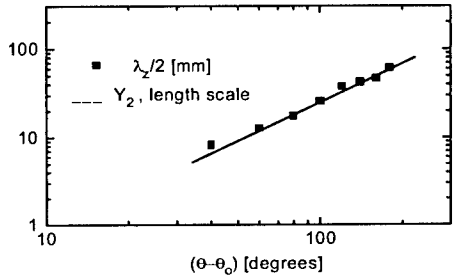

Figure 3b:The increase in size of the streamwise vortices with distance from the slot.

Nevertheless, when the same measurement was made in a plane wall-jet the minimum correlation recorded was only G_{33}=-0.10 and this was significantly lower than for the flow around the cylinder (figure 4).

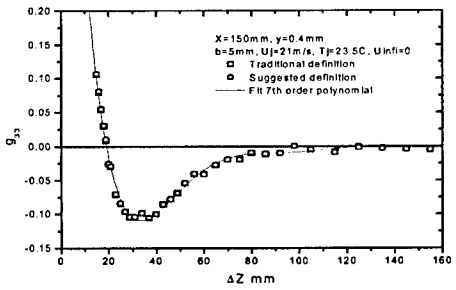

Figure 4: Traditional cross correlation in a Plane wall jet.

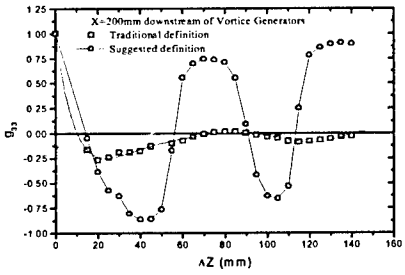

Figure 5: A comparison between The traditional G_{33} and the one based On a total W signal.

The traditional definition of the correlation function is based solely on velocity fluctuations, because turbulent flow was considered random in both time and space.

However a row stationery vortices would yield G_{33}=0. Since approximately 50% of the turbulent intensity is locked within the large streamwise vortices[1], and the latter only slowly meander along the span. Thus, the traditional definition of G_{33} has to be modified to account for spatial variations in the mean motion and this is achieved by correlating the entire signal instead of the fluctuations around the mean. Ming de Zhou[2] tested this hypothesis by placing vortex generators in the plane wall jet (figure 5). The conventional correlation measured 200mm downstream yielded G_{33}=-0.25 for the first minimum and less than -0.1 for the second. On the other hand, the time-average product of the **instantaneous velocity** gave a modified $< G_{33} > \approx \pm 0.9$ that did not diminish by increasing the distance between the two probes by a full wave length (figure 5).

In order to study the naturally developing interactions between the large, spanwise rollers and the longitudinal vortices, the flow was excited in a two-dimensional fashion by perturbations introduced through the slot. Two-dimensional PIV data was acquired from consecutive measurements in the x-y and y-z planes at 8 individual phases relative to the excitation signal. In this manner we have resolved the passage of the spanwise rollers. By maintaining the same phase reference in both planes, we hoped to combine the results and form a quasi three-dimensional flow field by post-processing. The excitation frequency was 35 Hz and the excitation level was 5%. All experiments were conducted at the angular downstream location of θ=80°.

Figure 6 shows four consecutive frames of phase averaged spanwise vorticity contours that are superimposed on streamlines drawn in the xy-plane at $\Delta\Phi$=45° for the latter half of the forcing cycle. The contours show a narrow belt of large positive vorticity in the wall boundary layer (clockwise rotation) and moderate negative vorticity in the outer shear layer (counter-clockwise rotation). During the first 1/4 of the forcing cycle ($0° \le \Phi \le 90°$) the streamwise, phase averaged velocity decelerated relative to the time-mean until the momentum in the jet was reduced to 65% of its mean value. This decay stopped just before the arrival of the spanwise roller (figure 6). During this phase the spanwise roller induces a strong velocity component normal to the surface which starts to redistribute the jet momentum. In fact, the streamwise velocity component increases continuously near the surface while it decays in the outer part of the shear layer. After the vortex core passed through the designated y-z plane (θ=80°), the streamwise velocity attained its maximum value (Φ=270°). At this moment the streamwise momentum reaches approximately 150% of its average value (i.e. it varies by a factor of 2.5 over the cycle). The appearance of the spanwise roller also affects the distribution of the Reynolds stresses and intensities of the various velocity components and those are discussed in reference [1].

The streamwise vortices shown in figure 6 were educed in the same manner as before, except that the data was phase locked to the two-dimensional perturbations. To the first order of approximation it would appear that these vortices are not affected by the excitation, they simply "bobbed up and down", periodically, like floats on a wavy lake surface. The distance of their cores from the solid surface varied periodically with Φ

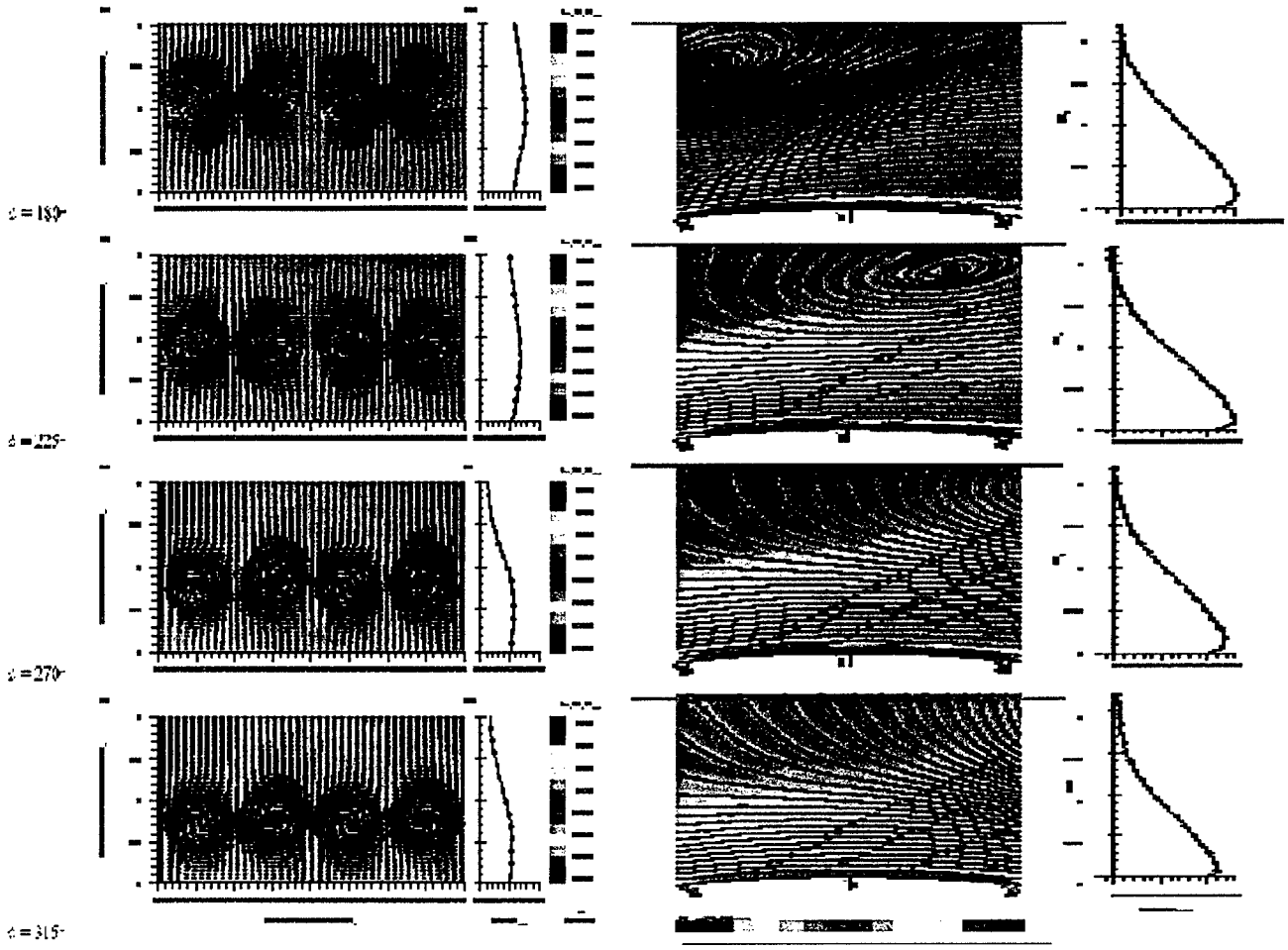

Figure 6: Phase locked and ensemble-averaged PIV data, collected during the passage of the large spanwise rollers in the x-yand y-z planes.

while the size of their cores did not appear to change throughout the forcing cycle. This distance corresponds to y/Y_2=1.15 at Φ=180° (fig.6) and to y/Y_2=0.7 at Φ=315°. Clearly the location of the cores is affected by the passage of the spanwise roller that induces an upwash ahead (downstream) of its arrival and a downwash in its wake (figure 6). Conventional correlation measurements, using a pair of hot-wire probes, in the excited wall jet suggest that there is an interaction between the streamwise vortices and the spanwise rollers.

The g_{11} correlation shown in the figure 7 refers to a normalized product of the streamwise

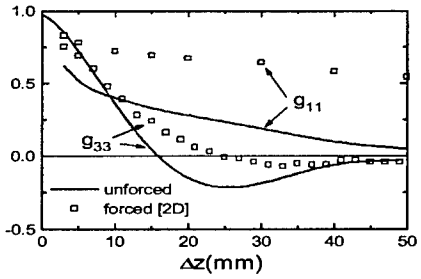

Figure 7: A comparison of correlations with and without excitation

velocity components, u_θ' separated by a distance Δz. The g_{11} correlation decayed exponentially with increasing probe separation and it only provided a measure of the scale of the naturally occurring spanwise vortices. These vortices are generated by the spanwise vorticity existing in the mean flow that leads to an instability (as is the case in the plane wall jet). Two-dimensional excitation emanating from the nozzle had a tremendous impact on the three-dimensionality of the flow. The g_{11} correlation at $\Delta z = 50mm$ increased 10 fold (from approximately 0.05 to 0.5), while the negative g_{33} decreased very significantly (by a factor of 4) and its spanwise wavelength increased somewhat. This suggests that plane periodic perturbations cause a diminution in the strength or in coherence of the streamwise vortices but these were not observed in the cursory data presented in figure 6. A three-dimensional PIV system would be helpful in this case as it would provide a check on the repeatability and quality of the data allowing one to assess better this type of vortex interaction.

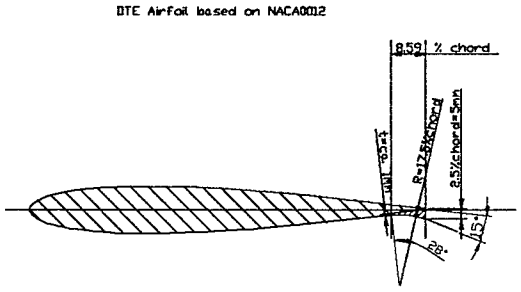

Figure 8: The DTE Airfoil

The Airfoil with the Divergent Trailing Edge

A NACA 0012 airfoils was modified to have a divergent trailing edge (DTE) as shown in Figure 8. This airfoil was chosen because of the availability of its aerodynamic performance at the low Reynolds numbers of interest. The trailing edge thickness is 2.5% of the chord and it represents a typical Gurny flap. A fillet that is tangential to the lower surface some 8% of chord upstream deflects the local flow by an angle of 15° to the chord at the trailing edge.

The aerodynamic characteristics of this airfoil are given in below and they are compared with the conventional NACA-0012 airfoil. The addition of the DTE moves the C_L-α to the left providing a C_L=0.45 at α=0°.The maximum C_L also increased by approximately 30% and the stall characteristics of the airfoil became much gentler. Although the drag penalty at low values of C_L is substantial (about 20% at C_L=0.5), the addition of the DTE enables one to cruise or loiter at C_L=1. A tiny fliperon was added to the airfoil at the trailing edge that is hinged to it at the upper surface. The fliperon does not exceed the 2.5% chord so it can be stowed when not in use. It is mainly intended to reduce drag at moderate values of α. A slot was also milled near the leading edge of the airfoil in order to provide traditional active flow control. It is meant to be used and to interact with the fliperon actuation only at high angles of attack in order to delay stall.

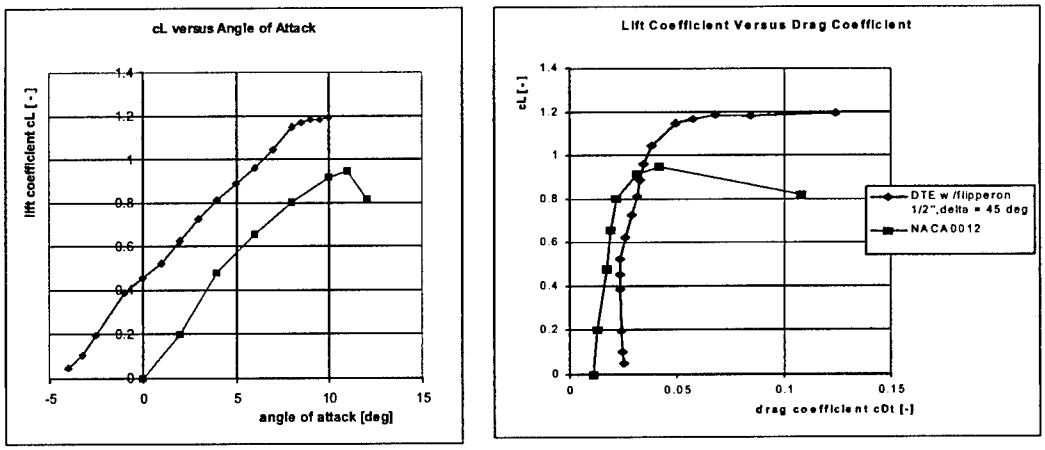

Figure 9: The Aerodynamic characteristics of the DTE airfoil.

Acknowledgment/Disclaimer

This work was sponsored by the Air force Office of Scientific Research, USAF, under contract number F 49620-00-1-0070. The views and conclusions contain herein are those of the author and should not be interpreted as necessarily representing the official policies and endorsements, either expressed or implied, of the Air Force Office of Scientific Research or the U.S. Government. The author is indebted to Professor L. Lourenco for his assistance in making the PIV measurements and to Professor Ming de Zhou for his redefinition of the G_{33} correlation.

References

1. "The Turbulent Wall Jet Along a Convex Curved Surface" by Ralf Neuendorf, a Ph.D. that was submitted to the Technical University of Berlin in Spring 2000 under an exchange agreement with the University of Arizona.

2. Ming de Zhou Private Communication, 2000

Personnel Supported

Olaf Lisser	Graduate Student, University of Arizona, Tucson
Sixiong Chen	Graduate Student, University of Arizona, Tucson
I. Wygnanski	Professor, University of Arizona, Tucson

Publications

Neuendorf, R. and Wygnanski, I., "On a Turbulent Wall Jet Flowing Over a Circular Cylinder", Journal Fluid Mechanics 381, 1-25, 1999

Seifert, A., Bachar, T., Wygnanski, I., Kariv, A., Cohen, H. and Yoeli, R., "Application of Active Separation Control to a Small Unmanned Air Vehicle", AIAA Journal of Aircraft, Vol. 36, No. 2, pp. 474-477, 1999.

O. Likhachev, D. Quintana, and I.Wygnanski, "On the Stability of a Laminar Wall Jet with Heat Transfer" Turbulence and Combustion 62: 137-162, 1999

Y.Guy, J.A. Morrow, T.E.McLauglin and I.Wygnanski., "Velocity measurements on a delta wing with periodic blowing and suction" AIAA Paper 2000-0550, 38th Aerospace Sciences Meeting Reno NV, 2000
H. Fasel, A. Ortega& I.Wygnanski , "Film Cooling in a Pulsating Stream-Recent Results for Laminar and Turbulent Wall Jet" 18 Symposium on Energy Engineering Sciences ; Argonne National Laboratory May 2000
P. Kjellgren, N. Anderberg and I. Wygnanski, "Download Alleviation by Periodic Excitation on a Typical Tilt –Rotor Configuration-Computation and Experiment." AIAA paper 2000-2697
I. Wygnanski, "Some New Observations Affecting the Control of Separation by Periodic Excitation." AIAA paper 2000-2314
A. Darabi, L. Lourenco & I. Wygnanski, " On the Mechanism of Flow Reattachment by Periodic Excitations" in Advances in Turbulence VIII, p.201-204 C.Dopazo (ed.) CIMNE, Barcelona. (Proceedings of ETC 8, Barcelona June, 2000)

Transitions

Active control of separation is undergoing transition research to the V-22 "Osprey", helicopter rotors and UAV technology. The control of turbulent mixing (IL patent 52613 from 1977 and US patent 4,257,224 granted 1981) undergoes transition to jet engines

MEMS-BASED CONTROL FOR AIR BREATHING PROPULSION: EXTERNAL JET FLOW

AFOSR Grant F49620-97-1-0526

Thomas C. Corke

University of Notre Dame
Aerospace & Mechanical Engineering Department
Hessert Center for Aerospace Research
Notre Dame, IN 46556

Background

This work has been motivated by two objectives:

1. To develop an efficient jet control strategy which couples the shear layer and column modes.

2. To develop a flow control actuator which is capable of controlling the initial conditions needed to accomplish the first objective in full-scale jet engines.

Both of these objectives have been met, and reported on in past contractors meetings. The final objective, which has been the focus of the past years efforts, has been to demonstrate the level of control in a jet at compressible Mach numbers. The following summarizes our steps in achieving this.

The target Mach number for the final experiments was Mach 0.8, which is representative of the primary air jet in high by-pass jet engines. The original proposal had planned to conduct the compressible jet experiments in the Anechoic Jet Facility at NASA Langley Research Center. When that facility became no longer available, the plan was changed to make use of the high-speed blow-down facility in the Hessert Center for Aerospace Research at the University of Notre Dame.

This facility had been used for the supersonic jet screech experiments reported by Walker and Thomas(1997) and Walker, Gordeyev and Thomas(1997). The air generation system consists of an Ingersoll-Rand Model ESH 3-stage industrial air compressor, which supplies air to a receiver at a pressure of 3.8×10^6Pa (550psi) and at a volumetric flow rate of 0.122 m^3/sec (4.4cfm). From the compressor, the air passes through an Ultra Air UHR 250 twin tower desiccant type gas dryer which lowers the dew point to $-73°$C. Dried and filtered air leaving the dryer then passes through an electric heater that is capable of raising the air temperature to any desired value up to 316 $°C$. The air receiver consists of a large cylindrical tank equipped with both wall trace heating and an insulated outer jacket to maintain a desired stagnation temperature.

A plenum chamber total pressure is preset and precisely maintained during receiver blowdown by two pressure regulators operating in tandem with a pneumatic feedback control loop.

The flow discharges into a large anechoic chamber formed by removable walls, ceiling and floor panels which are covered with polyurethane foam wedges. This

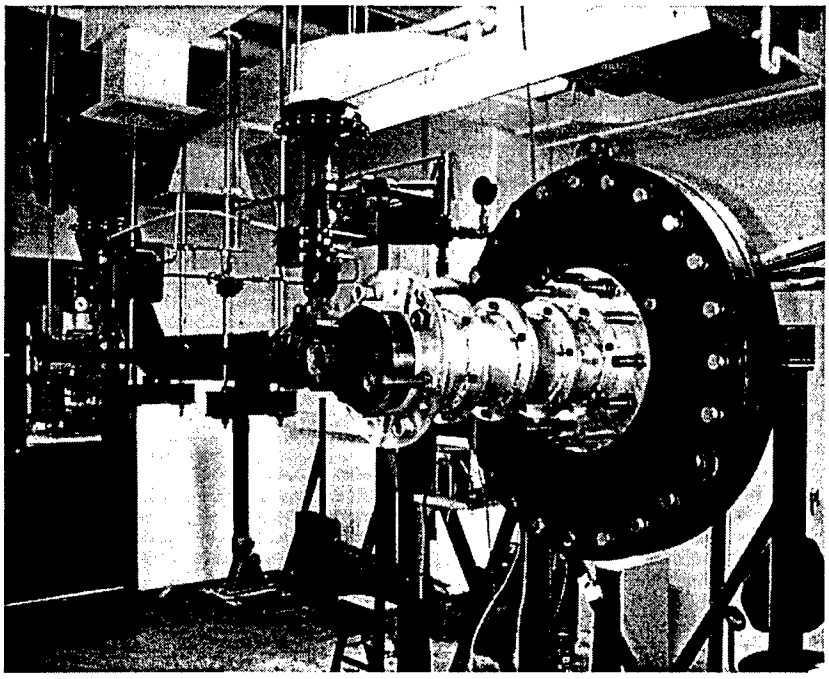

Figure 1: Photograph showing high pressure blow-down facility with added flow manipulation section and 5.08cm exit diameter nozzle.

arrangement has been demonstrated (Walker and Thomas, 1997) to provide an anechoic environment above a frequency of 250Hz. Air is ducted outside the chamber in sufficient volume to avoid any overpressure inside.

Facility Modifications

The modifications to the facility were intended to make use of the 5.08cm exit diameter nozzle used in the previous incompressible flow experiments. This nozzle has an area ratio of 6:1, giving it an inlet diameter of 15.24cm. A photograph of the modified facility is shown in Figure 1.

Two problems existed for the conversion of the facility to accommodate the larger nozzle:

1. Regulating the pressure to maintain a constant velocity over the time-duration of the run, and

2. Obtaining a uniform mean flow with low disturbance levels, both vortical and acoustic, at the nozzle exit.

The facility was initially designed for use with small supersonic jets. These produced a large pressure drop at low flow rates. The pressure regulating valves which control the flow rate had been sized based on this pressure drop.

In the conversion to the larger jet, the pressure drop through the system was lowered by an approximate order of magnitude. The pressure regulating valve system

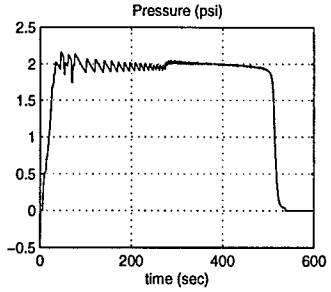

Figure 2: Time trace of settling chamber pressure before modifying valve feedback controllers.

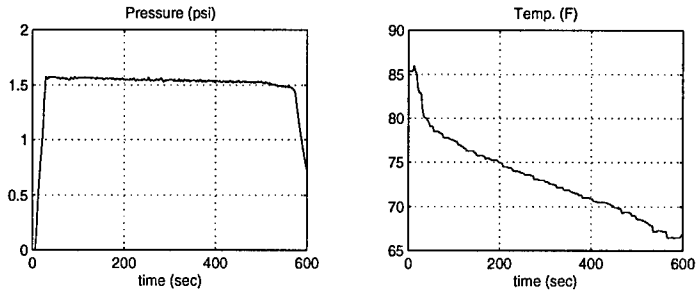

Figure 3: Time trace of settling chamber pressure (left) and temperature (right) after modifying valve feedback controllers.

uses the pressure drop as feedback in maintaining a constant velocity. The lower pressure drop that occurred for the larger subsonic jet reduced the sensitivity of the of the valve control system and as a result was not able to adequately maintain a constant jet velocity. An example of this is shown in Figure 2. This shows a time trace of the total pressure in the settling chamber upstream of the nozzle. The trace indicates oscillations in the pressure which were caused by the automatic valve control system as it alternated between its minimum set points. This eventually settled down near the end of the run, however more than half of the usable run-time was lost.

The solution to this problem was to modify the controllers for the valves to increase their sensitivity. Although this was a relatively expensive and time consuming step, the result documented in Figure 3, demonstrates its success. In this case the oscillations seen in the previous pressure time trace were eliminated. The total run time under these conditions, which gives Mach 0.8 in the 5.08cm jet, is approximately 6.5 minutes.

Also included in Figure 3 is a time trace of the total temperature in the settling chamber. Part of the appeal of this facility is the ability to change the temperature of the air stream. It is well understood that the amplification rates of the jet instabilities decreases with increasing temperature. Therefore from the point of view of control based on exciting instabilities, the air temperature is an issue. In addition, MEMs temperature sensors were one of the sensors considered for feedback control.

The temperature time trace in Figure 3 verifies that the temperature change in

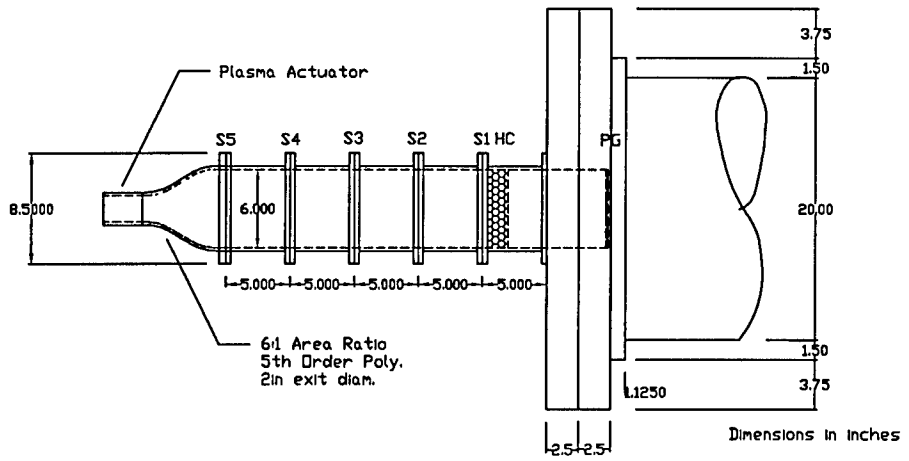

Figure 4: Scale drawing of turbulence manipulation section for the jet.

the central portion of a run, in the worst case, varied by approximately 7°F. This amount is not expected to have a drastic effect on the instabilities, and can be easily compensated for in hot-wire calibrations.

The second part of the facility modifications involved obtaining a uniform flow, and low turbulence intensity in the jet core. Figure 4 shows a scale drawing of the settling chamber, and turbulence manipulation components added to the facility.

The flow manipulators consisted of a honeycomb with 0.3175cm cell size, to remove any swirl in the approaching flow, followed by five low-solidity screens. The first screen is placed against the downstream side of the honeycomb, which based on Loehrke and Nagib (1972), significantly reduces the turbulence levels produced by the honeycomb. The screen are mounted in the flanges of the elements which make up the total manipulator section. The spacing between screens corresponds to 250 mesh lengths, which is optimum for the turbulence decay.

Particular issues with the flow quality of the facility for the larger subsonic jet are: the 90° bend upstream of the settling chamber, and the lack of any internal contouring at the settling chamber exit. Both of these contributed to having a nonuniform mean flow, and higher turbulence levels at the entrance of the flow manipulator section.

These issues with the flow conditions were dealt with by using a high solidity grid and multiple low solidity screens, to produce a high pressure drop at the entrance to the manipulation section. The grid and screen combination were located at the entrance of a straight section which extended into the settling chamber (see Fig. 4).

Figure 5 documents the mean velocity and turbulence intensity profiles across the exit of the straight section, downstream of the grid and screen combination, at the exit plane of the settling chamber. This represents the upstream initial condition to the manipulator section. Aside from the boundary layers on the side walls, the central portion of the profile is reasonable flat. The turbulence intensity in this region is also an acceptable level of approximately 2 percent.

The turbulence reduction factor for five screens is 0.21 (based on Loehrke and Nagib, 1972). With the addition of the 6:1 area ratio contraction, the turbulence reduction factor becomes 0.035. Therefore with the upstream turbulence level of

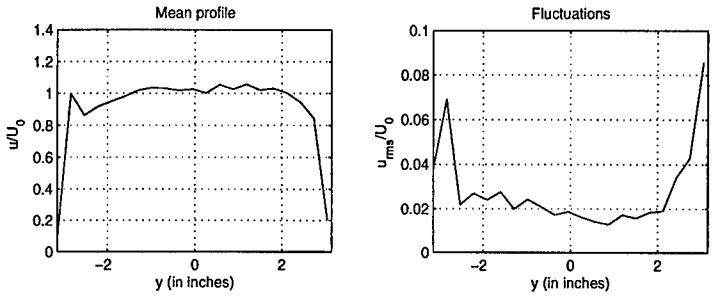

Figure 5: Mean velocity and turbulence intensity downstream of the grid and screen combination, at the exit plane of the settling chamber.

approximately 2 percent, following the 5 screens and honeycomb, the turbulence level in the jet core will be approximately 0.07 percent. This level is quite acceptable, and will allow minimum actuator amplitudes for controlling the jet unsteady initial conditions.

At the time of this writing, the fabrication of the last (fifth) manipulator section was being completed. Following that, we will verify that the expected turbulence level was achieved in the jet, and begin documentation of the flow downstream of the jet exit.

Proposed Final Measurements

With the completion of the facility modifications, and flow field documentation, the remaining measurements will deal with the active flow control using the phased plasma actuator array presented in the previous contractors meeting.

This last phase of the work will involve:

1. the documentation of the ability of the actuator to excite jet shear layer and column modes in a range of Mach numbers from 0.6 to 0.8,

2. the operation of the actuator with closed-loop feedback, similar to Corke and Chang (1998), and

3. the documentation of the changes in the integral properties of the jet due to excitation at these Mach numbers, such as presented at the previous contractors meeting, and by Corke and Matlis (1999).

These are expected to be completed in the next two months.

Acknowledgment/Disclaimer

This work is sponsored by the Air Force Office of Scientific Research under Grant F49620-97-1-0526, which is monitored by Dr. Thomas Beutner. The views and conclusions contained herein are those of the author and should not be interpreted as necessarily representing the official policies or endorsements either expressed or implied, of the Air Force Office of Scientific Research or the U.S. Government.

References

Corke, T. and Chang, A. 1998. Mode-coupled Feedback Excitation in an Axisymmetric Jet. Bulletin of the APS-DFD98.

Corke, T. and Matlis, E. 1999. Helical Mode Excitation of a Jet Core Instability using Phase-array Plasma Actuators. Bulletin of the APS-DFD99.

Loehrke R. and Nagib, H. 1972. On the Management of Free-stream Turbulence. AGARD Report.

Walker, S. H. and Thomas, F. O., 1997, Experiments Characterizing the Nonlinear Shear Layer Dynamics in a Supersonic Rectangular Jet Undergoing Screech. *Phys. of Fluids*, 9, 9, pp. 2562-2579.

Walker,S. H., Gordeyev, S. V. and Thomas, F. O., 1997, A Wavelet Transform Analysis Applied to Unsteady Aspects of Supersonic Jet Screech Resonance. *Experiments in Fluids*, 22, pp. 229-238.